Evaluation of Recycled Aggregate Base Courses Stabilized by Geosynthetics

By

Tanya N. Walkenbach

Submitted to the graduate degree program in Civil, Environmental, and Architectural Engineering and the Graduate Faculty of the University of Kansas in partial fulfillment of the requirements for the degree of Doctor of Philosophy.

Committee Members:

_____

Chair: Dr. Jie Han

_____

Co-Chair: Dr. Robert L. Parsons

_____

Dr. Masoud K. Darabi

_____

Dr. Steven D. Schrock

_____

Dr. Leigh A. Stearns

Date Defended: 24 March 2020

The dissertation committee for Tanya N. Walkenbach certifies that this is the approved version of the following dissertation:

Evaluation of Recycled Aggregate Base Courses Stabilized by Geosynthetics

_____

Dr. Jie Han, Chair

_____

Dr. Robert L. Parsons, Co-chair

Date Approved: 14 May 2020

Abstract

Both unpaved roads and pavement sustainability are dependent upon base course performance and longevity. With the depletion of natural resources and limited funding for necessary pavement rehabilitation, alternative aggregate resources, and addition of geosynthetics must be analyzed as potential solutions. Recycled concrete aggregate (RCA) and reclaimed asphalt pavement (RAP) are potential alternatives to virgin granular base (VGB) typically used. The addition of geosynthetics at the interface of the base course and subgrade can stabilize the base course section through separation, lateral restraint, and the tensioned membrane effect.

This large-scale box study focused on granular base options for roadway applications. All base course sections were constructed atop a laboratory-blended subgrade material of pulverized kaolin, ASTM C33 sand, and water using a known moisture content-CBR relationship. Locally sourced RCA, RAP, and VGB were tested with and without geosynthetics (nonwoven geotextile, woven geotextile, triaxial geogrid, and combined nonwoven geotextile with triaxial geogrid) installed at the base course- subgrade interface for cyclic plate load tests on unpaved roads at varying load magnitudes. Based on performance and economy, nonwoven geotextile was selected for analysis in concrete paved test sections under 40 kN cyclic loading both before and after a rainfall event; a VGB control section was compared against two nonwoven-geotextile-stabilized test sections, one with RCA and one with VGB. Earth pressure cells recorded changes in vertical stresses at the base course-subgrade interface at varying lateral distances from the center of the load plate for both unpaved and paved test sections. Vertical displacements were recorded at the plate for all tests; for the paved tests, vertical displacement transducers also recorded along the diagonal of the loaded concrete slab from the loaded corner to a distance of three times the radius from the center of the load plate as well as on the corner of the other non-

loaded slab nearest the loaded slab corner. Permanent and resilient deformation as well as interface stress reductions were analyzed for both the unpaved and paved test sections.

The unpaved test sections were first analyzed in terms of accumulated permanent deformation, their unique permanent-to-resilient deformation ratios, and interface stress reduction. Replacement of VGB with RAP did not limit permanent deformation, so RCA and VGB were focused on. In both VGB and RCA unpaved test sections, the addition of geosynthetics limited the permanent deformation as compared with control sections, but the resilient deformations were very similar. Interface stress reductions and thus increases in stress distribution angle were achieved through the addition of geosynthetics in both VGB and RCA. The replacement of VGB with RCA had a greater effect than the addition of geosynthetics to the VGB both on decreased permanent deformations and increased stress distribution angles. The stress reduction method was effective at calculating resilient moduli (M_r) of the unpaved sections, but the modified Burmister solution yielded M_r that more closely reflected reductions in permanent deformation through the addition of geosynthetics. AASHTO (1993) design charts and methods were used to estimate the composite subgrade reaction moduli for the unpaved test sections.

The three concrete paved test sections were then analyzed in terms of vertical displacements and base course-subgrade interface stress reduction. Permanent deformations in the concrete sections were reduced by the addition of nonwoven geotextile, and the replacement of VGB with RCA further reduced permanent deformation in the nonwoven-geotextile-stabilized sections before rainfall. Rainfall caused an increase in permanent deformation in the paved sections, but its effect disappeared within 1,000 load cycles. Interface stress reductions were observed through the addition of geosynthetics and the replacement of VGB with RCA in both

pre- and post-rainfall concrete paved sections. The Westergaard (1926) method and the measured vertical displacements were used to calculate the subgrade reaction moduli and estimate expected tensile stresses in the slabs. Subgrade reaction moduli in the paved sections were approximately 60% to 70% of those calculated for the unpaved sections using the AASHTO (1993) design chart. Both the unpaved and paved sections were simulated in the KENPAVE software to estimate slab tensile stresses and while the vertical displacement reductions were reflected in subgrade reaction moduli, the change in expected tensile slab stresses was very small.

Acknowledgment

A work of this magnitude could only be accomplished through the tremendous amount of support I was fortunate to receive in my time at the University of Kansas. I would like to thank Dr. Jie Han, Dr. Robert Parsons, Dr. Bruce McEnroe, and Dr. Dennis Lane for agreeing to award me the Chancellor's Fellowship and thus support my doctoral endeavor. Dr. Han and Dr. Parsons were very gracious in their commitment to my academic development; I am grateful for the time they spent instructing me as well as discussing the discoveries of this study. The support of the University of Kansas as a whole, through this Chancellor's Fellowship, allowed me to pursue a goal that otherwise may not have been possible.

The time and effort required of my committee to ensure that I am worthy of this Ph.D. title are greatly appreciated. In addition to Dr. Han and Dr. Parsons, I would also like to thank Dr. Masoud Darabi, Dr. Steven Schrock, and Dr. Leigh Stearns for their attention and support.

This study was greatly supported by material suppliers in the Lawrence, KS, area. Funds for this study came from the Kansas Department of Transportation's (KDOT) through the Kansas Transportation Research and New-developments (K-TRAN) Program. Virgin granular base was donated by Mid-States Materials. Recycled concrete aggregate was donated by R.D. Johnson Excavating Co. Reclaimed asphalt pavement was donated by Hamm Companies. ASTM C33 sand was donated by Midwest Concrete Materials. TenCate donated the geotextiles used in this study. Geogrid used in this study was donated by Tensar. This tremendous amount of support is greatly appreciated.

Kent Dye, David Woody, and the rest of the Civil, Environmental, and Architectural Engineering laboratory team are greatly appreciated for all of their time brainstorming experimental methods and solutions, keeping lab equipment functional, responding rapidly during breakdowns, and providing support and training to keep my group and myself safe.

The University of Kansas Geotechnical Society (KUGS) deserves many thanks for my professional development as well as the success of this study. I would like to thank the graduate KUGS members of this group for their feedback and moral support during my time at KU. Dr. Jun Guo and Dr. Madan Neupane taught me how to construct my experiments and properly used the instrumentation before their departure. Dr. Saif Jawad and Hao Liu assisted in the concrete pavement test section completion; Dr. Mahdi Al-Naddaf and Dr. S. Mustapha Rahmaninezhad must also be acknowledged for their assistance in test construction instrumentation support when malfunctions occurred. Test construction could not have been possible without my undergraduate research assistants, including Cassidy Diebold, Daniel Rich, Jesus Leos, Zeyad Dessouki, Ashley Underwood, Audrey Carroll, Brandon Tabor, and Luke Spriggs. Zexia Li is greatly appreciated for his tremendous support not only in physical construction of the unpaved large box tests but in scheduling, data analysis, and general project support even beyond his graduation.

Appreciation most of all goes to my family. I could not have succeeded without your patience, compassion, support, and love. All of you, including (but certainly not limited to) Mom, Dad, Tami, Rachael, Dan, Madeline, Danielle, Drew, and especially my children Olivia, Reese, and Jack: Thank You!

Table of Contents

List of Tables

List of Figures

Chapter 1. Introduction

Road construction and rehabilitation is necessary for the continued operation of personal and commercial vehicles. Sustainable, low-cost solutions are necessary to provide the most comprehensive roadway construction and rehabilitation and to ensure pavements will last for long periods of time. With technological advances as well as the depletion of natural resources to construct or rehabilitate roadways, alternatives must be considered to ensure pavement sustainability.

Road rehabilitation often involves tear-out of existing asphalt or concrete pavements. This removed pavement must then either be disposed of in a landfill or reprocessed and repurposed. Reclaimed asphalt pavement (RAP) is commonly recrushed and recycled into new asphalt production. Recycled concrete aggregate (RCA) is sometimes used as a base course material, but it is often placed into landfills due to difficulty of recrushing rebar-reinforced pavement. In both scenarios, the common practice is to back-haul these removed pavements, process them, and then transport them yet again, incurring additional haulage and processing costs. A potentially low-cost and sustainable solution would be to reuse these torn-out pavements as local aggregate sources for base course replacement. Recycled aggregates often have high variability and may degrade with time; therefore, they may be stabilized by chemicals, binders, or geosynthetics.

A plethora of geosynthetic products (e.g. geotextile, geogrid, and geocell) exist in the market that can improve the performance of a base course section. Many studies have displayed the reduction in rutting, prevention of intermixing, and overall improvement of base course

sections as compared with non-stabilized base course sections. Utilization of geosynthetics can reduce the aggregate demand for a base course section and/or increase the longevity of the pavement section. However, limited studies exist on the use of geosynthetics with recycled aggregate for base courses and their performance in unpaved and paved road applications.

This study focuses on the investigation of granular base options and their performance in unpaved roads and concrete pavements under simulated traffic loading through automated cyclic plate load testing. Recycled concrete aggregate (RCA) and virgin granular base (VGB) were stabilized using woven geotextile (W), nonwoven geotextile (NW), and triaxial geogrid (GG). Specific geosynthetics were selected from the Kansas Department of Transportation (KDOT) pre-approved materials list to assure typical materials in practice were used in this study. Base course sections were tested with each geosynthetic over controlled laboratory-manufactured subgrade. Results for each geosynthetic-stabilized base course section are compared against non-stabilized control sections. Weak subgrade with a California Bearing Ratio (CBR) at approximately 2% was selected and prepared beneath the base course sections. The quality and uniformity of the subgrade were controlled and determined by dynamic cone penetrometer (DCP) tests.

Initial testing included large-scale automated plate load tests on unpaved road sections. Laboratory-manufactures subgrade was compacted in six 150 mm lifts to a total height of 900 mm. If a geosynthetic was used, it was secured atop the subgrade prior to the installation of the base course. Earth pressure cells were embedded in the top of the subgrade to measure the stress reduction at the base course-subgrade interface. Either RCA or VGB 250 mm thick was compacted in two lifts atop the geosynthetic (or subgrade for non-stabilized sections). A hydraulic actuator affixed with a 300-mm-diamter rigid steel plate, an internal load cell, and a

displacement transducer applied automated cyclic plate loading to the surface of the base course in eleven load stages or until approximately 38 mm vertical displacement was achieved. The actuator system recorded automated applied loads and the resultant vertical displacements of the rigid plate under loading, while the earth pressure cells measured the deviator stresses at the base course-subgrade interface; all data was measured at ten readings per second. Vertical displacement data resulted in the measure of the permanent and resilient plate motion for each applied cyclic load. With the timestamps, the earth pressure cell data was normalized to the actuator data, and the resultant deviator interface stresses from the applied load could be observed; these measurements are then used to estimate stress distribution angle in the base course section, or the wider-spread area over which the applied surface load is propagated through the base course and reducing the resultant stress on the weak subgrade.

Based on the large-scale cyclic plate load test results of the unpaved roads with different granular base courses and geosynthetic products, one geosynthetic was chosen based on performance and economy for paved road plate load testing. Nonwoven-geotextile-stabilized VGB and RCA sections as well as a VGB non-stabilized section were constructed beneath 150 mm thick concrete pavement. These sections were subjected to cyclic loading after seven days of concrete curing, subjected to a rainfall event, and cyclic loaded again at eight days of curing. Permanent deformation and pavement section stiffness were improved both by the addition of nonwoven geotextile and further by the replacement of VGB with RCA.

The goal of the study is the identification of recycled materials' suitability for base course use beneath unpaved roads and concrete pavements with the addition of various geosynthetic stabilizations. This study serves to identify more cost-effective road rehabilitation options for areas of lower volume and/or funding. Geosynthetics provide the possibility of lower-cost or

more-readily-available base course materials in such areas. This research evaluates the measured performance data for geosynthetic-stabilized granular bases in terms of permanent deformation, resilient deformation, and stress reduction at the base course/subgrade interface under cyclic loading with various load magnitudes. These data were used to estimate resilient modulus and modulus of subgrade reaction for performance comparison and pavement design.

This dissertation includes eight chapters. The next chapter provides a literature review related to pavement design, use of recycled materials, and the applications of and design with geosynthetics. Chapter 3 describes the experimental design, procedures, and test matrix. Chapter 4 investigates the resilient and permanent deformations of the unpaved sections, displacements for the concrete paved sections, and the implications of these displacements for the design parameters in pavement design. Chapter 5 displays the interface deviator stresses, their implication for distribution angle in unpaved sections, and comparison in the deviator stress reductions in the paved sections. Chapter 6 estimates the resilient moduli of non-stabilized and geosynthetic-stabilized granular bases using the test data and the modified Burmister solution coded in MATLAB as well as compares the design values obtained using different correlation methods. Chapter 7 utilizes the KENPAVE software to determine the slab stresses and their implications for the design values obtained in the prior chapters. Finally, this dissertation will summarize the findings of these tests and their implications to the application of these materials in practice.

Chapter 2. Literature Review

2.1 Pavement Design

Several road design methods exist, including empirical, statistically based, and mechanistic-empirical. The focus of this document will be the geotechnical aspects of what happens beneath the concrete pavement. It is important to understand the reactions in the underlying base course, geosynthetics, and subgrade due to the effects these have on the overlying pavement.

2.1.1 Westergaard Concrete Pavement Models

Westergaard (1926) identified an early theoretical solution for the computation of stresses in a concrete pavement slab. He treated the pavement foundation (i.e. subgrade) as a series of springs and introduced the modulus of subgrade reaction, *k*, as a constant stiffness value across a homogeneous subgrade. This k-value multiplied by the deflection *z* at any point in the slab describes the subgrade reaction per unit area. Westergaard (1926) stated that variations of *k* up to 4 orders of magnitude (from 50 pci to 200 pci) yield only minor changes in the estimated stresses in a concrete pavement slab, so the assumption of a uniform modulus of subgrade reaction across the slab is valid. Radius of relative stiffness, *l*, was also identified as the relative stiffness of the slab that correlates to radius of gyration of a beam [Eq. (2.1)] (Westergaard 1926).

$$l = \sqrt[4]{\frac{Eh^3}{12(1-\mu^2)k}} \qquad (2.1)$$

where E = elastic modulus of the concrete slab, h = thickness of the concrete slab, μ= Poisson's ratio of concrete (0.15 in this study), and k = modulus of subgrade reaction.

Figure 2.1 depicts the three loading cases Westergaard considered in his 1926 theory. Critical tension in the slab was identified as top-of-slab tension for corner loading, bottom-of-slab tension for center loading, and bottom-of-slab tension under edge loading. His theory for the loading axes and slab behavior changes between load locations (Westergaard 1926).

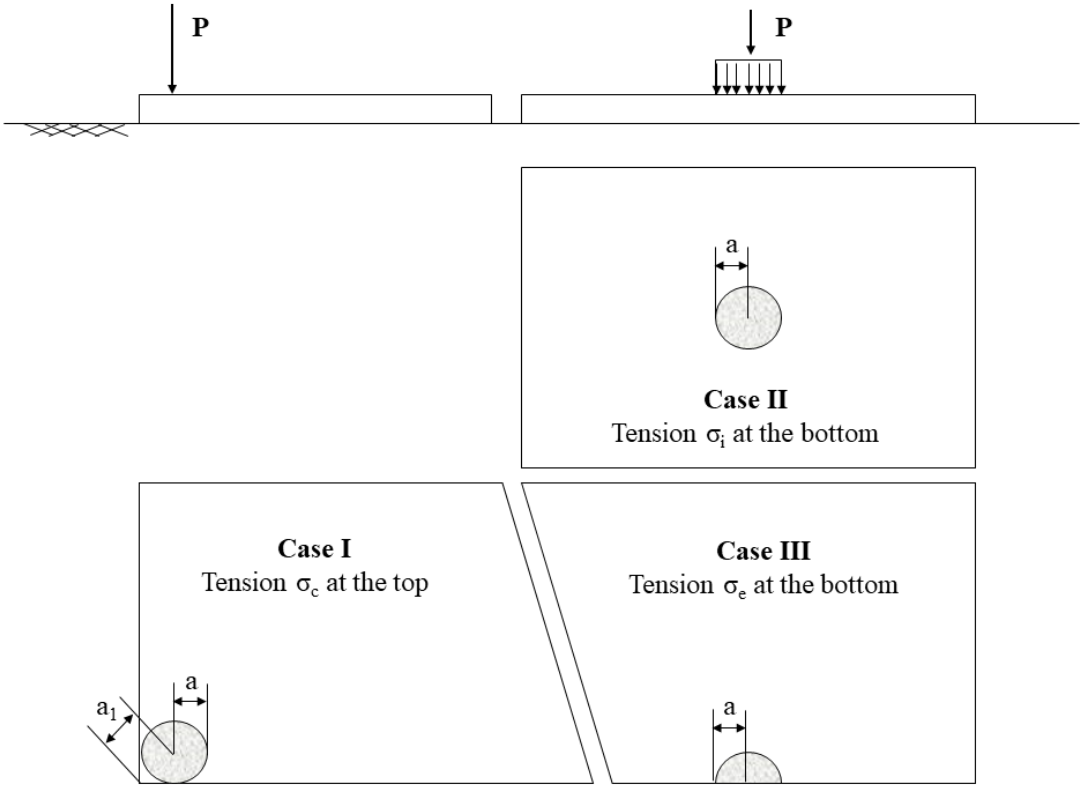

Figure 2.1. Loading Cases (Westergaard 1926).

Deflections and maximum stress in the concrete slab due to corner loading can be calculated using Eq. (2.2) and Eq. (2.3), respectively. These formulae consider the changes in bending moment per unit width and the secant modulus of the slab. The location of the maximum moment due to corner loading, x_1, is found based on incremental moments using Eq.

(2.4). Greater impact on the deflection and stress was observed by changing the value of a_1 from 0 to the formula listed below. Changes in *k* yielded minimal change in slab stress for corner loading (Westergaard 1926).

$$z_c = \frac{P}{kl^2}\left(1.1 - 0.88\frac{a_1}{l}\right) \tag{2.2}$$

where z_c= slab deflection at the corner due to corner loading, P= applied force, k= modulus of subgrade reaction, l= radius of relative stiffness, a_1= distance from the corner to the center of the loaded area = $a\sqrt{(2)}$, and a= radius of circular loaded area.

$$\sigma_c = \frac{3P}{h^2}\left[1 - \left(\frac{a_1}{l}\right)^{0.6}\right] \tag{2.3}$$

where σ_c is the maximum tensile stress in the slab due to corner loading.

$$x_1 = 2\sqrt{a_1 l} \tag{2.4}$$

where x_1 = maximum moment location due to corner loading, and a_1 = distance from loaded corner to center of load plate.

For interior-slab loading, two theories in accordance with the theory of elasticity are identified: “ordinary theory of slabs” and “special theory.” In the ordinary theory, there exists a neutral surface perpendicular to bending in a plane cross-section. The ordinary theory of slabs is said to apply to the stresses throughout the slab except for “in the immediate neighborhood of a concentrated load” and can determine deflections throughout the slab. The special theory is

applied for the thickness of the slab by accounting for finite tensile stresses at the bottom of the slab due to top loading; it assumes that modulus of elasticity and Poisson's ratio are constant and that the material maintains geometrical continuity. The ordinary theory utilizes "cones of equivalent distribution pressure" (see Figure 2.2) that estimate pressures at the base of the slab; this theory assumes that the critical stress will be at the slab base, which would be true for all but very small-radius (i.e. point) loads, and this would not apply to a tire load. Both loading theories may be considered using Eq. (2.5) to determine the applicable radius and Eq. (2.6) or Eq. (2.7) to determine the critical stress in the slab due to interior loading. In the special theory, concentrated loads create local stresses around a concentrated load and thus localized deformations; the critical slab stresses and deflections about this concentrated load [Eq. (2.8) and (2.9), respectively] are non-uniform as a result. As with the corner loading scenario, the load radius has a greater influence than the modulus of subgrade reaction (Westergaard 1926).

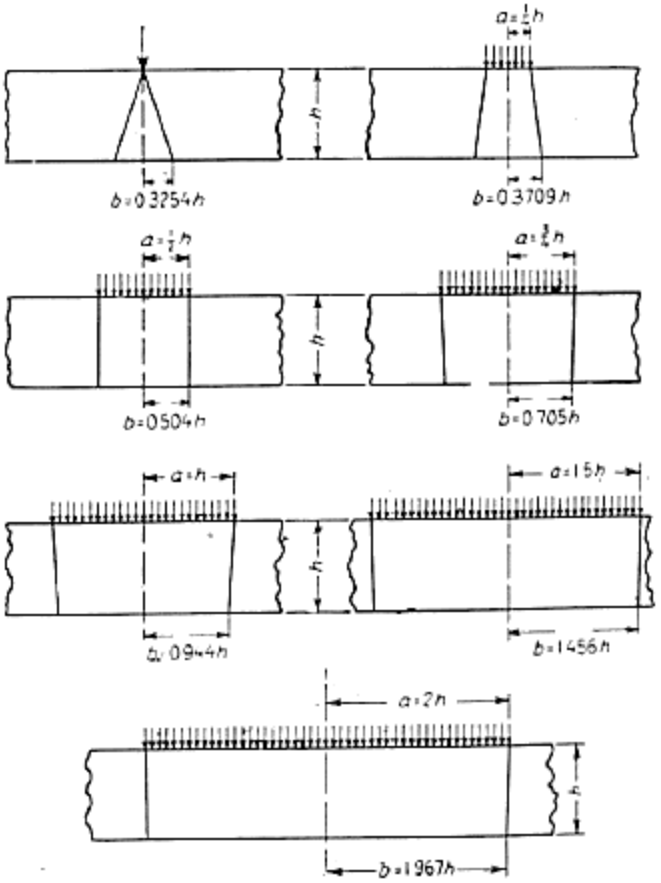

Figure 2.2. Westergaard (1926) cones of equivalent pressure distribution beneath center-loaded concrete pavement slab.

$$b = \begin{cases} \sqrt{1.6a^2h^2} - 0.675h & for\ a < 1.724h \\ a & for\ a \geq 1.724h \end{cases}$$

(2.5)

where b= radius of equivalent pressure distribution area at bottom of slab, a = radius of surface load, and h = slab thickness.

$$\sigma_i = \frac{3(1+\mu)P}{2\pi h^2}\left(\ln\frac{l}{b} + 0.6159\right)$$

(2.6)

where σ_i = critical stress in the slab under interior loading (ordinary theory, general form).

$$\sigma_i = 0.3162\frac{P}{h^2}(\log h^3 - 4\log a - \log k + 6.478) \tag{2.7}$$

where σ_i = critical stress in the slab under interior loading (ordinary theory where b=a, assuming E_{slab} = 3,000,000 psi and μ_{slab} = 0.15).

$$\alpha_i = 0.3162\frac{P}{h^2}\left(\log h^3 - 4\log\left(\sqrt{1.6a^2h^2} - 0.675h\right) - \log k + 6.478\right) \tag{2.8}$$

where α_i = critical stress in the slab under interior loading (special theory, assuming E_{slab} = 3,000,000 psi and μ_{slab} = 0.15).

$$z_i = \frac{P}{8kl^2} \tag{2.9}$$

where z_i = deflection under center loading.

Edge loading applies similar theory to that of interior loading with the equivalent radius *b* [Eq. (2.5)]. Due to the edge nature of the loading, the critical stress can be obtained using Eq. (2.10). The special theory that assumes concentrated stresses applies here. Deflection of the slab due to edge loading is observed in Eq. (2.11). Westergaard found that the case holds where the

greatest variation is due to changes in the surface load radius and the modulus of subgrade reaction is not as important. (Westergaard 1926)

$$\sigma_e = 0.572\frac{P}{h^2}\left(\log h^3 - 4\log\left(\sqrt{1.6a^2h^2} - 0.675h\right) - \log k + 5.767\right)$$

(2.10)

where σ_e = critical stress in the slab under edge loading (for E = 3,000,000 psi, μ = 0.15).

$$z_e = \frac{1}{\sqrt{6}}(1 + 0.4\mu)\frac{P}{kl^2} \approx 0.433\frac{P}{kl^2}\ when\ \mu = 0.15$$

(2.11)

where z_e = deflection due to edge loading.

Though Westergaard (1926) includes several deflection diagrams and discusses several case studies from the time, his models have their limitations. The system is considered perfectly elastic, so accumulated damage is not considered. Volume changes of the slab, such as those due to temperature fluctuation, are not accounted for. Varying thickness of the slab is not considered. Changes in subgrade stiffness including soft and hardened areas are not captured. The horizontal components of the system and their effects are omitted; only vertical stress and deflection are addressed. The above analysis tools do not consider dynamic loading effects, which could potentially increase the modulus of subgrade reaction in practice. These limitations must be considered when using the Westergaard (1926) theory and as a starting point for research advancement.

2.1.2 Burmister Layered Elastic Theory

Burmister (1945) published a series of three papers that address the continuity and reactions of layered soil systems. His theory was originally developed for the design of airport trafficways and foundations (Burmister 1945). Nonetheless, his two-layer theory has been widely used in the design of unpaved roads and asphalt pavement structures.

Burmister (1945) assumed that the soils in the two-layer system (see Figure 2.3) conform to the theory of elasticity and meet the following conditions:

- The soils in each layer are "homogeneous, isotropic, elastic materials, for which Hooke's law is valid"; in other words, the materials are consistent, their deformation properties exist in a single direction, their deformation is not permanent, and force is directly proportional to isotropic deformation multiplied by a constant (e.g. *k*) (Love 1892).
- Both layers in the system are assumed to have infinite horizontal extents .
- The vertical extents of the first layer are finite (height *h*) but the underlying layer has infinite height.
- Beyond the surface loading area, the surface of the first layer has no normal or shearing stress (boundary condition).
- The displacements at Layer 2 (the lower layer) are zero at infinite depth.

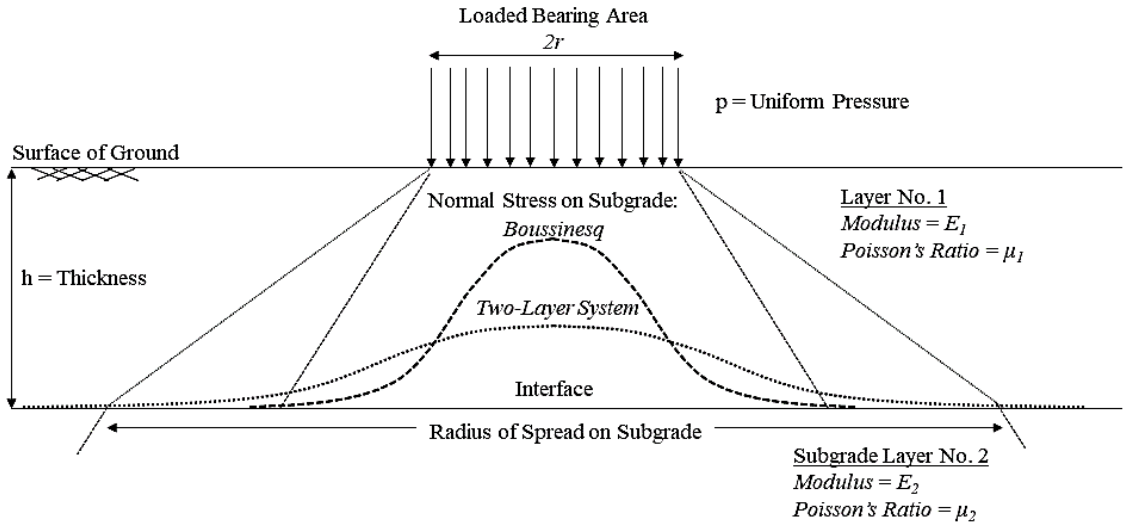

Figure 2.3. Schematic for two-layer soil system (Burmister 1945).

Continuity conditions must also be met. In the first case for continuity, it is assumed that both layers are in continuous contact and move together elastically at all contact locations; all displacements and stresses at the interface are equal. In the second continuity case, the two layers have a frictionless interface; only normal stress and displacement are continuous. Burmister's assumptions of continuity allow for the determination of engineering properties by determining values for elastic moduli, Poisson's ratio, displacements at the top and bottom of base course layers, and other mechanical properties and reactions. Burmister (1945) stated that stress equilibrium in the theory of elasticity must be met [see Eq. (2.12)]. Considering that experience and observation displayed a breakdown and loss of shear stress continuity between the layers occurred under large concentrated load from airplane wheels, the second case was assumed. The continuity equations were also detailed for a flexible three-layer system with the same criteria met layer-to-layer as in a two-layer system, but most of the discussion in Burmister (1945) focused on application to a two-layer system.

$$\frac{\delta\sigma_r}{\delta r} + \frac{\delta\tau_{rz}}{\delta z} + \frac{\sigma_r - \sigma_\theta}{r} = 0;\ \frac{\delta\tau_{rz}}{\delta r} + \frac{\delta\sigma_z}{\delta z} + \frac{\tau_{rz}}{r} = 0$$

(2.12)

Burmister (1945) confirmed the validity of the Boussinesq solution for surface deformation beneath a circular, flexible bearing area, with the assumption that Poisson's ratio (μ) of both soil layers is 0.5, with an applied correction factor F_w [Eq. (2.13)]. In Eq. (2.13), *w* denotes deflection at the center of the plate at the surface of Layer 1 (the upper surface), *p* denotes applied pressure, *r* denotes the radius of the circular load area, and E_1 and E_2 denote the elastic moduli of the upper and lower soil layers, respectively, for surface deflection beneath a circular surface load. The correction to Burmister's (1945) solution is modified to account for the ratio of the radius (*r*) of the load area to the height (*h*) of Layer 1 as well as the ratio of the elastic moduli; it thus takes into account the modulus derived from the base course layer overlying a weak soil and the relative thickness of the base course layer. Figure 2.4 depicts Burmister's (1945) original chart to determine the correction coefficient F_w based on the Case 1 (full continuity interface) continuity relationship of soil layers. Burmister (1945) noted that surface deformation would be a function of the radius of the applied pressure, the height of the stronger overlying section, the applied load magnitude, and the elastic moduli of both the base course and subgrade sections.

$$w_0 = \begin{cases} \frac{1.5qa}{E_2} F_2 = \frac{1.5pr}{E_2} F\left[\frac{r}{h}, \frac{E_2}{E_1}\right] & (flexible\ plate) \\ \frac{1.18qa}{E_2} F_2 = \frac{1.18pr}{E_2} F\left[\frac{r}{h}, \frac{E_2}{E_1}\right] & (rigid\ plate) \end{cases}$$

(2.13)

where w_0 = surface deflection of a two-layer system, q= p = applied pressure, a = r = radius of the circular loaded area, E_1 & E_2 = elastic modulus of the upper (1) and lower (2) soil layers, and

$F = F_2$ = settlement coefficient (a function of E_b/E_s and h_b/a), h = thickness of the upper soil layer; for a rigid plate, a factor of 1.18 should be used instead of 1.5.

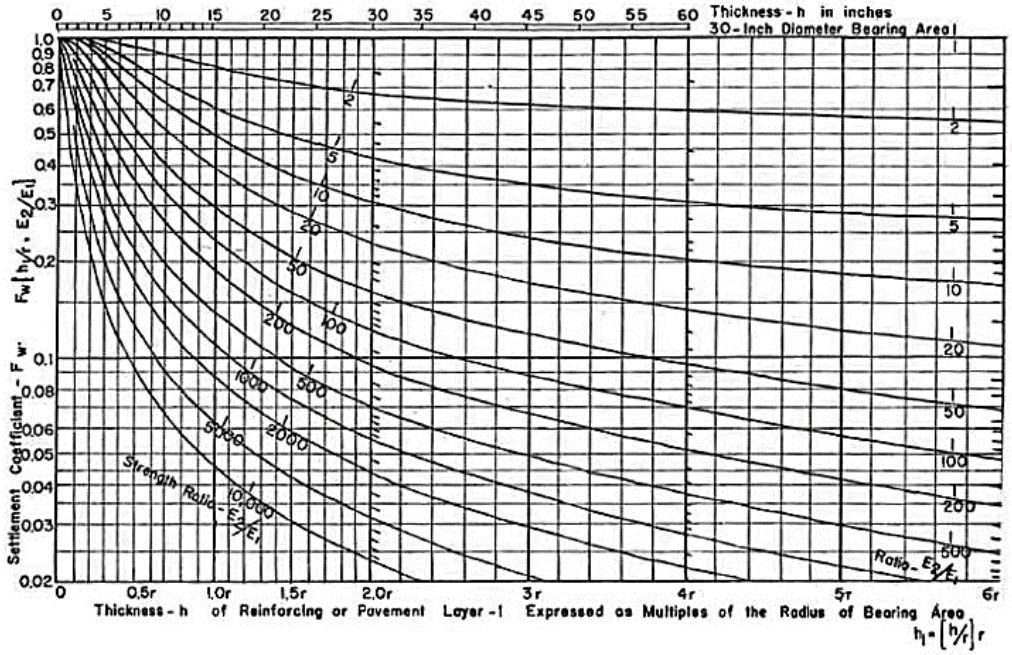

Figure 2.4. Settlement coefficient, F_w chart, assuming $\mu = 0.50$ (Burmister 1945).

Burmister (1958) expanded on his theory and applied it to the Western Association of State Highway Officials (WASHO) road test, one of the earliest "full-scale road test on flexible [asphalt] pavements with controlled truck traffic…" (Highway Research Board 1954). The concept of a stress distribution angle was discussed as depicted in Figure 2.5(a). Based on this theory, stress distribution angle can be calculated from a static applied load as displayed in Eq. (2.14). The reduction in stress as a function of the differences in elastic moduli of the three-layered pavement system were also discussed, as depicted in Figure 2.5(b). Based on Burmister (1945), a stiffer base course layer overlying a weaker subgrade layer will increase the stress distribution angle and thus reduce the measured change in vertical pressure at depth directly

beneath the center of the applied load. Analysis of the WASHO test data using his theory yielded expected results and thus validated his 1945 theories (Burmister 1958).

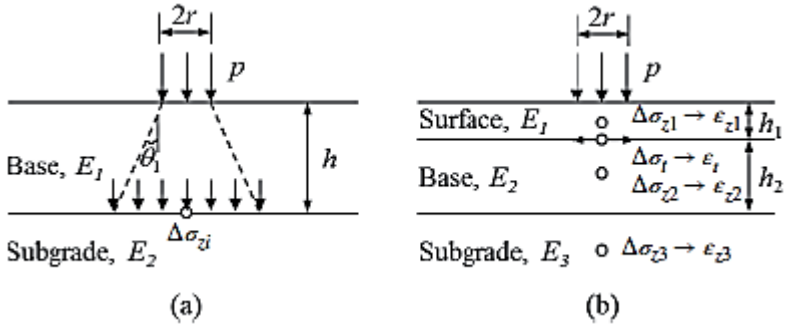

Figure 2.5. Stress Distribution in unpaved roads (a) and paved roads (b) (from Han 2015).

Burmister (1958) introduces several more design charts that relate vertical stress reduction at depth to the ratio of the elastic moduli of base course and subgrade layers, assuming the overlying layer has an equal or greater elastic modulus. Figure 2.6 displays the vertical stress reduction coefficient as the change in vertical stress at depth (σ_z) divided by the deviator stress at the surface (p), assumes that the radius of the loaded area (r) is equal to the height of the base course (h), and takes the stress reduction at a given depth (z) normalized to the load radius (r), and the ratio of the elastic moduli of the layers (E_1/E_2) can be estimated; the elastic modulus ratio decreases with the increase in the vertical stress reduction coefficient, pointing out that the stiffer the overlying layer in relation to the weakness of the underlying layer will result in greater stress reduction and a more widespread distribution at depth. Figure 2.7 is similar to Figure 2.6 except that the vertical stress is only observed at the interface between the base course and subgrade layers, so various radii in relation to the base course height may be evaluated; moving from left to right in this chart, as the radius of the applied load at the surface increases along the same stress reduction coefficient line, the modulus ratio increases, or conversely a constant radius-to-

height will result in an increase in stress reduction ratio (higher observed stress) at the interface moving upward through the chart and resulting in a decrease in the modulus ratio. Both charts assume Poisson's ratio of 0.50. These charts as well as Eq. (2.14) can be used to estimate stress distribution angle, interface stress, or elastic modulus ratio when the appropriate data has been gathered (Burmister 1958).

$$\tan\theta_1 = \frac{1}{h}\left[\sqrt{\frac{r^2 p}{\Delta\sigma_{zi}}} - r\right] \qquad (2.14)$$

where θ_1 = stress distribution angle, h = height of the base course, r = radius of the applied load at the base course surface, p = applied pressure at the base course surface, and $\Delta\sigma_{zi}$ = deviator stress at the base course / subgrade interface.

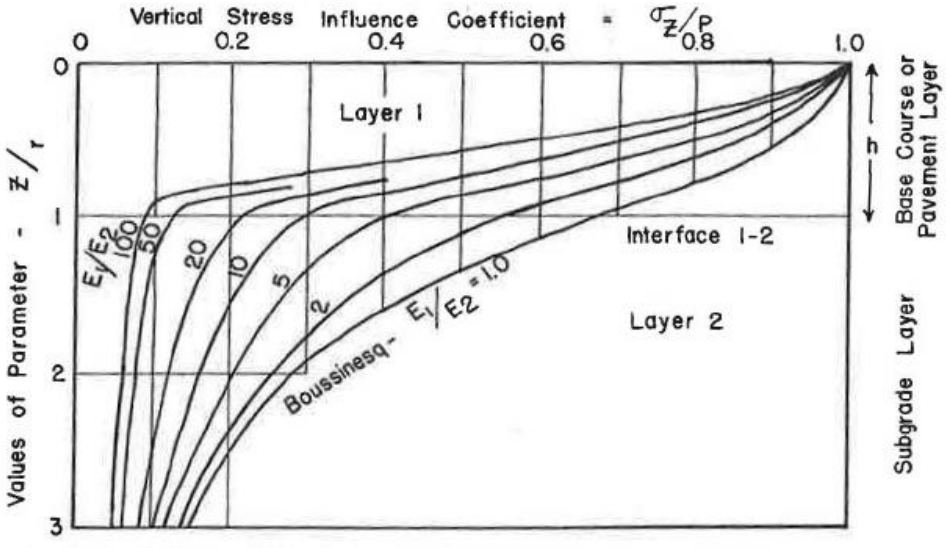

Figure 2.6. Vertical Stress Reduction Chart (from Burmister 1958). Assuming r/h=1.0 and μ=0.50.

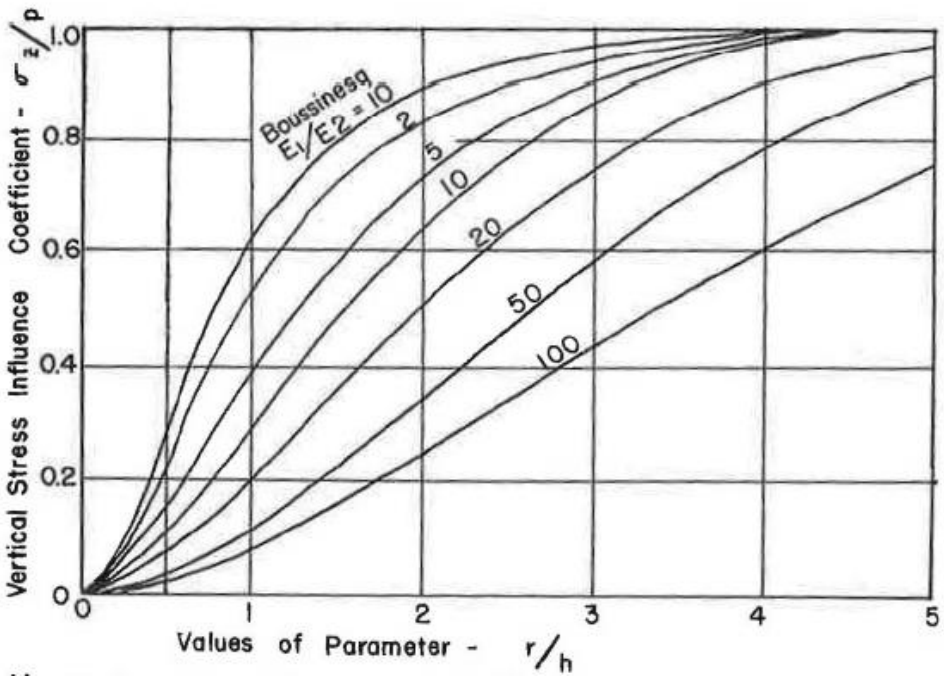

Figure 2.7. Vertical Stress Reduction at Interface (from Burmister 1958). Assuming μ=0.50.

In applying his theory and the field observations, Burmister (1958) made several additional interpretations of the behavior of the pavement sections. He noted that with the repetition of applied loads, consolidation of the subgrade "under a given pressure" as observed by displacement at the surface resulted in a strength increase or an observed increase in elastic modulus of the subgrade. He also pointed out that strength for the WASHO soils (modulus roughly 4,000 psi or 27.5 MPa) increased as the system consolidated until the applied pressure reached 51.9 psi (358 kPa), at which point the soil gained no more strength and yielded. Burmister (1958) observed the effect of plate size on plate load tests and the inability to compare results of plates with various applied pressure radii directly. Similar strength increase through compression was noted in the subbase sections; with the increase in subbase consolidation, the relative percentage of subgrade deflection as a function of surface deflection increased to 80-90%; this indicated that properly compacted base course transferred most of the deflection into

the subgrade, so deformation within the base course layer was considered minimal. It should be noted that load "cycles" for the WASHO tests was less than 50 (Burmister 1958).

Burmister (1945, 1958) used extensive mathematics and differential equations to create a layered reaction model and derive Figure 2.4 and Eq. (2.13). Sun et al. (2017) modified these equations to determine the equivalent resilient modulus of a geosynthetic-reinforced base course section through use of MATLAB coding. Permanent deformation at the surface of the base course and at the interface of the two layers (assuming the geosynthetic-reinforced base course acts as one layer) were measured and used in Burmister's set of equations to back-calculate the equivalent resilient modulus of the reinforced sections (Sun et al. 2017). The intention of the study by Sun et al. (2017) was prediction of the deformation behavior under cyclic loading by integrating the calculated elastic responses with pavement damage models. This integration into mechanistic-empirical design will be discussed in later sections.

2.1.3 AASHO Road Test

The American Association of State Highway Officials (AASHO), the precursor to AASHTO, created a famous test site that was the basis for many design guides used for current pavements. Seven miles of pavement were constructed in Ottawa, Illinois, consisting half of concrete and half of asphalt. Test sections varied in pavement and base/subbase thickness to divide the 6 loops and 16 bridges into 836 test sections. The test was conducted from October 1958 through November 1960. Test results became the "foundation for analytical evaluation of stresses and deflection from moving vehicles" (FHWA 2018), even for guides used today. No comparable test has been conducted to date (FHWA 2018). These road tests are the basis for the 1986 and 1993 AASHTO pavement design guides.

2.1.4 PCA

One of the earliest developed guides for concrete pavement structural design was published by the Portland Cement Association (PCA). The basis for the PCA methods includes theoretical studies (e.g. Westergaard), finite element analyses, PCA and agency full-scale tests, in-use pavement behaviors, and test road sections (including the AASHO road tests). Design factors that determine concrete pavement thickness are identified as: 1.) modulus of rupture of the concrete; 2.) composite modulus of subgrade reaction (k); 3.) number, magnitudes, and configurations of axle load passes; and 4.) design period (20 years if not otherwise specified). Method of design is trial-and-error by changing the design thickness and completing the worksheet in Table 2.1 until the maximum of fatigue or damage percent is near to, but not greater than, 100%. Pavement stresses are most critical when wheel loads are near the edge, centered between the joints. The most critical deflections occur when pavement corner loading exists; movement of loading location away from the edge even a few inches drastically reduces deflection. Nonrepetitive Static Plate Load Test (ASTM D1196) is identified to determine the modulus of subgrade reaction for the PCA design method (Packard 1984).

Table 2.1. PCA design guide worksheet (Packard, 1984).

Calculation of Pavement Thickness

Project _____

Trial Thickness	_____	in.	**Doweled joints:**	yes _____	no _____
Subbase-subgrade k	_____	pci	**Concrete shoulder:**	yes _____	no _____
Modulus of rupture, MR	_____	psi	**Design period:**	_____	years
Load safety factor, LSF	_____				

Axle Load, kips	**Multiplied by LSF**	**Expected Repetitions**	**Fatigue Analysis**		**Erosion Analysis**	
			Allowable Repetitions	**Fatigue, percent**	**Allowable Repetitions**	**Damage, percent**
1	***2***	***3***	***4***	***5***	***6***	***7***
Single Axles ***8. Equivalent stress*** _____ ***9. Stress ratio factor*** _____			***10. Erosion factor*** _____			
28-30						
26-28						
24-26						
22-24						
20-22						
18-20						
16-18						
14-16						
12-14						
10-12						
Tandem Axles ***11. Equivalent stress*** _____ ***12. Stress ratio factor*** _____			***13. Erosion factor*** _____			
48-52						
44-48						
40-44						
36-40						
32-36						
28-32						
24-28						
20-24						
16-20						
12-16						
			TOTAL =		TOTAL =	

Modulus of rupture of concrete is determined using ASTM C78 for samples cured in moisture-controlled conditions for typically 7 days and 14 days for quality control. The 28-day test results are commonly used in design of pavements; 90-day results are used for airfields. The curing time is important as concrete continues gaining strength over time (see Figure 2.8) (Packard 1984).

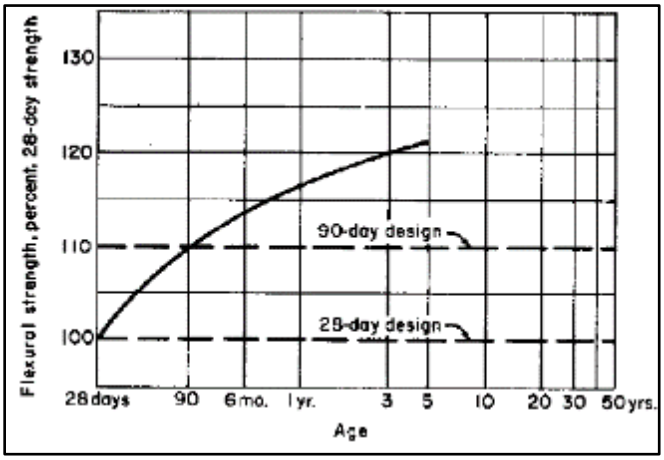

Figure 2.8. Flexural strength, age, and design relationships (Packard 1984).

Several key findings were noted in the investigation of concrete pavement design using the PCA method. The latest-published document appears to be the 1984 guide, with several technical notes to be appended to this method (PCA, 2018). Changes in slab thickness, applied stress changes with changes in axle load, and erosion are addressed (Packard 1984). Two failure modes (fatigue and erosion) of the slab are identified and evaluated separately; it is noted that one failure mode may prevail over the other (Packard 1984). Static load test results for modulus of subgrade reaction, using a 762 mm (30-in.) plate at deformations less than 1.27 mm (0.05 in.) are applied to a dynamically loaded traffic scenario; resilient modulus is not included (Packard

1984). The guide provides typical k-values for virgin and cement-treated base course, but it does not address the use of geosynthetics or alternative materials (Packard 1984).

2.1.5 USACE

Around the same time as the PCA manual publication, the U.S. Army Corps of Engineers (USACE) published an engineering manual addressing the design of concrete pavements. This manual published the same soil classifications listed in Figure 2.9 (with reference to PCA). Traffic loading places vehicles into design categories based on vehicle type as described in Table 2.2 and traffic volumes detailed in EM-1110-3-130 (USACE 1984a) and Table 2.3. Concrete pavement thickness is determined from Figure 2.10 using three inputs: flexural strength of the concrete slab, modulus of subgrade reaction, and the design index from Table 2.2 from the traffic weights. (USACE 1984a, 1984b)

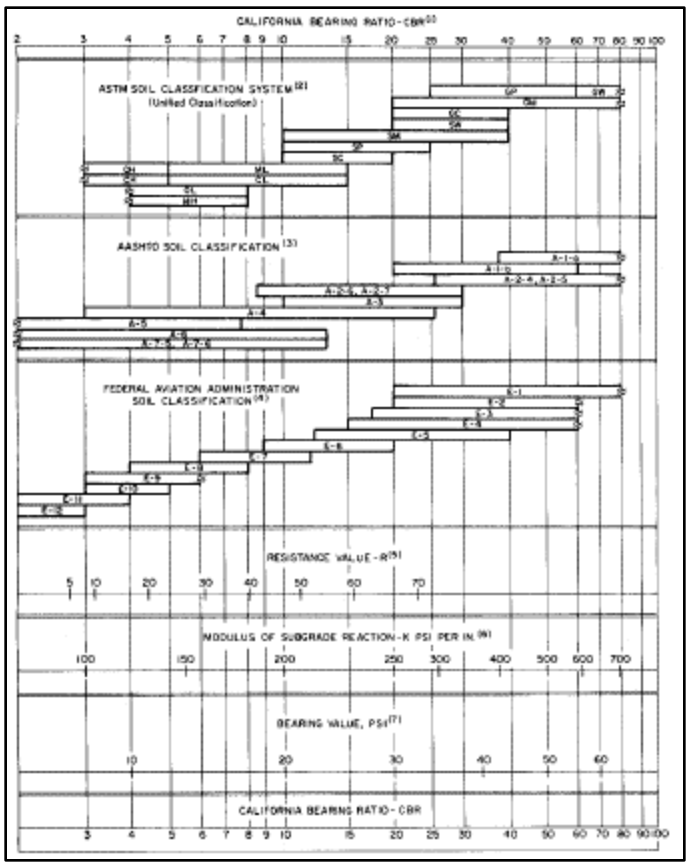

Figure 2.9: PCA correlation chart, modulus of subgrade reaction: typical soil (Packard 1984).

The USACE defines soil stabilization in terms of mixed-in additives such as cement, lime, or fly ash. Stabilization is defined as a core of the treated soil meeting minimum compressive strength and durability requirements outlined in USACE EM 1110-3-137. If these requirements are not met, then the soil is said to be modified, not stabilized, and the k-value should be adjusted as determined from the top of the modified layer; this scenario would apply to a geosynthetic-stabilized soil (USACE 1984b).

Table 2.2. Traffic categories (adapted from USACE 1984b).

Category	Group 1	Group 2	Group 3	Track-laying GVW (lb)	Forklift truck GVW (lb)
	Passenger cars, panel trucks, pickup trucks	*Two-axle trucks*	*3-, 4-, 5-axle trucks*		
I	Primarily	< 1%	0%		
II	Primarily	≤ 10%	0%		
III	Primarily	≤ 15%	≤ 1%	≤ 15,000	≤ 6,000
IV	Primarily	≤ 25%	≤ 10%	15,000-40,000	6,000-10,000
V				60,000	15,000
VI				90,000	20,000
VII				120,000	35,000

Table 2.3. Rigid (Concrete) Pavement Design Index (USACE 1984b).

Traffic Category	**Rigid Pavement Design Index for Road Classification**	
	B	***D-E***
I	1	1
II	1	1
III	3	2
IV	4	3
V:		
500/day	6	6
200/day	5	5
100/day	5	5
40/day	5	4
10/day	4	4
4/day	4	4
1/day	4	3
VI:		
200/day	8	8
100/day	7	7
40/day	6	6
10/day	5	5
4/day	5	5
1/day	4	4
1/week	4	3
VII:		
100/day	9	9
40/day	8	8
10/day	7	7
4/day	6	6
1/day	5	5
1/week	4	4

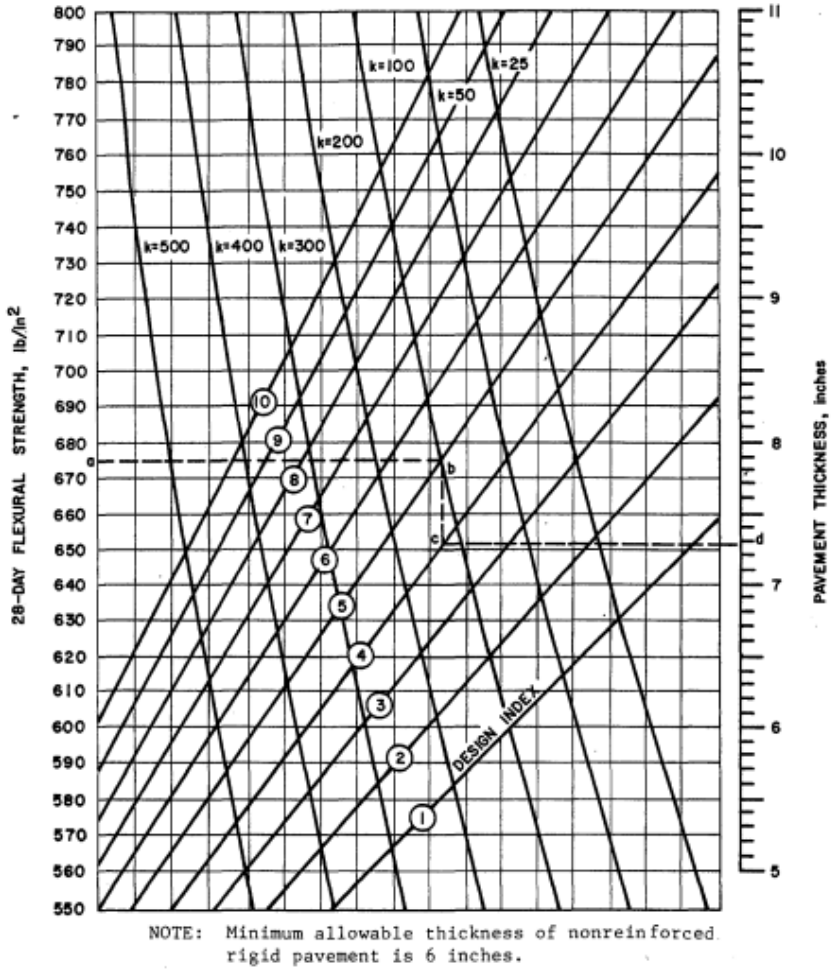

Figure 2.10. USACE (1984b) Rigid (Concrete) Pavement Thickness Design Chart.

2.1.6 AASHTO 1993 Pavement Design Guide

The American Association of State Highway and Transportation Officials (AASHTO) published their original pavement design guide in 1986, then updated and published the widely used design guide in 1993. The AASHTO design guides identify the number of 80-kN (18-kip) equivalent single axle loads (ESALs) that a given pavement section can undergo, based on engineering design values for a given pavement section, confidence in the model, and allowable change in serviceability over a given pavement lifespan. Data from the AASHO road tests and updates to

the original 1972 AASTHO interim design guide address many key design factors, including erosion loss of support (Figure 2.11), defining the resilient modulus of roadbed soil to AASTHO T274, traffic/ ESALs, pavement management, rehabilitation, reliability, serviceability, and the vision for mechanistic-empirical design procedures. (AASHTO 1986, 1993).

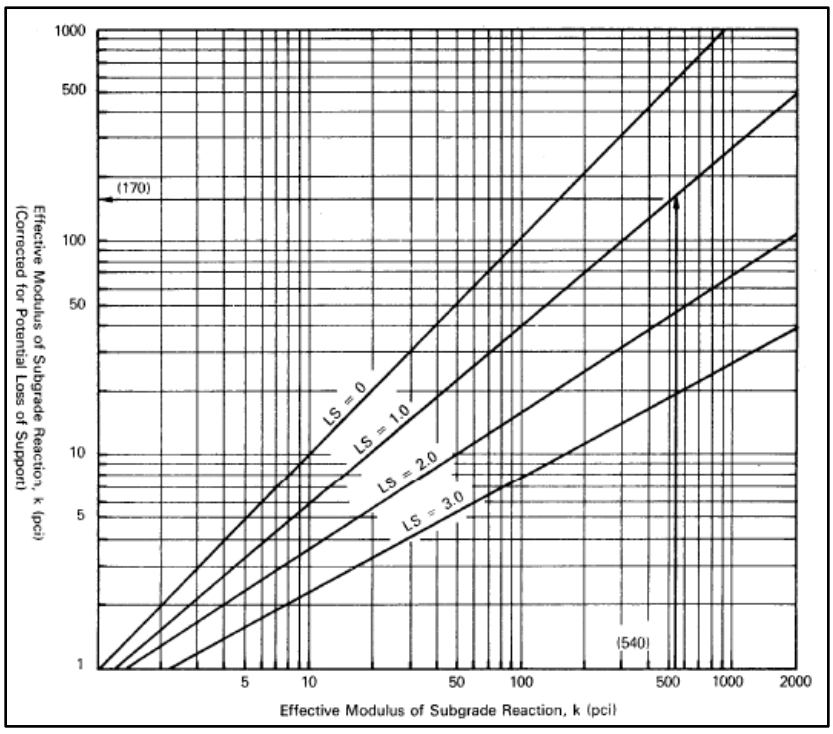

Figure 2.11. Loss of support correction for modulus of subgrade reaction (AASHTO 1993).

For concrete pavement design, the number of equivalent single axle loads (ESALS) a pavement section can endure is given by Eq. (2.15). This long equation focuses heavily on the properties of the concrete slab. The structure beneath the concrete slab is considered in the composite subgrade reaction modulus (*k*). Axle loads are converted to a single load magnitude using load equivalency factors (LEF) found in Appendix D of the 1993 design guide; traffic volumes of different axle load magnitudes are counted during traffic studies, converted to

ESALs, and summed. Additional details on estimation of traffic quantities can be found in the AASHTO 1993 guide. The emphasis on loss of support (Figure 2.11) due to erosion beneath the slab is of great importance for the design input k-value [Eq. (2.15)], indicating that a stabilizing geosynthetic layer could be imperative to sustainable concrete pavement.

$$\log_{10} W_{18} = Z_R S_0 + 7.35 \log_{10}(D+1) - 0.06 + \frac{\log_{10}\left(\frac{\Delta PSI}{4.5-1.5}\right)}{1+\frac{1.624\times 10^7}{(D+1)^{8.46}}} + (4.22 - 0.32 p_t)\log_{10}\left\{\frac{S_c C_d (D^{0.75}-1.132)}{215.63 J\left[D^{0.75} - 18.42 \Big/ \left(E_c/k\right)^{0.25}\right]}\right\} \quad (2.15)$$

where W_{18} = no. of Equivalent Single Axle Loads (ESALs), D = slab thickness, E_c = concrete slab elastic modulus, S_c = slab modulus of rupture, Δpsi = change in serviceability, p_t = terminal serviceability, C_d = drainage coefficient, S_0 = overall standard deviation, Z_R = normal standard deviate (based on reliability), and k = modulus of subgrade reaction [k (pci) for fine-grained subgrade = M_r (psi)/19.4].

Modulus of subgrade for this approach is a composite value for systems where a base or subbase exists above the subgrade (see Figure 2.12); it is explicitly stated in the AASHTO guide that direct measure of composite modulus of subgrade reaction using standard static plate load testing will not produce accurate results. AASHTO relates the resilient modulus to the modulus of subgrade reaction, assuming a 762-mm-diameter plate and 69-kPa (10-psi) applied pressure,

AASHTO (1993) correlates California Bearing Ratio (CBR) to the resilient modulus using Eq. (2.16) for fine-grained soils with CBR less than 10 and using Eq. (2.17) for base course.

$$M_r(psi) = 1500 \times CBR \rightarrow M_r(MPa) = 10.3 \times CBR$$

(2.16)

$$E_b(MPa) = 17.6CBR^{0.64}$$

(2.17)

Loss of support should also be applied to the k-value using Figure 2.11; recommended loss of support is 1.0 to 3.0 for unbound granular materials, 2.0 to 3.0 for natural subgrade, and 0.0 to 1.0 for cement- and bituminous-treated base courses (AASHTO 1993). The AASHTO 1993 design guide explicitly does not account for the addition of geosynthetic stabilization. The relationship between the composite modulus of subgrade reaction for 2% CBR subgrade and 250 mm (10 in.) base course thickness taken from Figure 2.12 yields Eq. (2.18) (AASHTO 1993).

$$k\ (pci) = 59 \ln\left(M_{r,Base,psi}\right) - 347$$

(2.18)

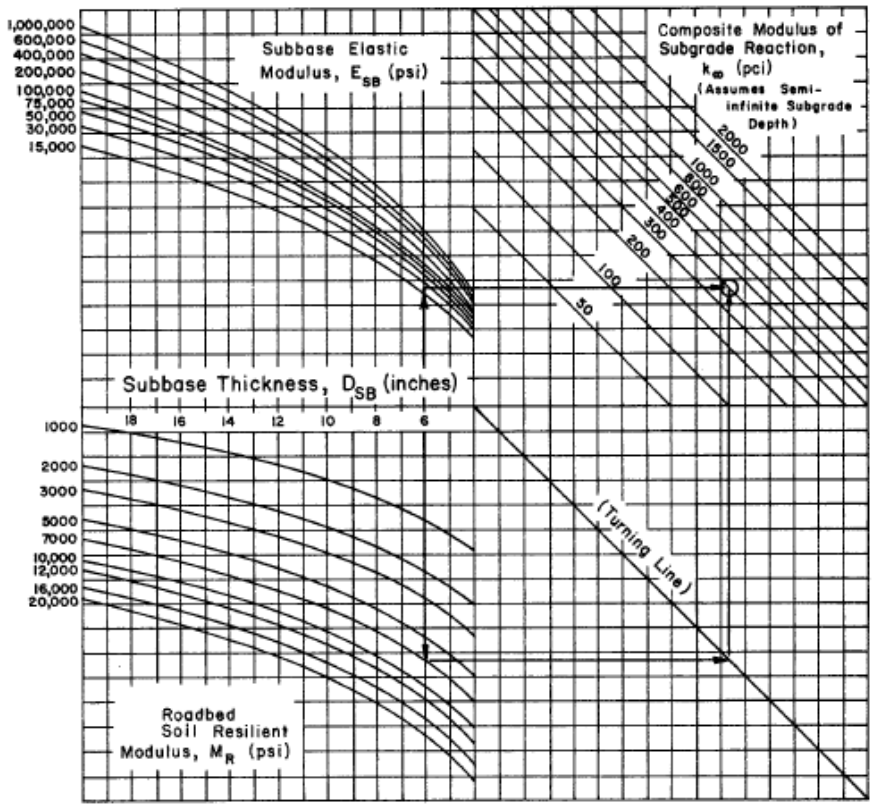

Figure 2.12. Chart for composite modulus of subgrade reaction (AASHTO 1993).

2.1.7 MEPDG

MEPDG provides design inputs and material parameters necessary for use in the AASHTOWare software and expands upon the principles in the AASHTO 1993 Pavement Design Guide. The software uses neural network structural response models based on ISLAB2000 finite element analysis runs. These values depend on the radius of relative stiffness and subgrade reaction as identified in Eq. (2.19) (NCHRP 2004).

$$l = \sqrt[4]{\frac{E_{PCC} h_e^3}{12(1-\mu_{PCC}^2)k}} \tag{2.19}$$

where l = radius of relative stiffness for AASHTOWare (560 to 2000 mm typically), E_{PCC} = elastic modulus of Portland cement concrete, h_e = slab thickness, μ_{PCC} = Poisson's ratio of concrete, and k = dynamic modulus of subgrade reaction.

MEPDG (NCHRP 2004) divides concrete pavements into jointed plain concrete pavement (JPCP) and continuously reinforced concrete pavement (CRCP). Critical design criteria for JPCP are transverse cracking (10% to 45%), transverse joint faulting (2.5 to 5 mm), and International Roughness Index (IRI) pavement smoothness (2.3 to 3.9 m per km). CRCP performance criteria include load transfer efficiency (LTE) (greater than 95%) and crack width (0.5 mm), IRI smoothness, and punchouts (6 to 12 per km). Design input parameters include climate, traffic, drainage, pavement structure and thermal expansion properties. Distance of the wheel path from the edge of the slab and the deviation of that path increase cracking potential in both JPCP and CRCP. Infiltration and drainage potential of the pavement estimates water entering the base course layer from precipitation at four levels: none, minor (10%), moderate (50%), or extreme (100%).

For pavement structure, the AASHTOWare converts the resilient moduli of multiple layers underlying the pavement and base course to a dynamic k-value. This value differs from the Westergaard (1926) static k-value as it is estimated based on multiple deflections from a 40-kN 150-mm falling weight deflectometer (FWD) model atop a concrete pavement structure. Despite the distinction between static and dynamic loads, the theory that the underlying layer acts like a series of springs beneath the concrete pavement structure matches the Westergaard (1926) method. The AASHTOWare similarly converts the pavement and base course into an equivalent rigid (concrete) layer atop the equivalent subgrade for neural network modeling [Eq. (2.20)] (NCHRP 2004).

$$h_{eff} = \sqrt[3]{h_{PCC}^3 + \frac{E_{base}}{E_{PCC}} h_{base}^3 + 12\left[h_{PCC}\left(x - \frac{h_{PCC}}{2}\right)^2 + \frac{E_{base}}{E_{PCC}}\left(h_{PCC} + \frac{h_{base}}{2} - x\right)^2 h_{base}\right]}$$

(2.20)

where h_{eff} = effective pavement thickness, h_{PCC} = concrete thickness, h_{base} = base course thickness, E_{base} = base course elastic modulus, E_{PCC} = concrete elastic modulus, x = distance between the neutral plane and the top surface of the PCC layer. This implies that reaction will occur between the base course and subgrade, and that the base course will not be the mode of failure due to pavement loading at the surface. The program accounts for both temperature and tire loading.

Behavior of pavement sections is dependent upon the applied stress, strength properties, and incremental damage incurred by repeated load cycles (i.e. traffic). Tseng (1988) acknowledged that the resilient behavior of a pavement section was stress-dependent as observed in Eq. (2.21).

$$E_r = a{\sigma_\theta}^b {\sigma_d}^c$$

(2.21)

where E_r = resilient modulus of subbase/subgrade layer, σ_θ = bulk stress, σ_d = deviator stress, and a, b, and c are regression constants.

Tseng and Lytton (1989) identified that permanent deformation for flexible, including unbound granular, layers is dependent upon the number of cycles and the relationship between the permanent and resilient deformation unique for each sample [see Eq. (2.22)].

$$\varepsilon_a = \varepsilon_0 e^{-(\rho/N)\beta}$$

(2.22)

where ε_α = accumulated permanent strain, N= number of load cycles, and ε_0, β, ρ are material parameters.

The damage model for unbound granular layers modified the original Tseng and Lytton (1989) model in the publication of the Mechanistic- Empirical Design Guide (MEPDG) (NCHRP 2004) as observed in Eq. (2.23) and (2.24); the original ρ, β, and ($\varepsilon_0/\varepsilon_r$) were modified and no longer consider the bulk or deviator stresses that Tseng and Lytton deemed important. Analysis can be performed at three levels: 1.) properties measured on-site; 2.) properties correlated to on-site measurements; 3.) typical values for the region (NCHRP 2004).

$$\delta_{p,3} = k_b \delta_{r,1} \left(\frac{\varepsilon_0}{\varepsilon_r}\right)_b e^{-\left(\rho_b/N\right)^{\beta_b}}$$

(2.23)

where $\delta_{p,3}$ = permanent deformation at surface of base course, k_b = calibration factor, $\delta_{r,1}$ = resilient deformation at surface of base course, N = number of cycles, and:

$$\begin{cases} \beta = 10^{\left(-0.61119-0.017638W_{c(b,s)}\right)} \\ \rho_{(b,s)} = 10^9 \left[\dfrac{-4.89285}{1-(10^9)^{\beta_b}}\right]^{1/\beta_b} \\ \left(\dfrac{\varepsilon_0}{\varepsilon_r}\right)_{(b,s)} = \dfrac{0.15 \cdot e^{\rho_b{}^{\beta_b}} + 20 \cdot e^{\left(\rho_b/10^9\right)^{\beta_b}}}{2} = \left(\dfrac{\varepsilon_p}{\varepsilon_r}\right)_{N\to\infty} \end{cases}$$

(2.24)

where $W_{c\,(b,s)}$ = moisture content of the base course (b) or subgrade (s), ε_p = accumulated permanent vertical strain at *N* cycles, and ε_r = (average) vertical resilient strain.

MEPDG (NCHRP 2004) designates that the evaluation of damage beneath the concrete slab should be performed separately from the damage of the concrete slab. Eq. *(2.23)* is the

rutting formula for asphalt pavements and unpaved roads. This model is recommended by NCHRP (2004) for modeling the damage in the base course and subgrade layers beneath concrete pavements.

MEPDG (NCHRP 2004) identifies three stages, as shown in Figure 2.13, of pavement deformation for a single material set, load, and environmental condition. The first or primary stage includes a high initial rutting rate, higher permanent deformations, and volumetric change. The secondary stage is marked by a relatively constant rutting rate and some volume change, but there is also an associated increase in the rate of shear deformations. The tertiary stage includes high plastic deformations due to shearing. Most current predictive models only include the primary and secondary deformation stages (NCHRP 2004).

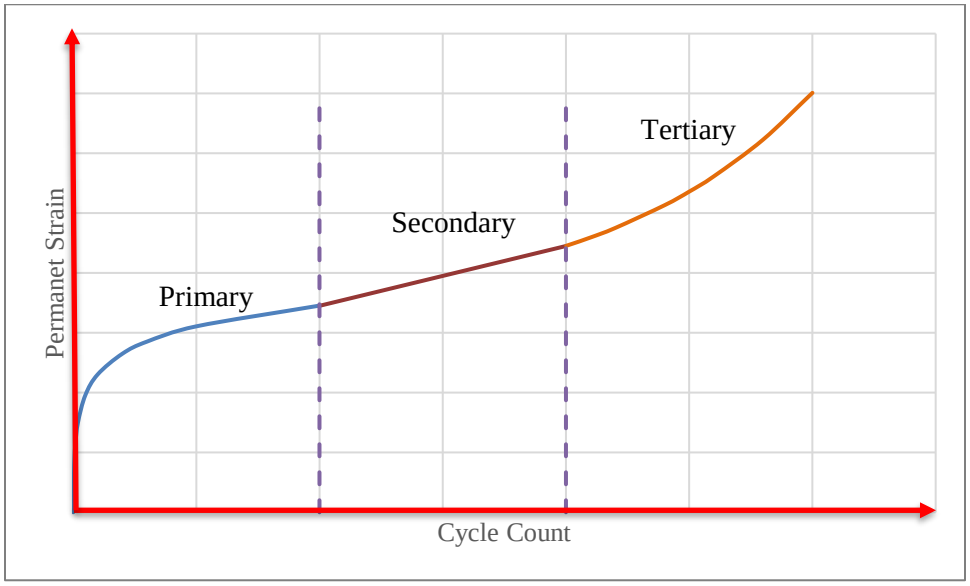

Figure 2.13. MEPDG Pavement Deformation Stages.

2.1.8 AASHTO T307 Resilient Modulus

While the design values listed in prior sections may be used to estimate resilient modulus and modulus of subgrade reaction, AASHTO T307 (2017) uses a triaxial shear machine with a dynamic load system to determine an aggregate's resilient modulus. The triaxial sample is prepared in the same way as that of a statically loaded undrained sample; a series of axial deviator stresses are applied based a series of confining pressures as outlined in the test method. Eq. (2.25) displays the resilient modulus calculation in accordance with AASHTO T307 (2017), which is simply the deviator stress divided by the resilient strain in the cylindrical sample.

$$M_r = \frac{\sigma_d}{\varepsilon_r} \tag{2.25}$$

where σ_d= axial deviator stress and ε_r = resilient axial strain.

Haversine axial loading is applied using a 0.1-second dwell force and a total load cycle of 1.0 to 3.1 seconds; confining stresses remain static (AASHTO T307 2017). It is important to note the definition of deviator stress as displayed in Eq. (2.26) (adapted from AASHTO T307 2017), as the pressure required to maintain contact with the sample is subtracted from the axial force to determine cyclic load.

$$\sigma_d = \frac{p_{cyclic}}{A} = \frac{p_{max} - p_{contact}}{A} \tag{2.26}$$

where p_{cyclic} = cyclic applied force, p_{max} = maximum applied load, $p_{contact}$ = load applied to the sample surface to maintain contact ($0.1p_{max}$ per test method), and A = original cross-sectional area of the specimen.

Resilient modulus is not an inherent soil property; stress conditions, like those simulated in the AASHTO T307 test (2017), will change the observed values. Testing at various lateral stress levels is thus important so that stress simulation of the pavement section (or other soil structure section subject to dynamic loading) are captured. While chemically stabilized base course, virgin base course, and subgrade materials can be tested using this method, geosynthetic-stabilized sections are not captured as a single aggregate material is tested using AASHTO T307 (2017).

2.1.9 Numerical Modeling

Huang (2004) developed KENPAVE, a computer program to estimate stresses both concrete and asphalt pavements. The program addresses base course and subgrade through the elastic moduli and Poisson's ratios of multiple layers beneath the concrete slab. Detailed inputs are available for the construction of the concrete slab; similar to the AASHTO (1993) design methods, there are limited inputs for the underlying layers but a plethora of variations for the concrete slab. Loss of support or contact at the bottom of the slab can be input as well if those values are known. As KENSLABS (the concrete pavement portion of KENPAVE) will be used to estimate performance for different base course combinations in this study, detailed input parameters can be found in Appendix B. (Huang 2004)

KENSLABS, in KENPAVE, treats the slab/layer interfaces a series of springs at node coordinate inputs. Tire location and size coordinates are also input on the slab surface so that loading location impacts can be analyzed. Outputs of the program include vertical and shears stress contours in the slab as well as peak stress magnitudes. (Huang 2004)

2.2 Foundations

Concrete pavement can be looked at as a rigid shallow foundation with complex cyclic loading. Principles of basic foundation design should thus be kept in mind when evaluating concrete pavement systems. Westergaard's corner loading theory for a pavement slab is similar to an eccentric load on a shallow foundation.

Westergaard (1926) identifies the moment for corner loading of a concrete pavement as described in Eq. (2.27). This moment is independent of slab dimensions, so the eccentricity in Eq. (2.28) for the length and width will be equal. Westergaard (1926) stated that the distribution of stress in a concrete pavement from a circular load with a radius (a) equal to the slab height (h) will be distributed at the pavement-subgrade interface over a circular area with a radius equal to 0.944 times the height of the slab.

$$M = -\frac{P}{2}\left[1 - \left(\frac{a_1}{l}\right)^{0.6}\right] \tag{2.27}$$

where M is the moment, P is applied force at the surface, a_1 is the distance from the corner to the center of the circular applied load, and l is the radius of relative stiffness.

$$e = \frac{M}{P + W_f} \tag{2.28}$$

where M is the moment of surface loading of the rigid foundation, P is the applied surface force, and W_f is the weight of the foundation.

For foundational analyses, the assumption for loading on a rigid footing is that eccentricity is a factor for corner loading and estimation of equivalent bearing pressure.

Eccentricity is defined by Coduto (2001) as the ratio of the bending moment to the sum of the applied load and the weight of the footing. Eccentricity of loading is first identified as described in Eq. (2.28). Once eccentricity is determined, the effective width (B') and length (L') can be determined using Eq. (2.29) (Meyerhof 1963). The equivalent bearing pressure, at depth, is then determined using the effective area of the slab calculated from eccentricity using Eq. (2.30) (Coduto 2001). The concept is that the eccentric load on the beam will apply stress at depth over a smaller footprint than a centrally loaded rigid foundation, in which the applied surface force would be distributed over the entire area. When this force is offset, as in the case of corner loading of a pavement slab, the moment is taken into effect, the load area at depth is adjusted, and the resultant applied force beneath the rigid foundation is adjusted accordingly.

$$\left.\begin{aligned} B' &= B - 2e_B \\ L' &= L - 2e_L \end{aligned}\right\}$$

(2.29)

where B is the measured width of the slab, L is the measured length of the slab, and e_B and e_L are the eccentricities in the width and length directions of the slab, respectively.

$$q_{eq} = \frac{P + W_f}{B'L'} - u_D$$

(2.30)

where q_{eq} is the equivalent bearing pressure induced by the rigid foundation at depth, P is the applied surface force, W_f is the weight of the foundation, B' and L' are the effective width and length of the slab, and u_D is the porewater pressure at the foundation embedment depth.

The stress q_{eq} is theoretically the surface load applied at the top of the base course by the rigid concrete pavement slab over the area B' multiplied by L'. As distribution angle is estimated

using the radius of an applied circular load [see Eq. (2.14)], the radius of the applied load at the surface of the base course (a') may be estimated using Eq. (2.31).

$$a' = \frac{\sqrt{B'L'}}{\sqrt{2}} \tag{2.31}$$

2.3 Recycled Base Course

Aggregates for road construction are in sustainable demand. Since 1995, the per capita usage of aggregates in the United States has not fallen below 7 tons (Ober 2017). In 2016, the U.S. produced 2.8 million tons of construction aggregates, and production occurred in all 50 states (Ober 2017). Construction aggregates comprised 34% of U.S. production by revenue and 87% of mineral production tonnage in 2016 (Ober 2017). It is estimated that a person born today in the U.S. will consume over 1.4 million pounds of stone, sand and gravel, or materials used in construction (Ober 2017). These steady trends in demand necessitate the identification of low-cost sources for continuing construction demands. With an established roadway system in the U.S., focus of road construction should include cost-saving and environmentally friendly measures for both rehabilitation of existing roads and construction of new roads.

Recycled (or reclaimed) concrete aggregate (RCA) (also known as reclaimed concrete material, RCM, or recycled concrete pavement, RCP) has been used as a base course material throughout the United States. The AASHTO has designated RCA as an aggregate base course material (AASHTO 2015). RCA has been suggested in (cement) stabilized subbase cases based on cost and environment by federal and state agencies (Jung et al., 2012). Use of this material in concrete pavement applications will differ from the existing work for unpaved roads or asphalt pavements.

Reclaimed asphalt pavement (RAP) is typically processed for recycle into new asphalt. Material is ground out of existing pavements, crushed, and screened into coarse and fine fractions as deemed necessary by the asphalt mix design. Recycling asphalt saves in raw aggregate needs but more importantly in the reduction in need for expensive asphalt oil. The finer fraction of processed RAP will have a greater oil recovery, but it also increases the amount of waste fines that must be rejected from the mix. Because RAP is crushed and screened, it can be produced to meet base course specifications for gradation and plasticity index. However, it is not frequently used as a base course because greater financial benefit is achieved through its reuse in asphalt mix.

2.4 Geosynthetic Stabilization of Roads

2.4.1 How Geosynthetics Stabilize Roads

Geosynthetics have widely been used for the stabilization of unbound and asphalt pavements. Han and Thakur (2014) provided a summary of the state-of-practice for geosynthetic-stabilized RCA, including numerical modeling of asphalt pavements over geogrid-stabilized RCA, cyclic plate load tests (CPLT) of geogrid-stabilized RCA over subgrade (SG), and dialect tests on asphalt pavement overlays over geogrid-stabilized RCA. Geosynthetics provide three major benefits when used to stabilize subbase: separation (Figure 2.14), lateral restraint (Figure 2.15), and tension membrane effect (Figure 2.16) (Maxwell et al. 2005). Separation and preservation of base course layers are vital to the longevity of concrete pavements; allowable vertical deformation (less than 13 to 25 mm) in pavement is not great enough to mobilize the tensioned membrane effect.

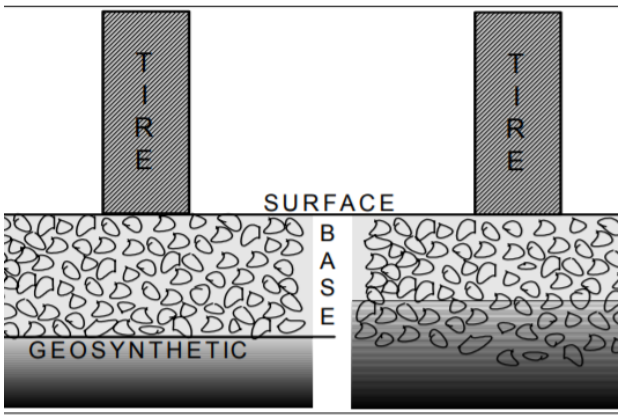

Figure 2.14. Geosynthetic separation effect (from Maxwell et al. 2005)

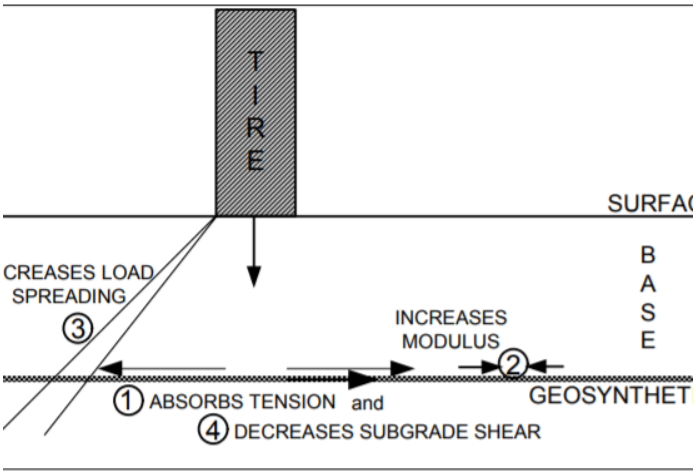

Figure 2.15. Geosynthetic lateral restraint effect (from Maxwell et al. 2005)

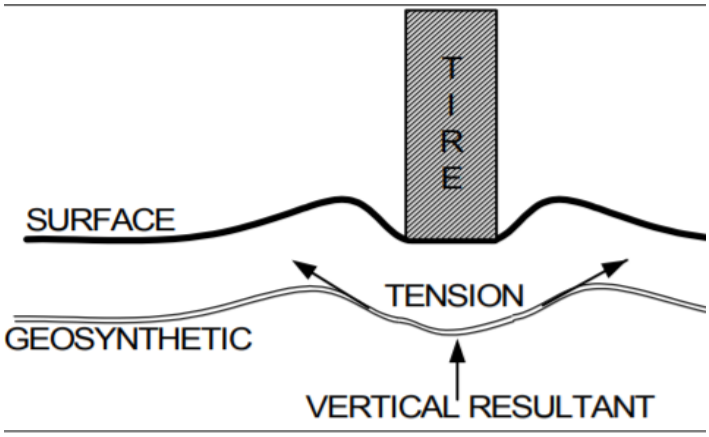

Figure 2.16. Geosynthetic tension membrane effect (from Maxwell et al. 2005)

2.4.2 Simplified Method

Giroud and Han (2004a, 2004b) did extensive work to develop design methods for unpaved roads when base course is stabilized with geosynthetics, particularly addressing the use of geogrid. The two papers work together to provide design methodology (Giroud and Han 2004a) and field calibration (Giroud and Han 2004b). The Giroud-Han method takes into account the use of geosynthetics, reduction in distribution angle with repeated cyclic loads, resilient moduli of the base course and subgrade, strength of the subgrade, applied load magnitude, and the ratio of the load radius to base course thickness (Giroud and Han 2004a,2004b). This design method is used extensively in the estimation of performance of stabilized base course sections in practice.

The Giroud-Han method serves to consider a comprehensive set of impacting variables on required base course thickness: stress distribution, base course material strength, geosynthetic/base course interlock, geosynthetic stiffness, traffic volume, tire pressure, wheel loads, strength of subgrade material, allowable rut depth, and geosynthetic-dependent failure mode (Giroud and Han 2004a). Eq. (2.32) displays the universal equation, along with typical values (Giroud and Han 2004a) (Giroud and Han, 2004b).

$$h = \frac{a + (b - dJ^2)\left(\frac{r}{h}\right)^{1.5} \log N}{f_E}\left[\sqrt{\frac{P}{\pi r^2 m N_c c_u}} - 1\right] r \qquad (2.32)$$

where: a = regression constant (1.26 for Gabr 2001 data set) (see Figure 2.17), b = regression constant (0.96 for Gabr 2001 data set) (see Figure 2.17), d = regression constant (1.46 for Gabr 2001 data set), J = aperture stability (m-N/^{o}) (0 for unreinforced and geotextile-reinforced sections) [*Note: b-dJ^2 must be greater than 0. This should be achieved by limiting J],* r = radius of equivalent tire contact pressure (m) = √[P/(πp)], h = (required) base course thickness (m), N =

number of axle passes, f_E = modulus ratio factor = 1 + 0.204 (R_E – 1), R_E =limited modulus ratio = *min*[(E_{bc}/E_{sg}), 5.0] = *min*[($3.48CBR_{bc}^{0.3}/CBR_{sg}$), 5.0], P = applied wheel load for half of one axle (kN) = P_A/ 2. P_A = axle load (kN), p = tire contact pressure (kPa), m = bearing capacity mobilization coefficient [Eq. (2.33)], N_c = bearing capacity factor (3.14 for unreinforced, 5.14 for geotextile-reinforced, 5.71 for geogrid-reinforced roads), c_u = undrained cohesion of subgrade (kPa) = f_C CBR_{sg} [(f_C = 30 kPa for this study) (CBR ≤ 5.0)].

$$m = \left(\frac{s}{f_s}\right)\left\{1 - \xi exp\left[-\omega\left(\frac{r}{h}\right)^n\right]\right\} \tag{2.33}$$

where: s = allowable rut depth (50 to 100 mm), f_s = 75 mm (constant), ξ = constant (0.9 to keep m from reaching 0 for small r/h), ω = regression constant [1.0 based on Giroud-Han data (2004b)], n = regression constant = [2.0 based on Giroud-Han data (2004b)].

The above equations can be calibrated using data from field testing and equivalent base course thickness (*h**) (Giroud and Han 2004b). Design thickness should also be checked against minimum base course thickness as described in Eq. (2.34) (Giroud and Han 2004b).

$$h_{min} = \frac{r}{\sqrt{\ln\left(\frac{0.9}{1 - \frac{f_s}{s}}\right)}} \geq 0.10m \tag{2.34}$$

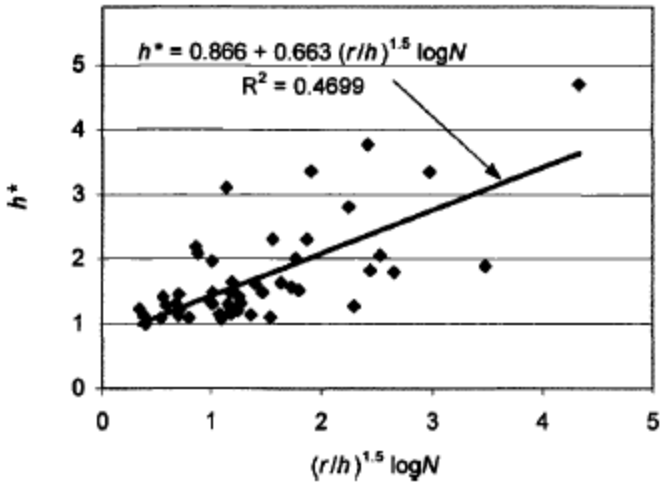

Figure 2.17. Calibration for a and b, assuming no geogrid, for Eq. (2.32) (Giroud and Han, 2004b).

One key point Giroud and Han (2004a) pointed out is the change in distribution angle with the number of applied load cycles. According to Giroud and Han (2004a), the initial stress distribution will be much larger at a typical index value and gradually decrease, focusing the load on a smaller area at the interface until a "failure" occurs. This phenomenon is described in Eq. (2.35). It should be noted that this equation is only valid for static loading, however.

$$\tan \alpha_1 = \tan \alpha_0 \left[1 + 0.204 \left(\frac{E_{bc}}{E_{sg}} - 1\right)\right] \quad (2.35)$$

where α_1 = stress distribution angle for static load, α_0 = reference distribution angle, E_{bc} = elastic modulus of base course, and E_{sg} = elastic modulus of subgrade.

Reference angle for different soils may be unique and can be estimated from control sections. Distribution angle for each load based on the measured change in vertical pressure at the base course-subgrade interface may be calculated using the Burmister (1958) formula [Eq.

(2.14)]. Plots of the inverse of the tangent of the distribution angle ($1/\tan \alpha_1$) against the log of the number of applied cycles (of a single magnitude) yields a linear trend; the common y-intercept determines the α_1 for N=1 for a "reference medium". Estimate of the ratio R_E of the medium and subgrade to back-calculate the reference angle using Eq. (2.35) for that material. For the material in Giroud and Han's study, the reference angle was determined to be 38.5° (Giroud and Han 2004a).

The commonly used reference angle in practice for α_0 is 26.7° (Han 2015). It is assumed for this study that an applicable reference angle for the given material will be that at which the deviator stress at the interface is equal to or greater than the bearing capacity of the subgrade. The relationship in Eq. (2.36) (Han 2015) identifies the relationship between stress distribution angle and the deviator stress at depth; rearranging the equation yields a solution for the reference angle at which failure should occur when the bearing capacity is fully mobilized (or m_{bc}=1) at the maximum applied surface load.

$$\Delta\sigma_{zi} = \frac{P}{\pi(r + h\,tan\,\theta)^2} = m_{bc}N_c c_u \rightarrow tan\,\theta = \frac{1}{h}\left[\sqrt{\frac{P}{\pi N_c c_u}} - r\right] \quad (2.36)$$

Change to base course elastic modulus may be estimated using the Giroud and Han (2004a) method. The elastic modulus ratio assumed from the previous paragraph and in Eq. (2.35) is now assumed to change with the change in distribution angle calculated using Eq. (2.14). Solving for the modulus ratio yields Eq. (2.37). Assuming that the modulus of the underlying layer does not change, the change in modulus over repetitive cycles can be estimated using Eq. (2.37). It should be noted that this method applies a formula for static loading to a

dynamically loaded road section; however, measured values used for this calculation are unique for the given applied load and the formulae used are not a function of the number of cycles.

$$E_{BC}/E_{SG} = \left[4.9\left(\frac{\tan\alpha_1}{\tan\alpha_0} - 1\right) + 1\right] \quad (2.37)$$

Several limitations exist with this method, despite its versatility and ability to be calibrated. One issue with Eq. (2.32) is that the base course thickness appears on both sides of the equation; continuity can be obtained using simple software (e.g. Microsoft Excel). Rut depths addressed in this method are between 50 and 100 mm (Giroud and Han 2004a); this would be too great a depth for concrete pavement design, which typically limits rut depth to 25 mm or less (AASHTO,1993). Subgrade CBR considered in this design method must be less than 5.0 (Giroud and Han 2004b); with improving technology such as lime stabilization that may increase bearing capacity of subgrades, this method may not be applicable without modification. Bearing failure within the base course section is not taken into consideration in this method; excessive deformation of the subgrade is assumed to be the failure mechanism (Giroud and Han 2004b). There is a mathematical limitation to the aperture stability modulus in Eq. (2.32) (Giroud and Han, 2004b); the full benefit of a stiffer geogrid may not be accounted for using this design method as a result. Despite these limitations, the method is widely applicable.

2.4.3 MEPDG Method

Sun et al. (2017a, b) applied Burmister's (1945) layered elastic solution along with the MEPDG damage model for cyclic plate loading tests with geosynthetic stabilization at the base course-subgrade interface. Sun et al. (2017a) discovered that due to larger rebound induced by geosynthetic reinforcement during cyclic loading, the resilient modulus back-calculated using

this elastic solution (Qian et al. 2011) did not reflect the resistance to permanent deformation and/or stress reduction of geosynthetic-stabilized base course sections. MATLAB code was written based on Figure 2.18 using MEPDG input parameters including load magnitude, number of load cycles, moisture contents, layer CBR's, base course thickness, and subgrade resilient modulus [assumed using Eq. (2.16)] combined with Burmister's settlement coefficient functions and the elastic modulus ratio E_1/E_2 (Sun et al. 2017a). Sun et al. (2017b) altered the damage model from MEPDG as displayed in Eq. (2.38). Calibration factor for the base course k_b was treated as a constant value for a given aggregate, but the subgrade calibration factor k_s was changes based on the interface stress using Eq. (2.39).

$$\delta_{p,1} = k_b \cdot p \cdot f_b(E_e, E_s, z, a)\left(\frac{\varepsilon_0}{\varepsilon_r}\right)_b e^{-\left(\rho_b/N\right)^{\beta_b}} + k_s \cdot p \cdot f_s(E_e, E_s, z, a)\left(\frac{\varepsilon_0}{\varepsilon_r}\right)_s e^{-\left(\rho_b/N\right)^{\beta_s}} \quad (2.38)$$

where $\delta_{p,1}$ = permanent deformation at surface of base course, $k_{b,s}$ = calibration factor, p= applied load, f_b = Burmister's settlement coefficient function, material properties are listed in Eq. (2.24).

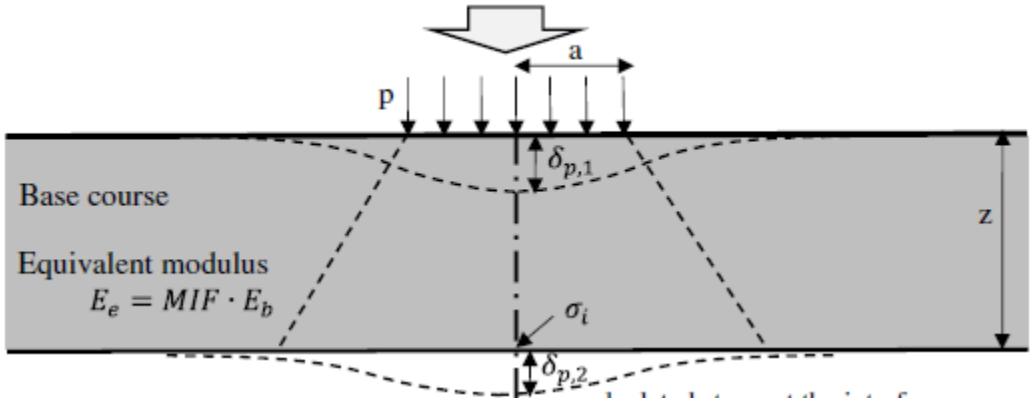

Figure 2.18. Base course and subgrade deformation under axial plate load (Sun et al. 2017a).

$$k_s = a \cdot e^{-b \cdot CBR_{SG}} \frac{p}{N_c c_u}$$

(2.39)

where k_s = subgrade calibration factor for MEPDG damage model, CBR_{SG} = California Bearing Ratio of the subgrade, p= applied load, N_c=3.14, c_u= 30*CBR_{SG} (kPa), and *a* and *b* are regression constants.

2.4.4 Test Evaluation

The moduli of geosynthetic-stabilized base courses can be determined using large-scale plate loading tests based on three methods: (1) resilient deformation, (2) vertical stress at the base-subgrade interface, and (3) permanent deformation.

Large scale tests have been used to determine resilient modulus through cyclic plate load tests (CPLTs). Qian et al. (2011) used the elastic solution for deformation on a half-space medium [Eq. (2.40)] to calculate subgrade resilient modulus without any geosynthetic from CPLTs using the measured resilient deformation (i.e. elastic rebound) and found their values close to commonly-used correlations in the literature. However, this method was found invalid for geosynthetic-stabilized roads because the inclusion of geosynthetic may increase the resilient deformations (rebounds) of the roads due to the release of lateral restraint and the tensioned membrane during unloading (Sun et al. 2015).

$$M_r = \frac{p_i B I (1 - \nu^2)}{\delta}$$

(2.40)

where p_i is applied vertical stress, B is the loading plate diameter, ν is the Poisson's ratio, δ is elastic displacement, and I is the displacement influence factor (0.79 for a rigid plate, 1.0 for a flexible plate).

Huang (2004) relates the modulus of subgrade reaction (k-value) to resilient modulus using Eq. (2.41) but warns that plates with radii smaller than 375 mm yield falsely high k-values.

$$k = \frac{q}{w_0} = \frac{2M_r}{\pi(1-\nu^2)a} = \frac{4p_i I}{\pi\delta} \tag{2.41}$$

where q = applied load (static); w_0 = δ = deflection; a = radius of plate; ν = Poisson's ratio (assumed to be 0.45 both by Huang and in this study); p_i = applied vertical stress; I = displacement influence factor.

To combat the issue of varying plate size for field and laboratory plate load tests (PLTs), Putri et al. (2012) conducted a study on plate size variation and resultant outputs. The relationship between plate size, deflection, and k-values are summarized in Eq. (2.42). Using this predictive relationship allows for the estimations of modulus of subgrade reaction and resilient moduli to be corrected to the standard 375 mm diameter plate used in Westergaard's (1926) tests and overcome the small plate size issue designated by Huang (2004).

$$\frac{\left(p/\delta\right)_1}{\left(p/\delta\right)_2} = \frac{k_1}{k_2} = \sqrt{\frac{A_2}{A_1}} = \frac{r_2}{r_1} \tag{2.42}$$

where p = applied surface pressure, δ = surface deflection, k = modulus of subgrade reaction, A= area of applied surface load, and r = radius of circular load plate.

Tamrakar et al. (2019) performed automated plate load tests in the field on both virgin and recycled aggregate base course sections with and without multiaxial geogrid, and they made several important discoveries. They denoted N* as the number of cycles required to reach a steady state of deformation where the incremental permanent vertical displacement and the resilient vertical displacement were linear, and this N* value was greatly reduced by the addition of geogrid at the base course-subgrade interface. Subsequently increasing load cycles and stress levels resulted in both greater permanent and resilient deformations for recycled concrete aggregate and virgin aggregate base course with and without geogrid stabilization. For a constant stress of 103 kPa, non-stabilized sections exhibited four times the permanent deformation of geogrid-stabilized sections at 10,000 cycles (Tamrakar et al. 2019).

Chapter 3. Experimental Design and Procedure

To evaluate the performance of geosynthetic-stabilized recycled granular bases in unpaved roads and concrete pavements, experimental tests were conducted in this study. The goal of the test method for these experiments is to replicate a field condition and/or standard test method. A large box was used in this study for constructing and cyclically loading test sections to simulate roadway traffic loading. Material properties were determined prior to testing, and a comprehensive plan to control the construction quality of the test sections was created. The following sections discuss the conception and development of the experiments for the given dataset.

3.1 Material Selection and Properties

For pavement applications, the materials used in this study include subgrade, granular base, concrete, and geosynthetic. Non-woven geotextile, woven geotextile, and triaxial geogrid were selected based on the KDOT pre-approval list. The virgin aggregate selected in this study follows the KDOT specification for granular base. Below are the descriptions of these materials.

3.1.1 Subgrade

To properly compare the base course options for unpaved roads and concrete pavements, additional variables for other materials need to be controlled or eliminated. To create a consistent subgrade, a blend of processed, powdered kaolin and ASTM C33 sand with water was used. Similar blending procedures for subgrade have been used in prior research (e.g., Guo et al. 2016).

The ASTM C33 sand came from an aggregate producer in the Lawrence, Kansas, area. Material was mined from the Kansas River. It is tan to orange in color, clean and free of debris. The sand material was tested as non-plastic using ASTM D4318 (2010). Gradation of the sand can be found in Figure 3.1 following the test procedures in ASTM D1140 (2017) and ASTM D421 (2007).

Kaolin for this blend was an EPK clay from Edgar Minerals out of Florida. This fine material had a mean particle size of 1.36 microns; it was extremely fine and was delivered in 23-kg (50-lb) bags (Edgar Minerals, 2018). Specific gravity of the kaolin is 2.65, pH is 5.5 to 6.5, and the water retention is 25% (Edgar Minerals 2018). Atterberg limit tests were performed for the different pallets received following ASTM D4318 (2010) and their test results are presented in Figure 3.2; the Liquid Limit (LL) is approximately 60%, and the Plasticity Index (PI) is approximately 25%.

To prepare subgrade, these two components were blended by weight at a ratio of 25% kaolin to 75% sand. Sand was weighed by a 19-L (5-gallon) bucket to fill a skid steer loader attachment and moisture content was taken; dry weight per skid steer bucket (136 kg or 300 lb) was thus determined. Bags of kaolin were weighed to confirm they contained 23 kg (50 lb) of material and added accordingly to measured piles of sand (by counting loader buckets). Mixing was then performed to uniformity using shovels, the skid steer, and fine water mist for airborne particle control.

Once the subgrade was mixed, index properties were obtained in the soils laboratory. Wet sieve analysis was performed on the mixed subgrade material grabbed from stockpile as displayed in Figure 3.3. Subgrade samples were compacted in a 150-mm (6-in) Standard Proctor

mold (ASTM D698 2012); these samples were used to perform California Bearing Ratio (CBR) tests (ASTM D1883 2016) as well as hand-held vane shear tests (ASTM D4648 2016). Unconfined Compression (UC) samples were also prepared and tested (ASTM D2166 2016). Figure 3.4, Figure 3.5, and Figure 3.6 show these test results. A relationship of 30 multiplied by the expected CBR yields the hand-held vane shear (VS) reading in kPa. Values for UC undrained shear strength are approximately half those obtained using the hand-held vane shear.

Full-scale testing in the big box reflects similar results to those obtained using the vane shear in the Proctor molds, as will be discussed in subsequent sections. Because target CBR for the subgrade in testing was 2%, this value was targeted for moisture content-density-undrained shear strength testing in the big box. As shown in Figure 3.5, tests were conducted wet of the optimum moisture content to achieve these CBR values. Quality control in the big box for the full-scale tests depended upon the hand-held vane shear and the dynamic cone penetrometer (DCP) values (ASTM D7380 2008).

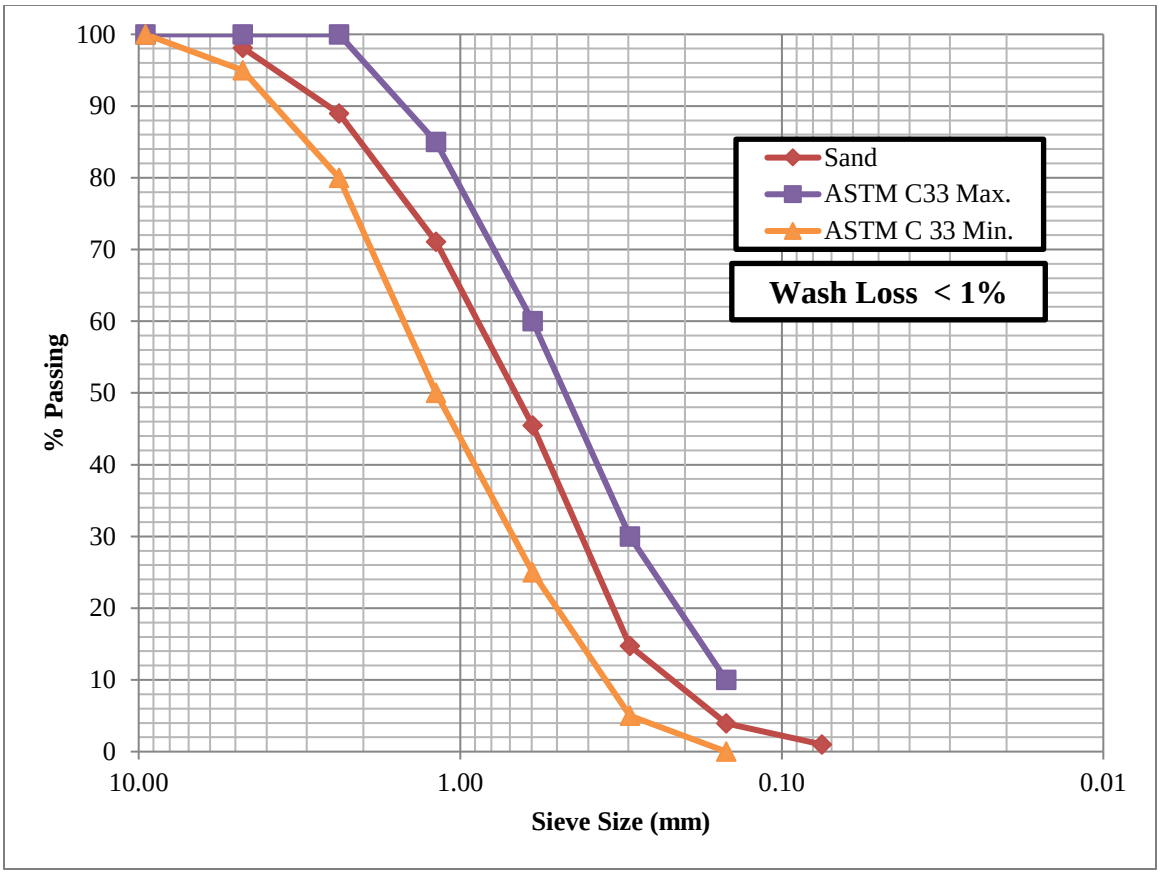

Figure 3.1. Gradation of As-Received Sand for Subgrade Blend.

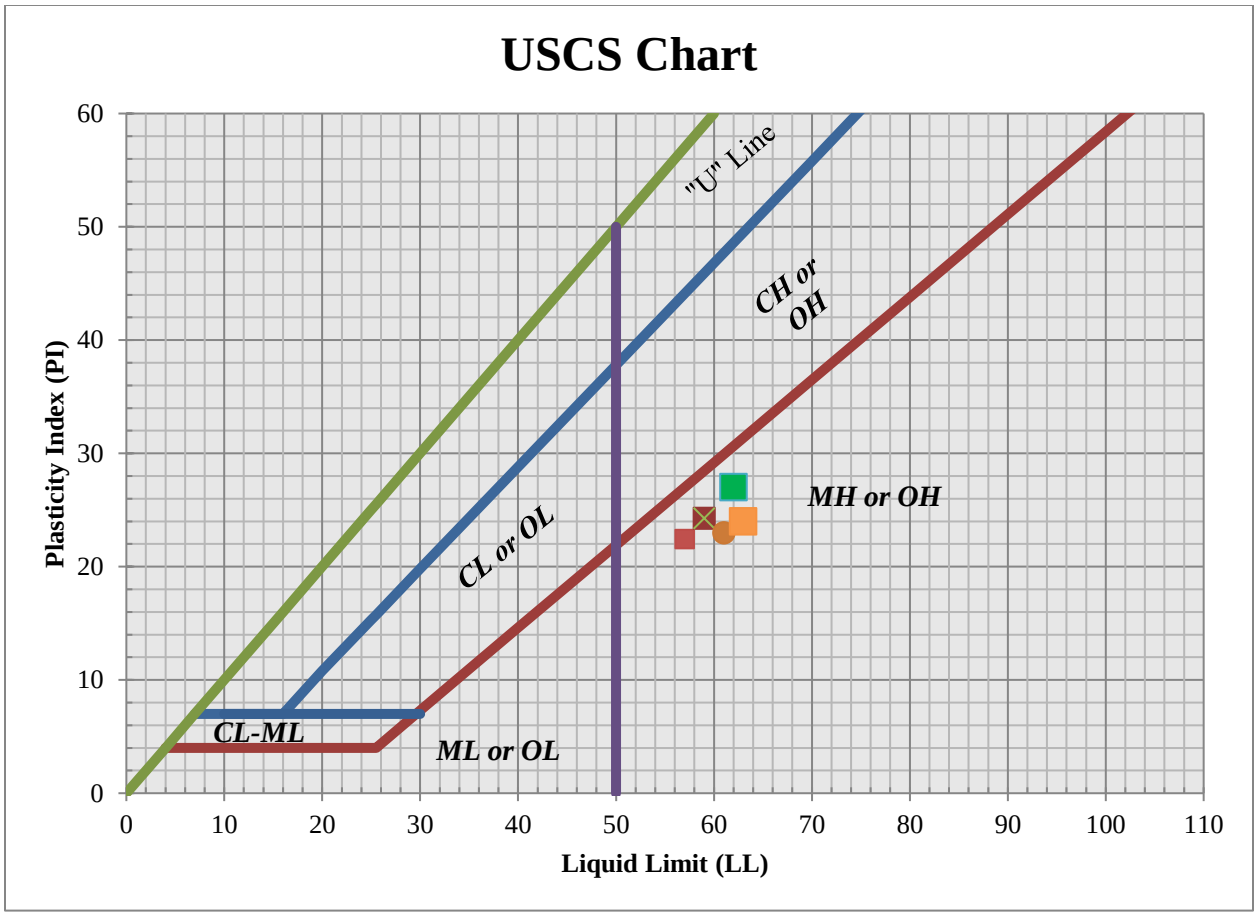

Figure 3.2. Atterberg Limits of EPK Kaolin As-Received from Edgar Materials.

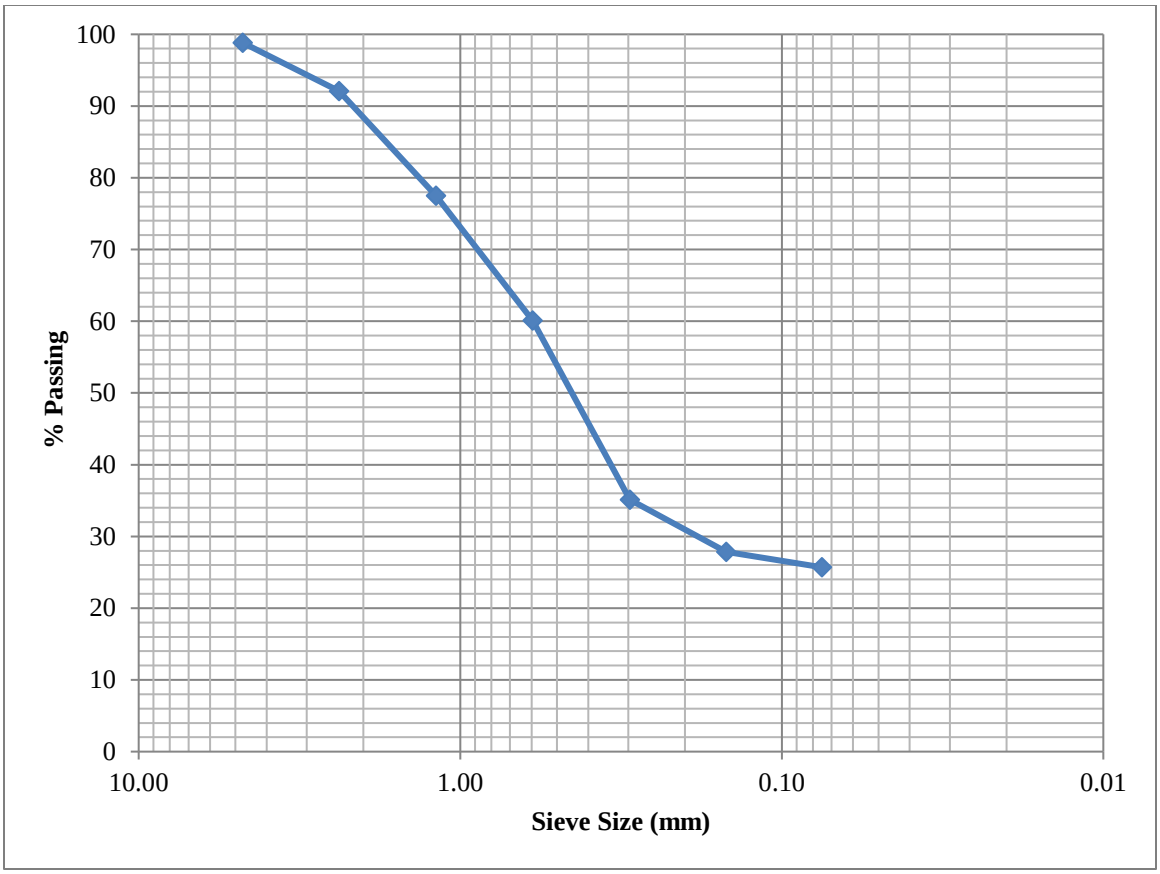

Figure 3.3. Subgrade Stockpile Sample Gradation.

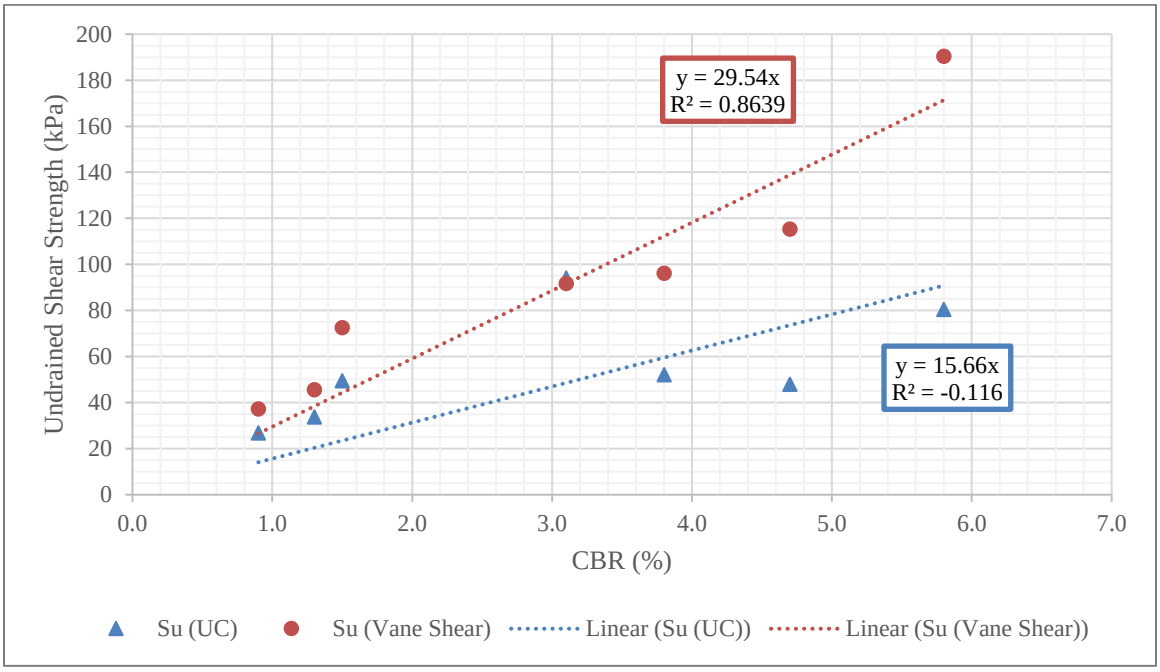

Figure 3.4. Subgrade Laboratory Undrained Shear Strength vs. CBR.

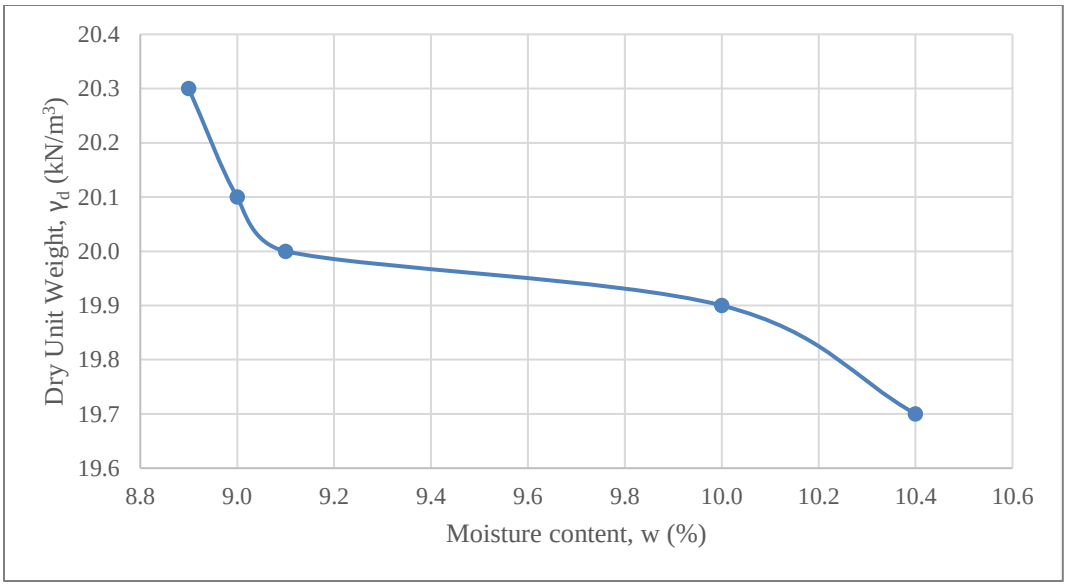

Figure 3.5. Subgrade Standard Proctor Dry Density vs. Moisture Content.

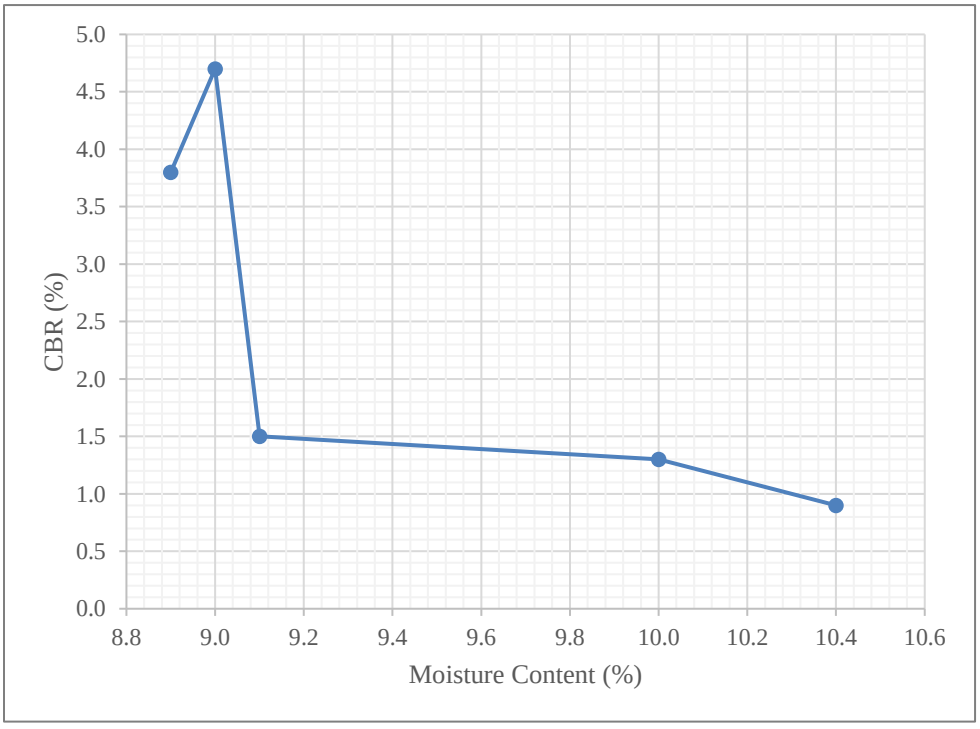

Figure 3.6. Subgrade Moisture Content vs. CBR from Standard Proctor Mold.

3.1.2 Virgin Granular Base (VGB)

Granular base material used in this study conforms to the Kansas Department of Transportation (KDOT) specification for granular base. This material consisted of crushed limestone from a local (near Lawrence) aggregate source. Sieve analysis following ASMT D1140 (2017) and ASTM D421 (2007) was conducted upon receipt of the base course material and during testing to assure the specification was met. Obtaining minimum 95% relative compaction based on the maximum dry density from the Standard Proctor (ASTM D698 2012) was necessary during the big box testing for accurate road simulation. The VGB Standard Proctor curve is shown in Figure 3.8. The optimum moisture content and maximum dry density of the VGB were 7.1% and 21.2 kN/m^3 (135 pcf), respectively. The dry density at 95% relative compaction was 20.2 kN/m^3 (128 pcf) and corresponded to a moisture content range of 6.6% to 7.5%.

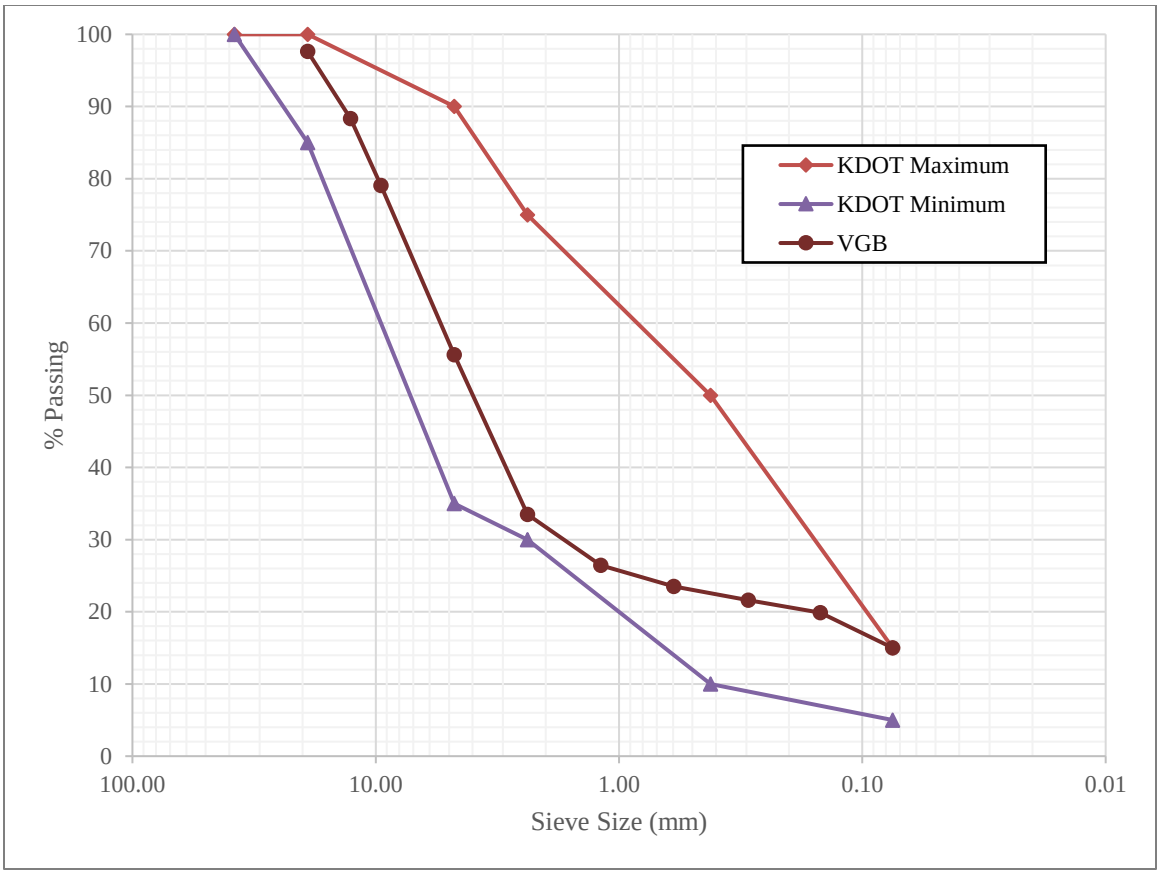

Figure 3.7. Virgin Granular Base (VGB) Sieve Analyses and KDOT Specification.

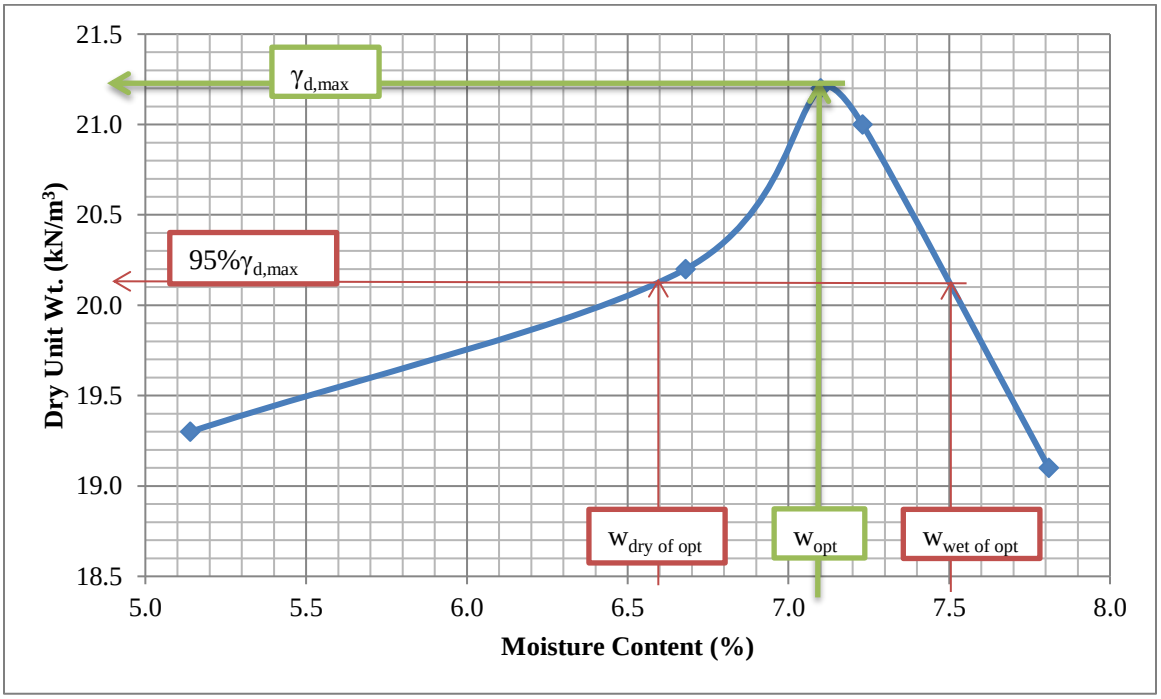

Figure 3.8. Virgin Granular Base (VGB) Moisture-Density Curve.

3.1.3 Recycled Concrete Aggregate (RCA)

Recycled Concrete Aggregate (RCA) was sourced from a local producer. As is typical, the source of the pavement crushed into RCA is unknown; inherent variability is part of using an RCA product, especially if the source is unknown. Water ran freely out of this RCA material, rendering it as non-plastic (NP) when attempting to run Atterberg limit tests (ASTM D4318 2010). Sieve analysis shows that the gradation of this material meets the KDOT specification for granular base (see Figure 3.9). Maximum dry unit weight and optimum moisture content from the Standard Proctor test (ASTM D698 2012) were 17.9 kN/m^3 (114 pcf) and 12.8%, respectively (see Figure 3.10). Relative compaction of 95% was achieved at 17.0 kN/m^3 (108 pcf) dry unit weight; the moisture content range to achieve compaction was 9.8% to 17.5%.When compared with the VGB in terms of the moisture range, the RCA is a more absorptive material and is less sensitive to changes in moisture content.

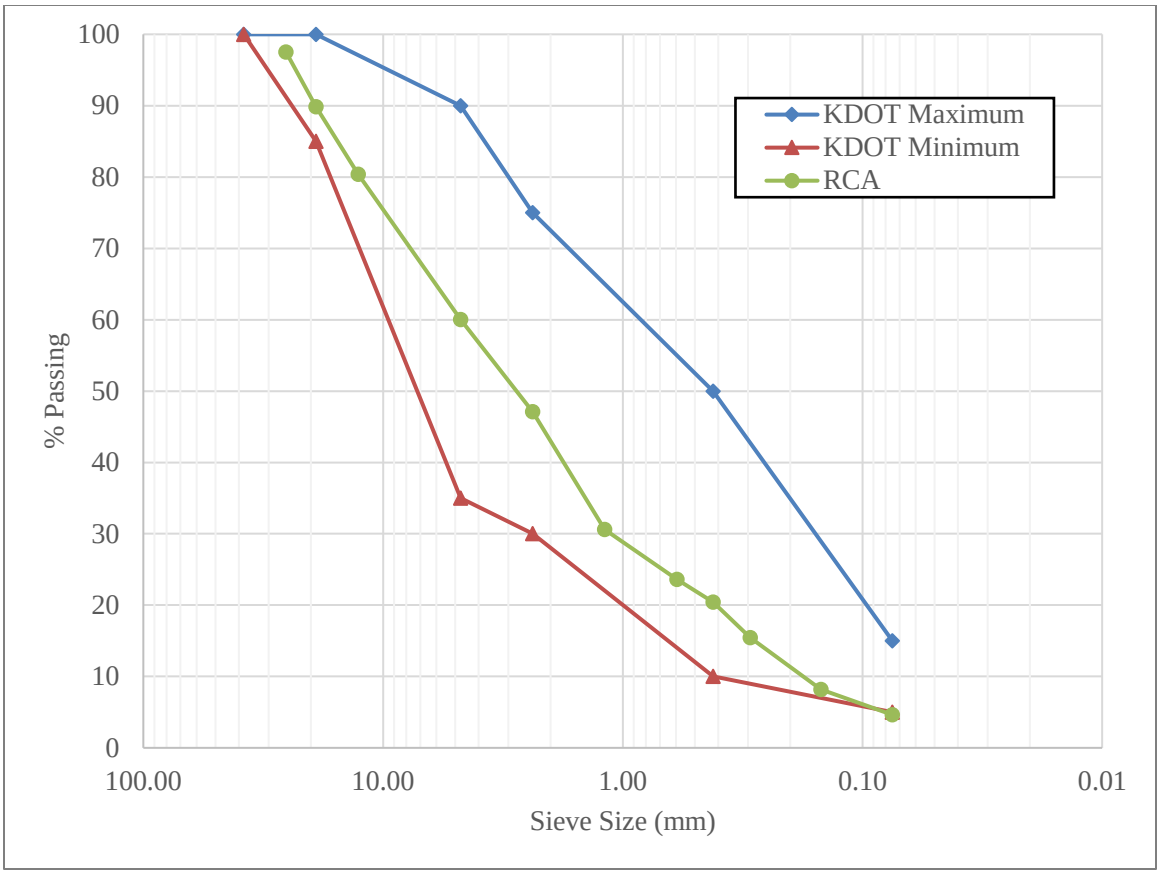

Figure 3.9. RCA Sieve Analysis vs. KDOT Granular Base Specification.

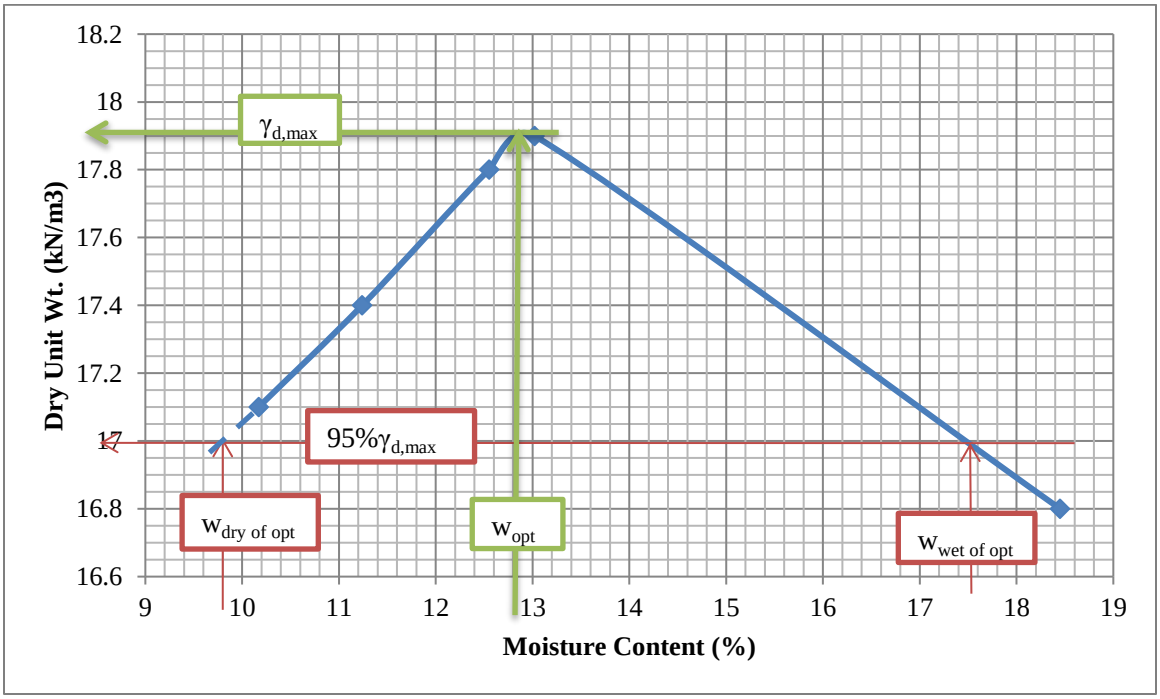

Figure 3.10. RCA Moisture-Density Curve.

3.1.4 Reclaimed Asphalt Pavement (RAP)

Reclaimed Asphalt Pavement (RAP) was also sourced from a local producer. While the pavement source is unknown, RAP is typically processed for reuse in asphalt pavement, so the quality is more closely controlled than in RCA products. The current trend for RAP processing is to fractionate into coarse and fine fractions; the coarse fraction provides more aggregate replacement, while the fine fraction allows for greater asphalt oil recovery. For this study, the "after-burn" gradation, or the aggregate gradation after the oil was burned off in an ignition oven, is used for comparison against the KDOT granular base specification (see Figure 3.11). To meet the specification, the coarse fraction RAP was selected for this study. The asphalt oil content was 4.56%, as determined by the RAP provider. A Standard Proctor test was performed to determine the moisture-density relationship for test section construction; the maximum dry unit weight and optimum moisture content of the RAP were 16.9 kN/m^3 and 1.95%, respectively. The hydrophobic nature of oil yielded a much drier optimum moisture content and a narrower range of moistures (0.6% to 3.2%) to achieve 95% relative compaction at 16.1 kN/m^3. The entrainment of fines in oil bound to the surface of larger aggregate particle hindered compaction.

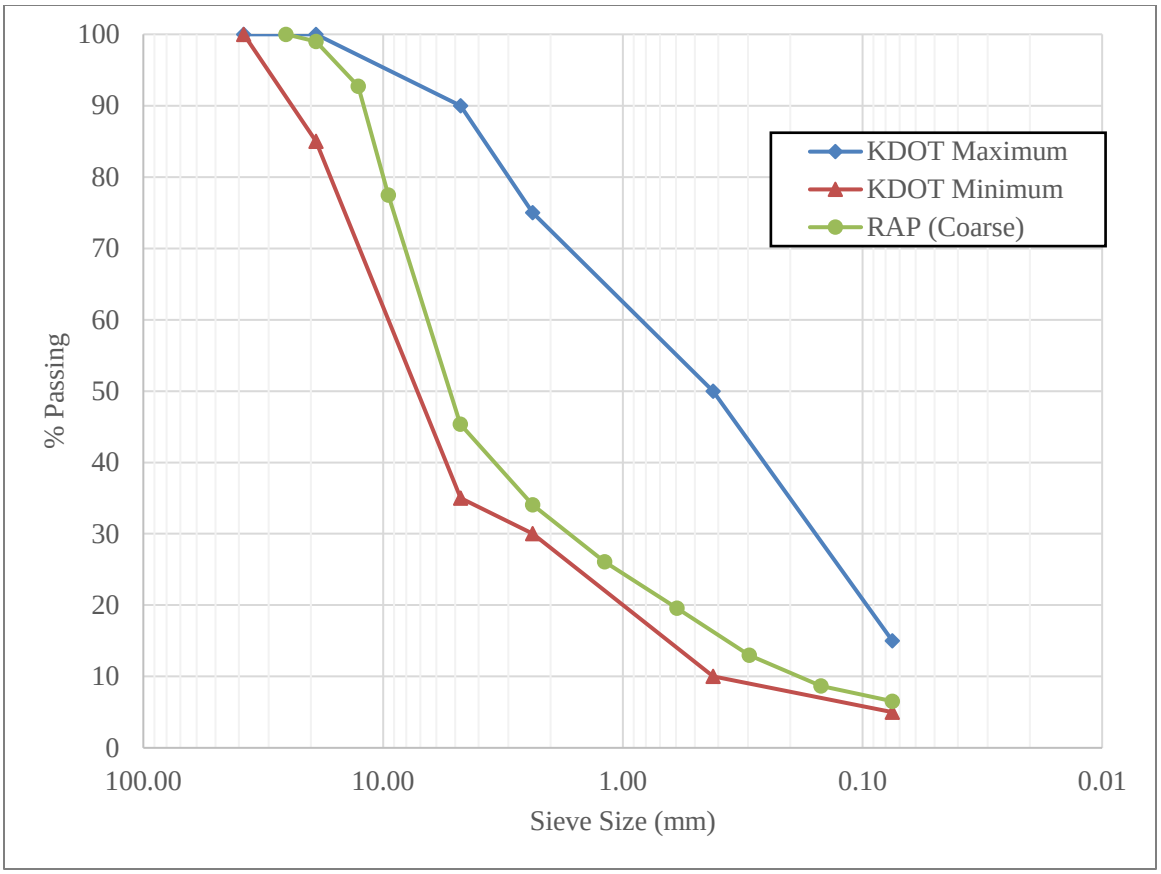

Figure 3.11. Coarse RAP Gradation vs. KDOT Granular Base Specification.

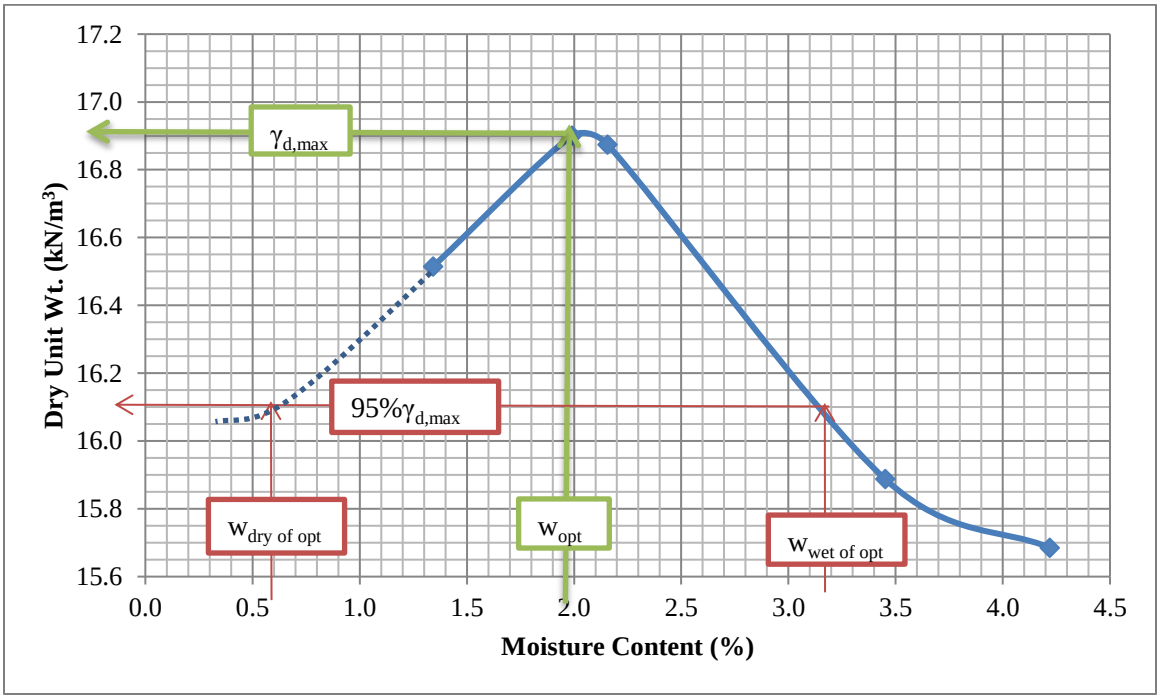

Figure 3.12. RAP Standard Proctor Moisture-Density Curve.

3.1.5 Geosynthetics

Geosynthetics for this project were chosen from the KDOT list of pre-qualified materials (KDOT 2018). This ensures that the testing is applicable to current practice. It also allows the results to be based upon inherent advantages and disadvantages of each type of geosynthetic typically used in practice, i.e. nonwoven geotextile (symbol: NW, Figure 3.13) vs. woven geotextile (symbol: W, Figure 3.14) vs. triaxial geogrid (symbol: GG, Figure 3.15). Table 3.1, Table 3.2, and Table 3.3 display the properties of each geosynthetic used.

Table 3.1. Nonwoven Geotextile Properties.

Geosynthetic Type	**Non-Woven Geotextile (NW)**
KDOT LIST?	Yes
Grab Strength (N)	710
Tear Strength (N)	270
Puncture Strength (N)	420
Burst Strength (kPa)	2,100
Permittivity (s^{-1})	1.4
AOS (mm)	0.212
UV Stability (%)	70

Figure 3.13. Nonwoven Geotextile.

Table 3.2. Woven Geotextile Properties.

Geosynthetic Type	Woven Geotextile (W)
KDOT LIST?	Yes
Tensile Strength (kN/m) @ 2% Strain	14
Tensile Strength (kN/m) @ 5% Strain	35
Tensile Strength (kN/m) @ 10% Strain	70
Tensile Strength (kN/m) ultimate	70
Permittivity (s^{-1})	0.4
AOS (mm)	0.600
UV Stability (%)	80

Figure 3.14. Woven Geotextile (after RAP Test).

Table 3.3. Triaxial Geogrid Properties.

Geosynthetic Type	Geogrid-Triaxial (GG)
KDOT LIST?	Yes
Junction Efficiency	93%
Radial Stiffness (kN/m @ 5% strain)	225
Rib Pitch (mm)	40
Mid-Rib Depth (mm)	1.2
Mid-rib Width (mm)	1.1
UV Stability (%)	70

Figure 3.15. Triaxial Geogrid (with VGB).

3.1.6 Concrete

A quick-cure, commercially available concrete mix was selected for timing purposes as well as to remove any human factors in mix design. Typical concrete pavement has a 28-day unconfined compressive strength of 21 MPa (Huang 2004); the goal for this study was to accelerate testing by achieving this minimum strength in 7 days instead of 28 days, so the commercial concrete

mix was selected that meets this minimum strength (see Figure 3.16). Water was added according to bag directions at 2 liters per 27.2 kg bag of concrete to yield 0.014 cubic meter per bag. Concrete and water were mixed to uniformity, poured into grease- and foam-lined wooden formwork inside the big box, hand-tamped and hand-smoothed to construct concrete slabs for a pavement.

Two samples were taken from the mixed concrete during pouring and cured in a humidity-controlled room for 8 days to confirm the unconfined compressive strength. Compressive strength (f'_c) was tested at an average of 28.5 MPa at 8 days, which is higher than the rated strengths from the manufacturer (see Figure 3.16). Using the American Concrete Institute (ACI) recommendations, the modulus of rupture (f_r) of standard-strength concrete using Eq. (3.1) is 3.31 MPa and the modulus of elasticity E_c is 25.3 GPa based on Eq. (3.2) (ACI 2019, Oluokun et al. 1991). By shifting the curve from the measured values (Figure 3.16), the 7-day f'_c was estimated as 27.7 MPa, the tensile strength from Eq. (3.1) was 3.26 MPa, and the modulus of elasticity from Eq. (3.2) was 24.9 GPa.

$$f_r = \begin{cases} 7.5\sqrt{f'_c(psi)} \\ 0.62\sqrt{f'_c(MPa)} \end{cases} \tag{3.1}$$

$$E = \begin{cases} 57{,}000\sqrt{f'_c(psi)} \\ 4{,}700\sqrt{f'_c(MPa)} \end{cases} \tag{3.2}$$

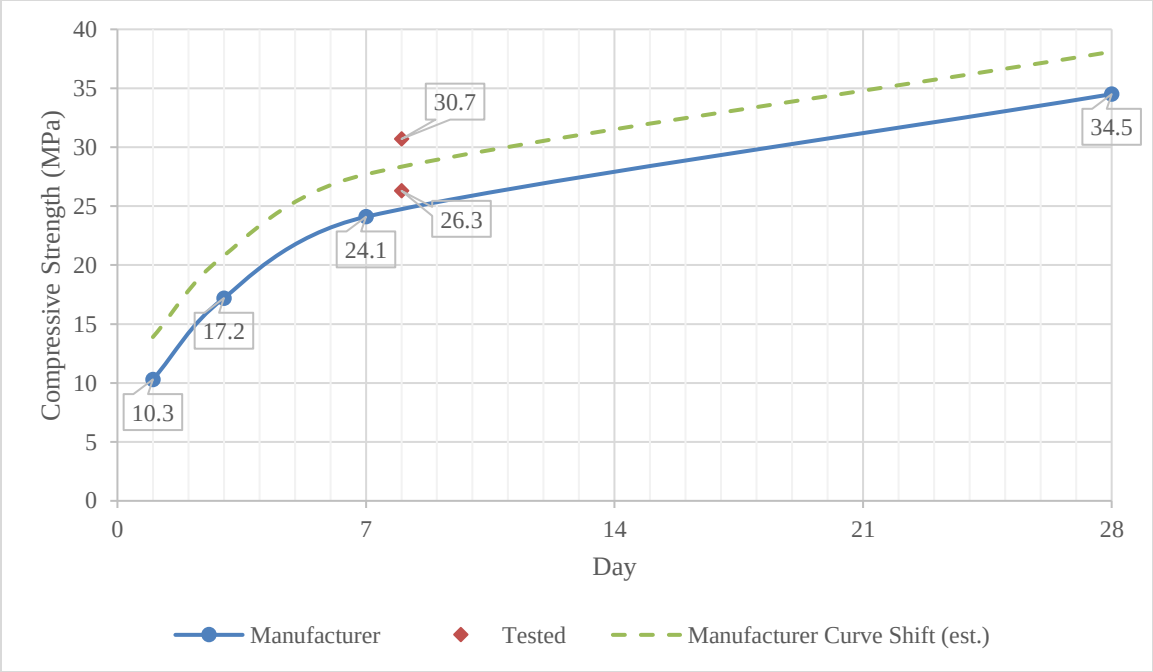

Figure 3.16. Concrete Compressive Strength.

3.2 Test Section Preparation in the Box

Figure 3.17 depicts the big box section for large-scale plate load testing. A steel plate 300 mm in diameter applies a rigid load to the surface of compacted base course via a 245-kN-capacity actuator. The base course section was 250 mm thick over 900 mm of weak (2%-CBR) subgrade. The actuator was hinged to allow for leveling of the plate and to prevent equipment damage in the event of a system overload. The following sections detail how the test section was constructed.

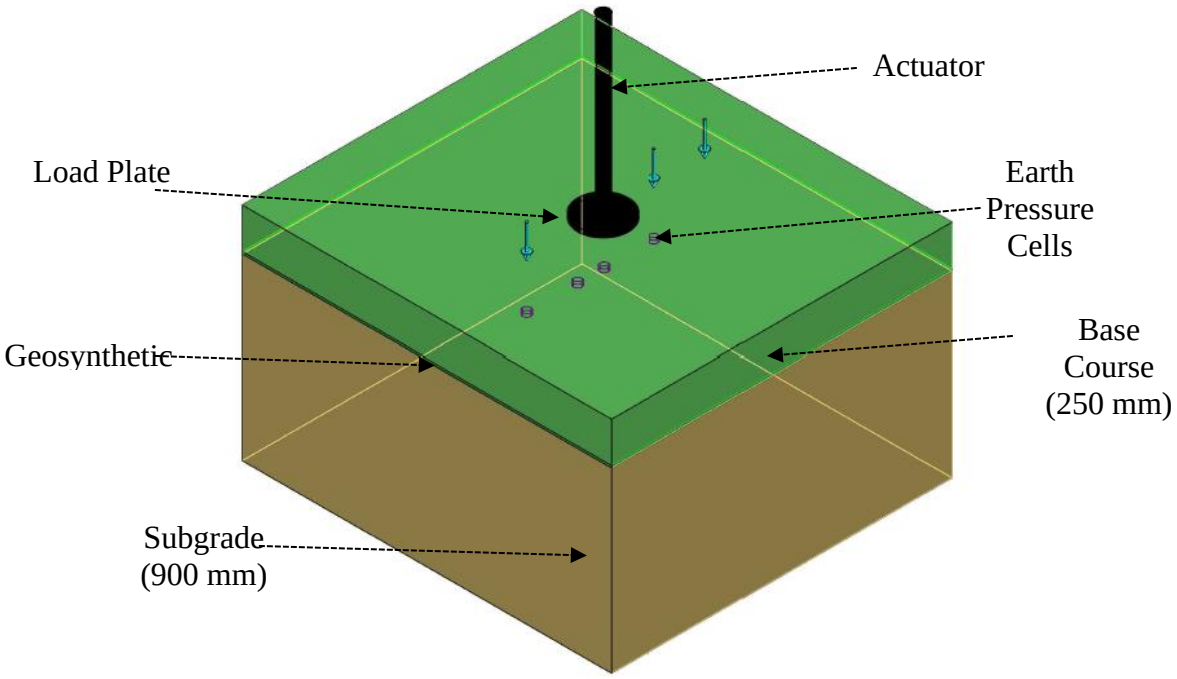

Figure 3.17. Test Section Construction

3.2.1 Subgrade

Subgrade was blended outdoors to the target moisture content based on the CBR-moisture content curve in Figure 3.6. It was noted during test construction and through DCP testing that the moisture content needed to be increased to 9.76% to achieve 2% CBR in the box; this varied slightly from the value obtained in laboratory testing in Figure 3.6. Once the target moisture content was confirmed, material for the subgrade lift was brought into the box using the skid steer and roughly leveled by hand tools. The layer was then compacted using a vibratory compactor. Six 150-mm lifts of subgrade were used. Quality control was performed on each layer using a hand-held vane shear device (see Figure 3.4), but quality assurance and determination of the section subgrade CBR was taken from DCP tests; these test results can be observed in Appendix A. Once the subgrade quality was assured, earth pressure cells (EPC) were installed in the surface of the subgrade to measure vertical interface stresses during loading.

3.2.2 Geosynthetic

When a geosynthetic product was part of the test section, it was placed at the top of the subgrade after the installation of earth pressure cells. To assure adequate coverage and anchoring, the geosynthetic was cut so that approximately 100 mm additional material was left on each of the four sides. The stabilizing geosynthetic layer (nonwoven geotextile, woven geotextile, or triaxial geogrid) was gently tensioned by holding the corners to the box edges and smoothing by hand. The geosynthetic was then secured in each corner through railroad spikes hammered through the geosynthetic into the subgrade.

3.2.3 Base Course

Two lifts of base course were then compacted in place atop the geosynthetic (or subgrade in the case of control sections). Prior to placement, vertical markers for 250 mm from top of subgrade or geosynthetic were marked along the inside of the big box. Each lift was 125 mm in thickness, creating a 250-mm-thick base course section over weak subgrade. Base course material was prepared to the optimum moisture content outside the lab, then brought in via skid steer and hand-leveled roughly. The same vibratory compactor was used on each lift. The surface layer was checked for level beneath the plate to assure full contact with the load plate. Quality assurance was performed for dry density using the sand cone test (ASTM D1556 2016) to assure 95% minimum relative compaction. Thickness of the section was also confirmed by direct measurement after removal of steel beams, as displayed in Figure 3.18.

Figure 3.18. Direct Measurement of Base Course Thickness Post-Test.

3.2.4 Concrete Slabs

When present, concrete slabs of 150-mm thick were poured in the box atop the compacted base course. No reinforcement was used in the concrete slabs, and no load transfer devices (such as dowel bars or tie bars) were installed at the joint. The slabs were poured such that the 150-mm loading plate applied a corner load to one slab. An adjacent slab was poured with an open (unreinforced) 12.5-mm joint. A rebar lifting hook was set in the center of each slab to help with extraction after the test (see Figure 3.23 and Figure 3.24). Concrete cured for 7 days beneath wetted burlap prior to applying the first load sequence. Loose aggregate was filled level next to the slabs as a pavement shoulder and hand tamped before loading. After the initial load sequence at Day 7 of curing, 300 liters of water were applied to the test section through a sprinkler system (see Figure 3.25). The wetted section was left overnight, and the second load sequence was applied at Day 8. Figure 3.19 through Figure 3.22 depict the layout of the big box with the concrete slabs. Figure 3.23 displays the framework and partially poured Slab 1. Slab 1 was the

loaded slab where most measurements were taken, while Slab 2 was the “other” slab present to simulate a joint and to measure adjacent slab displacements.

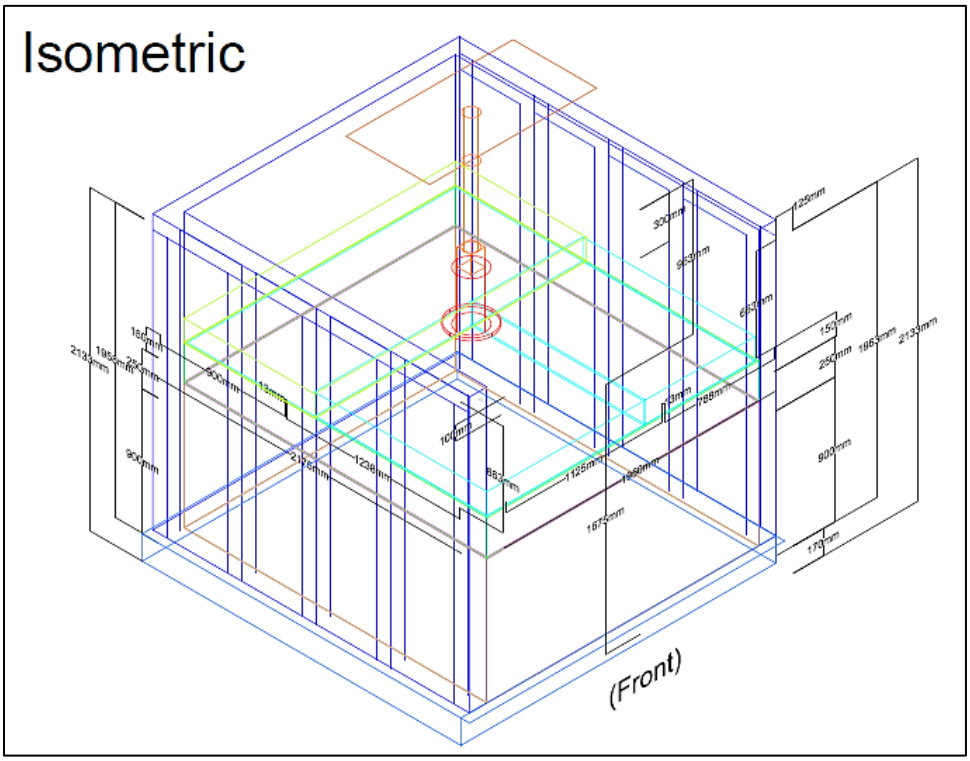

Figure 3.19. Big Box Layout with Concrete Slabs, Isometric View.

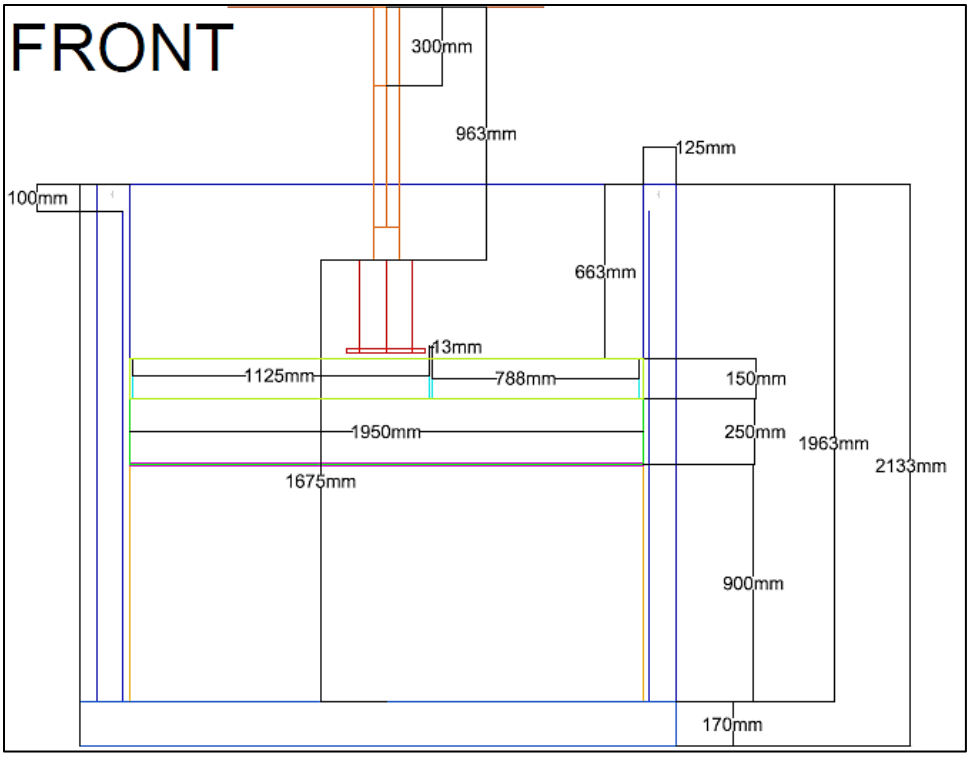

Figure 3.20. Big Box Layout with Concrete Slabs, Front View.

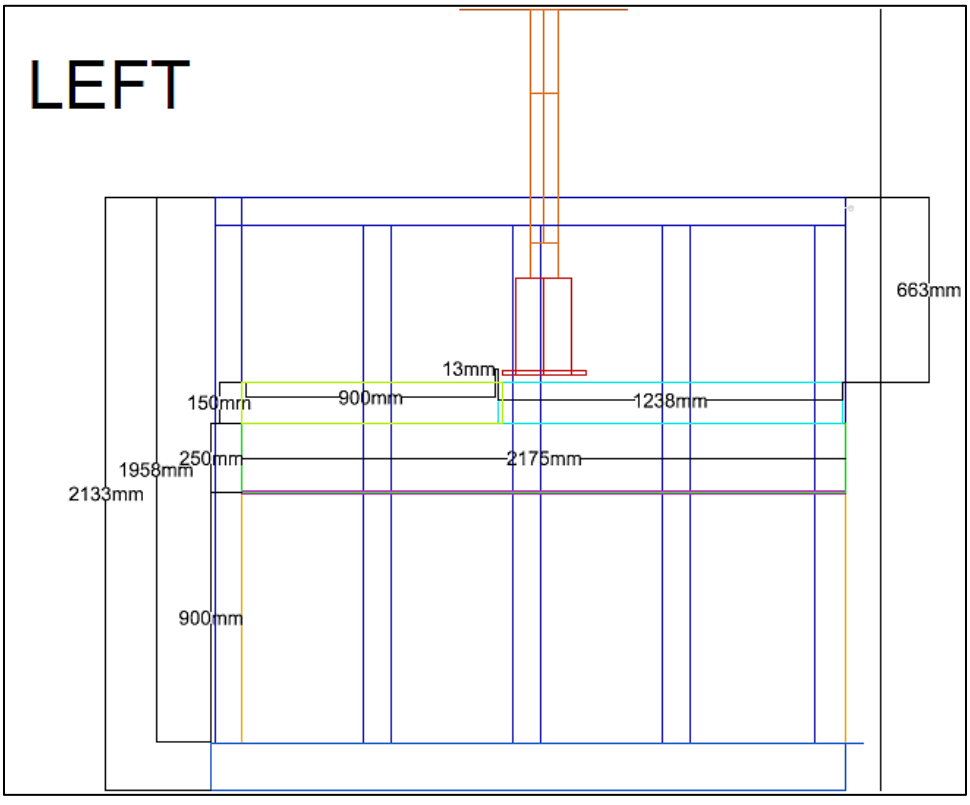

Figure 3.21. Big Box Layout with Concrete Slabs, Left View.

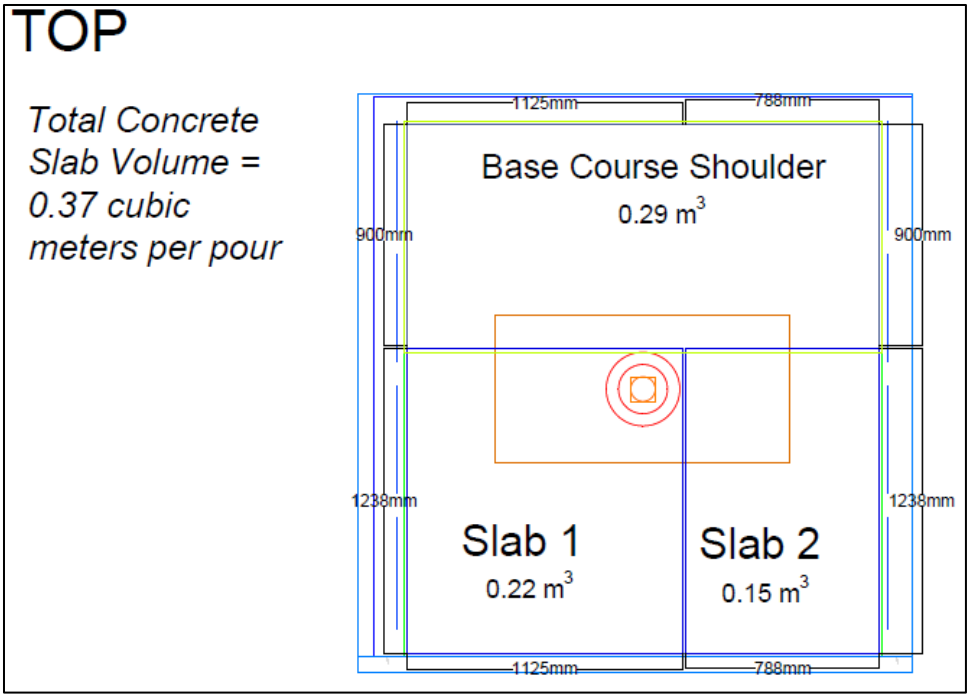

Figure 3.22. Big Box Layout with Concrete Slabs, Top View.

Figure 3.23. Loaded Concrete Slab During Pour and Compaction.

Figure 3.24. Concrete Slabs After Pour with Burlap Overlying to Preserve Moisture.

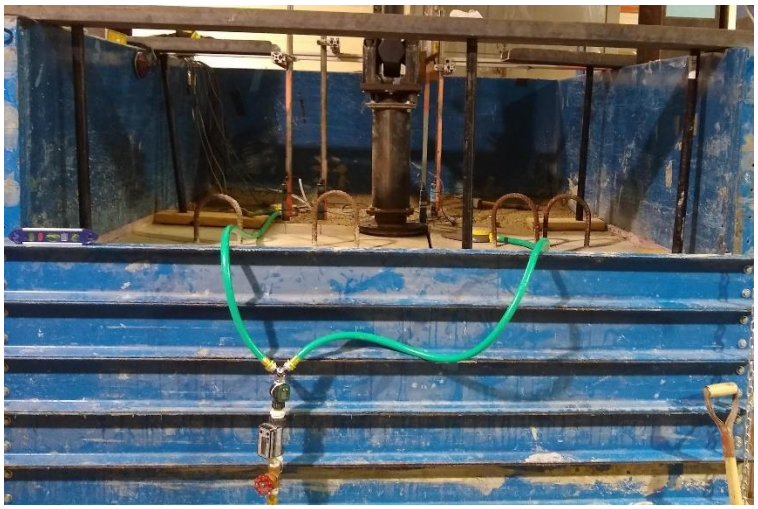

Figure 3.25. Sprinklers for Applying Rainfall.

3.2.5 Instrumentation

To understand how the base course section was performing, several instruments were installed at the surface of the base course (or pavement) and at the surface of the subgrade (interface). Once the subgrade quality was assured, 100-mm-diameter earth pressure cells (EPCs) (see Figure 3.30) were installed in the surface of the subgrade at 0-mm, 150-mm, 300-mm, and 450-mm offsets from center of the loading piston; readings were taken every 0.1 second during loading. Calibration factors for the earth pressure cells were provided by the factory.

Displacement transducers were placed at the surface of both test sections. In the unpaved tests (Figure 3.26), transducers measured displacements on the plate, at twice the radius from the center, and at thrice the radius from the center. For the paved sections (Figure 3.27), transducers were placed at the loaded corner of the slab, at twice and thrice the radius of the plate from the center of the plate along the diagonal of the loaded slab, and at the load-adjacent edge of the non-loaded ("Other") slab. From these measurements, the radius of relative stiffness, corner deformation, 2R, and 3R measurements could be found (Figure 3.28). Considering the definition of the radius of relative stiffness as a radius of gyration by Westergaard (1926) and the finite slab dimension used in this study, the distance from the loaded corner to the estimated point of slab rotation is assumed equal to the radius of relative stiffness, l, as shown in Figure 3.28; this assumption should be verified in future research. The fully assembled test sections can be observed in Figure 3.26, Figure 3.27, and Figure 3.29. A photo of an earth pressure cell is depicted in Figure 3.30. The data logging system for the earth pressure cells and displacement transducers is observed in Figure 3.31.

Figure 3.26. Surface of Base Course During Unpaved Test Sequence.

Figure 3.27. Displacement Transducers on Concrete Pavement Test.

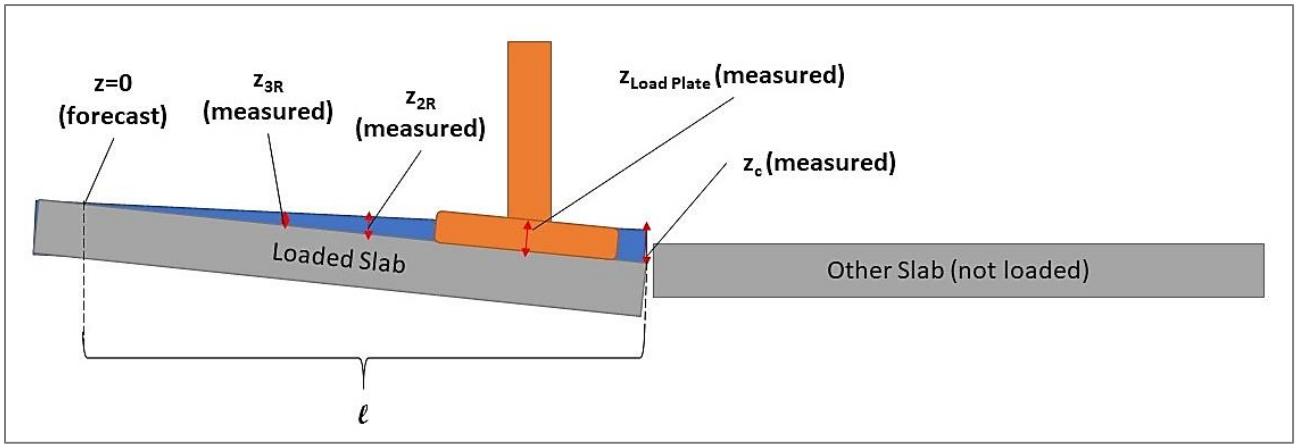

Figure 3.28. Instrumentation Layout for Paved Sections.

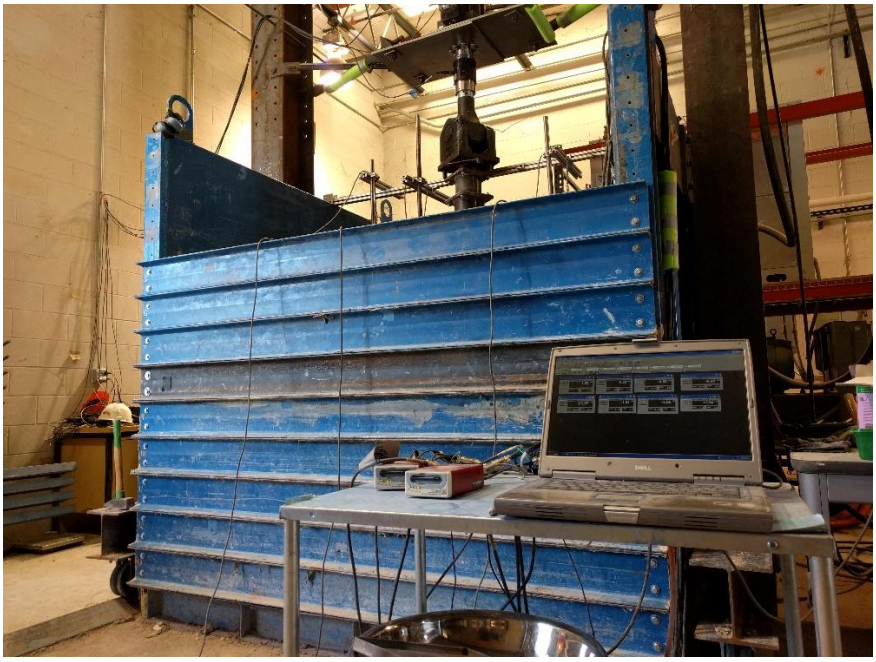

Figure 3.29. Test During Operation (Outside-Box View).

Two recording methods were used for readings from the actuator for the unpaved sections. During static loading, the computer controlling the actuator did not record but provided real-time readings on the display (see Figure 3.32), so static load sequence readings were manually adjusted and recorded by the operator. The 245-kN actuator measured and recorded the displacements at the load plate as well as the forces applied by the piston to the base course surface during cyclic loading; readings were taken by load cycle as well as by time every 0.1 second (see Figure 3.33). The actuator was professionally calibrated in June 2018 for both load and displacement readings.

Figure 3.30. Earth Pressure Cell Used in This Study.

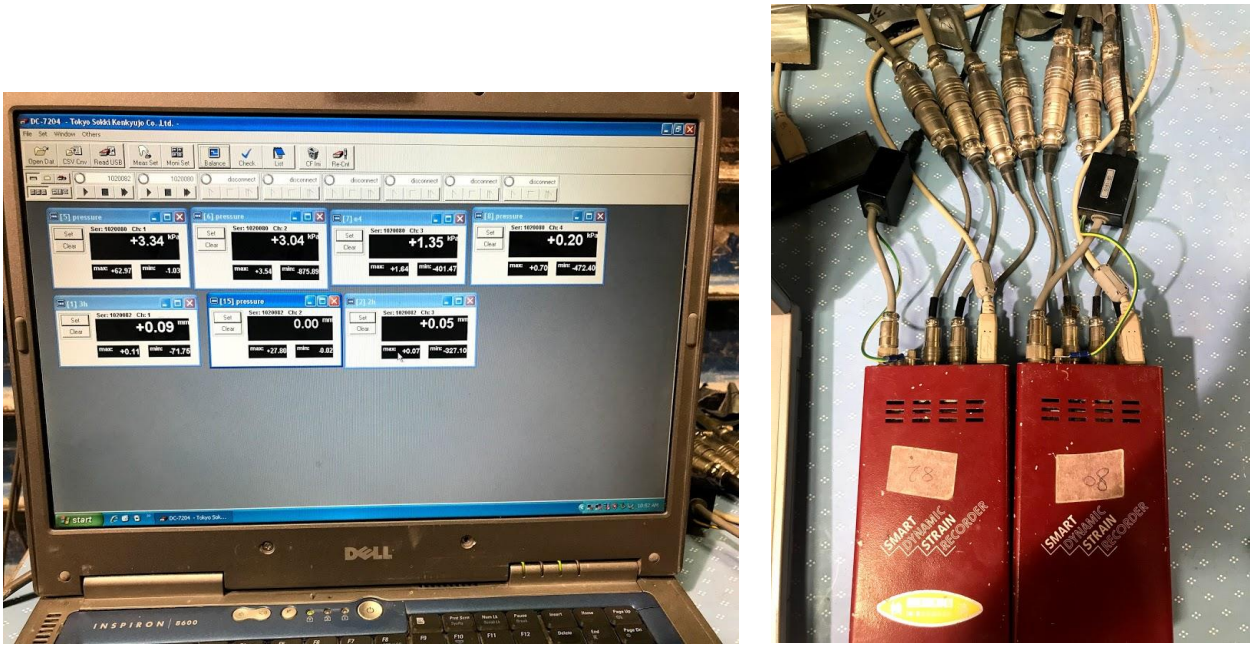

Figure 3.31. Datalogging Software (left) and Datalogger Recorders (right).

Figure 3.32. Actuator Manual Controls and Display Output.

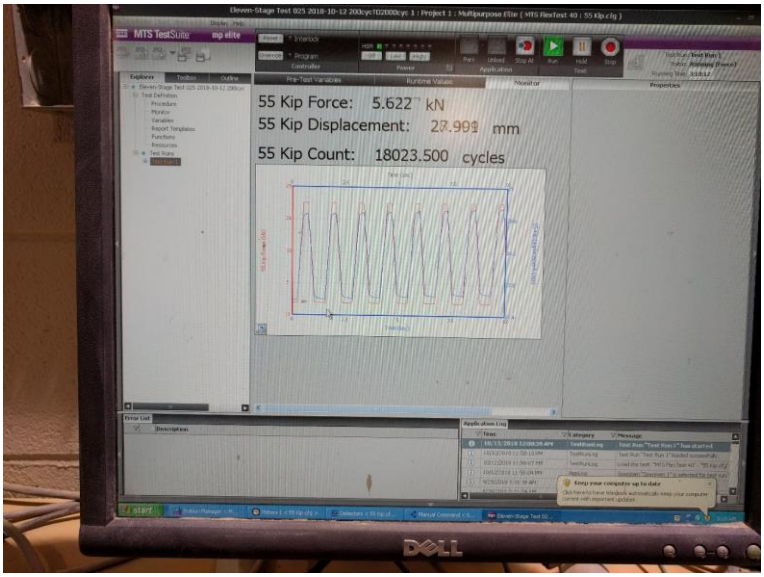

Figure 3.33. Actuator Computer Display during Cyclic Loading.

3.3 Load Sequence

3.3.1 Unpaved Sections

Static Load Test

Once the test section was constructed, its quality was assured, and the load plate was leveled, a static load sequence was applied to the test section surface. This loading served several purposes. AASHTO (1993) states that the static loading method should be used to determine the k-value of a uniform subgrade, but this method will not yield consistent or valid results for multi-layer pavement-underlying sections; running this sequence confirms the theory outlined in the AASHTO (1993) guide. This static sequence provides a seating preload identified in other studies; there has not been a consistent method of preload, whether it be static or cyclic loading, applied across field and smaller scale automated plate load tests, so this method was chosen to mimic the triaxial method of preloading a sample using static loads before applying a cyclic load sequence. Load increments for the static sequence are shown in Table 3.4. The load was manually entered using the actuator controls in a computer program; displacements and applied loads could be observed. The load was maintained until the displacement was 0.03 mm per minute for 3 consecutive minutes. Once the peak load was reached and the displacement was stabilized, unloading was performed in several stages to prepare for cyclic loading.

Table 3.4. Static Load Test Sequence.

Target Load (kN)	Target Load (kN)
0.00	3.75
1.50	4.50
3.00	5.25
0.00	6.00
0.75	6.75
1.50	4.00
2.25	2.00
3.00	0.02

Cyclic Load Test

After the section was preloaded and then unloaded, an automated program applied the cyclic load sequence. Load increments and number of cycles for each load stage are detailed in Table 3.5. The waveform for each 1.3-second load cycle (Figure 3.34) included a ramp up to the desired load for 0.3 second, maintenance of the load for 0.2 second, unload down to 0.02 kN over 0.3 second, and maintenance of the unloaded state for 0.5 second; reducing the load all the way to zero would cause the plate to lose contact with the subgrade and apply an impact load instead of pulsing and maintaining plate/base course contact. Maximum displacement of the plate was limited to approximately 38 mm in the unpaved tests to prevent damage to the instrumentation. Any displacement greater than 13 mm would likely result in damage of the concrete slab, so this displacement was enough to capture allowable displacement for concrete pavement applications. Load magnitudes used in this study reflect the stress increments of the resilient modulus test (AASHTO T307 2017).

Table 3.5. Cyclic Load Sequence Adopted in This Study.

Stage No.	Applied Load (kN)	Sim. Tire Pressure (kPa)	No. Cycles	Stage No.	Applied Load (kN)	Sim. Tire Pressure (kPa)	No. Cycles
1	1.0	14	200	6	7.5	103	2,000
2	2.0	28	200	7	10.1	138	2,000
3	3.0	41	200	8	15.1	207	2,000
4	4.0	55	200	9	20.1	276	2,000
5	5.0	69	200	10	25.2	345	2,000
				11	30.2	414	2,000

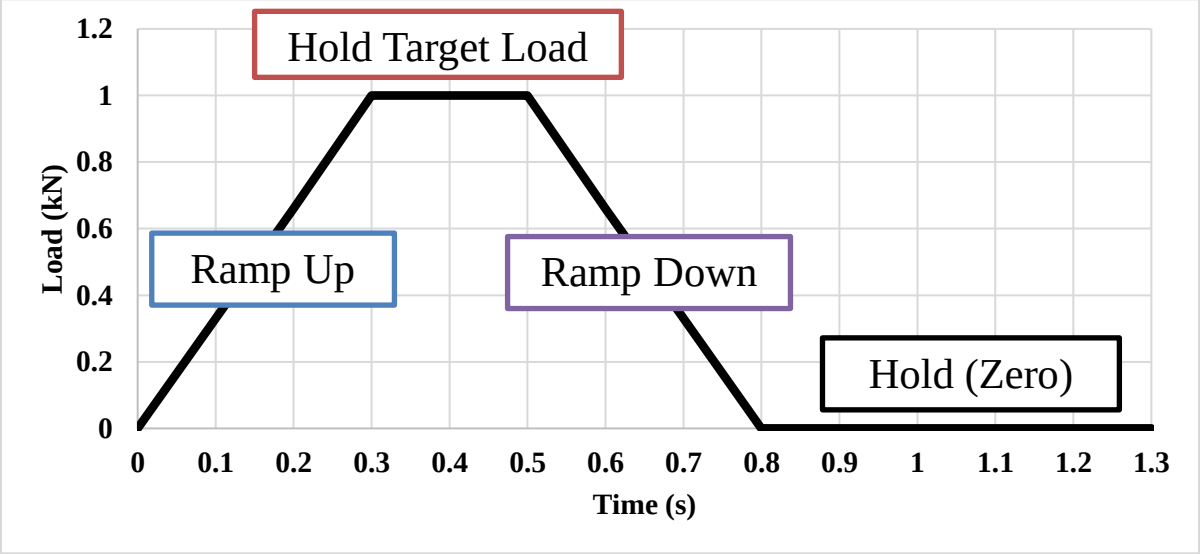

Figure 3.34. Single-cycle Load Waveform.

The initial testing plan had an alternate load sequence, as shown in Table 3.6. Permanent deformations were minimal at the small number of low-intensity cycles in the original, typically less than 10 mm (in some cases less than 5 mm). Surface imperfections in the base course did not have an opportunity to be smoothed with so few cycles, so no consistent pattern of behavior

could be determined for long-term pavement life. It was decided to increase the number of load cycles and stages to instigate more deformation. A trial test of VGB stabilized by woven geotextile was conducted using an initial alternate load sequence that allowed the final stage of cycles to run with a target 25 mm permanent deformation, as shown in Table 3.7; three thousand cycles was not enough to cause the desired permanent deformation (only 3.75 mm). The sequence was again modified to the current load sequence (Table 3.5) in order to observe any effects of load magnitude, reach at least 25 mm of permanent deformation due to cyclic loading, and to consider the time constraints of running a test (nearly 5 hours for the current cyclic load sequence).

Table 3.6. Original Cyclic Load Sequence.

Stage No.	Applied Load (kN)	Sim. Tire Pressure (kPa)	No. Cycles
1	1.0	14	200
2	2.0	28	200
3	3.0	41	200
4	3.5	48	200
5	5.0	69	200
6	7.6	103	200
7	10.1	138	200

Table 3.7. Alternate Load Sequence.

Stage No.	Applied Load (kN)	Sim. Tire Pressure (kPa)	No. Cycles
1	1.0	14	200
2	2.0	28	200
3	3.0	41	200
4	4.0	55	200
5	5.0	69	200
6	7.6	103	200
7	10.1	138	3,000

3.3.2 Concrete Pavement Sections

For test sections with a concrete slab atop the base course and subgrade, a single load magnitude was applied at Day 7 after the concrete slab was poured. Tests “A” and “B” refer to the initial or pre-rainfall (Day 7) and post-rainfall (Day 8) tests. The applied load of 40 kN corresponds to the equivalent single wheel load (ESWL) (AASHTO 1993). No static preloading was performed for the paved sections; the surface concrete layer was rigid and did not require preloading, and irregularities in the underlying base course section were removed through the installation and compaction of overlying concrete. Table 3.8 displays the load sequences for the paved test sections.

Table 3.8. Load Sequence for Concrete Pavement Sections.

Stage No.	Applied Load (kN)	Sim. Tire Pressure (kPa)	No. Cycles
1A	40	550	15,000
1B	40	550	15,000

3.4 Test Summary

Table 3.9 displays the large-scale box tests on unpaved road sections. As discussed previously, the load sequence was updated at Test 11 to induce additional deformation and to gain more insight regarding performance at higher load cycles and later stages. Test 15 will be discarded due to equipment malfunction; load readings were confirmed to be invalid, and the system suffered an unexpected shutdown during operation that could not be resolved (the equipment had since undergone professional repair and recalibration). This dissertation will focus on the results obtained in Tests 11 through 27 (not including Test 15) because the load sequences allow them to be compared most easily.

Table 3.9. Test Matrix for Unpaved Road Sections.

Test No.	Date	Base Course Material	Geosynthetic	SG CBR	BC CBR	Notes
Test 1	*6/28/2017*	*VGB*	*NW*	*5.4%*	*6.4%*	*Old Load Seq.*
Test 2	*6/30/2017*	*VGB*	*W*	*5.5%*	*6.7%*	*Old Load Seq.*
Test 3	*7/14/2017*	*VGB*	*NONE*	*5.1%*	*8.3%*	*Old Load Seq.*
Test 4	*7/20/2017*	*VGB*	*GG*	*5.4%*	*8.9%*	*Old Load Seq.*
Test 5	*7/26/2017*	*RCA*	*NONE*	*5.1%*	*12.4%*	*Old Load Seq.*
Test 6	*8/1/2017*	*RCA*	*W*	*5.5%*	*6.0%*	*Old Load Seq.*
Test 7	*8/4/2017*	*RCA*	*NW*	*5.3%*	*6.0%*	*Old Load Seq.*
Test 8	*8/9/2017*	*RCA*	*GG*	*6.2%*	*7.9%*	*Old Load Seq.*
Test 9	*8/17/2017*	*VGB*	*NW*	*1.8%*	*21.0%*	*Old Load Seq.*
Test 10	*4/20/2018*	*VGB*	*W*	*1.9%*	*11.1%*	*Alt. Load Sq.*
Test 11	5/1/2018	VGB	W	2.2%	11.6%	VALID.
Test 12	5/16/2018	RCA	W	2.0%	13.4%	VALID.
Test 13	5/19/2018	RCA	NONE	2.1%	13.1%	VALID.
Test 14	5/23/2018	VGB	NONE	1.9%	12.4%	VALID.
Test 15	*6/6/2018*	*VGB*	*GG*	*2.0%*	*16.3%*	*Equip. failure*
Test 16	6/15/2018	RCA	GG	2.0%	14.9%	VALID.
Test 17	6/20/2018	VGB	NW	2.2%	13.0%	VALID.
Test 18	6/28/2018	RCA	NW	2.0%	16.3%	VALID.
Test 19	7/6/2018	VGB	GG	2.1%	14.5%	VALID.
Test 20	7/27/2018	VGB	NW	2.9%	14.0%	VALID.
Test 21	8/15/2018	RCA	GG over NW	2.0%	17.2%	VALID.
Test 22	8/23/2018	VGB	GG over NW	1.9%	14.9%	VALID.
Test 23	9/19/2018	VGB	NONE	5.4%	12.6%	VALID.
Test 24	9/28/2018	VGB	NW	4.9%	11.0%	VALID.
Test 25	10/12/2018	RAP	NONE	4.9%	6.9%	VALID.
Test 26	10/17/2018	RAP	NW	2.2%	8.0%	VALID.
Test 27	10/24/2018	RAP	W	4.9%	15.3%	VALID.

Table 3.10 summarizes the concrete pavement test sections. Addition of nonwoven geotextile to VGB and replacement of VGB with RCA (with nonwoven geotextile) are compared against a non-stabilized VGB control section. CBR values listed in this table come from DCP results taken prior to concrete installation.

Table 3.10. Test Matrix for Concrete Pavements.

Test No.	Date	Base Course Material	Geosynthetic	SG CBR	BC CBR (DCP)
Test 28	*5/2/2019 5/3/2019*	*VGB*	*NONE*	*2.2%*	*8.5%*
Test 29	*5/20/2019 5/21/2019*	*VGB*	*NW*	*2.2%*	*10.8%*
Test 30	*6/12/2019 6/13/2019*	*RCA*	*NW*	*2.0%*	*15.2%*

Chapter 4. Resilient and Permanent Deformations of Road Sections

During the experiments, vertical deformations of the 300 mm rigid plate were measured. This chapter presents and evaluates these measured deformations of unpaved road sections under static loading. This chapter also covers these measured resilient and permanent deformations of unpaved roads and concrete pavements under cyclic loading.

4.1 Deformations of Unpaved Roads

4.1.1 Static Load Sequence

Although the static load test is not considered a reliable measure of composite modulus of subgrade reaction, the load-displacement curves for this sequence are included in this section. Figure 4.1 shows the comparison of the load-vertical displacement curves for the VGB sections while Figure 4.2 displays this same comparison of the RCA sections; the latter Figure can be used to compare the RCA sections with the VGB sections for reference.

For the VGB experiments, Figure 4.1 shows that the test sections with the nonwoven geotextile (NW), woven geotextile (W), and geogrid (GG) sections had smaller vertical displacements than the control section under static loading; the NW-stabilized section displayed the smallest displacement. Large displacements were noted in the combination GG/NW-stabilized section; this result is unforeseen and might be due to the reduced interlock between the geogrid and the aggregate on initial compaction, as the geotextile remained flush with the geogrid until the plate load was applied. This hypothesis was indirectly confirmed upon excavation when the imprint of the geogrid was observed in the surface of the subgrade, but the

aggregate imprints were not observed (see Figure 4.3). This result could also be attributed to the variability of base and subgrade strengths because this surprising result did not happen in the test sections with RCA. In the VGB/NW (i.e. without GG) section, aggregates were pushed on the geotextile into the surface of the subgrade but did not puncture the geotextile; therefore, the aggregates were locked into the geotextile while maintaining separation. This locked-in phenomenon was not observed in the VGB/GG/NW section. The maximum and permanent deformations for the unpaved sections with VGB over 2%-CBR subgrade are provided in Table 4.1, which shows that the permanent deformation after unloading was approximately 83% the maximum deformation under loading on average.

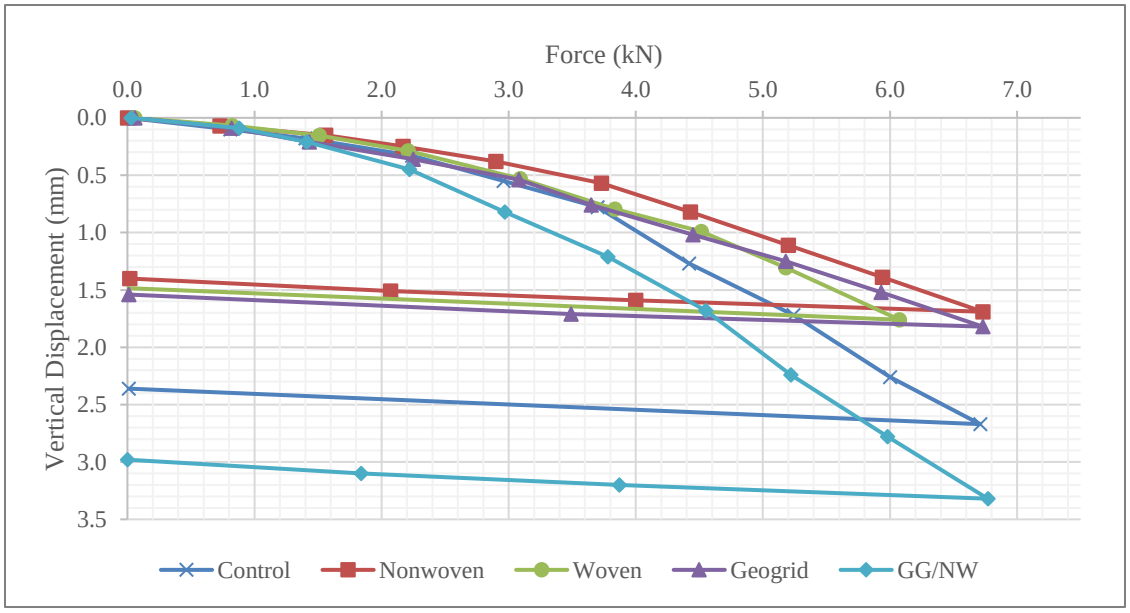

Figure 4.1. Load-Displacement Curves of VGB Sections on 2%-CBR Subgrade under Static Loading.

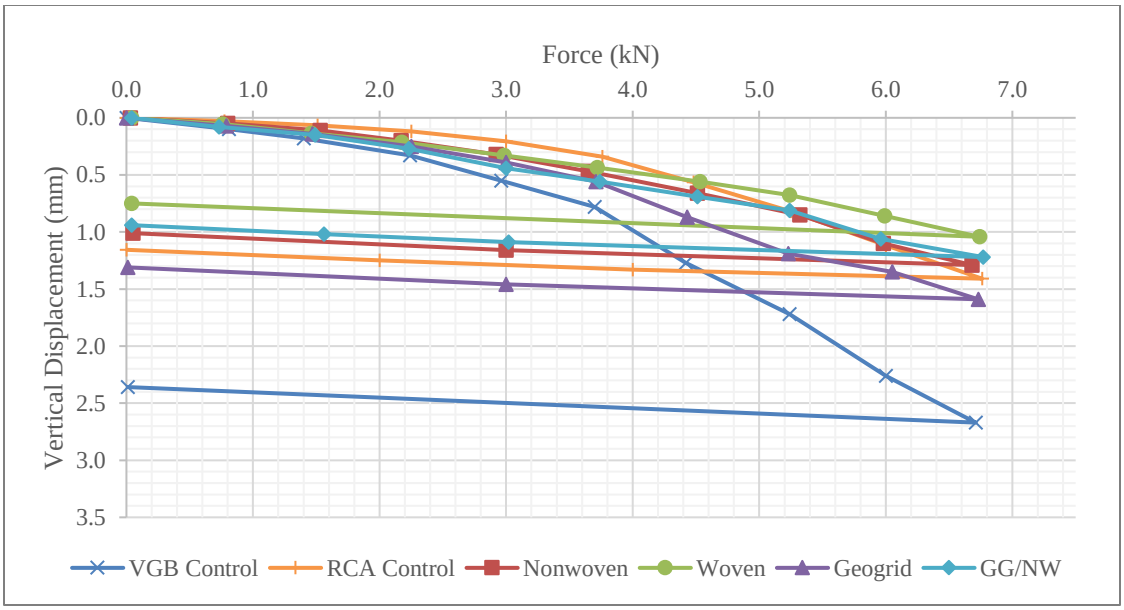

Figure 4.2. Load-Displacement Curves of RCA Sections on 2%-CBR Subgrade under Static Loading.

Figure 4.3. Subgrade Surface in the VGB/GG/NW Section after Loading and Excavation.

Table 4.1. Maximum and Permanent Deformations of Unpaved Sections with VGB on 2%-CBR Subgrade under Static Loading up to 6.75 kN and after Unloading.

Base Course CBR (%)	Subgrade CBR (%)	Geosynthetic	Maximum Deformation δ_{max} (mm)	Permanent Deformation δ_p (mm)	δ_p / δ_{max}
12.4	1.9	Control	2.7	2.4	0.89
13.0	2.2	NW	1.7	1.4	0.82
11.6	2.2	W	2.1 (extrapolated)	1.5	0.71
14.5	2.1	GG	1.8	1.5	0.83
14.9	1.9	GG/NW	3.3	3.0	0.91

The unpaved sections with RCA consistently outperformed the VGB sections in terms of maximum and permanent deformations as shown in Figure 4.1 and Figure 4.2. Static load-induced maximum deformations for the RCA sections stabilized by geosynthetics were more consistent, ranging from 1.0 to 1.6 mm. In the RCA comparison with different geosynthetic, the woven geotextile displayed the least maximum and permanent deformations, while the geogrid exhibited the most. As would be expected, the combined GG/NW section with RCA had the second least maximum and permanent deformations. The RCA aggregate/NW/subgrade interlock discussed in the VGB section above was observed upon excavation (see Figure 4.4) in the evidence of aggregate imprints on the subgrade surface.

In this series of tests, it is unexpected that the RCA control section (i.e. without geosynthetic) performed better than all the sections with geosynthetic when the load was lower than 4.5 kN. This result is likely due to the variability of base and subgrade strength. This and above discussions indicate that at small deformations, the performance of an unpaved road section with or without geosynthetic is influenced by compaction and variability of base and subgrade strengths.

Figure 4.4. Subgrade Surface of the RCA/GG/NW Section after Loading and Excavation.

The maximum and permanent deformations for the unpaved sections with RCA over 2%-CBR subgrade are provided in Table 4.2. This table shows that the permanent deformation after unloading was approximately 79% the maximum deformation under loading on average for RCA, which is slightly less than the 83% in the VGB sections.

Table 4.2. Maximum and Permanent Deformations of Unpaved Sections with RCA on 2%-CBR Subgrade under Static Loading up to 6.75 kN and after Unloading.

Base Course CBR (%)	**Subgrade CBR (%)**	**Geosynthetic**	**Maximum Deformation δ_{max} (mm)**	**Permanent Deformation δ_p (mm)**	**δ_p / δ_{max}**
13.1	2.1	Control	1.4	1.2	0.83
16.3	2.0	NW	1.3	1.0	0.78
13.4	2.0	W	1.0	0.8	0.75
14.9	2.0	GG	1.6	1.3	0.82
17.2	2.0	GG/NW	1.2	0.9	0.78

One section with RAP/NW on 2%-CBR subgrade was tested and its result is compared with those for the test sections with VGB/NW and RCA/NW in Figure 4.5. Maximum and permanent deformations of 11.5 mm and 11.2 mm, respectively, occurred in the RAP section and were excessive as compared with other sections. Similar to the combined VGB/GG/NW section (Figure 4.3), there was no observed aggregate/geotextile/subgrade interlock as evidenced by aggregate imprints in the surface of the subgrade (Figure 4.6). Adequate separation was achieved through use of the geotextile, but permanent deformation of the NW-stabilized RAP exceeded both the NW-stabilized VGB and RCA sections as well as the non-stabilized VGB section.

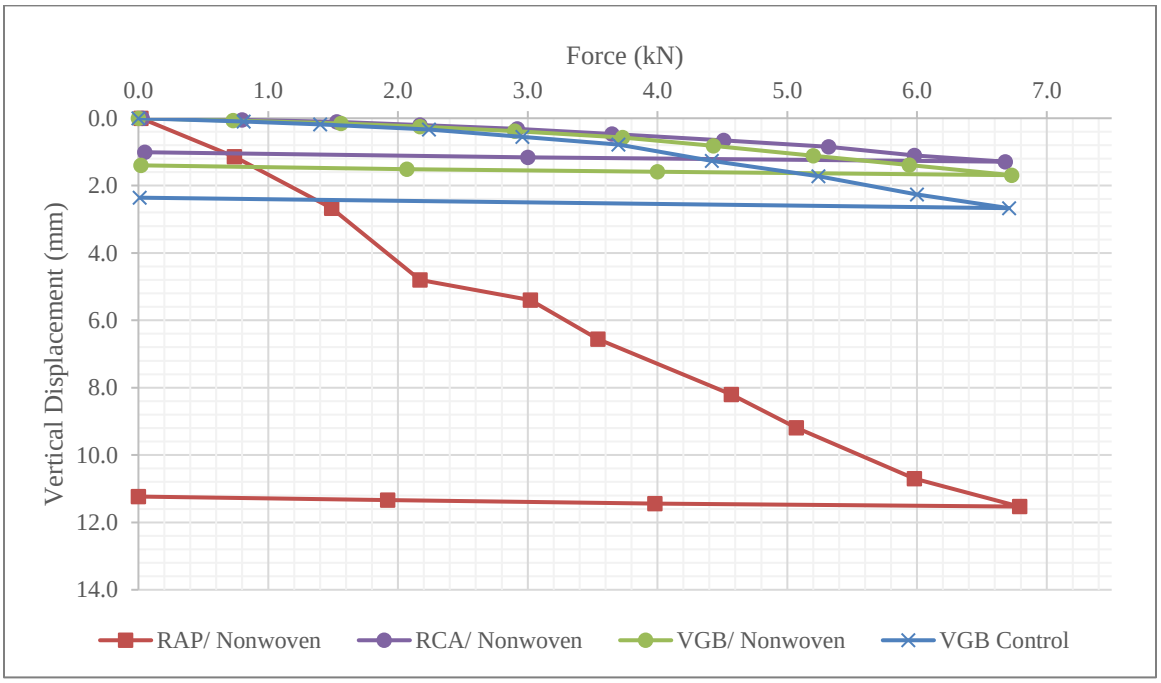

Figure 4.5. Load-displacement Curves of the RAP Section as Compared with Other Sections on 2%-CBR Subgrade under Static Loading.

Figure 4.6. Subgrade Surface of the RAP/NW Section after Loading and Excavation.

Several sections were constructed on 5%-CBR subgrade (see Table 3.9 in Chapter 3), and their static load-vertical displacement curves are displayed in Figure 4.7. As would be expected, static loading over a stronger subgrade (comparing the VGB control sections) resulted in smaller displacements under static loading. A similar large increase in the displacements for the RAP sections as compared with the VGB sections was observed with the stronger subgrade for both the non-stabilized and the woven geotextile-stabilized sections. The woven geotextile decreased the maximum deformation for the RAP sections (6.7 mm for the control vs. 5.5 mm for the woven geotextile-stabilized section), but the nonwoven geotextile in the VGB section resulted in a slightly larger maximum displacement from static loading than the control section (1.4 mm for the control vs. 1.8 mm for the nonwoven geotextile). These comparisons indicate that the test sections at small displacements could not consistently show the benefit of geosynthetics.

AASHTO (1993) does state that static load testing is unreliable for determining the modulus of subgrade reaction (or resilient modulus). As discussed earlier, the displacements induced by static loading were small, especially for 5%-CBR subgrade; thus, the benefits of

geosynthetic stabilization could not be consistently demonstrated. Therefore, cyclic loading is necessary to achieve the goal for this study. In addition, cyclic loading more closely replicates traffic loading. Considering poor performance of RAP as a base material in an unpaved road and its more viable option as an asphalt recycle component, RAP was not fully investigated in this study.

The test results from static loading are reported here in case the initial permanent deformation appeared to have an impact on the permanent deformation from cyclic loading. Additionally, this static loading sequence was performed as a prestress to the cyclic loading. Test results discussed subsequently in this dissertation will be focused on the data obtained in the cyclic loading tests.

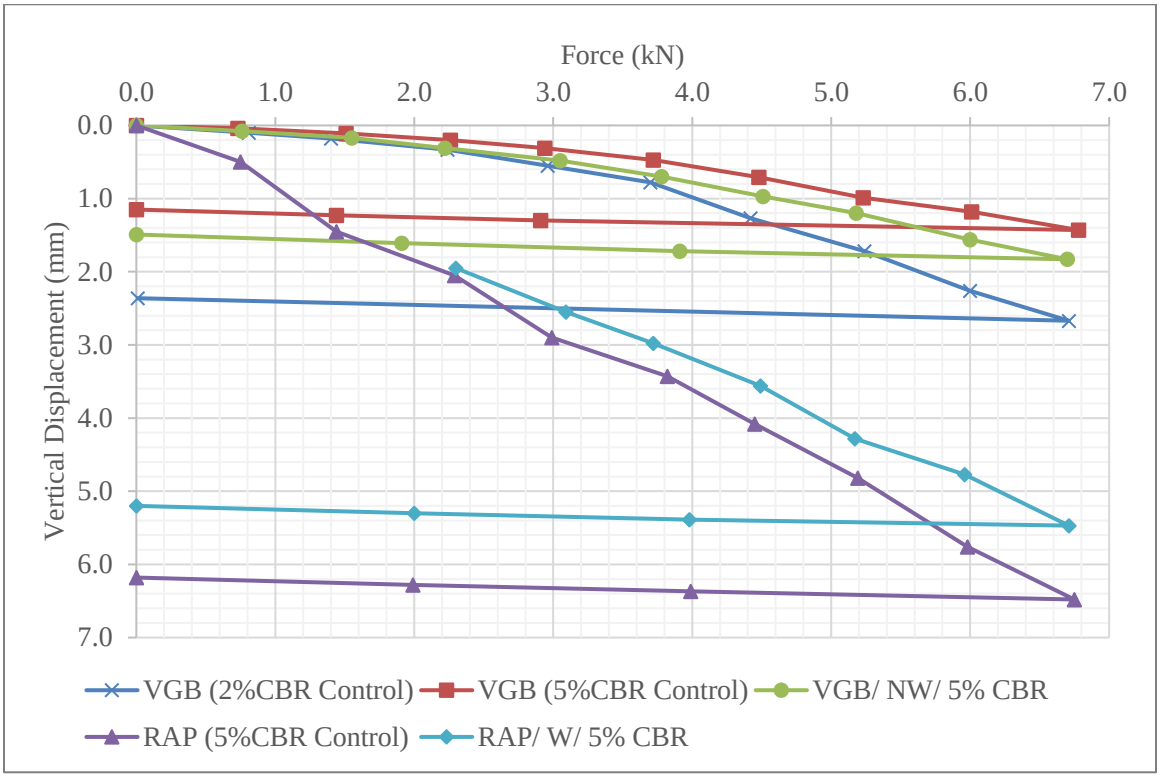

Figure 4.7. Load-displacement Curves of Different Base Courses on 5%-CBR Subgrade as Compared with VGB/ 2%-CBR Subgrade under Static Loading.

4.1.2 Cyclic Load Sequence

The combined displacement vs. load cycle curves for different unpaved sections with or without geosynthetic on 2%-CBR subgrade are displayed in Figure 4.8, Figure 4.9, and Figure 4.10 for VGB, RCA, and RAP, respectively. Resilient deformation can be observed in the thickness of each displacement "band", while accumulated permanent deformation is displayed as the distance between the x-axis and the displacement band. It should be noted that the VGB section with geogrid (GG) (i.e. Test 15 in Table 3.9) displays a strange displacement pattern as discussed in Section 3, and the data is considered invalid due to equipment failure; it has not been included in the analysis. A total of five cyclic loading tests for both RCA and VGB were completed along with one test for RAP (with nonwoven geotextile) over 2%-CBR subgrade.

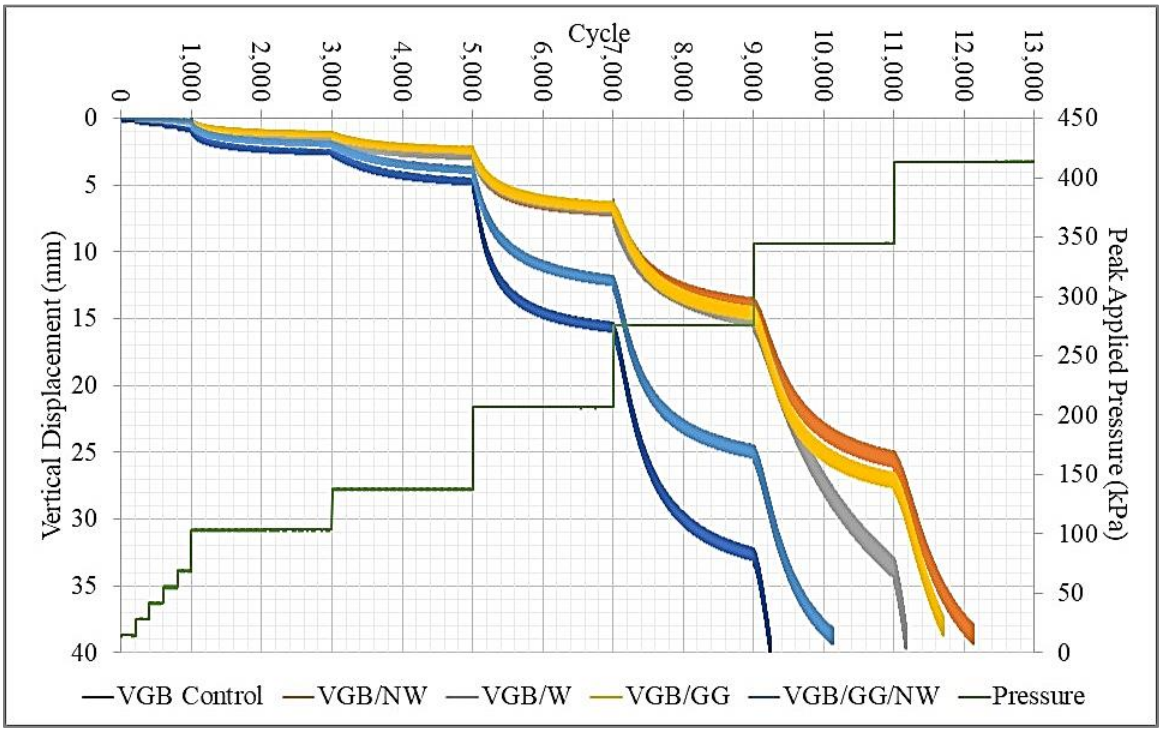

Figure 4.8. Deformation Results for VGB Unpaved Sections on 2%-CBR Subgrade under Cyclic Loading.

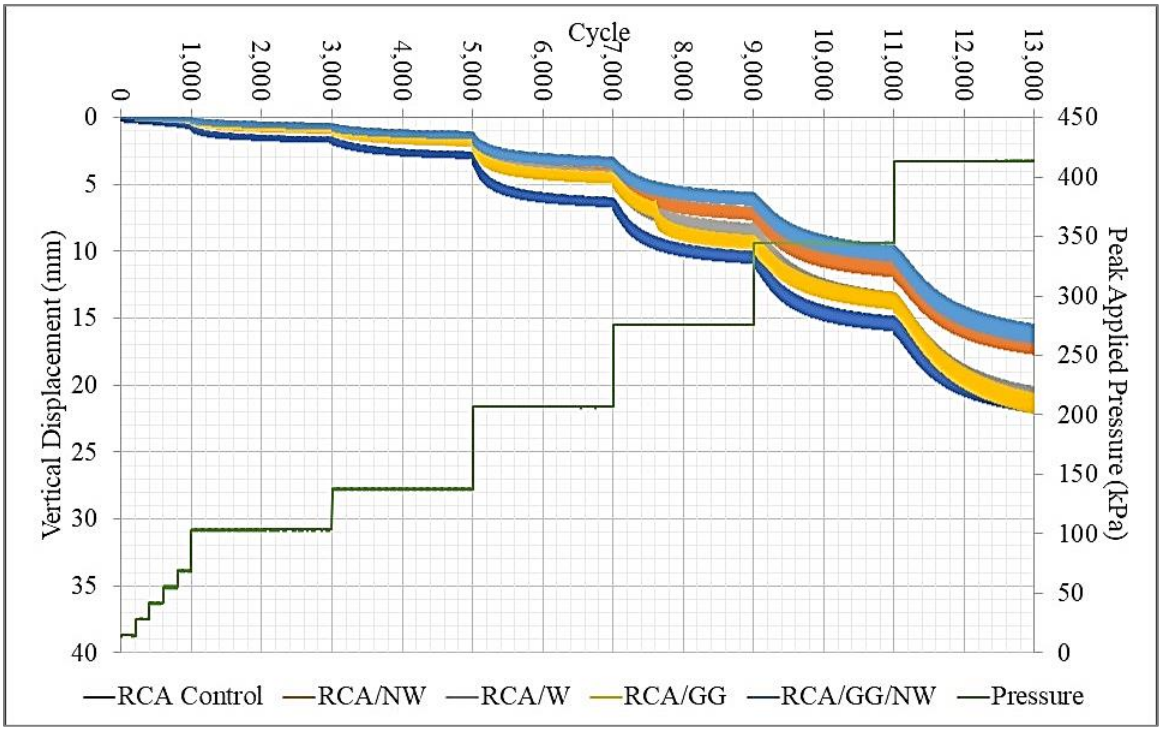

Figure 4.9. Deformation Results for RCA Unpaved Sections on 2%-CBR Subgrade under Cyclic Loading.

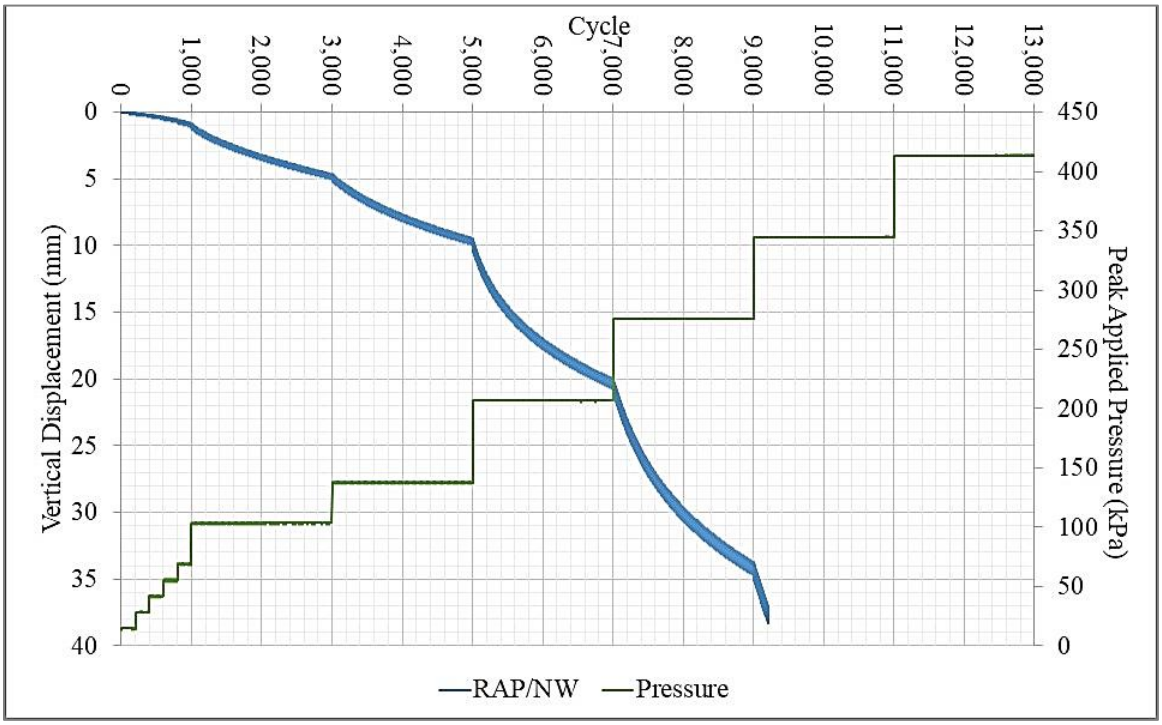

Figure 4.10. Deformation Results for Nonwoven Geotextile-Stabilized RAP Unpaved Section on 2%-CBR Subgrade under Cyclic Loading.

Permanent Deformation

The first item to note based on Figure 4.8 and Figure 4.11 is the comparison of the effect of the aggregate on permanent deformation of a test section. The unpaved sections with RCA generally resulted in smaller permanent deformations than the sections with VGB, and the section with RAP had much larger permanent deformation. Comparison of the VGB and RCA control sections shows that aggregate substitution of VGB by RCA alone greatly decreased the permanent deformation.

Accumulated permanent deformations under different load increments up to approximately 38 mm are displayed in Figure 4.11 for the tests performed. The RCA sections with nonwoven geotextile (NW and GG/NW) displayed the least permanent deformation after cyclic loading. Consistent with the static load results, the RAP sections exhibited more permanent vertical deformation than the VGB control sections on the subgrade of the respective strengths.

Looking closely at the early stages with fewer cycles, it is difficult to distinguish the performance of different base course sections. Deformations for all sections were minimal at less than 1 mm. In these early stages, the control sections with VGB and RCA on 2%-CBR subgrade displayed the largest permanent deformation, and a clear benefit of adding geosynthetics is displayed. After these control sections on weak subgrade, the RAP sections all displayed the largest deformations in this initial stage (e.g., the VGB/ W section on 2%-CBR subgrade displaying similar deformation to the RAP sections on 5% subgrade). The remaining base course sections displayed the deformations ranging from 0.05 to 0.15 mm after the first 1,000 cycles; such miniscule deformation increments created difficulty in distinguishing which section performed the best.

Using the deformation in the early stage of the load sequence, a linear trend is noted. The slope of this trend is displayed in Table 4.3. The RCA/GG/NW/2%CBR subgrade section shows the strongest response, which was far sturdier than even the next strongest RCA/GG/2%CBR subgrade section. Geosynthetics provided improvement in the performance of all aggregates tested. The RAP material exhibited the slope values greater than those for the other aggregates on similar subgrade.

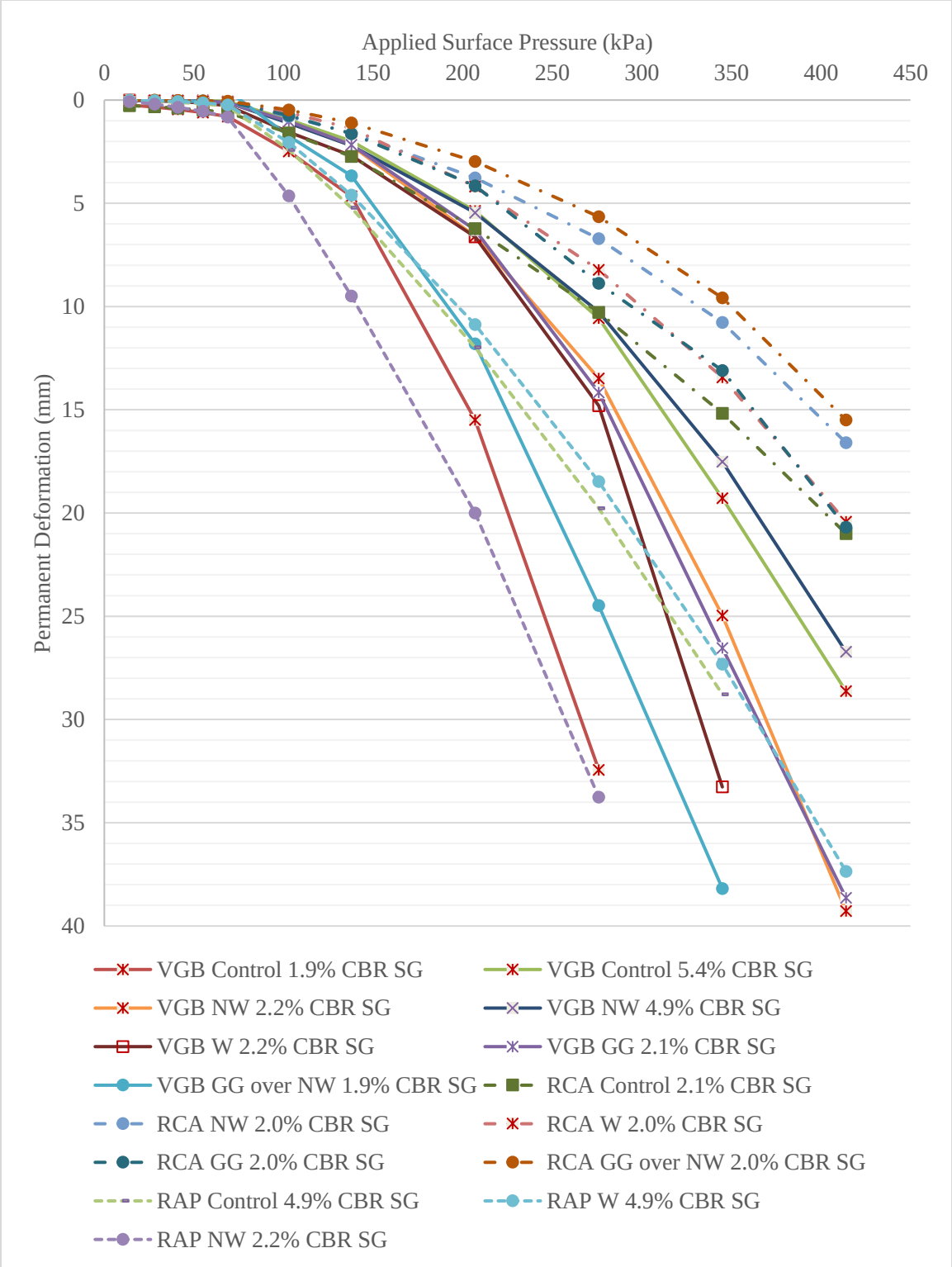

Figure 4.11. Accumulated Permanent Deformations under Different Load Increments.

Table 4.3. Slope of Initial Permanent Deformation Curve.

Test No.	Base Course Material	Base Course Stabilization	SG CBR	Slope of δ_p (mm)/ Applied Pressure (kPa)
Test 14	VGB	Control	1.9%	0.0101
Test 17	VGB	NW	2.2%	0.0018
Test 22	VGB	GG over NW	1.9%	0.0015
Test 11	VGB	W	2.2%	0.0047
Test 19	VGB	GG	2.1%	0.0020
Test 24	VGB	NW	4.9%	0.0021
Test 23	VGB	Control	5.4%	0.0013
Test 13	RCA	Control	2.1%	0.0061
Test 18	RCA	NW	2.0%	0.0019
Test 12	RCA	W	2.0%	0.0019
Test 16	RCA	GG	2.0%	0.0015
Test 21	RCA	GG over NW	2.0%	0.0010
Test 26	RAP	NW	2.2%	0.0136
Test 25	RAP	Control	4.9%	0.0050
Test 27	RAP	W	4.9%	0.0041

For further investigation, the permanent deformations incurred by each load sequence in all the tests are displayed in Figure 4.12 through Figure 4.22. At later load sequences where applied pressure magnitude increased, the VGB and RAP sections typically exhibited excessive deformations, while the RCA sections maintained more steady, smaller permanent deformations than the VGB sections. This phenomenon is also observed in Figure 4.8 through Figure 4.10 above; the "arc" of deformation steadily increased in magnitude with the increase in load magnitude for the VGB and RCA sections, but the difference in the permanent deformations by

the load sequence for the RCA sections was much smaller. Permanent deformations within the early stage (first 5 sequences) were greatest in the non-stabilized and in some woven geotextile-stabilized sections. RAP under-performed in terms of permanent deformation for all scenarios.

RAP had the greatest permanent deformation as well as the lowest resilient deformation (to be discussed in detail in the next section) as compared with the other two aggregate materials. RAP was also the most difficult to get to 95% relative compaction during test section preparation. Loose particles were observed at the surface of compacted RAP sections as well, despite excess effort by doubling the number of compaction lifts. It is likely that the laboratory setting might not truly mimic the application of RAP as base course in practice. In the field, ambient heat as well as that generated in the aggregate from sunlight make the remaining asphalt binder in the RAP more malleable; this increase in ductility would promote easier compaction and better packing. Additionally, compaction effort may be greater in the field than what was achieved with a hand-held vibratory compactor in the lab, which would decrease the effort to achieve density. When RAP is used as a base course, confinement of the overlying pavement layer could also improve RAP performance greatly, as the surface "loose" particles of RAP would no longer be free. Additional tests with different geosynthetics, gradations, compaction methods, environmental simulations, and pavement confinement are necessary to truly evaluate RAP performance but are beyond the scope of this study.

As previously mentioned, Figure 4.12 through Figure 4.22 display the permanent deformation accumulated under each load sequence for the different test sections. The legend should be read left to right, and the bars correspond left to right. When a gap exists where a given bar on the graph should be, there was negligible deformation accumulated for the test section listed.

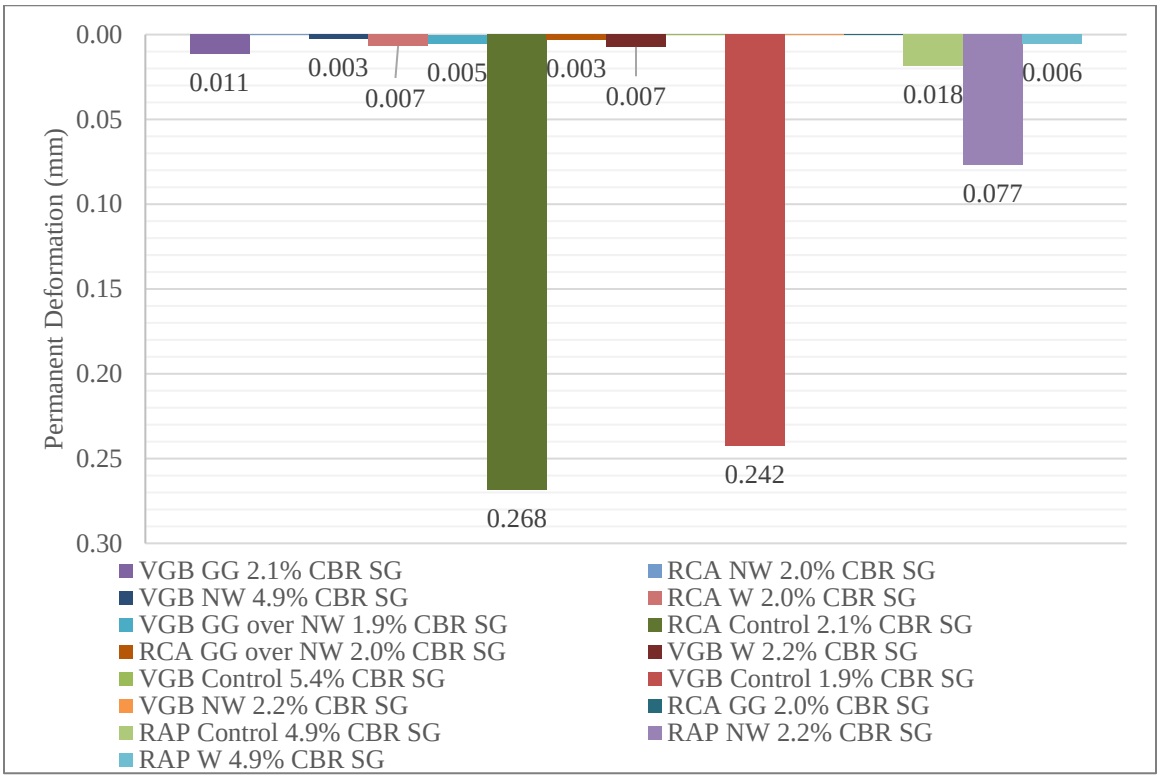

Figure 4.12. Permanent Deformation under Individual Load Sequence of 14 kPa.

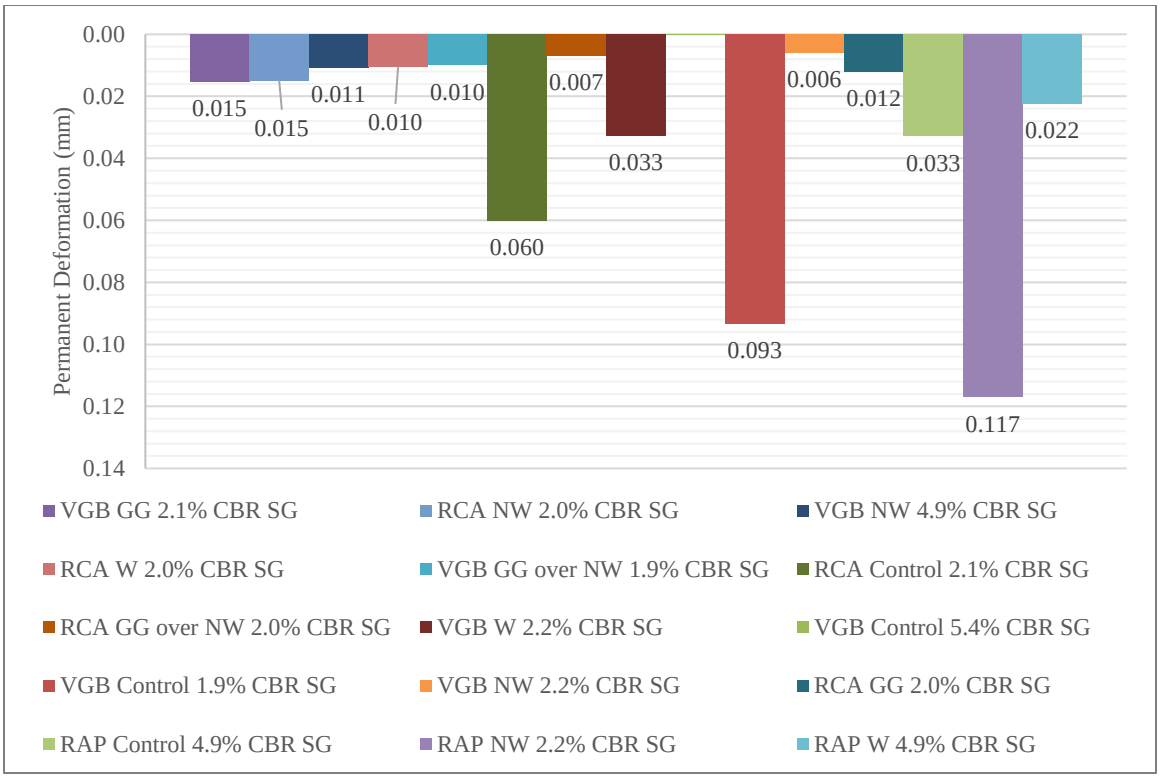

Figure 4.13. Permanent Deformation under Individual Load Sequence of 28 kPa.

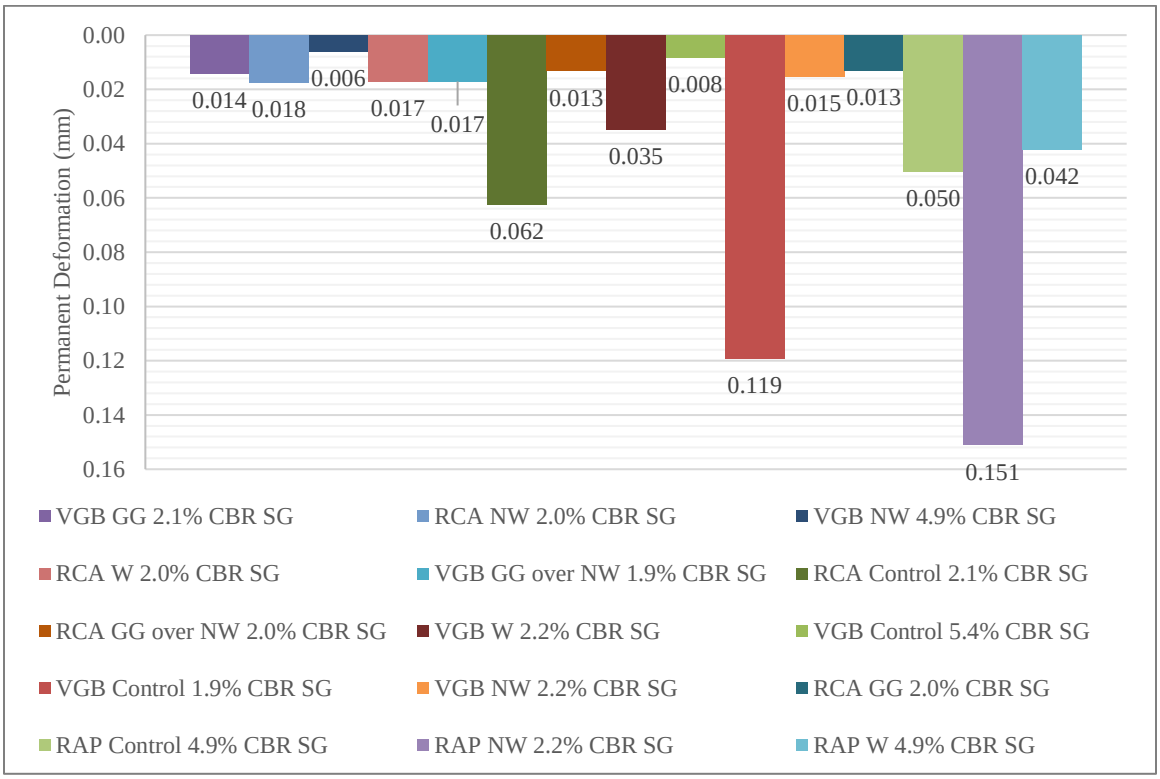

Figure 4.14. Permanent Deformation under Individual Load Sequence of 41 kPa.

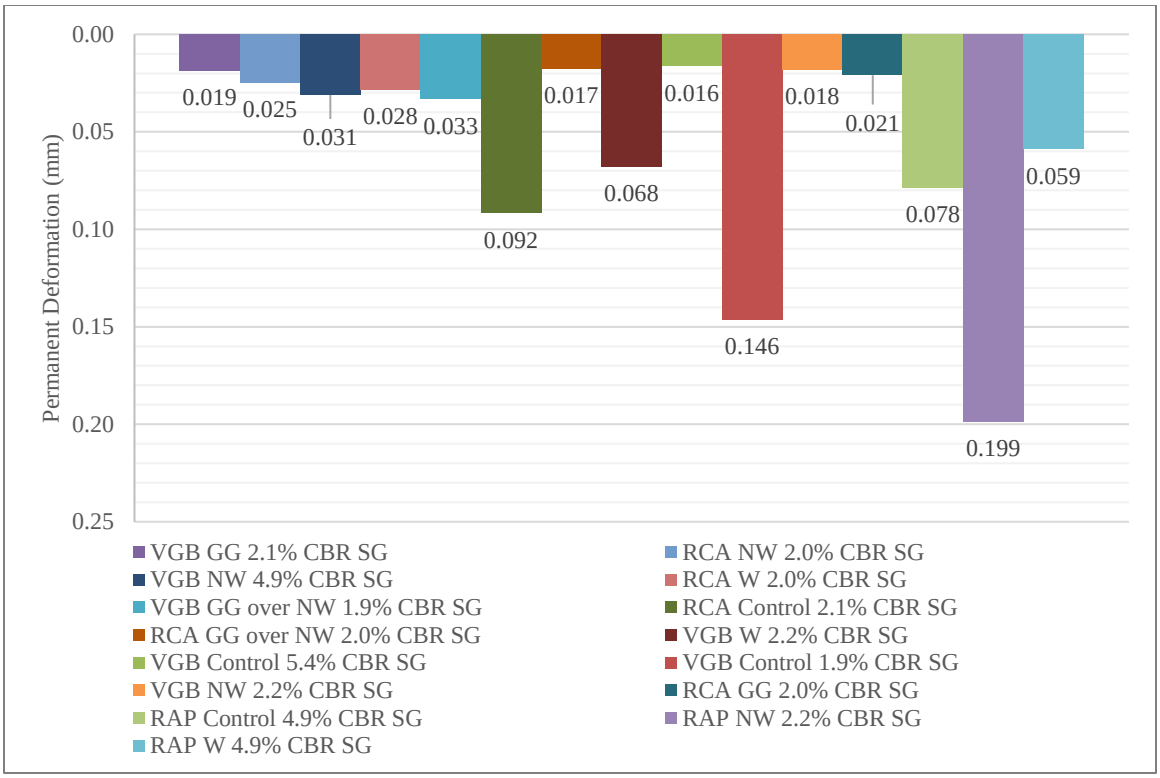

Figure 4.15. Permanent Deformation under Individual Load Sequence of 55 kPa.

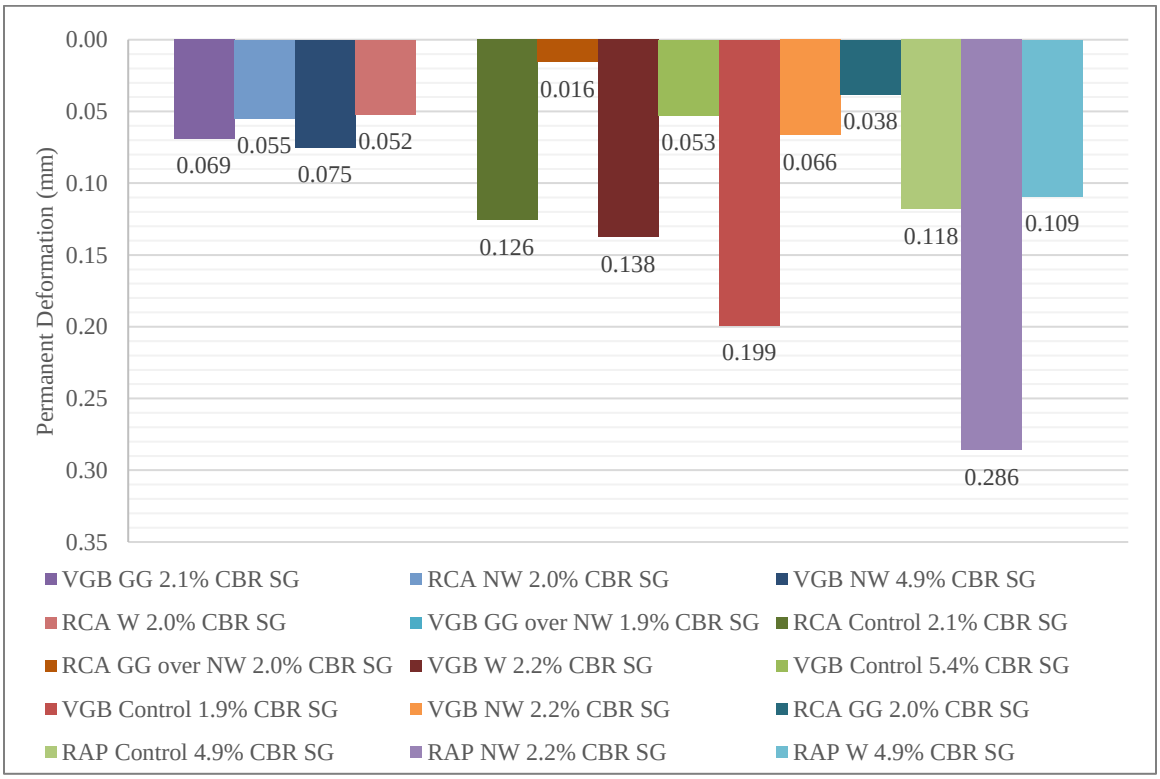

Figure 4.16. Permanent Deformation under Individual Load Sequence of 69 kPa.

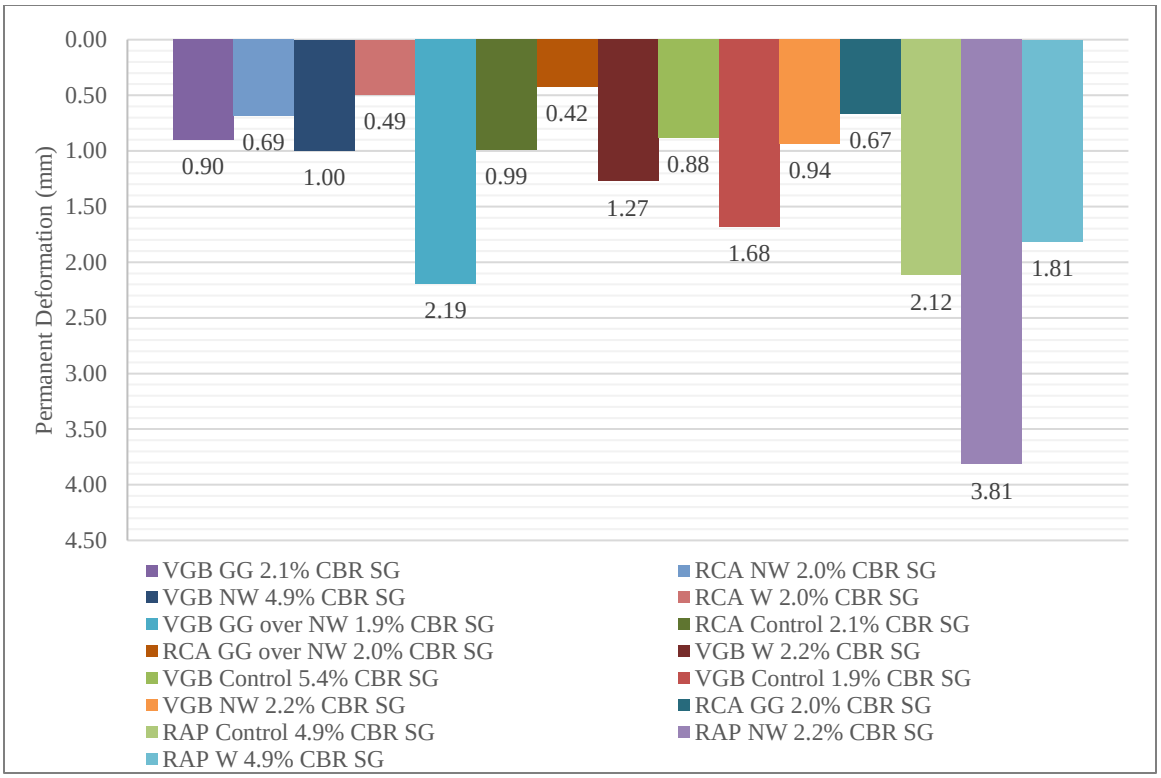

Figure 4.17. Permanent Deformation under Individual Load Sequence of 103 kPa.

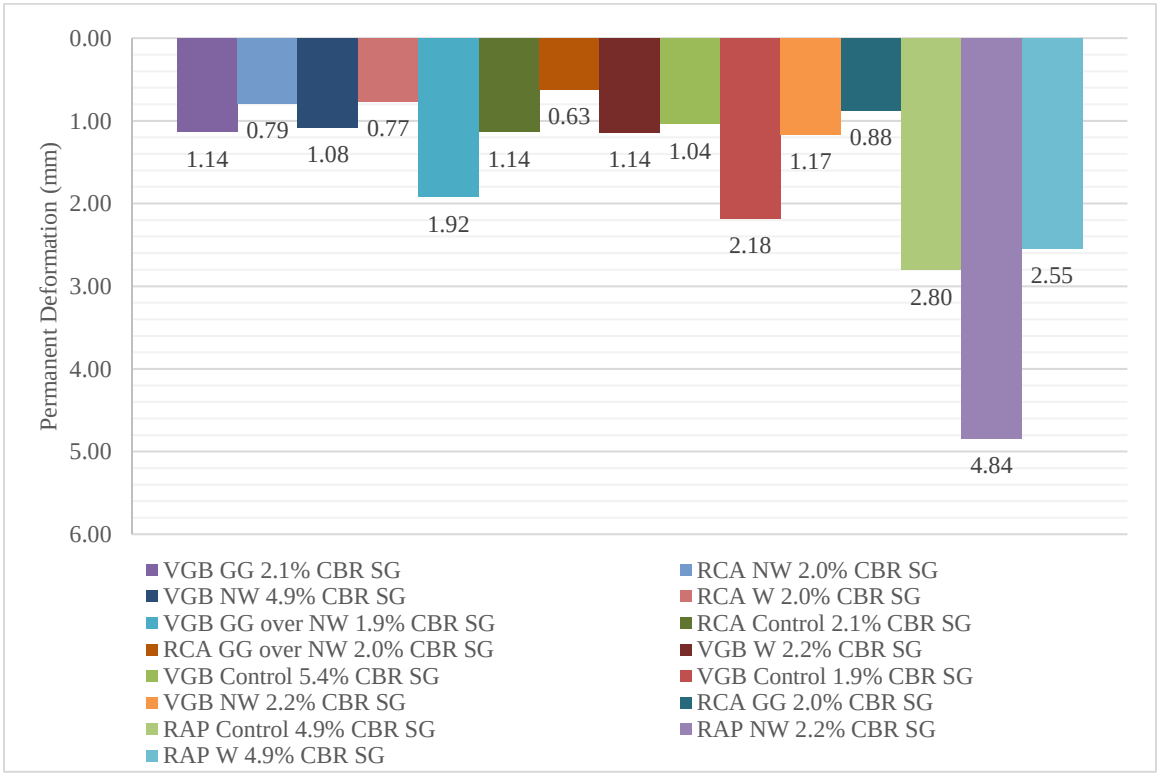

Figure 4.18. Permanent Deformation under Individual Load Sequence of 138 kPa.

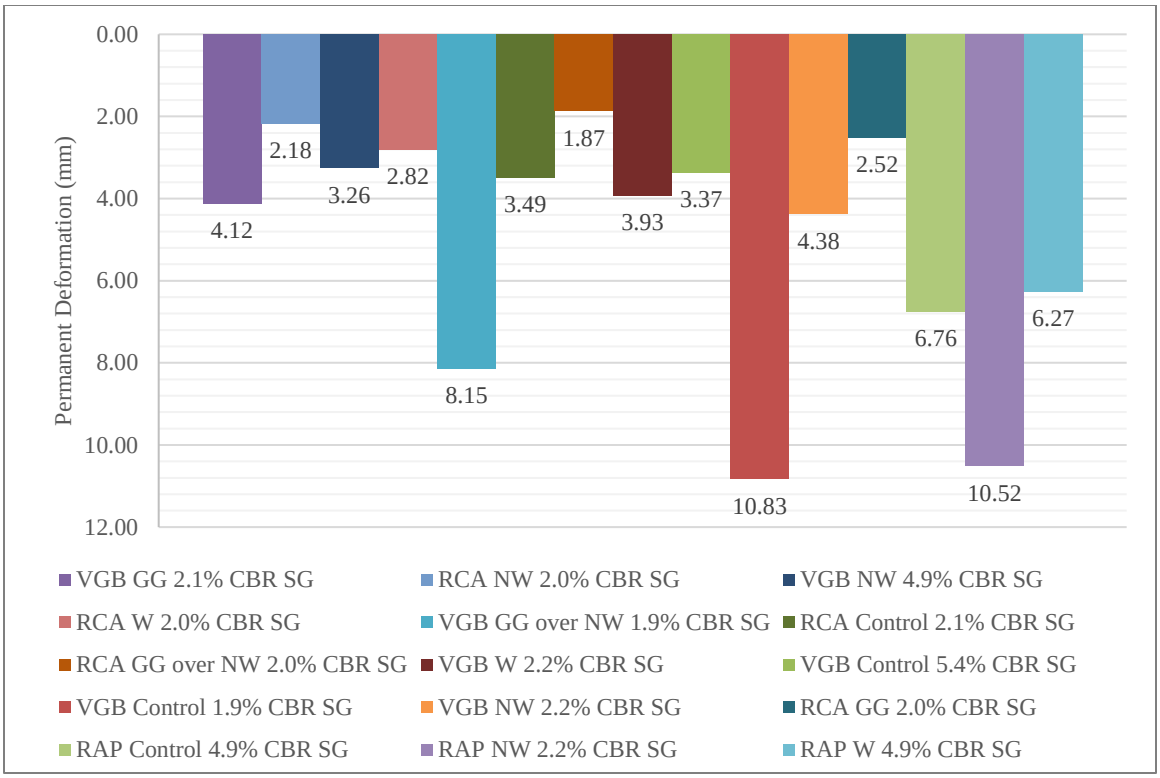

Figure 4.19. Permanent Deformation under Individual Load Sequence of 207 kPa.

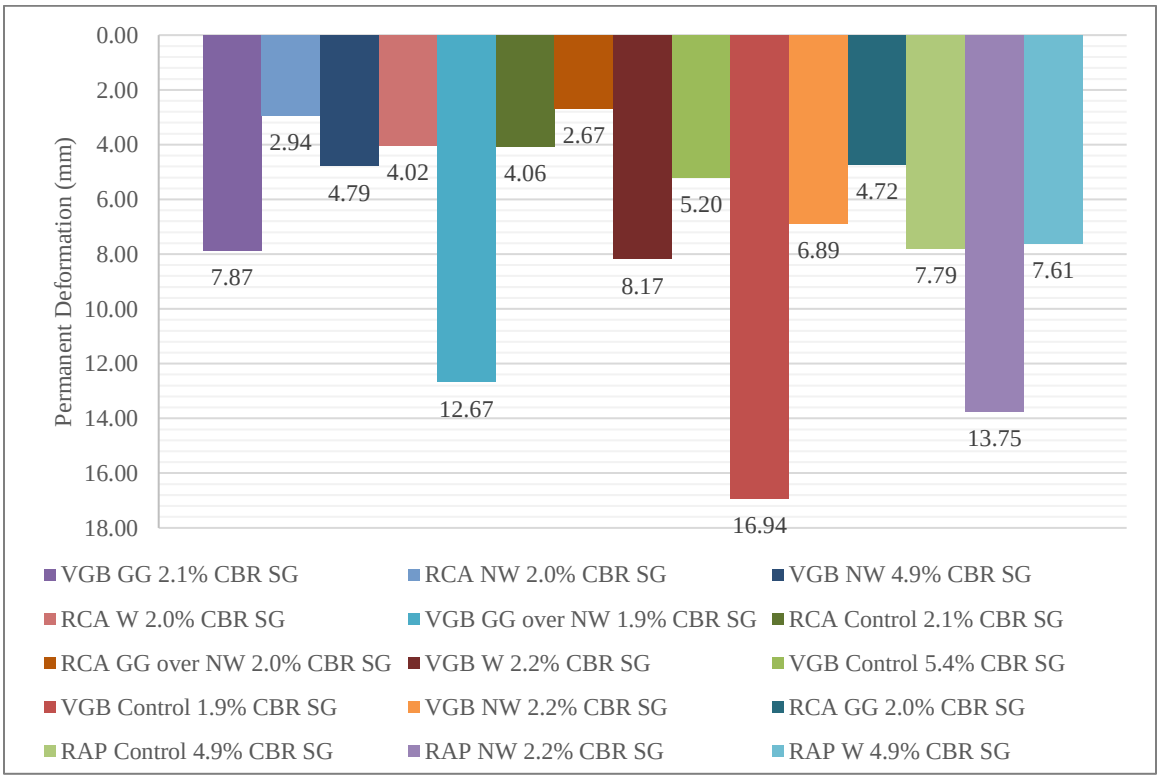

Figure 4.20. Permanent Deformation under Individual Load Sequence of 276 kPa.

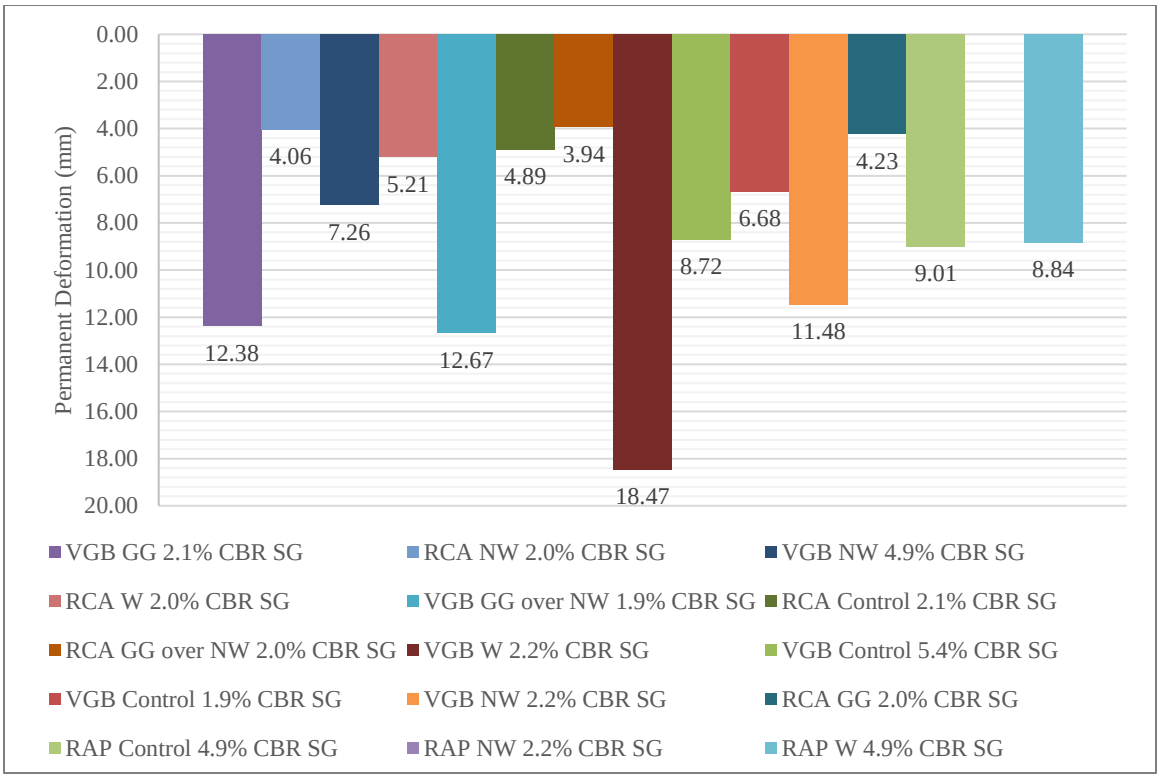

Figure 4.21. Permanent Deformation under Individual Load Sequence of 345 kPa.

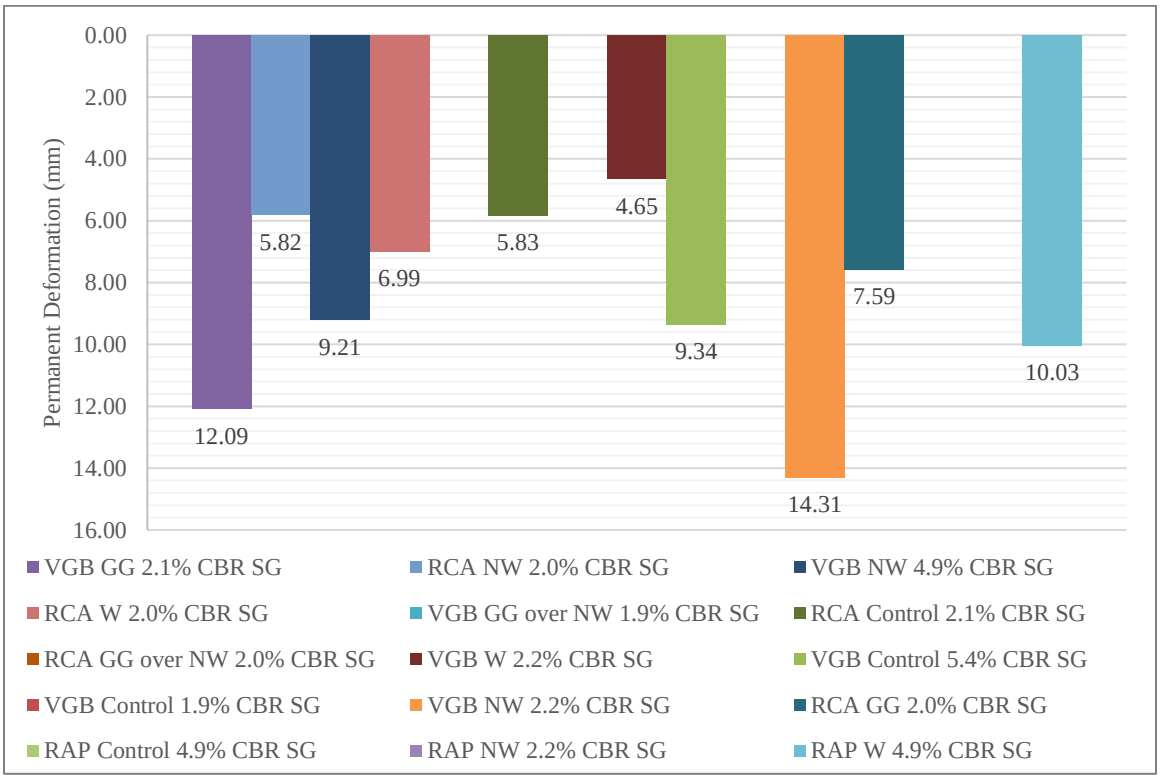

Figure 4.22. Permanent Deformation under Individual Load Sequence of 414 kPa.

At the later stages of the VGB sections, the permanent deformation greatly increased to beyond the 25 mm limit, indicating a failure of the section. This failure was exhibited visually by a punching failure (Figure 4.23), rapid increase in permanent deformation vs. cycle number (Figure 4.8), and change of the resilient deformation trend from linear to curved (Figure 4.25).

By contrast, the RCA sections did not display the punching failure but a more generalized depression as displayed in Figure 4.24. In later loading stages the displacement behavior kept a consistent form as the section accumulated more permanent deformation. Total deformations after 13,000 cycles for all RCA sections were below the 25 mm limit.

Figure 4.23. Punching Failure at Surface of the VGB Section Due to Cyclic Loading.

Figure 4.24. Surface Depression on the RCA Section after Cyclic Loading.

Resilient Deformation

Figure 4.25 shows the average resilient deformation of each test section by load sequence. The resilient deformations for different sections by applied load magnitude follow the same approximately linearly increasing trend with similar values. Virgin granular base with woven geotextile consistently displayed the largest resilient deformation, although the differences in magnitude of the resilient deformation were minimal. Even between the strong and weak subgrades and different types of geosynthetics, the differences in average resilient deformations are minimal. In the test sections that reached the largest permanent deformation (i.e. the ones that did not reach 13,000 cycles) the resilient deformation increased at a greater rate in the later stages. The RAP sections and the VGB control section displayed some of the smallest resilient deformation along with larger permanent deformation (see Figure 4.8); these sections that have lower resilient deformations display higher permanent deformations at earlier cycle numbers.

A closer look at the early stages shows a linear relationship of the resilient deformation of all base course sections. As with the permanent deformation, distinction between the resilient

deformations of the sections in the first 5 load sequences is not possible due to the similarity in deformation values. Resilient behavior appears more uniform throughout the cyclic load sequence in early, lower-magnitude load stages. There are several possibilities for this, but it is likely that the low loads induced small deformations that were not large enough to initiate the benefits of geosynthetics, which include lateral restraint and separation at such low displacements. When the accumulated deformation (see the previous section) is very small, the aggregate strength and compaction dominated the behavior of the base course, thus resulting in similar values.

The small differences in resilient deformations highlight the importance of the permanent deformation behavior, especially in terms of the MEPDG damage model and the mechanisms through which geosynthetics stabilize base course sections (see Chapter 2). The MEPDG damage model (NCHRP 2004) suggests that the permanent strain of a pavement layer is proportional to its resilient strain, and this relationship is unique for a given base course material. This relationship was developed based on isotropic materials. In this study, the resilient deformations for all test sections were similar but their permanent deformations were very different; therefore, the relationships of permanent deformation versus resilient deformation of geosynthetic-stabilized bases should be re-examined.

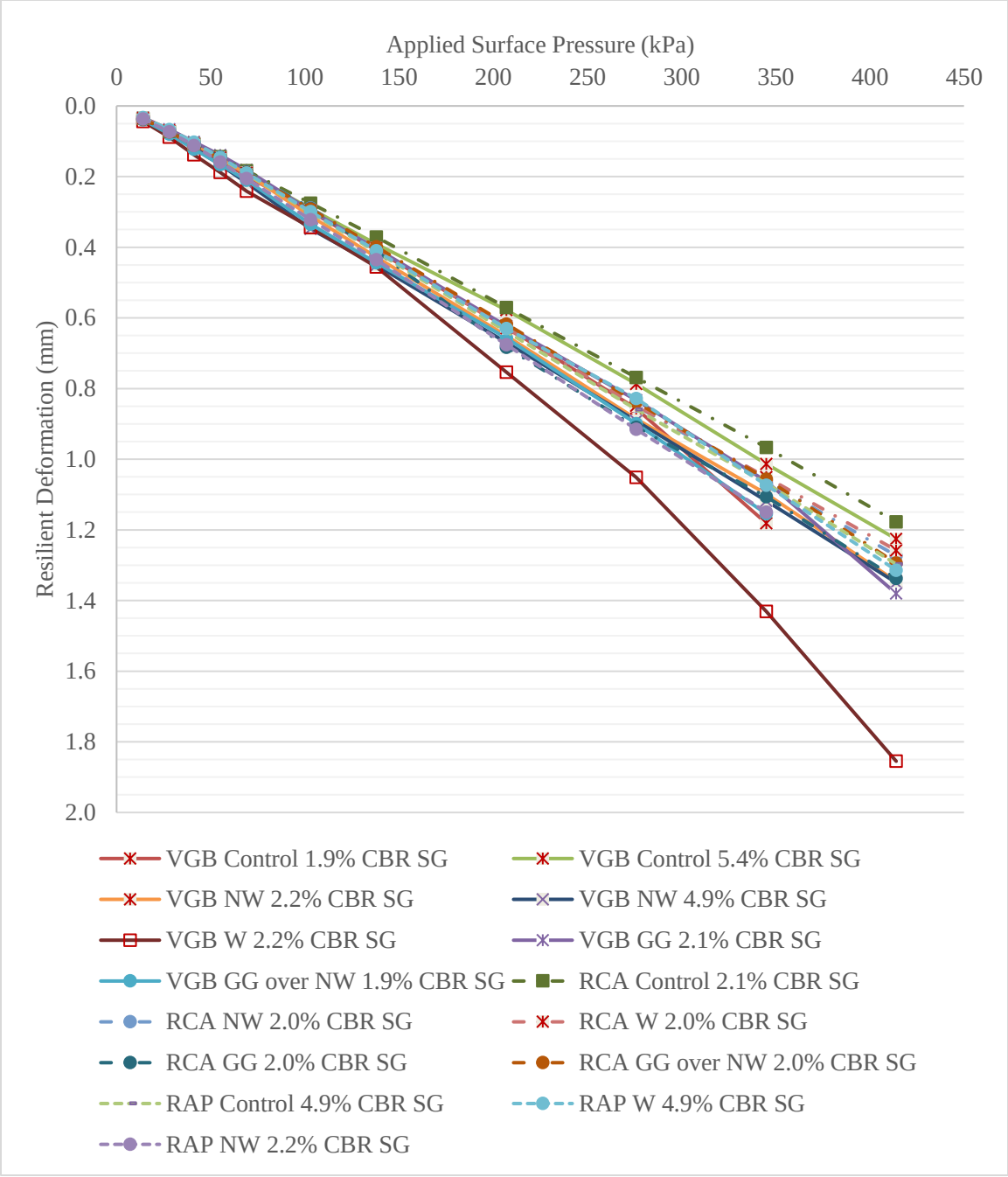

Figure 4.25. Average Resilient Deformations of Unpaved Sections under Different Load Increments.

Resilient deformation at the surface of the base course for each cycle may be used to calculate the composite resilient modulus (M_r) (Qian et. al. 2011). In this calculation, load plate diameter was 0.3 m and Poisson's ratio was assumed to be 0.45 (Huang 2004); the applied surface pressure and the measured resilient deformation were taken from the actuator readings in the experiment for each load cycle. These composite resilient moduli estimates are displayed in Figure 4.26. Resilient moduli over the loading process decreased over the earlier sequences of lighter loading and fewer cycles; as the test progressed at higher magnitudes and over a greater number of cycles, the modulus values become more consistent. As Burmister (1958) and later Tamrakar et al. (2019) noted, stress-related densification occurs until a base course section reaches a steady state or N* value where the incremental permanent as well as the resilient deformations become stable; this is believed to have occurred in these tests where the resilient moduli calculated using Eq. (2.38) became similar for increasing applied loads.

As is noted in the displacement curves (Figure 4.8), the addition of geosynthetics decreased the permanent deformation but increased the resilient deformation (the "band" became thicker). This flexibility allows for the geosynthetic-stabilized sections to resist permanent damage by acting in a more flexible manner. Because the resilient or load-by-load induced deformation is used in the Qian et al. (2011) method, minimal distinctions in calculated resilient moduli are shown in Figure 4.26 below. Based on this approach, the calculated resilient moduli for the stabilized sections were lower than those of the control sections despite smaller permanent deformations as a result of geosynthetic stabilization. This discussion indicates that the method using a resilient deformation to estimate resilient modulus for a geosynthetic-stabilized base may not be appropriate.

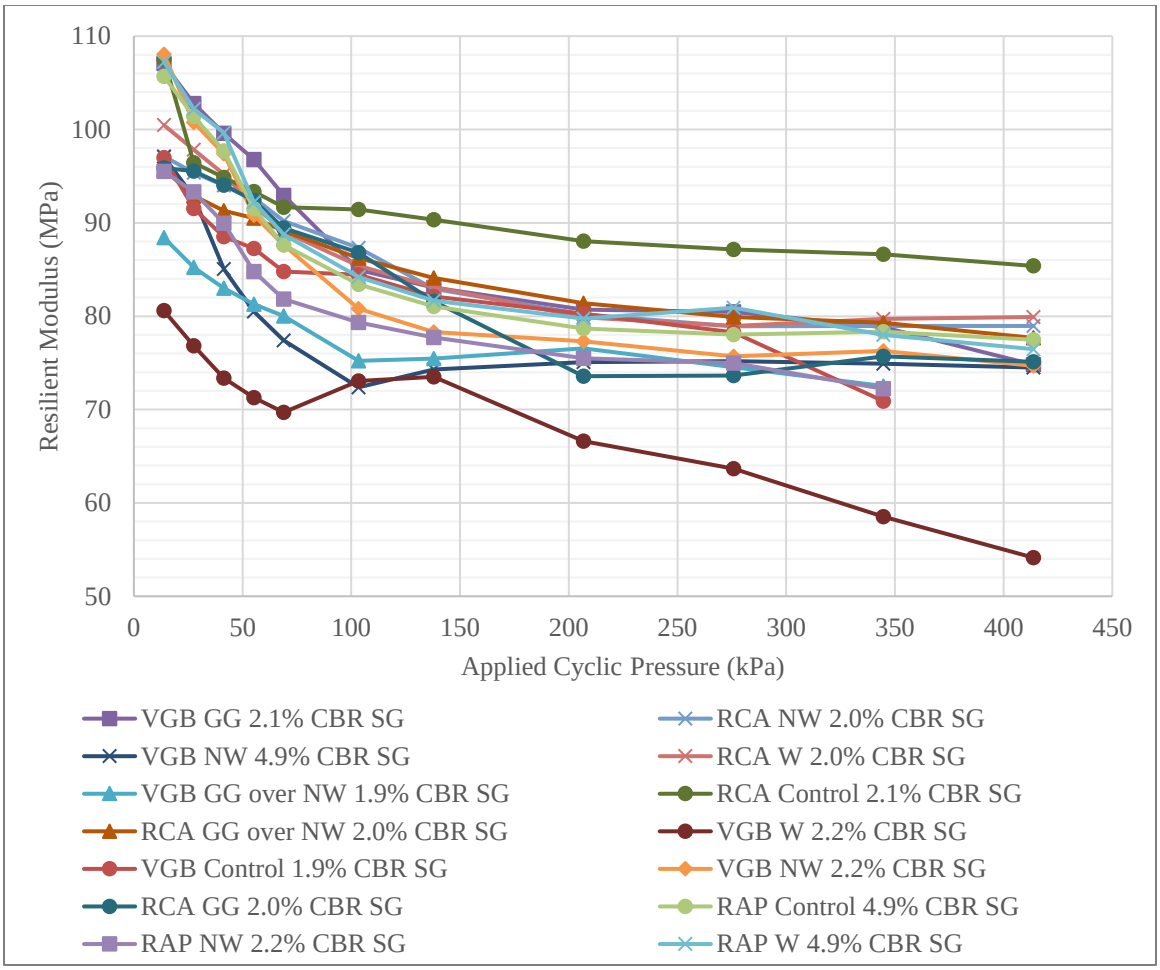

Figure 4.26. Composite Resilient Modulus of Unpaved Sections over 2%-CBR Subgrade vs. Cyclic Load using Surface Resilient Deformation.

Burmister's (1945) layered elastic theory for resilient surface deformation under a rigid plate may be used to estimate the resilient moduli of the base courses from the composite resilient moduli in Figure 4.26 as displayed in Figure 4.27. In this calculation, the two layers (base course and subgrade) were assumed to have Poisson's ratios of 0.50 in order to use the Burmister (1945) settlement coefficient chart. Applied surface pressure by load sequence, average resilient deformation for each sequence, plate radius of 0.15 m, and base course thickness of 0.25 m were used to solve for the settlement coefficient, F_w, and then the modulus

ratio of the base to the subgrade. The subgrade's resilient modulus was assumed to be its CBR multiplied 10.3 MPa (AASHTO 1993). The modulus ratio from Burmister (1945) was then multiplied by the estimated subgrade resilient modulus to determine the resilient modulus of the base course section. As Qian et al. (2011) observed, the resilient moduli reached a somewhat consistent value at later sequences (see Figure 4.27). As this method is dependent on the resilient deformations, geosynthetic-stabilized sections that exhibited larger resilient deformations than the control sections yielded lower resilient moduli. Therefore, this method has the same problem as discussed above because of the use of the resilient deformation. Consequently, other methods should be sought and will be discussed in Chapter 6 of this dissertation.

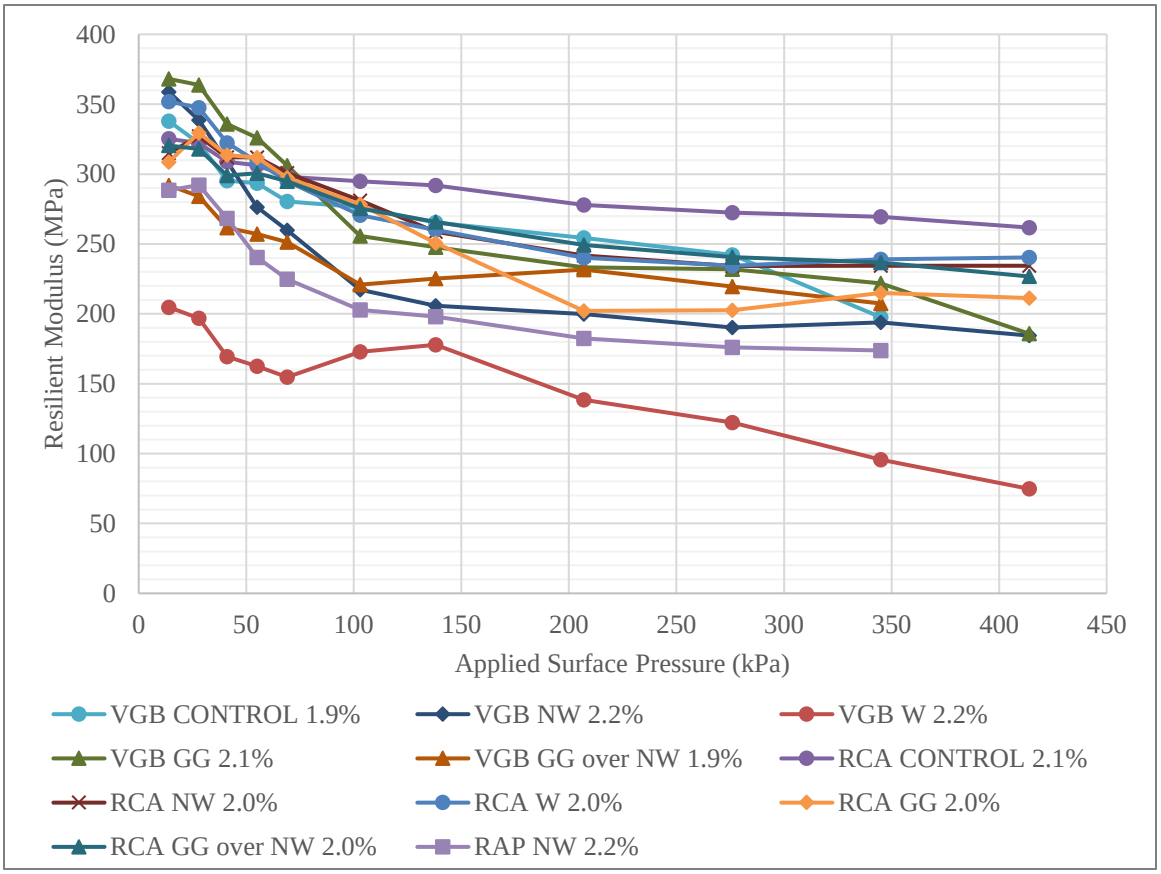

Figure 4.27. Load Sequence vs. Resilient Modulus of Unpaved Section using Layered Theory and Elastic Solution, Unpaved.

Because the thickness of the deformation bands in Figure 4.8 are difficult to compare, resilient deformations under each load increment for all the test sections are displayed in Figure 4.28 through Figure 4.38. These figures show the very small discrepancies in resilient deformation that will not be correlated to permanent vertical deformation of a section or show the stabilizing benefits of geosynthetics.

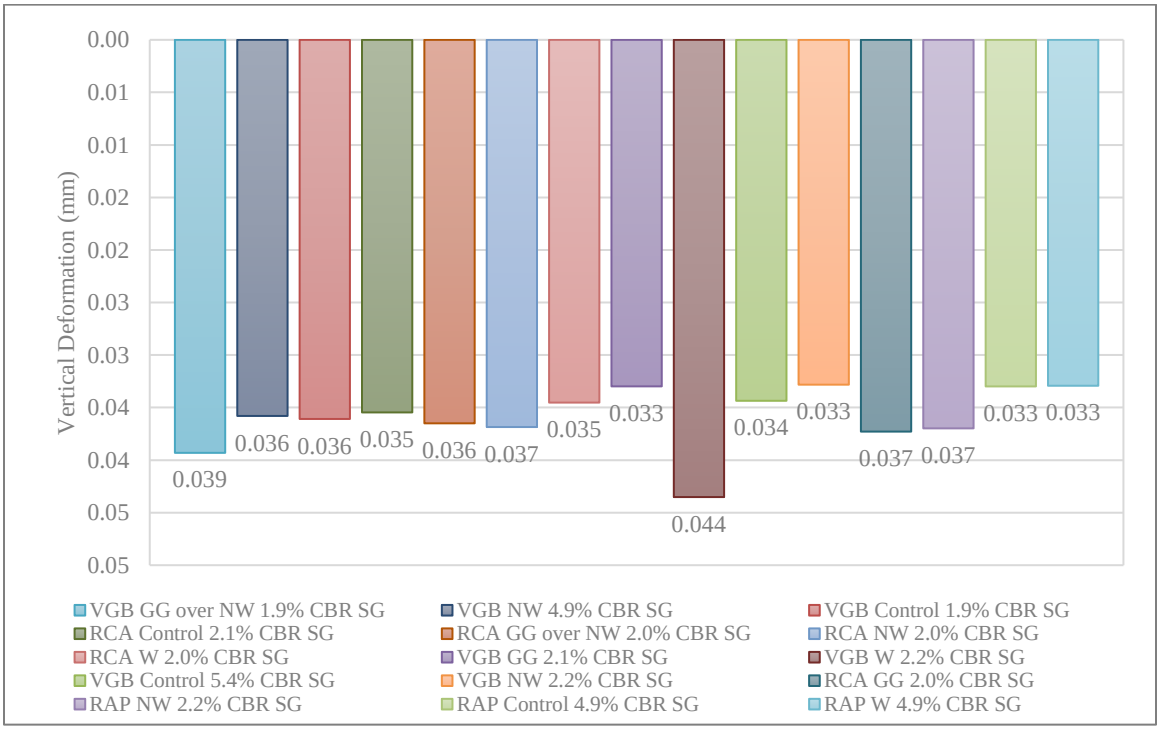

Figure 4.28. Average Resilient Deformation under Load Sequence of 14 kPa.

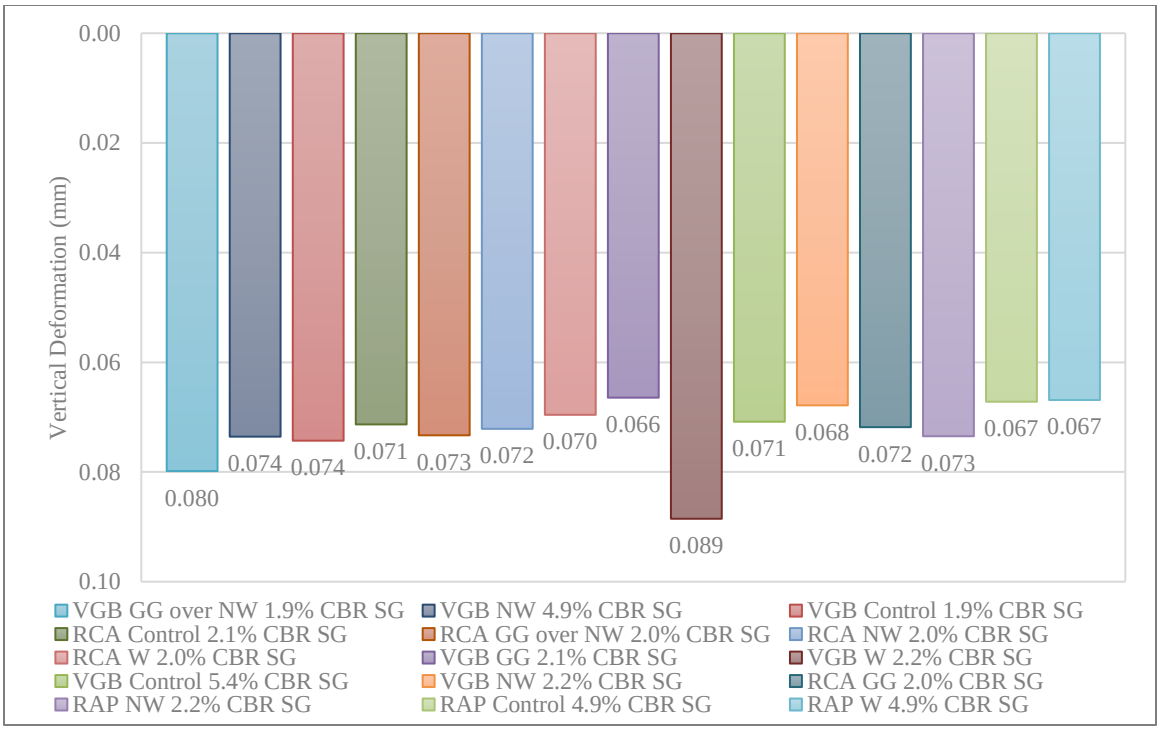

Figure 4.29. Average Resilient Deformation under Load Sequence of 28 kPa.

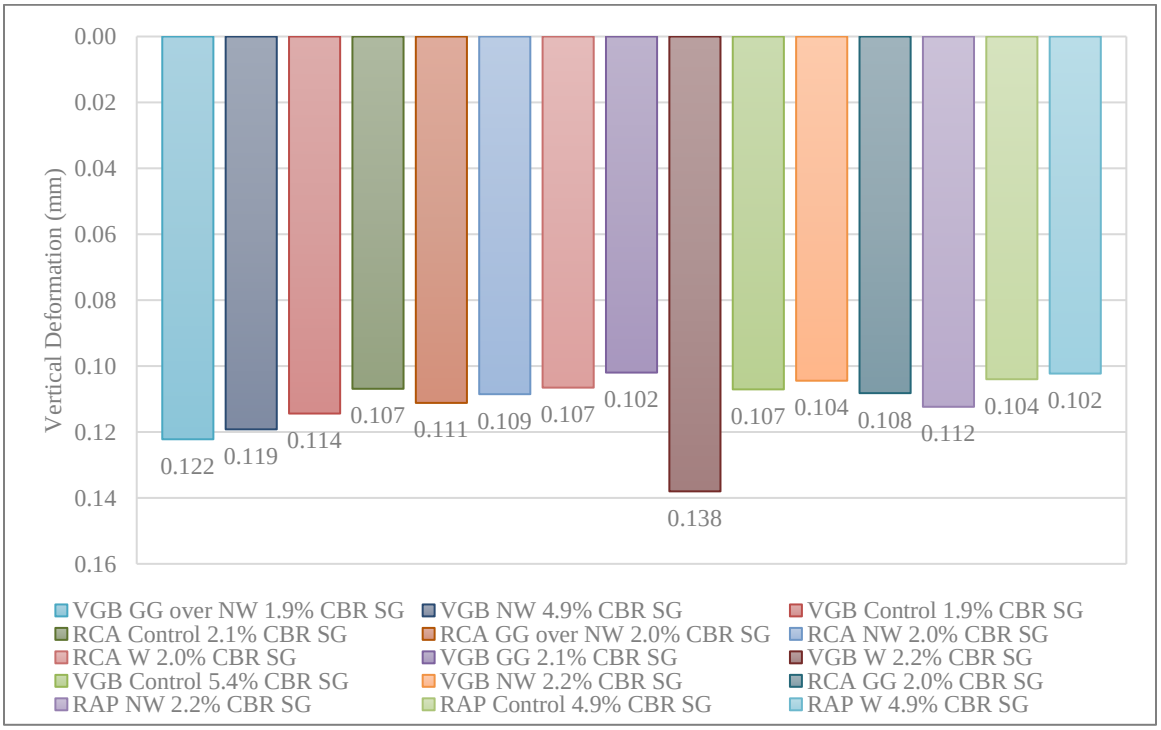

Figure 4.30. Average Resilient Deformation under Load Sequence of 41 kPa.

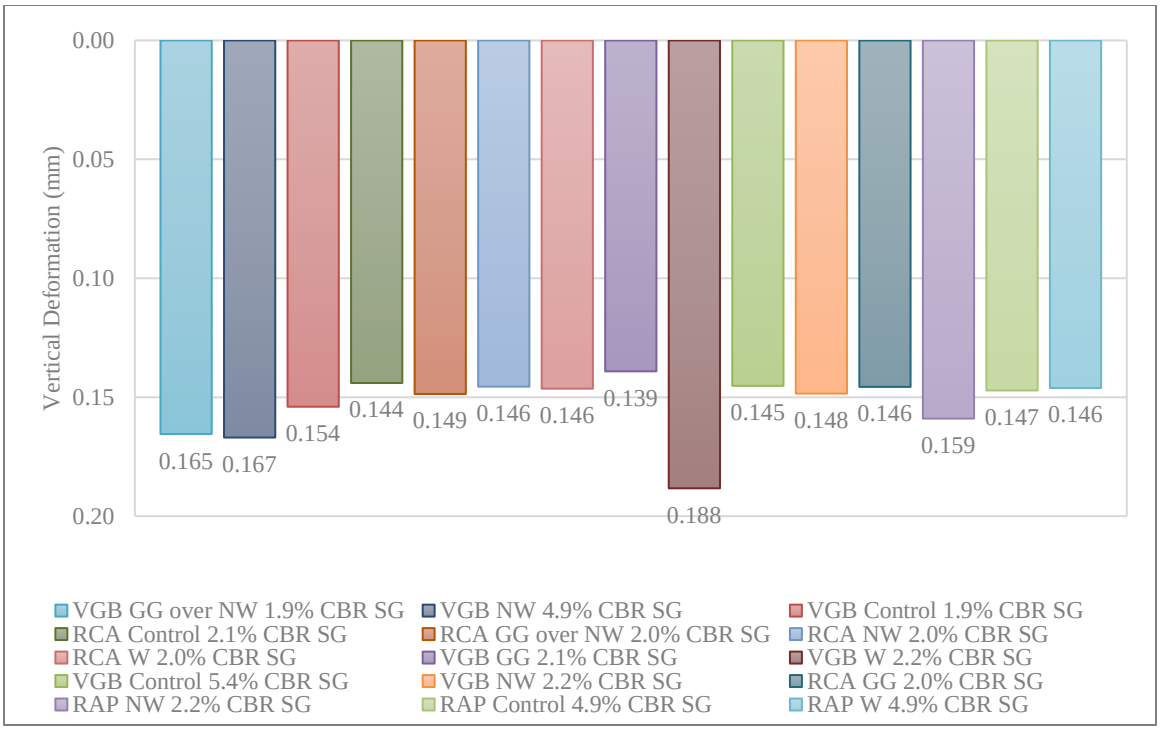

Figure 4.31. Average Resilient Deformation under Load Sequence of 55 kPa.

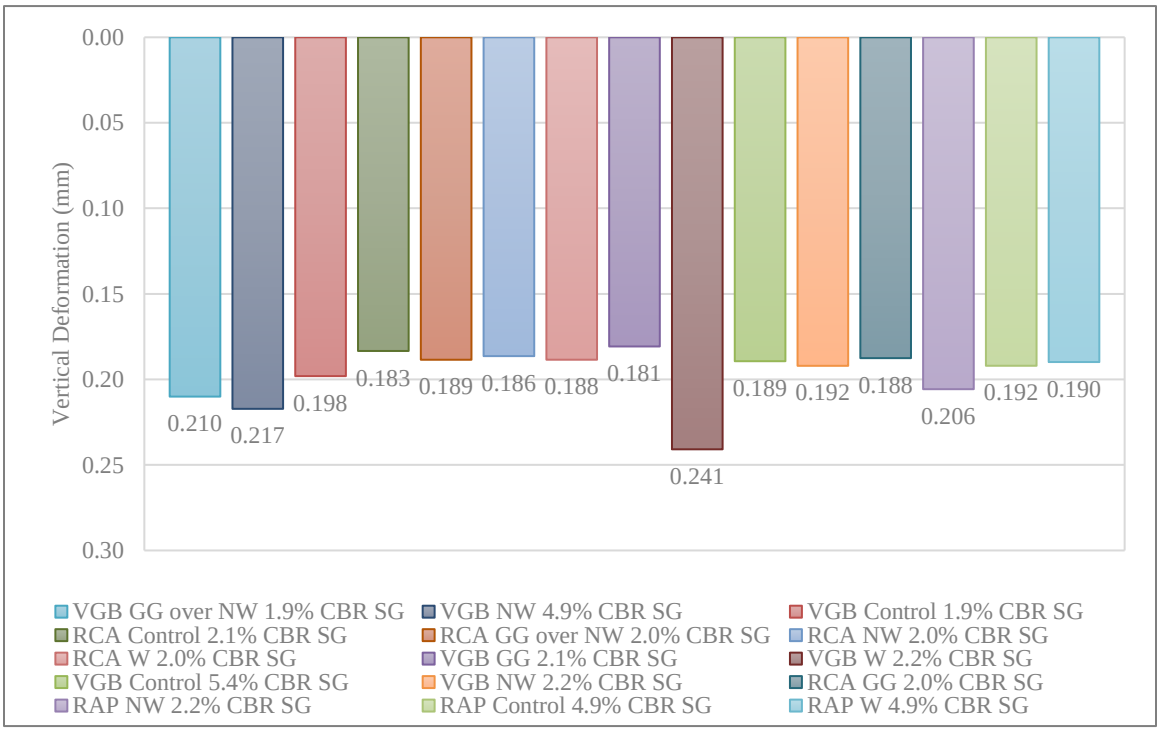

Figure 4.32. Average Resilient Deformation under Load Sequence of 69 kPa.

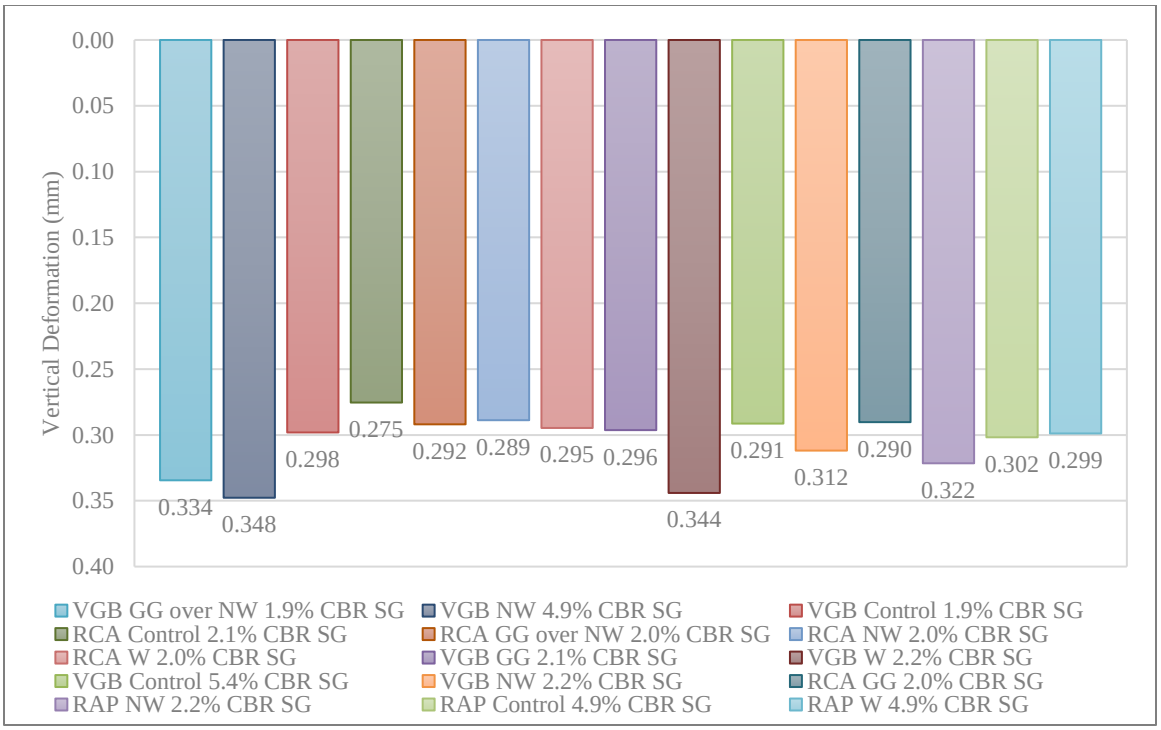

Figure 4.33. Average Resilient Deformation under Load Sequence of 103 kPa.

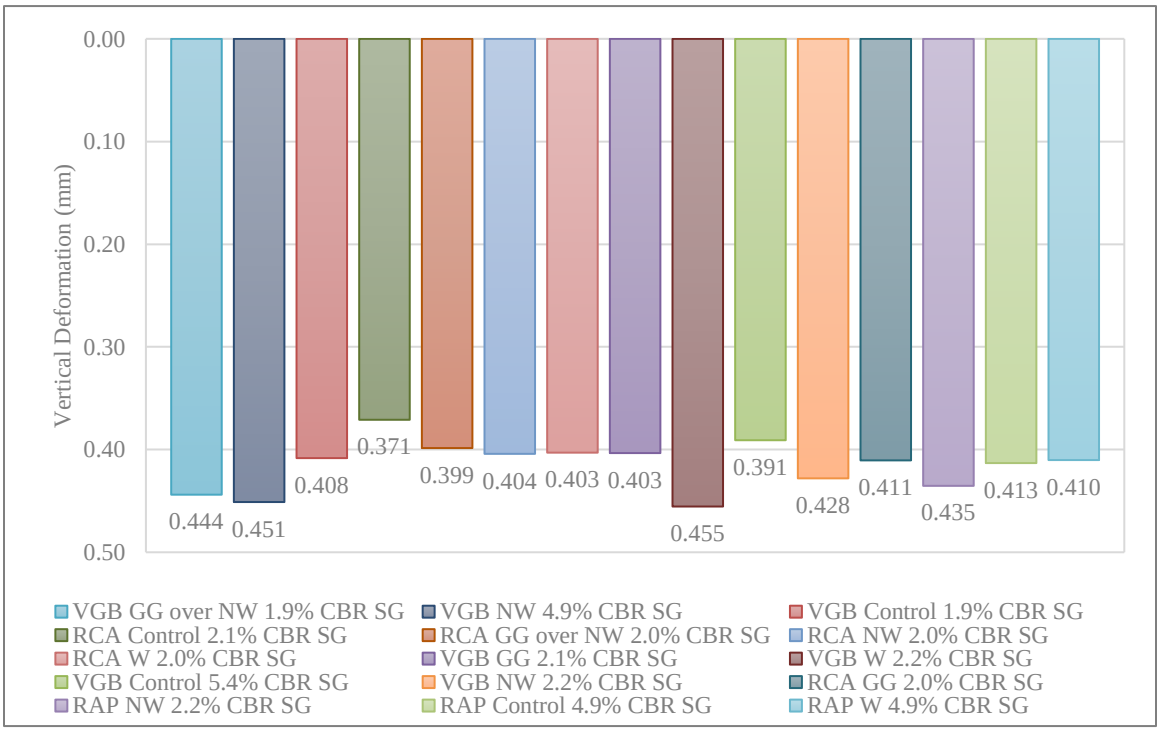

Figure 4.34. Average Resilient Deformation under Load Sequence of 138 kPa.

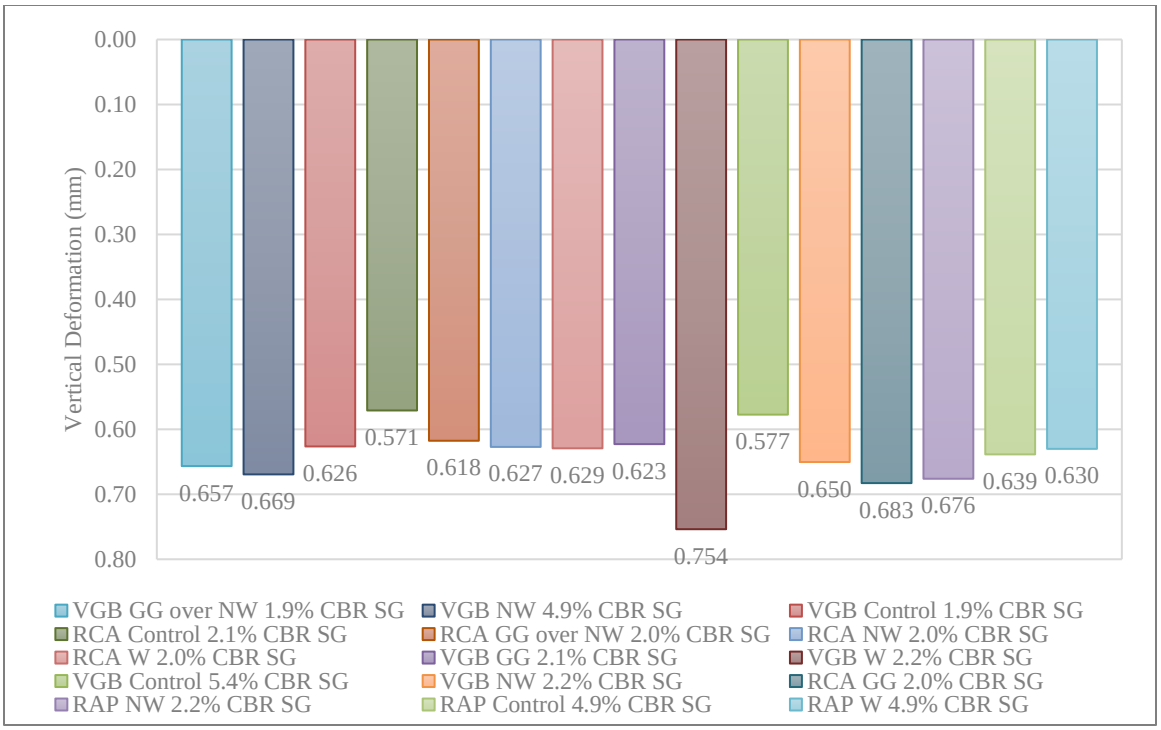

Figure 4.35. Average Resilient Deformation under Load Sequence of 207 kPa.

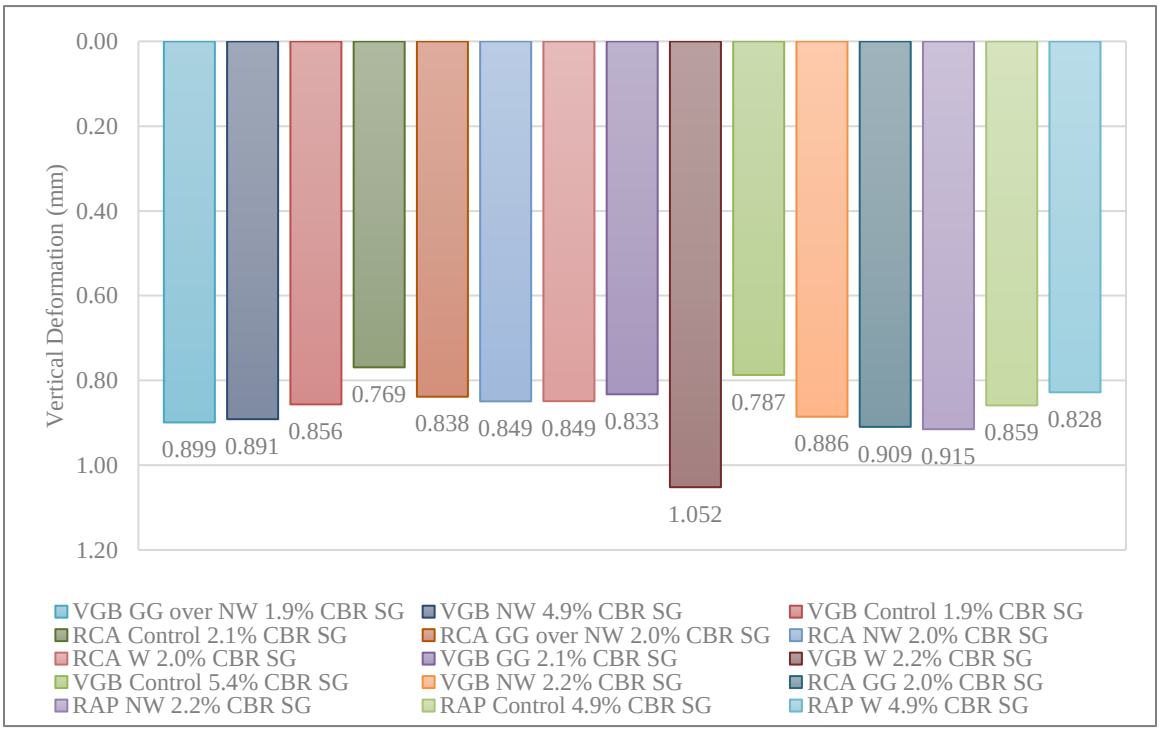

Figure 4.36. Average Resilient Deformation under Load Sequence of 276 kPa.

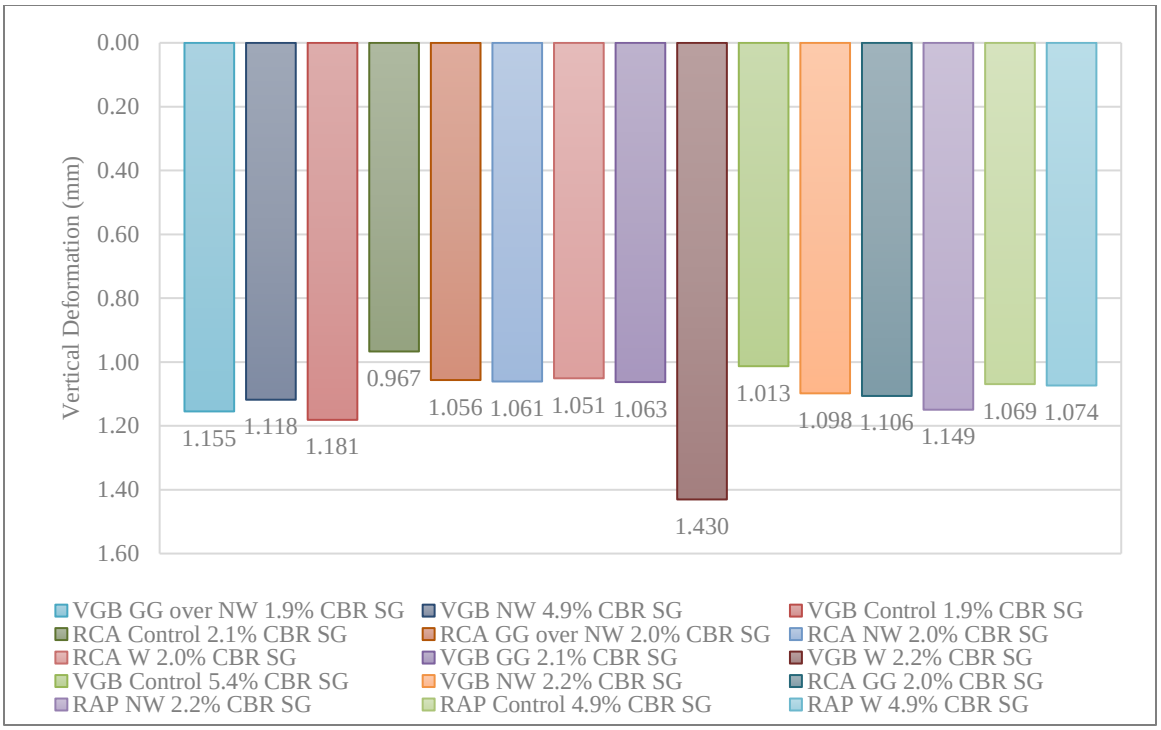

Figure 4.37. Average Resilient Deformation under Load Sequence of 345 kPa.

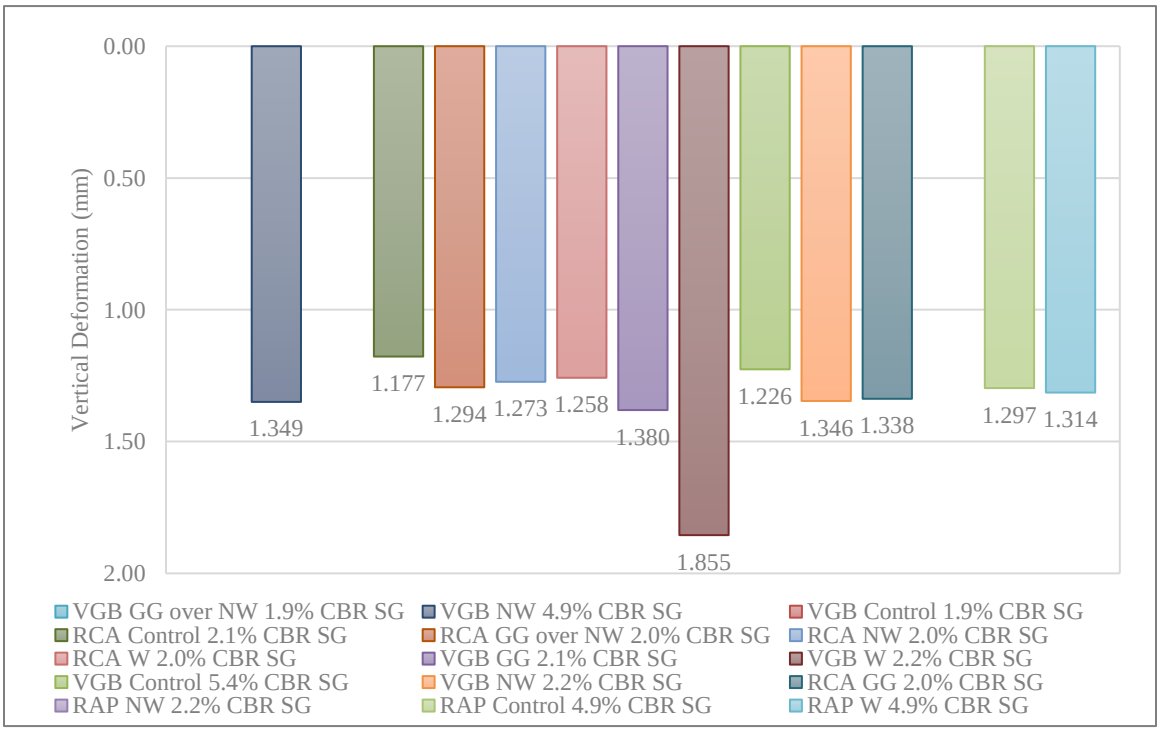

Figure 4.38. Average Resilient Deformation under Load Sequence of 414 kPa.

Deformation Ratios

As identified in the pavement damage model for rutting in the MEPDG (NCHRP 2004), there exists a unique relationship between the incremental permanent deformation and the average resilient deformation for a given unpaved road section. Figure 4.39 displays this incremental permanent deformation incurred against the average resilient deformation for each of the unpaved sections over 2% CBR subgrade. As discussed above, the differences in the resilient deformations among different test sections are minimal, but the slopes of the lines plotting incremental permanent deformation against resilient deformation are steeper for the sections that exhibited larger permanent deformations.

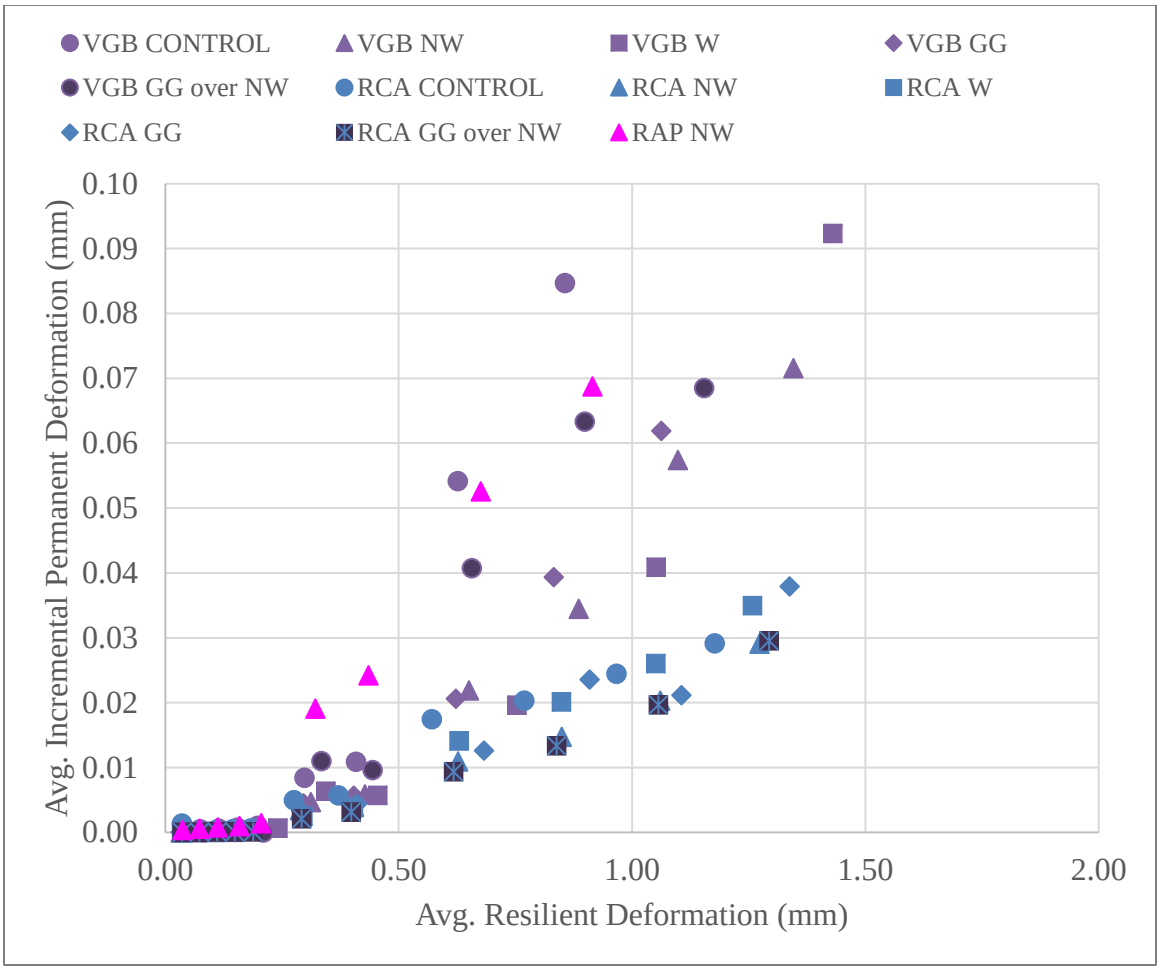

Figure 4.39. Average Resilient vs. Average Incremental Permanent Deformations for Unpaved Sections atop 2% CBR Subgrade.

To provide better evaluation of the data presented in Figure 4.39, Figure 4.40 and Figure 4.41 separate the data for the VGB and recycled base course (RCA and RAP) sections and show linear trend lines of the incremental permanent deformation against the average resilient deformation. Replacement of VGB by RCA consistently reduced the deformation ratios in all stabilization cases because addition of geosynthetics increased the resilient deformation but decreased the total permanent deformation (see Figure 4.8). When the slope of the trend line decreased, the ratio of permanent deformation to resilient deformation decreased and correlated

with the decrease in the total permanent deformation. This inverse relationship depicts the more malleable and thus resilient nature of geosynthetic-stabilized base course. Since the RCA sections displayed smaller permanent deformations than all the VGB sections, their ratios δ_{pi}/δ_r were correspondingly lower. This deformation rate correlation is unique to each aggregate and geosynthetic stabilization test section, confirming the relationship in Tseng and Lytton (1989) and subsequently the MEPDG damage model (NCRHP 2004).

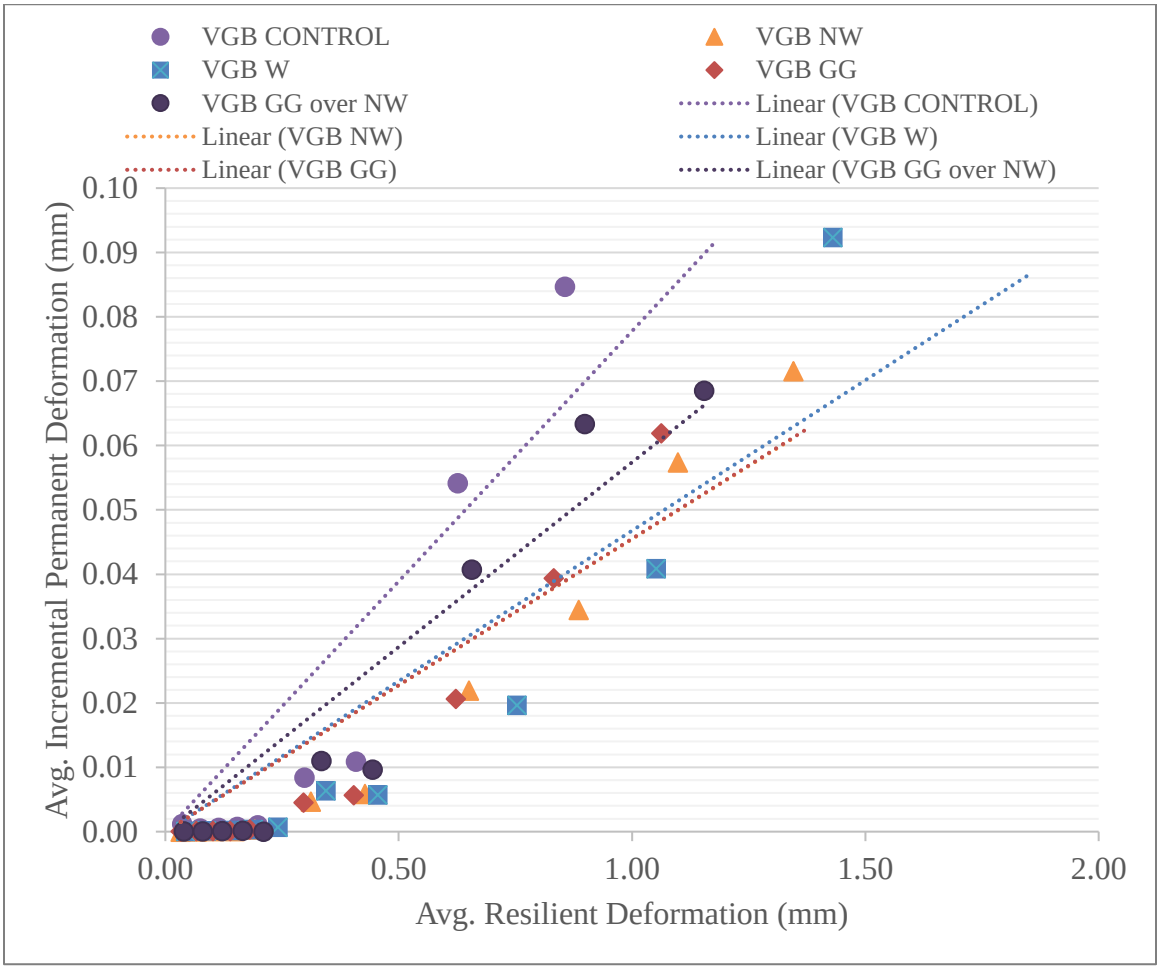

Figure 4.40. Average Resilient vs. Average Incremental Permanent Deformations of the VGB Sections atop 2% CBR Subgrade.

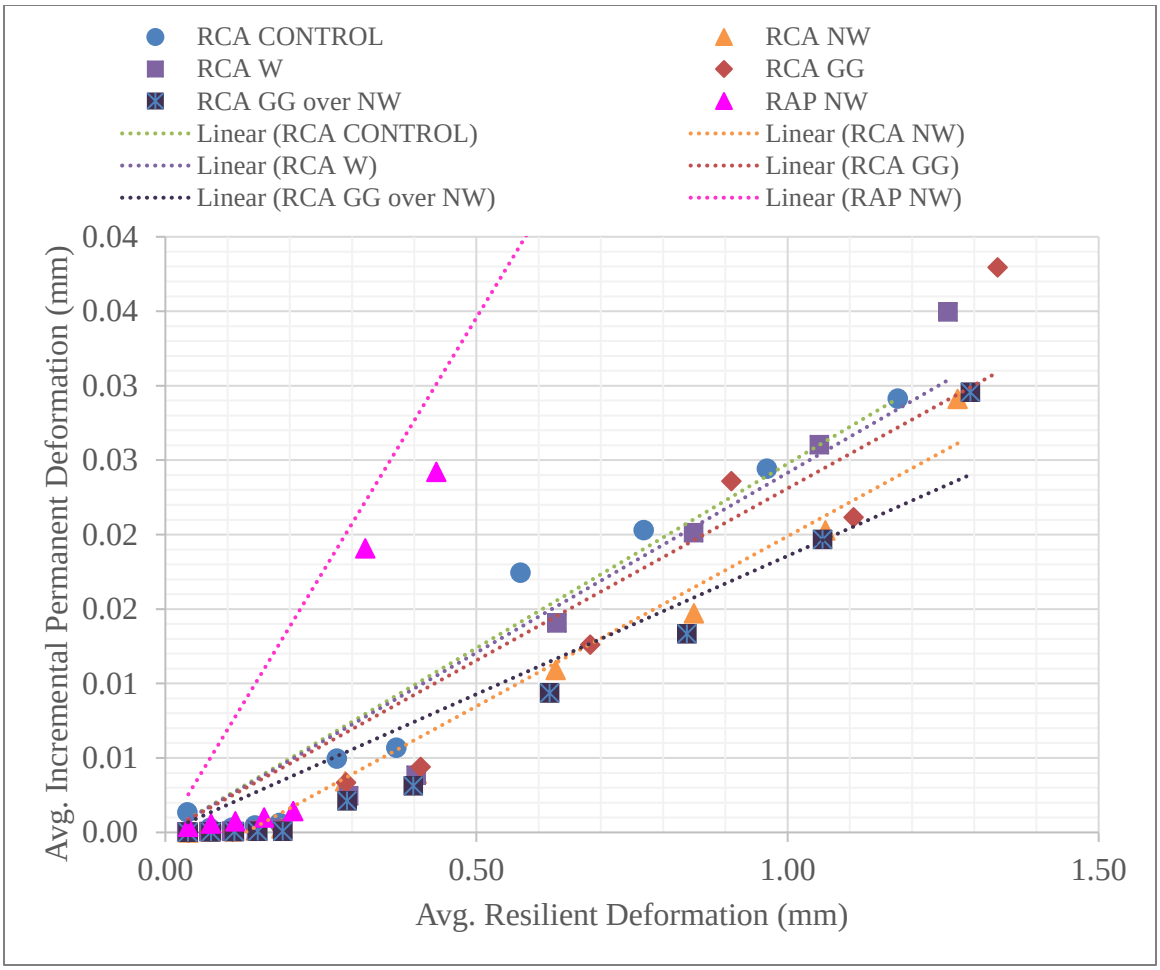

Figure 4.41. Average Resilient vs. Average Incremental Permanent Deformations of the RCA and RAP Sections atop 2% CBR Subgrade.

Figure 4.42 displays the relationship between the accumulated permanent deformation and the average resilient deformation for the 2,000-cycle load sequences in the unpaved test sections atop 2% CBR subgrade. In this figure, the numbers next to the data points indicate the corresponding load sequence and thus the applied load magnitude (see Table 3.5). Of note is the linear relationship observed between the permanent and resilient deformations in this figure for the same number of applied load cycles and magnitudes. The addition of geosynthetics for both the VGB and RCA increased the resilient deformation for the same accumulated permanent

deformation at later load stages; this relationship indicates that for a larger resilient deformation attained at a higher load magnitude, the accumulated permanent deformation was limited.

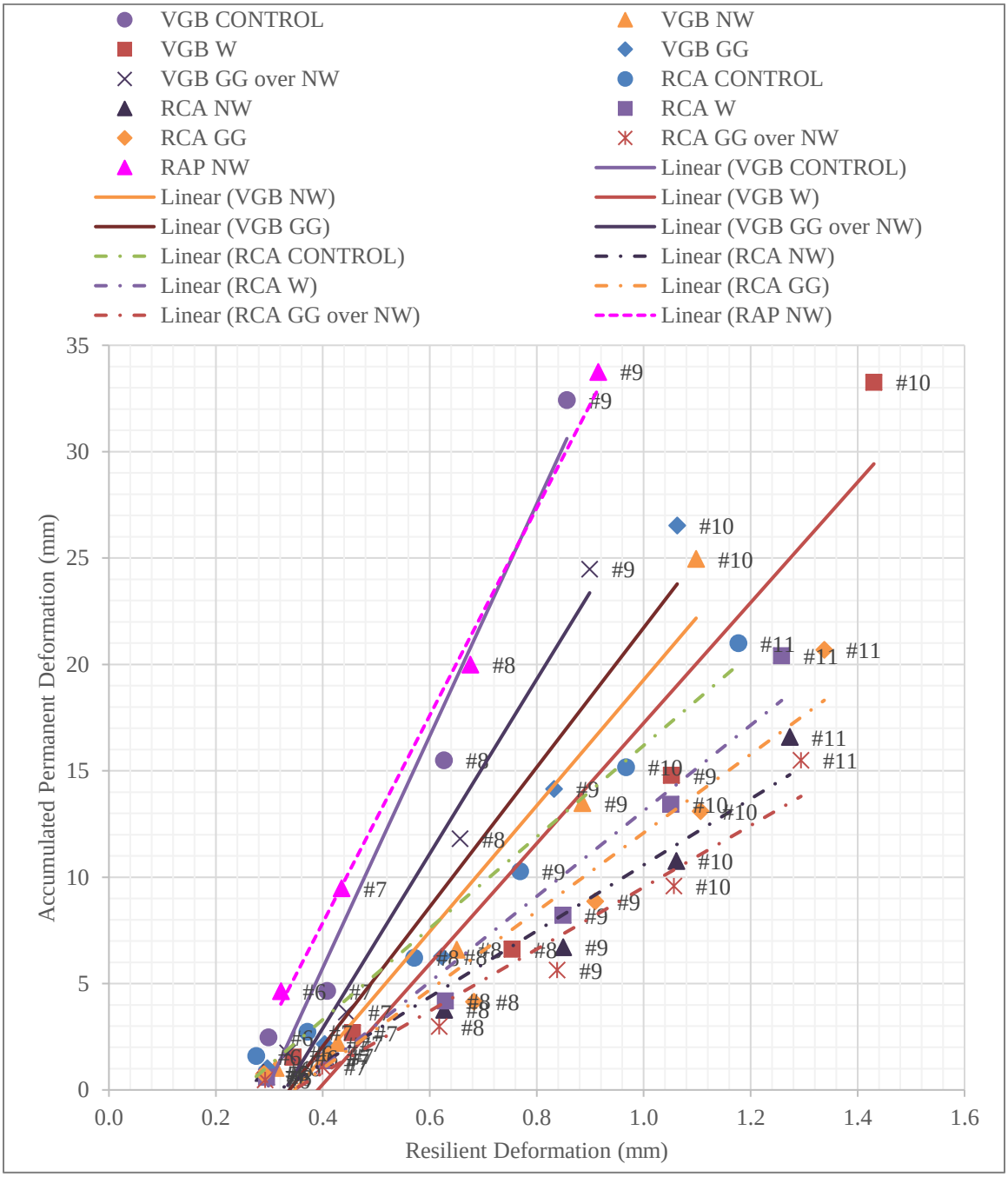

Figure 4.42. Average Resilient Deformation vs. Accumulated Permanent Deformation under 2,000-cycle Load Sequences for Unpaved Sections atop 2% CBR Subgrade.

In Figure 4.42, the permanent versus resilient deformations are plotted for the VGB (solid lines) as well as the RCA and RAP (dashed lines) sections over weak subgrade. It should also be noted that for both aggregates, the deformation ratios were reduced through the addition of geosynthetics. In the VGB sections the woven geotextile was most effective at reducing this ratio while in the RCA sections the nonwoven geotextile was most effective. Of note are the steeper slopes of the deformation ratios for the VGB sections when compared with those for the RCA sections: even with the shallowest-slope for the section stabilized by the woven geotextile, the replacement with RCA over VGB was more effective at reducing this permanent-to-resilient deformation ratio.

Figure 4.43 presents the deformation ratio relationships for the VGB test sections only over 2% CBR subgrade. Except for the woven geotextile, the resilient deformations for each load sequence are very similar; greater discrepancies occur in the permanent deformation by load sequence, as shown in the previous section. For woven geotextile, the magnitudes of both resilient and permanent deformations increased by load cycle, but the deformation ratio was the lowest for this geosynthetic in the VGB sections. The inherently strong woven geotextile allowed a great amount of resilient strain when a surface load was applied and released, while permanent deformation was not significantly reduced. This increase in resilient deformation was not as pronounced in the VGB sections stabilized with triaxial geogrid and nonwoven geotextile. In addition to the separation function, the nonwoven geotextile might have a similar mechanism as the geogrid by providing lateral restraint as interlock occurred both with the particles in the geogrid and the “punching interlock” of nonwoven geotextile and aggregate into the soft subgrade.

Further investigation of Figure 4.43 shows that the deformation ratio is not the only indicator of base course section stabilization with the addition of geosynthetics. While the slope of the line may be similar for different road sections, the load sequence number should also be noted. For example, the woven geotextile trendline is shallower in Figure 4.43 than all of the other trendlines, but the magnitude of both the nonwoven geotextile-stabilized and the geogrid-stabilized sections for Load Sequence #10 are lower for both resilient and accumulated permanent deformations. This accumulated deformation ratio must thus be calibrated to predict deformation in the field, as this ratio alone does not account for applied pressure.

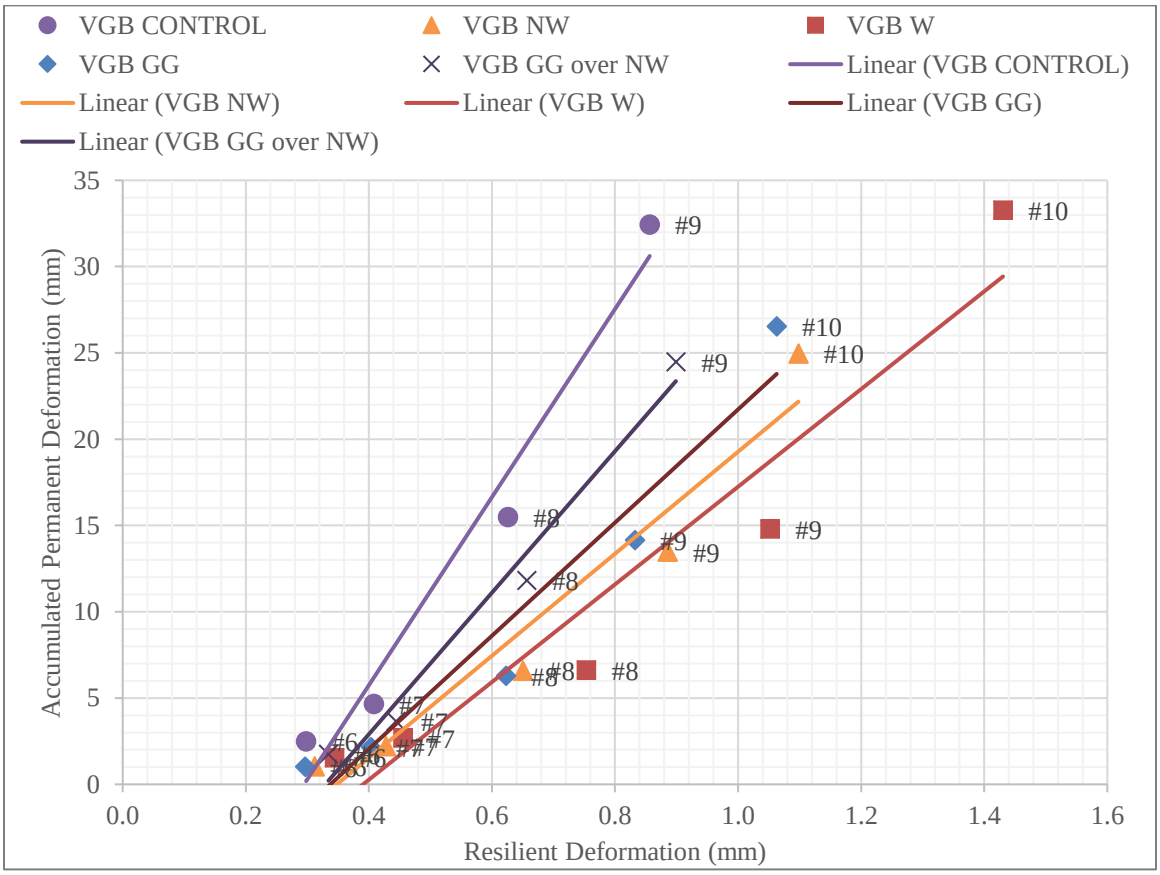

Figure 4.43. Average Resilient Deformation vs. Accumulated Permanent Deformation under 2,000-cycle Load Sequences for the VGB Sections atop 2% CBR Subgrade.

It would be expected that the VGB section with both geogrid and nonwoven geotextile (GG over NW) stabilization would display the lowest permanent-to-resilient-deformation ratio, but this was not the case as discussed earlier and shown in Figure 4.43. Although minimum allowable relative compaction was achieved, the aggregate particles did not sufficiently penetrate the geogrid apertures or push the nonwoven geotextile into soft subgrade; as a result, the aggregate was not fully engaged with the dual geosynthetics so that larger vertical deformation occurred in this test but might not occur in the field.

Figure 4.44 plots the deformation ratios for the RCA and RAP sections over 2% CBR subgrade for closer analysis. For these sections, the nonwoven geotextile and the combination of nonwoven and geogrid exhibited the lowest permanent-to-resilient deformation ratios, and woven geotextile exhibited the highest deformation ratios among all the geosynthetic-stabilized sections. In all RCA sections, similar to the VGB sections, the deformation ratios were reduced through the addition of geosynthetics. When compared against the non-stabilized section, the RCA sections exhibited larger resilient deformations for the same load cycle number for all geosynthetic-stabilized sections. Like in the VGB sections, woven geotextile exhibited one of the largest increases in both permanent and resilient deformations, but unlike the VGB sections, geogrid stabilization increased these deformations in the RCA sections. For both nonwoven-geotextile-stabilized sections (with and without geogrid), there were clear reductions in the accumulated permanent deformation with small increases in the resilient deformation when compared with the control section. As discussed earlier, the aggregate indented into the soft subgrade with the nonwoven geotextile was achieved with the RCA, providing a combination of lateral restraint and separation. Instead, the woven geotextile provided good separation without effective lateral restraint while geogrid provided good lateral restraint with less effective

separation. These phenomena have been evidenced by the imprints and no inter-mixing on the subgrade surface during the excavation of the RCA sections.

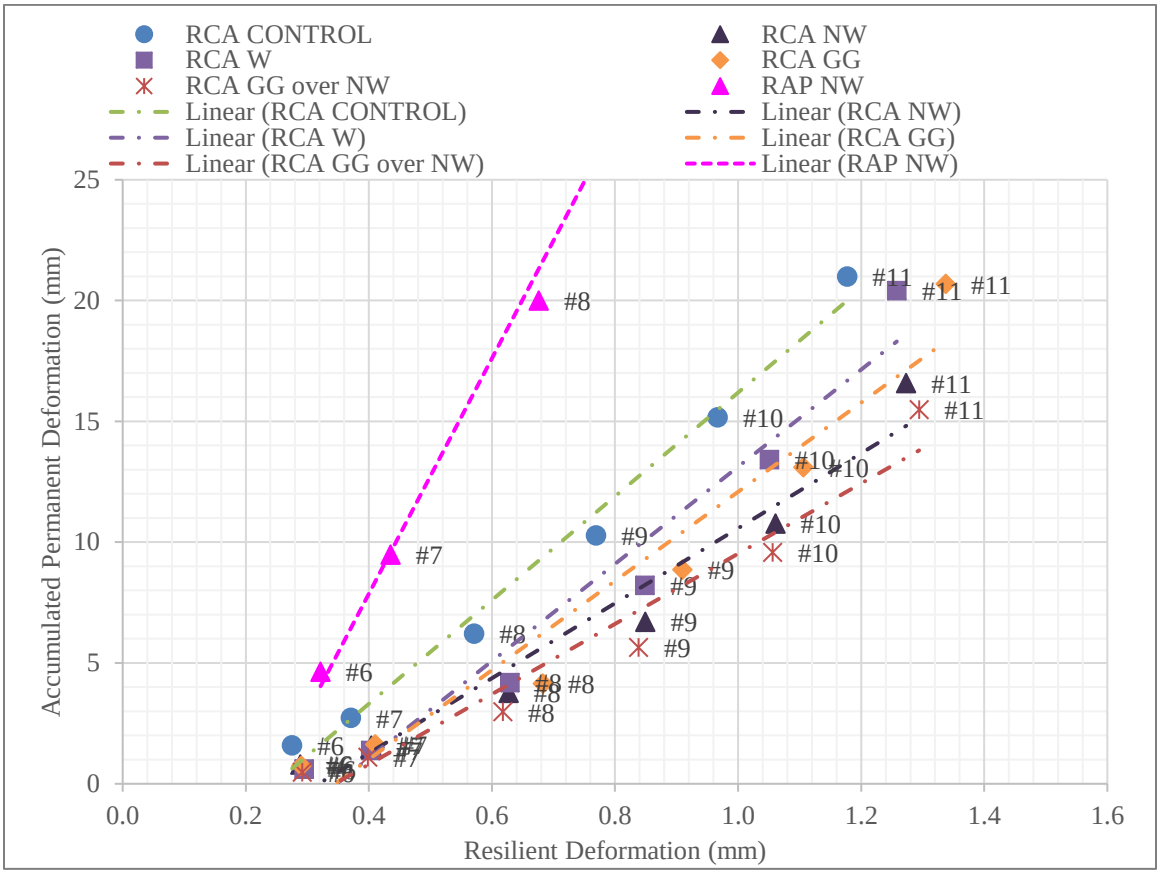

Figure 4.44. Average Resilient Deformation vs. Accumulated Permanent Deformation under 2,000-cycle Load Sequences of the RCA and RAP Sections atop 2% CBR Subgrade.

Each incremental deformation versus average resilient deformation ratio (δ_{pi}/δ_r) is plotted against the applied surface load in Figure 4.45. The magnitudes of the resilient and incremental permanent deformations increased linearly with load magnitude as described previously; thus, the δ_{pi}/δ_r ratios are relatively the same across the applied load magnitudes. This ratio is thus unique but independent of load magnitude.

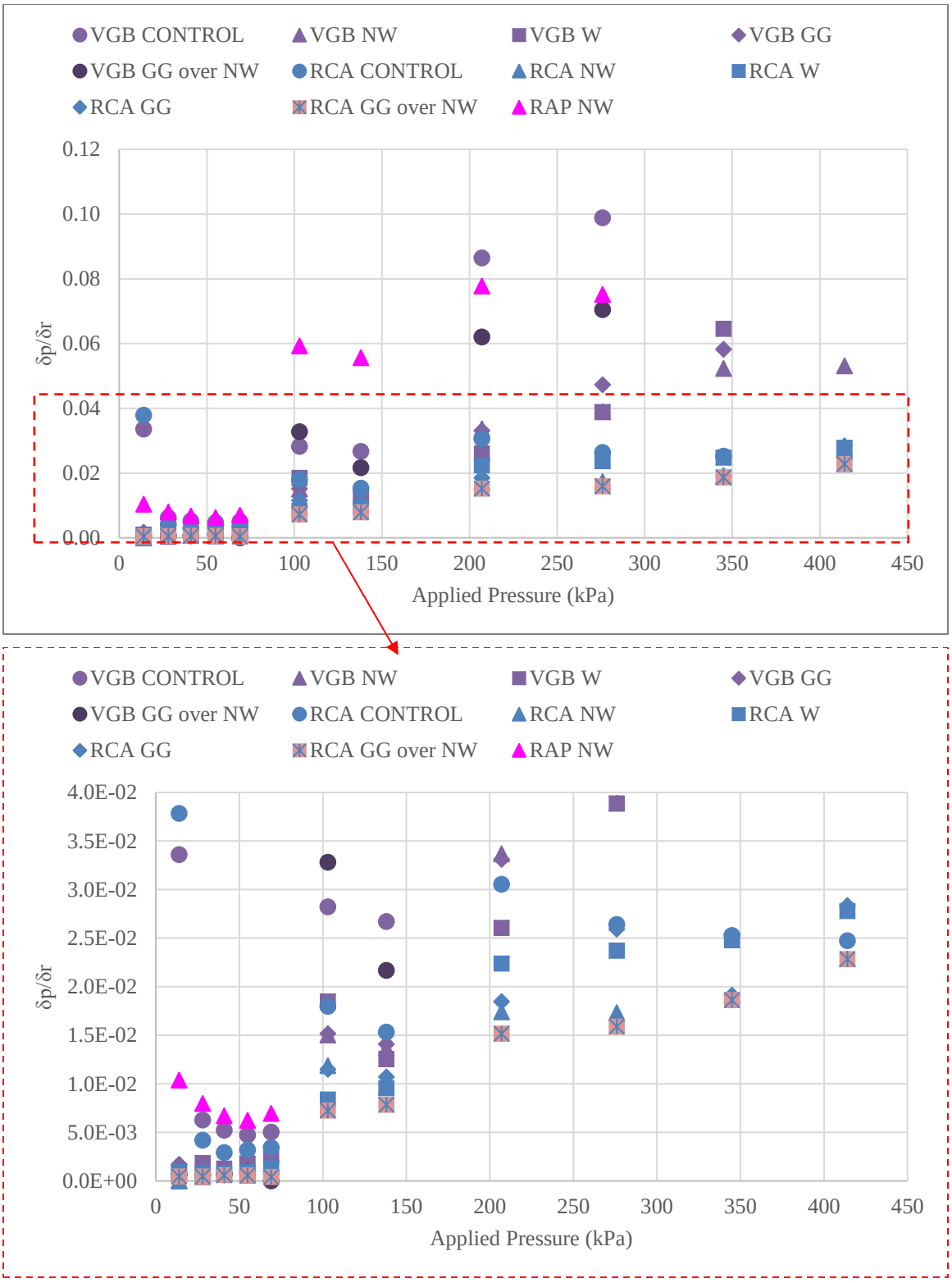

Figure 4.45. Deformation Ratio vs. Applied Surface Pressure for the Unpaved Sections atop 2% CBR Subgrade.

4.2 Deformations of Concrete Pavements

4.2.1 Plate Displacements

For the concrete pavement sections, the actuator readings can be observed in Figure 4.46. Resilient deformations were adjusted for these sections to account for the flexible padding between the loading plate and the concrete pavement using the displacement transducer data in conjunction with the recordings from the actuator system. Unlike the unpaved test sections, the largest deformations occurred at the corner of the concrete slab and not beneath the plate. Therefore, the deformations in Figure 4.46 are not the maximum deformation measured on the slab. Continuing with the numbering of unpaved road tests, Tests 28, 29, and 30 refer to the concrete pavements on non-stabilized VGB, nonwoven-geotextile-stabilized VGB, and nonwoven-stabilized RCA sections, respectively. By plotting the pre- and post-rainfall displacements together, initial rebound can be observed between tests if present. Figure 4.46 shows that less rebound was observed in all three tests post-rainfall than pre-rainfall.

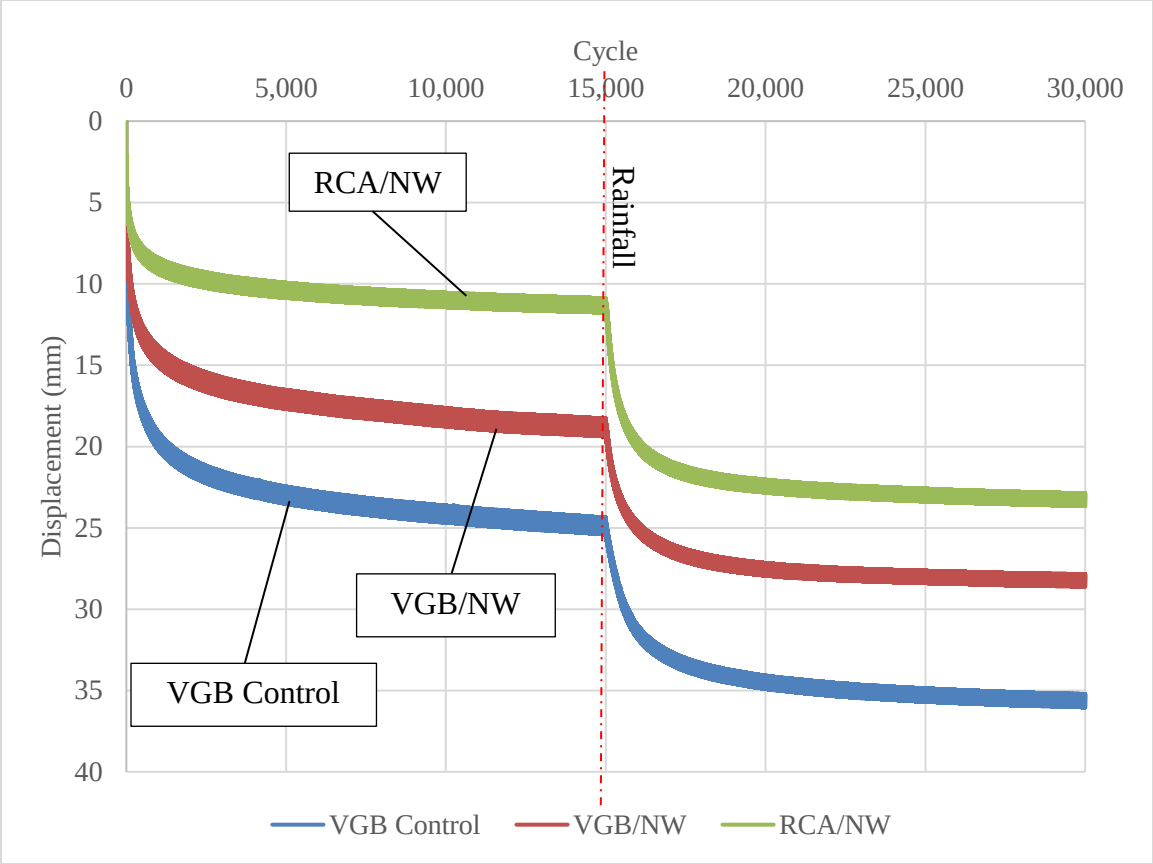

Figure 4.46. Displacements of the Loading Plate on Concrete Pavement Sections.

Like the unpaved sections, the permanent deformations of the concrete pavement on the VGB were reduced by the addition of nonwoven geotextile and further reduced by the replacement of the VGB with the RCA. Figure 4.46 shows that the displacement rate became roughly constant after 3,000 cycles in the load sequence. To better investigate the pavement response, the permanent deformations pre- and post-rainfall within the first 3,000 load cycles are plotted in Figure 4.47 and Figure 4.48.

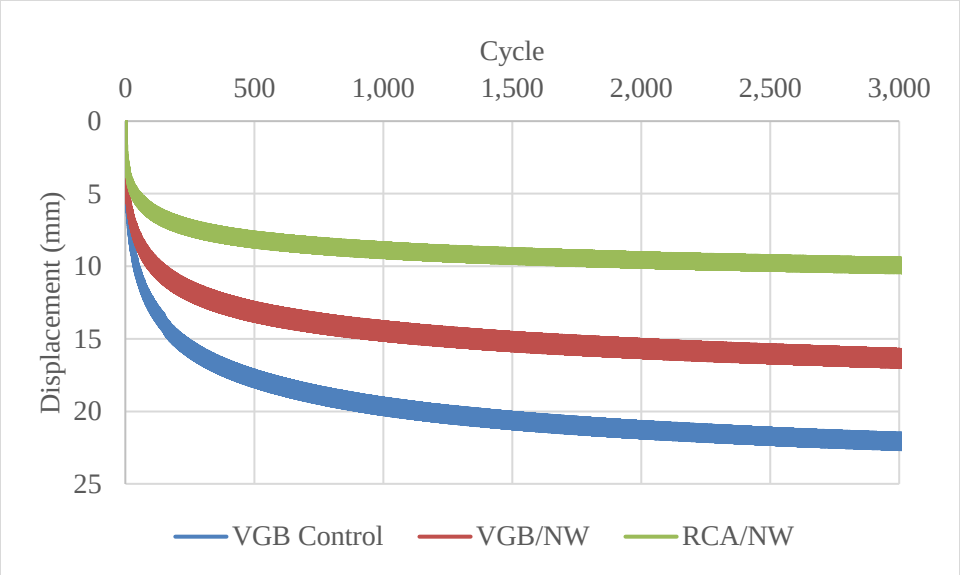

Figure 4.47. Displacement of the Loading Plate on the Concrete Pavements within the First 3,000 Cycles of Pre-rainfall Tests.

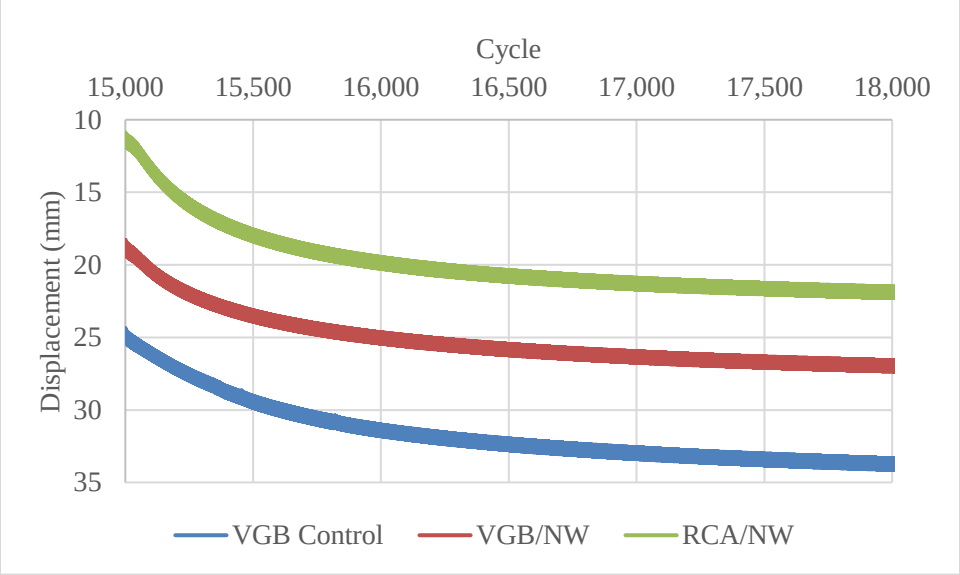

Figure 4.48. Displacement of the Loading Plate on the Concrete Pavements within the First 3,000 Cycles of Post-rainfall Tests.

Displacement discrepancies were investigated for the early cycle stages to assure that excessive initial deformation did not falsely increase the permanent deformation due to imperfect contact with the concrete pavement, as shown in Figure 4.49 and Figure 4.50 for the pre- and

post-rainfall sequences, respectively. For the pre-rainfall test sequence, a normal curve is observed with no indication of surface irregularities falsely increasing deformation. In the post-rainfall test, there is a shallower initial portion of the curve in all three tests due to pre-compression of the test sections.

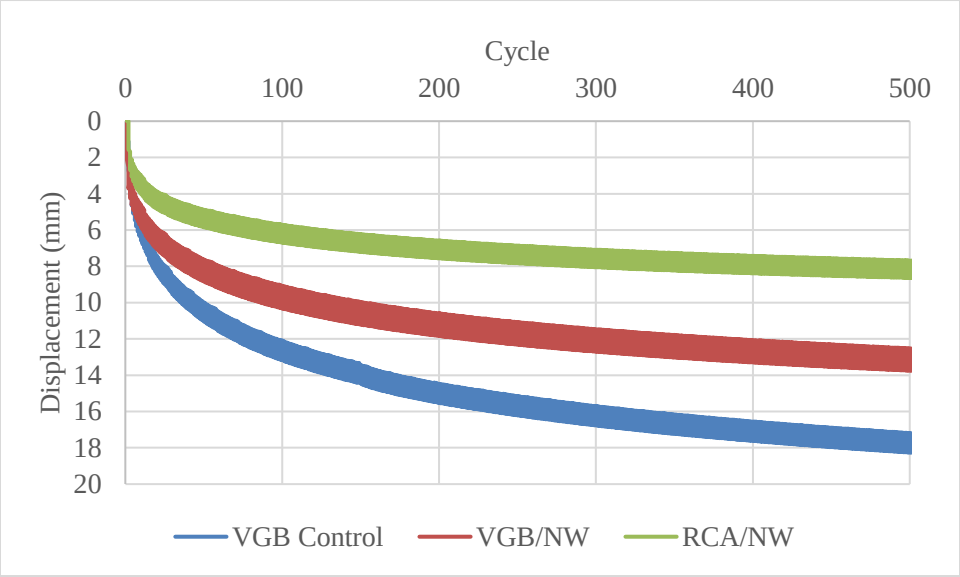

Figure 4.49. Displacement of the Loading Plate on the Concrete Pavements within the First 500 Cycles of Pre-rainfall Tests.

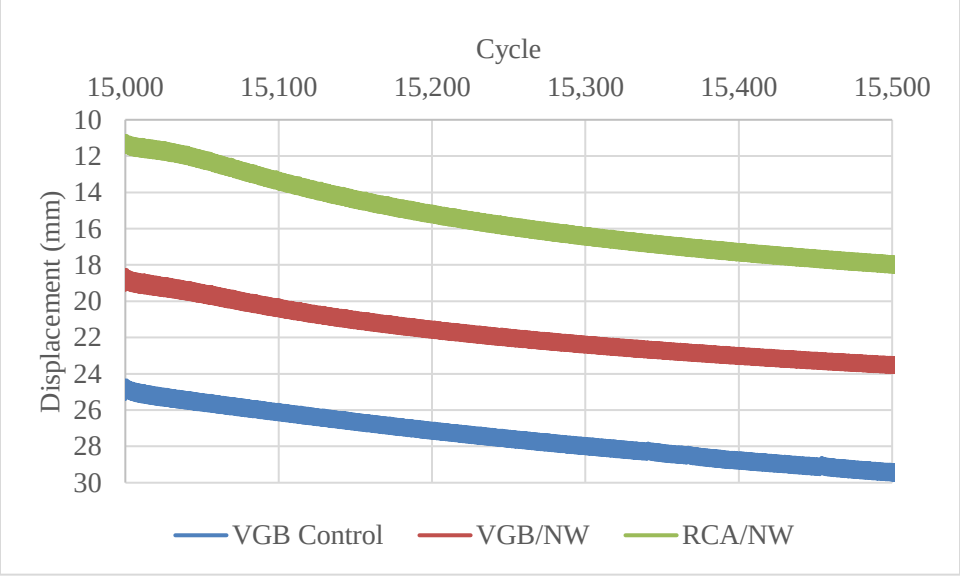

Figure 4.50. Displacement of the Loading Plate on the Concrete Pavements within the First 500 Cycles of Post-rainfall Tests.

4.2.2 Corner and Slab Displacements

Displacement transducers along the slab are necessary to measure the displacements at the corner and the reaction of the slab system in order to determine the modulus of subgrade reaction. Maximum displacement of the slab due to corner loading occurred at the corner of the slab, so this point displayed the maximum vertical displacement incurred in the paved tests. Stiffness of the concrete pavement required multiple measurements on the slab to evaluate the rotation of the slab.

Maximum displacement of the slab occurred at the loaded corner of the concrete slab. These maximum displacements are summarized in Figure 4.51. The pre-rainfall loading ("A" group) of the concrete pavement on VGB exhibited the most pronounced permanent deformation, while the pre-rainfall load stage of the concrete pavement on RCA showed much less permanent deformation. Details of slab displacement behavior are shown and discussed below.

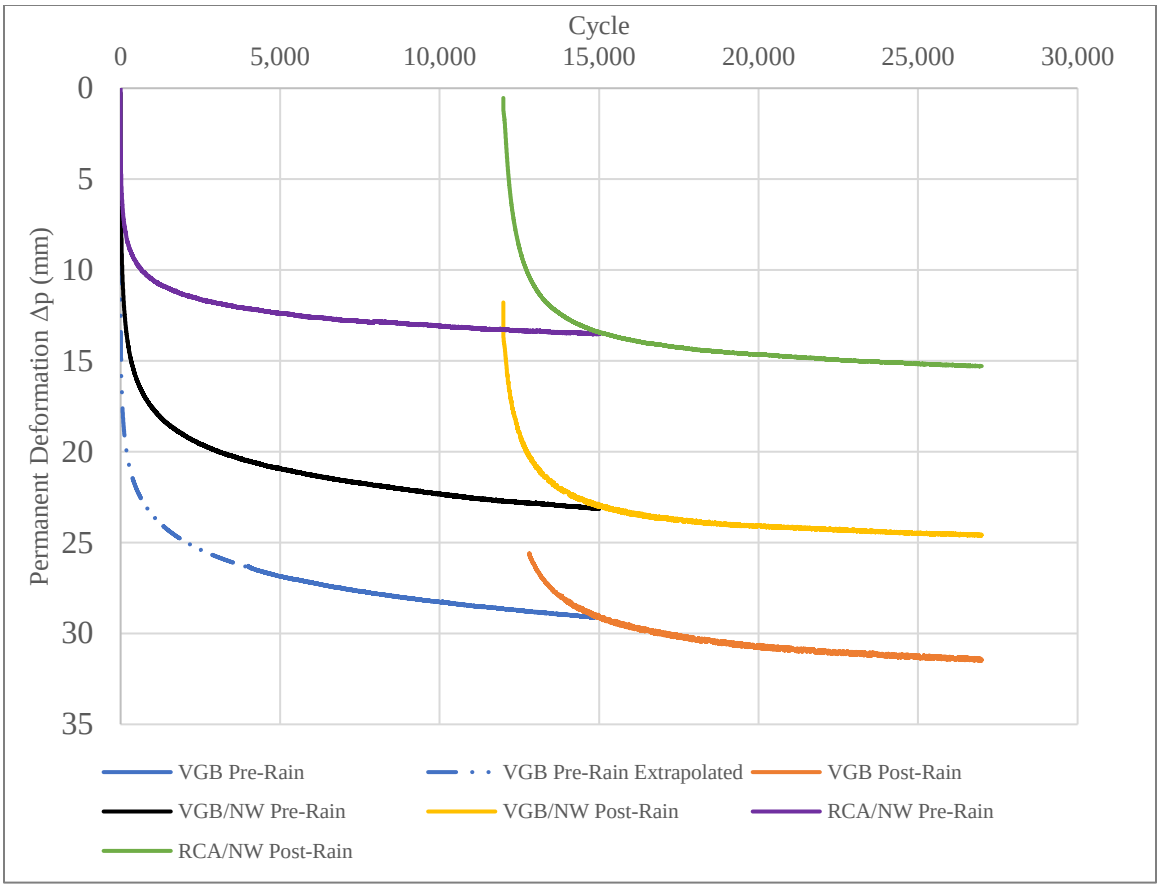

Figure 4.51. Loaded Slab Corner Permanent Deformation Summary.

Figure 4.52 through Figure 4.57 display the recorded vertical displacements of the loaded slab at "Corner" of the loaded slab, "2R" at twice the radius from the center of the load plate atop the loaded slab, and "3R" at thrice the radius from the center of the load plate atop the loaded slab, and the adjacent corner of the surcharge slab ("Other Slab") along with the actuator measurements of the plate displacement ("Actuator") for each paved test. In the control (non-stabilized VGB) test pre-rainfall, which was the first test for the concrete pavement study, the displacements are shown in Figure 4.52. Initially the corner displacement was not measured as the displacement transducer was used atop the plate (see "Plate" in Figure 4.52); this measure was taken to confirm the validity of the actuator-measured displacements of the plate and that no

frame bending due to load magnitude occurred by matching the displacement curves as shown. The displacement transducer was then moved to the corner of the loaded slab (see "Corner" in Figure 4.52) to obtain the maximum displacement in the slab for this test and to account for the flexibility of the rubber pad between the concrete slab and the actuator plate. This test also provides the baseline for comparison of the subsequent attempts at pavement structure improvement through geotextile addition and RCA replacement. Results appear valid as the vertical displacements dissipate with distance from the corner in the 3R direction.

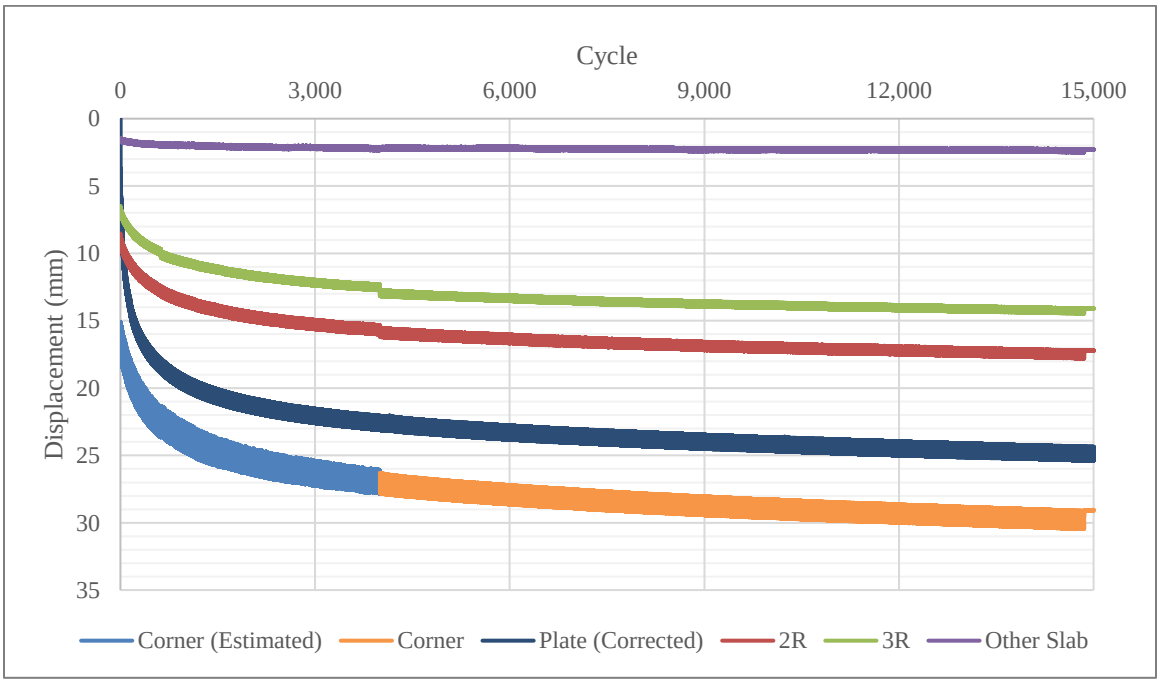

Figure 4.52. Vertical Surface Displacements of the Concrete Pavement on the Control VGB Pre-rainfall.

The pre-rainfall test results for the addition of nonwoven geotextile to the VGB-subgrade interface reduced deformations as shown in Figure 4.53. The number of load cycles for the displacements to reach a somewhat linear behavior was reduced from the control VGB section, indicating a more stable section. The magnitudes of the displacements at 2R and 3R were smaller

than those of the control section, and the corner and plate displacements were reduced. This result indicates a stiffer section as the slope and bending/rotation in the displaced slab were reduced with the geotextile addition to the pavement structure. Despite the reduction in the permanent deformation, the band thickness of the corner displacement curves and thus the resilient deformations were very similar for the control VGB section.

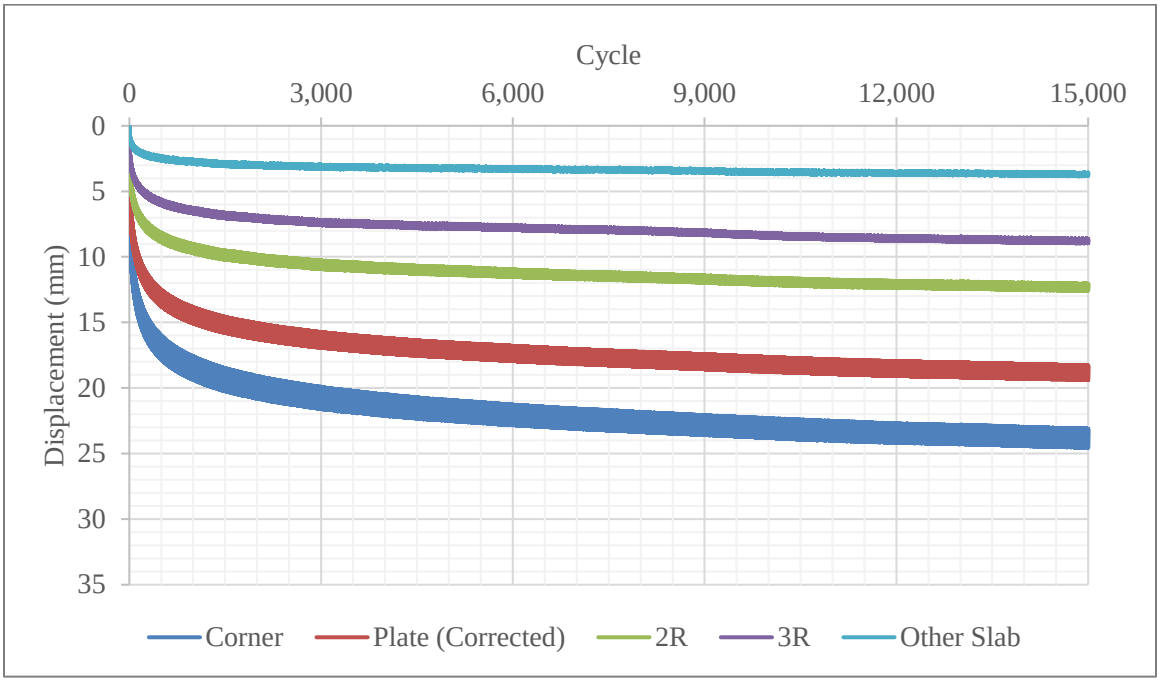

Figure 4.53. Vertical Surface Displacements of the Concrete Pavement on the VGB/NW Section Pre-Rainfall.

Replacement of the VGB with RCA considerably reduced the pre-rainfall deformation compared with both VGB sections pre-rainfall as shown in Figure 4.54. Displacements of the loaded slab at different locations were greatly reduced. The thicknesses of the displacement bands were also reduced when compared with the VGB sections to show less resilient deformation and a stiffer pavement foundation that would provide more bending/rotational resistance to the concrete slab under cyclic loading. Initial portions of the displacement curves

were further steepened compared with both VGB sections, indicating that a stable pavement state was sooner reached over the load stage.

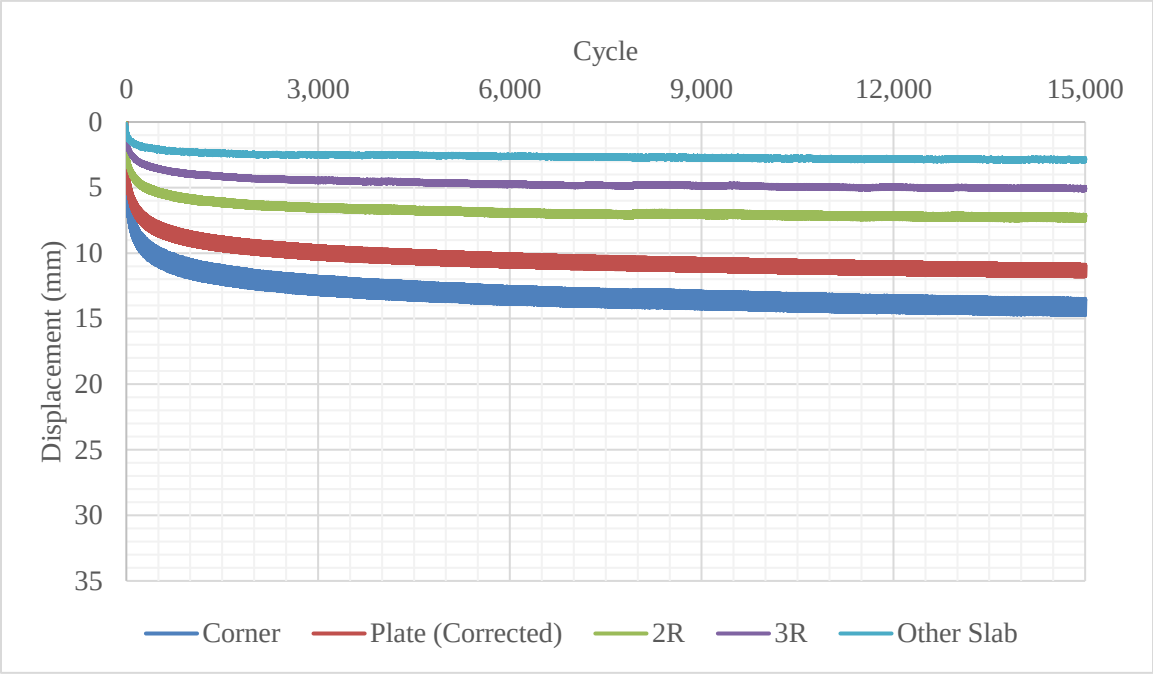

Figure 4.54. Vertical Surface Displacements of the Concrete Pavement on the RCA/NW Section Pre-Rainfall.

Before the second stage of the test, 15,000 cycles had already been applied to the pavement sections to compress the materials beneath the concrete pavement. Addition of rainfall had the possibility to change the state of the materials underlying the slabs by weakening the section and inducing greater deformation rates despite the preloading in the first stage. The joint between the slabs and the unpaved surface of the shoulder provided paths for water to seep into the pavement structure after rainfall, and traffic loading over a wet pavement structure could induce pumping and loss of support. On the other hand, the pavement structure had the opportunity to drain overnight.

The displacements of the concrete pavement on the VGB after rainfall are displayed in Figure 4.55 and will serve as the comparative reference for the addition of nonwoven geotextile and nonwoven-stabilized RCA replacement. Equipment malfunction prevented readings in the early cycles, but the trends have been extrapolated in the figure. The displacement transducer at 2R lost contact with the slab after 1,940 cycles and was extrapolated in the figure. Actuator readings were consistent, however. The displacements after rainfall should be compared with those at the end of the test pre-rainfall. The differences in the displacements post-rainfall can be considered as additional displacements due to rainfall. Therefore, rainfall induced additional displacements especially with the initial 3000 cycles. After 3,000 cycles, the rates of displacements returned to those pre-rainfall. These are true for the resilient and permanent deformations.

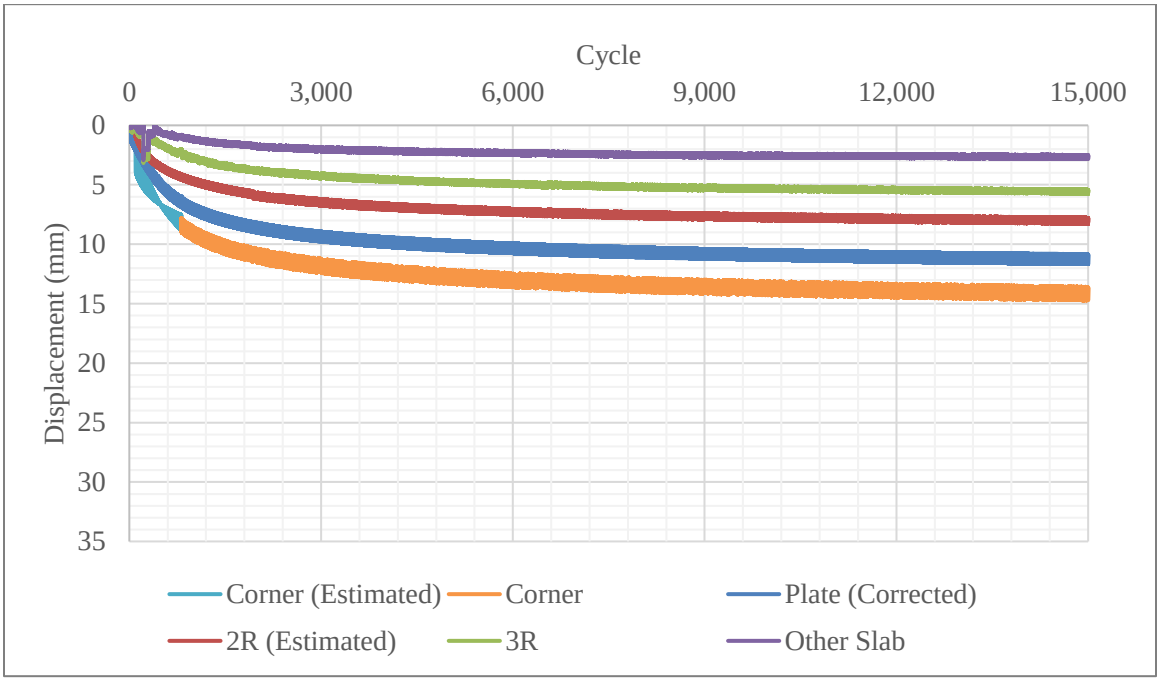

Figure 4.55. Vertical Surface Displacements of the Concrete Pavement on the Control VGB Section Post-Rainfall.

Addition of nonwoven geotextile reduced vertical surface deformations as shown in Figure 4.56. Rate of deformation (i.e. slope of the linear portion of the displacement curves) was lower compared with that in the control section. Adjacent ("other" unloaded) slab deformation was greater than loaded slab deformation at 3R and near loaded slab deformation at 2R. The other slab displacement was greater in the stabilized section than the control, but the deformations on the loaded slab decreased; the difference in the displacements between the other unloaded slab and the loaded slab was reduced, indicating a stronger pavement structure more resistant to breakdown from corner slab loading. The corner resilient deformation appeared to decrease with the geotextile, which would be desirable for a rigid pavement to reduce stresses in the slab.

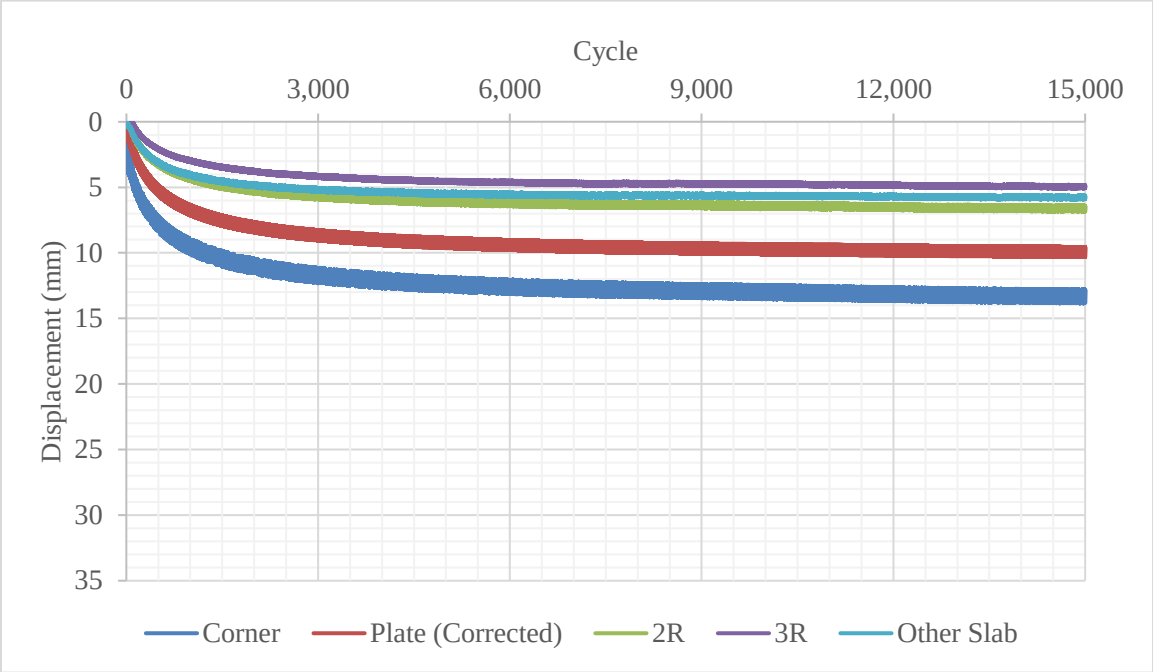

Figure 4.56. Vertical Surface Displacement of the Concrete Pavement on the VGB/NW Section Post-Rainfall Test.

The displacements of the concrete pavement on the RCA/NW section post-rainfall are shown in Figure 4.57. After rainfall, additional permanent deformation was noted when compared with that at the end of the pre-rainfall test. All deformations post-rainfall in the RCA/NW section were larger than those of the VGB/NW section. The measurement at the plate indicates that the VGB/NW section had the least post-rainfall permanent deformation, followed by the RCA/NW section and then the control VGB section. In any case, the deformation in the post-rainfall stage for the RCA/NW section was greater than that in the pre-rainfall stage. Unlike in the VGB/NW section post-rainfall, the other slab displayed less permanent deformation than at 3R of the loaded slab; this behavior is consistent with that of the control VGB section where the differential deformation across the slab was larger and the base course might not be as resistant to local degradation at the corner.

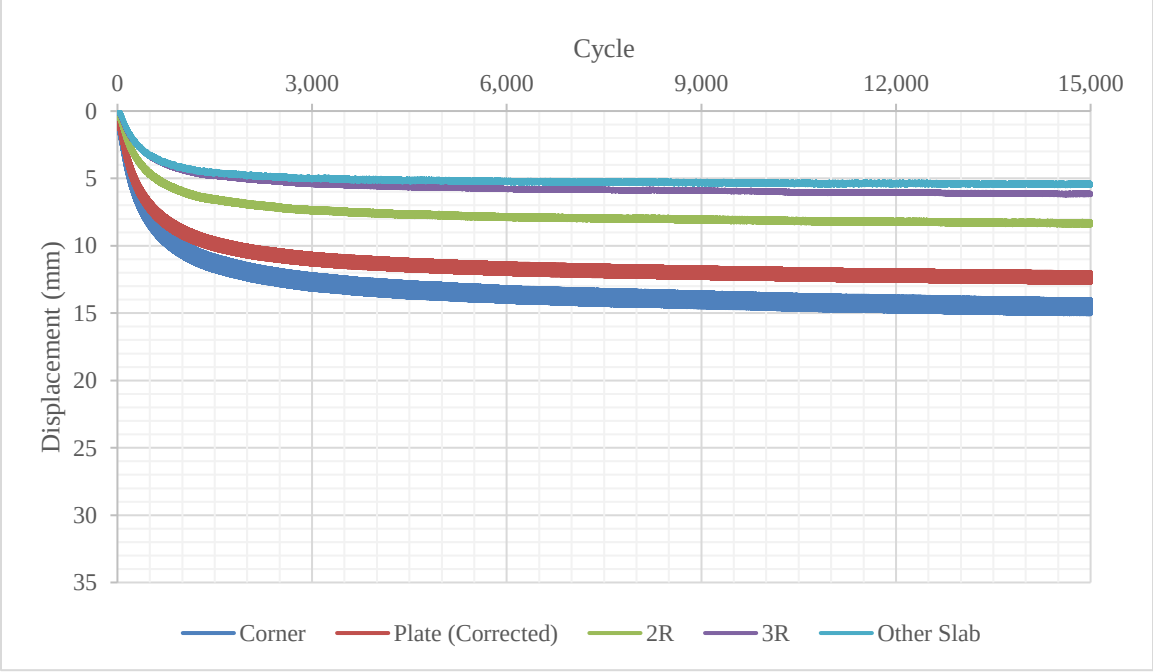

Figure 4.57. Vertical Surface Displacements of the Concrete Pavement on the RCA/NW Section Post-Rainfall.

Displacement trends of the adjacent other slab in Figure 4.52 through Figure 4.57 show whether the vertical deformation of the loaded slab was inducing heave or creating a depression over the loading sequence. In all three tests both pre- and post-rainfall, no vertical heave of the adjacent slab was induced in the downward displacement of the loaded slab. Figure 4.52 through Figure 4.57 show that the other slab displacement was considerably less than any observed change in the loaded slab within three times the radius of the loading plate. Despite lack of direct loading, the effect on adjacent slabs, structures, shoulders, or other portions of a roadway cannot be ignored based on these test results. The maximum displacement of this adjacent slab at the end of loading was very similar (less than 4 mm) in all pre-rainfall tests.

The other slab post-rainfall displacements were larger in both the VGB/NW and the RCA/NW tests than the control test. This result may be explained that the geotextile provided a tensioned membrane effect to bridge over the displacement from the loaded slab to the nearby other slab. This is also why the geotextile could reduce the displacement of the loaded slab. The smaller differential displacement (Δ_p) between two slabs on the stabilized sections in Figure 4.58 indicates these two slabs moved together as a whole as opposed to moving separately locally at the corner in the control VGB section. When this differential displacement was observed, the pre-rainfall tests for both VGB sections were similar. There was a reduction in this differential displacement from the pre-rainfall to the post-rainfall load stages in all test sections, but this difference was least pronounced in the RCA/NW section because the overall displacement was small.

Permanent deformation results at the load plate are summarized in Table 4.4 and Table 4.5. As previously discussed, deformation rates became constant at roughly 3,000 cycles, so the results are discussed below in these terms. For the pre-rainfall tests, the nonwoven geotextile

decreased the permanent deformation by 27% in the initial 3,000 cycles and 10% after 3,000 cycles; for the post-rainfall tests, nonwoven geotextile decreased the additional permanent deformation by 26% for the first 3,000 cycles and 48% after 3,000 cycles. Replacement of VGB with RCA along with nonwoven geotextile stabilization for the pre-rainfall test sequence decreased the permanent deformation from the control VGB section by 56% pre-3,000 cycles and 50% post-3,000; for the post-rainfall tests, the pre-3,000-cycle and post-3,000-cycle additional permanent deformations decreased by 6% and 44%, respectively. Over the 30,000-cycle test sequence, nonwoven geotextile decreased the total permanent deformation by 27% while RCA replacement of VGB along with nonwoven geotextile stabilization decreased the permanent deformation by 40%.

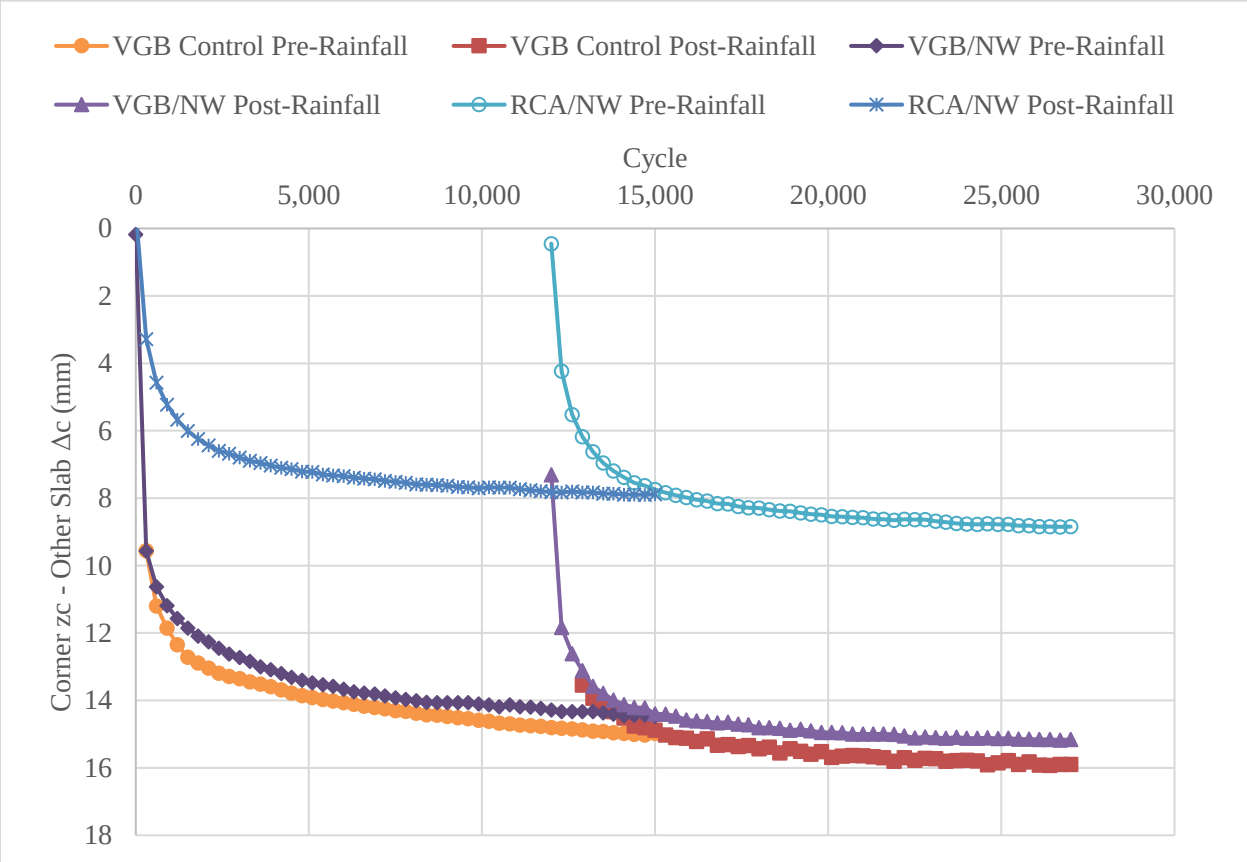

Figure 4.58. Differential Vertical Displacements of Concrete Pavements Pre- and Post-rainfall.

Greater permanent deformation was observed in the initial 3,000 cycles of the RCA/NW section post-rainfall than in the VGB/NW section. Table 4.6 summarizes the moisture content of the section as they were installed, as they were excavated roughly two days after the rainfall event (one day after plate loading), and the optimum moisture content from the standard Proctor curves (see Chapter 3). Both VGB sections were installed within 0.2% of their optimum moisture content. The RCA was installed a full percent dry of its optimum moisture content. When water was applied to the section, a large initial volume change under loading occurred as the RCA moved toward a lower void ratio. This volume change is expected to occur when a granular base course section is compacted dry of its optimum moisture content, water is applied, and vertical loading occurs (Han 2015).

Table 4.4. Plate Permanent Deformations of Concrete Pavement Tests.

Test	**Permanent Deformation BEFORE 3,000 Cycles (mm)**	**Permanent Deformation AFTER 3,000 Cycles (mm)**	**Total Permanent Deformation (mm)**
28A: VGB	21.54	2.83	24.37
28B: VGB	11.26	2.45	13.71
TOTAL 28: VGB	*32.80*	*5.28*	38.08
29A: VGB/NW	15.75	2.54	18.29
29B: VGB/NW	8.28	1.28	9.56
TOTAL 29: VGB/NW	*24.03*	*3.82*	27.85
30A: RCA/NW	9.48	1.42	10.90
30B: RCA/NW	10.60	1.38	11.98
TOTAL 30: RCA/NW	*20.08*	*2.80*	22.88

Table 4.5. Permanent Deformation Rates of Concrete Pavement Tests.

Test	Deformation Rate BEFORE 3,000 Cycles (mm/cycle)	Deformation Rate AFTER 3,000 Cycles (mm/cycle)
28A: VGB	7.18×10^{-3}	2.36×10^{-4}
28B: VGB	3.75×10^{-3}	2.04×10^{-4}
29A: VGB/NW	5.25×10^{-3}	2.12×10^{-4}
29B: VGB/NW	2.76×10^{-3}	1.07×10^{-4}
30A: RCA/NW	3.16×10^{-3}	1.18×10^{-4}
30B: RCA/NW	3.53×10^{-3}	1.15×10^{-4}

Table 4.6. Moisture Content Summary of Concrete Paved Tests.

Moisture Content (%)	VGB Control	VGB/NW	RCA/NW
Initial (as installed)	7.2	6.9	11.80
Excavation: Joint	8.98	9.76	12.46
Excavation: Under Slab	7.83	7.72	12.18
Optimum (Standard Proctor)	*7.1*	*7.1*	*12.8*

Performance of the paved sections should be compared against that of the unpaved sections. The control VGB was selected as a baseline case for this comparison. The RCA/NW section reduced the permanent deformation of the concrete pavement pre-rainfall by 55% as compared with the control VGB section, which is close to 59% decrease in the permanent deformation at the end of unpaved cyclic Load Stage 8 (207 kPa) and 68% at the end of unpaved cyclic Load Stage 9 (276 kPa). In the unpaved sections at mutual load stages, the addition of nonwoven geotextile to the VGB section displayed 56% and 58% decrease in the permanent deformation for Load Stages 8 and 9, respectively; however, the paved section only displayed

27% total decrease and 25% pre-rainfall decrease in the permanent deformation between the control VGB and VGB/NW sections. Total deformations in the unpaved sections at the end of the 207 kPa load stage were approximately 6.2 mm, 6.5 mm, and 15 mm for RCA/NW, VGB/NW, and control VGB, respectively. Total deformations in the unpaved sections at the end of the 276 kPa load stage were approximately 10.3 mm, 13.5 mm, and 32 mm for RCA/NW, VGB/NW, and control VGB, respectively. The permanent deformations incurred in the paved sections under the 550 kPa load stage were 10.9 mm to 24.4 mm after 15,000 cycles of equivalent single wheel loads (ESWL) and without rainfall, indicating that performance at higher loads in the unpaved sections was more comparable than at earlier stages.

Permanent deformation discrepancies were more pronounced in the unpaved sections than those in the pre-rainfall paved test sequence. Base course – subgrade interface vertical stresses will be discussed in Chapter 5, but the unpaved sections at Load Stages 8 and 9 had similar interface stresses to those observed in the corresponding pre-rainfall paved tests and thus confirming these stages for comparison with the pre-rainfall load sequence for paved roads.

When rainfall is considered, the benefits of geosynthetics become apparent. The post-rainfall permanent deformation was reduced similarly by both the addition of nonwoven geotextile in the VGB and the replacement with nonwoven-stabilized RCA by 30% and 13% (4.2 mm and 1.7 mm), respectively. Increase in lateral restraint through friction is one of the benefits of adding a geotextile layer; when water is added to a granular base course section with low to no plasticity, particle-to-particle friction is expected to decrease, and the geotextile could minimize some of this friction reduction in these tests due to drainage. Addition of water could also promote intermixing of base course and subgrade; in the unpaved tests, excavation revealed intermixing without rainfall for the control sections and full separation in the nonwoven-

geotextile-stabilized sections of all aggregates. In the RCA/NW section, the permanent deformation was very close (within 0.1 mm) to that of the VGB/NW section after 3,000 cycles. The addition of geotextile to the VGB brought the base course section to a stable state earlier in load stages (see

Table 4.5) than in the nonwoven-stabilized RCA section and indicate that for areas subject to high rainfall geotextile would be beneficial to pavement longevity regardless of aggregate source consistent with Tamrakar et al. (2019).

4.2.3 Incremental Permanent Deformation

Figure 4.59 and Figure 4.60 display the incremental permanent deformations incurred by cyclic loading at the corner of the loaded slab and at the plate, respectively. Both results are included as the maximum displacement occurred at the corner and the plate displacement was frequently measured and more stable due to larger surface area at the measurement. The plate displacements also confirm the values measured by the corner displacement transducer, as they should be of smaller magnitudes than those at the corner. Deformation per cycle was calculated by averaging the measurements over 1,000 cycles so that values may be viewed and compared. It should be noted that the deformation trends for the plate and the corner match. Incremental deformations continued to decrease as the number of cycles increased for all tests, indicating a densification and strengthening beneath the slab toward a stable state; a full failure of the section was not reached with the paved sections.

From 13,000 to 15,000 cycles, the incremental deformation trend is roughly linear for all paved tests. Late in the sequences, the control and VGB/NW sections displayed the greatest

incremental permanent deformation pre-rainfall. However, the smallest incremental permanent deformation during this phase was observed in the VGB/NW section post-rainfall, followed by the RCA/NW section post-rainfall. Once a stable, consistent deformation rate was reached, both replacement of RCA and nonwoven geotextile stabilization proved effective.

Prior to the linear portion of these incremental permanent deformation curves (e.g. in the first 3,000 cycles), the incremental deformations for the VGB/W section had greater deformation than the control VGB pre-rainfall, however the VGB/NW had consistently less deformation post-rainfall. The effect of water that would be seen in practice can thus not be ignored as the nonwoven geotextile provided a large incremental deformation reduction post-rainfall. RCA with nonwoven geotextile pre-rainfall displayed the lowest incremental deformation early on, but in later stages the values converged both with those for the control VGB section post-rainfall and the nonwoven-stabilized RCA section post-rainfall. The benefit of nonwoven geotextile in the improved performance of concrete pavements is quite apparent as a result.

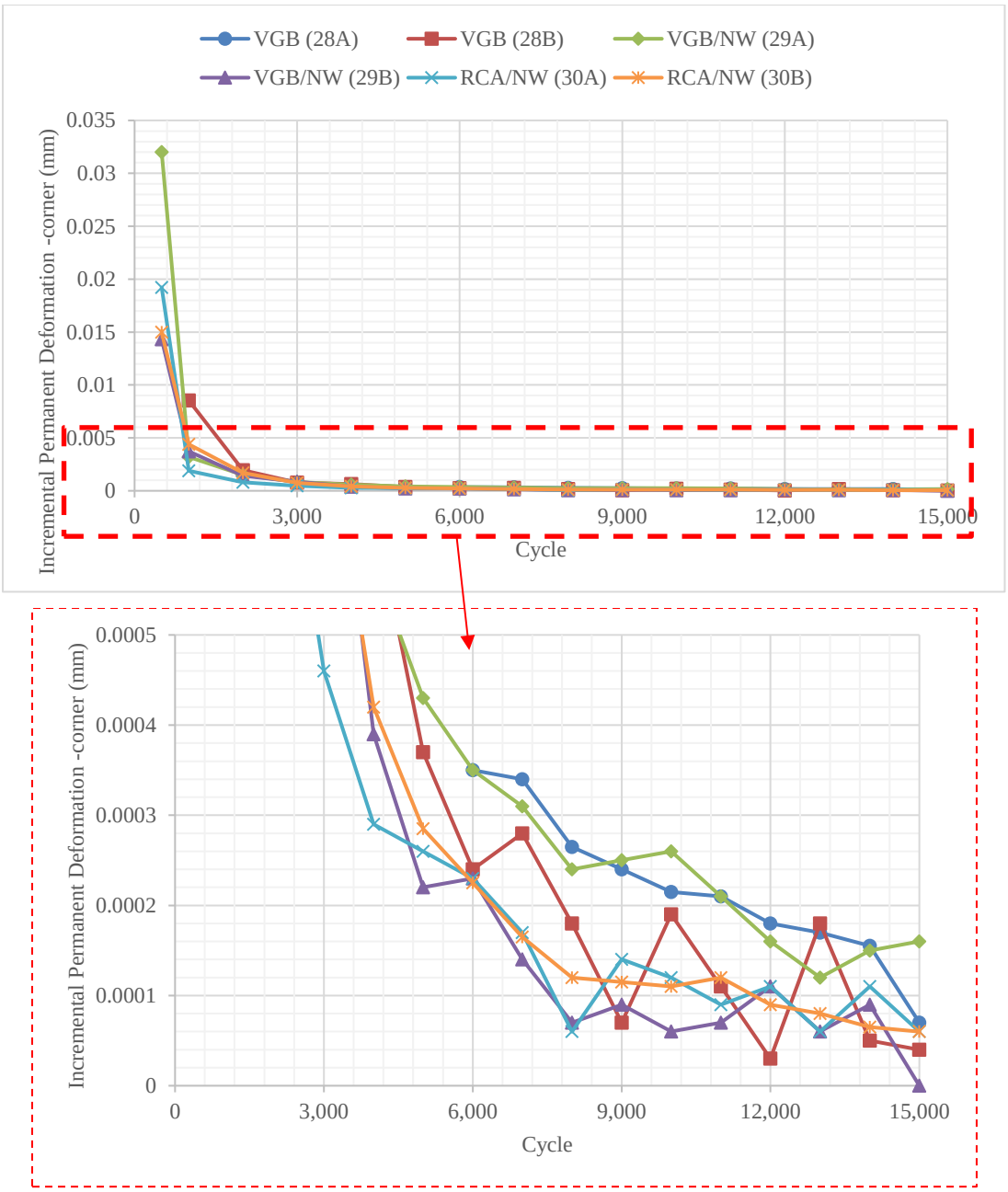

Figure 4.59. Incremental Permanent Deformations at the Loaded Corner in the Paved Tests.

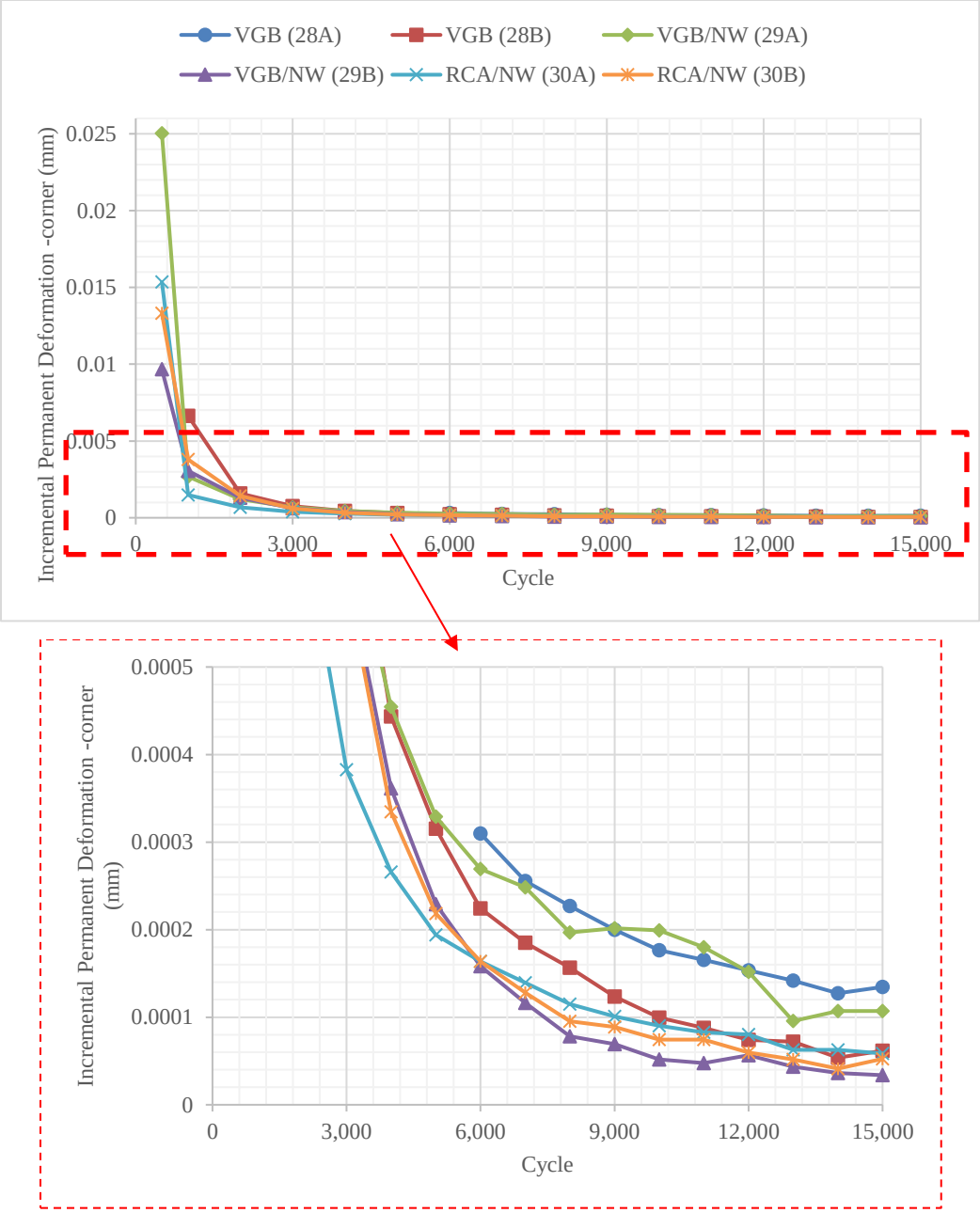

Figure 4.60. Incremental Permanent Deformations at the Plate Plates in the Paved Tests.

4.2.4 Resilient Deformation

As discussed in Chapter 2, there are multiple ways to determine the vertical deformation of a pavement system under a single wheel load. AASHTO resilient modulus testing identifies the

resilient deformation as the total induced strain in a sample with the non-recovered plastic strain subtracted; this interpretation of values for the paved tests can be found in Figure 4.61. Westergaard (1926) developed a solution to calculate pavement displacement as the total induced deformation for a single static load. In this study, this displacement was considered as the total vertical displacement readings for a given load cycle (not only the resilient deformation); these values are presented in Figure 4.62. The deformation presented in in Figure 4.62 was used for the Westergaard analysis. With the small incremental displacement values displayed above, the use of total or only resilient deformation are very close to equal on a cycle-by-cycle basis. The percentage change between the total deformation and resilient deformation by cycle are shown in Figure 4.63 and range from 0% to 3% for the paved tests.

Resilient deformation values (Figure 4.61) fall in the same range as those observed during the cyclic testing of unpaved sections above (see Figure 4.25). The VGB/NW section exhibited the highest resilient deformations pre-rainfall as well as the lowest resilient deformations post-rainfall. RCA/NW and control VGB sections also exhibited lower resilient deformations post-rainfall than pre-rainfall. Resilient deformations in the RCA/NW were most consistent with each other pre- and post-rainfall. While the resilient deformation values continued to decrease over number of cycles in all three pre-rainfall tests, these values became somewhat consistent in the post-rainfall tests after approximately 4,000 cycles.

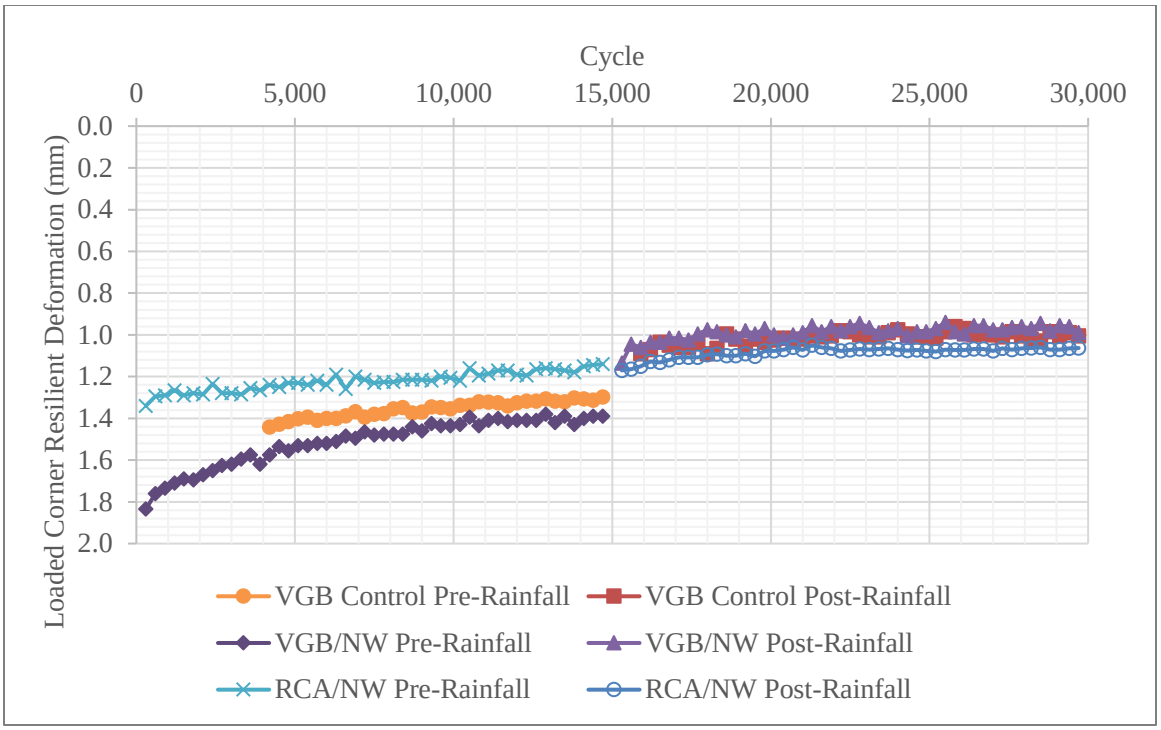

Figure 4.61. Resilient Deformations at the Loaded Corner in the Paved Tests.

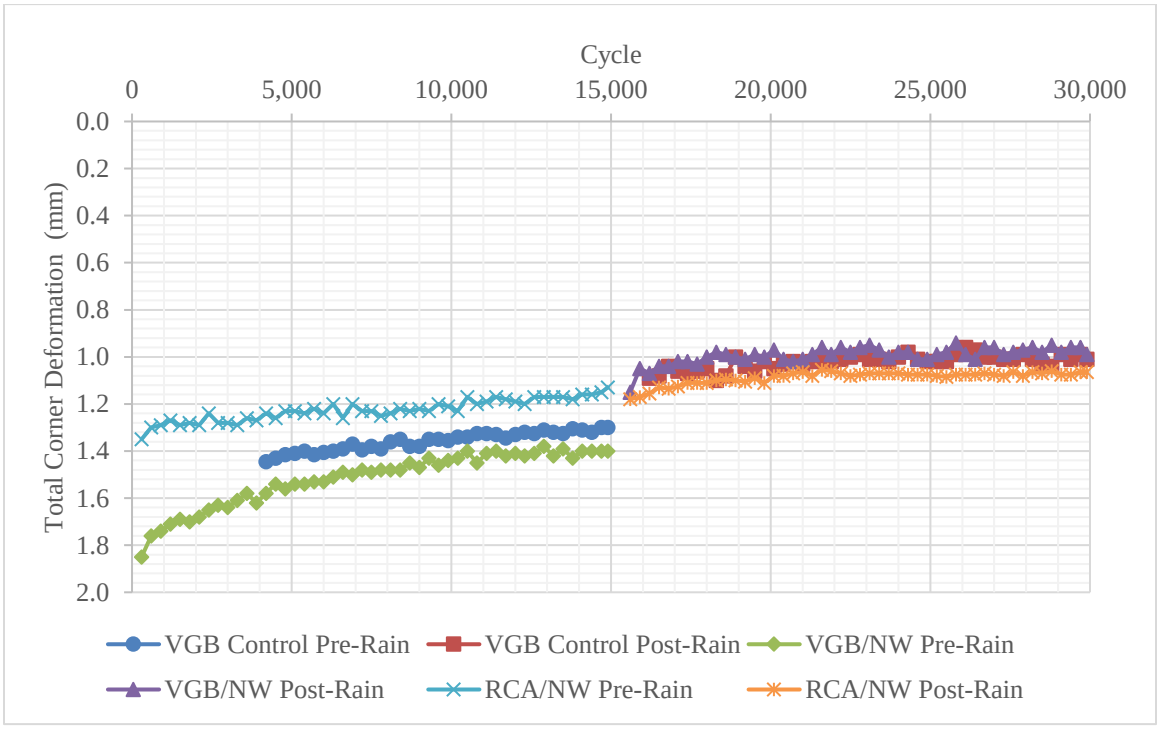

Figure 4.62. Induced Vertical Displacements at the Loaded Corner in the Paved Tests.

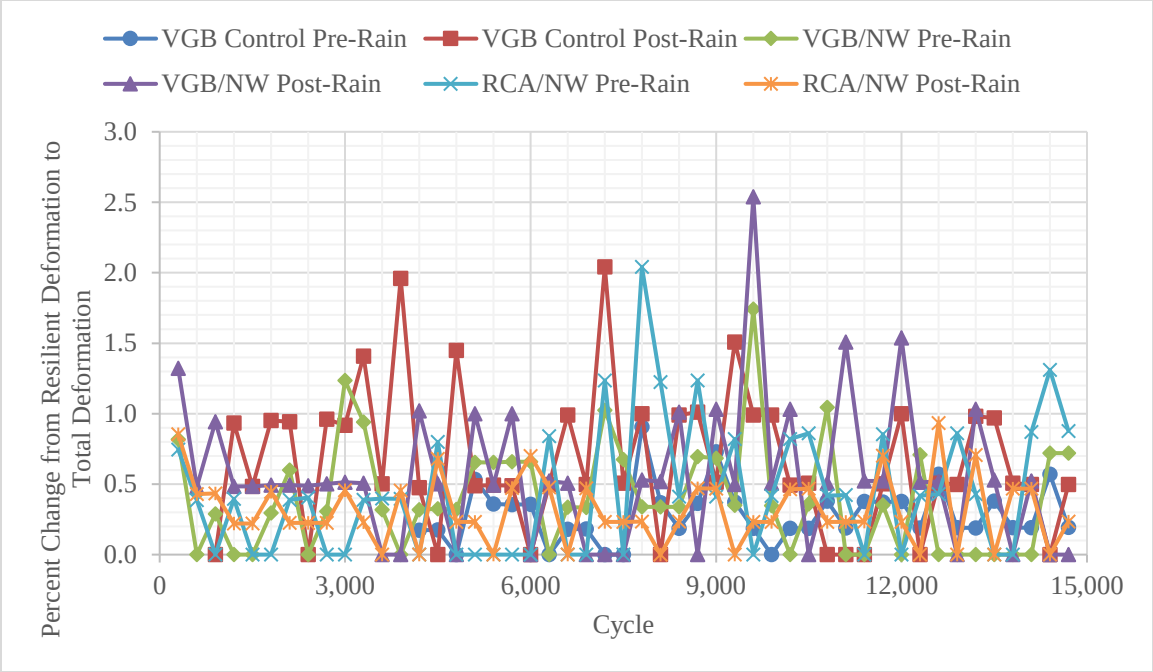

Figure 4.63. Percent Increase from Resilient Deformation to Total Deformation.

Relationship of permanent and resilient deformations for the paved tests is described in Figure 4.64 and Figure 4.65. As permanent deformation accumulated, the resilient deformation decreased for all three tests, both pre-rainfall and post-rainfall. This rate of decrease was greater for the pre-rainfall tests. The sections displayed stiffer behavior over the load sequences.

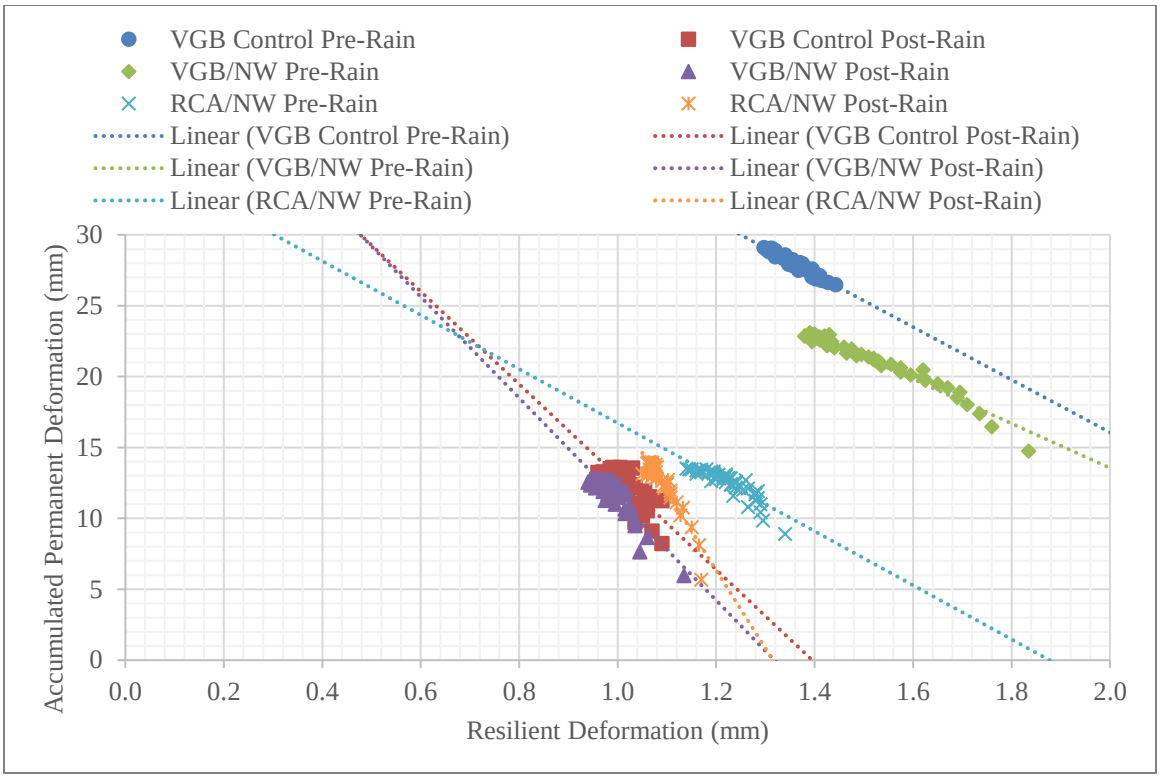

Figure 4.64. Accumulated Permanent Deformation vs. Resilient Deformation for the Paved Tests.

With the decrease in resilient deformation over number of cycles came a decrease in the magnitude of incremental deformation, as shown in Figure 4.64. There is a smaller deformation change noted in the post-rainfall tests than in the pre-rainfall tests. Although this behavior indicates that these sections were stiffened by preloading, there is evidence that they were softened by rainfall by the initial deformation increase; if the rainfall had no effect, then the deformation curve post-rainfall would simply be a continuation of the pre-rainfall cycle-deformation curve. Effects of rainfall cannot be ignored, however, as the section with the least deformations (RCA/NW) pre-rainfall displayed the highest resilient deformations and middle permanent deformation post-rainfall when compared against both the control VGB and

VGB/NW sections of corresponding rainfall scenarios. RCA with nonwoven geotextile displayed the least variation in deformation values, indicating a stable section.

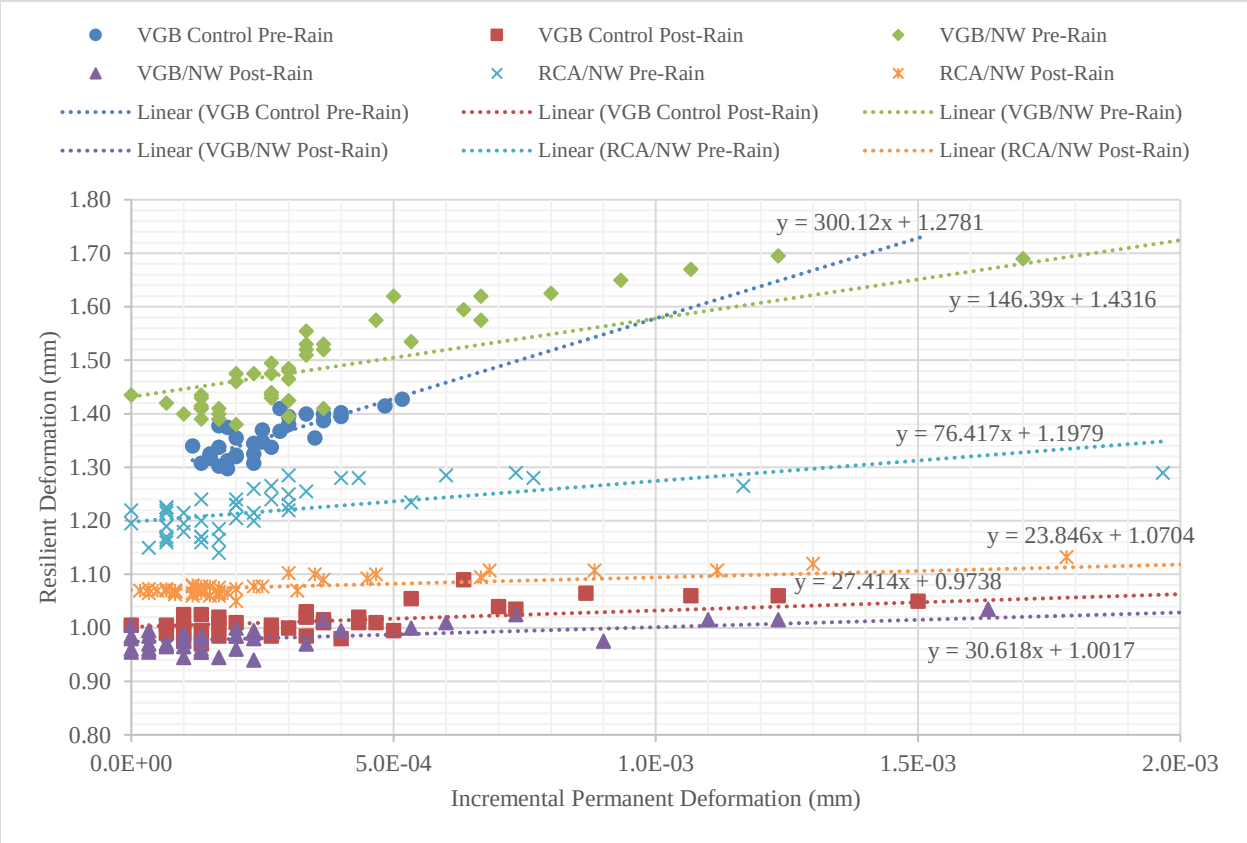

Figure 4.65. Incremental Permanent Deformation vs. Resilient Deformation in the Paved Tests.

4.2.5 Modulus of Subgrade Reaction (k-value)

From Westergaard's early analysis to the current MEPDG and other concrete pavement design methods, the impacts of underlying base course and/or subgrade are accounted for through the modulus of subgrade reaction (i.e. k-value). The analysis in this study was based on the displacement measurements at the corner of the slab due to corner loading that would result in maximum slab displacement and breakdown of the underlying aggregate-subgrade structure; focus was on the degradation of the subgrade rather than maximum induced slab stresses. Using

the recorded displacements at the slab surface and through linear extrapolation and considering the Westergaard (1926) definition of radius of relative stiffness as a radius of gyration, the radii of relative stiffness for each test were determined by linearly forecasting the distance *l* from the corner where the induced displacement *z* for a given applied load cycle is equal to zero as shown in Figure 3.28 (Chapter 3). The resulting *l* values are displayed in Figure 4.66. The radii of relative stiffness decreased with increased number of applied cycles. Radius of relative stiffness values were somewhat consistent for each test section, as these values were based on how the entire slab was moving.

Behavior of the entire slab's reaction to corner loading is indicated by the radius of relative stiffness. Lower l-values indicate that a smaller distance away from the load plate was displaced and thus the underlying pavement structure (base course, geosynthetic, and subgrade) was stiffer. The highest l-values were observed in the non-stabilized VGB sections both pre- and post-rainfall. Nonwoven-stabilized RCA displayed the lowest l-values in these tests and thus the stiffest behavior. VGB behaved differently than the RCA in that the radius of relative stiffness decreased post-rainfall. Despite the post-rainfall l-value decrease, VGB/NW permanently deformed the least (Figure 4.51) of the six paved tests. RCA/NW post-rainfall displayed greater permanent deformation than the pre-rainfall test, but the l-value decreased post-rainfall as the section was densified.

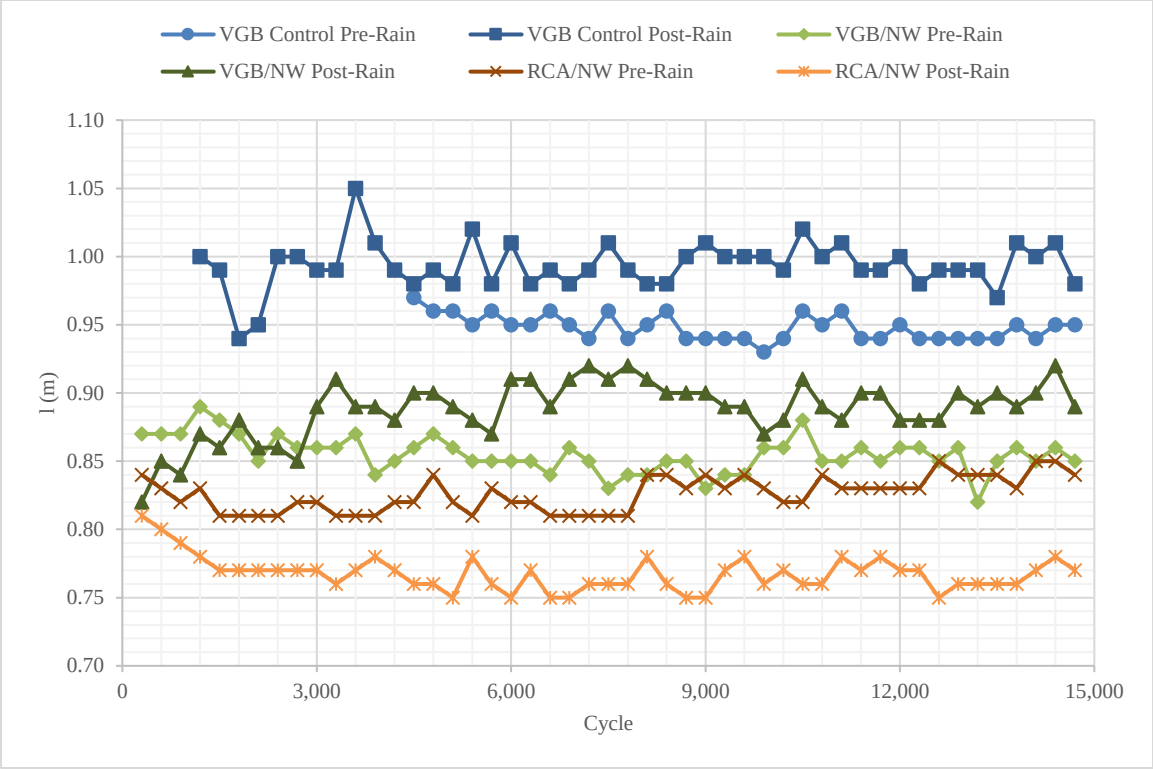

Figure 4.66. Radii of Relative Stiffness, l, in the Paved Tests.

From the corner displacements and radii of relative stiffness, the moduli of subgrade reaction were determined. The Westergaard (1926) estimation method for corner loading of concrete pavements described in Chapter 2 was used for this back-calculation as displayed in Eq. (4.1), where the applied load P was 40 kN, the distance from the corner to center of the load plate a_1 was 0.216 m, the corner displacement z_c was measured in each load cycle from a displacement transducer, and the radius of relative stiffness *l* was described above. These values were determined on a cycle-by-cycle basis to most closely mimic the Westergaard static load method. The values obtained are dynamic k-values because they came from cyclic load testing. Higher k-values indicate stiffer sections and less displacement.

$$k = \frac{P}{z_c l^2}\left(1.1 - 0.88\frac{a_1}{l}\right) \tag{4.1}$$

Dynamic k-values from the six tests are displayed in Figure 4.67. All calculated values fall near the range observed in the Westergaard (1926) pavement study. The k-value was greatest for the post-rainfall nonwoven-stabilized RCA at 55 MPa/m followed by the post-rainfall VGB/NW at 45 MPa/m; lowest values were observed in the pre-rainfall VGB control (30 MPa/m) followed by the pre-rainfall nonwoven-stabilized VGB (34 MPa/m). In all sections, post-rainfall k-values increased by 20% to 30% when compared with the pre-rainfall values.

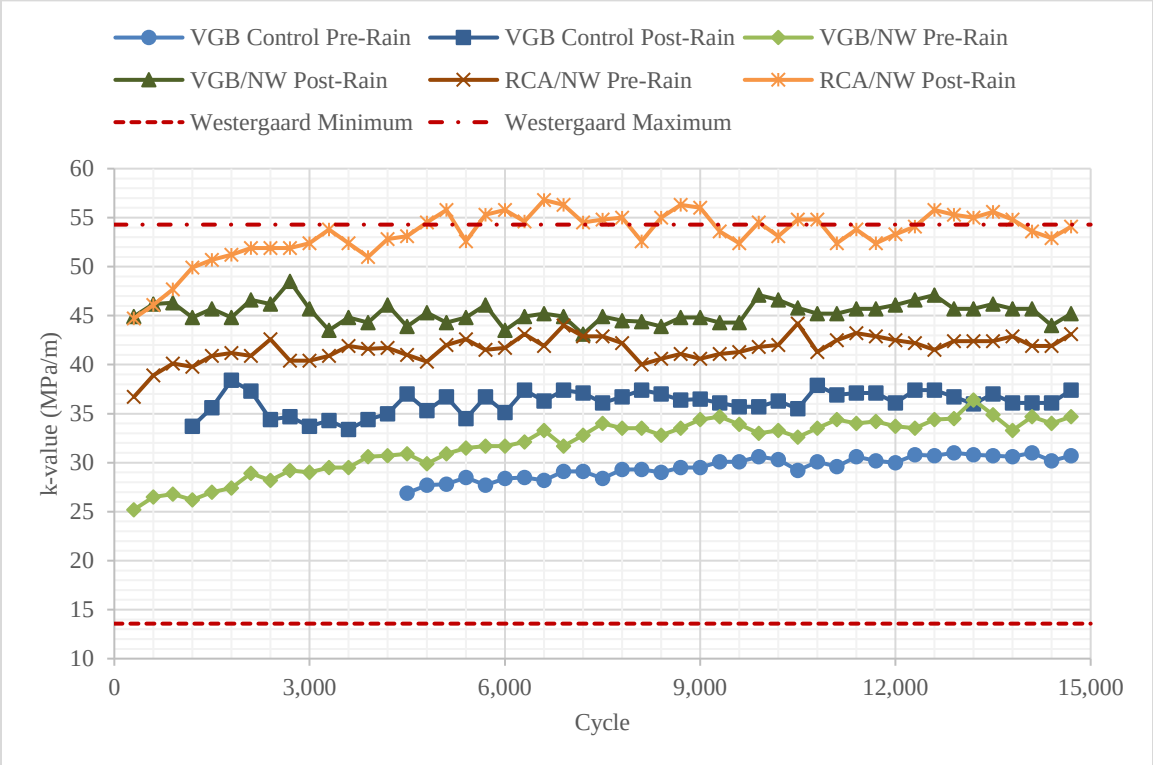

Figure 4.67. Moduli of Subgrade Reaction (k-value) from the Paved Tests.

4.2.6 Maximum Slab Stress Implications

Based on the concrete pavement testing, the values for the subgrade reaction modulus (k-value) increased both with the addition of geotextile and with the replacement of recycled concrete aggregate for virgin granular base. Maximum stresses in the slab due to corner loading using Westergaard's theory [Eq. (2.3)] are displayed in Figure 4.68; these values are well below the 2.9 MPa tensile strength of the concrete slabs, indicating that breakage of the concrete should not be observed. It should be pointed out that these tests were conducted under the following two conditions: one post-concrete-cure and one after a single rainfall event assuming no barriers to free drainage flow. In reality, field conditions may be different from the above conditions.

The measured total permanent deformation and the calculated maximum tensile stress in the slab may not indicate the same best performer for these tests, as some sections had a stiffer behavior despite an overall increase in the vertical displacement. The RCA/NW section is the prime example of this comparison. The post-rainfall total permanent deformation was greater, but the incremental deformation rate during the linear stage and the relative stiffness indicate a stronger pavement structure than both VGB sections.

Modulus of subgrade reaction is important in concrete pavement design assuming full homogeneous subgrade reaction. However, displacements are an indication of pavement structure deterioration over the pavement life that will create a heterogeneous subgrade reaction, potential differential stresses in the slab, and concrete pavement breakdown.

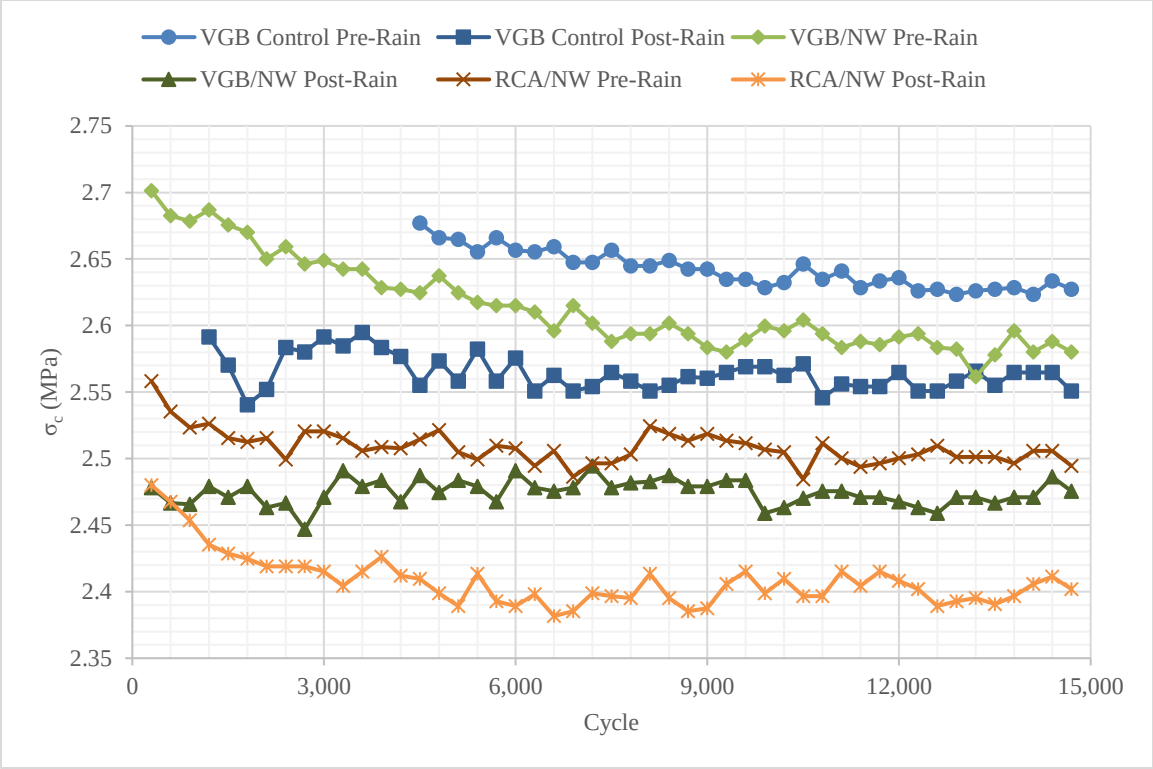

Figure 4.68. Maximum Tensile Stresses in the Concrete Slab Due to Corner Loading using the Westergaard Solution.

Chapter 5. Measured Vertical Interface Stresses and Analysis

Earth pressure cells were placed between base course and subgrade as described in Chapter 3 to monitor changes of vertical interface stresses in unpaved road sections and concrete pavements during cyclic loading. This chapter presents the measured vertical interface stresses and analysis based on the measured data.

5.1 Unpaved Road Sections

This section first presents measured earth pressure cell (EPC) readings at the interface of the subgrade (SG) and the base course in each section and then provides evaluation of these measured readings. The readings for the pressure cells for each test along with the stress reduction are noted at the center of the plate at depth. From the EPC results, the distribution angle (θ) was calculated as described in Eq. (2.13) based on the center reading. To eliminate the applied pressure effect, the stress reduction ratio (Δσ/p) at the center of the plate is also displayed; this value indicates the ability of the base course to distribute the applied surface load and represents a similar concept of wider-spread load at depth for higher distribution angles. For a comparison purpose, the estimated subgrade elastic limit using Eq. (5.1) (Giroud and Noiray 1981, Giroud and Han 2004a) is plotted on the load graphs. The results of each test section are subsequently discussed. All the measured results are from the test sections on 2%-CBR subgrade.

$$q_e = \pi c_u = \pi f_c (CBR)_{SG} \tag{5.1}$$

where q_e = elastic limit of the subgrade, c_u = undrained cohesion of subgrade (kPa) = f_C CBR_{sg} [(f_C = 30 kPa for this study) ($CBR \leq 5.0$)].

5.1.1 Control VGB Section

The VGB control section (Test 14) will be used as the point of comparison for subsequent test sections. Earth pressure cell results at various offset distances and the stress reduction ratio at load center at the interface are displayed in Figure 5.1. Each load magnitude sequence displays gradually decreasing vertical interface stress at the subgrade surface over the total number of cycles; an initial spike and then a leveling trend are consistent with initial permanent deformation that levels off. High variability in $\Delta\sigma/p$ was observed in initial load stages, ranging from 0.25 to 0.40; this is attributed to the changing load magnitudes over smaller number of total cycles for the first five stages, as closer inspection shows a similar leveling-off trend later in the stage as in the 2000-cycle stages. In load stage 6 and beyond, the average $\Delta\sigma/p$ was 0.35. Even in later stages for this base course material, $\Delta\sigma/p$ did not stabilize for the control VGB section. Earth pressure cell readings decreased in magnitude as distance from the center increased; the greatest interface stress measured at depth was at the center directly beneath the plate.

Behavior of the base course section varied slightly when looking at the entire load program versus the behavior within one load magnitude stage. With the leveling of interface stress (or in some cases reduction at the end of the load stage), it is noted that the repeat cycles initiated an increase in stress distribution angle θ as shown in Figure 5.2. Increase in surface load magnitude shows a decrease in θ and an increase in $\Delta\sigma/p$. There was a spike in the early load cycles for a given sequence in $\Delta\sigma/p$ of roughly 0.5, indicating that the section might not be fully stabilized and that the aggregate particles in this control section were moving past each other as the load magnitude increased. Stress distribution angle peaked at 25 degrees but reached approximately 22 degrees at the final applied load.

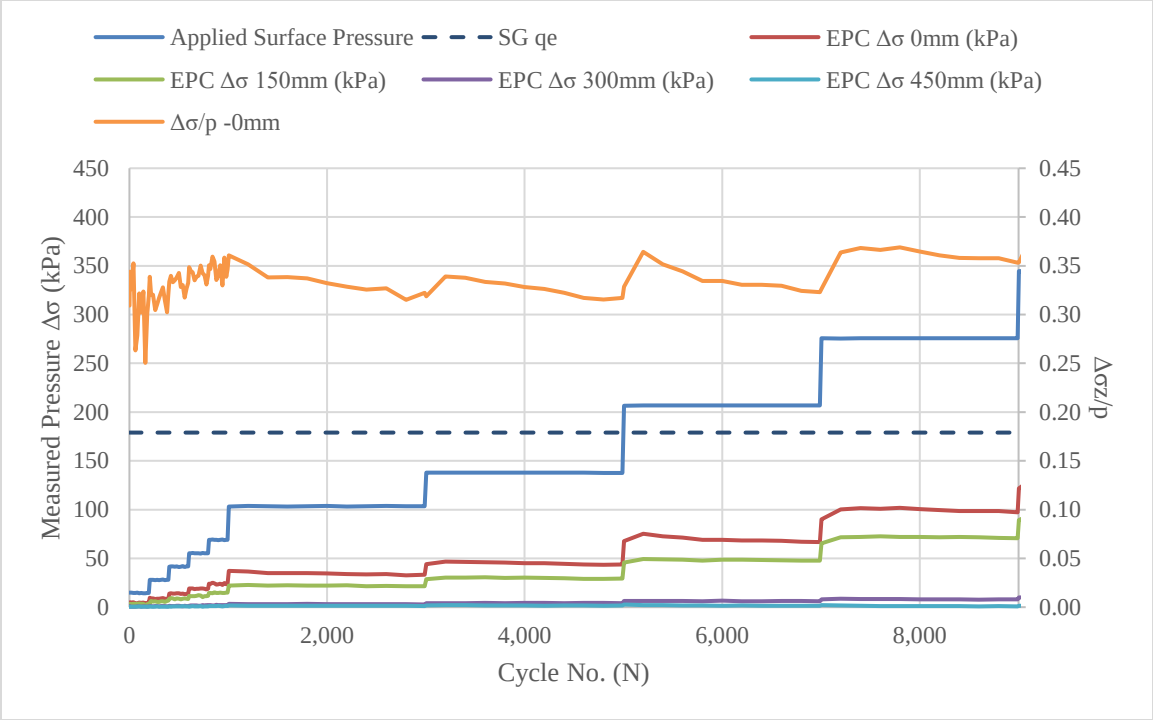

Figure 5.1. Measured Vertical Interface Stress and Stress Reduction Ratio for the Control VGB Section.

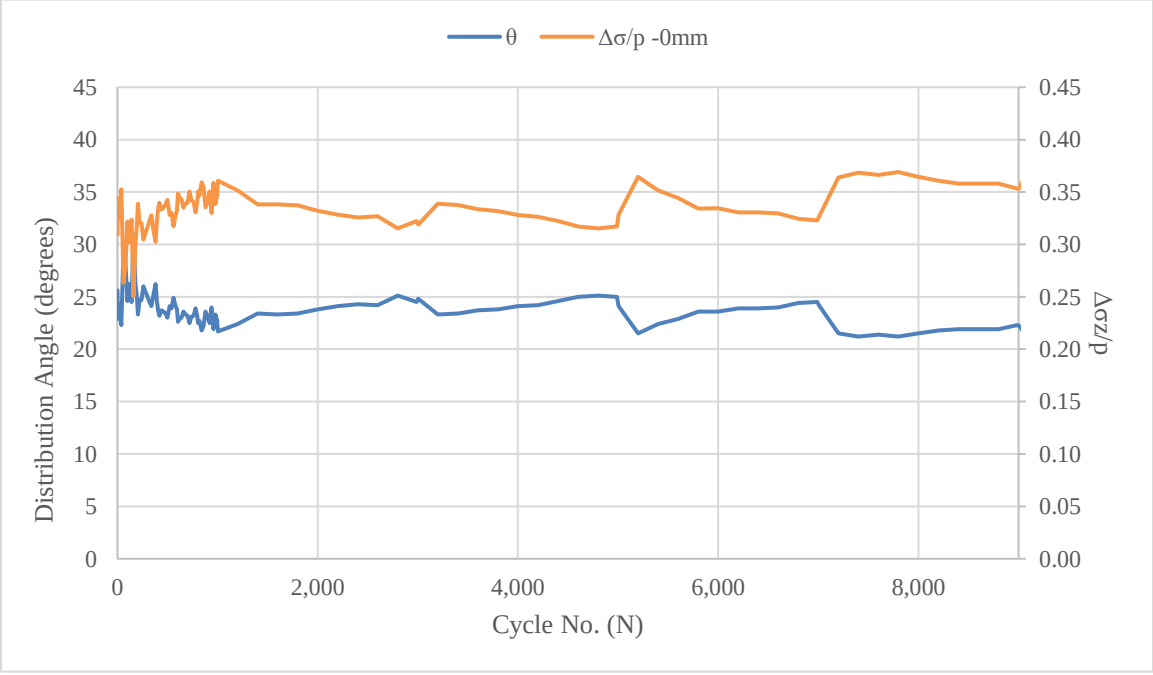

Figure 5.2. Stress Distribution Angle and Stress Reduction Ratio Based on the Vertical Interface Stress at the Center for the Control VGB Section.

5.1.2 VGB/NW Section

When nonwoven geotextile was added at the VGB/subgrade interface in Test 17, the behavior of the section changed (Figure 5.3 and Figure 5.4). In the earliest stages, the variation in stress reduction ratio only varied from 0.25 to 0.30, a much smaller range and a reduction ratio from the control section values of 0.25 to 0.40 for the same load stages. The overall trend of $\Delta\sigma/p$ was downward and stabilizing for the first 8 load stages, where the base course section clearly reached a stabilized 0.24 value (compared with 0.35 in the control section). At load stage 9, the applied surface load exceeded the estimated elastic limit of the subgrade, as clearly shown in Figure 5.3; at this point the section appeared to start degrading as $\Delta\sigma/p$ increased. As in the control section, the interface pressures decreased as distances from the center of the load plate increased.

The interface stresses observed in this test section correspond to the deformation behavior from Chapter 4. Before the applied surface load exceeded the subgrade elastic limit, the VGB/NW section underwent a primary strain (see Chapter 4) as well as interface stress (see Figure 5.3) increase stage, then the section became relatively stable in the second stage, and finally the section yielded in the tertiary stage in accordance with MEPDG as described in Chapter 2 (NCHRP 2004). The stress distribution angle reflects these stages as it increased to a stable value of 32 degrees and then reached a minimum of 22 degrees (Figure 5.4), as compared with the 20-to-25-degree range of the control section. The nonwoven geotextile was effective at further stabilizing the VGB over weak subgrade, but with the stress and displacement (see Chapter 4) behavior the section still appeared to yield with the applied load when it exceeded the subgrade elastic limit.

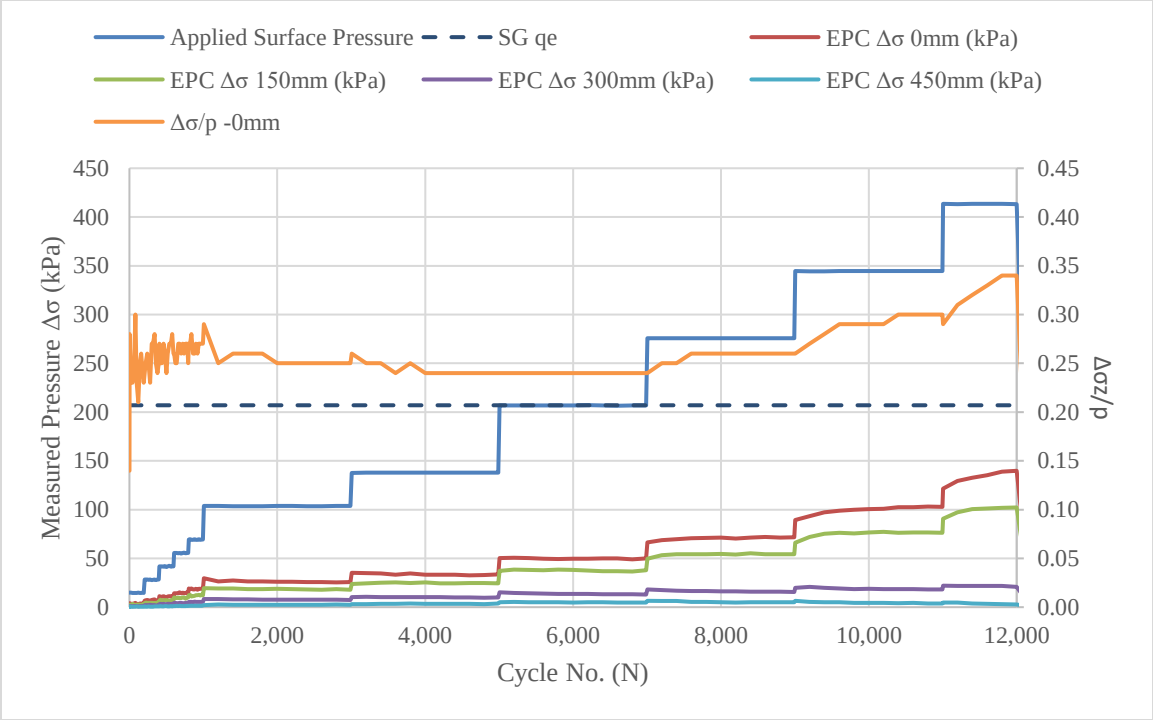

Figure 5.3. Measured Vertical Interface Stress and Stress Reduction Ratio for the VGB/ NW Section.

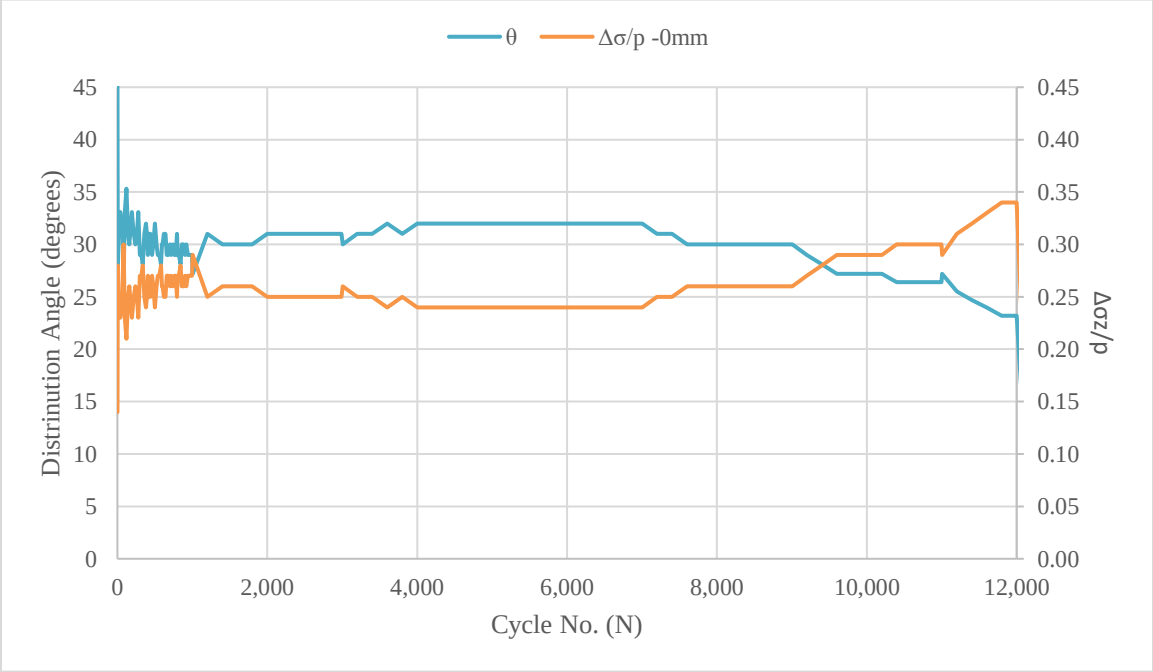

Figure 5.4. Stress Distribution Angle and Stress Reduction Ratio Based on the Vertical Interface Stress at the Center for the VGB/NW Section.

5.1.3 VGB/W Section

Although the displacement of the woven (W) geotextile VGB section (Test 11) limited the number of applied load cycles, the stress reduction behavior is interesting to observe. The stress reduction ratio decreased to a roughly stable level earlier on, reaching 0.24 to 0.26 (vs. 0.35 in the control) until the 10^{th} load stage when values began climbing to nearly 0.30 before maximum displacement was reached. More variability was noted in the readings for this section than the VGB/NW section but less than in the control section. Interface stress at the edge of the plate was very similar to that of the center and even surpassed the center pressure around the point where the applied surface load met or exceeded the estimated subgrade elastic limit; this indicates a better ability of this stabilization method to distribute the load.

The stress distribution angle (Figure 5.6) shows an initial decrease, then a leveling and somewhat increasing with the packing of particles under repeat loads, then a decline again as the section began to fail. The initial and final declines in stress distribution angle mimic the behavior theorized in Giroud and Han (2004a) initially where number of applied load cycles causes a decrease; the interim leveling/ minor increase in distribution angle does not. The stress distribution angle averaged from 28 to 33 degrees in the most level portion of the θ curve (compared with 20 to 25 degrees in the control and 22 in the VGB/NW); this confirms that pressure was distributed more evenly at the subgrade with the woven geotextile. Failure behavior appears to coincide less with the magnitude of the applied surface load for this material than it does for the number of cycles; despite the load magnitude exceeding the estimated subgrade elastic limit greatly, the base course section remained stable until surface load was roughly 1.5 times the subgrade elastic limit.

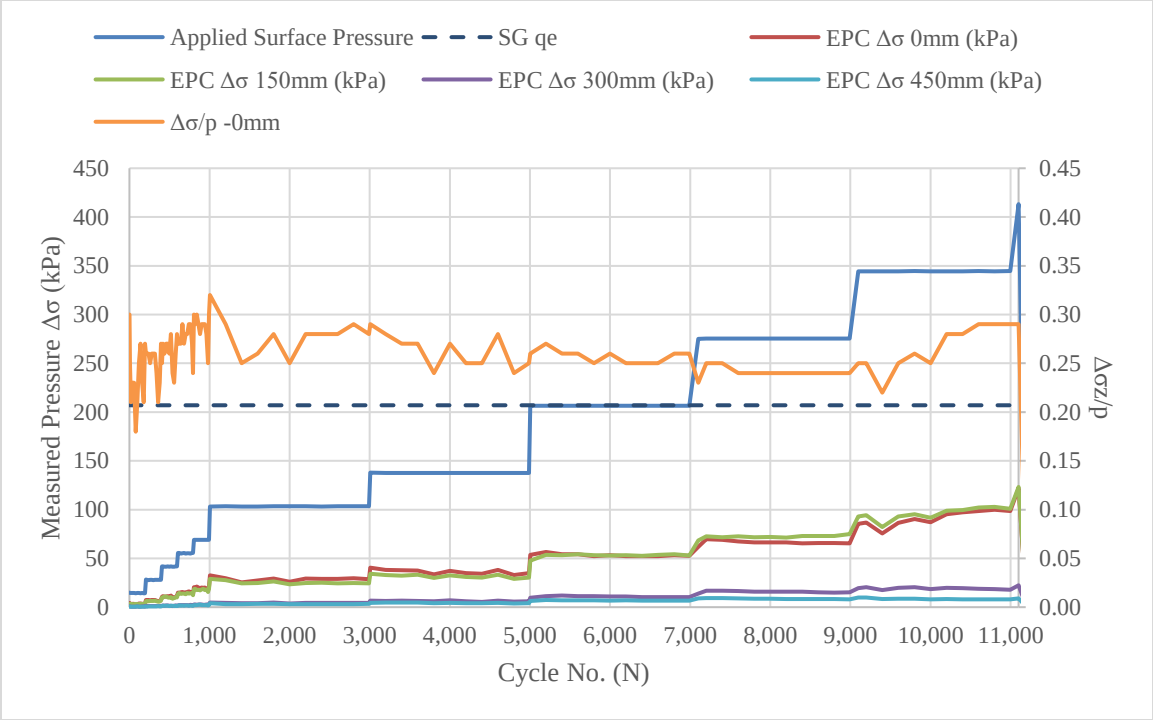

Figure 5.5. Measured Vertical Interface Stress and Stress Reduction Ratio for the VGB/ W Section.

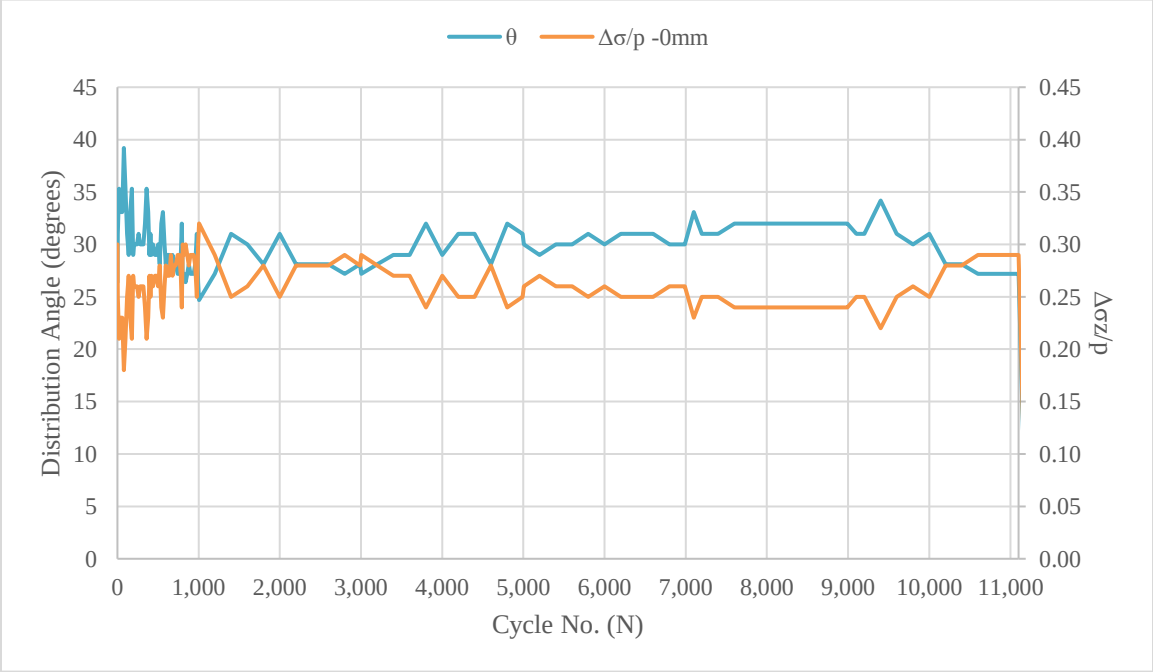

Figure 5.6. Stress Distribution Angle and Stress Reduction Ratio Based on the Vertical Interface Stress at the Center for the VGB/W Section.

5.1.4 VGB/GG Section

Placement of geogrid at the VGB-subgrade interface (Test 19) resulted in the pressure distribution displayed in Figure 5.7. Like the control and VGB/NW sections, the interface pressures decreased as horizontal distances from the plate center increased. The stress reduction ratio increased initially, but with repeat cycles exhibited a decreasing trend through the entirety of the load sequence. As discussed in Chapter 4, the displacement maximum was reached before the end of the load program, but from a pressure standpoint the section was quite stable; only the primary and secondary stages of the MEPDG model (NCHRP 2004) appear to be reached; this implies that although the maximum displacement was reached, the section was continuing to reposition and maintain strength.

Figure 5.8 highlights how both $\Delta\sigma/p$ and θ are the most stable for this section The value of $\Delta\sigma/p$ was roughly 0.29 for the section after the first 1000 cycles, and while this is greater than the VGB/W and VGB/NW sections, this is still an improvement over the control sections and did not deteriorate. Stress distribution angle was also fairly stable at 27 degrees; this was slightly lower than those for the two geotextile-stabilized sections, but the angles for these two sections were peaks that deteriorated in later load stages.

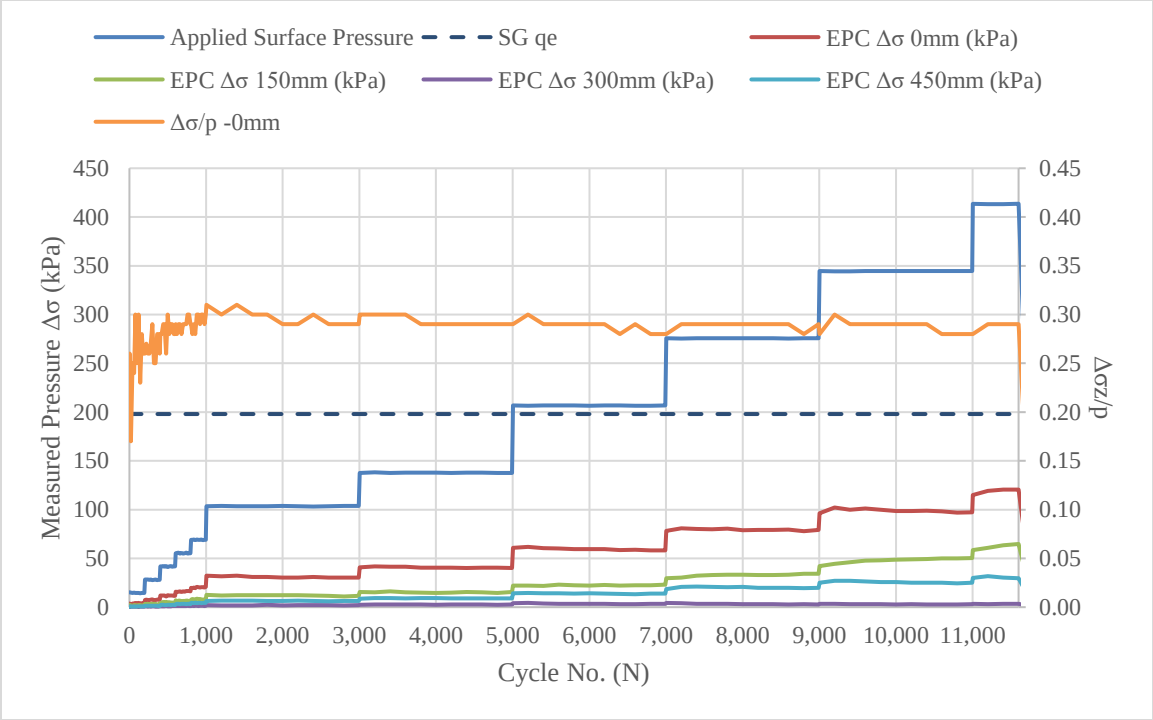

Figure 5.7. Measured Vertical Interface Stress and Stress Reduction Ratio for the VGB/ GG Section.

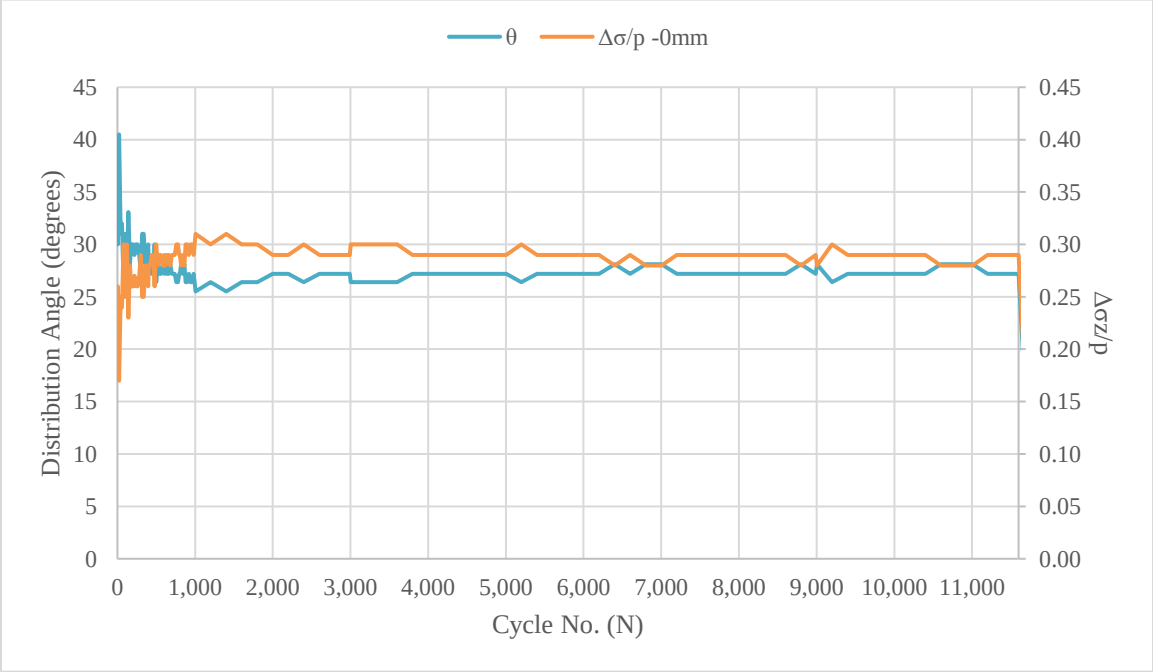

Figure 5.8. Stress Distribution Angle and Stress Reduction Ratio Based on the Vertical Interface Stress at the Center for the VGB/GG Section.

5.1.5 VGB/ GG/ NW Section

Use of double geosynthetics (GG and NW) in the VGB section (Test 22) yielded results displayed in Figure 5.9. The section appears more stable and displays a lower $\Delta\sigma/p$ than the control section. However, the magnitude of the stress reduction ratio was higher than those of the other three stabilized VGB sections. As was discussed previously, this could be attributed to the lack of interlock achieved between the aggregate and the geogrid with the geotextile sitting flush with the geogrid. Like the VGB/W section, the interface pressure at the plate edge was nearly equal to and even slightly surpassed the pressure measured at the center. While the magnitude of stress reduction ratio was not lower, the distribution area and the more uniform distribution indicate a more stable section than the control. It is noted that in the 10^{th} load stage $\Delta\sigma/p$ started to incline, exhibiting the behavior noted in the other two geotextile-stabilized sections; this could be an indication of failure, but due to total vertical displacement limit, the load program was terminated at approximately 10,000 of the 13,000 total cycles for other sections. Magnitude reduction of the measured vertical interface stress was similar to that of the VGB/GG section while the distribution was wider spread like that of the VGB/NW section where the stresses at distances of 0 mm and 150mm were very similar.

In this test section, the stress distribution angle remained fairly steady but low at 25 degrees prior to the 10^{th} load stage (see Figure 5.10). The measured pressures indicated a better load distribution, but more pressure seems to be transferred to the interface for this base course section.

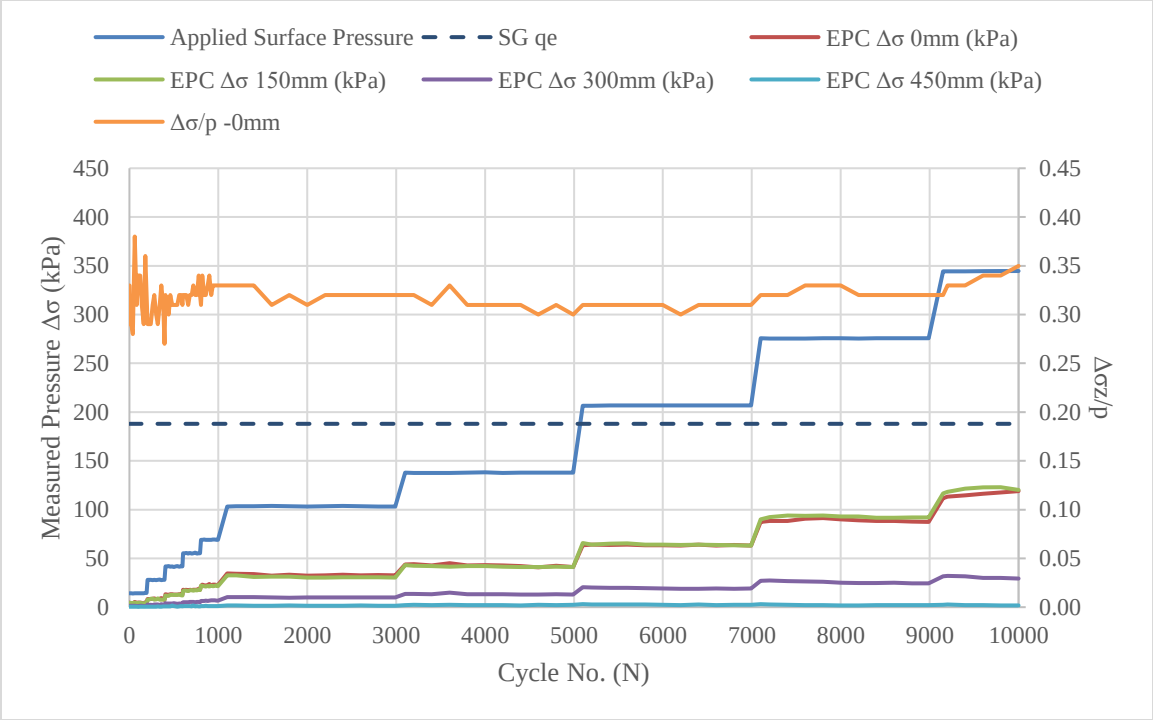

Figure 5.9. Measured Vertical Interface Stress and Stress Reduction Ratio for the VGB/ GG/ NW Section.

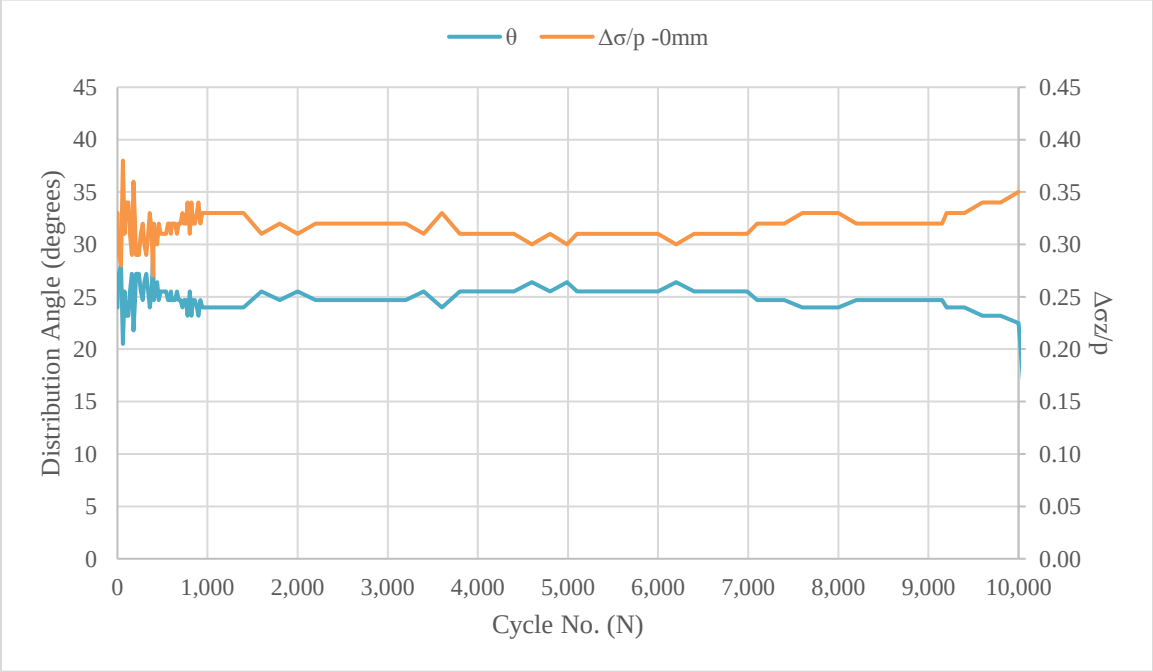

Figure 5.10. Stress Distribution Angle and Stress Reduction Ratio Based on the Vertical Interface Stress at the Center for the VGB/ GG/ NW Section.

5.1.6 Control RCA Section

A control section of RCA over 2%-CBR subgrade (Test 13) yielded a different stress response from all VGB sections, as displayed in Figure 5.11. At the interface, the stress reduction ratio consistently decreased from a high value of 0.25 until a stable value of 0.20 was reached in the 10^{th} load stage; this is an improvement over all the VGB sections over 2%-CBR subgrade in this study. While the RCA had smaller vertical displacement (the control section achieved all 13,000 cycles with less than 38 mm displacement), it also distributed the load better. The earth pressure cell at the edge of the plate measured almost as high as that at the center.

Figure 5.12 highlights the stability of the RCA section in terms of θ and $\Delta\sigma/p$. The steady increase in θ and decrease in $\Delta\sigma/p$ indicate strengthening of the RCA base course section with repeat load cycles. This is the opposite to the Giroud and Han (2004a) theory that the stress distribution angle deteriorates with number of load cycles. This aggregate material displays a different behavior than that expected from virgin VGB materials by exhibiting this strengthening behavior. Another possible reason is that its permanent deformation was smaller so that deterioration of the material was not significant. More testing to attempt to increase $\Delta\sigma/p$ and reduce θ at some number of cycles would be recommended, but for this study, the same number of applied loads as even the geosynthetic-stabilized VGB sections yielded a reduction in interface stresses.

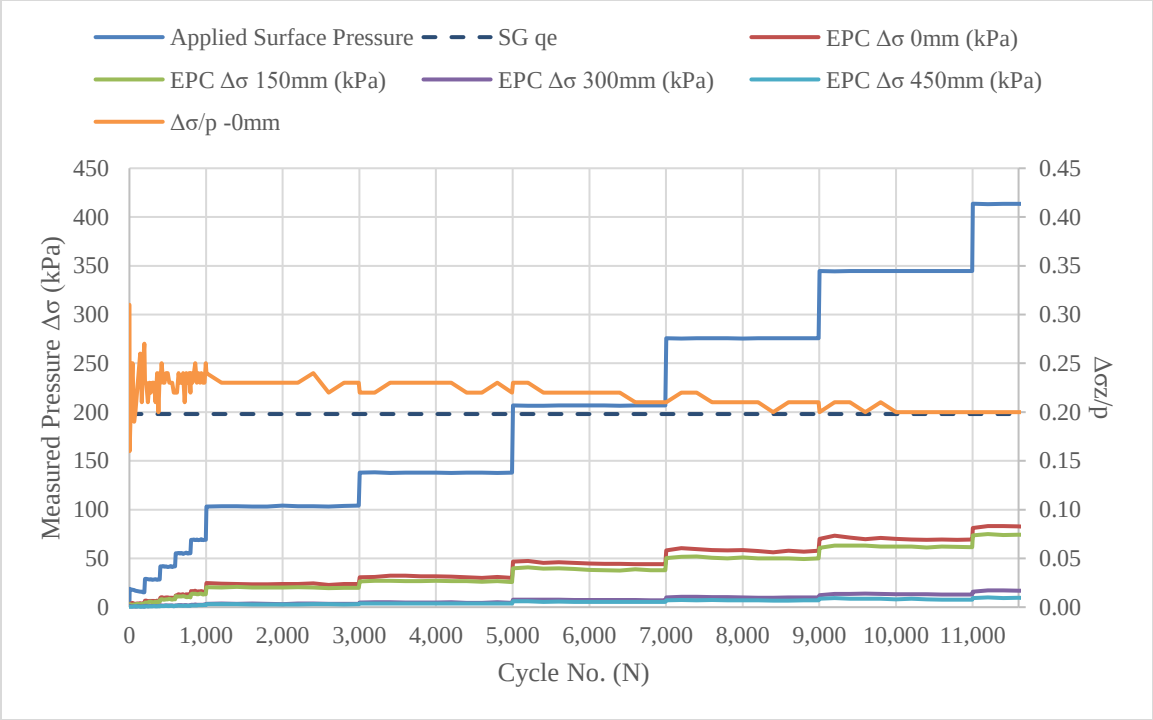

Figure 5.11. Measured Vertical Interface Stress and Stress Reduction Ratio for the Control RCA Section .

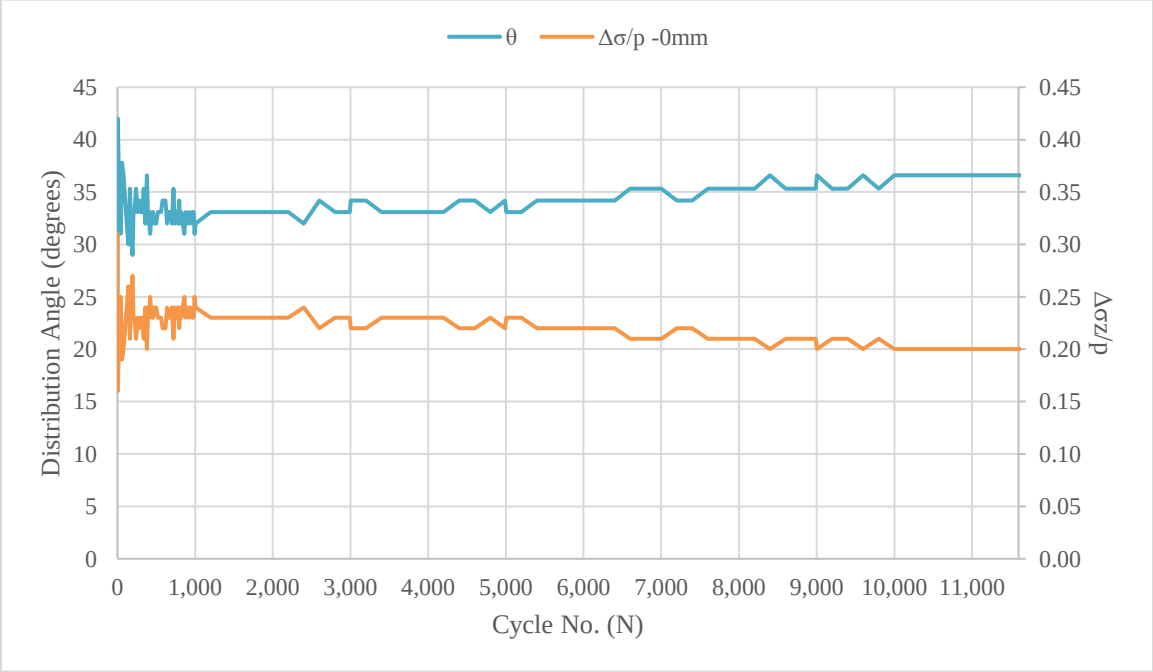

Figure 5.12. Stress Distribution Angle and Stress Reduction Ratio Based on the Vertical Interface Stress at the Center for the RCA Section.

5.1.7 RCA/NW Section

Addition of nonwoven geotextile at the RCA-subgrade interface (Test 18) yielded very similar results from an interface stress perspective as shown in Figure 5.13. The interface stresses were slightly reduced moving away from the center, but the stress was increased at a larger offset distance (300 mm) that indicates a larger stress distribution area. The stress reduction ratio was very similar to the RCA control section at 0.20 and achieved very close to the 1,000-cycle mark; the section remained relatively stable over the remaining 12,000 cycles. Figure 5.14 shows stress distribution angle and stress reduction based on the vertical interface stress at the center for the RCA/NW section. The distribution angle is similar to the 35 degrees obtained for the control RCA section.

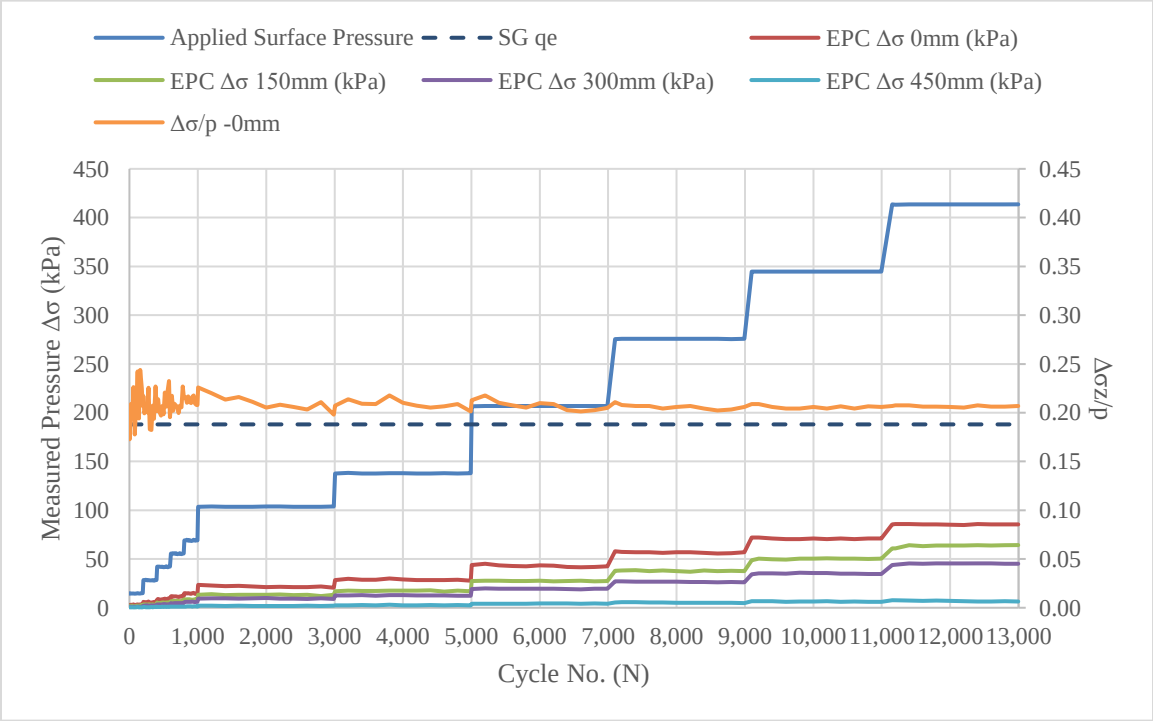

Figure 5.13. Measured Vertical Interface Stress and Stress Reduction Ratio for the RCA/NW Section.

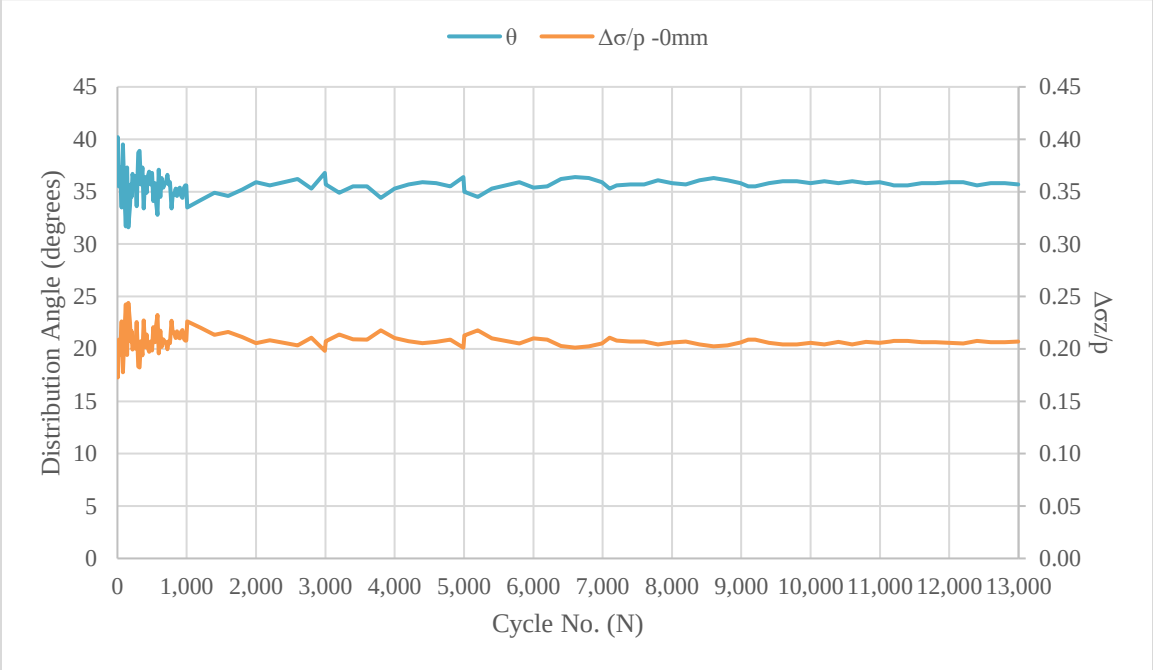

Figure 5.14. Stress Distribution Angle and Stress Reduction Ratio Based on the Vertical Interface Stress at the Center for the RCA/NW Section.

5.1.8 RCA/W Section

While the permanent displacement of the RCA/W section (Test 12) was greater than that of the RCA/NW section (see Chapter 4), interface stresses as shown in Figure 5.15 were lower than those of the nonwoven geotextile- and non-stabilized RCA sections. The earth pressure cell readings at 0 and 150 mm were similar in magnitude for the duration of the test, and the readings at 150 mm exceeded those at 0 mm for the last three load stages. The greater displacement could be causing the tensioned membrane effect at the plate edge at depth, resulting in these higher readings when compared with the center. Reduction in deformation and continued decrease in $\Delta\sigma/p$ and increase in distribution angle θ (Figure 5.16) indicate further stabilization and

strengthening in the base course section. The measured interface stresses indicate that the distribution angle increased to more than 40º as compared with 35º in the control and nonwoven geotextile-stabilized RCA sections and 30º in the VGB/W section.

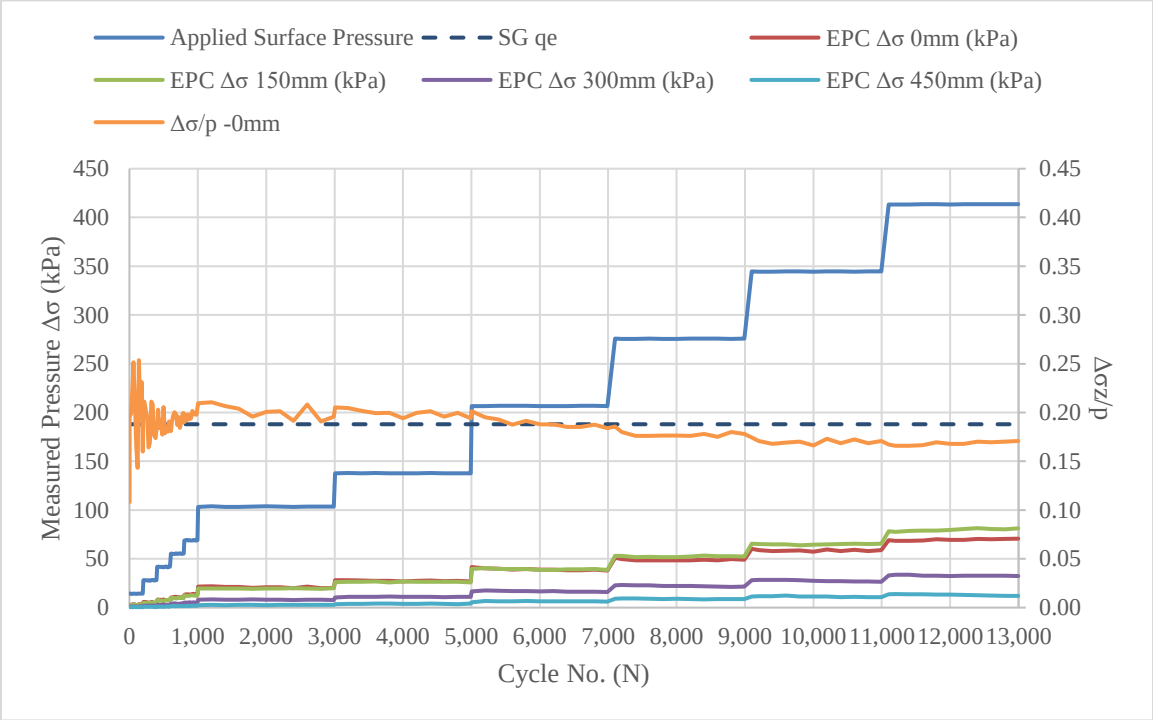

Figure 5.15. Measured Vertical Interface Stress and Stress Reduction Ratio for the RCA/W Sections.

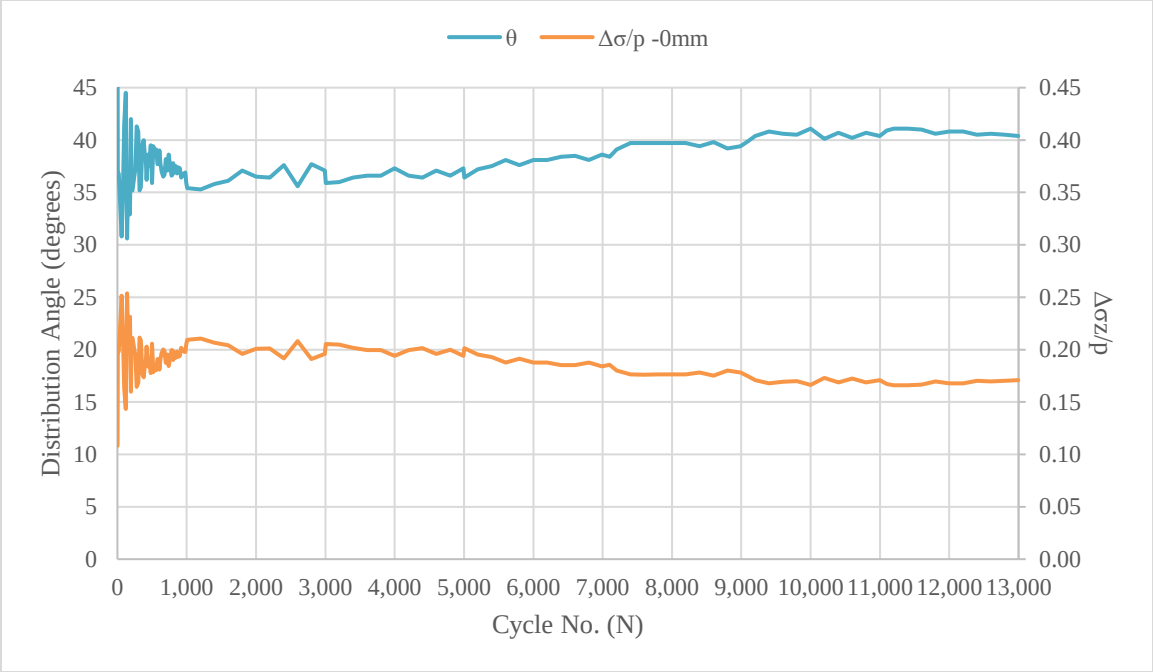

Figure 5.16. Stress Distribution Angle and Stress Reduction Ratio Based on the Vertical Interface Stress at the Center for the RCA/W Section.

5.1.9 RCA/GG Section

Geogrid stabilization of the RCA (Test 16) reduced the stress at 0 mm similarly to the woven geotextile, as displayed in Figure 5.17. The interface stresses at the greater offset distances in this section were reduced further than those in other RCA sections; however, the measured stresses at 150 and 300 mm were similar and of lower magnitude. This behavior indicates the wider angle of stress distribution until approximately Cycle 9,000 where the stress at 150 mm began to increase with the decrease in stress distribution area. The stress increase at 150 mm could be the effect of the tensioned membrane as permanent deformation increased as well, as this offset was located at the plate edge. The interface stresses at the center indicate the peak distribution angle of approximately 39^{o} occurred at near 9,000 cycles (see Figure 5.18) with a decrease to roughly 37^{o} by the end of loading.

The stress reduction ratio increases combined with the higher interface stresses at 150 mm indicate that the section was weakening over the 9,000 to 13,000 cycle sequence. This behavior indicates that the addition of geotextile was more effective at stabilizing the RCA base course than the geogrid in these tests. From the previous section, geogrid allowed high resilient deformations and was effective at stabilizing permanent deformation over control sections. Despite the increase in $\Delta\sigma/p$ and thus the reduction of the distribution angle, θ obtained over the load sequence are still greater than those of the control and RCA/NW sections. Increased load applications for all sections would be recommended to see the longer-term behavior of the sections and whether the geogrid or nonwoven geotextile would be more effective for stabilization.

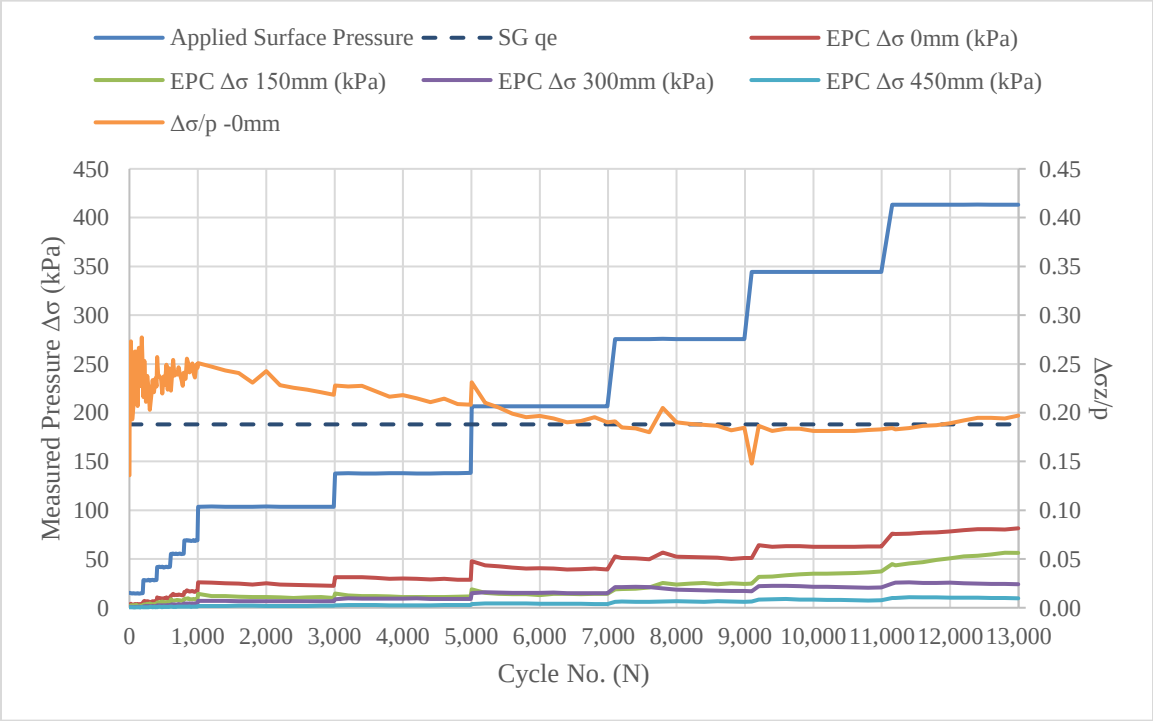

Figure 5.17. Measured Vertical Interface Stress and Stress Reduction Ratio for the RCA/GG Section.

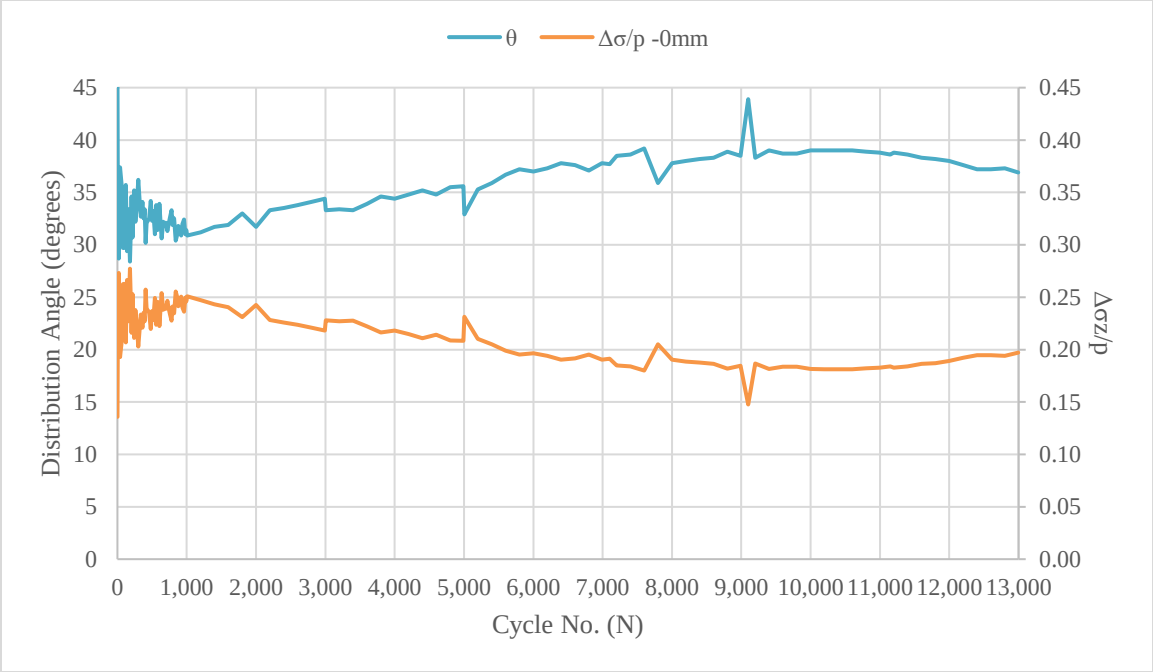

Figure 5.18. Stress Distribution Angle and Stress Reduction Ratio Based on the Vertical Interface Stress at the Center for the RCA/GG Section.

5.1.10 RCA/ GG/ NW Section

The addition of both geogrid and nonwoven geotextile (Test 21) resulted in the least permanent deformation in the tests performed, but the interface stresses displayed in Figure 5.19 were the second greatest noted in the RCA sections. The measured interface stresses at 150 mm approached those at the center, indicating the reduction of stress distribution area at depth. The stress at 300 mm was also the greatest observed, indicating wide area of distribution for interface stresses. A central concentration and membrane tensioning with greater displacement, while occurring at a higher cycle number, indicate that this section had high interlocking of the aggregate particles and the geosynthetics as well as small permanent deformation (see Chapter 4). The interface stress indicates that the distribution angle was only approximately 35^{o} (see Figure 5.20), a value similar to those for the RCA/NW and control RCA sections. The continued

decline of stress reduction ratio over the load sequence indicates a long-term strengthening and stabilization of this geogrid- and nonwoven geotextile-stabilized sections that may reach a distribution angle (35^{o}) or even greater than those observed in the RCA/GG and RCA/W sections above (roughly 40^{o}).

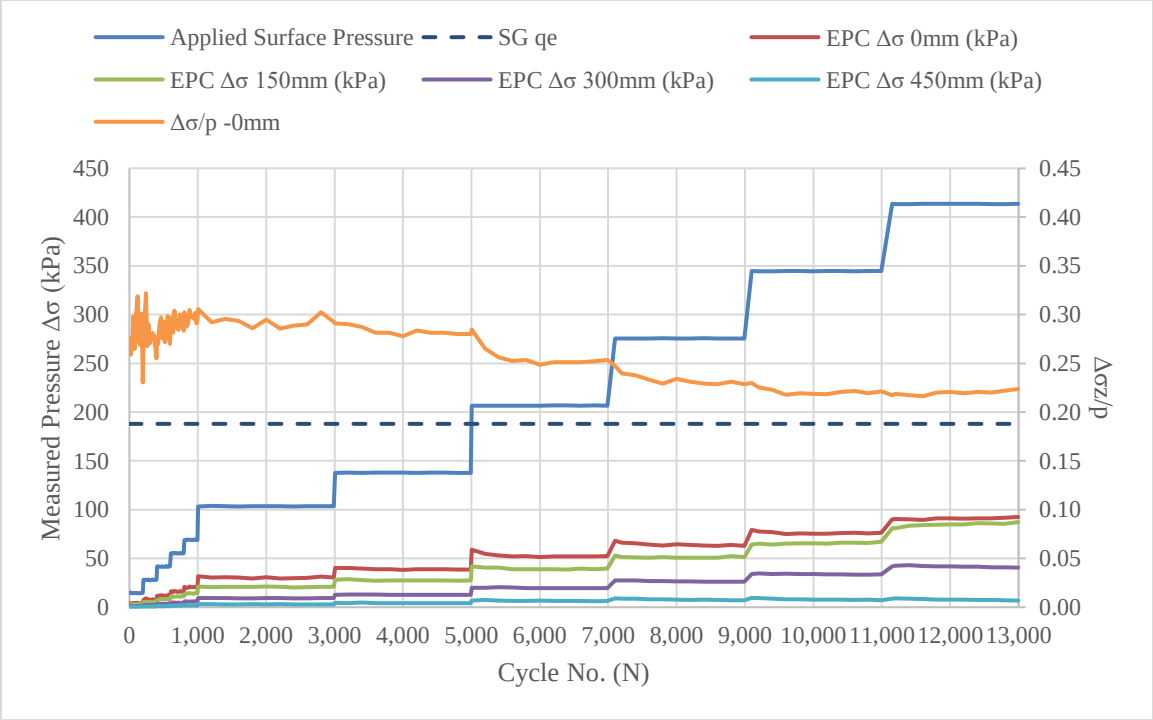

Figure 5.19. Measured Vertical Interface Stress and Stress Reduction Ratio for the RCA/GG Section.

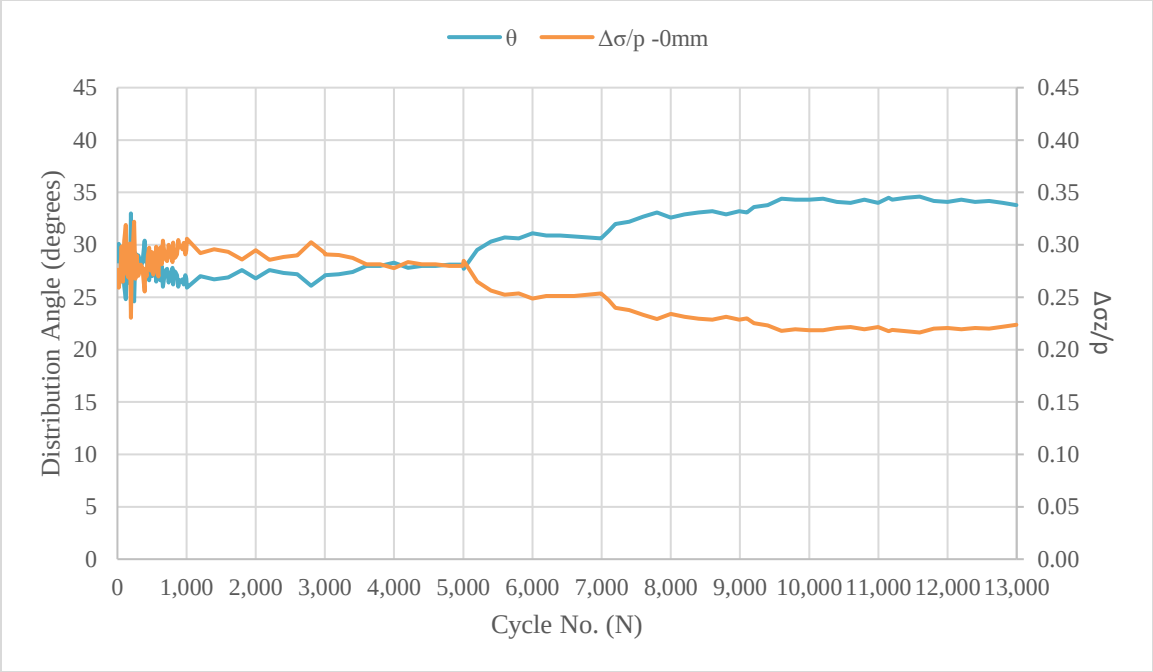

Figure 5.20. Stress Distribution Angle and Stress Reduction Ratio Based on the Vertical Interface Stress at the Center for the RCA/GG/NW Section.

5.1.11 RAP/ NW Section

With difficulties in achieving high relative compaction, the test section with nonwoven geotextile under RAP (Test 26) is compared with prior sections as displayed in Figure 5.21. Based on the increased deformations, the high increase in the interface stress reduction ratio is expected. The addition of the geotextile, however, appears to have increased the stress distribution area at the interface out to 300 mm offset from the center of the load plate. Distribution angle in this section decreased steadily from 25^{o} to roughly 18^{o} over the course of the loading sequence (Figure 5.22) as described in Giroud and Han (2004a and 2004b). Interface stresses at only the ninth load stage exceeded those of any other base course section tested, but the wide interface influence area indicates that the geotextile was adding stabilization to the section. These increased interface stresses combined with the greater surface deformation

indicate the poorer performance due to the lateral spreading of RAP under the given test conditions.

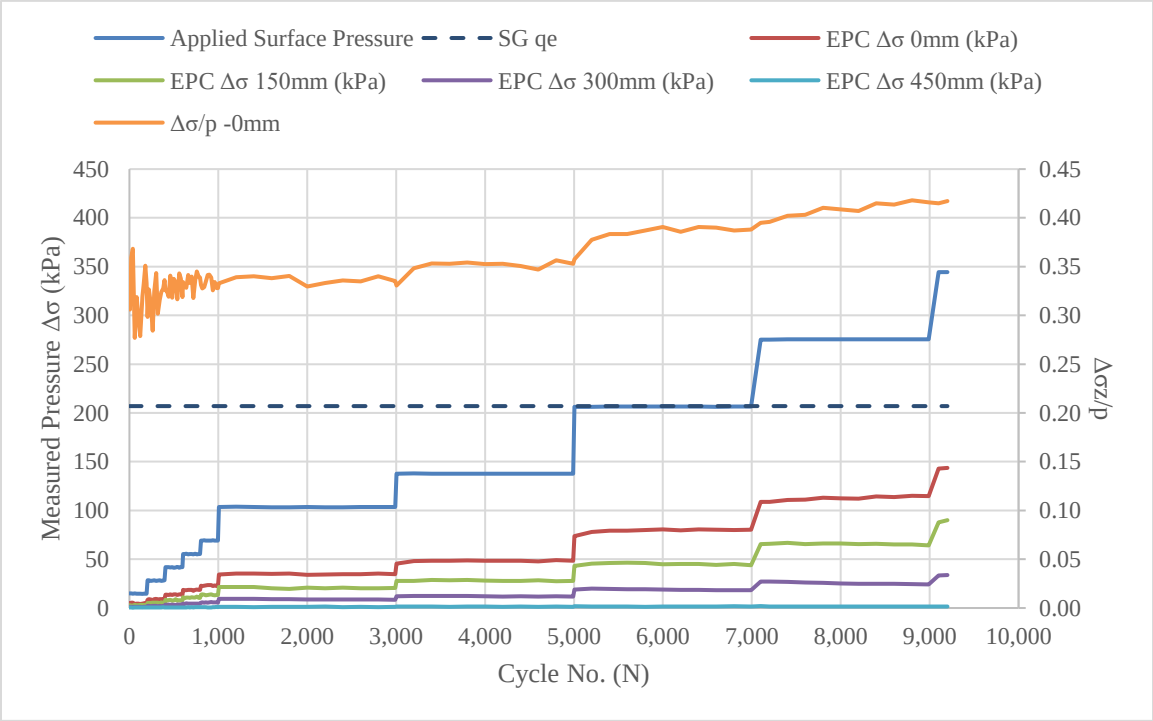

Figure 5.21. Measured Vertical Interface Stress and Stress Reduction Ratio for the RCA/GG Section for the RAP/NW Section.

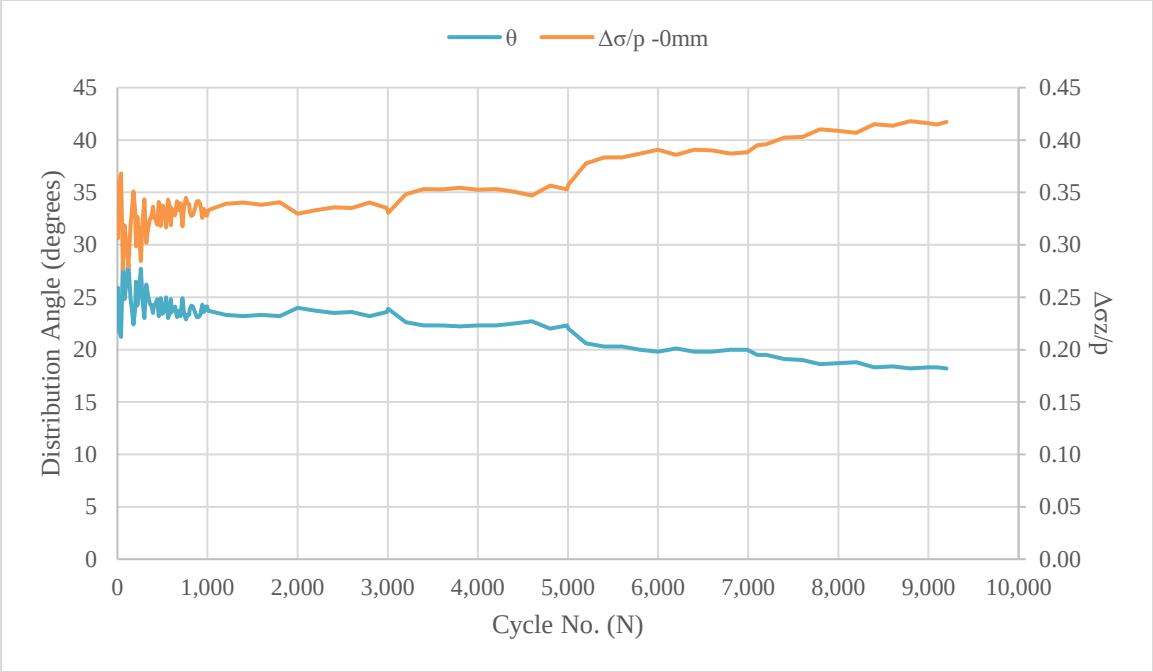

Figure 5.22. Stress Distribution Angle and Stress Reduction Ratio Based on the Vertical Interface Stress at the Center for the RAP/NW Section

5.1.12 Comparison of Measured Vertical Interface Stresses

Estimated stress distribution angles based on stress reduction at the interface between base and subgrade for the unpaved sections are summarized in Figure 5.23. Estimated distribution angles for a range of CBR from 1.8% to 2.2% at 40 kN (550 kPa) applied surface load are plotted as the two dashed lines in Figure 5.23 for reference; these values (21 to 26 degrees) were based solely on the undrained strength of the underlying subgrade and the dimensions of the base course and applied load as described in Chapter 2, Eq. (2.36). Distribution angle estimates are compared against these values at 40 kN applied surface load as this would be the equivalent single wheel load defined by AASHTO (1993).

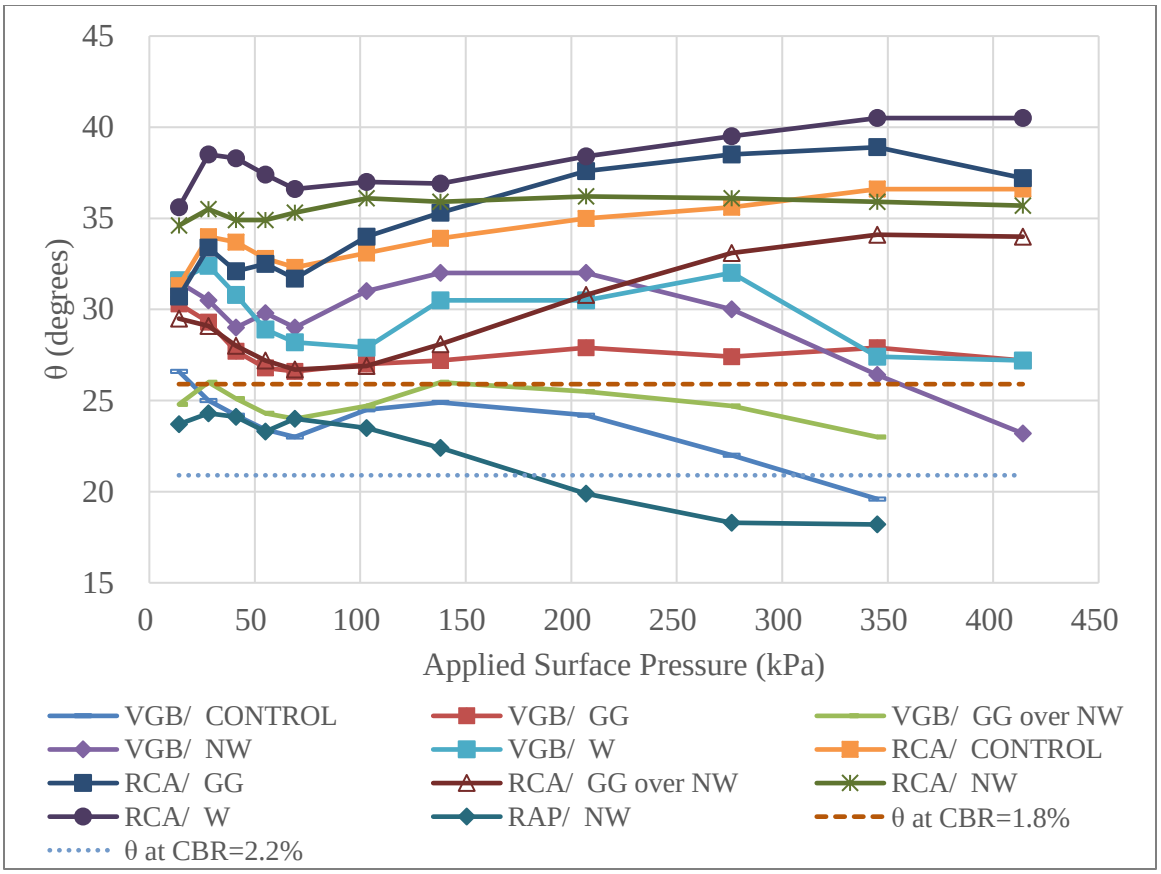

Figure 5.23. Distribution Angle versus Applied Surface Pressure Based on Interface Stress Reduction for Unpaved Sections.

VGB sections exhibited distribution angles in the range of 20 to 32 degrees, as shown in Figure 5.23. VGB control section distribution angles based on stress reduction fall within the estimates of distribution angle for the given CBR range. All the VGB sections except for the VGB/GG had a downward trend in stress distribution angle with increasing load magnitude and accordingly with more load cycle applications; this behavior indicates a deterioration of the base course in later load stages. VGB/GG exhibited the steadiest load distribution angle, indicating a strong base course structure resistant to deterioration. Geotextile stabilization (both W and NW) exhibited the highest distribution angle values, but terminally the distribution angle with W geotextile converged with that with GG and the angle with NW geotextiles was lower. As the

VGB sections with geogrid and nonwoven geotextile displayed similar and the least amount of permanent deformation, the interface stress reduction results support that the addition of nonwoven geotextile or geogrid was effective for improvement. In the last load sequences, where the distribution angle of the section with the woven geotextile exceeded that with the nonwoven geotextile, the following occurred regarding the permanent deformation rate: that of the VGB/NW section increased, that of the VGB/W section decreased, and that of the VGB/GG section remained stable. Based on the terminal distribution angle (19.6 degrees) of the control section, the angle of the VGB was improved by the addition of geosynthetics by 18% (nonwoven geotextile) to 39% (geogrid or woven geotextile).

RCA sections displayed similar increasing distribution angle trends, as shown in Figure 5.23. Decrease in interface stress reduction ratio over the number of applied load cycles is a trait common for RCA, indicating that the aggregate was inherently more resistant to loading. This discovery was confirmed in the displacement reductions discussed previously (see Chapter 4). The distribution angles for the RCA sections ranged from 27 to 41 degrees in these tests. Replacement of VGB with RCA increased the distribution angle more than 20% and over 70% at the minimum terminal distribution angle values. The increase in distribution angle (indicated by subsequent decrease in interface stress reduction ratio) was approximately 5 degrees for all RCA sections. Magnitudes of θ for the control and RCA/NW sections were terminally similar, but the value for the nonwoven-stabilized section was nearly constant (36 degrees); this section exhibited one of the lowest permanent deformations, and this stable section is further confirmed in the EPC results. The RCA/GG/NW composite section had the least permanent deformation, but the distribution angles were the lowest of the RCA sections. This same phenomenon was observed in the final load stage of the geogrid-stabilized RCA section. Addition of geosynthetics

to RCA did improve the sections based on the interface stress decreases up to 30%. This phenomenon indicates that lateral restraint to base course is a dominant mechanism for geogrid-stabilized bases.

Behavior in these sections is confirmed both by the permanent deformation and the stress reduction behavior. When rate of deformation increased, a subsequent decrease in distribution angle based on stress reduction was observed. The decrease in distribution angle shows a load concentration beneath the load plate as the section distributed the load at depth over a narrower area and the load magnitude atop weaker underlying subgrade more likely caused the subgrade to yield or fail. While the magnitude of distribution angle may be slightly greater or less, a stable section exhibited constant or increasing values as the base course maintained its integrity over more and greater-magnitude load applications.

5.1.13 Modulus of Test Section

As described in Chapter 2 [Eq. (2.35)], the stress distribution angle can be applied to back-calculate the modulus ratio of base course to subgrade. Using Giroud and Han's (2004a) method, the resilient modulus of the base course layer may be estimated using the distribution angle from the stress reduction method, the ratio of the base course to the subgrade resilient modulus, and the estimated resilient modulus of the subgrade. For a given cycle, this method has been applied to the test sections, and the resultant resilient moduli are displayed in Figure 5.24.

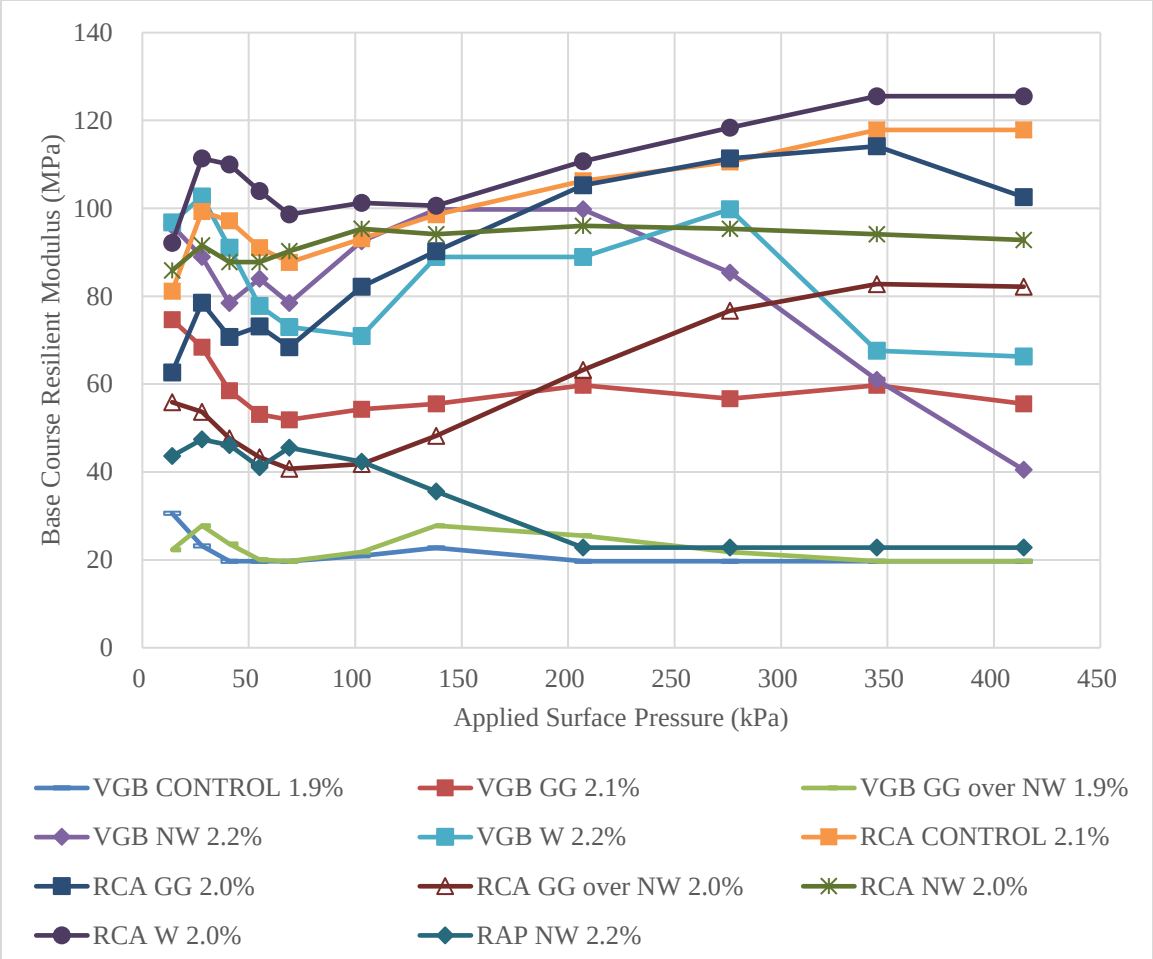

Figure 5.24. Resilient Modulus Calculated using Interface Stress Reduction for the Unpaved Sections.

Corresponding k-values for the unpaved sections were calculated using the stress distribution method to estimate the elastic modulus of the non-stabilized or geosynthetic stabilized base course and the AASHTO (1993) design chart based on the elastic modulus of the base course and the subgrade resilient modulus; these k-values are shown in Figure 5.25. When only stress reduction was considered for this calculation, the use of RCA either with or without geosynthetic stabilization yielded the greatest k-value at more than 50 MPa/m. In both VGB and RCA sections, the highest k-values resulted from the addition of woven geotextile. Addition of

geogrid yielded the most consistent EPC results in the VGB sections, while nonwoven geotextile yielded the most consistent EPC results in the RCA sections. VGB had a small plastic fines fraction (as discussed in Chapter 3) that RCA did not contain any fines. The plastic fines in VGB might cause apparent cohesion in the VGB/GG section that improved stability where the RCA acted in a cohesionless manner with the same geogrid stabilization. RCA might have both the separation and lateral restraint benefit through the addition of nonwoven geotextile that resulted in consistent interface stress reduction and k-values right around 55 to 60 MPa/m. Estimated k-values of VGB control sections range from 33 to 40 MPa/m using the AASHTO (1993) design chart.

Typical values of 14 to 60 MPa/m from Westergaard (1926) and up to 270 MPa/m are identified for composite k-values of control sections in AASHTO (1993) (see Chapter 2). Comparatively, the addition of geosynthetics and the replacement of VGB with RCA increased the k-value to double that identified in AASHTO (1993) for non-stabilized aggregate.

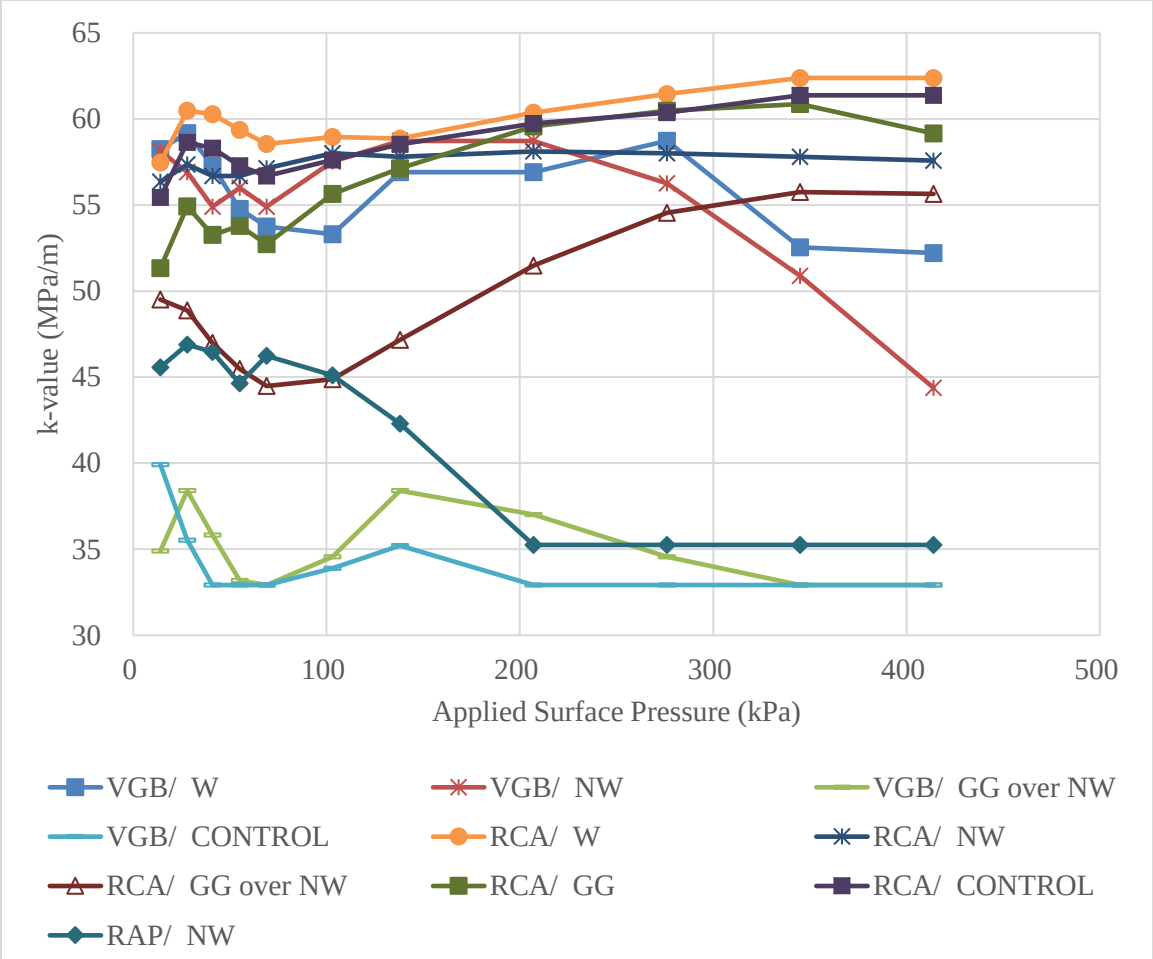

Figure 5.25. Modulus of Subgrade Reaction (k-value) for the Unpaved Sections, Calculated from Base Course Elastic Modulus Based on Interface Stress Reduction and the AASHTO (1993) Design Chart.

5.1.14 Deformation vs. Interface Stress Reduction

The above section estimated the distribution angle based on the interface stress reduction ratio according to Burmister (1958) and evaluated the change of this angle with number of applied load cycles following Giroud and Han (2004a). The MEPDG damage model relates the ratio of permanent to resilient deformation from AASHTO T307 resilient modulus testing for a given

aggregate material, but the addition of geosynthetics and the relationships of these deformations to interface stresses have not been thoroughly studied.

Figure 5.26 displays the relationship between the average resilient deformation and the interface stress at the base course- subgrade interface directly beneath the load plate for each load sequence. In a similar trend to the deformation ratios, the replacement with RCA for VGB exhibits an overall reduction in the ratio of interface stress to resilient deformation. Both replacement and geosynthetic stabilization resulted in interface-stress-to-resilient-deformation ratio reduction. There is a very good linear correlation between the induced resilient deformation and the interface deviator stress for all of the unpaved sections. This relationship is especially important in the context of bearing capacity of a weak underlying subgrade soil and the potential for yielding due to excess applied surface load-induced subgrade pressures.

The best relationship between interface stress and deformation is achieved by taking the total cycle deformation (i.e. the sum of the average resilient and incremental permanent deformations) as displayed in Figure 5.27. To only look at this figure, one would note that there is an inverse relationship from the testing between the total cycle deformation and the interface stress. In viewing Figure 5.27 in the context of Figure 5.26, the ability for a base course section to take on more resilient strain allows the section to reduce the stress applied to the surface of the subgrade (i.e. tensioned membrane effect). It is also important to note the good relationship between total cyclic deformation and interface deviator stress, as for the RCA/NW section compared with very similar data points for the VGB/W section; although their relationships are nearly identical, it should be noted that the surface stresses on the subgrade were reduced more in the RCA than in the VGB, as noted by each data point referring to a given load sequence (see Chapter 3). The magnitude change in deformation from Figure 5.26 to Figure 5.27 (i.e. resilient

deformation to total deformation for each cycle) was minimal in all cases, so it is expected that the interface deviator stresses relationship will be dominated by the resilient deformation and not the incremental permanent deformation for a given applied surface load cycle.

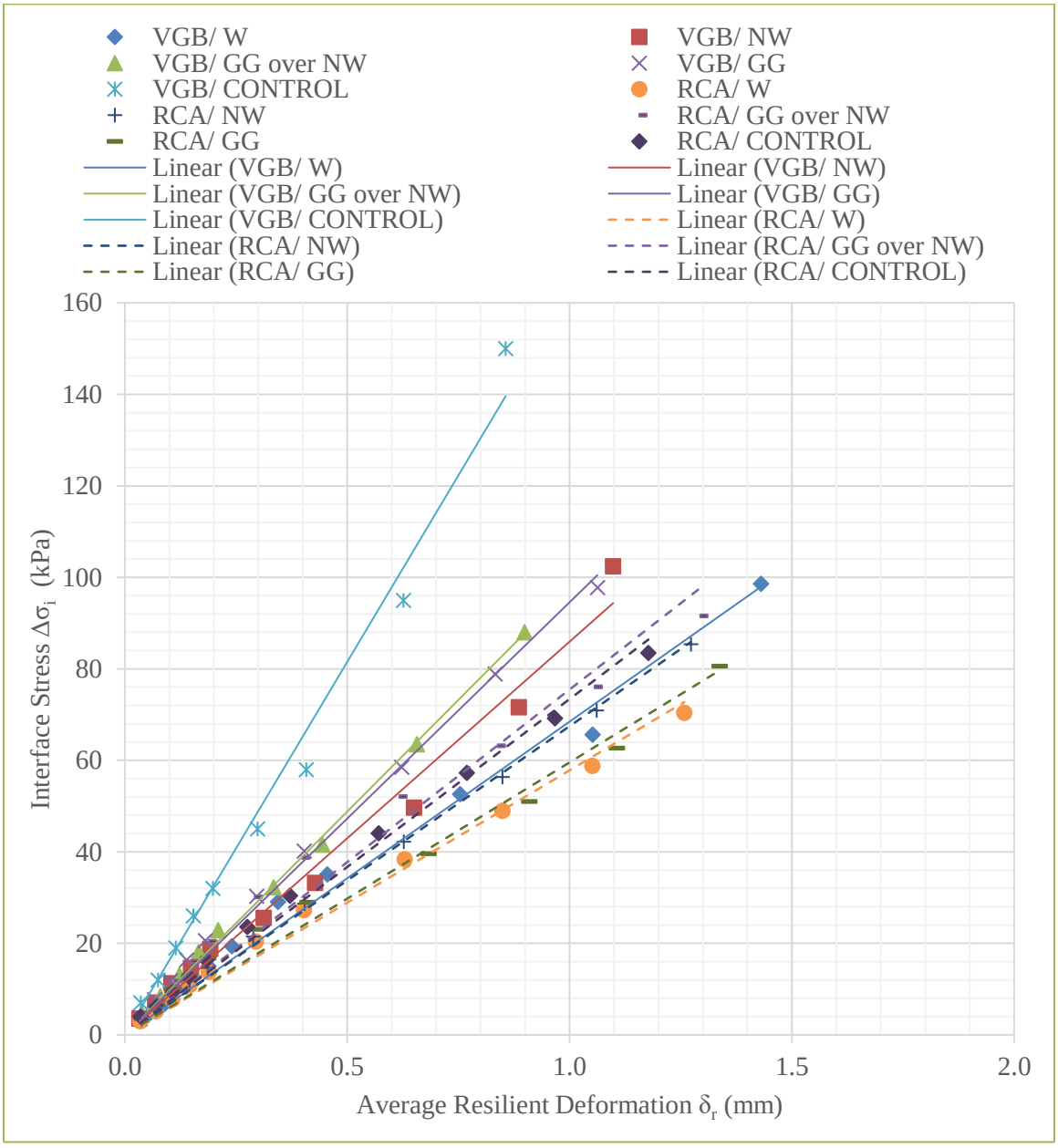

Figure 5.26. Average Resilient Deformation vs. Interface Deviator Stress for Unpaved Sections.

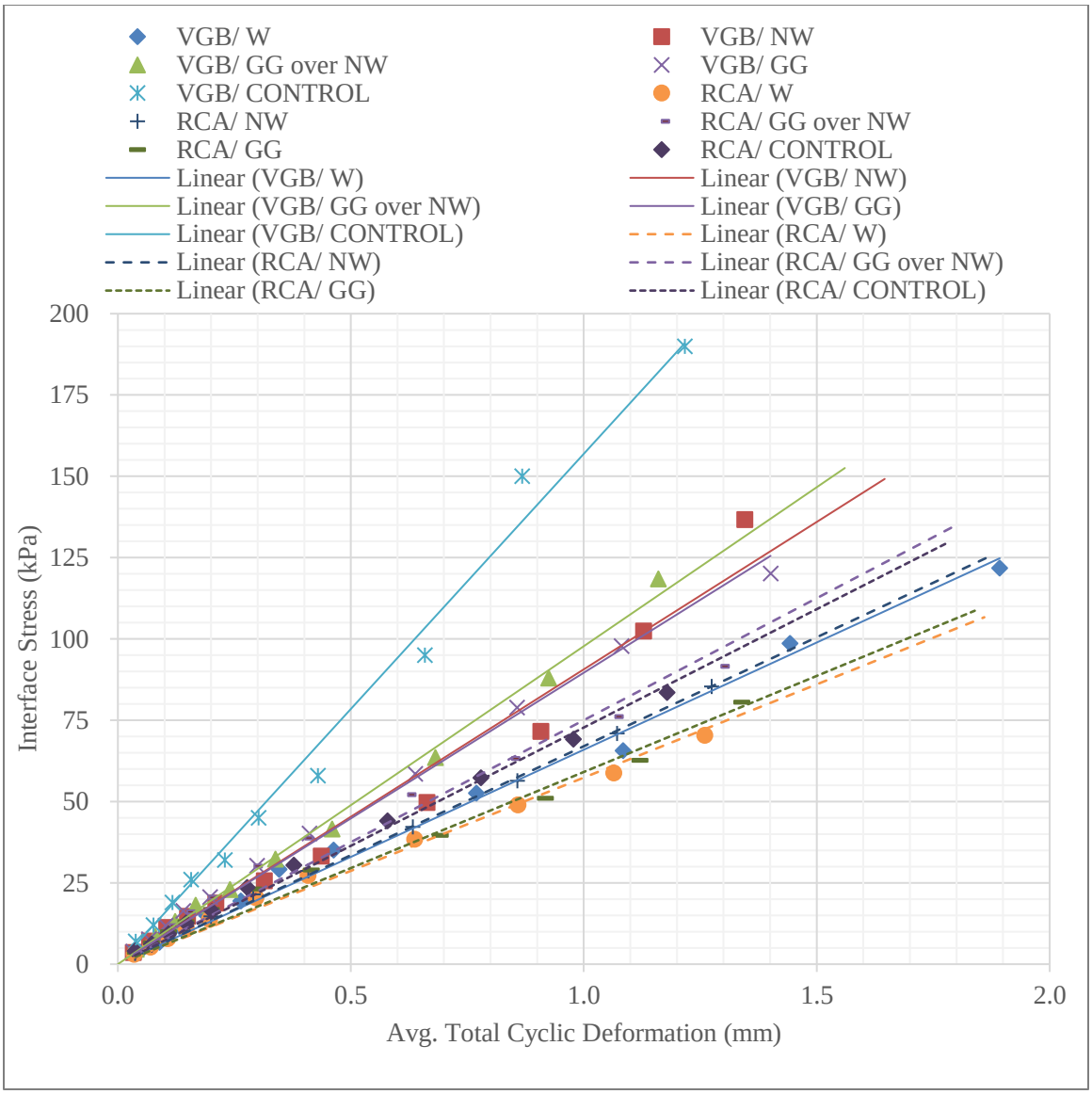

Figure 5.27. Average Total Deformation vs. Interface Deviator Stress for Unpaved Sections.

Figure 5.28 displays the relationship between interface deviator stress reduction and resilient deformation for the VGB only, and the equations for the linear trends are listed in the order on the legend. Woven geotextile displayed the greatest resilient deformation but also exhibited the lowest interface stresses, decreasing both the stress-deformation ratio and the interface deviator stress by over 55%.

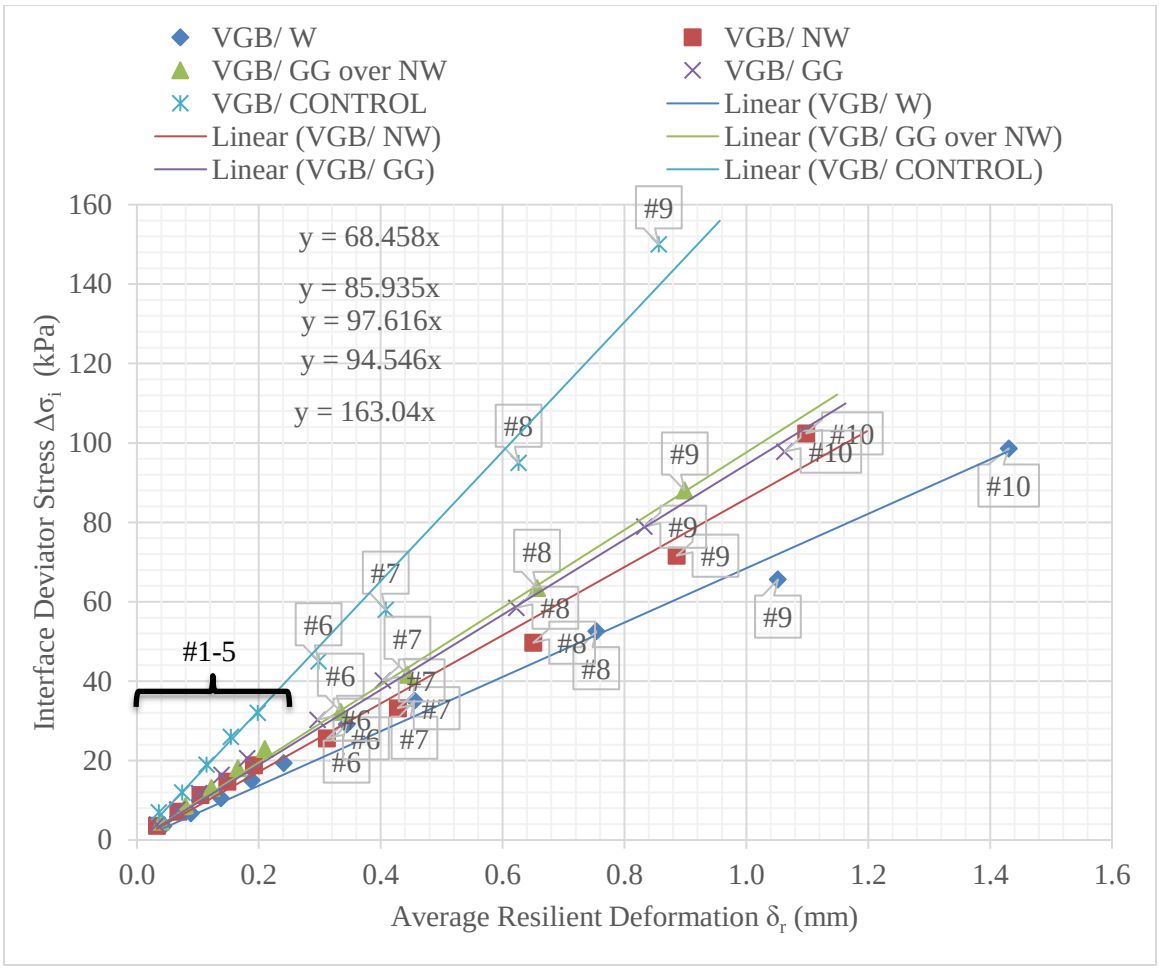

Figure 5.28. Resilient Deformation vs. Interface Deviator Stress for Unpaved Sections with VGB.

Figure 5.29 displays the relationship between interface deviator stress reduction and resilient deformation for the RCA only; the equations for the linear trends are listed in the order on the legend. When compared against the sections with VGB, slope of the stress-deformation relationship reduced through RCA replacement by over 50%. The discrepancy in the interface-stress-resilient-deformation relationships is much smaller in the RCA than in the VGB, but the addition of geosynthetics did reduce the slope of this relationship in most cases by about 10%.

In the sections with RCA, the exception to the trend of stress reduction with increase in resilient deformation was the section with the combination of nonwoven geotextile and geogrid

in the RCA (Figure 5.29). However, the permanent deformation for this section was the least for the unpaved road sections. Stress concentrations may be to blame for the larger earth pressure cell readings; while the exact reason for this phenomenon is unclear, it may be caused by the combined effect of more lateral restraint and less tensioned membrane effect.

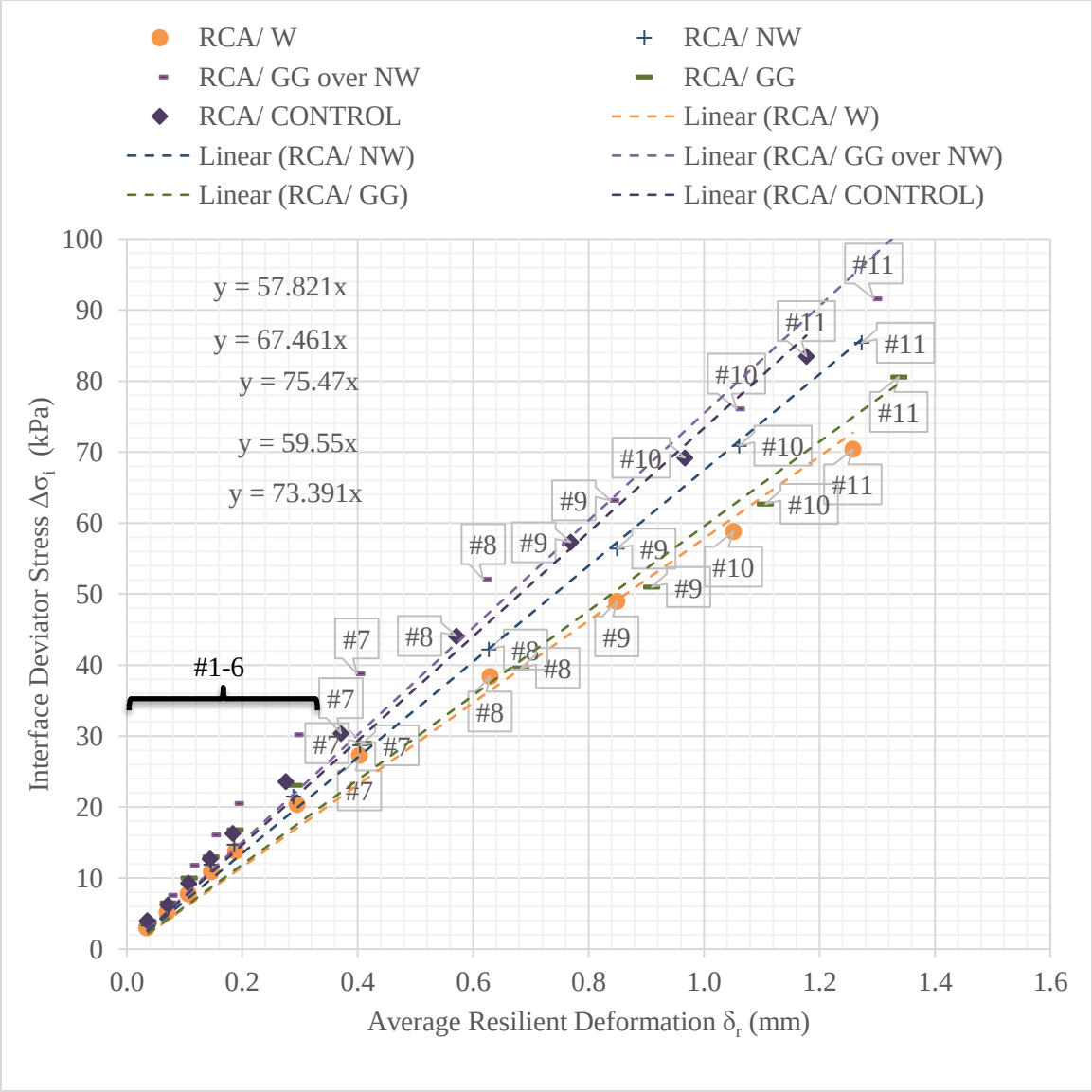

Figure 5.29. Resilient Deformation vs. Interface Deviator Stress in RCA Unpaved Tests.

5.2 Concrete Pavement Sections

Pressure readings were taken at the interface between the base course and subgrade beneath the loaded slab at the same intervals as in the unpaved sections. Load magnitude for all 15,000 cycles was 40 kN at the pavement surface. The 150-mm thick concrete pavement combined with the base course and geosynthetic (if present) is expected to distribute the load to the base course-subgrade interface.

5.2.1 Control VGB Section

The measured vertical interface stresses under the concrete slab over the non-stabilized VGB section during cyclic loading are presented in Figure 5.30. The magnitudes of the interface stresses at the center, 150 mm, and 300 mm from the plate center were similar, with a 40% reduction at the distance of 450 mm. From the loaded corner toward the center of the slab (i.e. away from the loading plate), the displacement of the slab decreased and the interface stresses under the slab decreased. When compared with the interface stresses in the unpaved VGB section, the control VGB section under the concrete slab exhibited approximately half of the maximum vertical stress at 0 mm (50 kPa vs. 100 kPa). As would be expected, $\Delta\sigma/p$ was much lower at 0.11 in the concrete pavement test as opposed to 0.35 in the unpaved test at the maximum applied surface pressure of 276 kPa . The interface stresses during the concrete pavement testing were relatively constant over the load sequence, slightly increasing over the first 3,000 cycles when the displacement was the greatest. This behavior indicates that the pavement system reached a relatively stable state, which covered over 80% of the load sequence.

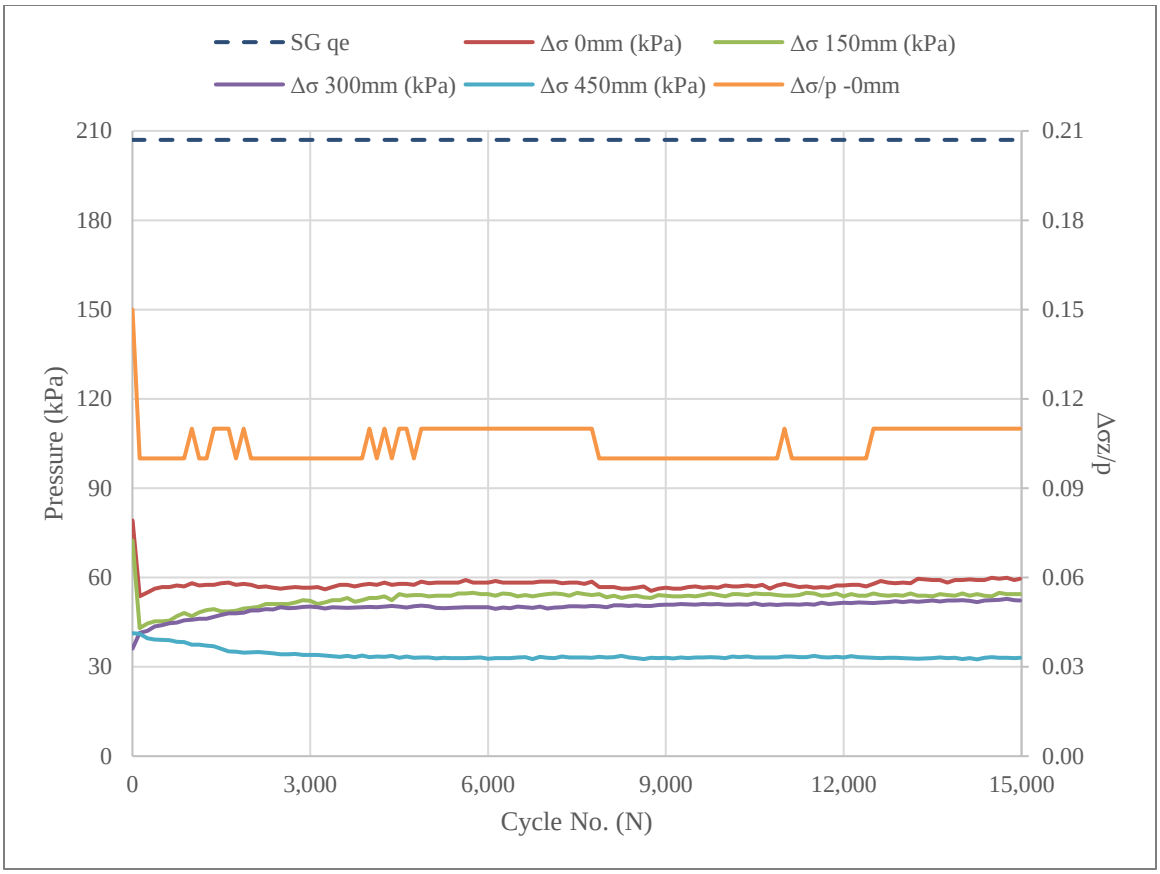

Figure 5.30. Measured Vertical Interface Stresses in the Control VGB Section under the Concrete Slab during Cyclic Loading Pre-rainfall.

When water was added to study the effects of a rainfall event, the stresses at the interface responded differently than in the control section pre-rainfall as shown in Figure 5.31. The magnitude disparity of the vertical interface stresses from the distances of 0 mm to 300 mm changed 10-15 kPa, and the load magnitudes measured by all four EPCs increased steadily by 2-5 kPa over the last 80% of the load sequence. Higher pressure increases were observed in the post-rainfall test sections. The increase in interface stresses observed beneath the plate increased the potential for breakdown of this material. Although the total deformation of this post-rainfall loading did not exceed those of the initial loading, the stresses at depth increased at the interface

post-rainfall; had this been a continuation without a rainfall event, interface stresses would have been maintained at the pre-rainfall levels rather than increase.

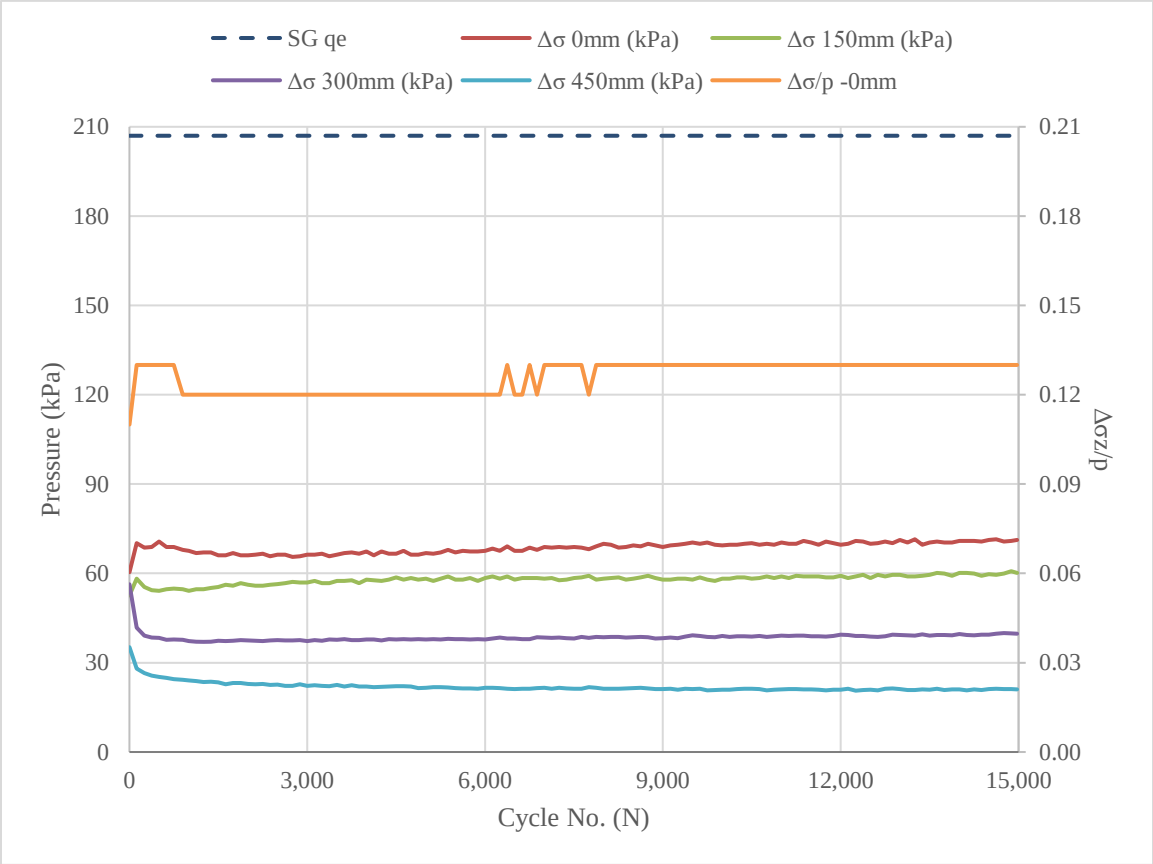

Figure 5.31. Measured Vertical Interface Stresses in the Control VGB Section under the Concrete Slab during Cyclic Loading Post-rainfall.

5.2.2 Nonwoven Geotextile Stabilized VGB

The addition of nonwoven geotextile to the VGB-subgrade interface resulted in the interface stresses observed in Figure 5.32. Magnitudes of the stresses at the distances of 0 mm and 150 mm from the plate center were similar at 70 to 75 kPa over the entire load sequence. The magnitude of the vertical stress at 300 mm steadily increased from 41 to 47 kPa. The steady stress state of the distances of 0 mm and 150 mm could indicate a stronger pavement structure, as

a decrease in the permanent deformation from the control VGB section was observed. The increase in the interface stress at 300 mm might be induced by tensioning of the geotextile; the increase in the stresses at the interface resulted in a decrease in the deformation. The relative stress reduction ratio for this section was 0.13 on average slightly greater than 0.11 in the control section.

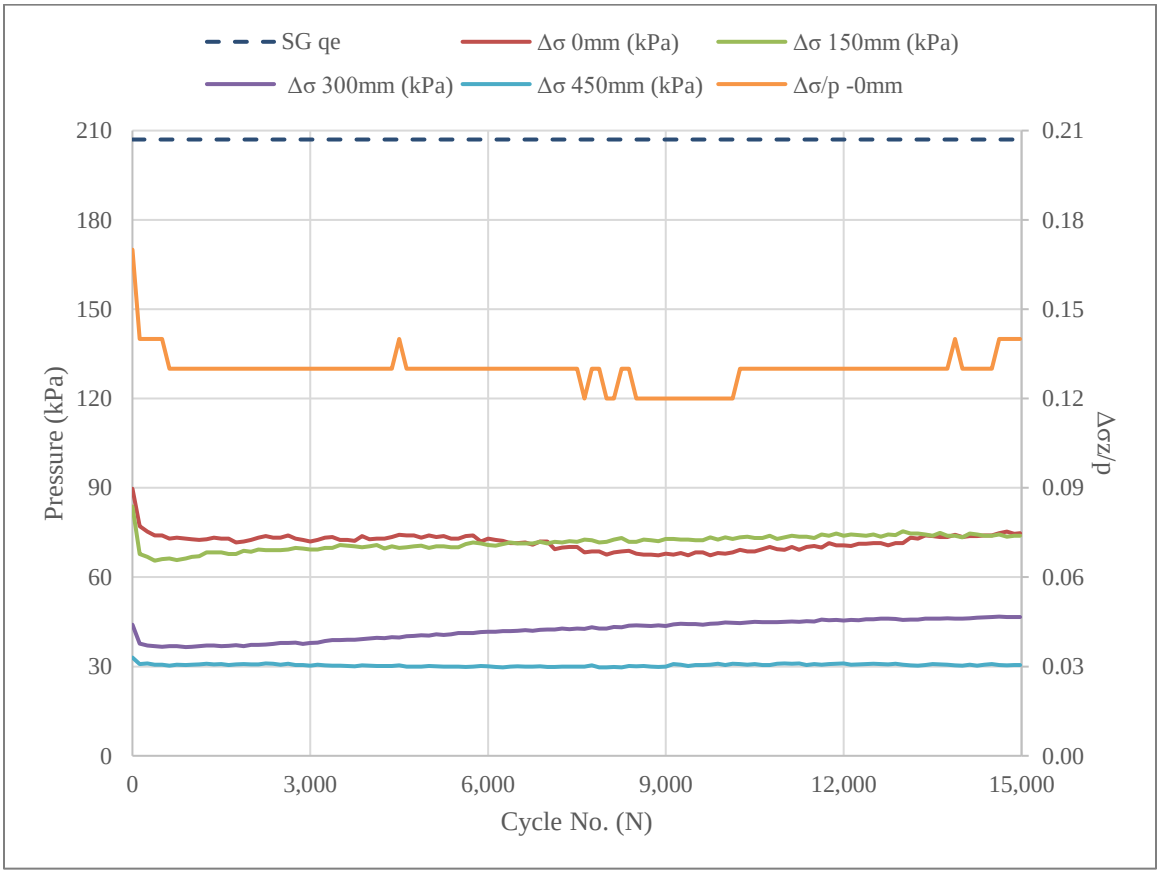

Figure 5.32. Measured Vertical Interface Stresses in the VGB/NW Section under the Concrete Slab during Cyclic Loading Pre-rainfall.

Rainfall, like in the control section, induced increased base course-subgrade interface stresses in the VGB/NW section as shown in Figure 5.33. Interface stress reduction ratio further increased to 0.17 as opposed to 0.13 in the control VGB post-rainfall test. Similar stress decrease

from the center of the plate along the diagonal of the loaded slab was observed with well-distributed stress magnitudes of 100 kPa to 25 kPa, respectively.

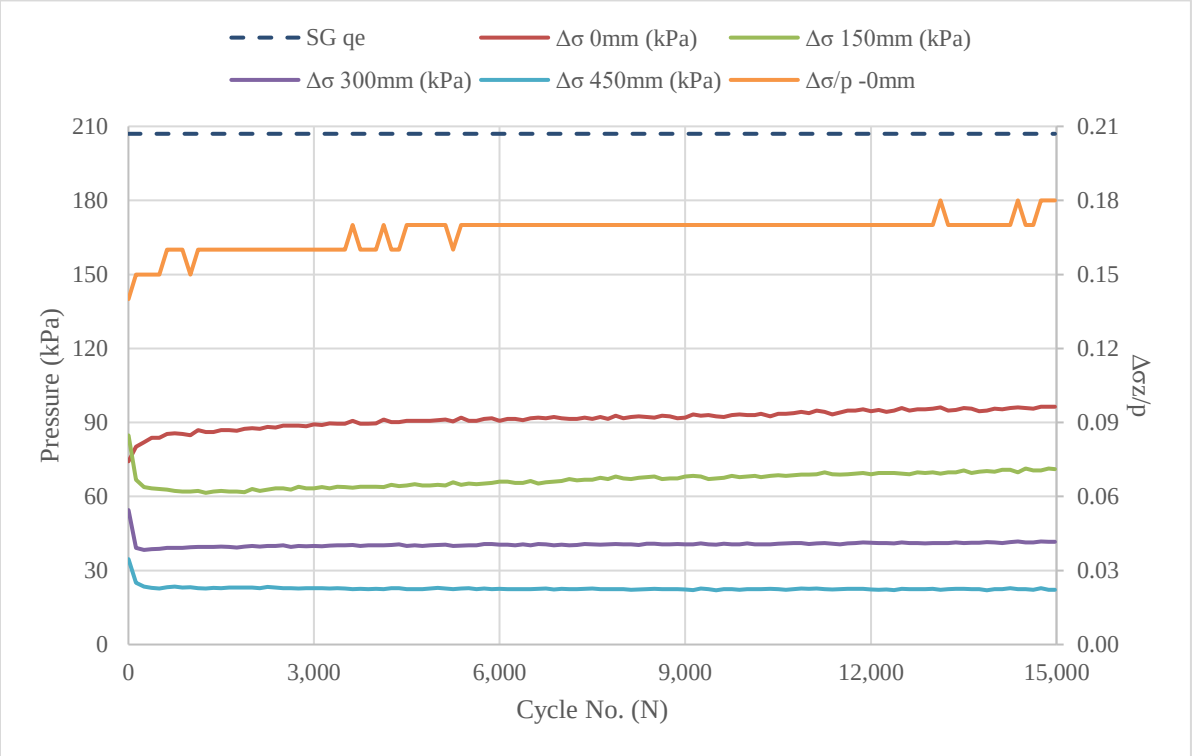

Figure 5.33. Measured Vertical Interface Stresses in the VGB/NW Section under the Concrete Slab during Cyclic Loading Post-rainfall.

5.2.3 Nonwoven-stabilized RCA Section

The earth pressure cell readings at the interface between base and subgrade for the nonwoven-stabilized RCA section pre-rainfall are exhibited in Figure 5.34. The vertical interface stress at 0 mm in this section was similar to that of the nonwoven geotextile-stabilized VGB pre-rainfall (approximately 75 kPa) and higher than those in the control VGB section (approximately 50 kPa). The vertical interface stresses at 150 mm and 300 mm in the RCA section was similar to

each other (near 50 kPa) with a decrease to less than 25 kPa at 450 mm. This distribution of interface stresses indicates that the stresses were concentrated beneath the load plate, but the base course provided load resistance out to the distance of 300 mm.

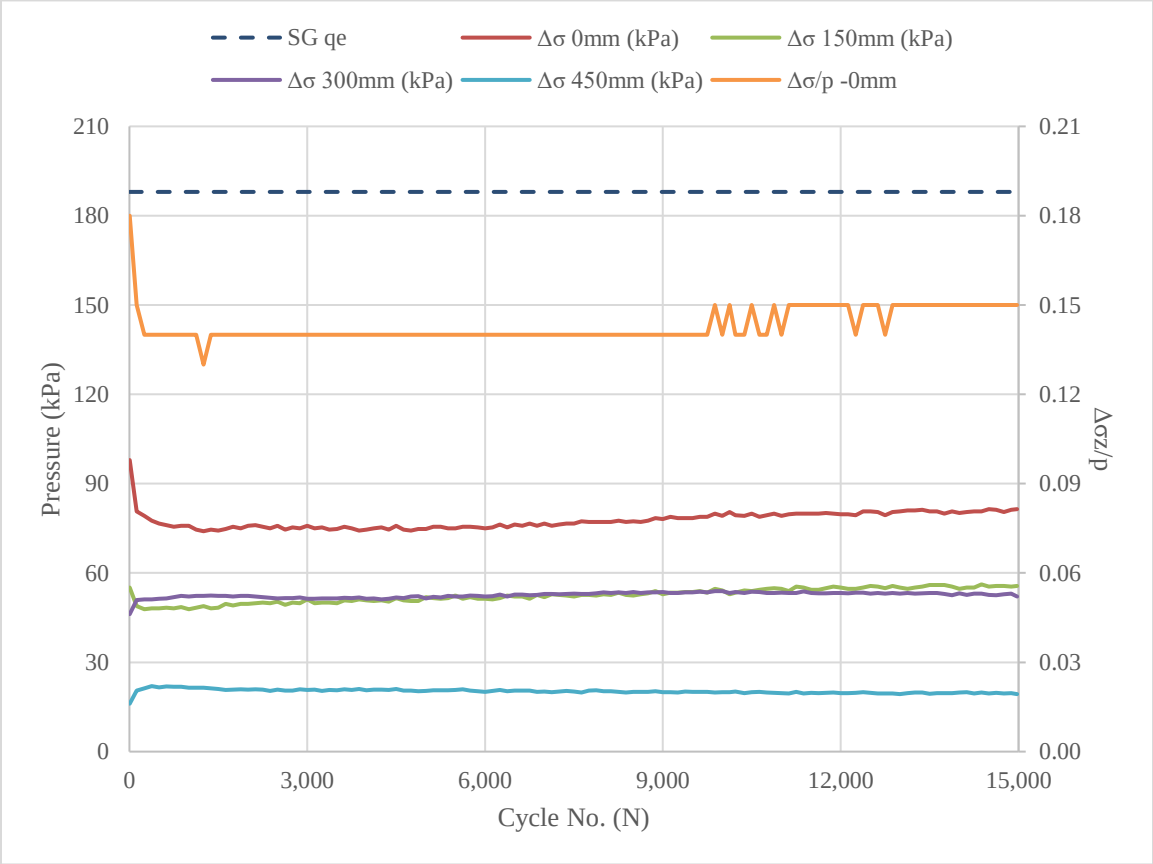

Figure 5.34. Measured Vertical Interface Stresses in the RCA/NW Section under the Concrete Slab during Cyclic Loading Pre-rainfall.

After rainfall, the nonwoven-stabilized RCA section exhibited lower interface pressure readings than the section pre-rainfall as displayed in Figure 5.35. The distribution pattern post-rainfall more closely resembled the pre-rainfall pattern in the nonwoven-geotextile-stabilized VGB section at the distances of 0 mm and 150 mm, exhibiting similar pressure readings at an intermediate distance of 300 mm and a decreased pressure at 450 mm.

While the initial 3,000 load cycles post-rainfall exhibited a higher permanent deformation, the reduction of the interface stress, the similar magnitudes of the stresses at different distances (40-50 kPa), and the lower permanent deformation occurred after 3,000 cycles. This result indicates that while some initial reorganization of particles to a denser state occurred post-rainfall, the non-plasticity nature of the RCA material allowed for fast drainage of water, which was further accelerated by loading and helped the section recovery to a strong pavement structure post-rainfall. Stress concentrations induced by a geotextile membrane pressing on the EPCs were not observed as those in the geotextile-stabilized VGB section; therefore, stress increases at the interface were not observed. As both sections contained geotextile, they recovered after the wetting of the material. The nonwoven-stabilized RCA section post-rainfall better distributed the load through the base course section than the VGB section. Interface stress reduction thus indicates the good performance of the nonwoven-geotextile-stabilized RCA section in rainfall applications.

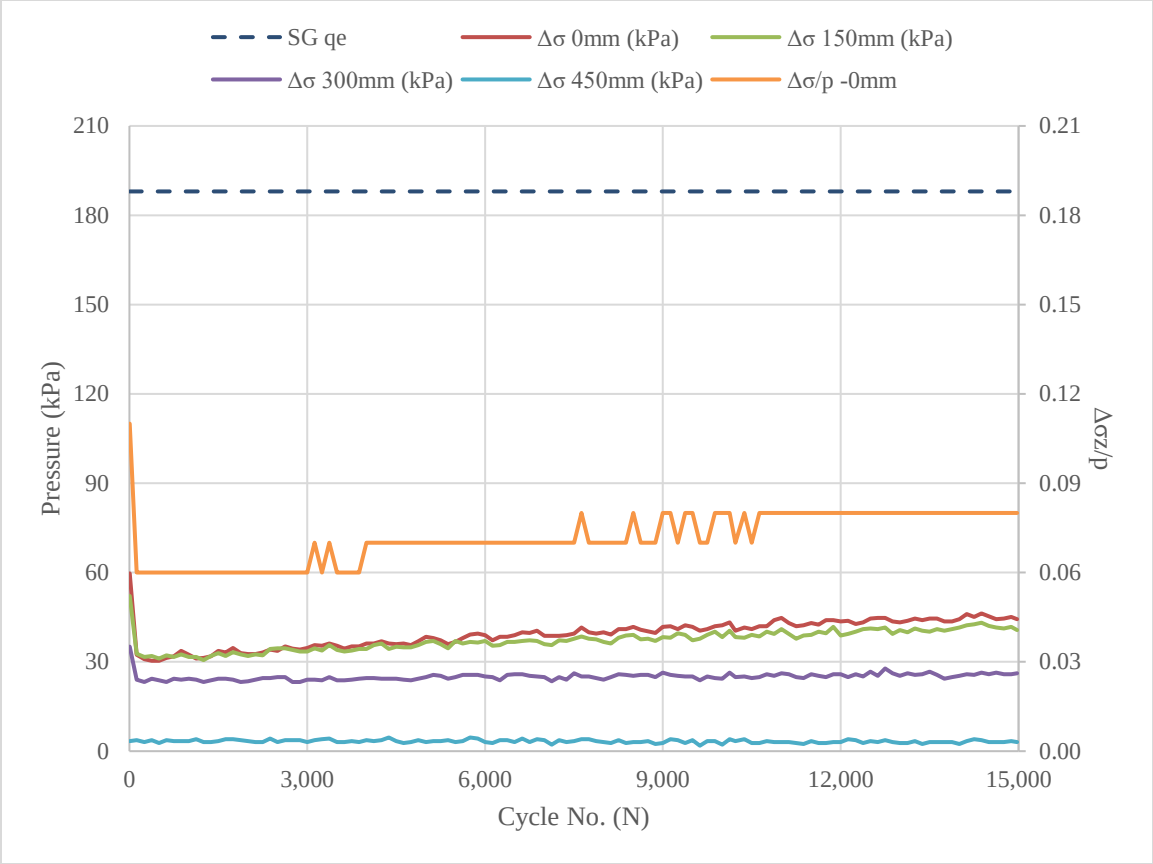

Figure 5.35. Measured Vertical Interface Stresses in the RCA/NW Section under the Concrete Slab during Cyclic Loading Post-rainfall.

5.2.4 Comparison of Measured Vertical Interface Stresses

Interface stress reduction ratios under the concrete slab during cyclic surface loading of 40 kN can be observed in Figure 5.36 as estimated at the pavement-base course interface as described in Chapter 2. Figure 5.37 displays interface stress reduction ratios as measured at the base course-subgrade interface. Estimated stresses at the bottom of the pavement were more similar to each other (0.15 to 0.20) than those at the subgrade surface (0.05 to 0.19). Variations were expected for the estimated pavement-base course interface stresses due to the stiffness component that is a function of the reaction of the rigid pavement with the underlying base course-subgrade. Stress

reduction ratio at the subgrade surface was smaller than that estimated at the base course surface, so the evaluation presented herein is valid as more load dissipation was observed at depth. The surface stiffness is not fully reflected in the base course-subgrade interface stress (Figure 5.37), as some sections display higher interface stresses at lower displacements (e.g. post-rainfall VGB with nonwoven geotextile) as was discussed previously. Initially, from an interface stress standpoint, the VGB appears to decrease the top-of-subgrade interface stress more effectively than the RCA replacement or the addition of nonwoven geotextile at the interface. Post-rainfall, the nonwoven-stabilized RCA reduces base course-subgrade interface stress the most; but the VGB/NW, which displayed the least post-rainfall surface deformation at the corner, had the highest interface stress directly below the plate.

Previous sections show some variation in the top-of-subgrade earth pressure cell readings when moving radially from the center of the plate up to 450 mm. If the pavement section is stiffer, the eccentricity will be reduced and more similar readings will be observed at depth (e.g. VGB/NW pre-rainfall in Figure 5.37); concentrated load readings that decreased radially (e.g. VGB/NW post-rainfall in Figure 5.37) indicate more bending of the slab over weaker base course.

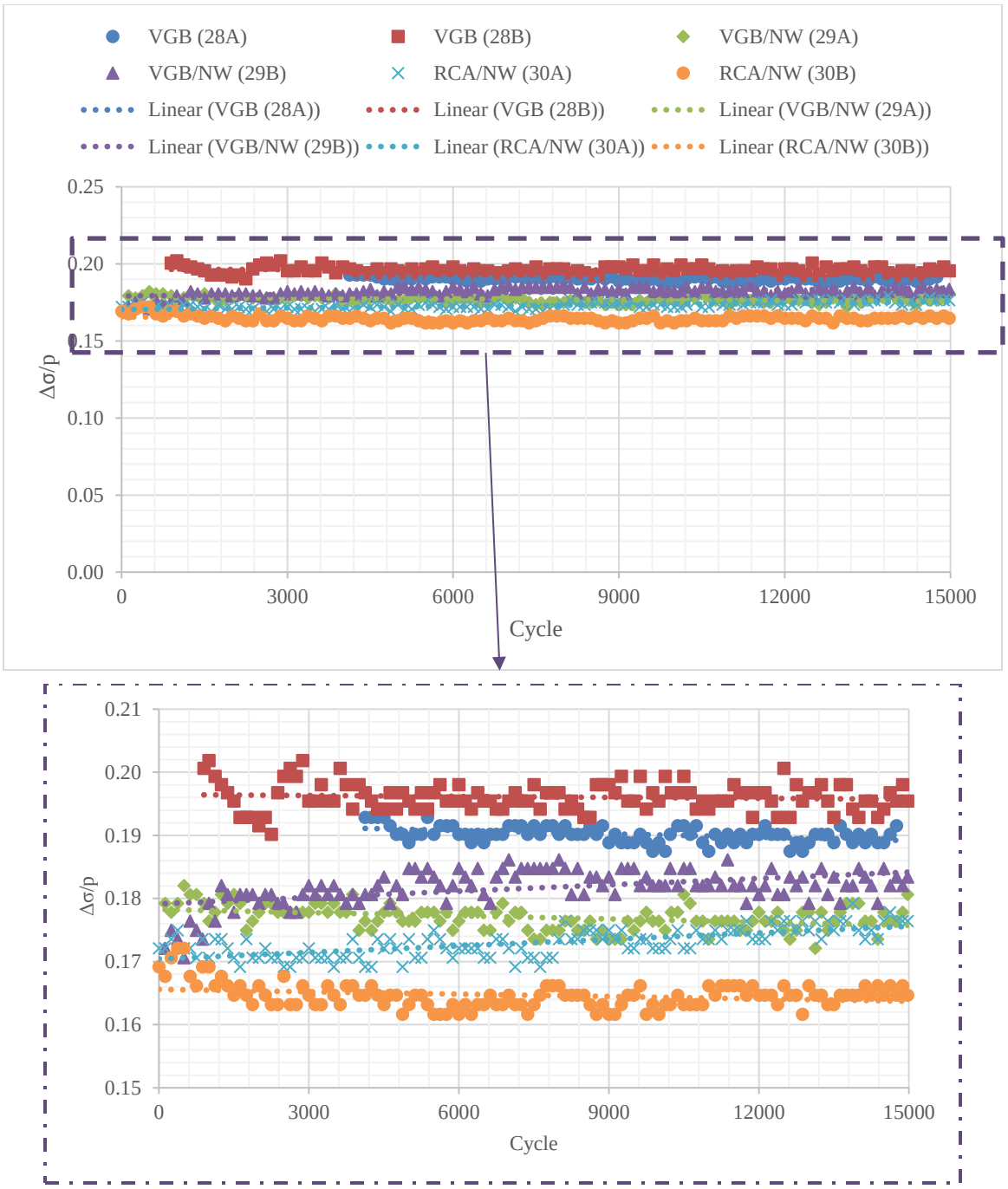

Figure 5.36. Estimated Stress Reduction Ratios at the Pavement-Base Course Interface under the Concrete Slab under Cyclic Loading.

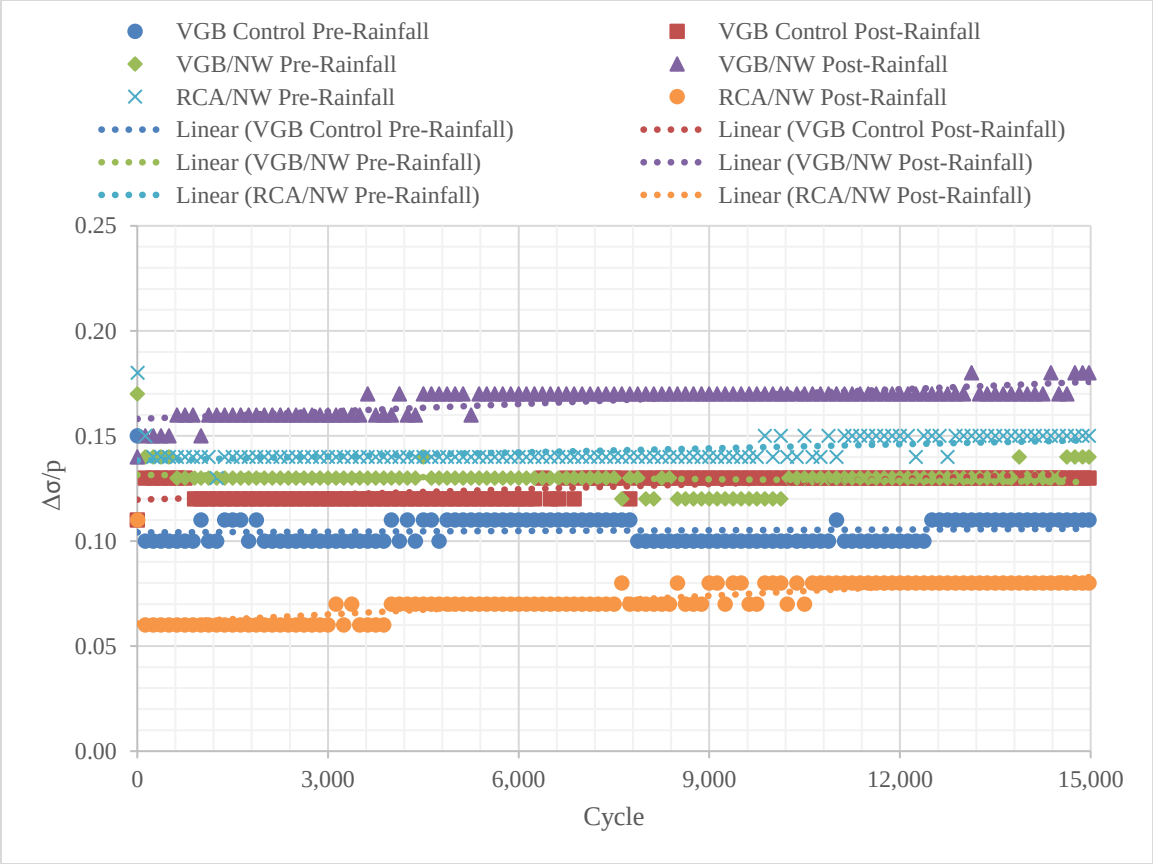

Figure 5.37. Measured Stress Reduction Ratios at the Base Course-Subgrade Interface under the Concrete Slab during Surface Loading.

5.2.5 Interface Stress vs. Permanent and Resilient Deformations

For design of concrete pavements, stresses and deflections of the slab are the focus as the breakdown of the slab determines pavement longevity; k-value is thought to have minimal effect on slab stresses (Westergaard 1926). Interface stresses between base course and subgrade are not considered in the current design of concrete pavement with the use of a composite or effective k-value, and charts and modeling for this application are more limited than they are for unpaved roads. As previously discussed, the tensioning of geotextile and the rigidity of the pavement create different behavior and stress distribution than unpaved roads; this is further proven by the

reduced stress reduction ratio ($\Delta\sigma/P$) and the base course-subgrade interface stress when compared against the unpaved tests. Lateral homogeneity is not present in this corner loading scenario, either, as a joint and free shoulder exist adjacent to the load plate. While interface stress reduction can be an indicator of improved or reduced pavement performance, design values for pavement structure are not determined on this basis using current methods.

Figure 5.38 displays the relationship between accumulated permanent deformation and stress reduction ratio at the base course-subgrade interface. For the pre-rainfall tests, lower permanent deformations corresponded to higher interface stress reduction ratios. Post-rainfall, interface stress ratio displays the same inverse relationship to accumulated deformation because the highest permanent deformation of the RCA/NW section exhibited the lowest interface stress reduction ratio while the VGB/NW section exhibited the highest interface stress reduction ratio and lowest permanent deformation. Before and after rainfall, both VGB sections exhibited an increase in interface stress reduction ratio but a decrease in permanent deformation; the nonwoven-geotextile stabilized RCA section exhibited a post-rainfall permanent deformation similar to the pre-rainfall one but a significant decrease in $\Delta\sigma/p$.

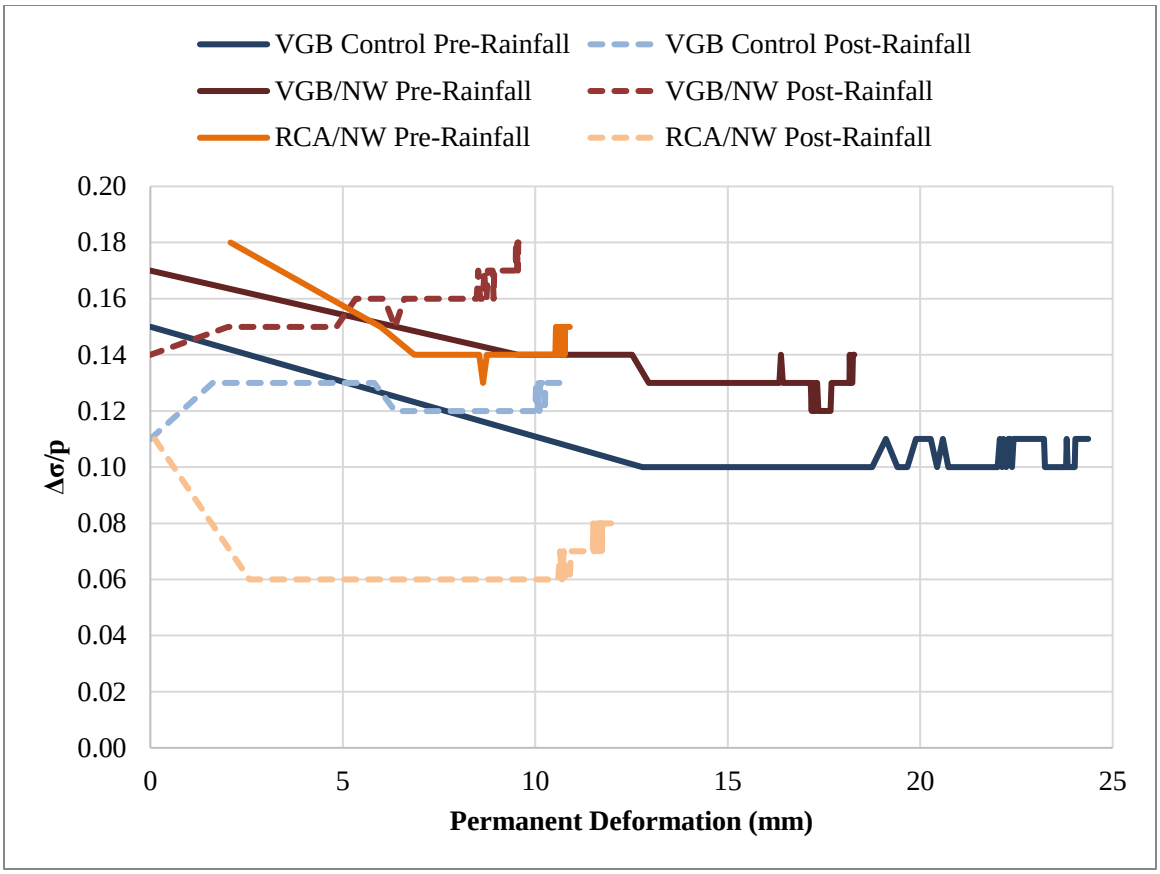

Figure 5.38. Permanent Deformation versus Stress Reduction Ratio for the Concrete Pavement Sections.

Figure 5.39 exhibits the resilient deformation plotted against the interface stress reduction ratio. Like the permanent deformation trend, the VGB sections exhibited a reduction in resilient deformation corresponding to an increase in interface stress reduction ratio post-rainfall. Resilient deformation increased with the addition of nonwoven geotextile but also increased the interface stress reduction ratio. The RCA/NW section exhibited the least resilient deformation and average interface stresses as compared with other sections pre-rainfall, but post-rainfall both the resilient deformation and the interface stress reduction ratio decreased. The stiffer behavior based on the reduction in the radius of relative stiffness of the RCA/NW section post-rainfall could account for the increased permanent deformation.

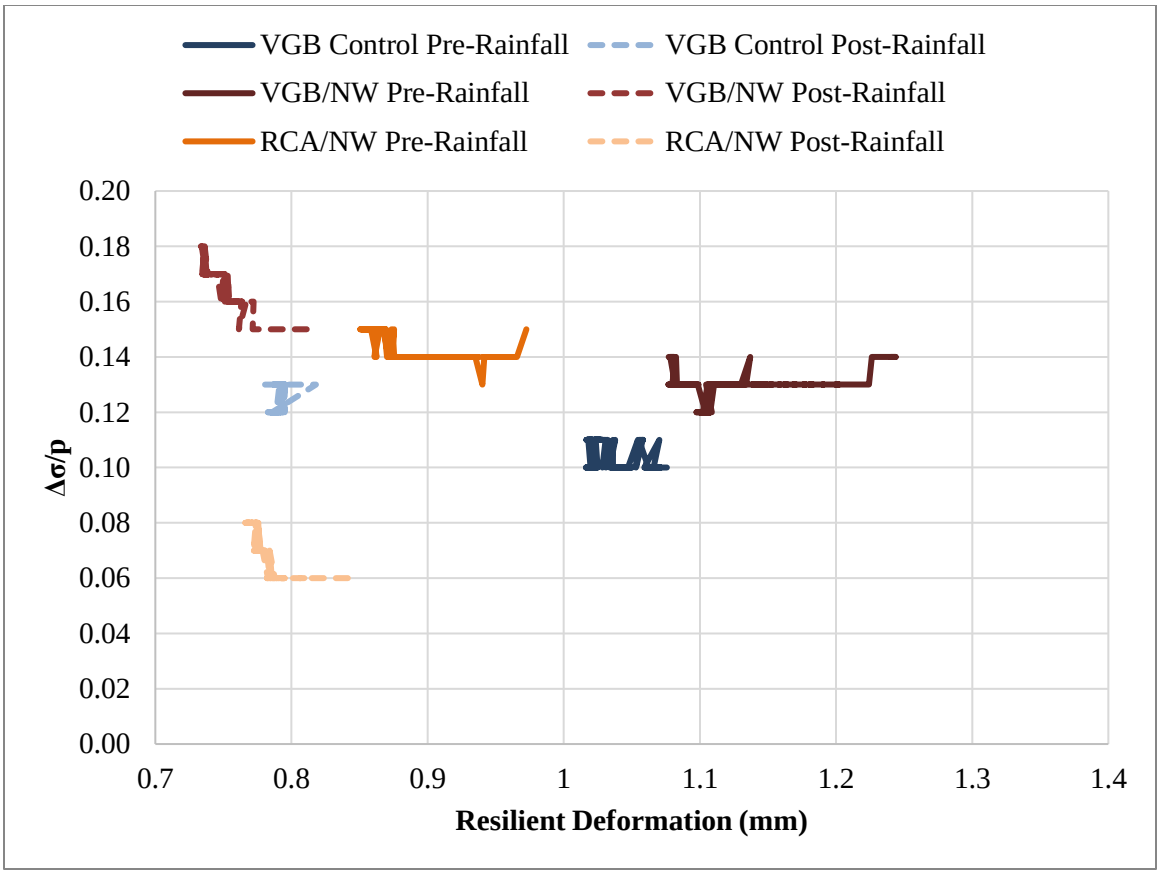

Figure 5.39. Resilient Deformation versus Stress Reduction Ratio for the Concrete Pavement Sections.

The relationship of deformation ratio (permanent to resilient deformation) at the pavement corner versus the base course-subgrade interface stress reduction ratio are plotted in Figure 5.40. The same trend of the prior two charts is observed, where the lower interface stress reduction ratio corresponds to lower ratio of permanent-to-resilient deformation.

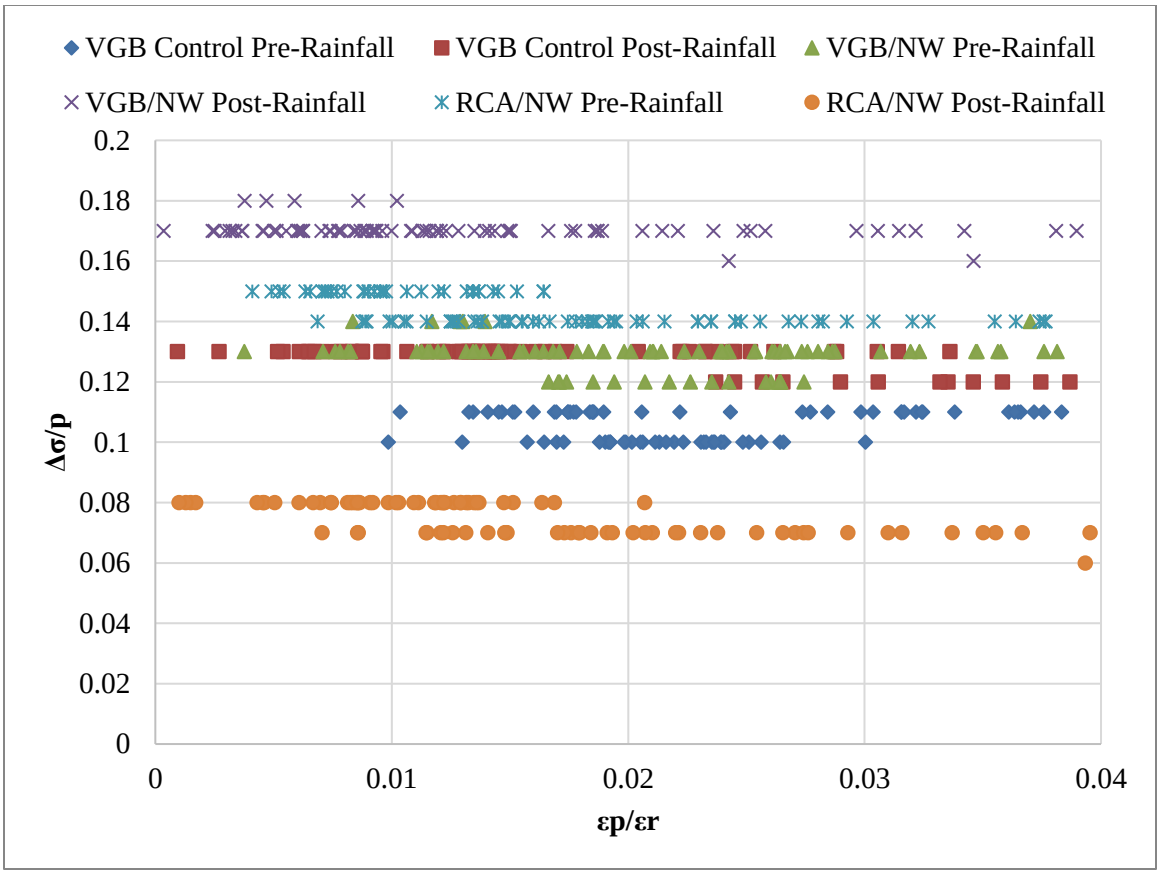

Figure 5.40. Deformation Ratio vs. Base Course-Subgrade Interface Stress Reduction Ratio for the Concrete Pavement Sections.

Chapter 6. Equivalent Resilient Modulus of Geosynthetic-Stabilized Granular Base

6.1 Theoretical Background

Burmister (1945) developed a layered elastic theory for analysis of layered pavements under wheel loads. In this theory, no geosynthetic is included in layered pavements. Sun et al. (2017) and Sun and Han (2019a, b) modified the Burmister solution by incorporating a geosynthetic layer at the interface between a base and a subgrade. The modified solution has been incorporated in a MATLAB code (Sun et al. 2017), which can be used to determine equivalent resilient modulus of the base course layer, especially when geosynthetics are involved.

Burmister (1945) developed his simplified equations based on continuity in a two-layer elastic system as Eq. (6.1).

$$w_0 = \begin{cases} \dfrac{1.5qa}{E_2} F_2 & (flexible\ plate) \\ \dfrac{1.18qa}{E_2} F_2 & (rigid\ plate) \end{cases} \tag{6.1}$$

where w_0 = surface deflection of a two-layer system, q = applied pressure, a = diameter of loading area, E_2 = elastic modulus of the underlying layer, and F_2 = settlement coefficient, a function of: 1.) the elastic modulus of the base course divided by that of the subgrade (E_b/E_s), and 2.) the height of the base course divided by the diameter of the loading area (h_b/a).

Number of load cycles can be adjusted using an equivalent axle load factor (EALF) and represented by equivalent single axle loads (ESALs) (AASHTO 1993). However, load magnitude impacts pavement damage or performance changes uniquely (NCHRP 2004). To account for deformation incurred before each load sequence, the number of cycles for prior load

stages is converted to a cyclic number corresponding to the initial permanent deformation value under an equivalent load [see Eq. (6.2), (6.3), and (6.4)] (Sun et al. 2015).

$$EALF = \left(\frac{p_j}{p_{target}}\right)^n \tag{6.2}$$

$$n = 0.2775e^{0.2152 \cdot CBR_{SG}} \tag{6.3}$$

$$N_{fs} = \sum_{i=1}^{m} \left(\frac{p_i}{p_t}\right)^n \tag{6.4}$$

where N_{fs} = number of cycles at equivalent load p_t, *m* = number of cycles, p_i = load for cycle *i*, p_t = target (equivalent) load (138 kPa for this study), and n = EALF regressed power [from Eq. (6.3).

Target load for this adjustment is the magnitude of the load for the current load sequence phase. A theoretical curve is then fit with a measured curve using calibration factors k_b and k_s for base course and subgrade, respectively, and by adjusting the base course over subgrade modulus ratio, E_1/E_2. Burmister's method, while including variation in the number of load cycles, cannot handle the change in magnitude between cycles; in accordance with the MEPDG (NCHRP 2004), k_b is adjusted as necessary for each load cycle and section construction to create the best-fit curve. Subgrade calibration factors k_s was maintained at 7.4 according to Sun et al. (2017).

Attempting to adjust *N* cycles for prior loading stages proved challenging from a curve-fitting perspective. Increase in load magnitude from stage-to-stage created an initial jump in permanent displacement. The goal of this curve-fitting was to capture the permanent deformation within the stage. Attempts at fitting the curve with the inclusion of prior loading displacement,

even adjusting using Eq. (6.5) and (6.6) created curves that do not display the steep increases in permanent deformation with the increase in load magnitude. Weakening of the section has been incurred from prior stages (Sun et al. 2015); this is better handled using the damage model from the MEPDG as displayed in Eq. (6.5) (NCHRP 2004).

$$\delta_{p,1} = k_b \cdot p \cdot f_b(E_e, E_s, z, a) \left(\frac{\varepsilon_0}{\varepsilon_r}\right)_b e^{-\left(\rho_b/N\right)^{\beta_b}} \tag{6.5}$$

where $\delta_{p,1}$ = permanent deformation at surface of base course, k_b = calibration factor for base course, $\delta_{r,1}$ = resilient deformation at surface of base course, N = number of cycles, f_b = Burmister's settlement coefficient function based on: 1.) elastic modulus of the base course, E_1 or E_e, 2.) elastic modulus of the subgrade, E_2 or E_s, 3.) height of the base course, z, and 4.) surface load radius, a. $(\varepsilon_0/\varepsilon_r)_b$, ρ_b, and β_b are base course material properties defined in Eq. (2.24) (Chapter 2).

The damage model included in NCHRP (2004) and described in Eq. (6.5) includes the terms from Burmister (1945); the functions of continuity for the factor 'F' are famously found in Burmister's simplified graph but were calculated using MATLAB along with the modified damage equation. [The damage model was originally developed by Tseng and Lytton (1989) and further modified by Sun et al. (2017) as Eq. (6.5).] The current MEPDG damage model (NCHRP 2004) only predicts the first and second stages of permanent deformation (see Figure 2.13 in Chapter 2). The settlement coefficient developed by Burmister (1945, 1958) is dependent upon applied load, so each load sequence should be considered individually when the elastic solution and damage model are applied; changes to the elastic properties (E_1/E_2) due to incurred damage in prior sequences are observed and reported. Sun (2015) recognized the effect of

possible yielding of subgrade on its permanent deformation under loading and developed the load-dependent k_s value as displayed in Eq. (6.6). This equation captures the subgrade yielding in terms of its CBR that occurs with load repetition as well.

$$k_s = \begin{cases} a \cdot e^{-b \cdot CBR_{SG}} \dfrac{p}{N_c c_u} \ (finegrained) \\ a \cdot e^{-b \cdot CBR_{SG}} \ (granular) \end{cases} \tag{6.6}$$

where k_s = subgrade calibration factor for MEPDG damage model, CBR_{SG} = California Bearing Ratio of the subgrade, p= applied pressure, N_c=3.14, c_u= 30*CBR_{SG} (kPa), and *a* and *b* are regression constants.

Resilient modulus of the subgrade (E_2 or M_r) in this study and also included in MATLAB was calculated using the correlation for fine-grained subgrade as shown in Eq. (6.7) (AASHTO 1993). AASHTO (1993) correlates the granular base course CBR to its resilient modulus (M_r) using Eq. (6.8).

$$M_r(psi) = 1500 \times CBR \rightarrow M_r(MPa) = 10.3 \times CBR \tag{6.7}$$

$$M_r(psi) = 2555 \times CBR^{0.64} \rightarrow M_r(MPa) = 17.6 \times CBR^{0.64} \tag{6.8}$$

Qian (2011) applied an elastic solution for a loaded plate on an elastic medium to estimate resilient modulus of subgrade as described in Eq. (6.9). This elastic solution does not account for large resilient deformation that may occur in certain pavement sections with geosynthetics that are effective at reducing permanent deformation. This calculation most closely replicates the definition of resilient modulus in the AASHTO 307 resilient modulus test standard, which defines M_r as the ratio of the axial deviator stress to the resilient strain.

$$M_r = \frac{p_i BI(1-\nu^2)}{\delta} \tag{6.9}$$

where p_i is applied vertical stress, B is the loading plate diameter, ν is Poisson's ratio (0.45 in this study), δ is resilient displacement at the surface, and I is the displacement influence factor (0.79 for a rigid plate, as used in this study; 1.0 for a flexible plate).

In this study, a damage model for each load sequence was fit to the permanent deformation curve for the number of load cycles within the sequence so that k_b, k_s, and E_1/E_2 were estimated. These parameters at different load magnitudes were investigated. Once the model was calibrated and the model was matched to the actual vertical deformation curve by load cycle, the modulus ratio E_1/E_2 was multiplied by the subgrade resilient modulus assumed based on the subgrade CBR and the relationship in Eq. (6.7). The estimated resilient moduli using this damage model method are also compared against the elastic solution as described in Eq. (6.9) (Qian et al. 2011). This following section describes the data analysis and the result comparison.

6.2 Unpaved Road Sections

6.2.1 Subgrade Only

A large-scale box test was performed with subgrade only. The subgrade had a CBR value of 2.8% estimated using the DCP method and a moisture content of 9.2%. The thickness of the base course and the k_b value were set to 0 for the MATLAB analysis. As a result, the displacement of the base course matched the displacement of the subgrade, as no base course existed. Through trial and error, the k_s value leading to a best fit for the given load magnitudes was determined to

be 1.50 for the subgrade material used in this test; this value yielded deformation prediction near measured values while being conservative in minimizing underprediction of deformation. The measured and predicted permanent deformations can be observed in Figure 6.1. It should be noted in Figure 6.1 that the best-fit curve under-predicted the permanent deformation in early loading stages while it over-predicted the permanent deformation in later stages.

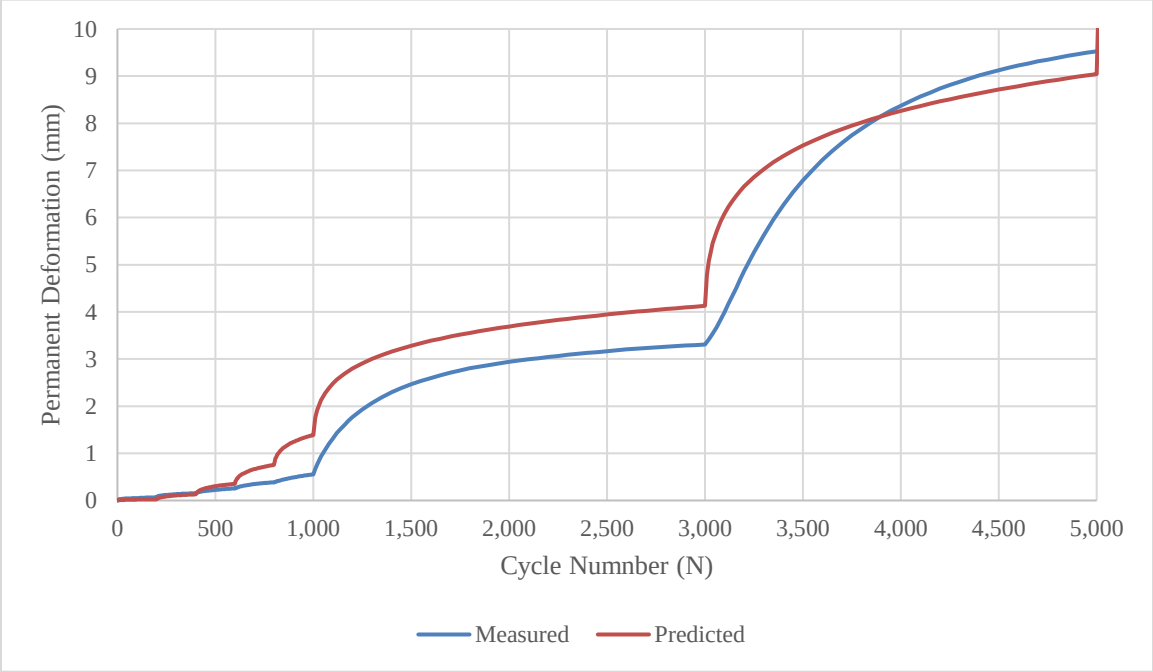

Figure 6.1. Predicted vs. Measured Permanent Deformations for Applied Load Stages Using a Single k_s Value of 1.50.

Figure 6.2 displays the displacement comparison for a less conservative k_s value of 1.10; the displacements were more accurately predicted in the earlier stages, but at the final load sequence permanent deformation was greatly under-predicted. This comparison creates a stronger case for a load-magnitude-dependent fit for each set of load cycles in order to accurately capture the behavior of the measured values.

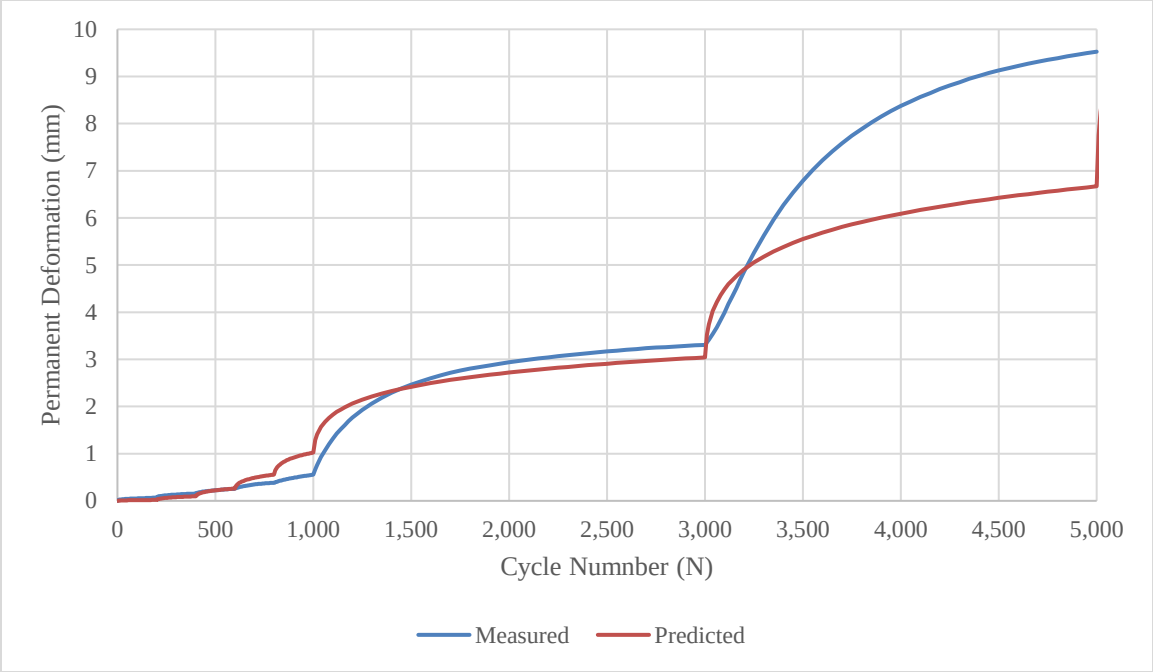

Figure 6.2. Measured versus Predicted Subgrade Permanent Deformation Using a Single k_s Value of 1.10.

Prediction of permanent deformation using the same k_s value from the above was attempted with adjusted values for N, assuming an equivalent wheel load of 20 kN (275 kPa). The load cycle numbers (N) for lower load magnitudes were adjusted using Eq. (6.2) and Eq. (6.3) (Sun et al. 2015). Applying the same k_s value (1.50) resulted in a vast over-prediction of permanent deformation, as exhibited in Figure 6.3. Therefore, the permanent deformation of the subgrade under varying loads was poorly characterized using this correlation.

The load cycle numbers were then adjusted using Eq. (6.2) with *n* of 4, as recommended for flexible pavements by AASHTO (1993). The equivalent load was kept at 40 kN and k_s remained 1.50. A much closer comparison was observed near the end of the load cycles, as exhibited in Figure 6.4. While the overall predicted and measured permanent deformation trends were similar, the steep deformation change at the increase in load magnitudes was not captured

by the prediction. It is thus valuable to further investigate the theoretical model for each cyclic load stage.

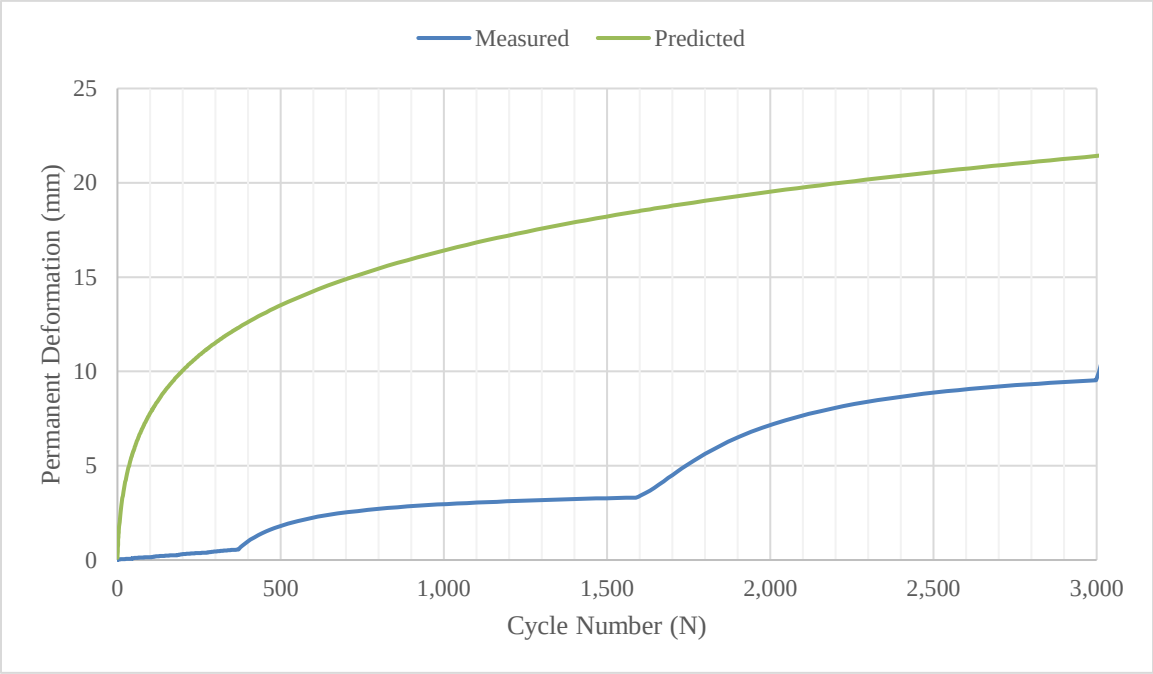

Figure 6.3. Measured versus Predicted Permanent Deformations of Subgrade using the Adjusted Load Cycles according to Sun et al. (2015).

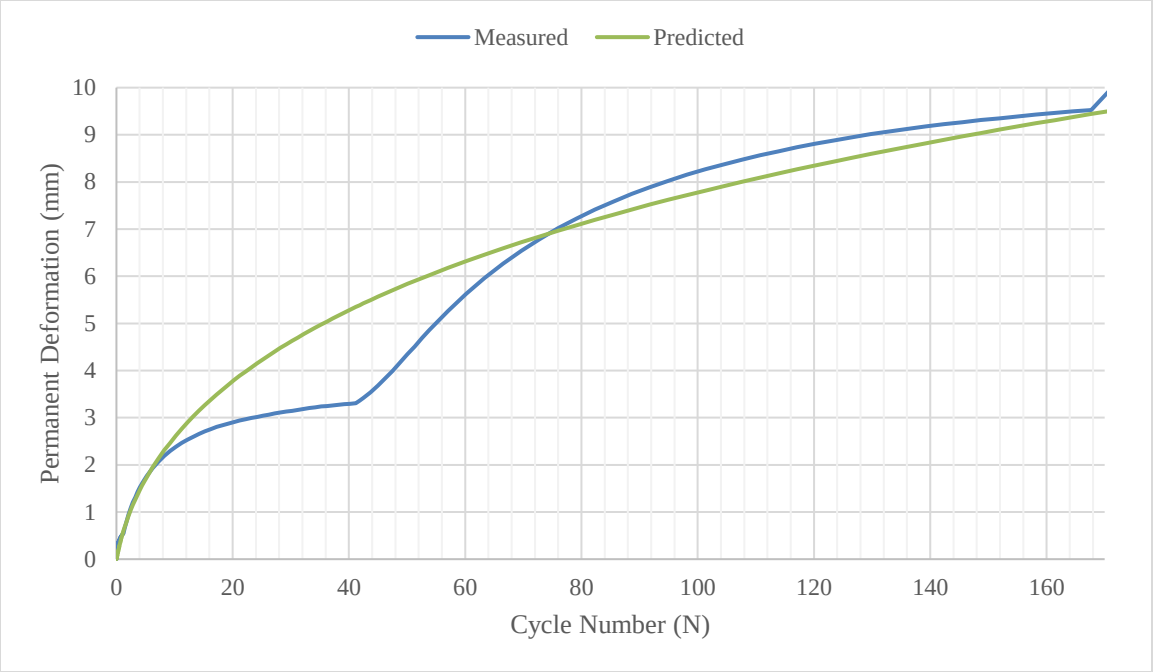

Figure 6.4. Measured versus Predicted Permanent Deformations of Subgrade using the Adjusted Load Cycles according to AASHTO (1993).

Each loading stage can be considered individually in MATLAB, and k_s can be varied to create a best-fit curve for each loading stage. Best-fit values of k_s for the given subgrade using a resilient modulus of 29 MPa are provided in Table 6.1. It is important to note that the resilient moduli obtained by Eq. (6.7) and Eq. (6.9) do not agree, as displayed in Table 6.1; the resilient modulus obtained based on the measured resilient deformation was almost twice that estimated based on the CBR value. The CBR-M_r correlation (29 MPa) was used for calibration in this deformation analysis per Sun et al. (2017).

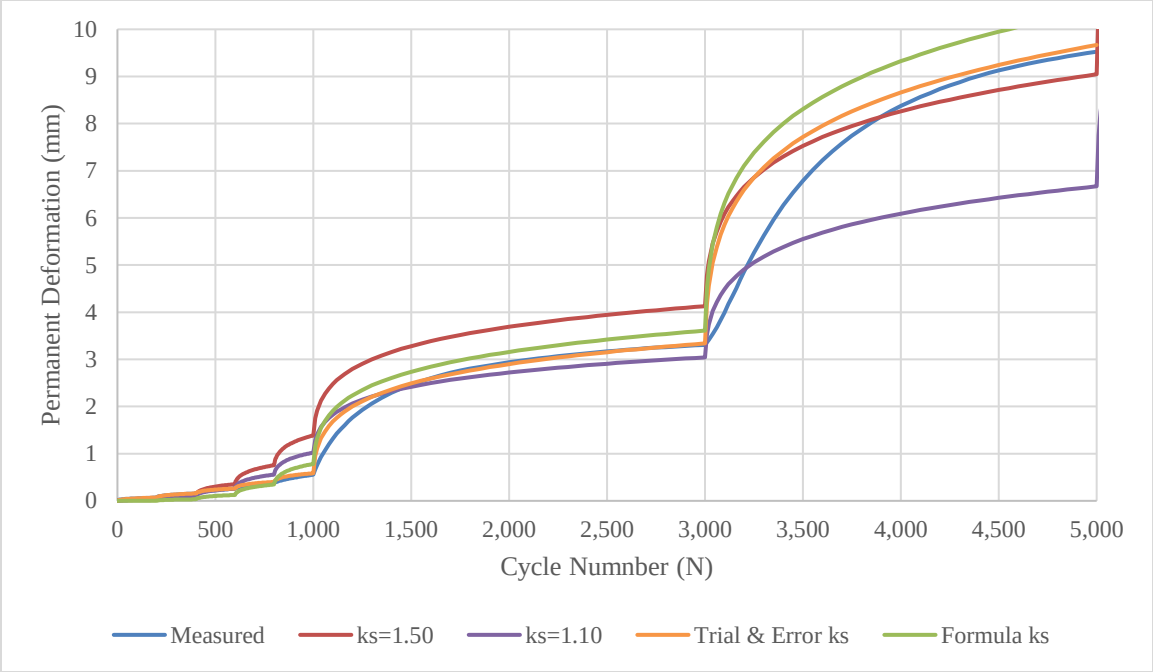

(a) Full Sequence

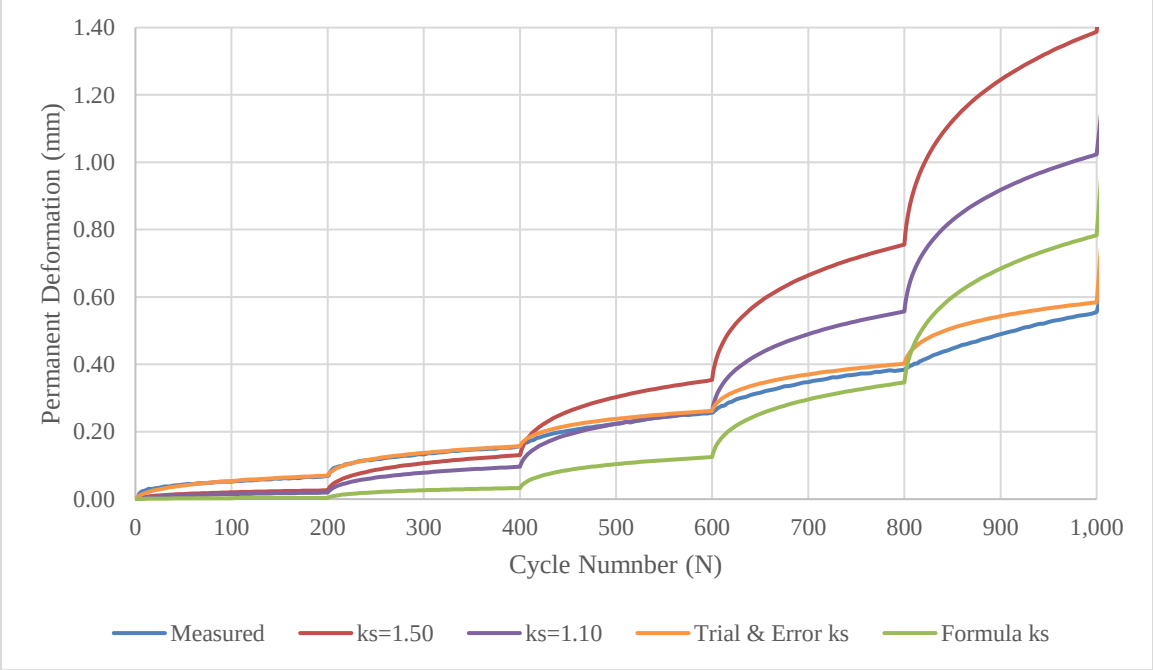

(b) Early Stage

Figure 6.5. Measured vs. Predicted Permanent Deformations using Different k_s Values.

Table 6.1. Resilient Modulus M_r and k_s Values for Subgrade.

Load Stage	Applied Pressure (kPa)	Resilient Modulus: Eq. (6.9) (MPa)	Resilient Modulus: Mr = 10.3*CBR (MPa)	MATLAB Trial & Error k_s	Formula [Eq. (6.6)] k_s
1	14	61.7	29	4.00	0.209
2	28	56.6	29	1.25	0.418
3	41	53.4	29	0.700	0.613
4	55	51.5	29	0.520	0.822
5	69	50.2	29	0.430	1.031
6	103	52.9	29	1.50	1.539
7	138	54.8	29	1.92	2.062
Combined/ Avg.	*Varies*	*54.4*	*29*	*1.47*	*0.956*

Based on Tseng and Lytton (1989), deformation of subgrade layers is sensitive to applied load even though this load effect is not considered in the MEPDG (NCHRP 2004). The subgrade calibration factor k_s in Eq. (6.6) is plotted against that obtained through trial and error in the MATLAB code. Since *a* and *b* in Eq. (6.6) were unknown, the MATLAB code was used to create best-fit curves based on the measured results. Figure 6.6 shows a reasonable correlation of the calculated k_s values using *a* of 10.5 and *b* of 0.35 as compared with those determined using MATLAB. A good correlation is discovered at later loading stages, as displayed in the deformation comparisons in Figure 6.5; this may be attributed to large initial settlements at the surface that increased the reaction coefficient during the initial stage of loading, where volume change still occurred despite adequate compaction. It is thus recommended to use Eq. (6.6) to determine k_s for each loading stage with applied pressure equal to that measured by the earth pressure cell located directly beneath the plate (at 0 mm) at the top of the subgrade in a base course over subgrade section. The subgrade calibration factor for each load stage can be observed in Table 6.1.

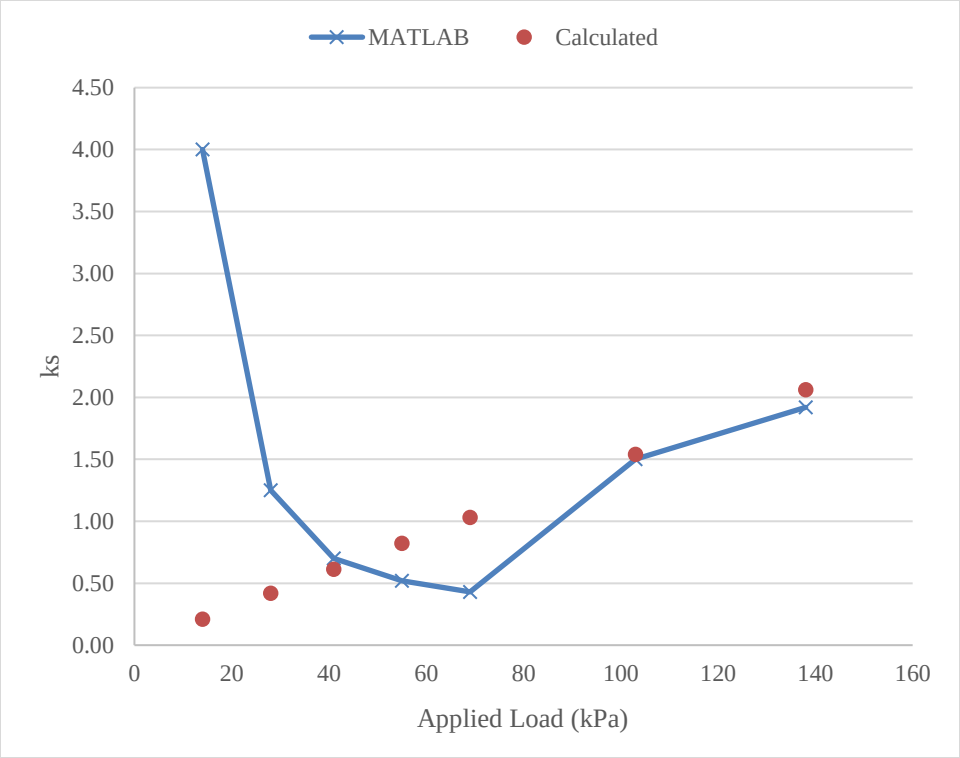

Figure 6.6. Subgrade Calibration Factors from MATLAB vs. Calculated by Formula for Different Applied Pressures.

6.2.2 Control Sections with VGB and RCA

Tseng and Lytton (1989) noted in their original damage model that the reaction of the upper base course layer is less stress-sensitive than the weaker, plastic underlying subgrade layers. The resilient modulus of an infinitely deep (relative to the applied load width) underlying subgrade layer will remain relatively constant because it is a fine-grained soil not overly sensitive to confining stress. However, degradation will occur in the upper base course layer under the load applied at the surface, resulting in reduction in its resilient modulus. One of the goals in this study was thus to find a single calibration factor k_b applicable for each base material (VGB, RCA) that is unique to the base course and will allow for data analysis by altering the ratio of E_1/E_2 in the continuity equations in the MATLAB code (Sun et al. 2017). Eq. (6.7) and (6.8)

were used to estimate an initial modulus ratio for the VGB and RCA; however, both the modulus ratio and k_b were iteratively changed to create best fit deformation curves against the measured values until a single k_b was achieved.

In this study, subgrade was handled as follows. Values of k_s were reduced based on the reading of the earth pressure cell located on the center at the interface of the subgrade and the base course using Eq. (6.6). Resilient modulus of the subgrade was determined using Eq. (6.6). Moisture contents of the subgrade (and base course) were measured during construction.

The calibration factor of the VGB was determined to be 1.40. Figure 6.7 displays the measured permanent deformation at the surface of the base course against the predicted deformation from MATLAB. Each load sequence was modeled individually and resultant modulus ratios (E_1/E_2) were determined. A single value for k_b for all load sequences was identified through trial-and-error such that a best-fit curve could be obtained for all sequences.

Table 6.2 details the resultant MATLAB variables determined to create the best-fit curves in Figure 6.7.

Table 6.2 shows that the modulus ratio first increased with the load due to the densification of the base and then decreased due to its degradation.

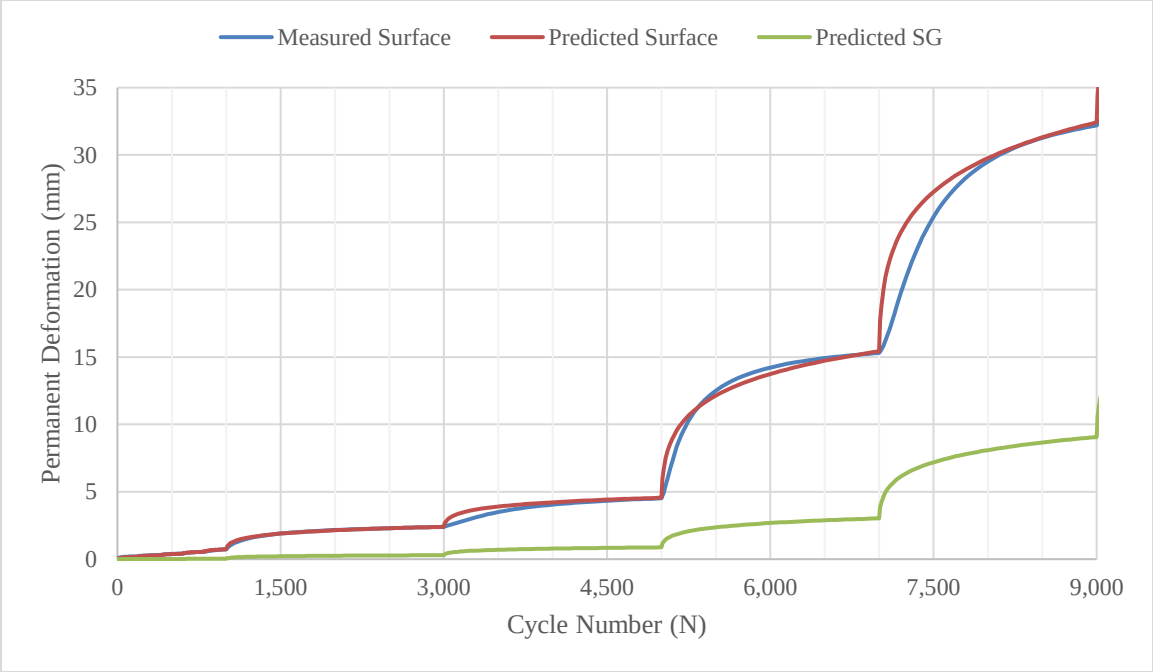

Figure 6.7. Measured vs. Predicted Permanent Deformations of the VGB Base over 2% CBR Subgrade.

Table 6.2. MATLAB Input Variables for the Control Section with VGB.

Load Sequence	Applied Pressure (kPa)	k_s	k_b	E_1/E_2
1	14	0.211	1.40	4.50
2	28	0.362	1.40	7.50
3	41	0.573	1.40	7.80
4	55	0.784	1.40	10.50
5	69	0.965	1.40	9.50
6	103	1.358	1.40	4.00
7	138	1.750	1.40	4.50
8	207	2.866	1.40	1.75
9	276	4.526	1.40	2.25
10	345			
11	414			

RCA was treated in the same manner as the VGB above. Through trial and error, k_b for the RCA was determined to be 1.25. A good correlation was obtained by holding this value constant and varying the modulus ratio, as shown in Figure 6.8. Table 6.3 shows the input parameters as well as the best fit modulus ratios. Permanent deformation of the RCA section was lower than that of the VGB section; the reduced k_b prevents an overestimation of resilient modulus [using Eq. (6.8) as a reference].

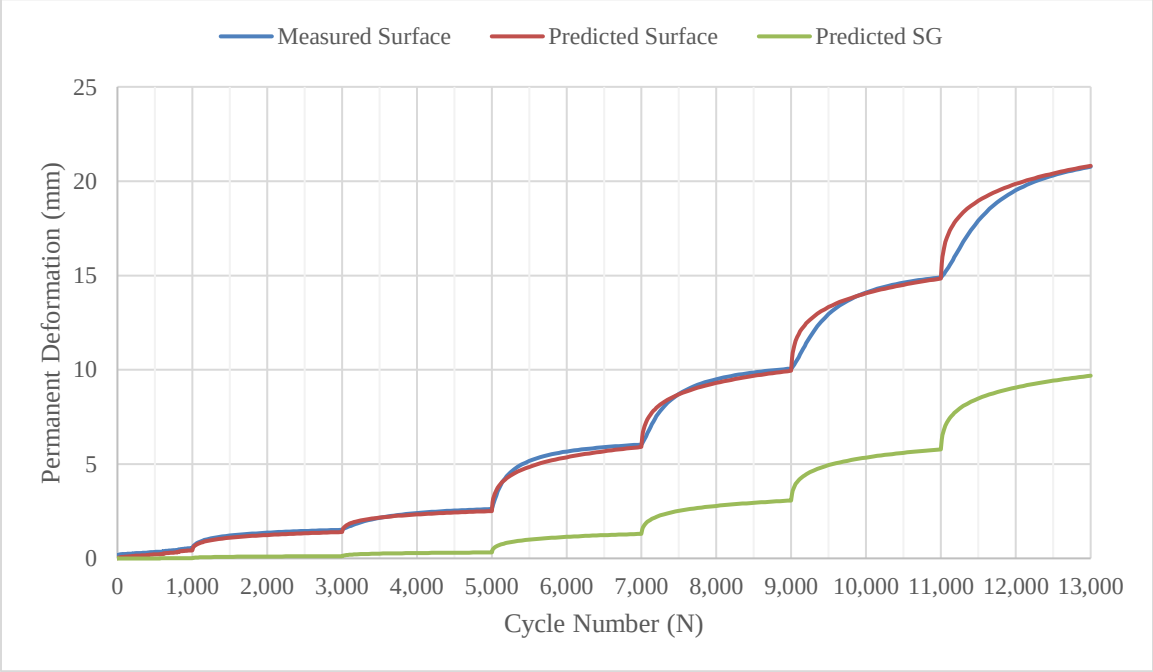

Figure 6.8. Cycle Count vs. Permanent Deformation for RCA/ 2%-CBR Subgrade.

Table 6.3. MATLAB Input Variables for the Control Section with RCA.

Sequence no.	Applied Load (kPa)	k_s	k_b	E_1/E_2
1	14	0.102	1.25	2.35
2	28	0.158	1.25	9.75
3	41	0.237	1.25	11.30
4	55	0.323	1.25	10.80
5	69	0.415	1.25	11.00
6	103	0.601	1.25	4.22
7	138	0.774	1.25	5.25
8	207	1.122	1.25	3.12
9	276	1.458	1.25	4.30
10	345	1.761	1.25	5.50
11	414	2.125	1.25	6.80

Once the calibration factors for the base course (k_b) and the fitting factors for the calibration factor of the subgrade (k_s) were determined, the modulus ratios of the geosynthetic-stabilized sections were estimated. The k_b was kept constant for either VGB (1.40) or RCA (1.25), and the k_s relationship based on interface pressure at the top of the subgrade was used as displayed in Eq (6.10), calibrated from Eq. (6.6). The predicted permanent deformation was matched to the measured surface deformation by iteratively adjusting the modulus ratio E_1/E_2. It was thus assumed that the addition of geosynthetics altered the modulus E_1 of the base course section, and thus the changes in the section based on the permanent deformation are reflected in this altered modulus ratio from the control section for the given base course (VGB or RCA).

$$k_s = 10.5 \cdot e^{-0.35 \cdot CBR_{SG}} \frac{p}{3.14 * (30\ kPa) CBR_{SG}} \quad (6.10)$$

where k_s = calibration coefficient of the subgrade, CBR_{SG} = California Bearing Ratio of the subgrade as determined by DCP, and p = measured interface pressure at 0 mm offset beneath the load plate.

6.2.3 Stabilized VGB Sections

Figure 6.9 through Figure 6.12 display the measured versus predicted permanent deformations for the VGB sections stabilized by geosynthetics, and Figure 6.13 shows the comparison of the resilient moduli of the VGB that produced these results. For reference, the calibration factors and resultant modulus ratios are given in

Table 6.2 and Table 6.4 through Table 6.7. Good comparison is achieved for all sections. In the first five load stages the displacement curves do not level off in the low number of load cycles (200 instead of 2,000) and thus much higher resilient moduli, as compared with later load stages, were required to best fit the curves. The predicted results provided resilient modulus trends more consistent with the accumulated permanent deformation and interface stress reduction, where the more stable sections (geogrid and geotextile-stabilized sections) yielded higher resilient moduli than the control section. Resilient modulus values for the VGB ranged from approximately 40 MPa (control section) to approximately 80 MPa (GG and NW-stabilized sections). For this analysis, the VGB/GG and VGB/NW sections had very comparable resilient moduli. Geosynthetics provided 1.5 times to over twice the resilient moduli in the VGB when compared with the control section using the modified Burmister method.

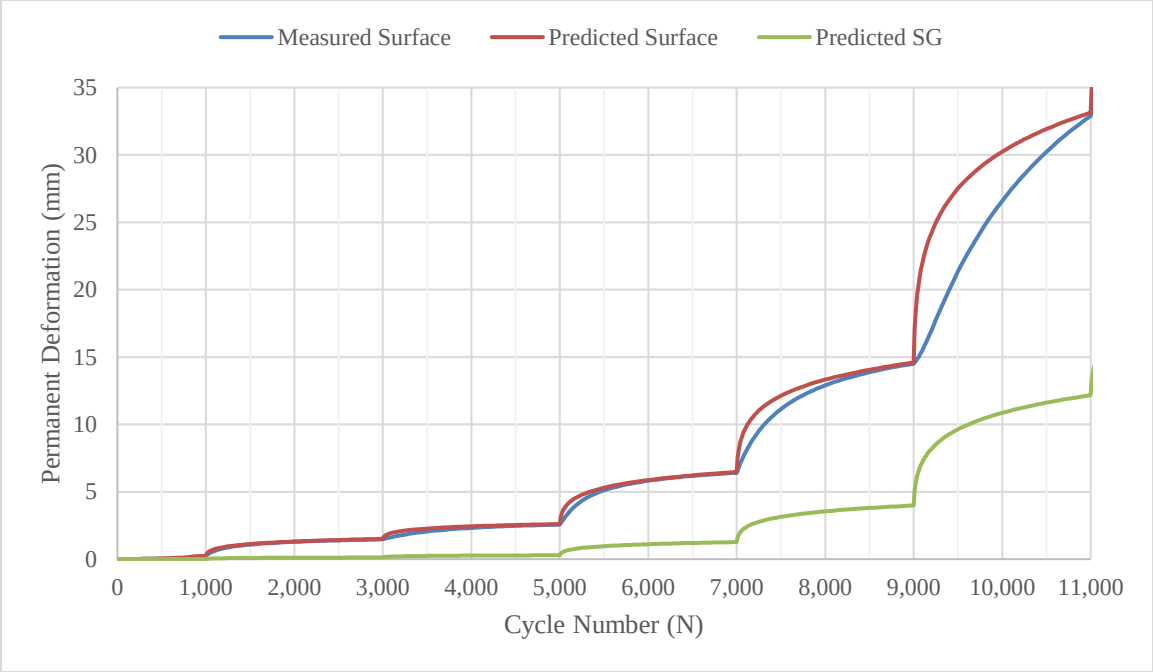

Figure 6.9. Measured versus Permanent Deformations of the VGB/W Section over 2% CBR Subgrade.

Table 6.4. MATLAB Input Variables for the VGB/ W Section over 2% CBR Subgrade.

Load Sequence	Applied Pressure (kPa)	k_s	k_b	E_1/E_2
1	14	0.082	1.40	29.00
2	28	0.157	1.40	31.50
3	41	0.246	1.40	29.00
4	55	0.352	1.40	19.00
5	69	0.455	1.40	13.50
6	103	0.683	1.40	4.10
7	138	0.823	1.40	6.50
8	207	1.234	1.40	3.35
9	276	1.539	1.40	2.45
10	345	2.313	1.40	1.65

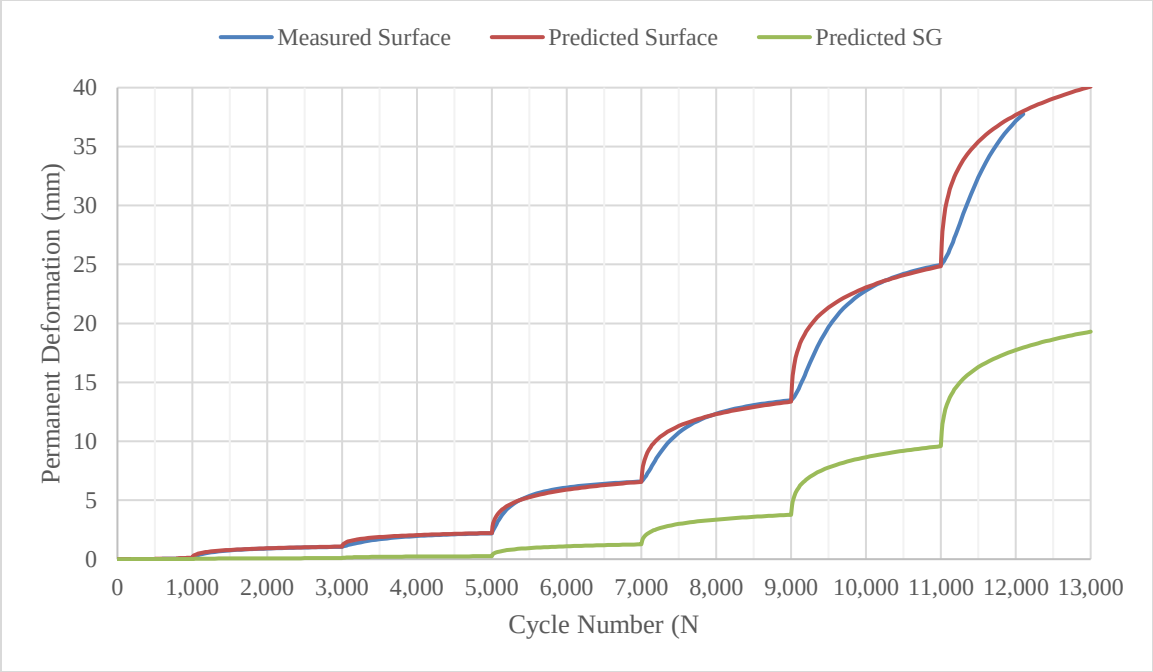

Figure 6.10. Measured versus Permanent Deformations of the VGB/NW Section over 2% CBR Subgrade.

Table 6.5. MATLAB Input Variables for the VGB/ NW Section over 2% CBR Subgrade.

Load Sequence	Applied Pressure (kPa)	k_s	k_b	E_1/E_2
1	14	0.084	1.40	60.00
2	28	0.167	1.40	60.00
3	41	0.265	1.40	57.00
4	55	0.345	1.40	51.00
5	69	0.441	1.40	22.00
6	103	0.601	1.40	5.25
7	138	0.779	1.40	6.10
8	207	1.166	1.40	2.90
9	276	1.680	1.40	3.00
10	345	2.402	1.40	2.85
11	414	3.207	1.40	3.45

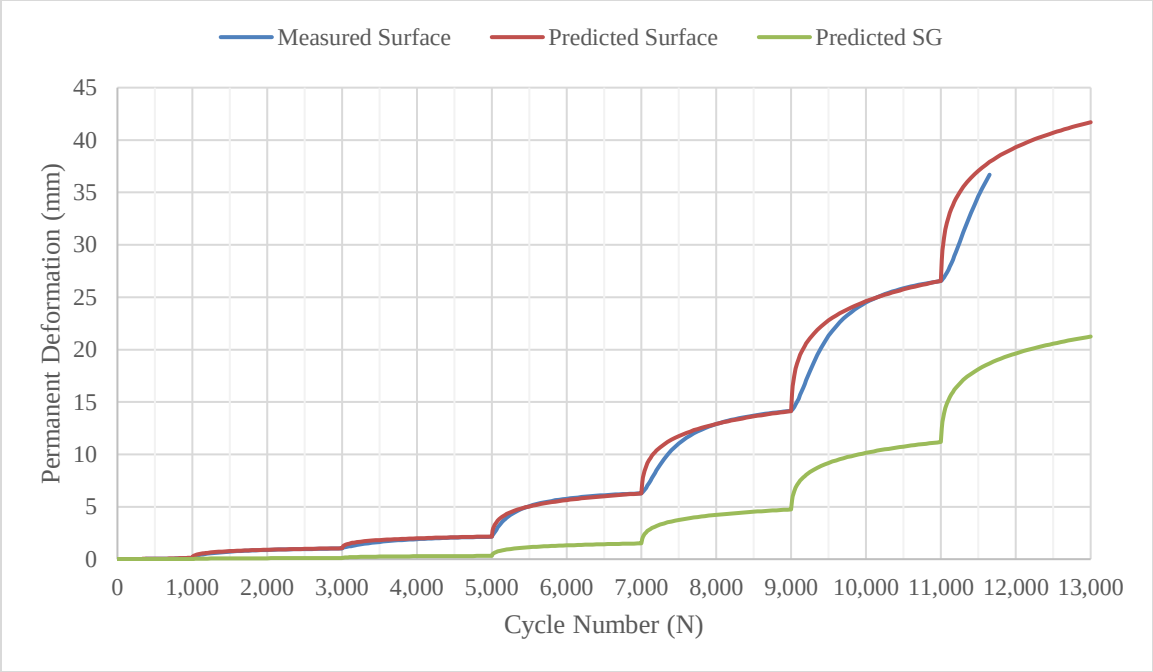

Figure 6.11. Measured versus Permanent Deformations of the VGB/GG Section over 2% CBR Subgrade.

Table 6.6. MATLAB Input Variables for the VGB/ GG Section over 2% CBR Subgrade.

Load Sequence	Applied Pressure (kPa)	k_s	k_b	E_1/E_2
1	14	0.099	1.40	26.50
2	28	0.196	1.40	33.00
3	41	0.300	1.40	60.00
4	55	0.417	1.40	63.00
5	69	0.524	1.40	25.00
6	103	0.771	1.40	6.00
7	138	1.023	1.40	7.00
8	207	1.489	1.40	3.52
9	276	2.008	1.40	3.00
10	345	2.489	1.40	2.90
11	414	3.057	1.40	4.00

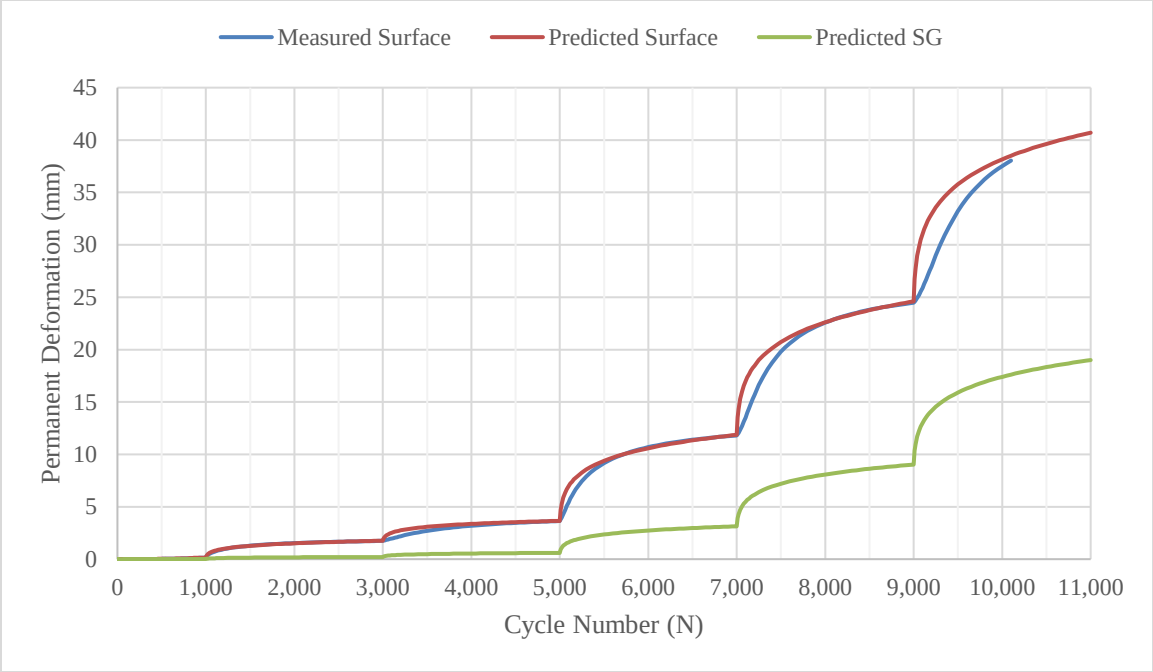

Figure 6.12. Measured versus Permanent Deformations of the VGB/GG/NW Section over 2% CBR Subgrade.

Table 6.7. MATLAB Input Variables for the VGB/ GG/NW Section over 2% CBR Subgrade.

Load Sequence	Applied Pressure (kPa)	k_s	k_b	E_1/E_2
1	14	0.139	1.40	63.00
2	28	0.256	1.40	56.00
3	41	0.395	1.40	52.00
4	55	0.546	1.40	37.50
5	69	0.691	1.40	24.00
6	103	0.974	1.40	3.94
7	138	1.255	1.40	4.85
8	207	1.916	1.40	2.08
9	276	2.655	1.40	2.28
10	345	3.572	1.40	3.10

Figure 6.13, Figure 6.14, and Figure 6.15 display the summary of the resilient moduli for the VGB sections calculated using the modified Burmister solution with continuity equations, the

elastic solution based on surface resilient deformation (Qian et. al. 2011), and the stress reduction method, respectively. While the resilient moduli based on the surface resilient deformation display a more regular relationship with the applied pressure (Figure 6.14), the resilient modulus values calculated based on the modified Burmister solution (Sun et al., 2017) are more reflective of the interface stress and permanent deformation patterns.

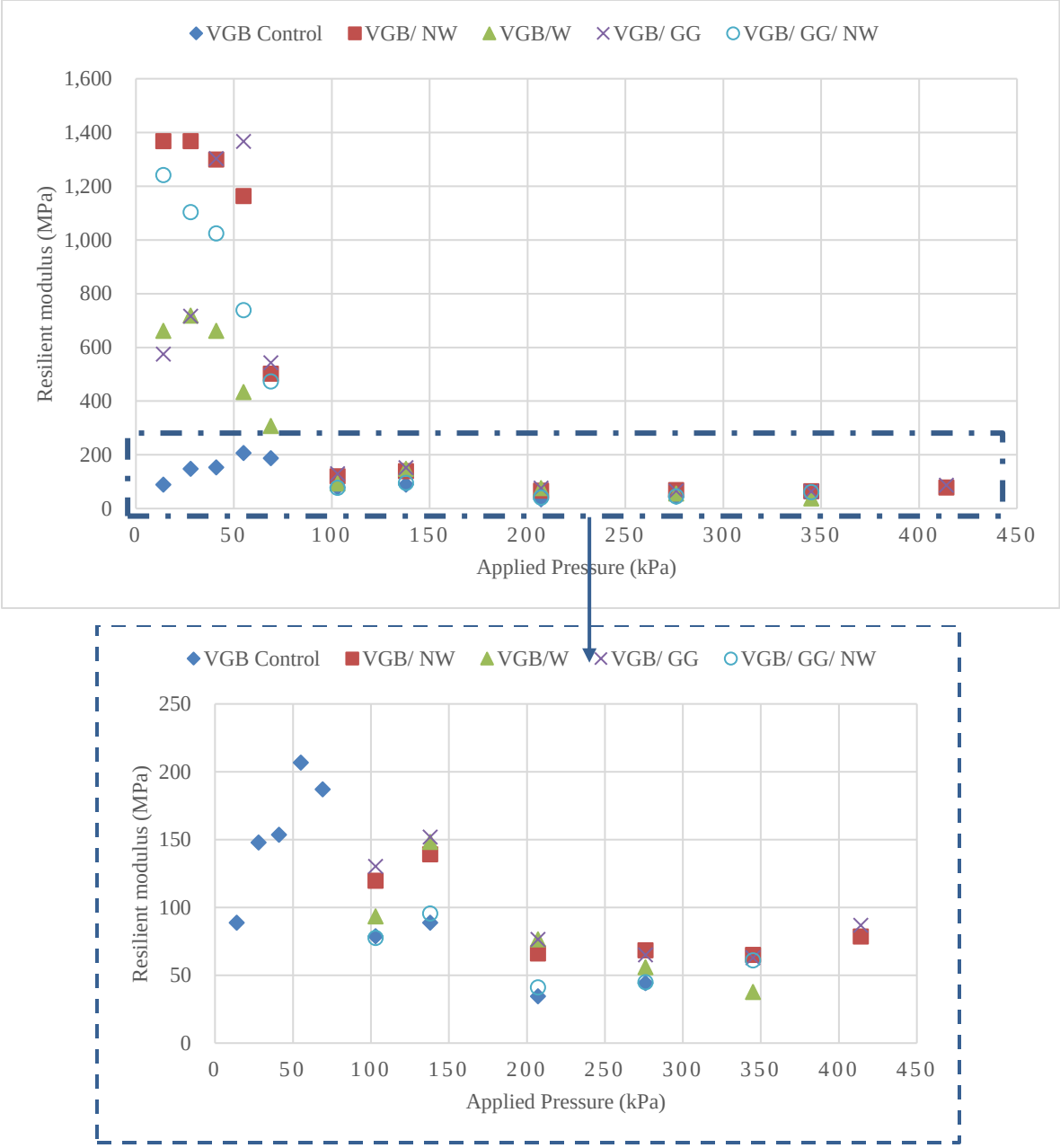

Figure 6.13. Resilient Moduli Calculated Based on the Modified Burmister Solution for the VGB Sections.

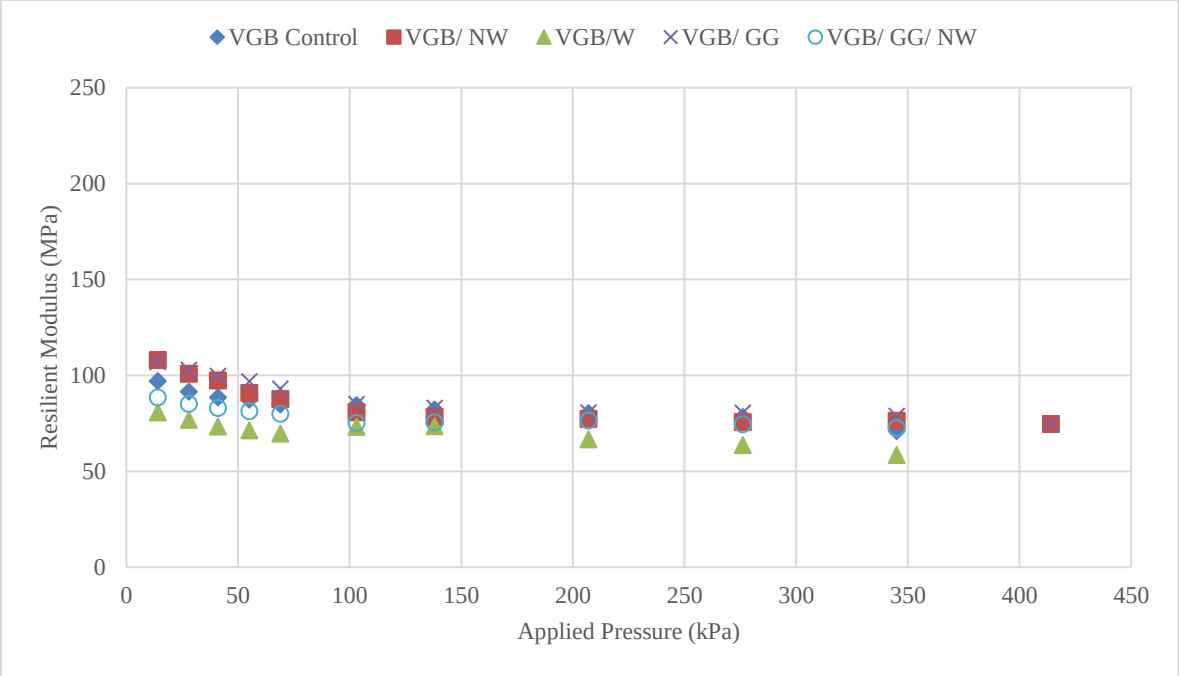

Figure 6.14. Resilient Moduli Calculated Based on the Surface Resilient Deformation for the VGB Sections.

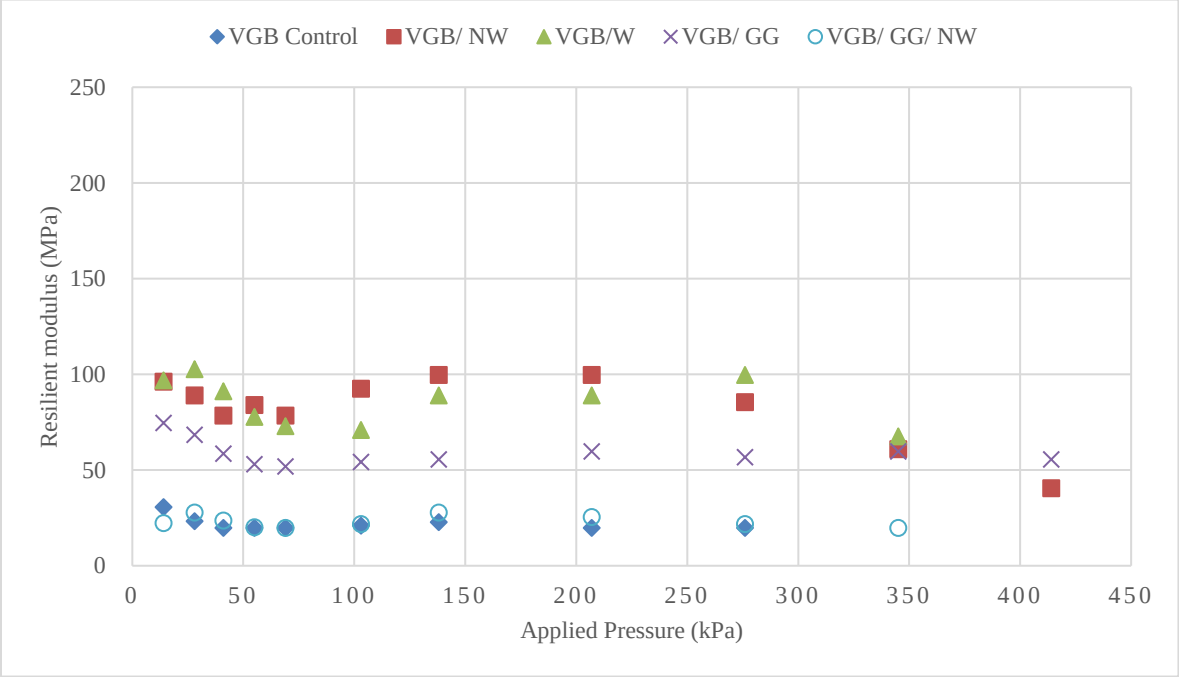

Figure 6.15. Resilient Moduli Calculated Based on the Interface Stress Reduction Method for the VGB Sections.

6.2.4 Stabilized RCA Sections

Figure 6.16 through Figure 6.19 depict the permanent deformation results calculated by the modified Burmister solution (Sun et al., 2017) best fit to those measured in the test sections at different load stages. Table 6.8 through Table 6.11 display the MATLAB input parameters for the best-fit curves. These tables show that the modulus ratios for each test section decreased with the applied surface pressure.

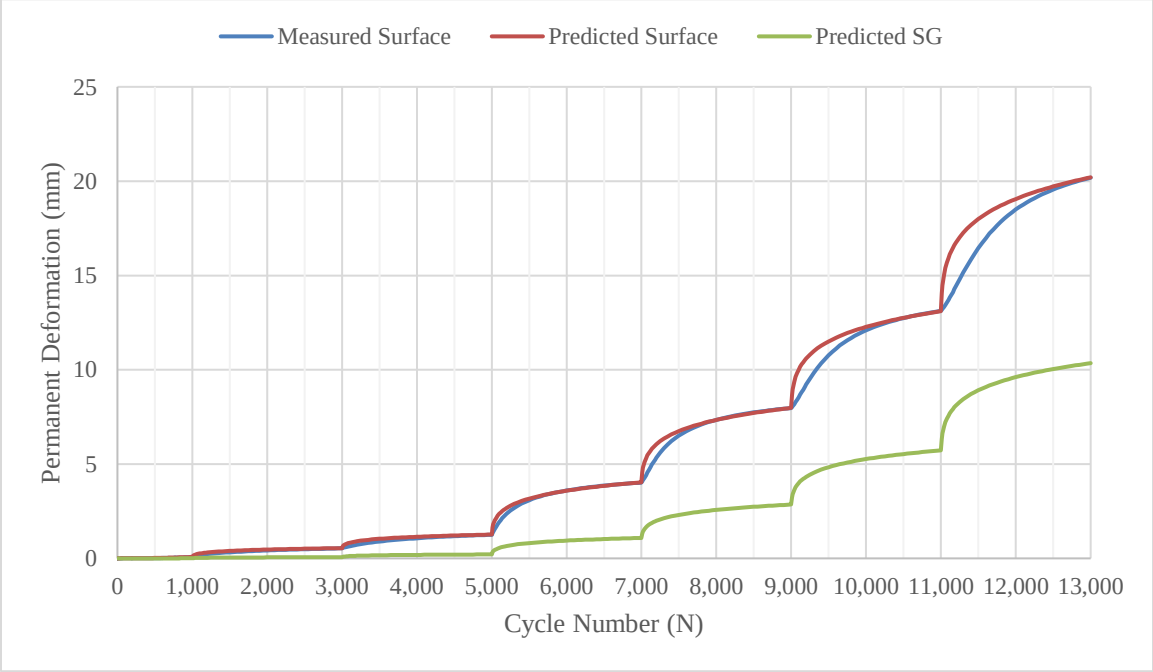

Figure 6.16. Measured versus Permanent Deformations of the RCA/W Section over 2% CBR Subgrade.

Table 6.8. MATLAB Input Variables for the RCA/ W Section over 2% CBR Subgrade.

Sequence no.	Applied Pressure (kPa)	k_s	k_b	E_1/E_2
1	14	0.084	1.25	48.00
2	28	0.144	1.25	66.00
3	41	0.216	1.25	48.00
4	55	0.302	1.25	43.20
5	69	0.382	1.25	35.30
6	103	0.565	1.25	7.95
7	138	0.756	1.25	7.71
8	207	1.063	1.25	3.71
9	276	1.356	1.25	4.27
10	345	1.627	1.25	5.08
11	414	1.948	1.25	5.50

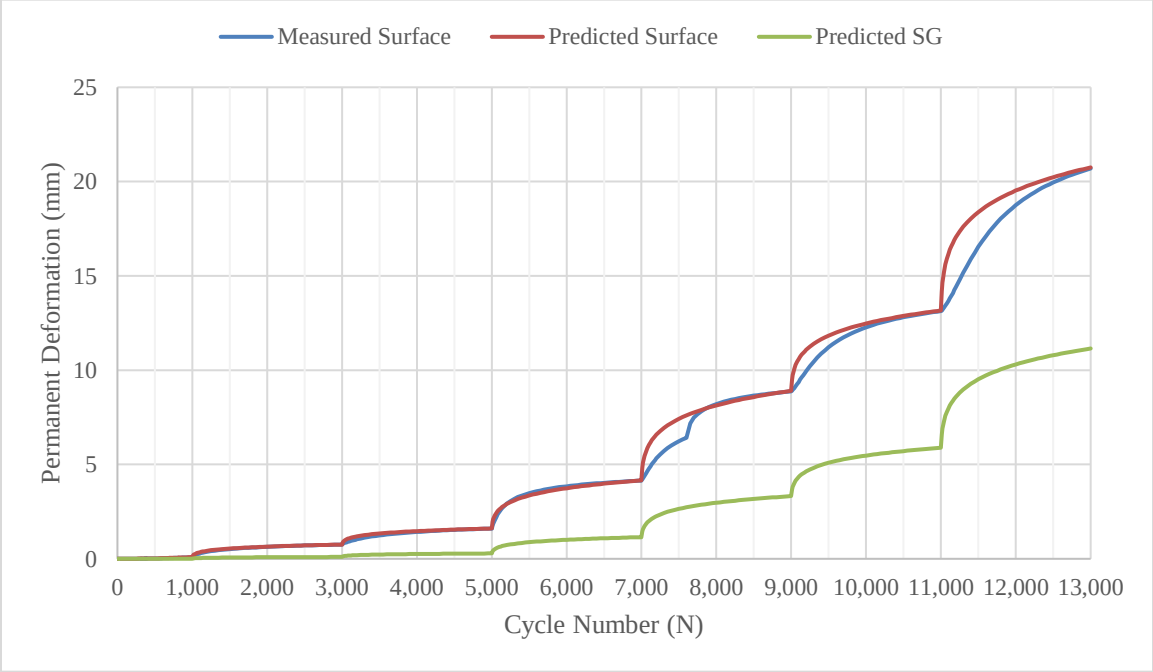

Figure 6.17. Measured versus Permanent Deformations of the RCA/GG Section over 2% CBR Subgrade.

Table 6.9. MATLAB Input Variables for the RCA/ GG Section over 2% CBR Subgrade.

Sequence no.	Applied Pressure (kPa)	k_s	k_b	E_1/E_2
1	14	0.102	1.25	40.00
2	28	0.180	1.25	38.00
3	41	0.277	1.25	38.00
4	55	0.360	1.25	36.10
5	69	0.465	1.25	32.40
6	103	0.639	1.25	5.46
7	138	0.803	1.25	6.32
8	207	1.096	1.25	3.89
9	276	1.411	1.25	3.44
10	345	1.735	1.25	6.19
11	414	2.231	1.25	5.50

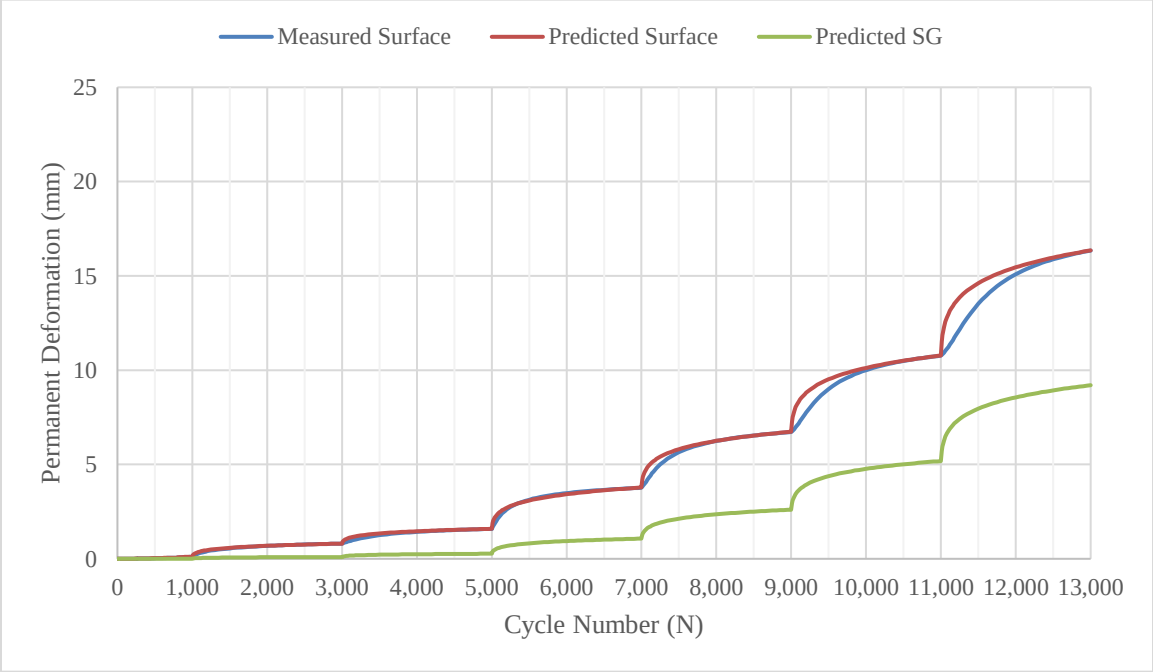

Figure 6.18. Measured versus Permanent Deformations of the RCA/NW Section over 2% CBR Subgrade.

Table 6.10. MATLAB Input Variables for the RCA/NW Section over 2% CBR Subgrade.

Sequence no.	Applied Pressure (kPa)	k_s	k_b	E_1/E_2
1	14	0.091	1.25	37.00
2	28	0.163	1.25	31.00
3	41	0.252	1.25	29.80
4	55	0.329	1.25	30.90
5	69	0.407	1.25	23.00
6	103	0.595	1.25	5.24
7	138	0.794	1.25	6.82
8	207	1.168	1.25	4.65
9	276	1.561	1.25	5.95
10	345	1.962	1.25	7.09
11	414	2.364	1.25	7.95

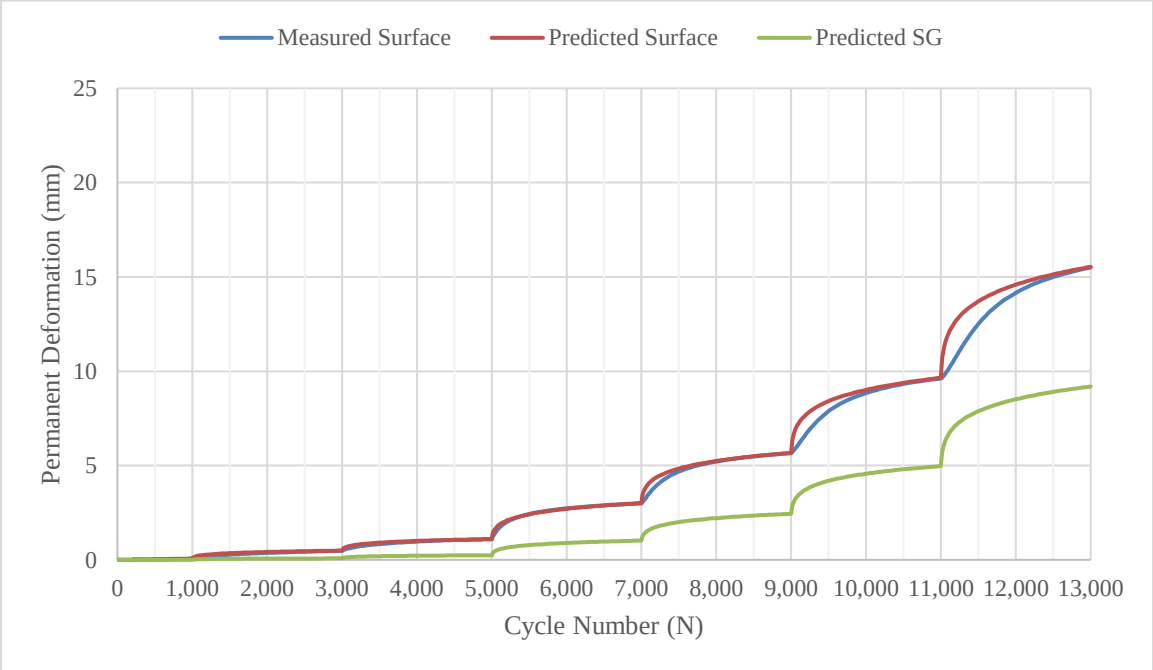

Figure 6.19. Measured versus Permanent Deformations of the RCA/ GG/ NW Section over 2% CBR Subgrade.

Table 6.11. MATLAB Input Variables for the RCA/ GG/ NW Section over 2% CBR Subgrade.

Load Sequence	Applied Pressure (kPa)	k_s	k_b	E_1/E_2
1	14	0.108	1.25	35.00
2	28	0.210	1.25	45.00
3	41	0.327	1.25	44.00
4	55	0.446	1.25	50.00
5	69	0.567	1.25	77.00
6	103	0.836	1.25	9.40
7	138	1.074	1.25	9.80
8	207	1.442	1.25	6.10
9	276	1.749	1.25	7.31
10	345	2.106	1.25	7.76
11	414	2.535	1.25	8.09

Figure 6.20 shows the resilient moduli calculated based on the modified Burmister solution (Sun et al., 2017) for the RCA sections. Figure 6.21 displays the resilient modulus results using the elastic rebound solution adopted by Qian et al. (2011). Figure 6.22 shows the resilient moduli calculated based on the interface stress reduction method for the RCA Sections. Like the VGB sections, the RCA sections displayed an initial spike in the resilient moduli due to the early stage of the load program at only 200 cycles instead of 2,000. Estimation of the resilient modulus by the modified Burmister solution is more aligned with the permanent deformation and the interface stress reduction results, displaying that the RCA/GG/NW provided the most effective stabilization. This result is opposite to that from the elastic rebound solution; in this case, the RCA control section had the highest modulus due to its lowest elastic rebound. Use of the RCA replacement of the VGB increased the resilient modulus of the base course to 60 MPa for the control RCA section or to as high as over 150 MPa for the RCA/NW section and the

RCA/GG/NW section. The change in the aggregate from VGB to RCA improved the performance by 1.5 times. Geosynthetics in the RCA improved resilient moduli by roughly 60%.

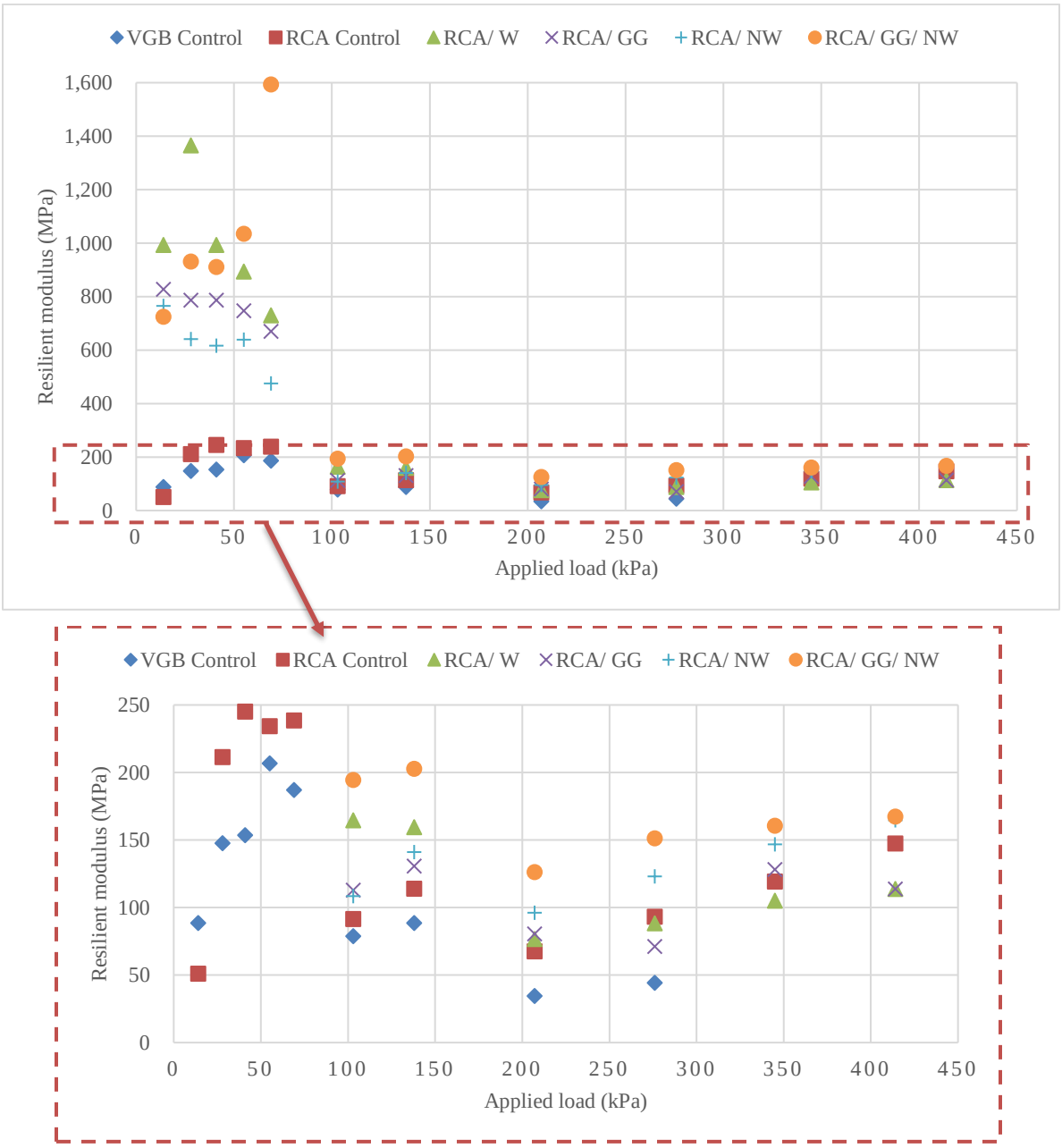

Figure 6.20. Resilient Moduli Calculated Based on the Modified Burmister Solution in the MATLAB Code for the RCA Sections.

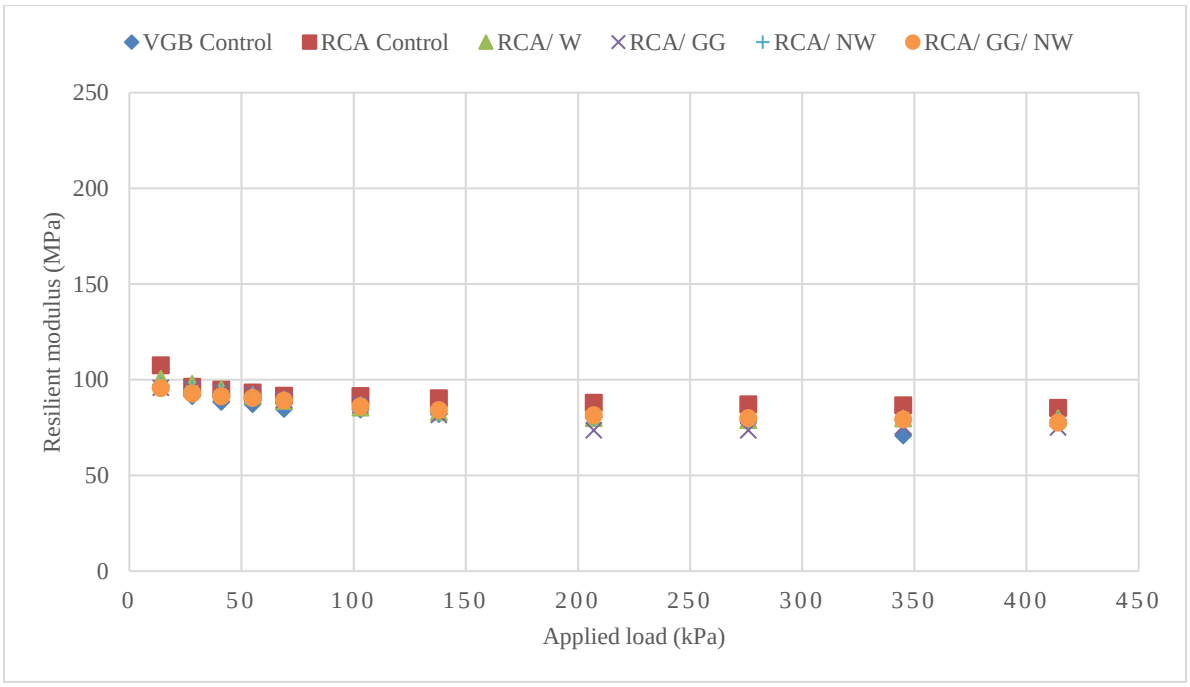

Figure 6.21. Resilient Moduli Calculated Based on the Elastic Rebound Solution for the RCA Sections.

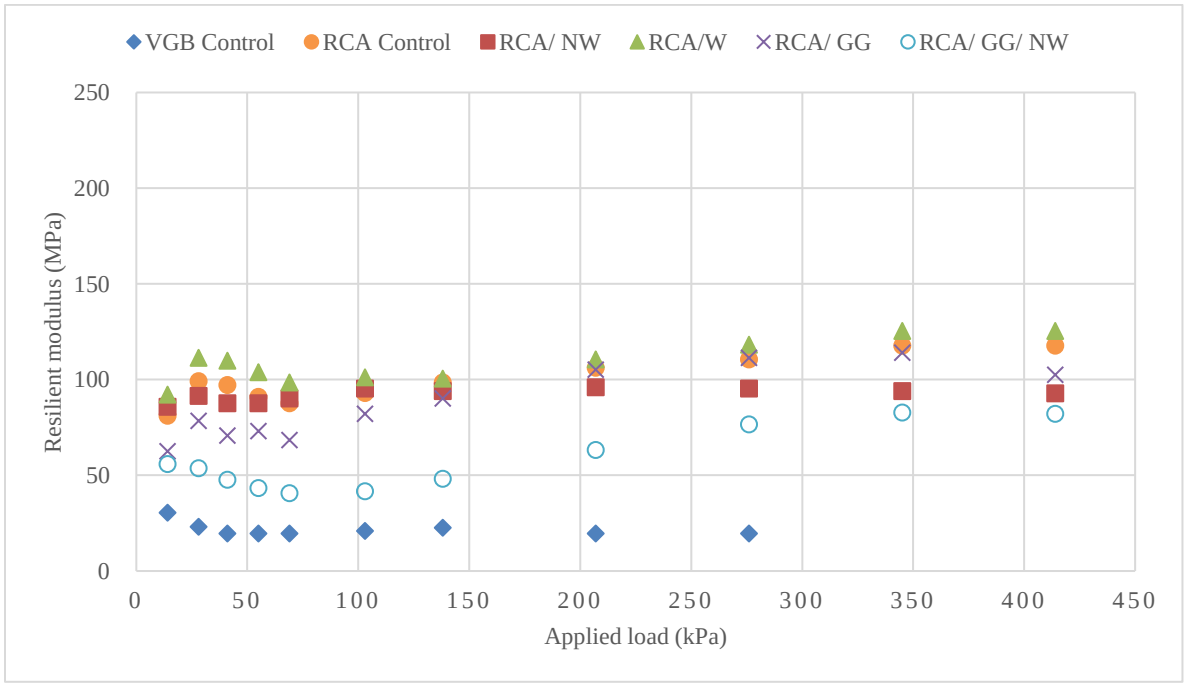

Figure 6.22. Resilient Moduli Calculated Based on the Interface Stress Reduction Method for the RCA Sections.

6.2.5 Modulus Comparison with Permanent Deformation

The average resilient moduli of the base course sections for the 2,000-cycle load sequences are compared along with the permanent deformation after 9,000 cycles in Figure 6.23. The relationship between the lower permanent deformation and the higher resilient modulus is most closely reflected using the modified Burmister solution (Sun et al., 2017). The magnitudes of the calculated moduli using the interface stress reduction method are most variable, but the benefits of using geosynthetic as well as the replacement of VGB with RCA are highlighted. The magnitudes of the resilient moduli are quite comparable for the control VGB section and the stabilized VGB section with the combination of nonwoven geotextile and geogrid despite the different methods used; these two tests displayed the largest permanent deformations at 9,000 load cycles.

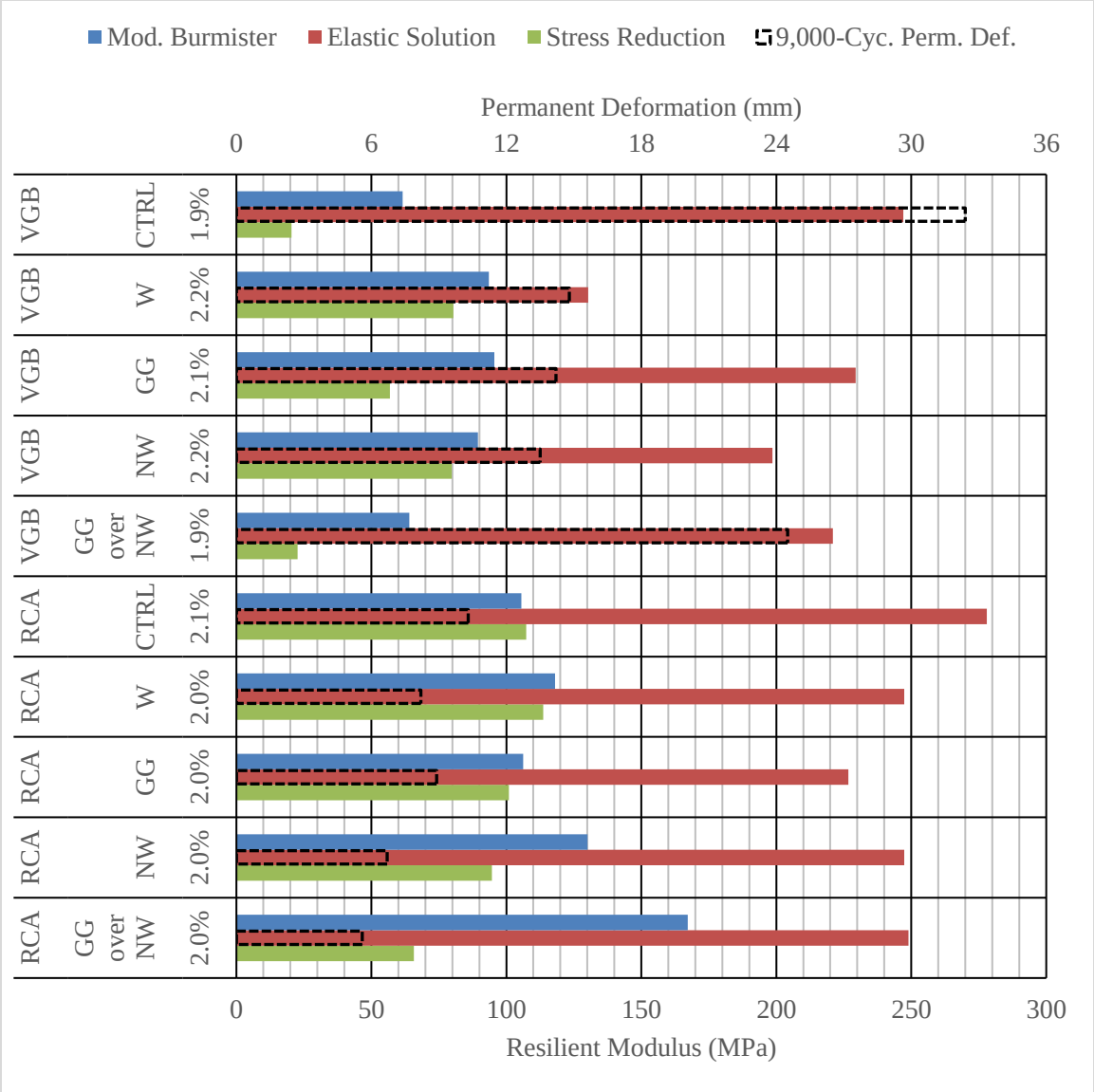

Figure 6.23. Average Resilient Moduli of the Base Courses from the 2,000-Cycle Sequences as Compared with Permanent Deformations at 9,000 Load Cycles.

Modulus of subgrade reaction can be estimated from the resilient moduli of the subgrade and the base course using the AASHTO charts as discussed in Chapter 2. The calculated moduli of subgrade reaction for different sections using different methods are shown in Figure 6.24. These calculated modulus values are in line with the typical values found in the AASHTO (1993) guide and in the Westergaard (1926) paper.

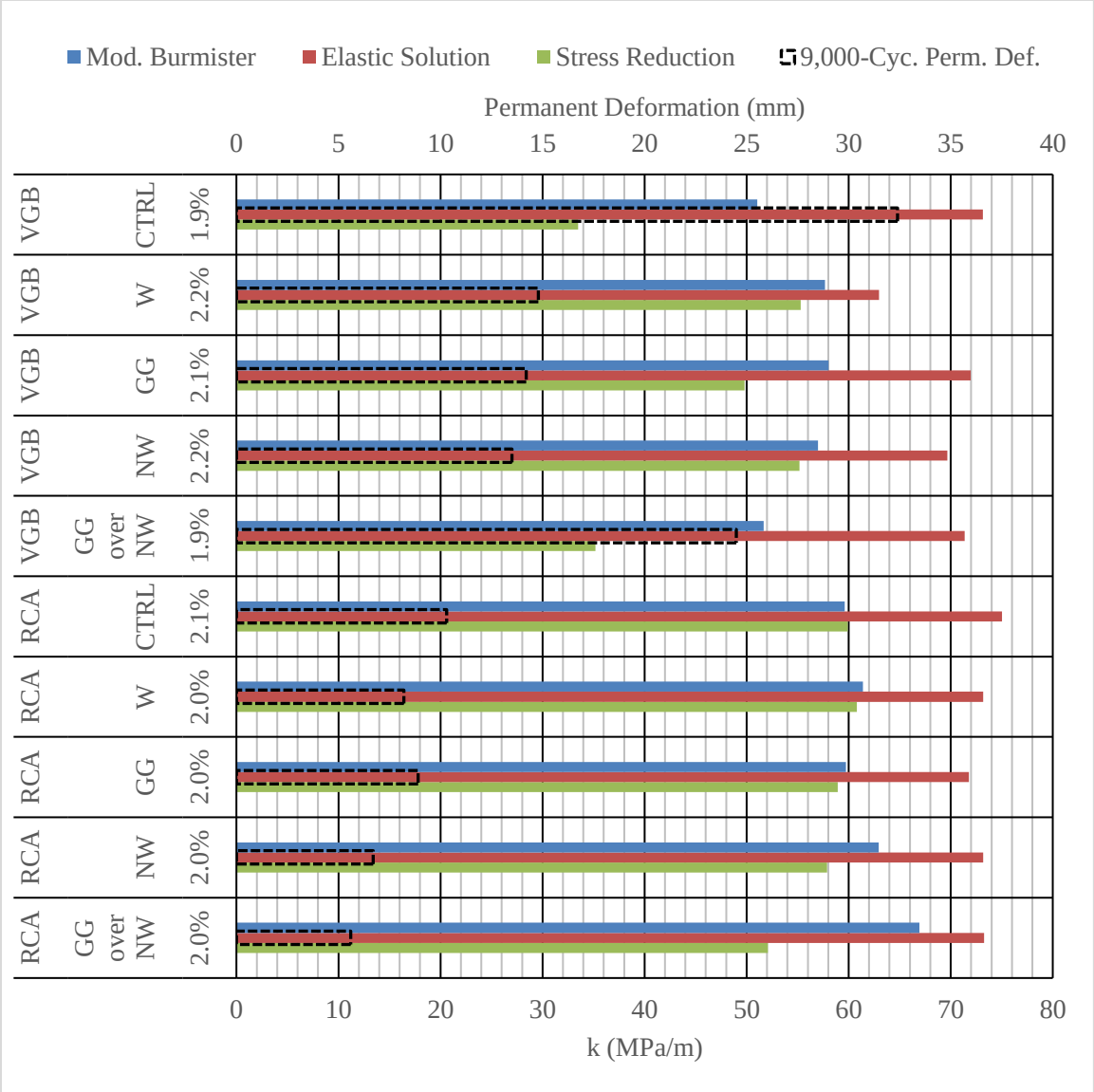

Figure 6.24. Composite k-values for Different Sections Using the AASHTO Design Chart Based on the M_r Values from Various Methods.

While the k-values in Figure 6.24 are of similar magnitude to those in the Westergaard (1926) and the AASHTO (1993), the small changes in the k-values resulted in large discrepancies in the permanent deformations in unpaved road sections. However, Westergaard (1926) indicated that the increase of k-value by four times from the minimum value had minimal impact on concrete pavement performance. This comparison indicates that concrete pavements

perform differently from unpaved roads. The relationship between the composite k-values using the AASHTO chart based on the M_r values from different methods and the accumulated permanent deformations at 9,000 cycles for all unpaved road sections is displayed in Figure 6.25. Both the interface stress reduction method and the modified Burmister method had an inverse relationship between the accumulated permanent deformation and the k-value.

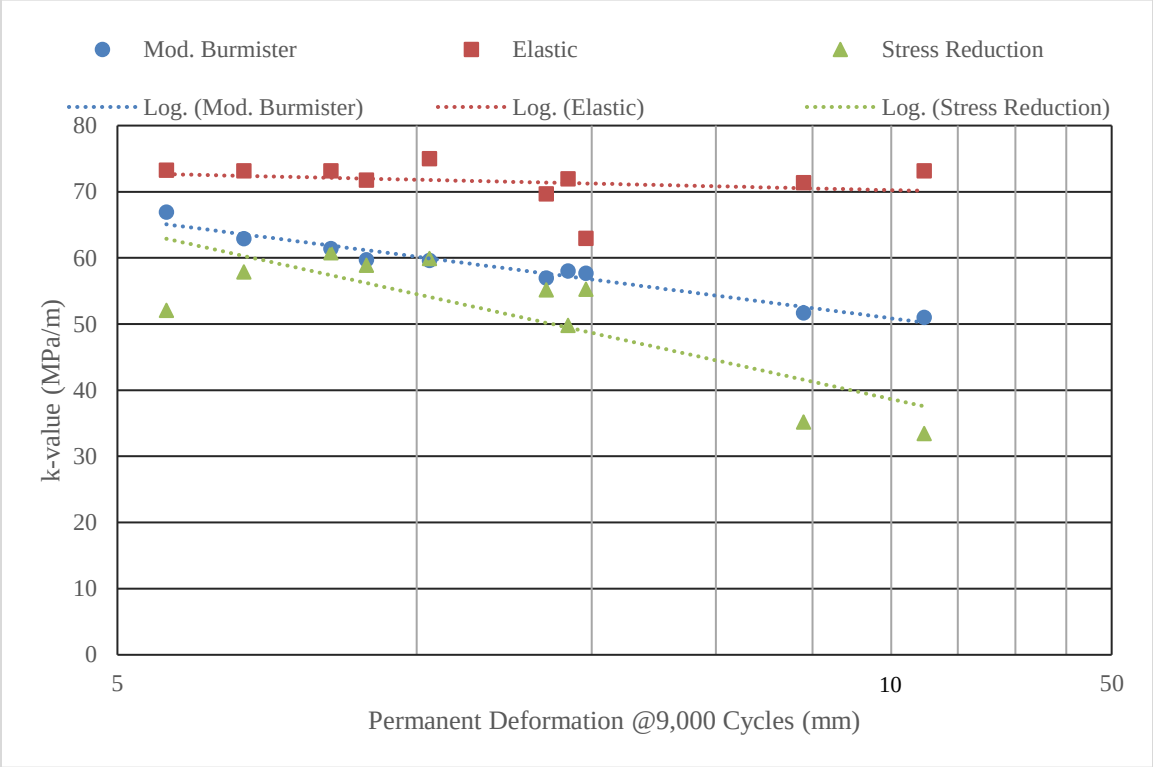

Figure 6.25. Subgrade Reaction Modulus vs. Accumulated Permanent Deformation at 9,000 Cycles for Unpaved Road Sections.

The variability in the calculated k-values varies based on the method of calculation, as displayed in Figure 6.26. As discussed previously, the elastic rebound method (Qian et al. 2011) of determination shows minimal change in the calculated k-values, as the spread of values for the various geosynthetics and base course aggregates is very small in Figure 6.26. There is greater distinction between the expected performance for different road sections using both the modified

Burmister and stress reduction methods, as depicted in the larger range of values. The stress reduction method displays a slightly lower range of k-values overall than the modified Burmister method.

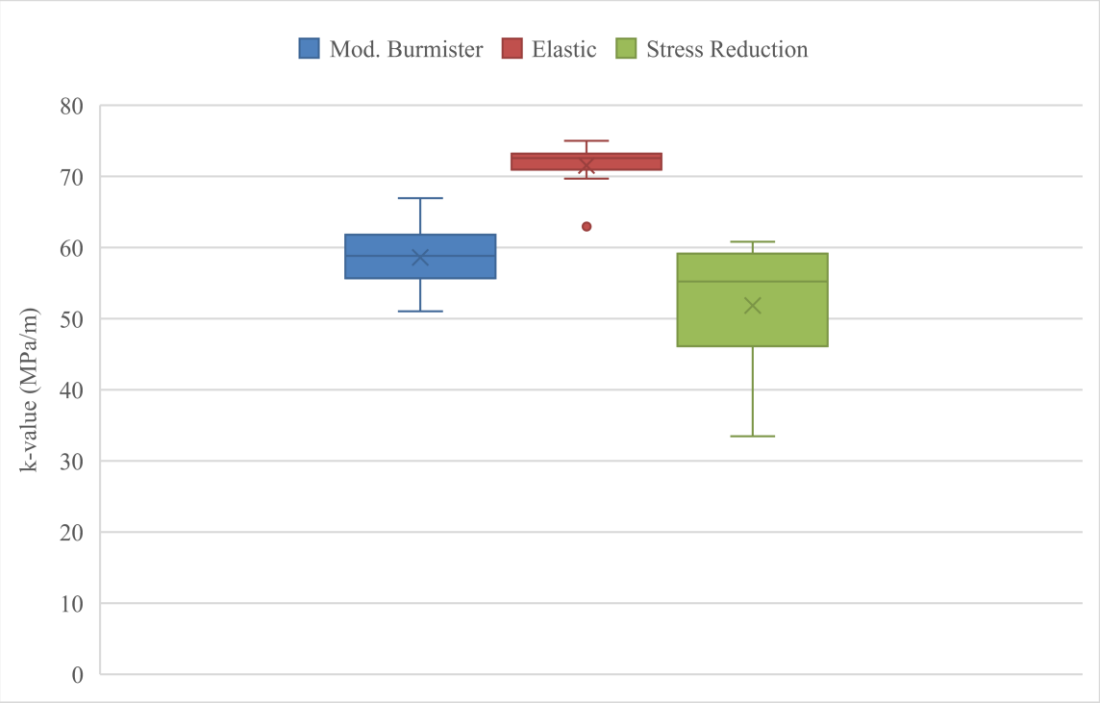

Figure 6.26. Ranges of Composite Subgrade Reaction Moduli Calculated Using the AASHTO Chart Based on the Base M_r Values from Different Methods.

Chapter 7. Analysis of Concrete Pavements on Geosynthetic-stabilized Granular Bases

7.1 Determination of Subgrade Reaction Modulus from Loading Tests

Both unpaved and paved road sections were tested in this study. Westergaard (1926) developed a solution to estimate the deflection of the concrete slab at the corner as described in Chapter 2. These k-values for the paved tests were determined using the Westergaard (1926) method, and these results can be found in Chapter 4. For the unpaved tests, the AASHTO (1993) design chart based on subgrade resilient modulus, base course elastic modulus, and base course thickness were used to estimate k-values in Chapter 6. Because the modified Burmister method of estimating equivalent resilient modulus of base course in the unpaved sections was most reflective of permanent deformation, the modulus values from this method were applied to this concrete pavement analysis.

Based on the measured deflection at the corner of the concrete slab and the thickness and properties of the concrete slab, the moduli of subgrade reaction (k-values) were estimated for the three test sections. The calculated k-values by the Westergaard (1926) method are listed in Table 7.1. The equivalent resilient modulus of the base course was estimated from the Westergaard k-values using the AASHTO (1993) design charts and are also shown in Table 7.1.

Table 7.1. Base Course k-values and Estimated Resilient Moduli from Paved Tests.

Test No.	Base Course	Geosynthetic	Rainfall	Westergaard k-value (MPa/m)	Resilient Modulus (MPa)
28A	VGB	NONE	Pre-rain	30.0	16.1
28B	VGB	NONE	Post-rain	36.6	24.3
29A	VGB	NW	Pre-rain	33.9	20.5
29B	VGB	NW	Post-rain	45.3	41.8
30A	RCA	NW	Pre-rain	42.1	34.1
30B	RCA	NW	Post-rain	54.3	73.0

Modulus of subgrade reaction as estimated in the unpaved tests are compared with those obtained in the pre-rainfall concrete paved tests in Figure 7.1. Values estimated using the Stress Reduction (Burmister 1958) and Modified Burmister (Sun et al. 2017) for the unpaved tests are displayed. Values estimated in the unpaved tests were approximately 35% greater than those estimated in the paved tests from this experimental study.

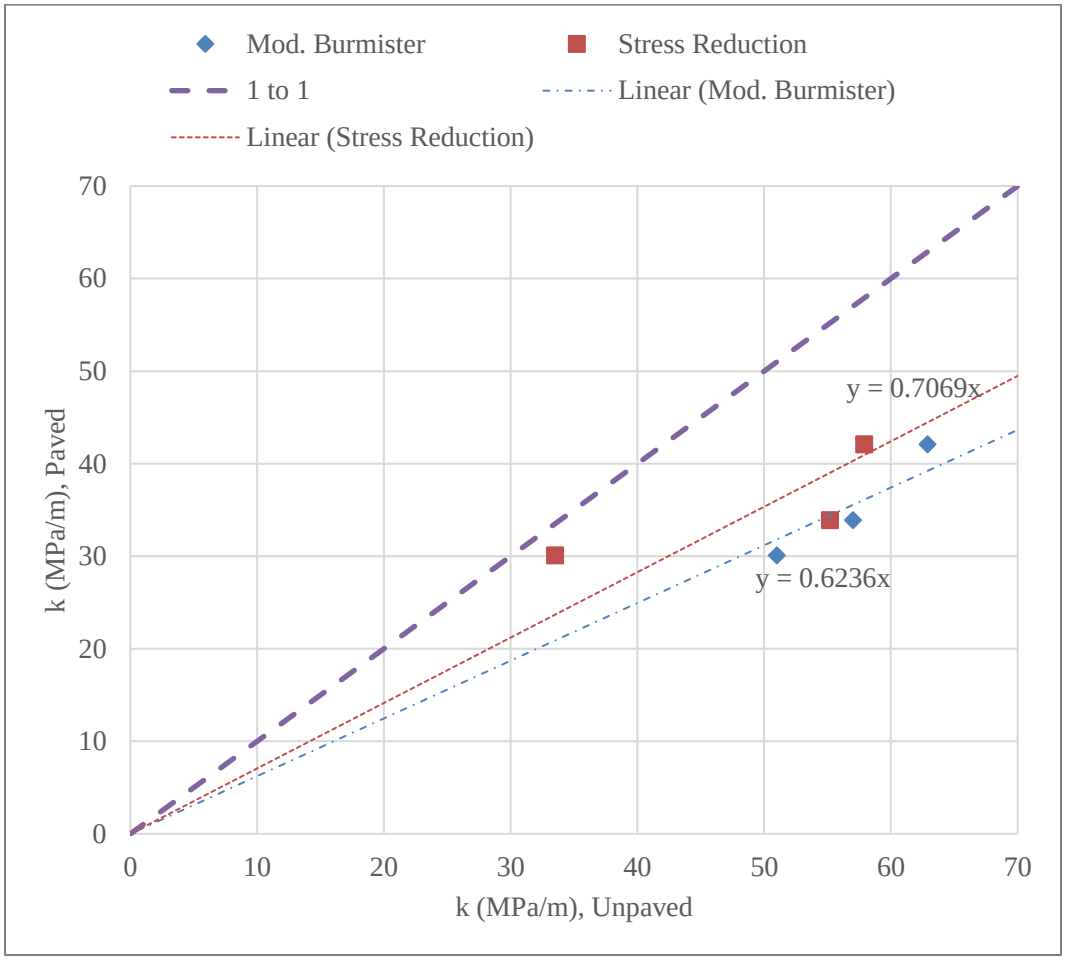

Figure 7.1. Moduli of Subgrade Reaction, Unpaved vs. Paved.

Although the subgrade reaction modulus is used to estimate the maximum tensile stresses in the loaded concrete slab, the effect on permanent deformation based on k-value changes must be acknowledged. As displayed in Figure 7.2, subgrade reaction moduli have a significant impact

on the measured deformations in both the unpaved and paved sections. The accumulated deformation increases at a greater rate for lower k-values or weaker base course-subgrade sections. This relationship must be considered when determining pavement section performance to avoid excessive deformations of the underlying pavement structure.

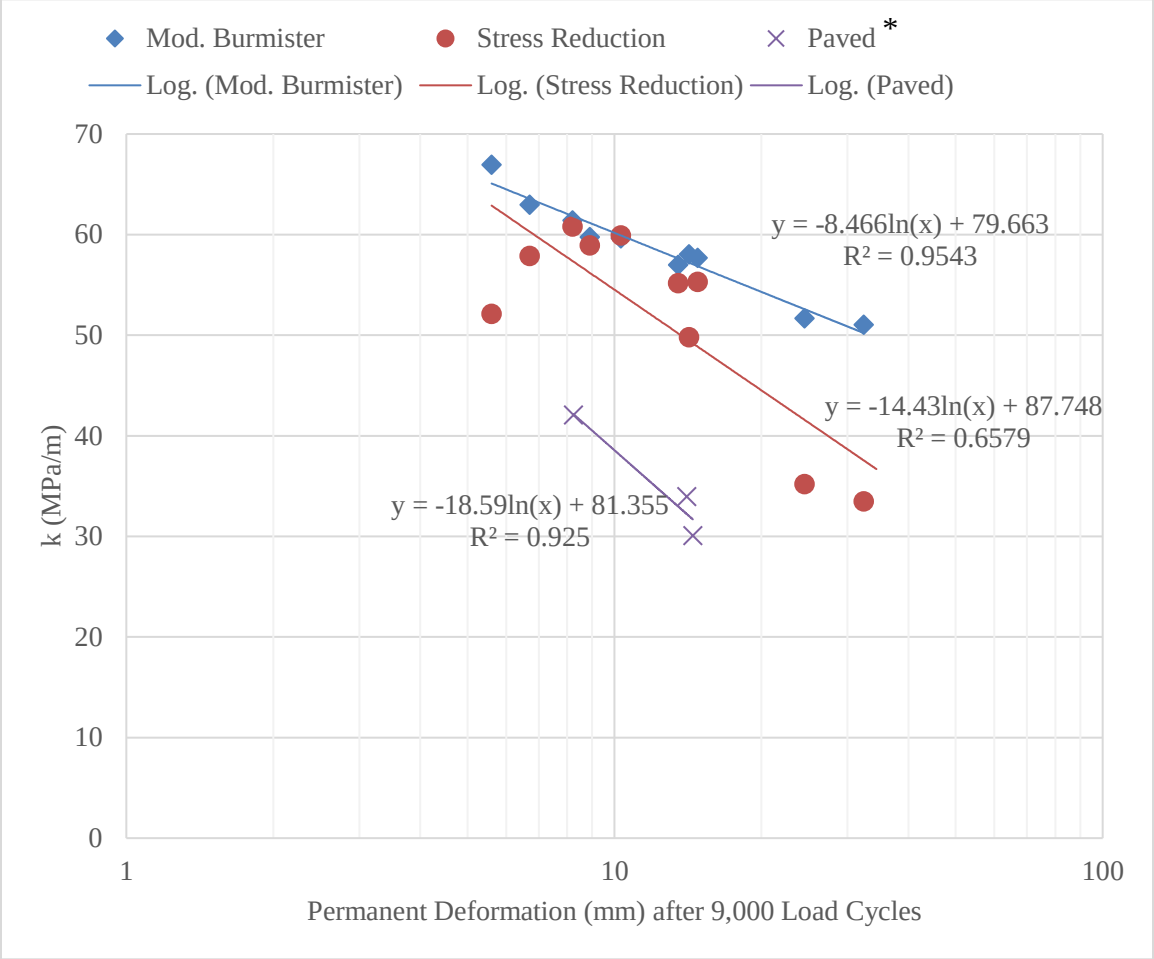

*Figure 7.2. Permanent deformation after 9,000 Load Cycles vs. Subgrade Reaction Modulus. *Paved sections had one larger load magnitude, while unpaved had multiple load stages of varying load magnitudes and cycle numbers.*

7.2 Tensile Stresses in Concrete Slabs

A load applied at the corner of a concrete pavement on a base course over subgrade will induce tensile stresses in the concrete slab (Westergaard, 1926) , as described in Chapter 2. Modulus of rupture of the slab, f_r, was estimated in Chapter 3 as 3.26 MPa and 3.31 MPa at 7 days and 8 days, respectively. Westergaard (1926) uses the k-value to estimate the tensile stress as described in Chapter 2, while the KENPAVE software by Huang (2004) relies on the resilient modulus (M_r) input either as a single composite value or for each base course and subgrade layer for pavement analysis. Based on the k-values from the Westergaard method, the resilient moduli of the base courses from the paved tests are displayed in Table 7.1.

The simplified solution by Westergaard (1926) was used for estimating the maximum induced tensile stresses in concrete due to corner loading (σ_c), which are shown in Figure 7.3. Factors of safety, defined as the modulus of rupture divided by the tensile stress in the concrete slab (see Figure 7.3), are greater than 1.0 for all sections. Factors of safety increased 0.03 through the addition of nonwoven geotextile to the VGB and a further 0.04 through the replacement of VGB/NW with RCA/NW. Less than 10% reduction in the stresses in the slab from the control VGB section was estimated. This small reduction in slab tensile stresses despite more significant changes to base course and subgrade strength/modulus was indicated by Westergaard (1926). Further analysis is recommended to compare the sections, especially with the consideration of accumulated damage, loss of support, and other external slab fracture mechanisms listed in the MEPDG (NCHRP 2004).

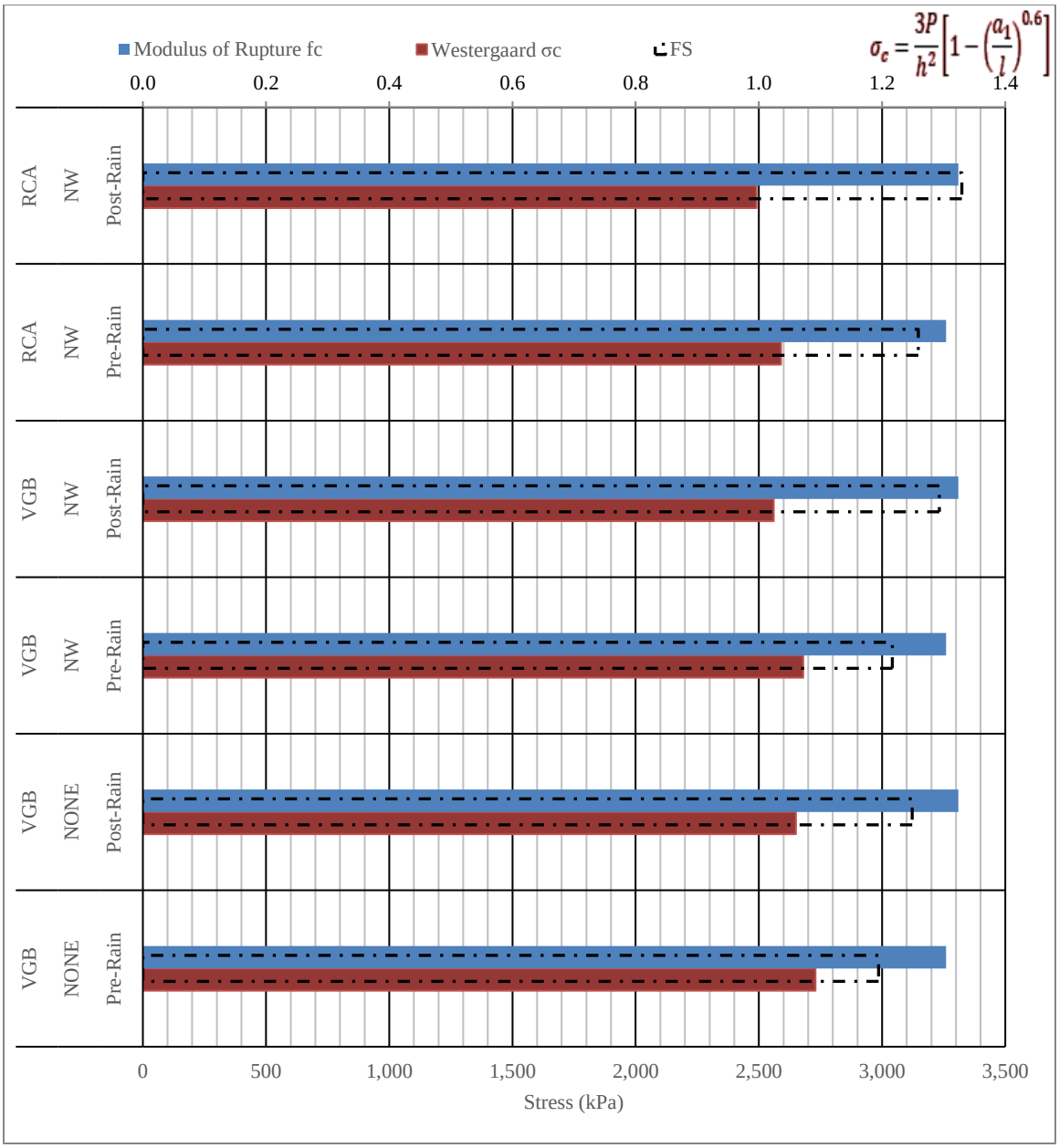

Figure 7.3. Maximum Slab Tensile Stresses due to Corner Loading Calculated by the Westergaard (1926) Solution.

The k-values estimated for the unpaved roads were used with the Westergaard (1926) formulas to estimate the tensile stresses in the pavement slab, as displayed in Figure 7.4. While these unpaved road test k-values were an average of 35% higher than those from the concrete

paved tests (see Figure 7.1), the difference in the corresponding estimated slab tensile stresses was only 4% to 5%.

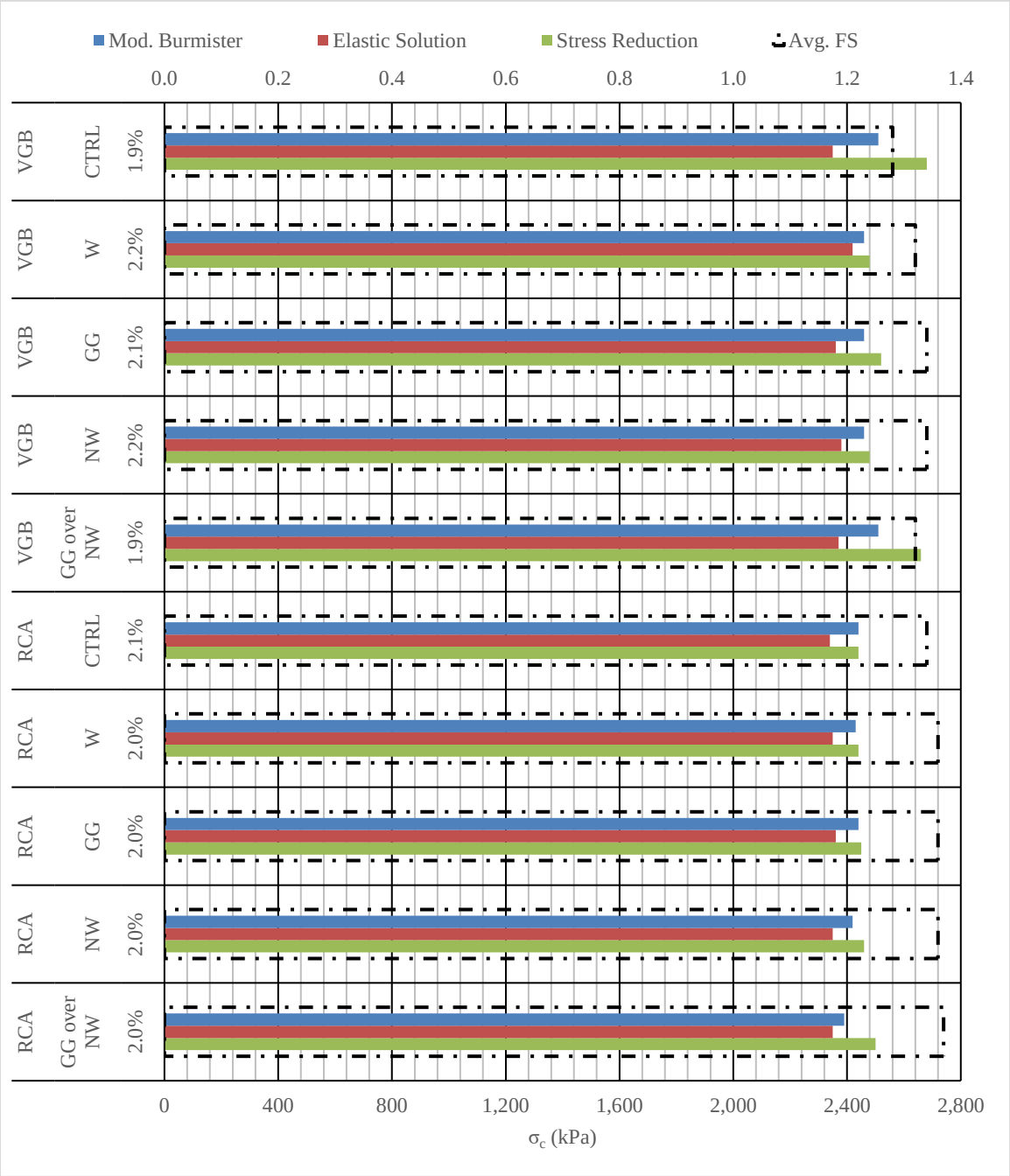

Figure 7.4. Maximum Slab Tensile Stresses due to Corner Loading Calculated by the Westergaard (1926) Solution using the k-values from the Unpaved Road Tests.

The KENPAVE software in Huang (2004) utilizes nodal analysis to estimate the stresses in a concrete slab based on slab dimensions, load parameters, and the subgrade reaction modulus estimated from the modulus (or moduli) of underlying layer(s). All input parameters used in these KENPAVE simulations can be found in Appendix B. Figure 7.5 compares the outputs of the tensile stresses from KENPAVE and the Westergaard solution using the composite k-values from the concrete paved road tests, listed in Table 7.1, in a "solid foundation" (single underlying layer) scenario. The good agreement of the calculated tensile stresses in the concrete slab from these two methods confirms the KENPAVE model setup was valid. Figure 7.5 plots the values obtained using the Westergaard (1926) formulas and the KENPAVE outputs for σ_c, and they are very near the 1:1 curve of matching exactly.

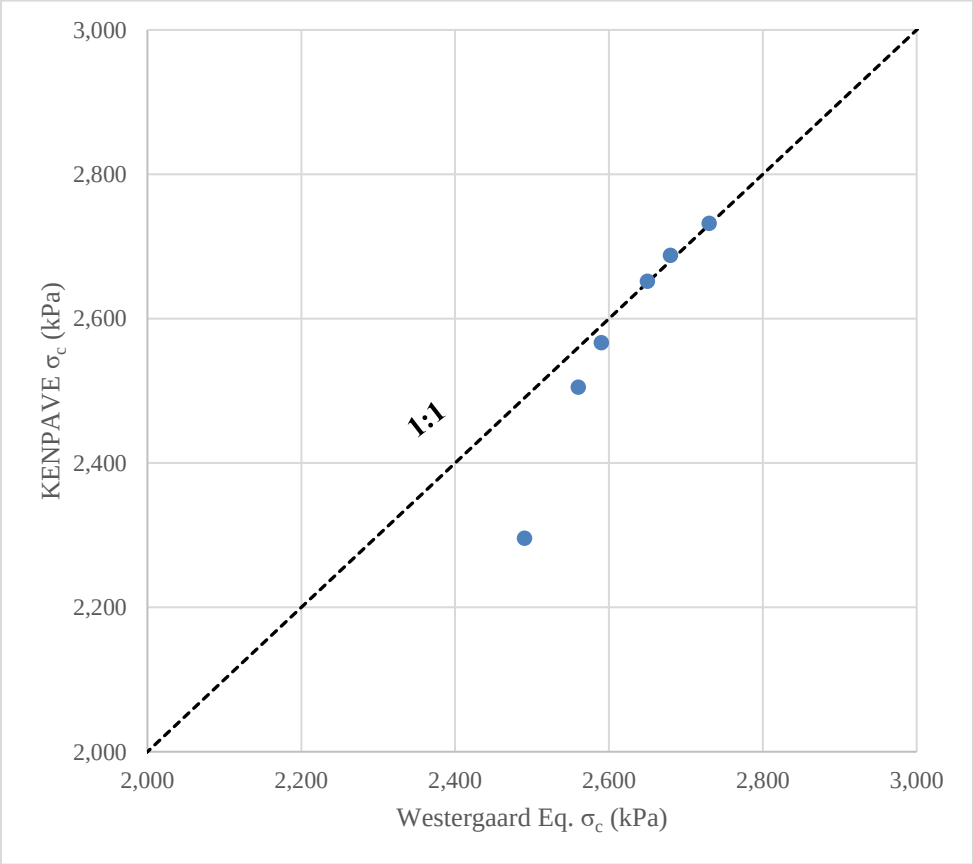

Figure 7.5. Calculated Tensile Stresses in the Concrete Slab using the Westergaard (1926) Equation vs. the KENPAVE Software.

Figure 7.6 displays the KENPAVE outputs for the large-scale box tests on the concrete pavements as-constructed in this study. Locations of the maximum stress in the slab, the applied load, the joint, the other (not-loaded) slab, and the loaded-slab corner stabilized by pole at the far corner in the box (estimated stabilizing load is 25 kN) are displayed. Deviations between the formula calculations and the KENPAVE program might be due to the variations in the corner stabilizing load that only resulted from rotation of the loaded slab under corner displacement (Figure 7.5). Details on the variables listed in the outputs are listed in Appendix B.

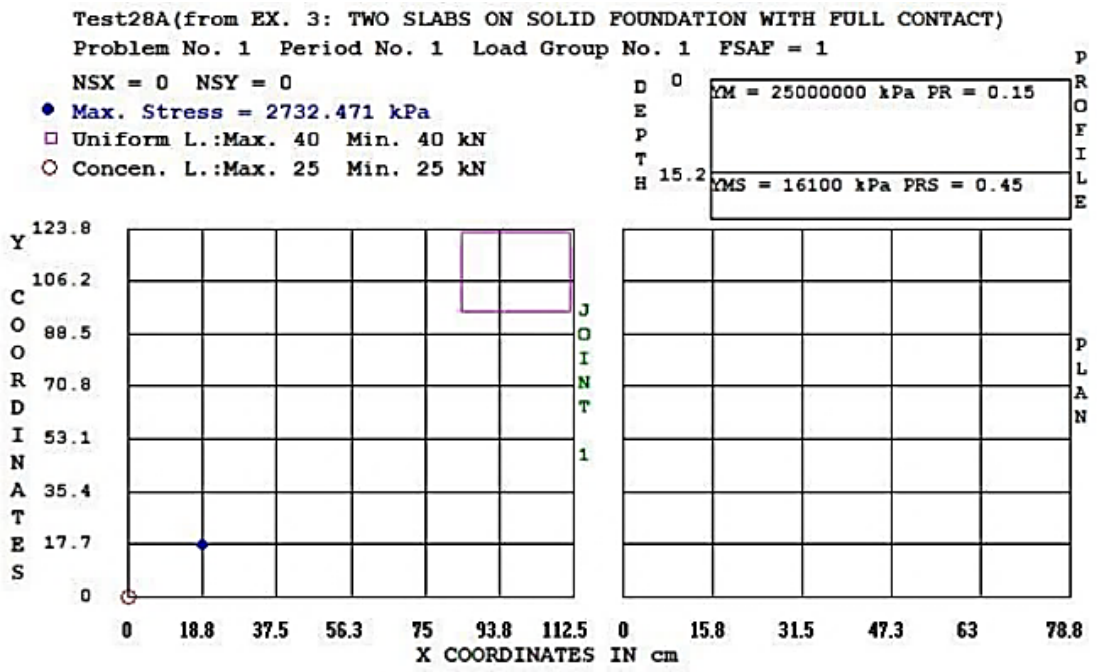
Test28A(from EX. 3: TWO SLABS ON SOLID FOUNDATION WITH FULL CONTACT)
Problem No. 1 Period No. 1 Load Group No. 1 FSAF = 1
NSX = 0 NSY = 0
Max. Stress = 2732.471 kPa
Uniform L.:Max. 40 Min. 40 kN
Concen. L.:Max. 25 Min. 25 kN
DEPTH
0
15.2
YM = 25000000 kPa PR = 0.15
YMS = 16100 kPa PRS = 0.45
PROFILE
Y COORDINATES
123.8
106.2
88.5
70.8
53.1
35.4
17.7
0
JOINT 1
PLAN
0 18.8 37.5 56.3 75 93.8 112.5 0 15.8 31.5 47.3 63 78.8
X COORDINATES IN cm

(a)

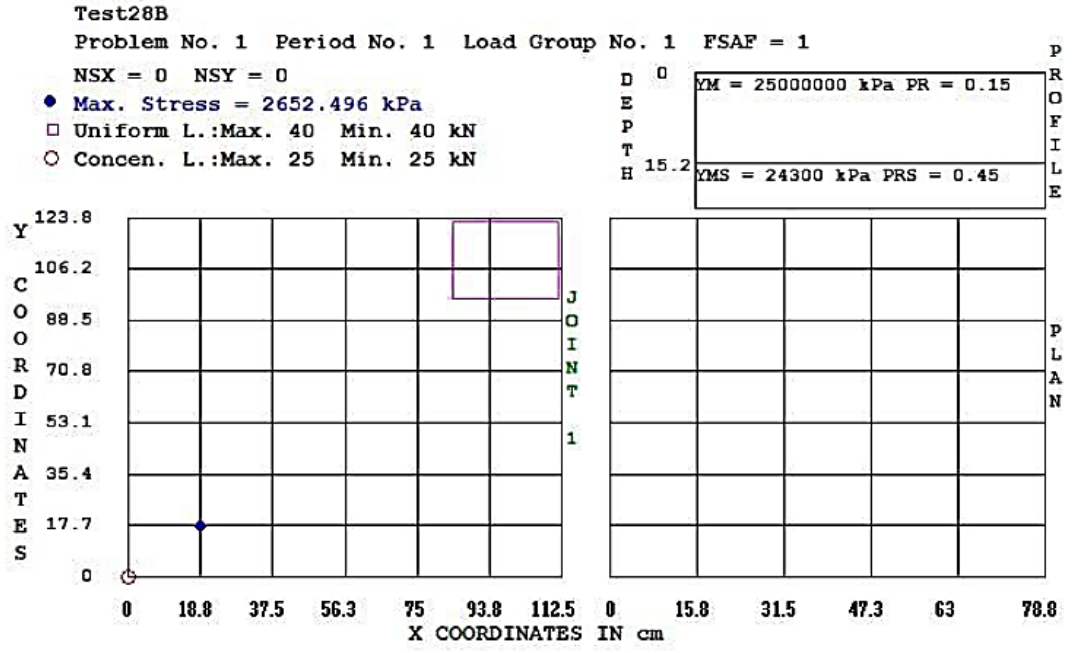
Test28B
Problem No. 1 Period No. 1 Load Group No. 1 FSAF = 1
NSX = 0 NSY = 0
Max. Stress = 2652.496 kPa
Uniform L.:Max. 40 Min. 40 kN
Concen. L.:Max. 25 Min. 25 kN
DEPTH
0
15.2
YM = 25000000 kPa PR = 0.15
YMS = 24300 kPa PRS = 0.45
PROFILE
Y COORDINATES
123.8
106.2
88.5
70.8
53.1
35.4
17.7
0
JOINT 1
PLAN
0 18.8 37.5 56.3 75 93.8 112.5 0 15.8 31.5 47.3 63 78.8
X COORDINATES IN cm

(b)

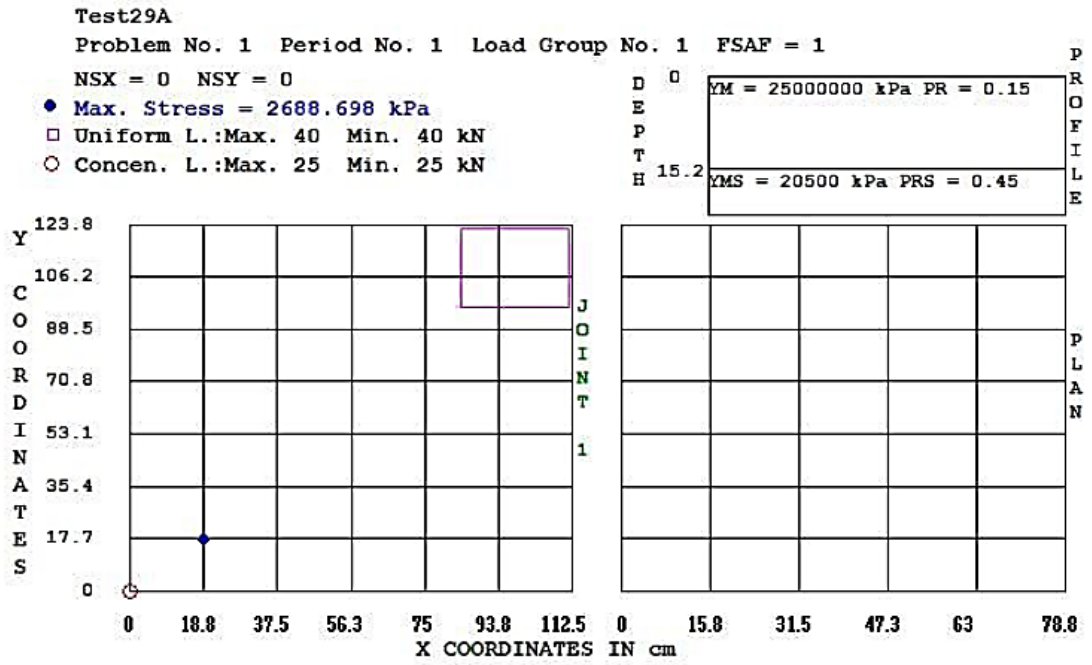
Test29A
Problem No. 1 Period No. 1 Load Group No. 1 FSAF = 1
NSX = 0 NSY = 0
Max. Stress = 2688.698 kPa
Uniform L.:Max. 40 Min. 40 kN
Concen. L.:Max. 25 Min. 25 kN
DEPTH
0
15.2
YM = 25000000 kPa PR = 0.15
YMS = 20500 kPa PRS = 0.45
PROFILE
Y COORDINATES
123.8
106.2
88.5
70.8
53.1
35.4
17.7
0
JOINT 1
PLAN
0 18.8 37.5 56.3 75 93.8 112.5
0 15.8 31.5 47.3 63 78.8
X COORDINATES IN cm

(c)

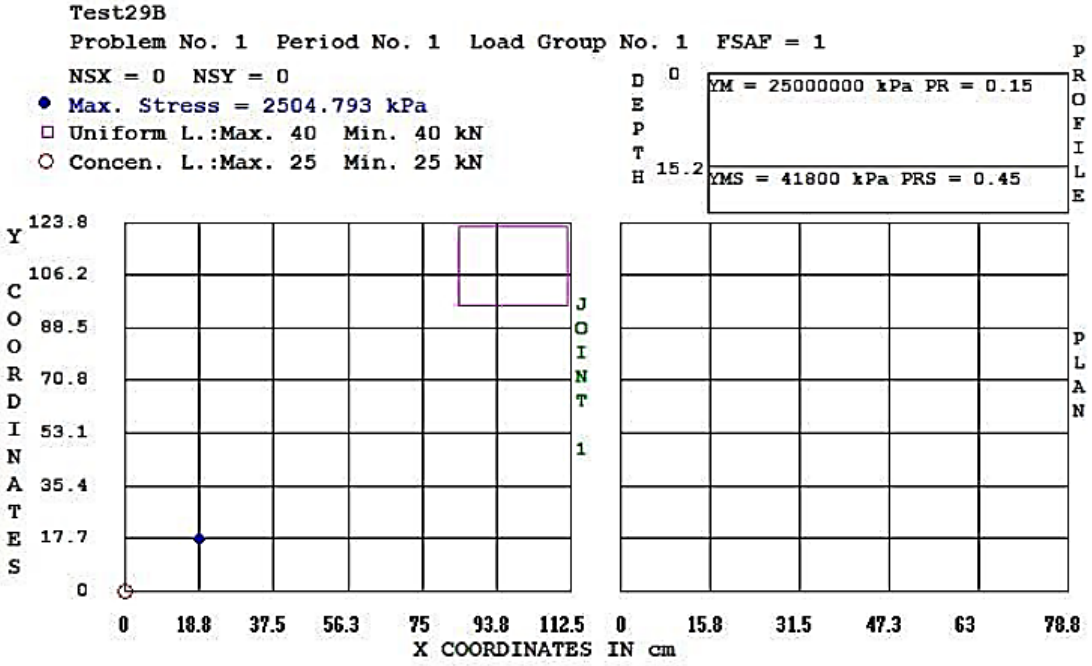
Test29B
Problem No. 1 Period No. 1 Load Group No. 1 FSAF = 1
NSX = 0 NSY = 0
Max. Stress = 2504.793 kPa
Uniform L.:Max. 40 Min. 40 kN
Concen. L.:Max. 25 Min. 25 kN
DEPTH
0
15.2
YM = 25000000 kPa PR = 0.15
YMS = 41800 kPa PRS = 0.45
PROFILE
Y COORDINATES
123.8
106.2
88.5
70.8
53.1
35.4
17.7
0
JOINT 1
PLAN
0 18.8 37.5 56.3 75 93.8 112.5
0 15.8 31.5 47.3 63 78.8
X COORDINATES IN cm

(d)

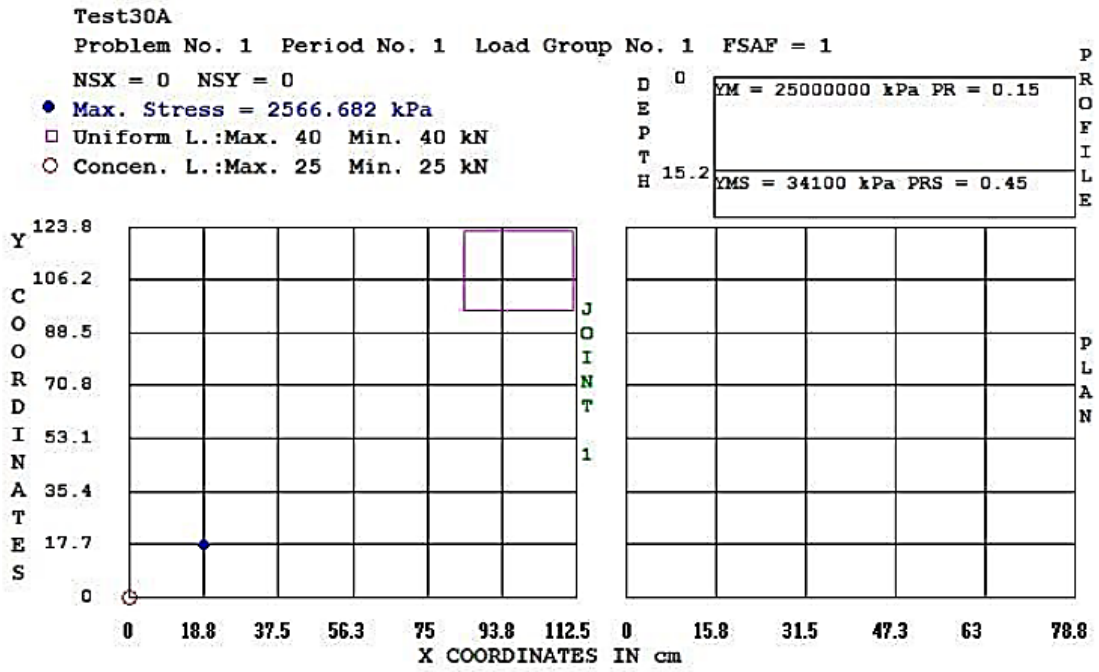

(e)

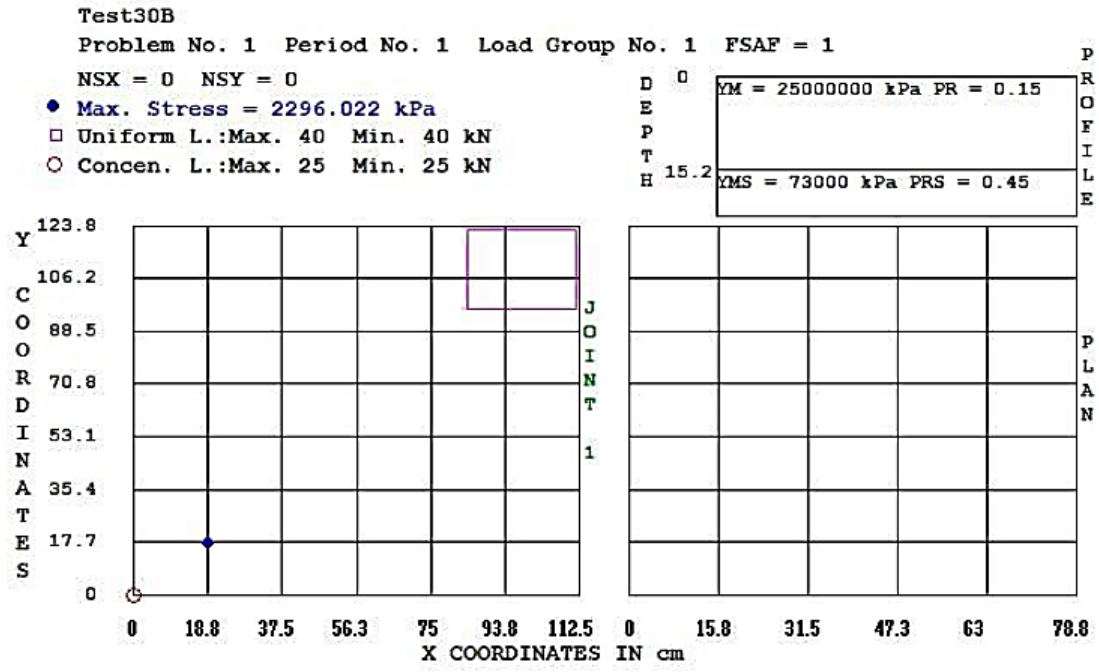

(f)

Figure 7.6. KENPAVE Inputs and Outputs for the Concrete Pavement Sections on Single Foundation Layer.

for (a) Control VGB Section Pre-rainfall, (b) Control VGB Section Post-rainfall, (c) VGB/NW Section Pre-rainfall, (d) VGB/NW Section Post-rainfall, , (e) RCA/NW Section Pre-rainfall, and (f) RCA/NW Section Post-rainfall.

7.3 Verification Study of Paved Test Sections

To validate the field representativeness of the method used in the large box test with corner loading and subsequent induced slab tensile stresses, a single axle load model with the same solid foundation was modeled in KENPAVE. The concrete slab dimensions were increased to 3 m by 3 m to simulate typical joint spacing in field, and one axle of two wheels with a typical wheel spacing distance of 1.4 m and a contact pressure of 550 kPa (i.e., a wheel load of 40 kN) atop each wheel area for the 80 kN equivalent single axle load (ESAL) was applied in accordance with the AASHTO (1993) design guide examples. One wheel was located at the same loaded corner as in the large box tests for these simulations. The slab tensile stress outputs with corner loading and the theoretical single axle load setup are compared in Figure 7.7. With only small variations in the calculated magnitudes of these slab tensile stresses between the single axle setup and the actual experiment construction with the single load and the opposite-corner stabilizing load, it can be confirmed that the test setup and reactions in the pavement system are reflective of single axle loading simulated in the field. Adjusted input parameters for KENPAVE are detailed in Appendix B.

Based on the validation presented in the previous section, the outputs from KENPAVE for each simulated concrete pavement experiment in this study using single-axle of wheel loads are shown in Figure 7.8. The single solid-layer model underlying the slab is kept the same for this single-axle simulation. Maximum tensile stress in these simulations was estimated to occur beneath the inner wheel (i.e. the wheel not located in the corner) at a distance similar to the radii of relative stiffness in Chapter 4. The consistency of these simulations between test setups is reflected in the small variation in slab tensile stress outputs estimated. These results support Westergaard's theory (1926) that small variations in slab tensile stresses are achieved through

significant changes in base course/subgrade k-values; however, these results do not reflect the permanent deformation reductions observed in the tests with the addition of geosynthetics and the replacement of VGB with RCA.

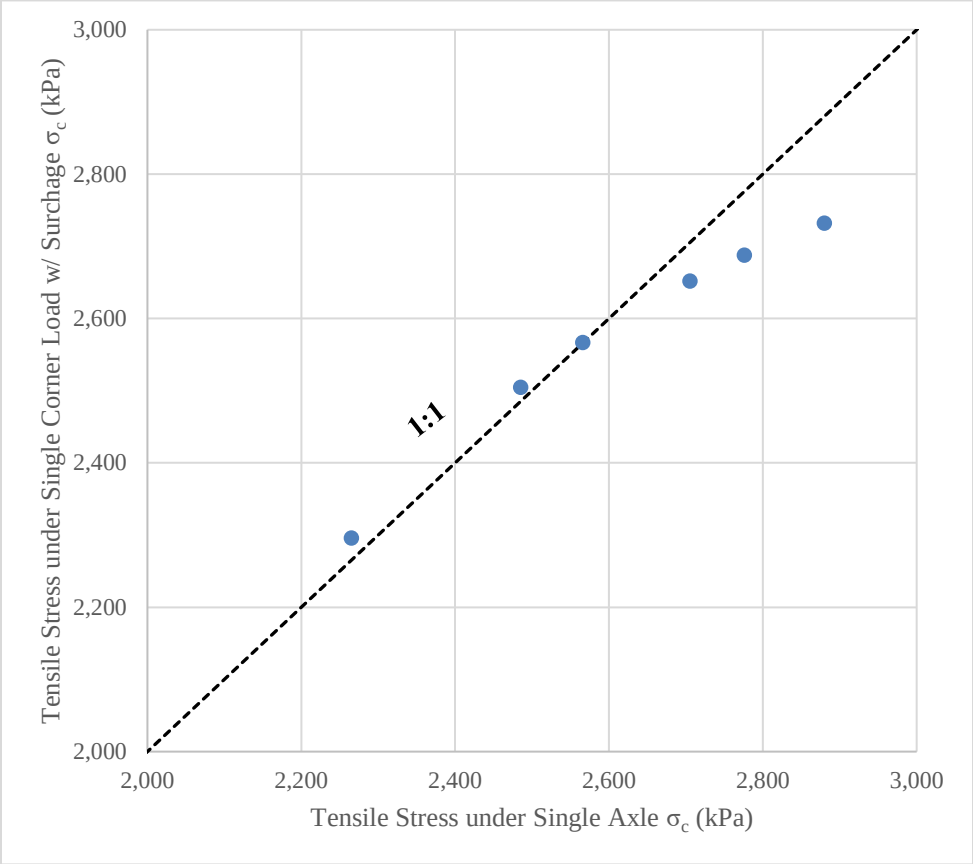

Figure 7.7. Tensile Stresses in the Concrete Slab Calculated by KENPAVE for Single Corner Load in the Box Test vs. Axle Load Simulated in Field.

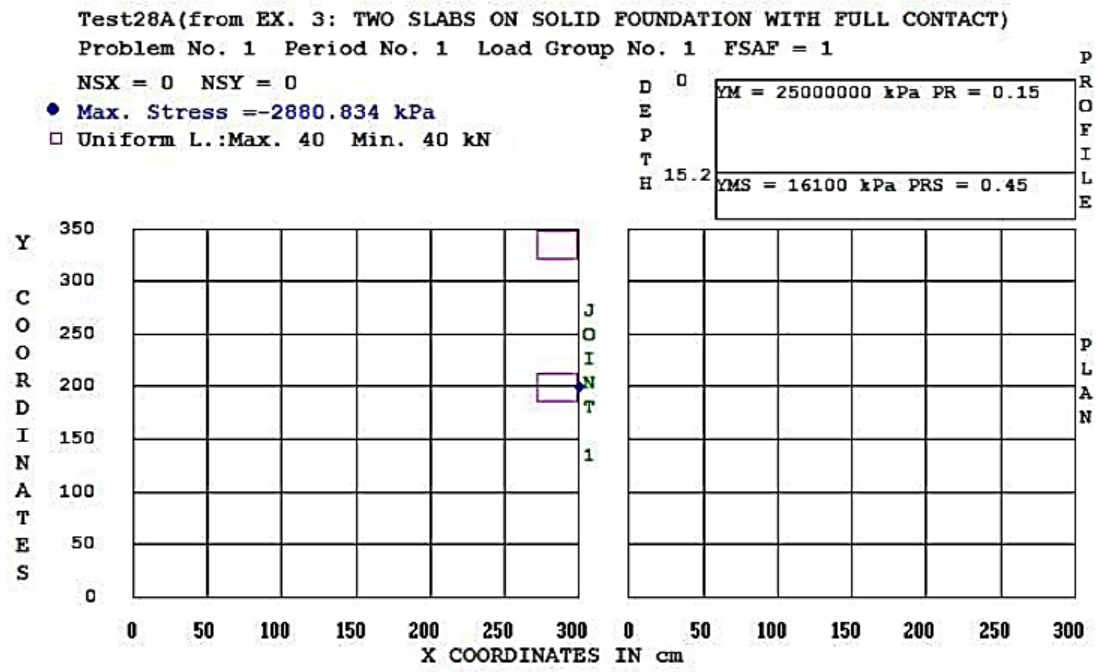
Test28A(from EX. 3: TWO SLABS ON SOLID FOUNDATION WITH FULL CONTACT)
Problem No. 1 Period No. 1 Load Group No. 1 FSAF = 1
NSX = 0 NSY = 0
Max. Stress =-2880.834 kPa
Uniform L.:Max. 40 Min. 40 kN
DEPTH
0
15.2
YM = 25000000 kPa PR = 0.15
YMS = 16100 kPa PRS = 0.45
PROFILE
Y COORDINATES
350
300
250
200
150
100
50
0
JOINT 1
PLAN
0 50 100 150 200 250 300
X COORDINATES IN cm

(a)

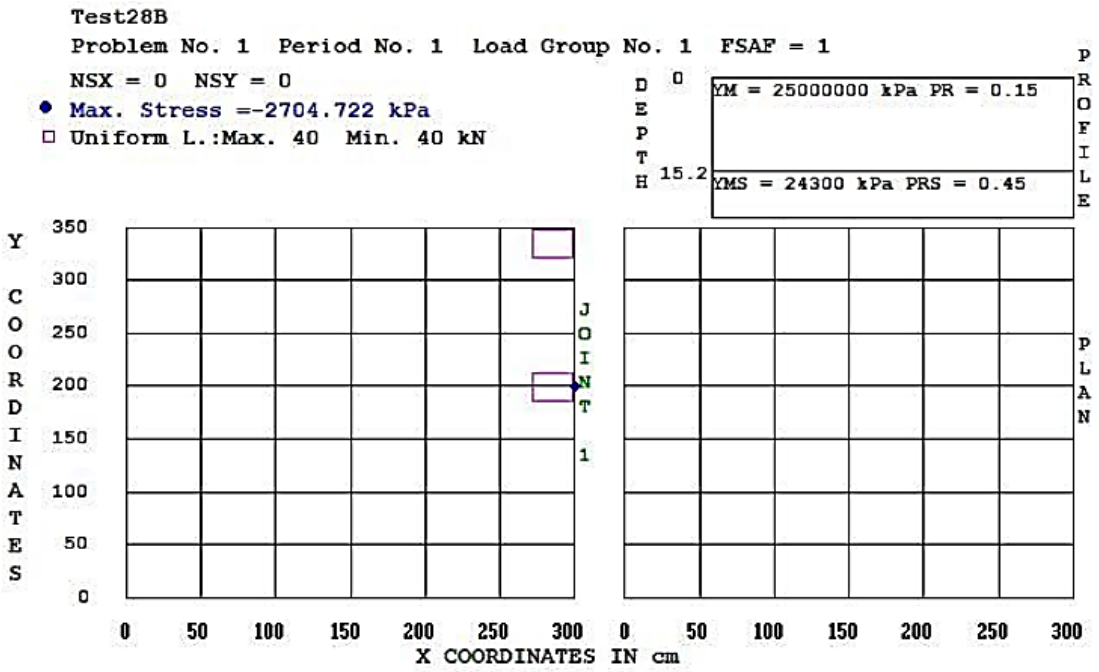
Test28B
Problem No. 1 Period No. 1 Load Group No. 1 FSAF = 1
NSX = 0 NSY = 0
Max. Stress =-2704.722 kPa
Uniform L.:Max. 40 Min. 40 kN
DEPTH
0
15.2
YM = 25000000 kPa PR = 0.15
YMS = 24300 kPa PRS = 0.45
PROFILE
Y COORDINATES
350
300
250
200
150
100
50
0
JOINT 1
PLAN
0 50 100 150 200 250 300
X COORDINATES IN cm

(b)

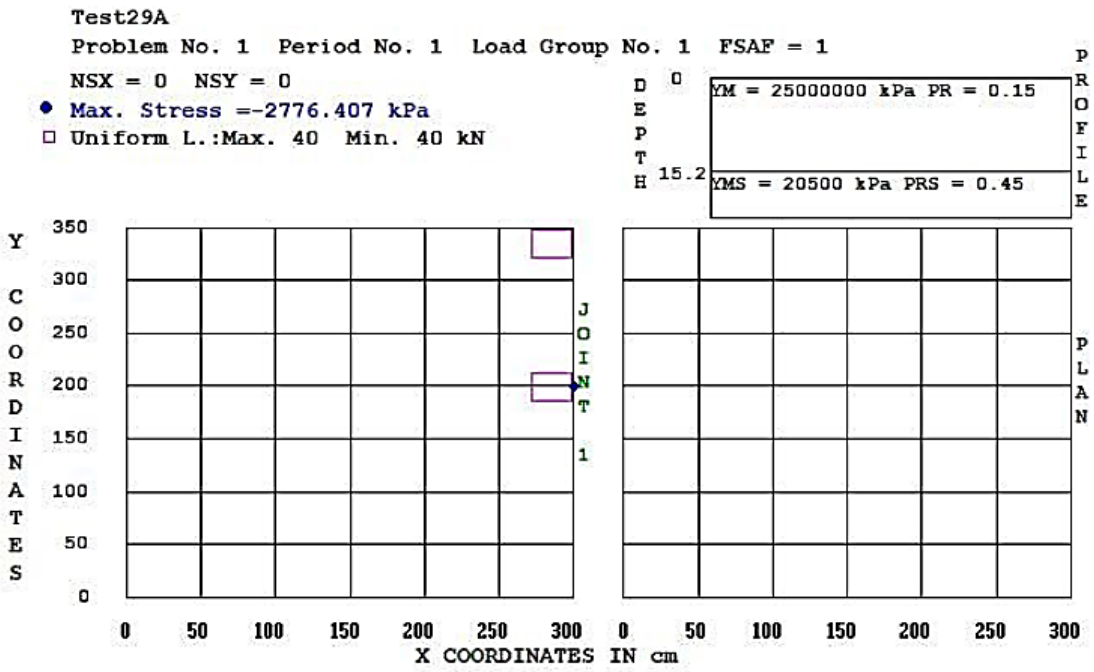
Test29A
Problem No. 1 Period No. 1 Load Group No. 1 FSAF = 1
NSX = 0 NSY = 0
Max. Stress =-2776.407 kPa
Uniform L.:Max. 40 Min. 40 kN
DEPTH
0
15.2
YM = 25000000 kPa PR = 0.15
YMS = 20500 kPa PRS = 0.45
PROFILE
Y COORDINATES
350
300
250
200
150
100
50
0
JOINT 1
PLAN
0 50 100 150 200 250 300
X COORDINATES IN cm

(c)

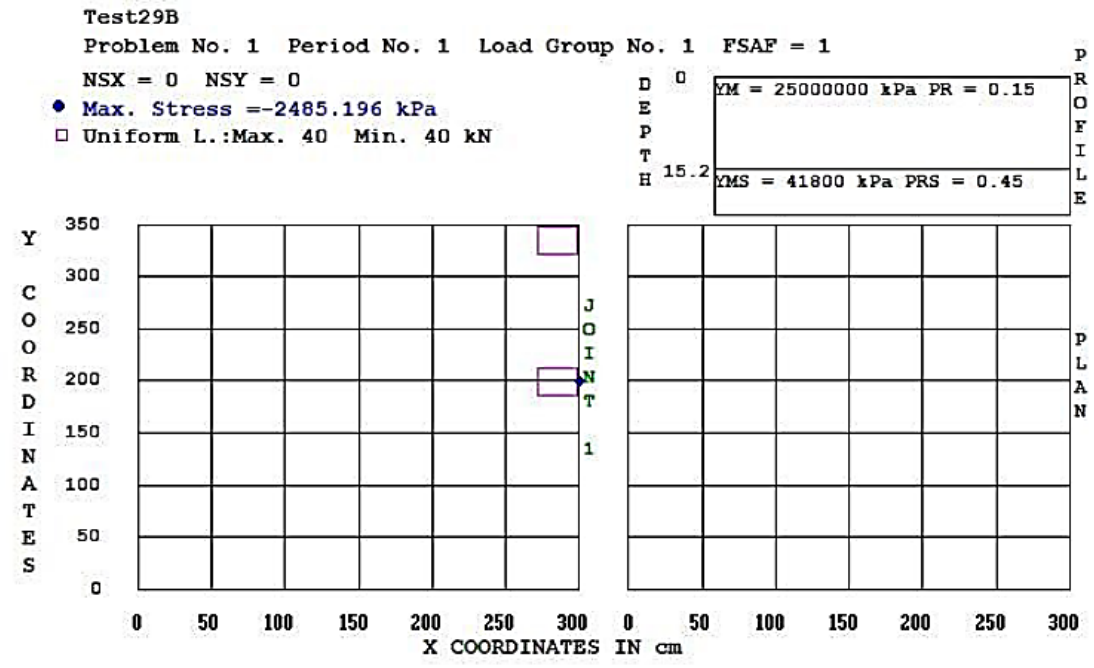
Test29B
Problem No. 1 Period No. 1 Load Group No. 1 FSAF = 1
NSX = 0 NSY = 0
Max. Stress =-2485.196 kPa
Uniform L.:Max. 40 Min. 40 kN
DEPTH
0
15.2
YM = 25000000 kPa PR = 0.15
YMS = 41800 kPa PRS = 0.45
PROFILE
Y COORDINATES
350
300
250
200
150
100
50
0
JOINT 1
PLAN
0 50 100 150 200 250 300
X COORDINATES IN cm

(d)

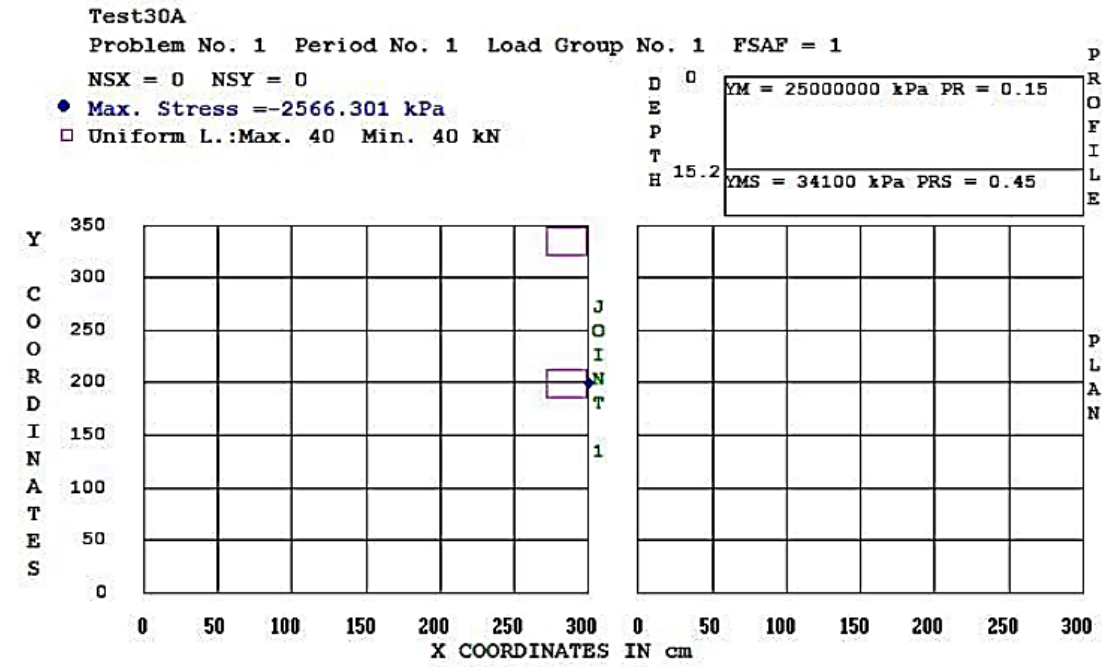

(e)

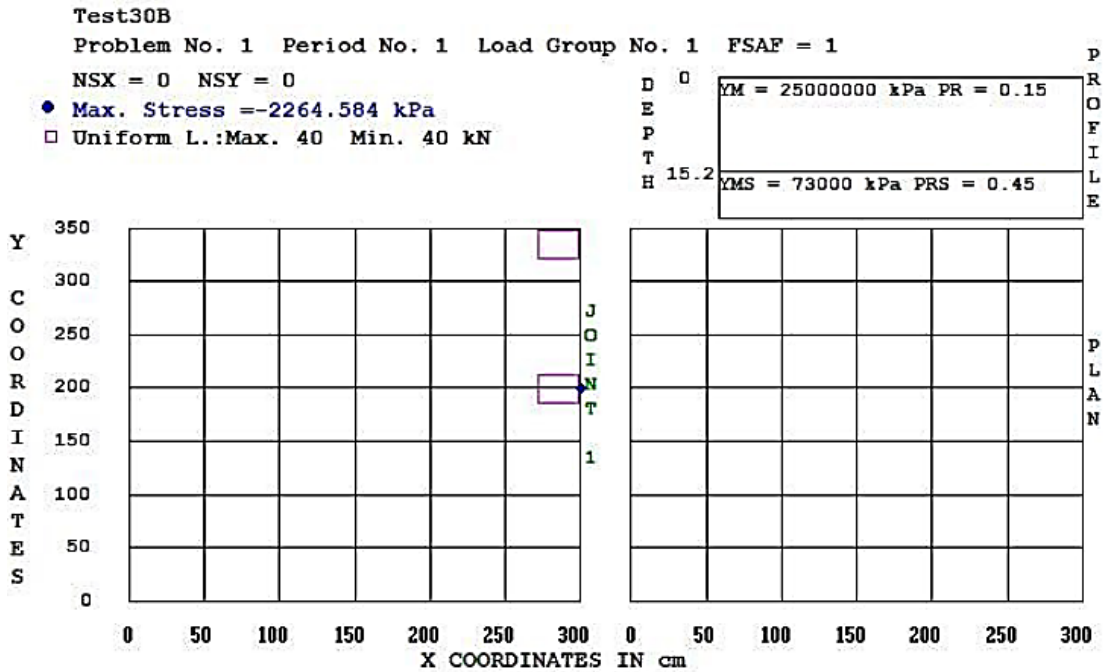

(f)

Figure 7.8. KENPAVE Inputs and Outputs for the Concrete Pavement Sections under An Axle Load using the k-values Calculated by the Westergaard (1926) Method for (a) Control VGB Section Pre-rainfall, (b) Control VGB Section Post-rainfall, (c) VGB/NW Section Pre-rainfall, (d) VGB/NW Section Post-rainfall, , (e) RCA/NW Section Pre-rainfall, and (f) RCA/NW Section Post-rainfall.

7.4 Analysis of Concrete Slab Based on Unpaved Road Design Values

In the preceding sections, the responses of concrete slabs under corner or edge loading were analyzed by considering the pavement foundation as springs with a subgrade reaction modulus. The responses of concrete slabs under the same loading can be analyzed by considering the pavement foundation as a layered soil with varying resilient moduli. In this analysis, the same single axle load setup was used with a layered system based on the M_r values for base course and subgrade from the unpaved road tests in this study to estimate the changes in slab tensile stresses expected. The M_r values for the base course are those achieved through the modified Burmister solution for unpaved roads as described in Chapter 6. A single subgrade modulus was used in order to compare the expected changes in induced slab tensile stresses. The KENPAVE inputs and outputs for the VGB and the RCA sections are displayed in Figure 7.9 and Figure 7.10, respectively. Maximum slab tensile stresses for this single axle loading are expected in the same location as those based on the subgrade reaction modulus in the paved tests, beneath the inner wheel load.

These KENPAVE outputs for the concrete pavement sections using the M_r values from the unpaved tests are summarized in Figure 7.11 for a single estimated 2% CBR subgrade M_r at 10,300 kPa multiplied by the CBR (AASHTO 1993). The overall increased base course moduli estimated from unpaved plate load testing indicate general reductions in expected slab tensile stresses when compared against those estimated based on the subgrade reaction modulus from the paved tests. The calculated tensile stresses in the concrete slab on the RCA/NW section pre-rainfall based on the k-value from the paved road test was nearly equal to those based on the M_r values from the unpaved layered section test. The calculated tensile stresses in the slab based on the Mr values for the unpaved VGB sections were 6% to 8% lower than those estimated using

the k-values from the paved tests. Even though variations in slab tensile stresses are limited to 5% or less based on these estimates, lower slab tensile stresses are expected through RCA replacement as well as geosynthetic stabilization based on these KENPAVE simulations.

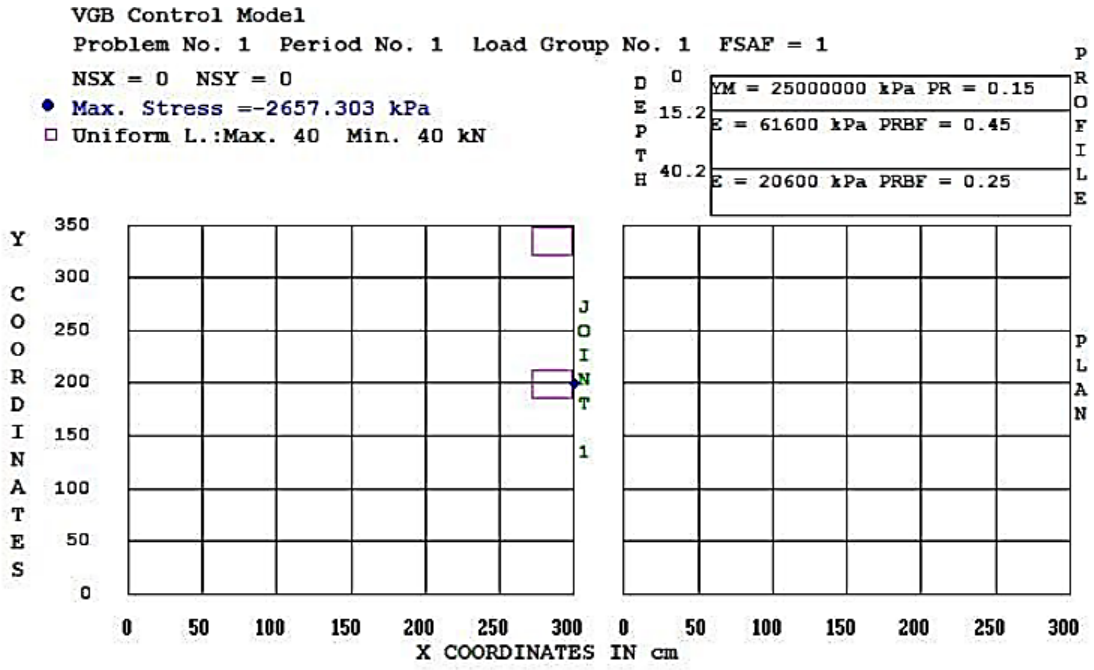

(a)

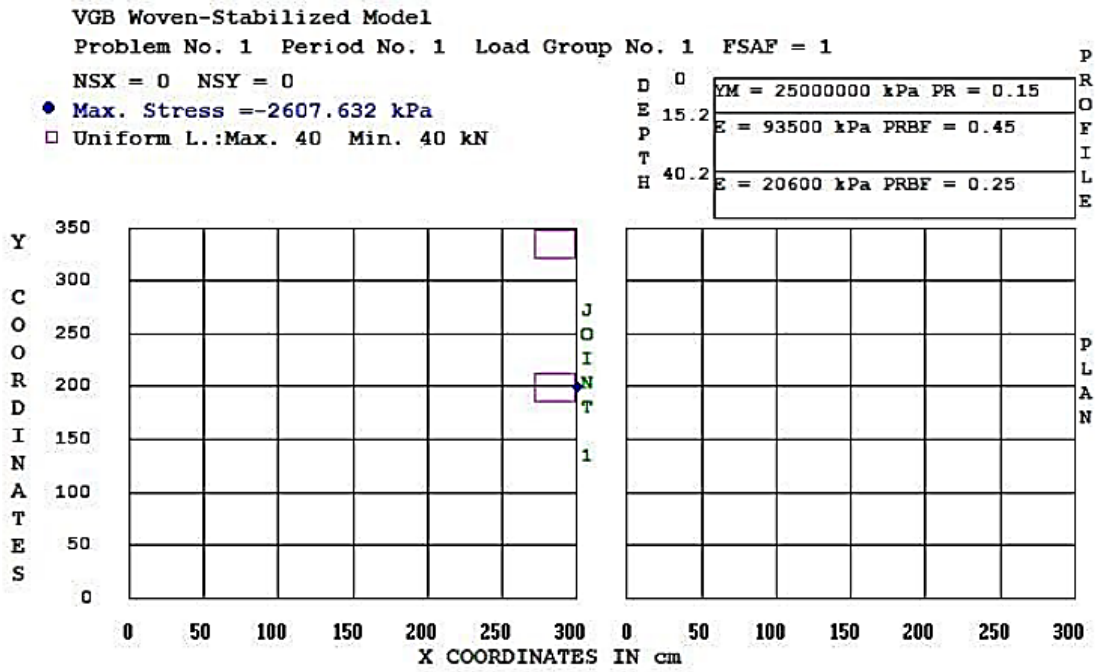
VGB Woven-Stabilized Model
Problem No. 1 Period No. 1 Load Group No. 1 FSAF = 1
NSX = 0 NSY = 0
Max. Stress =-2607.632 kPa
Uniform L.:Max. 40 Min. 40 kN
DEPTH
0
15.2
40.2
YM = 25000000 kPa PR = 0.15
E = 93500 kPa PRBF = 0.45
E = 20600 kPa PRBF = 0.25
PROFILE
Y COORDINATES
350
300
250
200
150
100
50
0
JOINT 1
PLAN
0 50 100 150 200 250 300
X COORDINATES IN cm

(b)

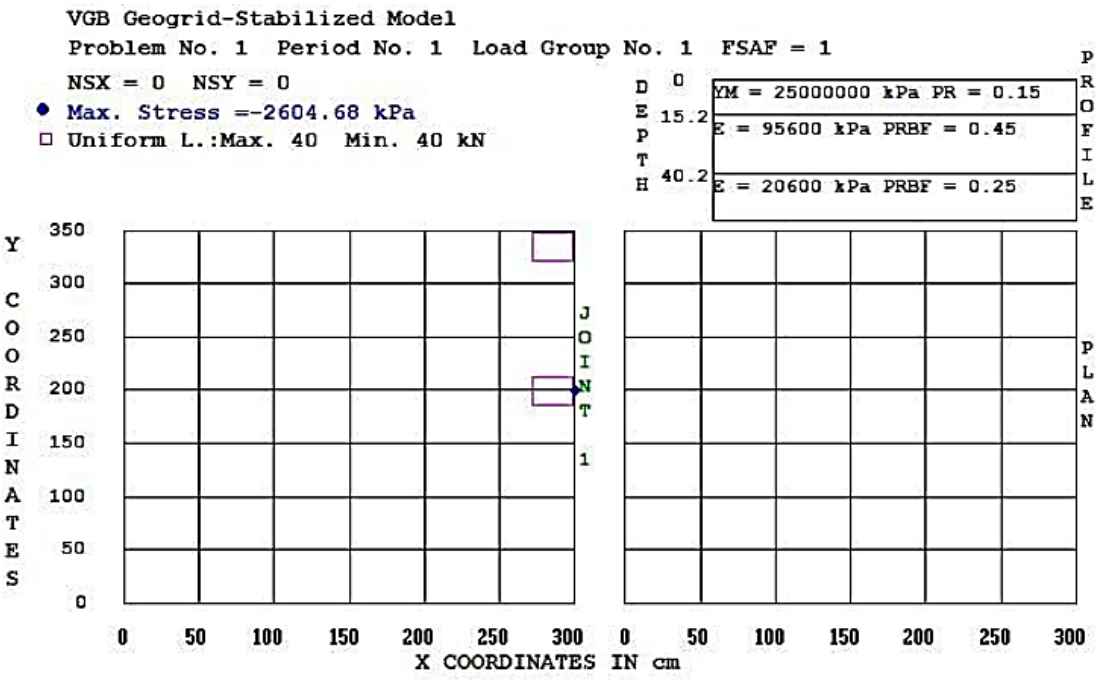
VGB Geogrid-Stabilized Model
Problem No. 1 Period No. 1 Load Group No. 1 FSAF = 1
NSX = 0 NSY = 0
Max. Stress =-2604.68 kPa
Uniform L.:Max. 40 Min. 40 kN
DEPTH
0
15.2
40.2
YM = 25000000 kPa PR = 0.15
E = 95600 kPa PRBF = 0.45
E = 20600 kPa PRBF = 0.25
PROFILE
Y COORDINATES
350
300
250
200
150
100
50
0
JOINT 1
PLAN
0 50 100 150 200 250 300
X COORDINATES IN cm

(c)

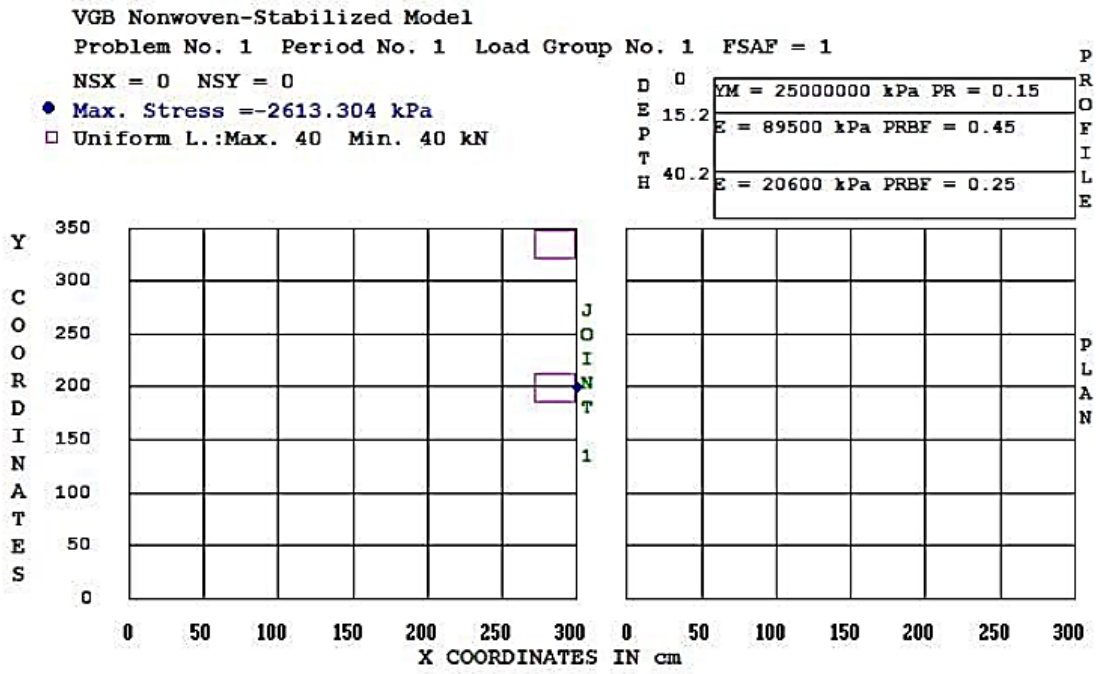

(d)

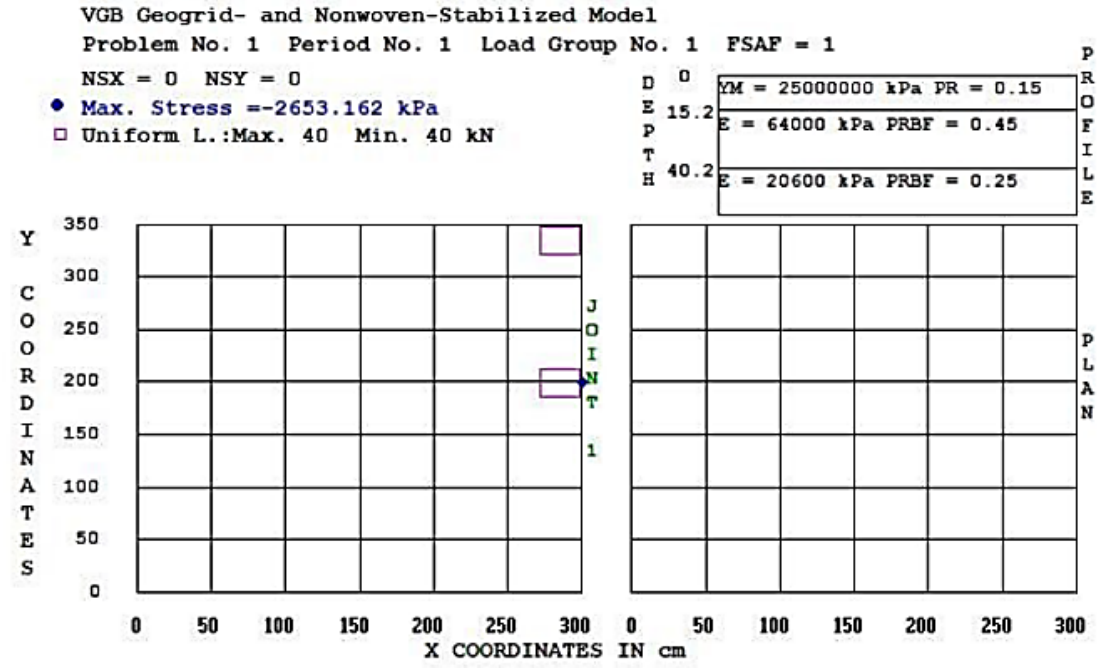

(e)

Figure 7.9. KENPAVE Inputs and Outputs for Slab Tensile Stresses using the M_r Values from Unpaved VGB Sections on Equal CBR Subgrade.
for (a) Control VGB Section (b) VGB/W Section, (c) VGB/GG Section, (d) VGB/NW Section, and (e) VGB/GG/NW Section.

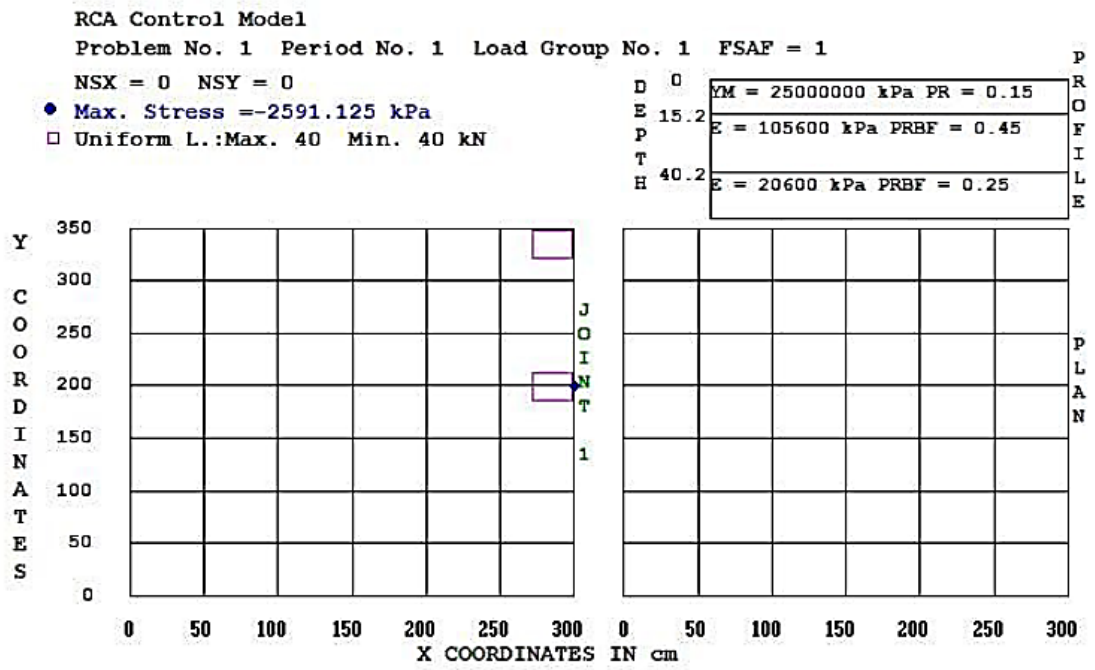
RCA Control Model
Problem No. 1 Period No. 1 Load Group No. 1 FSAF = 1
NSX = 0 NSY = 0
Max. Stress =-2591.125 kPa
Uniform L.:Max. 40 Min. 40 kN
DEPTH
0
15.2
40.2
YM = 25000000 kPa PR = 0.15
E = 105600 kPa PRBF = 0.45
E = 20600 kPa PRBF = 0.25
PROFILE
Y COORDINATES
350
300
250
200
150
100
50
0
JOINT 1
PLAN
0 50 100 150 200 250 300
X COORDINATES IN cm

(a)

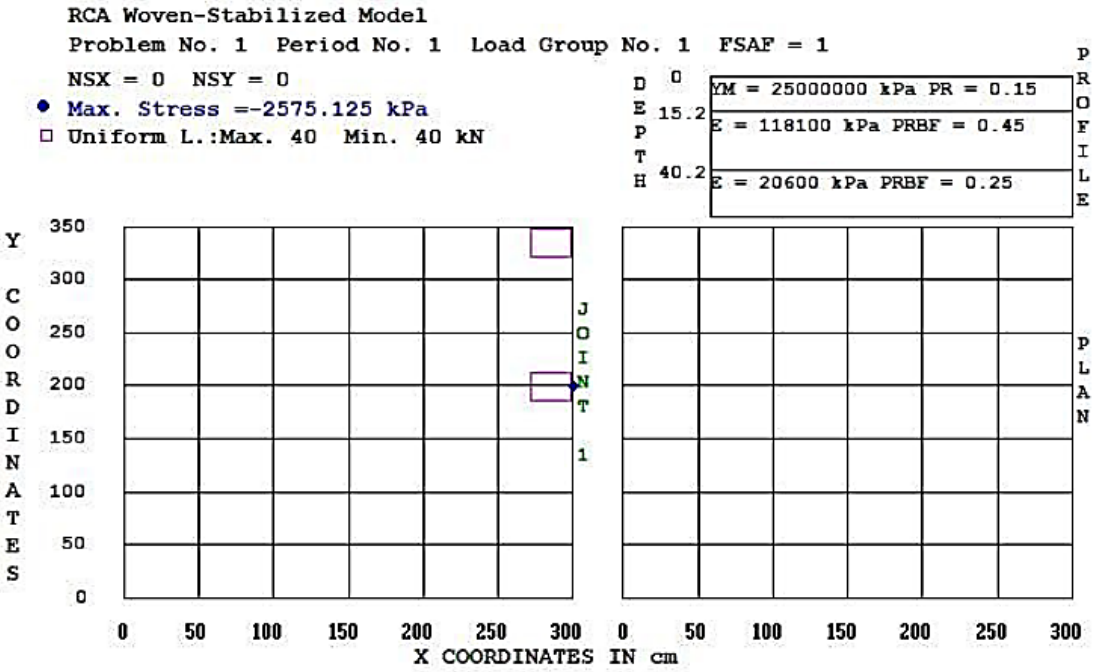
RCA Woven-Stabilized Model
Problem No. 1 Period No. 1 Load Group No. 1 FSAF = 1
NSX = 0 NSY = 0
Max. Stress =-2575.125 kPa
Uniform L.:Max. 40 Min. 40 kN
DEPTH
0
15.2
40.2
YM = 25000000 kPa PR = 0.15
E = 118100 kPa PRBF = 0.45
E = 20600 kPa PRBF = 0.25
PROFILE
Y COORDINATES
350
300
250
200
150
100
50
0
JOINT 1
PLAN
0 50 100 150 200 250 300
X COORDINATES IN cm

(b)

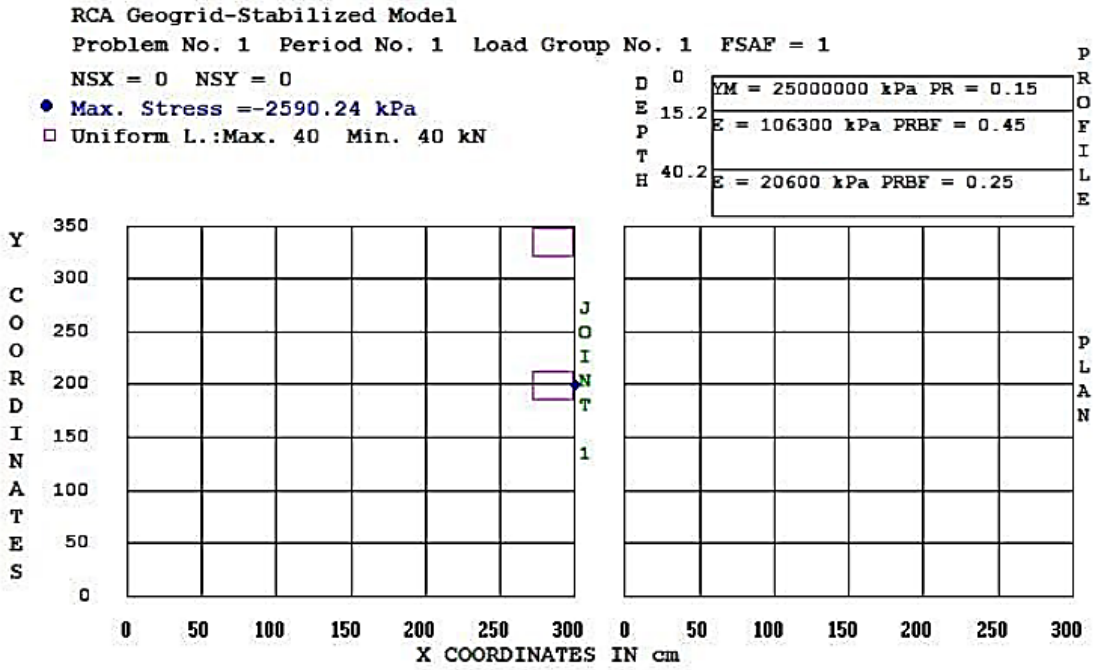
RCA Geogrid-Stabilized Model
Problem No. 1 Period No. 1 Load Group No. 1 FSAF = 1
NSX = 0 NSY = 0
Max. Stress =-2590.24 kPa
Uniform L.:Max. 40 Min. 40 kN
DEPTH
0
15.2
40.2
YM = 25000000 kPa PR = 0.15
E = 106300 kPa PRBF = 0.45
E = 20600 kPa PRBF = 0.25
PROFILE
Y COORDINATES
350
300
250
200
150
100
50
0
JOINT 1
PLAN
0 50 100 150 200 250 300
X COORDINATES IN cm

(c)

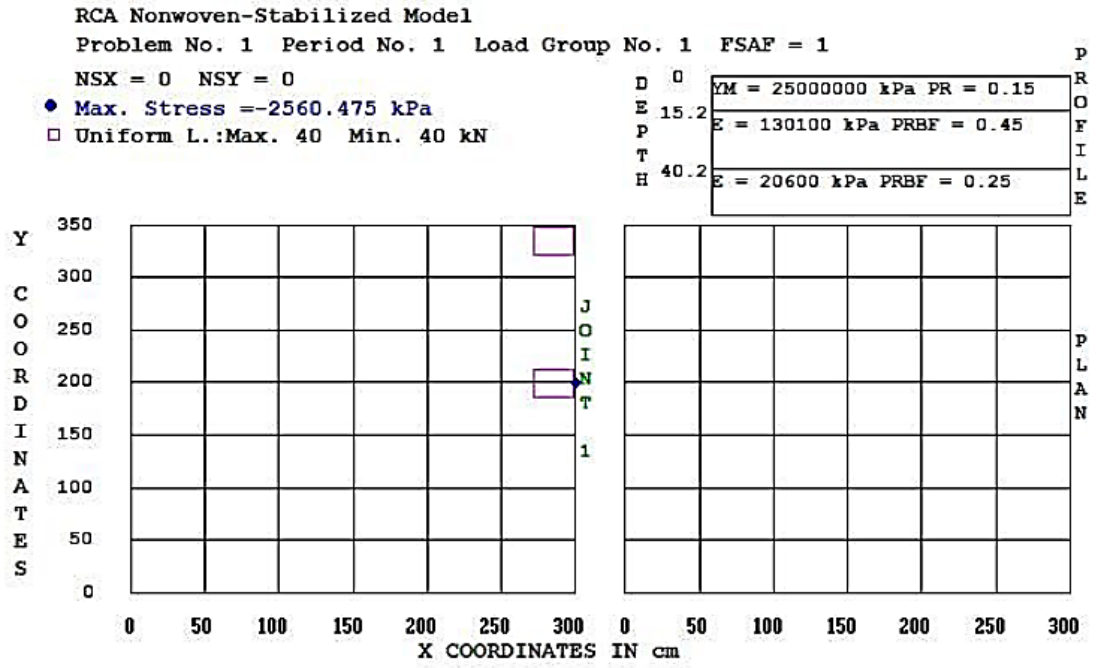
RCA Nonwoven-Stabilized Model
Problem No. 1 Period No. 1 Load Group No. 1 FSAF = 1
NSX = 0 NSY = 0
Max. Stress =-2560.475 kPa
Uniform L.:Max. 40 Min. 40 kN
DEPTH
0
15.2
40.2
YM = 25000000 kPa PR = 0.15
E = 130100 kPa PRBF = 0.45
E = 20600 kPa PRBF = 0.25
PROFILE
Y COORDINATES
350
300
250
200
150
100
50
0
JOINT 1
PLAN
0 50 100 150 200 250 300
X COORDINATES IN cm

(d)

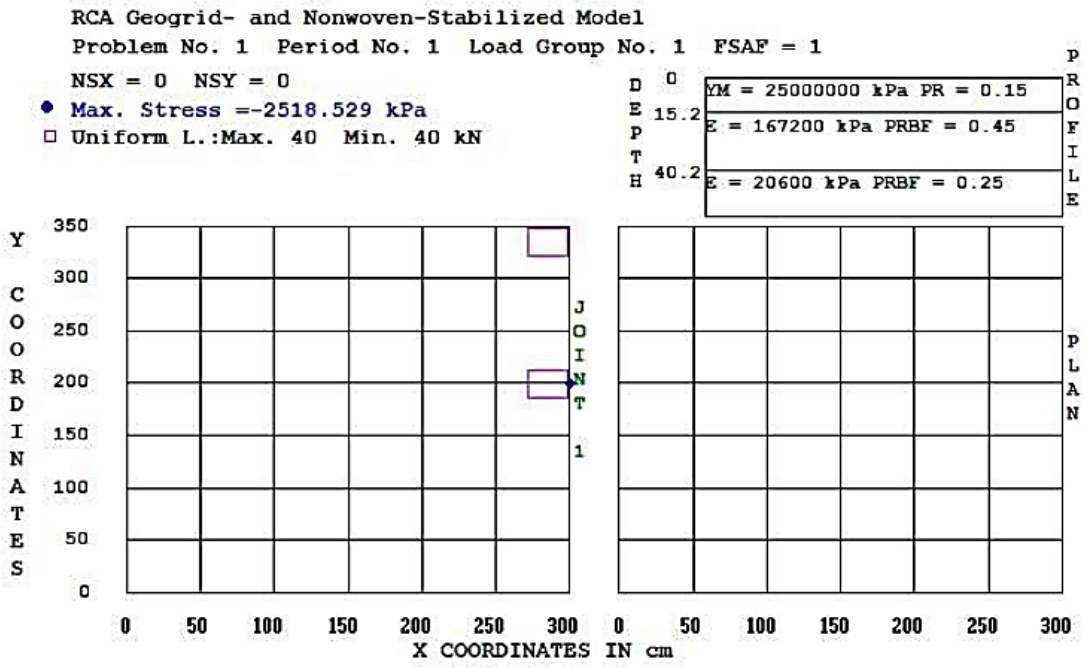

(e)

Figure 7.10. KENPAVE Inputs and Outputs for Slab Tensile Stresses using the M_r Values from Unpaved RCA Sections on Equal CBR Subgrade.
for (a) Control RCA Section (b) RCA/W Section, (c) RCA/GG Section, (d) RCA/NW Section, and (e) RCA/GG/NW Section.

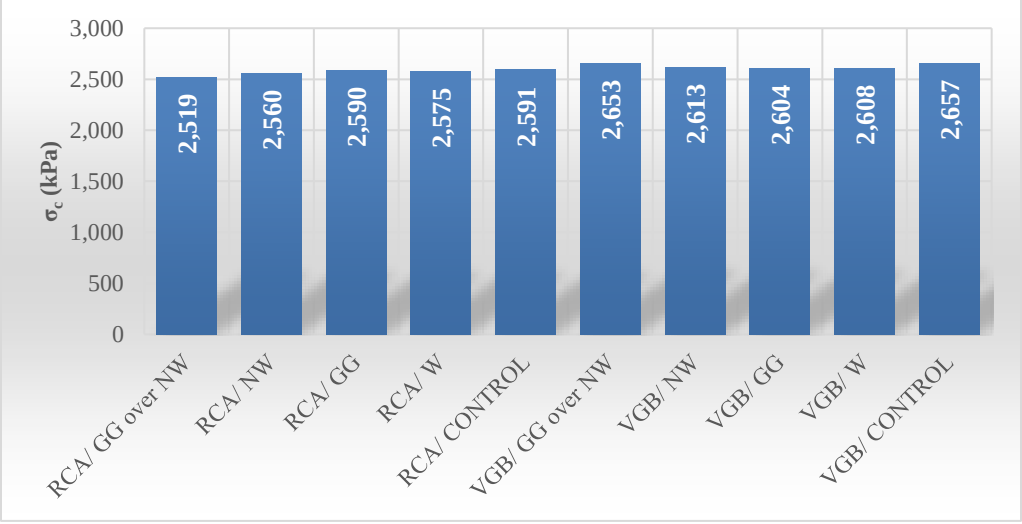

Figure 7.11. Calculated Tensile Stresses in Concrete Slabs under An Axle Load of 80 kN Based on the M_r Values of Base Course Sections on 2%-CBR Subgrade in Unpaved Tests.

The relationship between the calculated slab tensile stress and the measured permanent deformation is displayed in Figure 7.12. The permanent deformation at 9,000 load cycles is plotted against the slab tensile stress calculated in KENPAVE using the actual subgrade resilient moduli calculated from the DCP-estimated CBR. This figure shows that even a small change in the slab tensile stresses could occur with a great change in the permanent deformation incurred from load cycles. When full contact between the concrete slab and the base is maintained, the slab tensile stress changes might be minimal. Subgrade/base uneven displacements would minimize consistent contact between the slab and the underlying foundation layer, and this change in underlying support would induce higher slab tensile stresses and the likelihood for concrete slab cracking. Due to limited number of load cycles used in this study, support loss beneath the concrete slab might not be induced and the impact of support loss was not evaluated.

A consistent relationship between slab tensile stress and incurred permanent deformation is shown in Figure 7.12. The closed large-scale box test system with a contained non-erodible shoulder and base course in this study prevented loss of contact between the concrete slab and the foundation layer that the KENPAVE model would estimate from prior finite element models that the nodal system is based on.

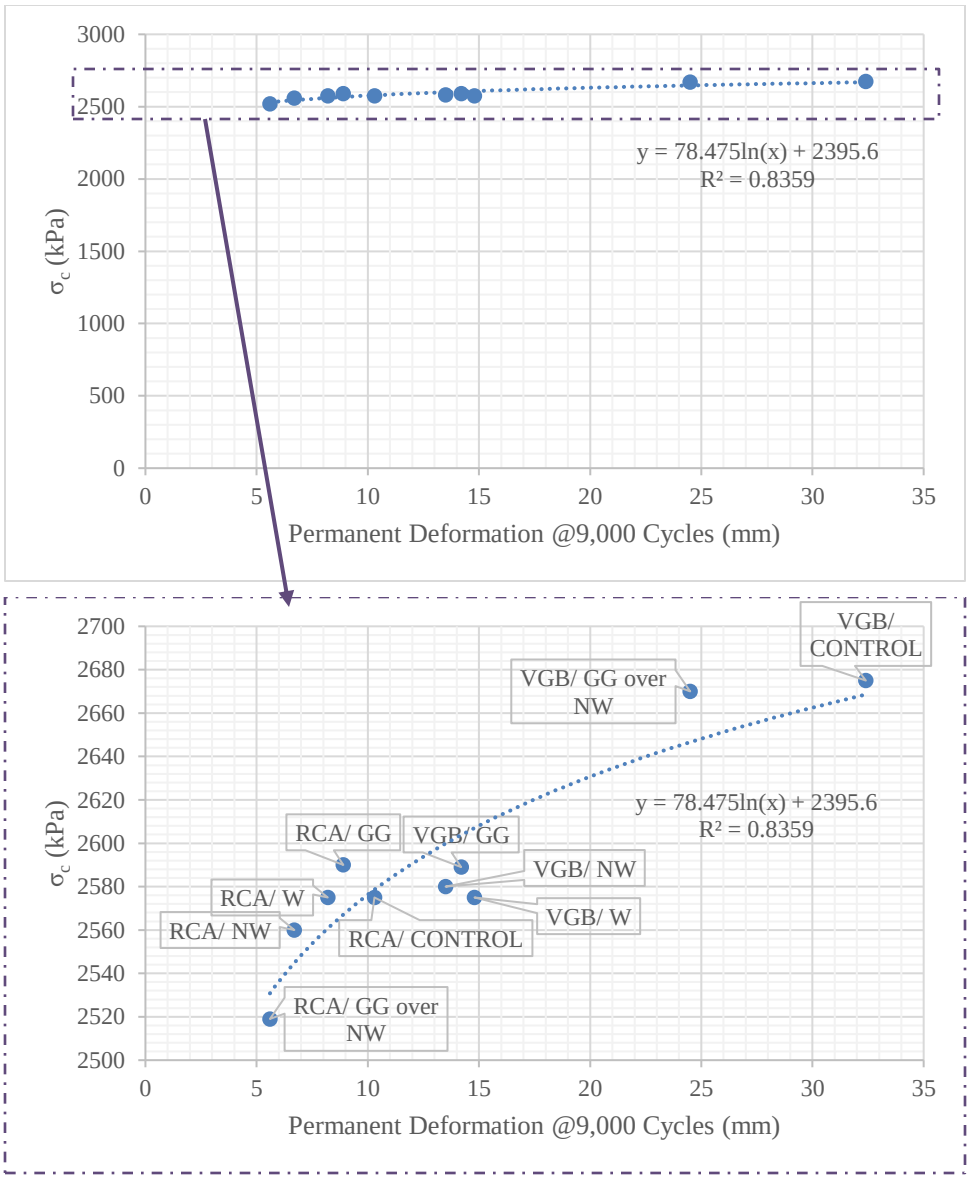

Figure 7.12. Calculated Tensile Stresses in Concrete Slabs Based on the M_r values from Unpaved Road Tests versus Permanent Deformation after 9,000 Load Cycles.

Chapter 8. Conclusions and Recommendations

8.1 Conclusions

This study investigated the performance of unpaved and concrete paved roads with geosynthetic-stabilized recycled aggregate bases over weak subgrade under cyclic loading using a large-scale test box compared against non-stabilized virgin granular base course. Nonwoven geotextile (NW), woven geotextile (W), geogrid (GG), and a combination of geogrid and nonwoven geotextile (GG/NW) were adopted in unpaved road test sections. Nonwoven geotextile was used in concrete pavement test sections. Recycled concrete aggregate (RCA) and reclaimed asphalt pavement (RAP) were used and compared with virgin granular base (VGB). Most test sections were evaluated on weak subgrade with 2% CBR. Below are the main conclusions from this study.

1. The reduction in permanent deformations of unpaved roads and concrete pavements under cyclic loading was achieved by the replacement of VGB with RCA, indicating that the RCA is more resistant to load-repetition breakdown and subsequent damage. RCA replacement of VGB reduced permanent deformation 50% in unpaved sections and 18% in paved sections.
2. The addition of a geosynthetic layer at the interface between base course and subgrade minimized the permanent deformations of the unpaved roads as well as the concrete pavement under cyclic loading. Separation, lateral restraint, and tensioned membrane played roles in the performance of these road sections. The importance of these functions depended on the magnitudes of load and deformation as well as the adequate compaction of the base course in the test section preparation. In the unpaved sections, the addition of

geosynthetics reduced permanent deformations an average of 48% in VGB and 29% in RCA. In paved sections, nonwoven geotextile reduced permanent deformation in VGB by 27%.

3. Both the replacement of VGB with RCA and the use of geosynthetic layer generally reduced the vertical interface stresses underneath the loading plate and increased their stress distribution angles. Replacement of VGB with RCA in unpaved sections increased stress distribution angles over 30%. Addition of geosynthetics to VGB in unpaved sections increased stress distribution angles 49%.
4. The modified Burmister solution was used in this study to address the added geosynthetic layer at the interface between base course and subgrade and back-calculated the equivalent resilient moduli of control and geosynthetic-stabilized aggregate bases. This method correlated well with the permanent deformations of the test sections at a large number of load cycles. The stress reduction method, based on the measured vertical interface stresses, could also back-calculate the resilient moduli in reasonable magnitudes; however, those values did not correlate as well to the permanent deformations as the modified Burmister solution. The elastic solution, based on the elastic rebound (or resilient deformation) of a test section, did not back-calculate the resilient modulus reasonably because the geosynthetic-stabilized section had larger resilient deformation than the control section.
5. The moduli of subgrade reaction of the unpaved test sections were estimated by the AASHTO (1993) design chart based on the back-calculated equivalent resilient modulus of the base course by the modified Burmister solution or the stress reduction method and the estimated resilient modulus of the subgrade. These subgrade reaction moduli were

within a reasonable range of those in the literature. The replacement of VGB by RCA and the use of a geosynthetic layer increased the modulus of subgrade reaction of the base course.

6. RCA and nonwoven geotextile improved the performance of concrete pavements on granular bases over weak subgrade by the reduction of permanent deformations under cyclic loading. Rainfall caused immediately increased permanent deformations in the paved sections subjected to cyclic loading, but its effect disappeared after less than 3,000 load cycles.
7. The modulus of subgrade reaction of the base course over the subgrade under a concrete pavement back-calculated using the Westergaard (1926) solution based on the assumption of the radius of relative stiffness equal to the distance from the loaded corner to the point of rotation was approximately 65% that estimated based on the AASHTO chart using the resilient moduli of the base and the subgrade in an unpaved road section.
8. Westergaard's (1926) theory for the estimated concrete slab tensile stresses that are minimally altered with significant changes in the k-values of the foundation layer was confirmed by the KENPAVE software in Huang (2004). Despite differences in slab stresses under 5% and well below the tensile strength of the concrete slab, there were significant changes in permanent deformation with changes in subgrade reaction modulus.

8.2 Recommendations

This study investigated the geosynthetic-stabilized recycled aggregate bases over weak subgrade in unpaved roads and concrete paved roads under limited number of cyclic loads in a laboratory setting. The benefits of the replacement with recycled concrete aggregate and the use of

geosynthetics in field may be different due to different aggregate sources, construction practice, and environmental conditions. Therefore, the results and conclusions from this study should be verified through field tests and evaluations in the future. Recycled concrete aggregate may degrade under repeated loading and environmental conditions in the long term, and these effects were not evaluated in this study. One of the main failure mechanisms for concrete pavements is loss of support due to soil erosion, but this possible effect was not investigated in this study. The Westergaard solution was developed based on infinite concrete slabs; the slab size effect was approximately considered. Further research is recommended to investigate these issues.

References

ACI Committee 318 (2019). *Building Code Requirements for Structural Concrete (ACI 318-19)*. American Concrete Institute, Farmington Hills, MI.

AASHTO (1986). *Guide for Design of Pavement Structures*. American Association of State Highway and Transportation Officials, Washington, D.C.

AASHTO (1993). *Guide for Design of Pavement Structures*. American Association of State Highway and Transportation Officials, Washington, D.C.

AASHTO (2015). *Mechanistic-Empirical Pavement Design Guide: A Manual of Practice*. American Association of State Highway and Transportation Officials (AASHTO), Washington, D.C.

AASHTO T307 (2017). *Standard Method of Test for Determining the Resilient Modulus of Soils and Aggregate Materials*. American Association of State Highway and Transportation Officials (AASHTO), Washington, DC.

ASTM D1140 (2017). *Standard Test Methods for Determining the Amount of Material Finer than 75-mu-m (No. 200) Sieve in Soils by Washing.* West Conshohocken, PA: American Society for Testing and Materials (ASTM) International.

ASTM D1556. (2016). *Standard Test Method for Density and Unit Weight of Soil In Place by Sand-Cone Method.* West Conshohocken, PA: American Society for Testing and Materials (ASTM) International.

ASTM D1883. (2016). *Standard Test Method for California Bearing Ratio (CBR) of Laboratory-Compacted Soils.* West Conshohocken, PA: American Society for Testing and Materials (ASTM) International.

ASTM D2166. (2016). *Standard Test Method for Unconfined Compressive Strength of Cohesive Soil.* West Conshohocken, PA: American Society for Materials and Testing (ASTM) International.

ASTM D421. (2007). *Standard Practice for Dry Preparation of Soil Samples for Particle-Size Analysis and Determination of Soil Constants.* West Conshohocken, PA: American Society for Testing and Materials (ASTM) International.

ASTM D4318. (2010). *Standard Test Methods for Liquid Limit, Plastic Limit, and Plasticity Index of Soils.* West Conshohocken, PA: American Society for Materials and Testing (ASTM) International.

ASTM D4643. (2017). *Standard Test Methods for Determination of Water Content of Soil and Rock by Microwave Oven Heating.* West Conshohocken, PA: American Society for Materials and Testing (ASTM) International.

ASTM D4648. (2016). *Standard Test Methods for Laboratory Miniature Vane Shear Test for Saturated Fine-Grained Clayey Soil.* West Conshohocken, PA: American Society for Materials and Testing (ASTM) International.

ASTM D698. (2012). *Standard Test Methods for Laboratory Compaction Characteristics of Soil Using Standard Effort (12,400 ft-lbf/ft3 (600 kN-m/m^3)).* West Conshohocken, PA: American Society for Testing and Materials (ASTM) International.

ASTM D7380. (2008). *Standard Test Method for Soil Compaction Determination at Shallow Depths Using 5-lb (2.3 kg) Dynamic Cone Penetrometer.* West Conshohocken, PA: American Society for Testing and Materials (ASTM) International.

Burmister, D. M. (1945). "The General Theory of Stresses and Displacements in Layered (Soil) Systems. I, II, III." *Journal of Applied Physics,* 16(2), pp. 89–94; 16(3) pp. 126-127; 16(5), pp. 296-302.

Burmister, D.M. (1958). “Evaluation of Pavement Systems of the WASHO Road Test by Layered System Methods.” *Highway Research Board Bulletin*, Highway Research Board (HRB), 177, pp. 26-54.

Coduto, D.P. (2001). *Foundation Design Principles and Practices, Second Edition*. Prentice-Hall, Inc., Upper Saddle River, NJ.

Crum, R.W., Taragin, A., Sutherland, E.C., Cashell, H.D., Burggraf, F. (1951). “Report on Maryland Road Test One-MD.” Highway Research Board, 36th Annual Meeting of the Michigan Highway Conference, Grand Rapids, Michigan.

Edgar Minerals. (2018, April). *EPK Clay*. Retrieved from http://www.edgarminerals.com/EPK-Clay.html

FHWA (1997a). *LTPP Data Analysis Phase I: Validation of Guidelines for k-value Selection and Concrete Performance Prediction*. FHWA-RD-96-198, Federal Highway Administration (FHWA), McLean, VA.

FHWA (1997b). *Design Pamphlet for the Determination of Design Subgrade in Support of the 1993 AASHTO Guide for the Design of Pavement Structures.* FHWA-RD-97-083, Federal Highway Administration (FHWA), McLean, VA.

Federal Highway Administration (FHWA) (2018, July). https://www.fhwa.dot.gov/infrastructure/50aasho.cfm .

Finney, E. A. (1951). *Report on Maryland Road Test One-MD*. Progress Report Summary, La Plata, MD: Michigan State Highway Department/ Highway Research Board.

Giroud, J.P., and Han, J. (2004a). "Design Method for Geogrid-Reinforced Unpaved Roads. I. Development of Design Method." *Journal of Geotechnical and Geoenvironmental Engineering*, American Society of Civil Engineers (ASCE), 130(8), pp. 775-786.

Giroud, J.P., and Han, J. (2004b). "Design Method for Geogrid-Reinforced Unpaved Roads. II. Calibration and Applications." *Journal of Geotechnical and Geoenvironmental Engineering*, American Society of Civil Engineers (ASCE), 130(8), pp. 787-797.

Han, J. (2015). *Principles and Practice of Ground Improvement*. John Wiley and Sons, Inc., Hoboken, NJ.

Han, J., and Thakur, J.K. (2014). "Sustainable roadway construction using recycled aggregates with geosynthetics." *Sustainable Cities and Society*, 14 (February), pp. 342-350.

Highway Research Board (1954). “Special Report 18: The WASHO Road Test, Part 1: Design, Construction, and Testing Procedures.” *Publication 310*, Fred Burggraf and W. J. Miller ed., National Academy of Sciences- National Research Council, Washington, D.C.

Huang, Y. H. (2004). *Pavement Analysis and Design, Second Edition*. Pearson Prentice Hall/ Pearson Education, Inc., Upper Saddle River, NJ.

Huang, Y.H. (2004). *KENPAVE* [Computer software]. University of Kentucky, Lexington, KY.

Jones, A. (1962). “Tables of Stresses in Three-Layer Elastic Systems.” *Bulletin 342*, Highway Research Board, pp. 176-214.

Jung, Y., Zollinger, D.G., Cho, B.H., Won, M., and Wimsatt, A.J. (2012). *Subbase and Subgrade Performance Investigation and Design Guidelines for Concrete Pavement*. FHWA/TX-12/0-6037-2, Technical Report, Texas Department of Transportation Research and Technology Implementation Office, Austin, TX.

Kansas Department of Transportation (KDOT) (2018, April). *LIST OF PREQUALIFIED GEOTEXTILE FABRICS*. Retrieved from Kansas Department of Transportation (KDOT) Index of Prequalified Materials and Material Sources: <http://www.ksdot.org/burmatrres/pql/default.asp>.

Kansas Department of Transportation (KDOT) (2018). *Standard Specifications for State Road and Bridge Construction*. https://www.ksdot.org/burconsmain/specprov/2015specprov.asp#1100.

Love, A.E.H. (1892). *A Treatise on the Mathematical Theory of Elasticity*. Cambridge: C.J. Clay, M.A. and Sons at the University Press.

MATLAB [Computer software]. MathWorks, Natick, MA.

Maxwell, S., Kim, W.H., Edil, T.B. and Benson, C.H. (2005). *Effectiveness of geosynthetics in stabilizing soft subgrades*. Wisconsin Highway Research Program #0092-45-15, Technical Report, Wisconsin Department of Transportation, Madison, WI.

Meyerhof, G.G. (1963). "Some Recent Research on the Bearing Capacity of Foundations." *Canadian Geotechnical Journal*, NRC Research Press, Vol. I, No. I., pp. 16-26.

NCHRP (National Cooperative Highway Research Program) (2004). *Guide for Mechanistic-Empirical Design of New and Rehabilitated Pavement Structures*. Final Rep. NCHRP 1-37A, Washington, D.C.

Ober, J.A. 2017. "Annual Review 2016: Mining Review." *Mining Engineering*, Society for Mining, Metallurgy, & Exploration (SME), 69 (5), pp. 50-59.

Oluokun, F.A., Burdette, E.G., and Deatherage, J.H. (1991). "Elastic Modulus, Poisson's Ratio, and Compressive Strength Relationships at Early Ages." *ACI Materials Journal*. American Concrete Institute (ACI), Vol. 88-M1, pp. 3-10.

Packard, R. G. (1984). *Thickness Design for Concrete Highways and Street Pavements*. Skokie, IL: Portland Cement Association.

PCA (2018). “Tech Note on Soil Sub Grade Modulus.” Portland Cement Association, July 24, 2018. http://www.cement.org/docs/default-source/th-bldgs-structures/da-reinforced-concrete/tech-note-on-soil-sub-grade-modulus.pdf .

Peattie, K.R. (1962). “Stress and Strain Factors for Three-Layer Elastic Systems.” *Bulletin 342*, Highway Research Board, pp. 215-253.

Putri, E.E., Rao, N.S.V.K., and Mannan, M.A. (2012). “Evaluation of Modulus of Elasticity and Modulus of Subgrade Reaction of Soils using CBR Test.” *Journal of Civil Engineering Research*, Scientific & Academic Publishing, 2(1): pp. 31-40.

Qian, Y., Han, J., Pokharel, S.K., and Parsons, R.L. (2011). "Determination of resilient modulus of subgrade using cyclic plate loading tests." *Proceedings of Geo-Frontiers*, ASCE, 4743-4751.

Sun, X. (2015). *Resilient Behavior and Permanent Deformations of Triaxial Geogrid Stabilized Bases over Weak Subgrade*. Ph.D. dissertation, Univ. of Kansas, Lawrence, KS.

Sun, X. and Han, J. (2019a). “Mechanistic-empirical analysis of geogrid-stabilized layered system: Part I. Solution development.” *Geosynthetics International*, 26(3), pp. 273–285.

Sun, X. and Han, J. (2019b). “Mechanistic-empirical analysis of geogrid-stabilized layered system: Part II. Solution verification and discussion.” *Geosynthetics International*, 26(3), pp. 286–296.

Sun, X., Han, J., Crippen, L., and Corey, R. (2017a). "Back-Calculation of Resilient Modulus and Prediction of Permanent Deformation for Fine-Grained Subgrade under Cyclic

Loading." *Journal of Materials in Civil Engineering*, American Society of Civil Engineers (ASCE) 29 (5): pp. 04016284-1 through 04016284-10.

Sun, X., Han, J., Crippen, L., Corey, R. (2017b). "Back-calculation of resilient modulus and prediction of permanent deformation for fine-grained subgrade under cyclic loading." *Journal of Materials in Civil Engineering*, American Society of Civil Engineers (ASCE), pp. 01016284-1: 04016284-10.

Sun, X., Han, J., Parsons, R.L., Thakur, J. (2018). "Equivalent California bearing ratios of multiaxial geogrid-stabilized aggregates over weak subgrade." *Journal of Materials in Civil Engineering* 30(11), American Society of Civil Engineers (ASCE), pp. 0401828-1: 0401828-10.

Sun, X., Han, J., Wayne, M.H., Parsons, R.L., Kwon, J. (2015). "Determination of load equivalency for unpaved roads." *Transportation Research Record: Journal of the Transportation Research Board*, No. 2473, Transportation Research Board of the National Academies, Washington, D.C., pp. 233–241.

Tseng, K.H. (1988). *A Finite Element Method for the Performance Analysis of Flexible Pavements*. Ph.D. Dissertation, Texas A&M, College Station, TX.

Tseng, K.H. and Lytton, R.L. (1989). "Prediction of permanent deformation in flexible pavement materials." *Implication of Aggregates in the Design, Construction, and Performance of Flexible Pavements, ASTM STP 1016*, H.G. Schreuders and C.R. Marek, Eds., American Society for Testing and Materials (ASTM), Philadelphia, PA, pp. 154-172.

USACE (1984a). *Engineering and Design: Geometrics for Roads, Streets, Walks, and Open Storage Areas: Mobilization Construction*. EM 1110-3-130, Department of the Army, U.S. Army Corps of Engineers, Washington D.C. 20314.

USACE (1984b). *Engineering and Design: RIGID PAVEMENTS FOR ROADS, STREETS, WALKS AND OPEN STORAGE AREAS: Mobilization Construction*. EM 1110-3-132, Department of the Army, U.S. Army Corps of Engineers, Washington D.C. 20314.

Walkenbach, T.N., Han, J., Li, Z., and Parsons, R.L. (2019). "Evaluation of Composite Subgrade Reaction Modulus of Geosynthetic-stabilized Recycled Subbase over Subgrade." *Geo-Congress 2019: Geoenvironmental Engineering and Sustainability*, American Society of Civil Engineers (ASCE), pp. 212-221.

Walkenbach, T.N., Han, J., Parsons, R.L., and Li, Z. (2020). "Effect of Geogrid Stabilization on Performance of Granular Base Course over Weak Subgrade." *Geo-Congress 2020: Geotechnical Earthquake Engineering and Special Topics*, American Society of Civil Engineers (ASCE), pp. 527-535.

Webster, S.L., Grau, R.H., Williams, T.P. (1992). *Description and Application of Dual Mass Dynamic Cone Penetrometer*. Instruction Report GL-92-3, Geotechnical Laboratory, Department of the (US) Army, Waterways Experiment Station, Corps of Engineers, Vicksburg, MS.

Westergaard, H.M. (1926). "Computation of Stresses in Concrete Roads." *Proceedings of the Fifth Annual Highway Research Board Held at Washington, D.C. December 3-4, 1925,*

Part I: Reports of Research Committees and of Special Investigation, Highway Research Board 5 (1), pp. 90-112.

Appendix A. Dynamic Cone Penetrometer (DCP) Results for Quality Assurance of Test Section Construction

Description of Method

Dynamic cone penetrometer (DCP) testing was chosen as the acceptance test method for proper construction of test sections in the big box. California Bearing Ratio (CBR) was the target for subgrade construction, and as testing progressed became a check for adequate base course installation (compaction). Equation (A.1) (Webster et. al., 1992) was used to determine CBR from the Dynamic Cone Penetration Index (DCPI) in mm/blow for the base course and subgrade sections. DCPI was taken as the slope of the line of blow count versus penetration depth in mm; base course and subgrade sections were separated graphically to determine DCPI for each location in the box. The average or mean of the several locations within each test setup was taken as the CBR for the test, as shown in Equation (A.2). Standard deviation (σ) and coefficient of variation (CV) were determined for each test section by Equations (A.3) and (A.4) , respectively.

$$CBR = \frac{292}{[DCPI(mm)]^{1.12}} \tag{A.1}$$

$$Mean = \bar{x} = \frac{\sum_{i=1}^{N} x_i}{N} \tag{A.2}$$

$$\sigma = \sqrt{\frac{\sum_{i=1}^{N}(x_i - \bar{x})^2}{N-1}} \tag{A.3}$$

$$CV = \frac{\sigma}{\bar{x}}$$

(A.4)

Summary of Data

Table A.1. Quality Assurance Summary of Test Sections.

Test No.	Paved?	Base Course	Geosynthetic	SG CBR	SG w[1]	Base Course Thickness (m)	Base Course C_r[2]	Base course CBR	Base Course w[1]
0		NONE-Subgrade only	NONE	2.8%	9%	0	n/a	n/a	n/a
11		VGB	W	2.2%	9.4%	0.254	97%	11.6%	6.5%
12		RCA	W	2.0%	9.7%	0.254	103%	13.4%	11.6%
13		RCA	CONTROL	2.1%	9.7%	0.254	106%	13.1%	9.8%
14		VGB	CONTROL	1.9%	9.8%	0.254	96%	12.4%	6.7%
15		VGB	GG	2.0%	9.8%	0.254	98%	16.3%	6.1%
16		RCA	GG	2.0%	9.8%	0.254	98%	14.9%	12.8%
17		VGB	NW	2.2%	9.8%	0.254	99%	13.0%	6.7%
18		RCA	NW	2.0%	9.7%	0.254	99%	16.3%	12.8%
19		VGB	GG	2.1%	9.6%	0.254	99%	14.5%	6.2%
20		VGB	NW	2.9%	9.1%	0.102	92%	14.0%	5.8%
21		RCA	GG over NW	2.0%	9.8%	0.254	102%	17.2%	11.2%
22		VGB	GG over NW	1.9%	9.8%	0.254	101%	14.9%	6.3%
23		VGB	NONE	5.4%	8.4%	0.102	95%	12.6%	5.4%
24		VGB	NW	4.9%	8.6%	0.102	99%	11.0%	6.9%
25		RAP	NONE	4.9%	8.7%	0.102	92%	6.9%	2.1%
26		RAP	NW	2.2%	9.4%	0.254	93%	8.0%	2.1%
27		RAP	W	4.9%	8.7%	0.102	97%	15.3%	1.6%
28	x	VGB	NONE	2.2%	9.64%	0.254	102%	8.5%	7.2%
29	x	VGB	NW	2.2%	9.68%	0.254	103%	10.8%	6.9%
30	x	RCA	NW	2.0%	9.77%	0.254	96%	15.20%	11.2%

[1] *w = Moisture Content*

[2] *C_r = Relative Compaction*

Subgrade Only Test

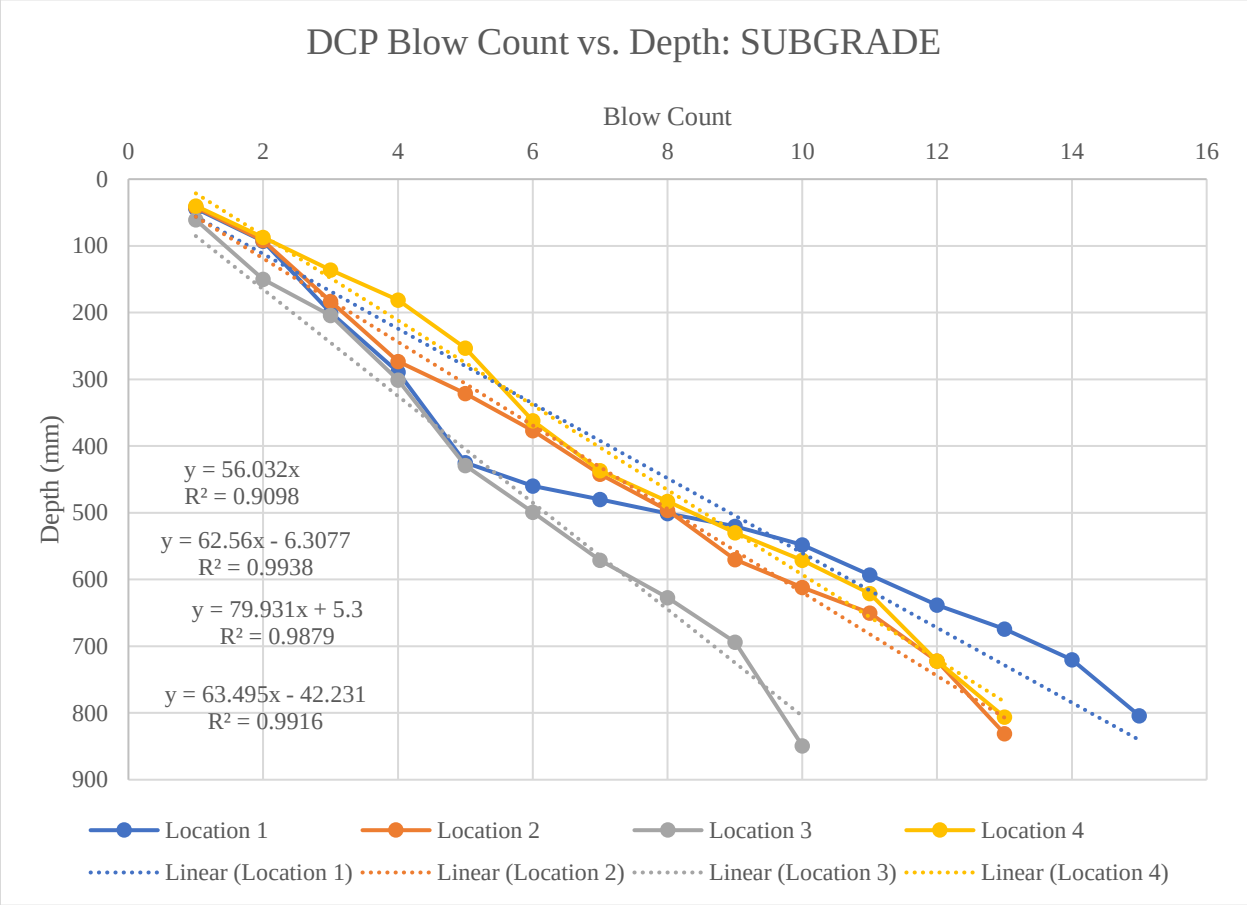

Figure 1. DCP Blow Count vs. Penetration Depth for Subgrade Only Test.

Table A.2. DCPI and CBR for Subgrade Only Test.

	DCPI (mm/Blow): SG	**CBR (%): SG**
Loc. 1	56.032	3.2
Loc. 2	62.56	2.8
Loc. 3	79.931	2.2
Loc. 4	63.495	2.8

Table A.3. CBR, Standard Deviation, Coefficient of Variation for Subgrade Only Test.

	Subgrade
Mean CBR (%)	2.8
Std. Dev. (σ)	0.438
CV	15.91%

Test 01: VGB/ NW/ 5%-CBR SG (old load sequence)

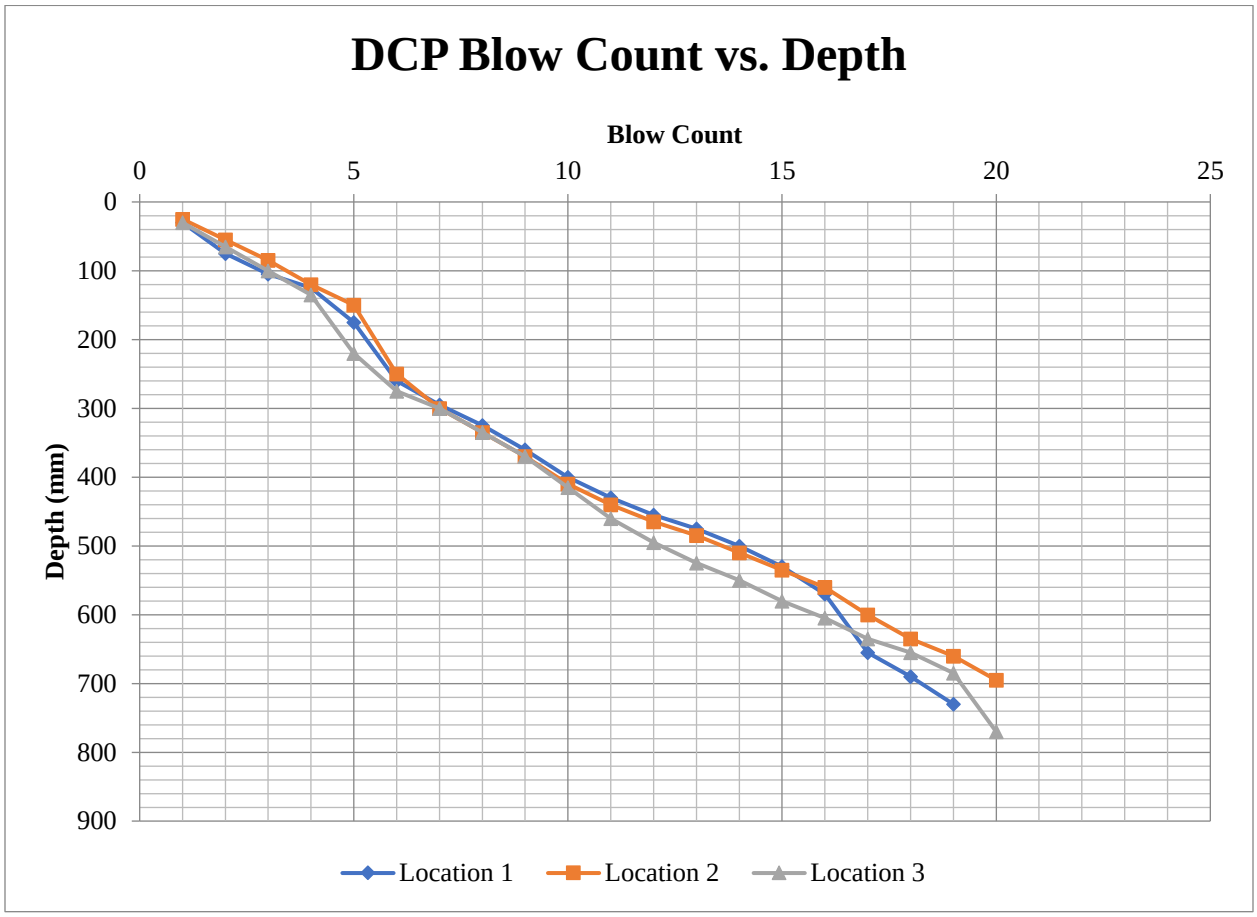

Figure 2. Test 01 DCP Blow Count vs. Penetration Depth.

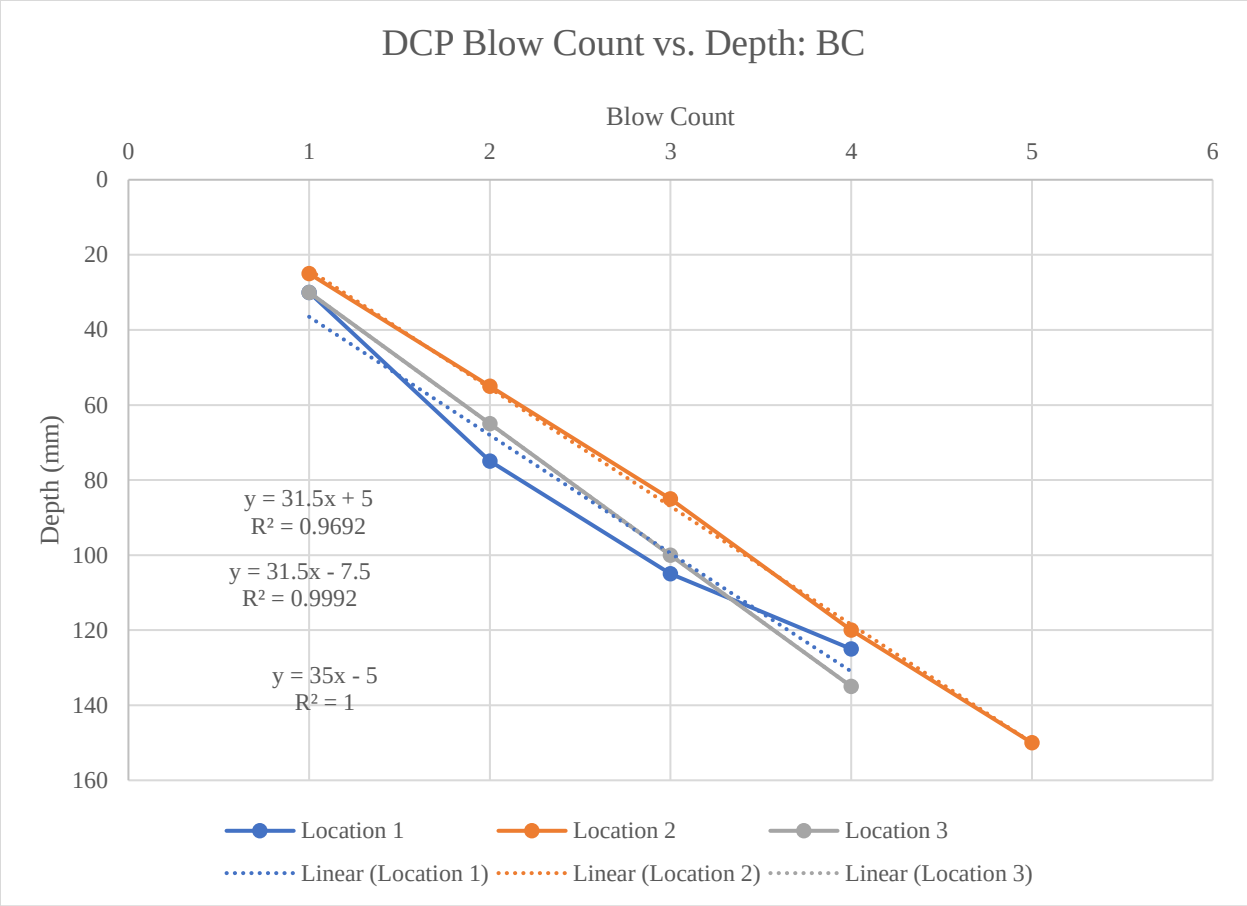

Figure 3. Test 01 DCPI: Base Course.

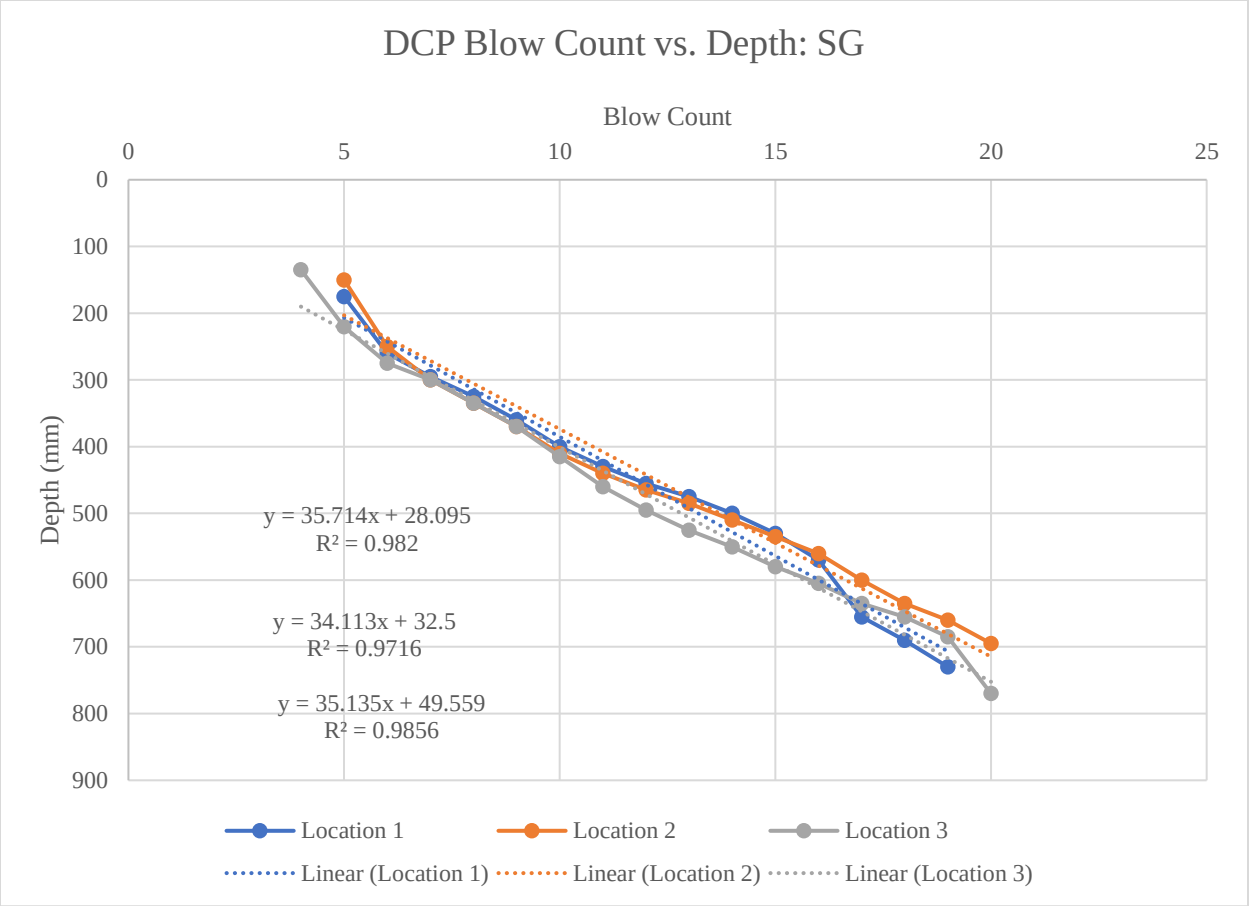

Figure 4. Test 01 DCPI: Subgrade.

Table A.4. Test 01 DCPI and CBR.

	DCPI (mm/Blow): BC	**DCPI (mm/Blow): SG**	**CBR (%): BC**	**CBR (%): SG**
Loc. 1	31.5	35.714	6.1	5.3
Loc. 2	31.5	34.113	6.1	5.6
Loc. 3	35	35.135	5.4	5.4

Table A.5. Test 01 CBR Output, Standard Deviation, Coefficient of Variation.

	Base Course	**Subgrade**
Mean CBR (%)	5.9	5.4
Std. Dev. (σ)	0.394	0.142
CV	6.67%	2.61%

Test 02: VGB/ W/ 5%-CBR SG (old load sequence)

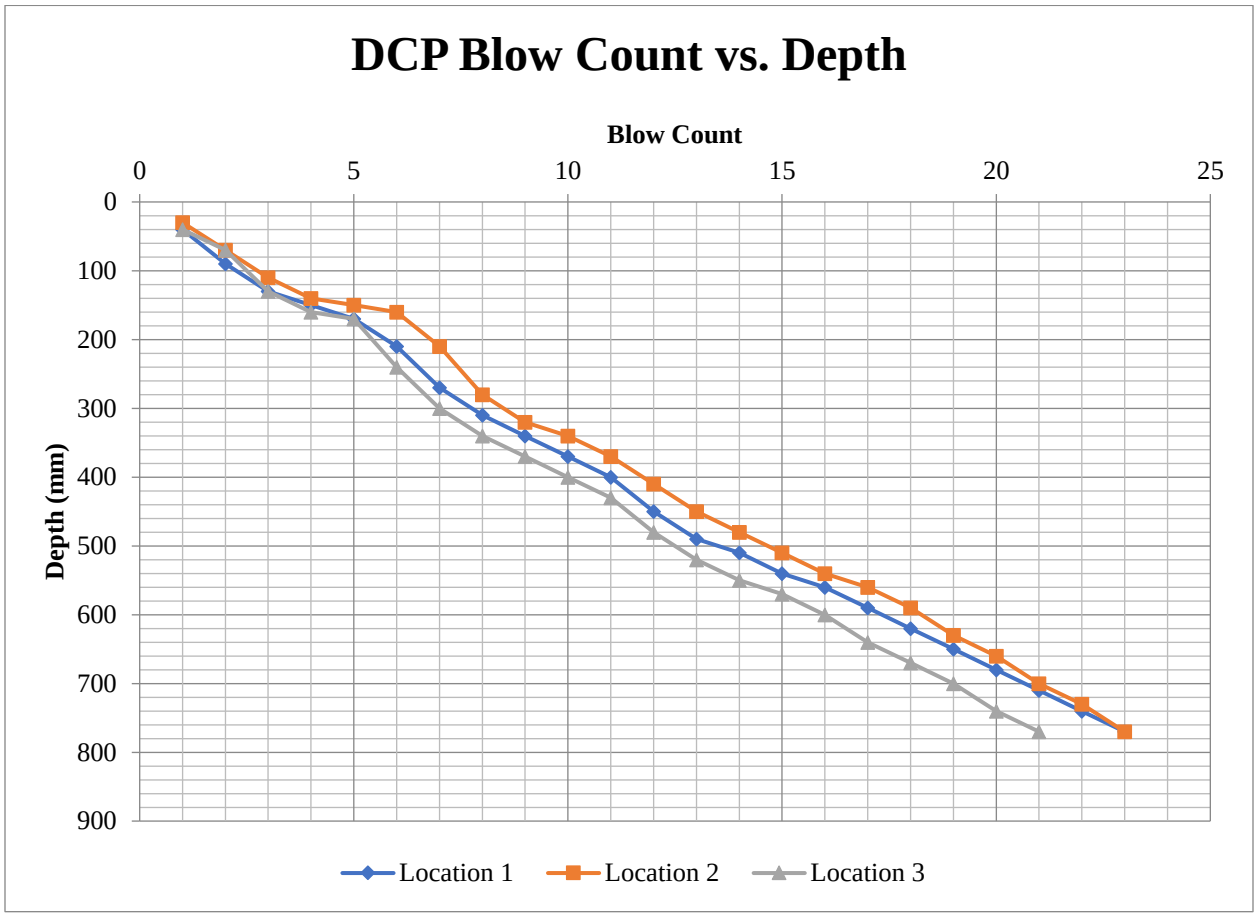

Figure 5. Test 02 DCP Blow Count vs. Penetration Depth.

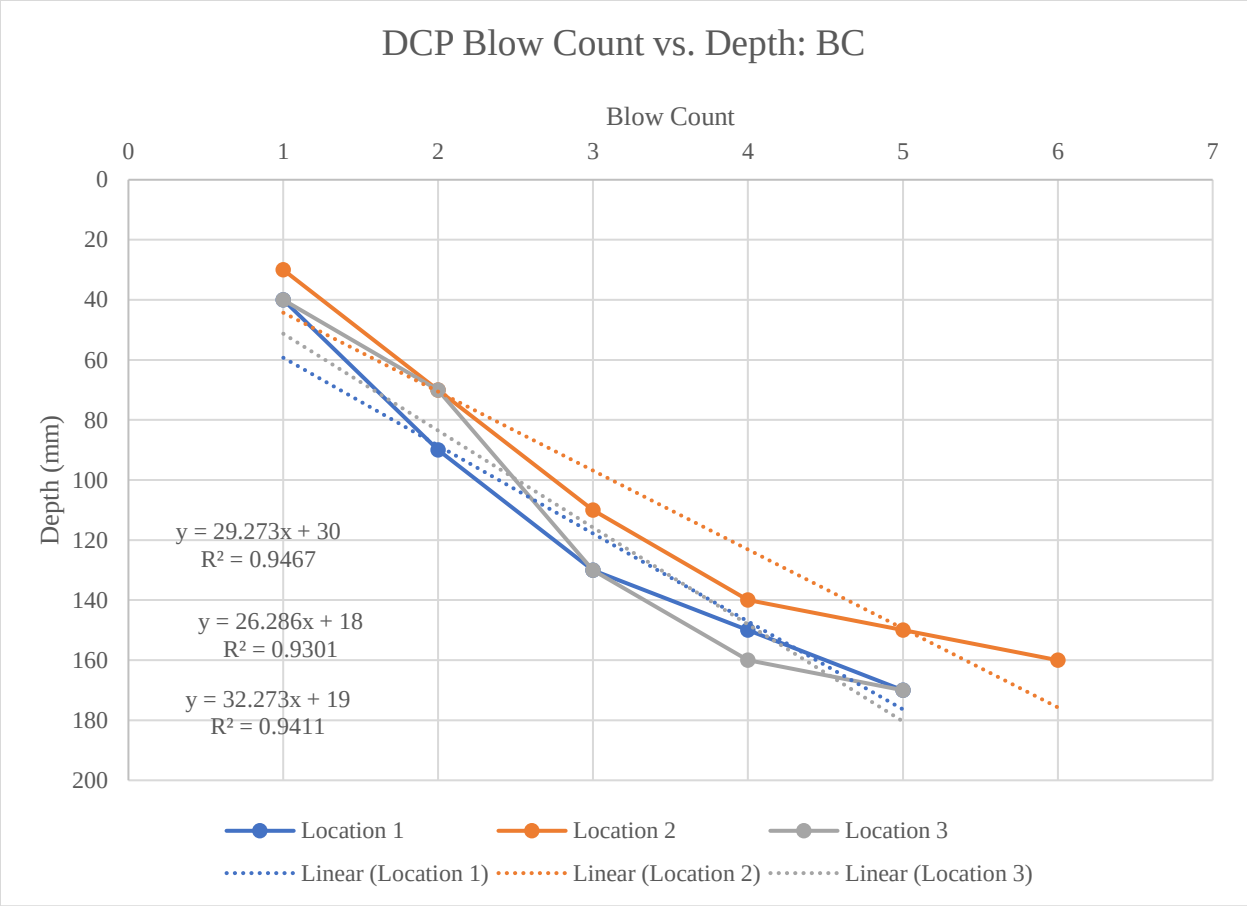

Figure 6. Test 02 DCPI: Base Course.

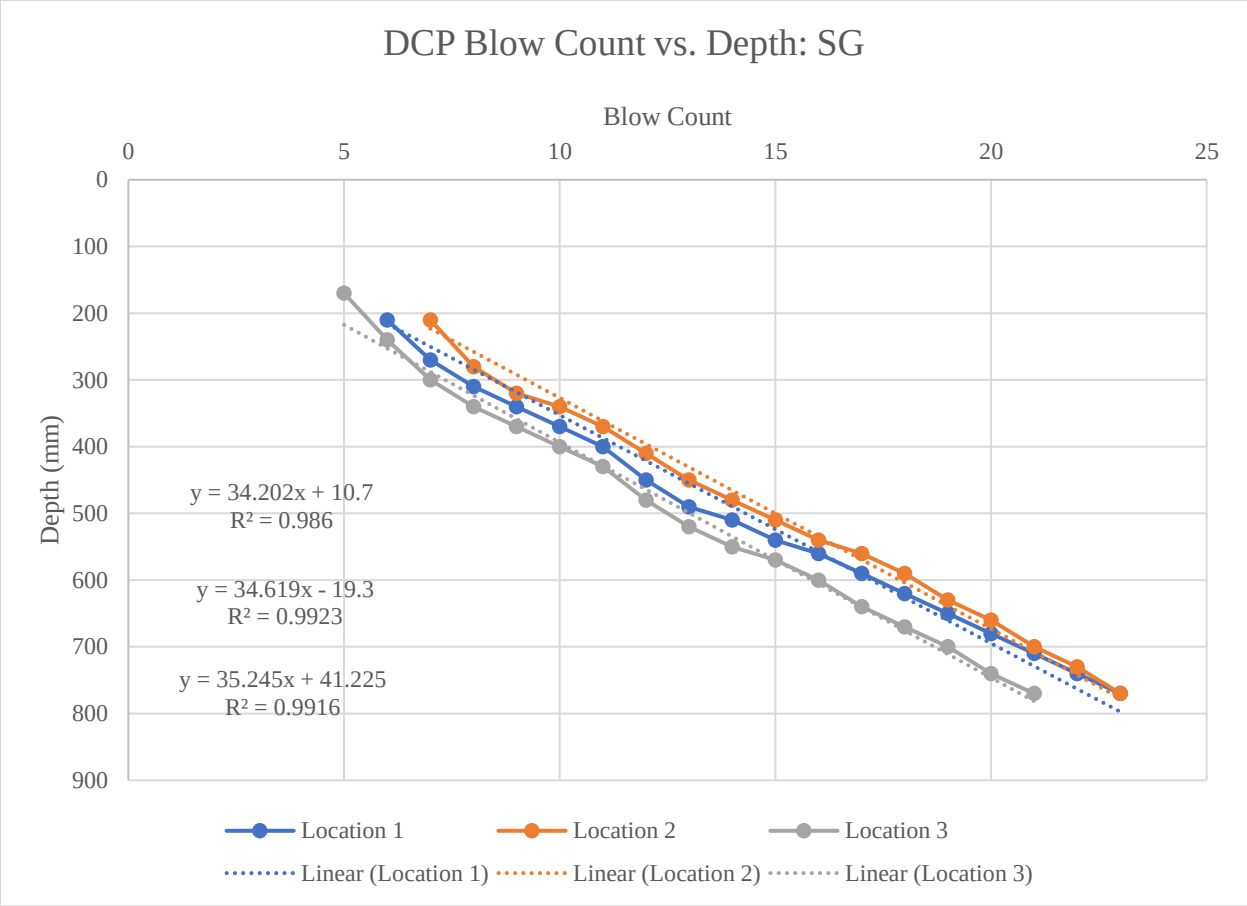

Figure 7. Test 02 DCPI: Subgrade.

Table A.6. Test 02 DCPI and CBR.

	DCPI (mm/Blow): BC	**DCPI (mm/Blow): SG**	**CBR (%): BC**	**CBR (%): SG**
Loc. 1	29.273	34.202	6.7	5.6
Loc. 2	26.286	34.619	7.5	5.5
Loc. 3	32.273	35.245	6.0	5.4

Table A.7. Test 02 CBR Output, Standard Deviation, Coefficient of Variation.

	Base Course	**Subgrade**
Mean CBR (%)	6.7	5.5
Std. Dev. (σ)	0.772	0.093
CV	11.51%	1.69%

Test 03: VGB/ 5%-CBR SG (Control) (old load sequence)

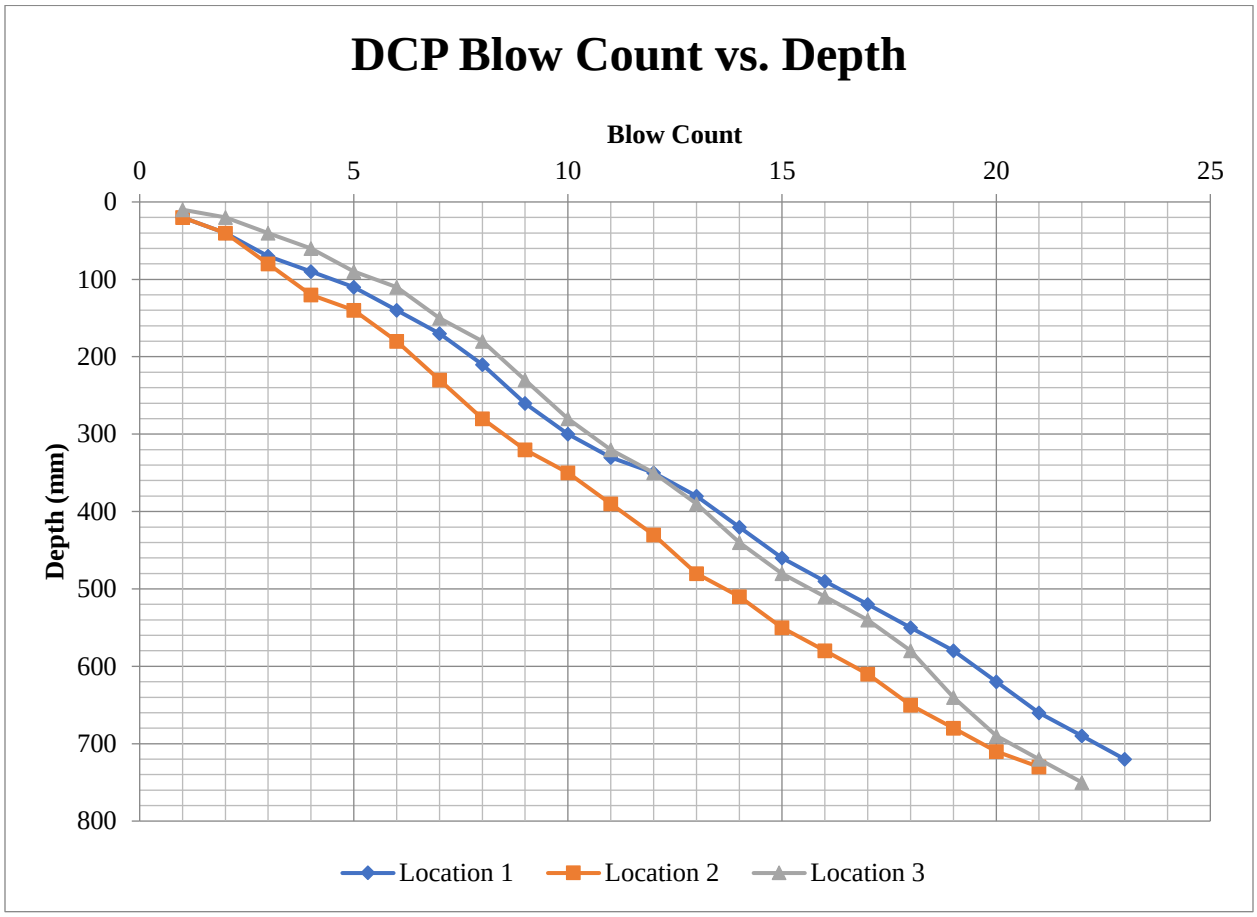

Figure 8. Test 03 DCP Blow Count vs. Penetration Depth.

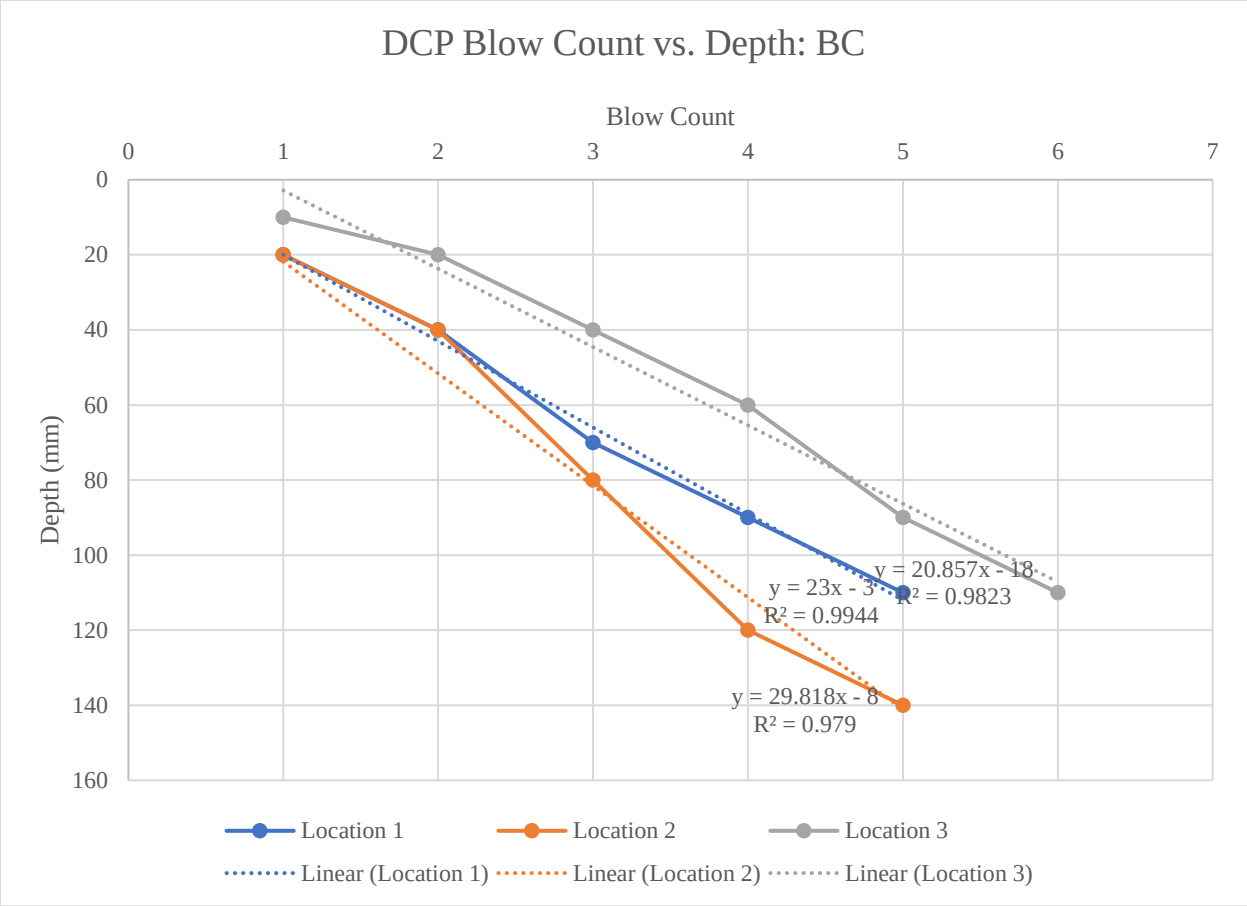

Figure 9. Test 03 DCPI: Base Course.

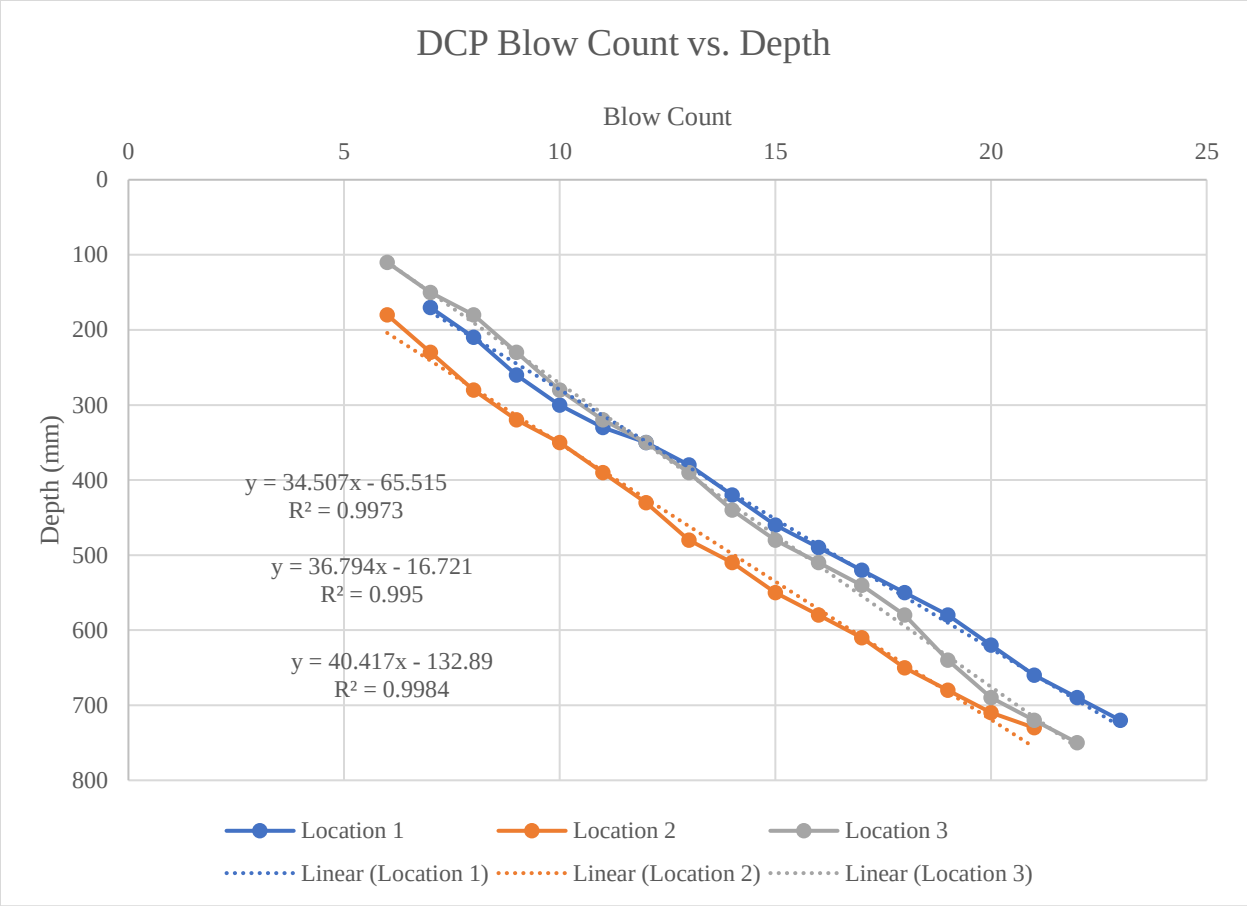

Figure 10. Test 03 DCPI: Subgrade.

Table A.8. Test 03 DCPI and CBR.

	DCPI (mm/Blow): BC	**DCPI (mm/Blow): SG**	**CBR (%): BC**	**CBR (%): SG**
Loc. 1	23	34.507	8.7	5.5
Loc. 2	29.818	36.794	6.5	5.1
Loc. 3	20.857	40.417	9.7	4.6

Table A.9. Test 03 CBR Output, Standard Deviation, Coefficient of Variation.

	Base Course	**Subgrade**
Mean CBR (%)	8.3	5.1
Std. Dev. (σ)	1.640	0.450
CV	19.72%	8.82%

Test 04: VGB/ GG/ 5%-CBR SG (old load sequence)

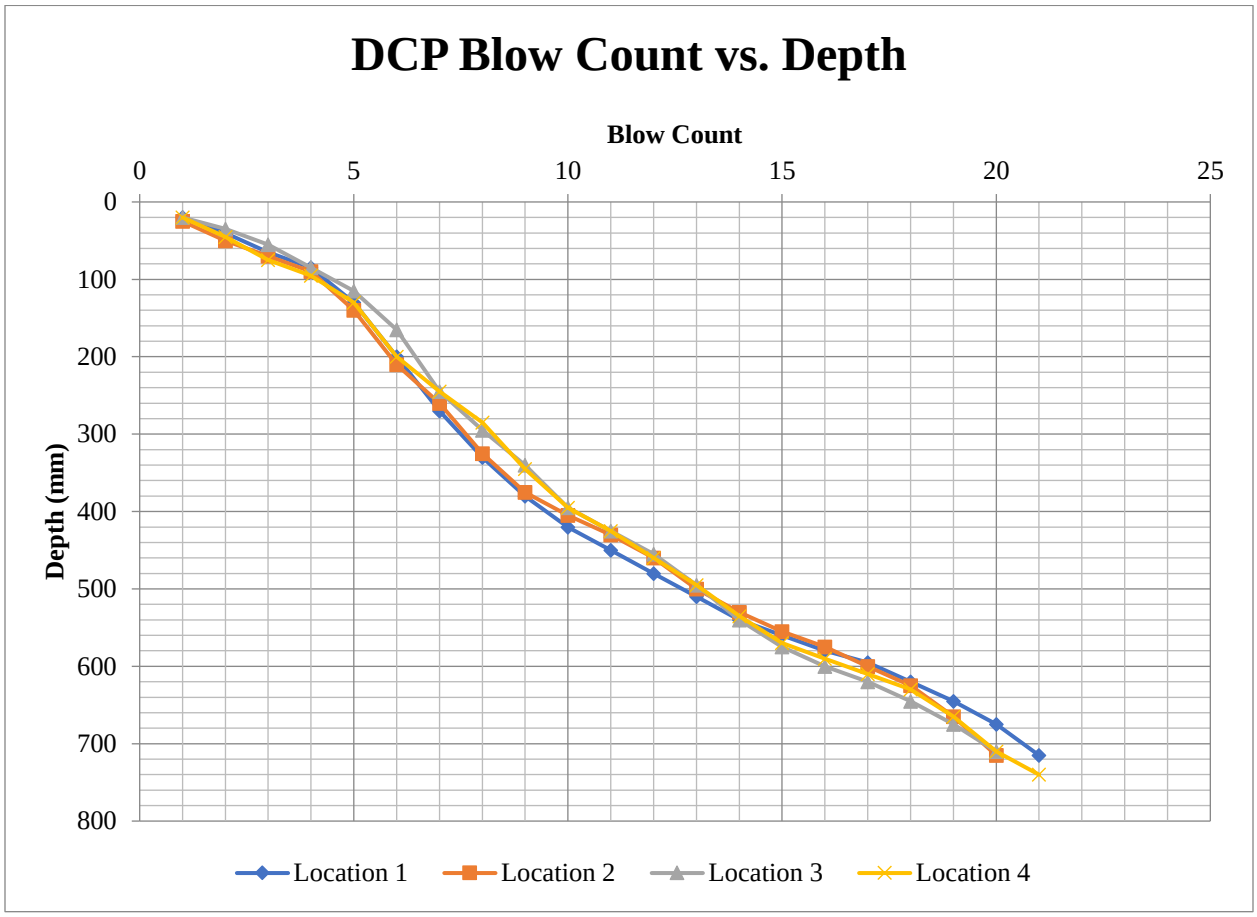

Figure 11. Test 04 DCP Blow Count vs. Penetration Depth.

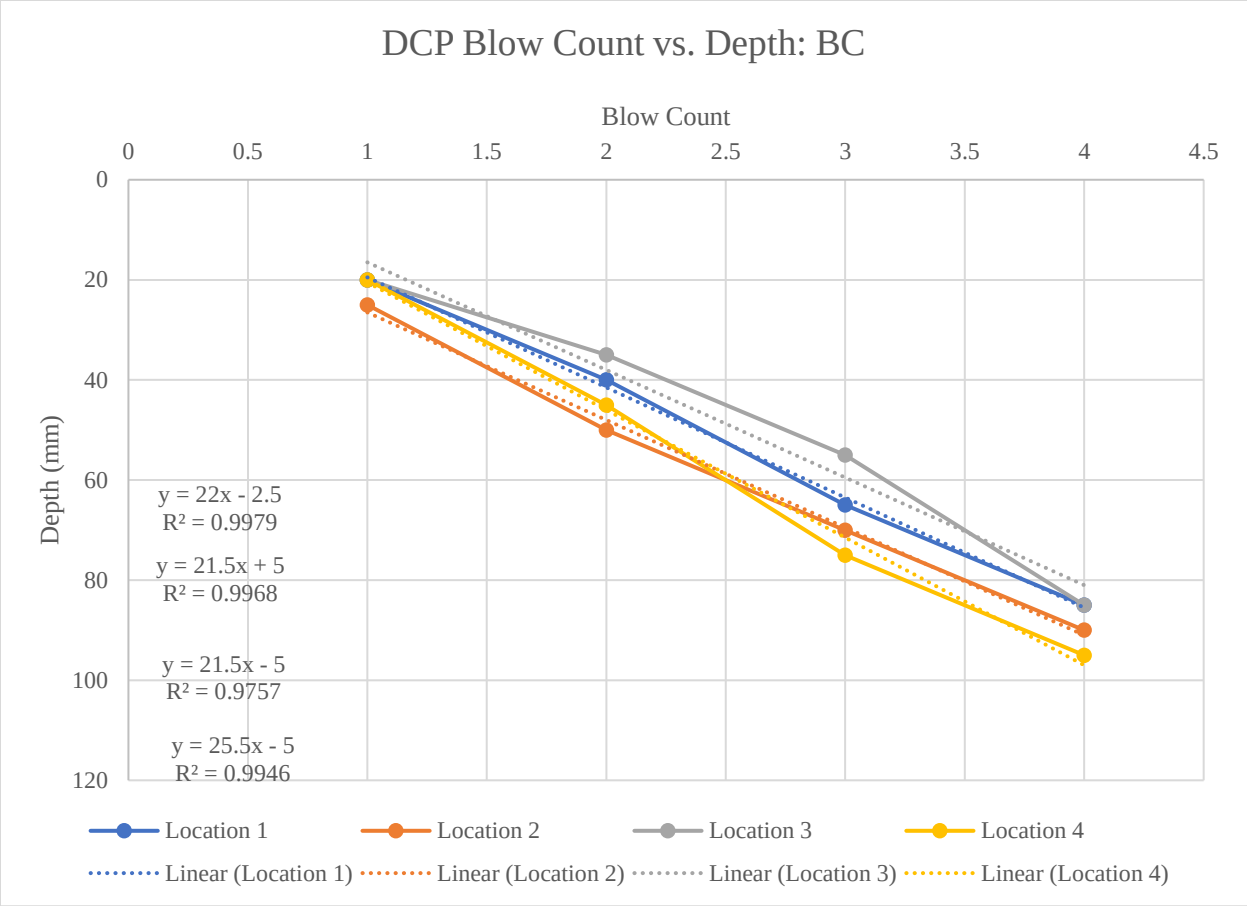

Figure 12. Test 04 DCPI: Base Course.

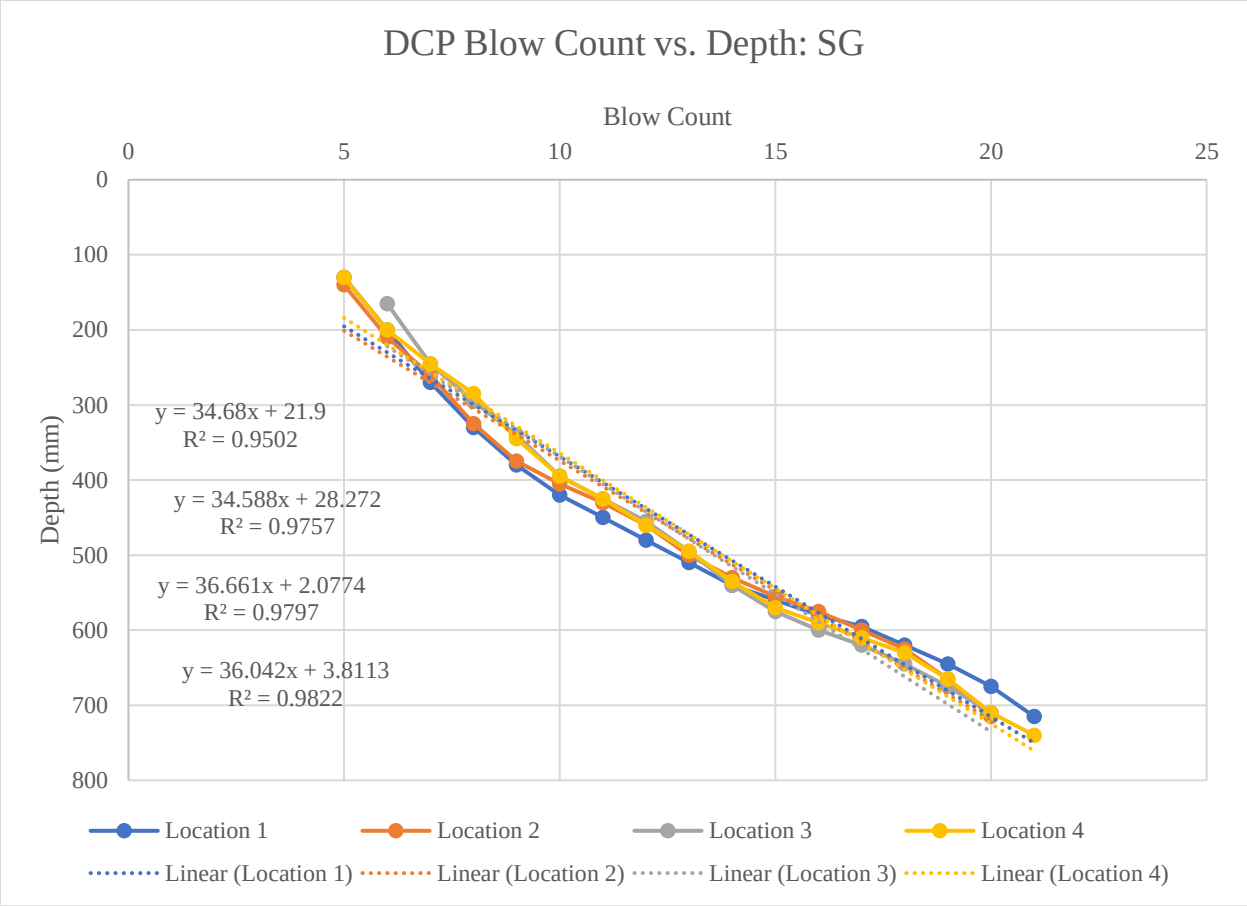

Figure 13. Test 04 DCPI: Subgrade.

Table A.10. Test 04 DCPI and CBR.

	DCPI (mm/Blow): BC	**DCPI (mm/Blow): SG**	**CBR (%): BC**	**CBR (%): SG**
Loc. 1	22	34.68	9.2	5.5
Loc. 2	21.5	34.588	9.4	5.5
Loc. 3	21.5	36.661	9.4	5.2
Loc. 4	25.5	36.042	7.8	5.3

Table A.11. Test 04 CBR Output, Standard Deviation, Coefficient of Variation.

	Base Course	**Subgrade**
Mean CBR (%)	8.9	5.4
Std. Dev. (σ)	0.786	0.173
CV	8.80%	3.22%

Test 05: RCA/ 5%-CBR SG (Control) (old load sequence)

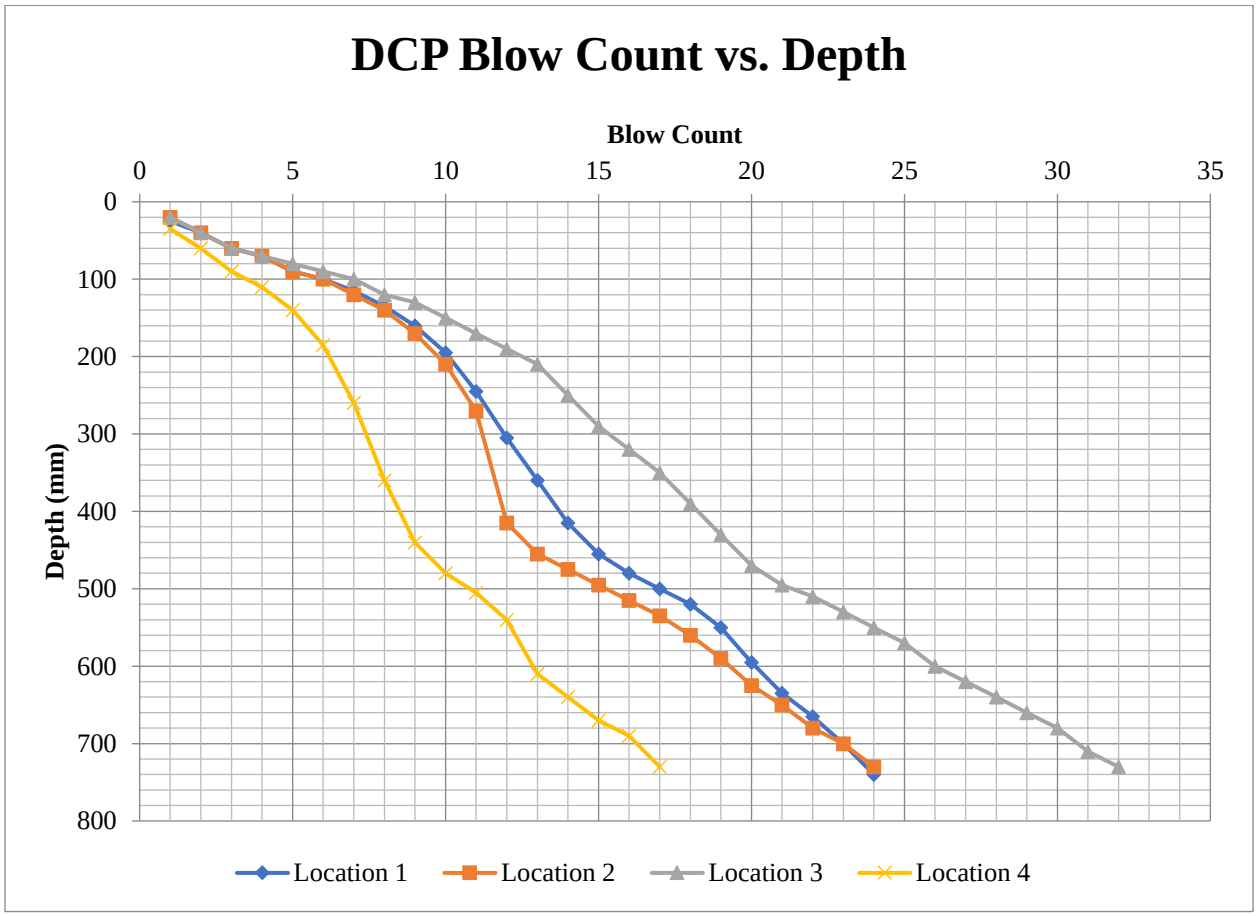

Figure 14. Test 05 DCP Blow Count vs. Penetration Depth.

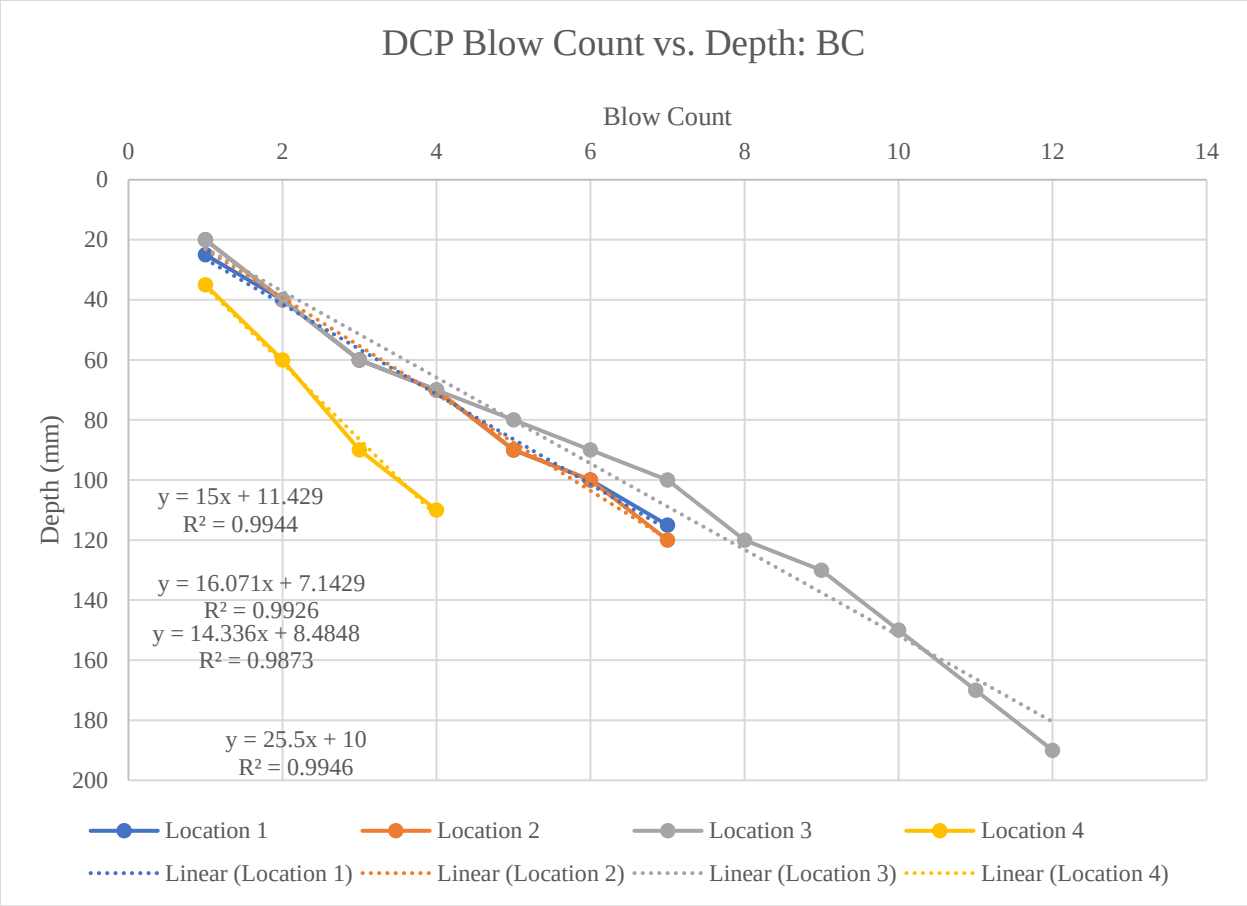

Figure 15. Test 05 DCPI: Base Course.

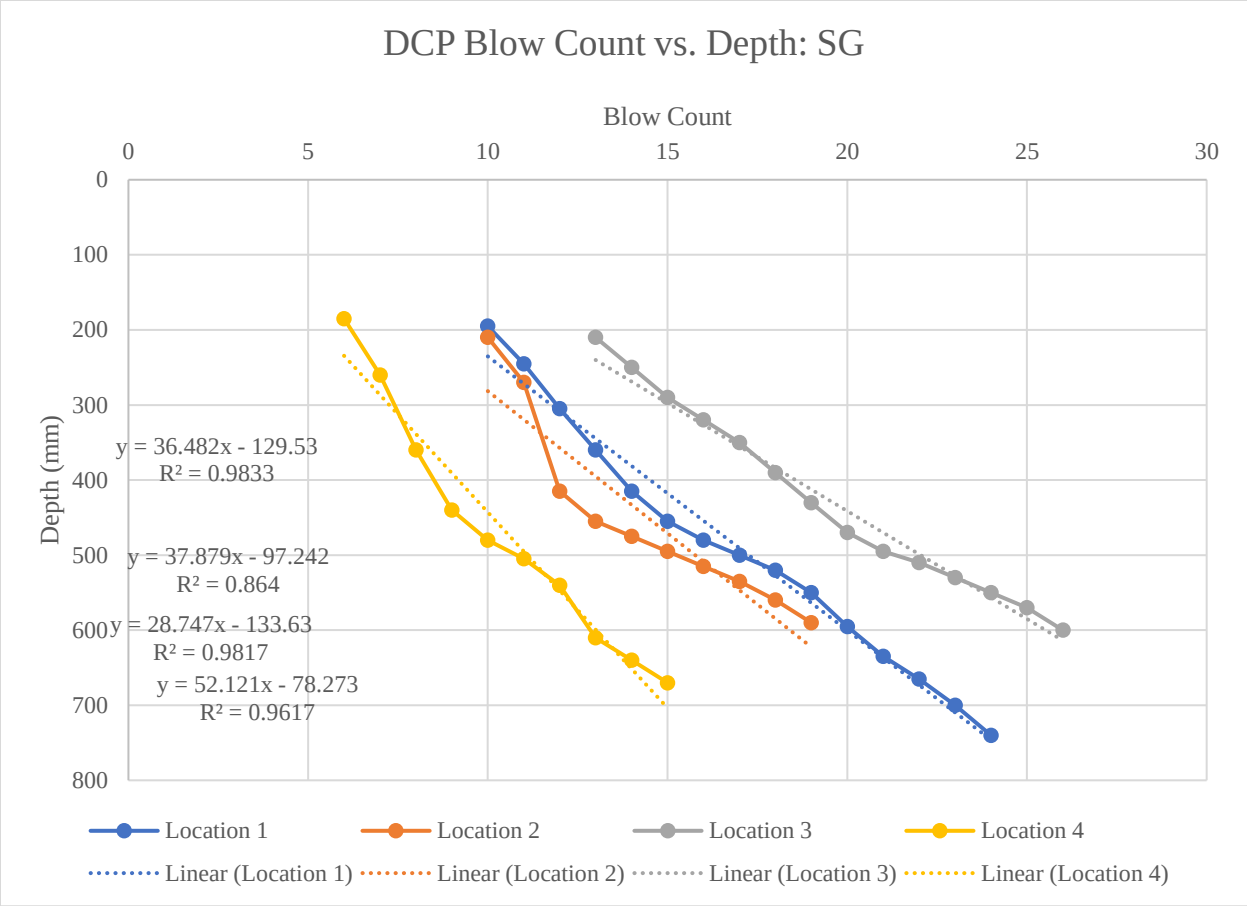

Figure 16. Test 05 DCPI: Subgrade.

Table A.12. Test 05 DCPI and CBR.

	DCPI (mm/Blow): BC	**DCPI (mm/Blow): SG**	**CBR (%): BC**	**CBR (%): SG**
Loc. 1	15	36.482	14.1	5.2
Loc. 2	16.071	37.879	13.0	5.0
Loc. 3	14.336	28.747	14.8	6.8
Loc. 4	25.5	52.121	7.8	3.5

Table A.13. Test 05 CBR Output, Standard Deviation, Coefficient of Variation.

	Base Course	**Subgrade**
Mean CBR (%)	12.4	5.1
Std. Dev. (σ)	3.183	1.351
CV	25.65%	26.42%

Test 06: RCA/ W/ 5%-CBR SG (old load sequence)

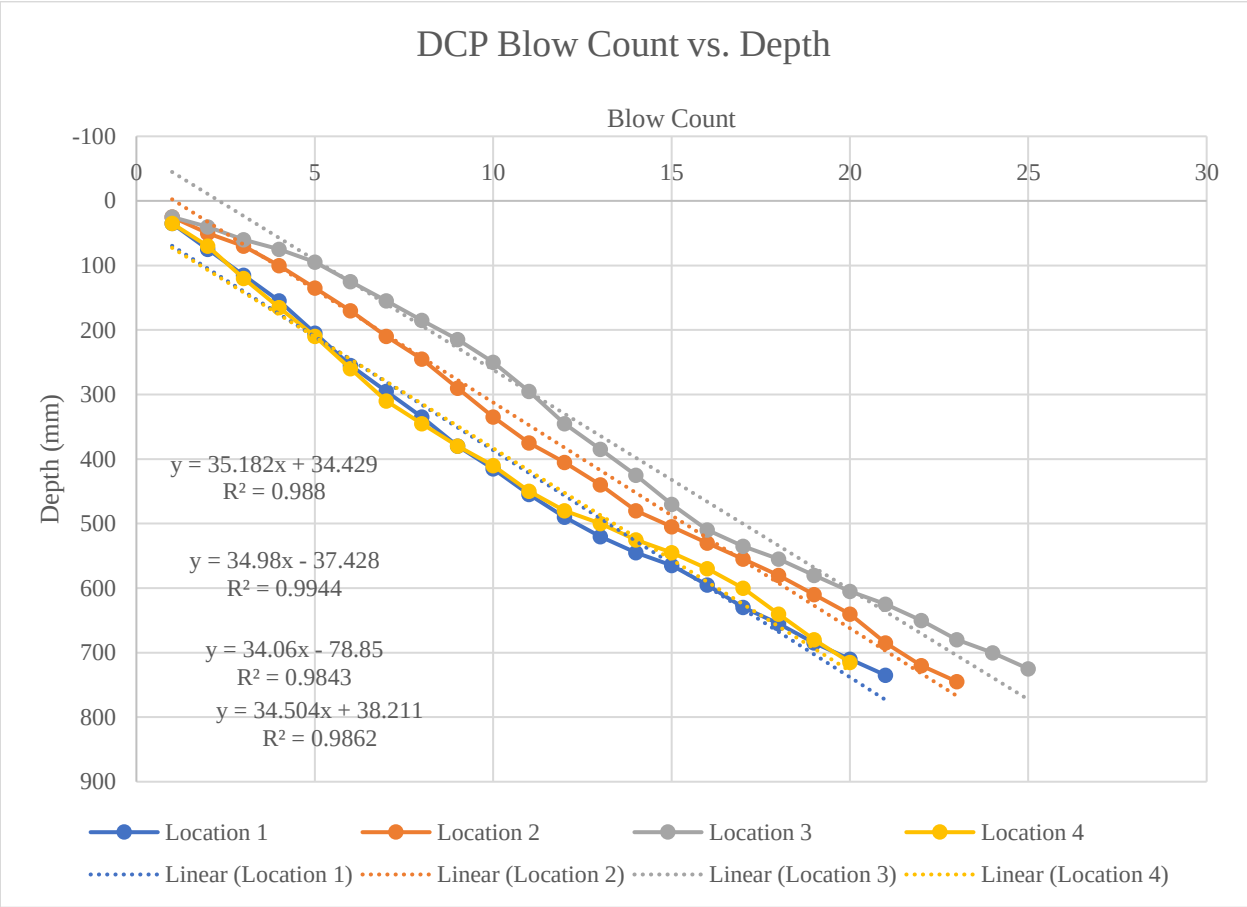

Figure 17. Test 06 Subgrade DCP Blow Count vs. Penetration Depth and DCPI.

Table A.14. Test 06 DCPI and CBR (Subgrade Only).

	DCPI (mm/Blow): SG	**CBR (%): SG**
Loc. 1	35.182	5.4
Loc. 2	34.98	5.4
Loc. 3	34.06	5.6
Loc. 4	34.504	5.5

Table A.15. Test 06 CBR Output, Standard Deviation, Coefficient of Variation (Subgrade Only).

	Subgrade
Mean CBR (%)	5.5
Std. Dev. (σ)	0.090
CV	1.63%

Test 07: RCA/ NW/ 5%-CBR SG (old load sequence)

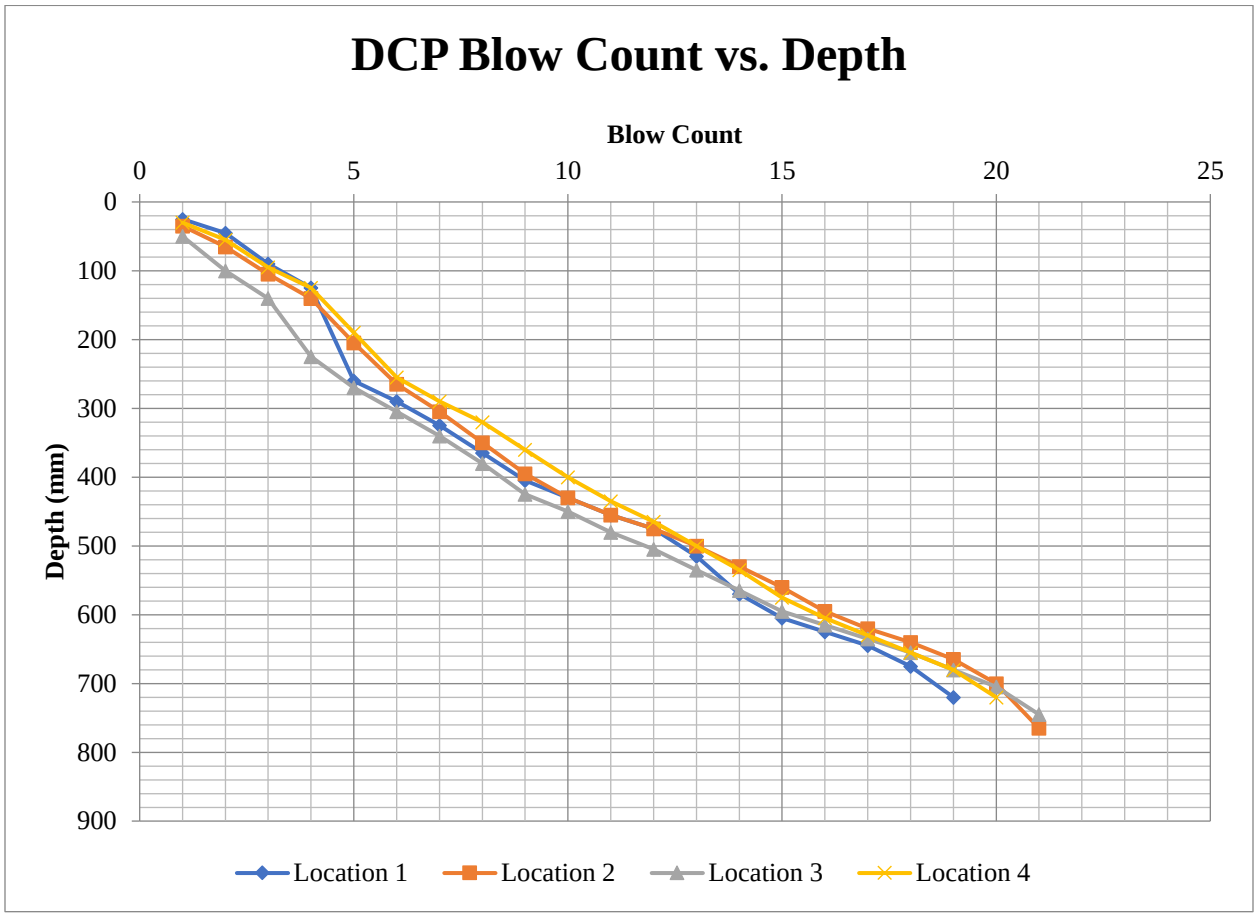

Figure 18. Test 07 DCP Blow Count vs. Penetration Depth.

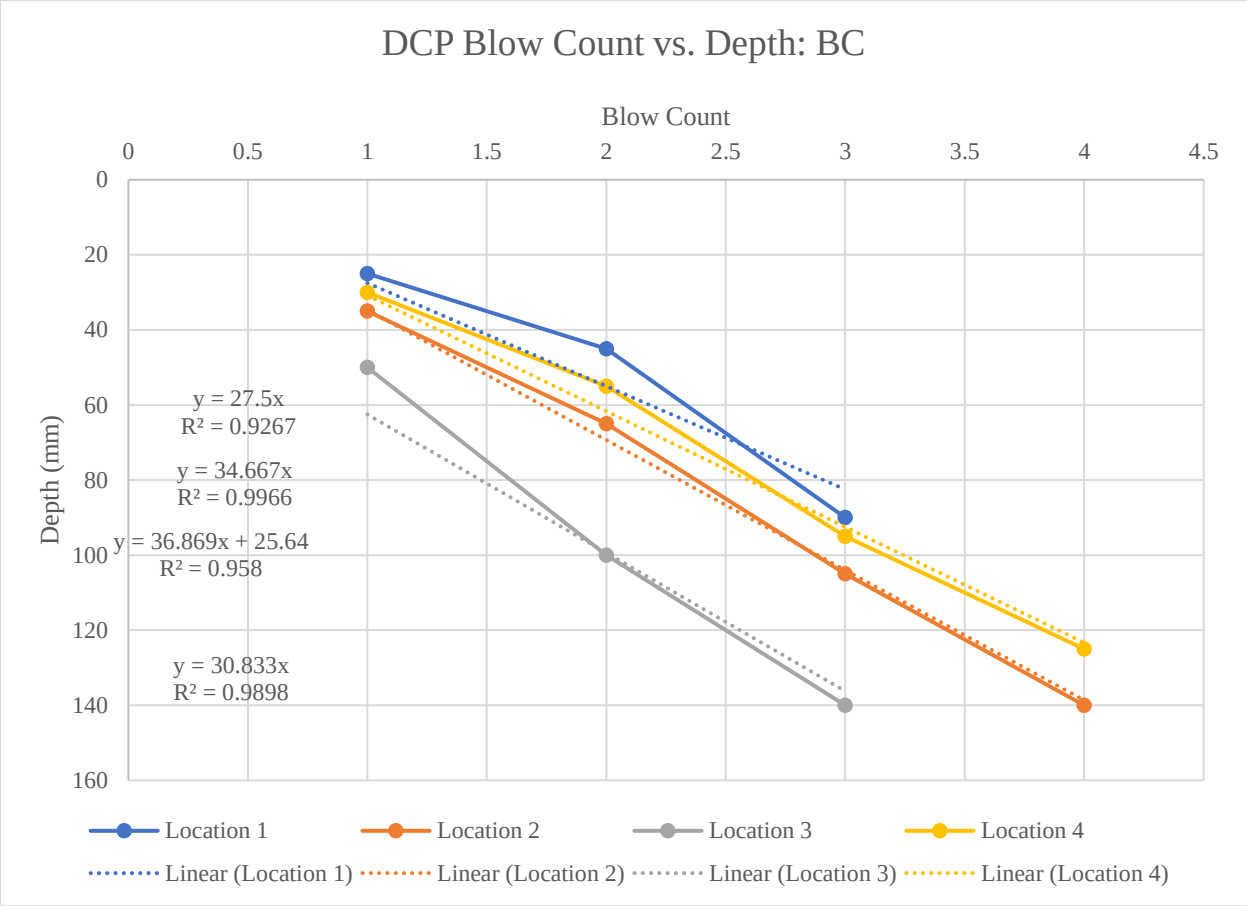

Figure 19. Test 07 DCPI: Base Course.

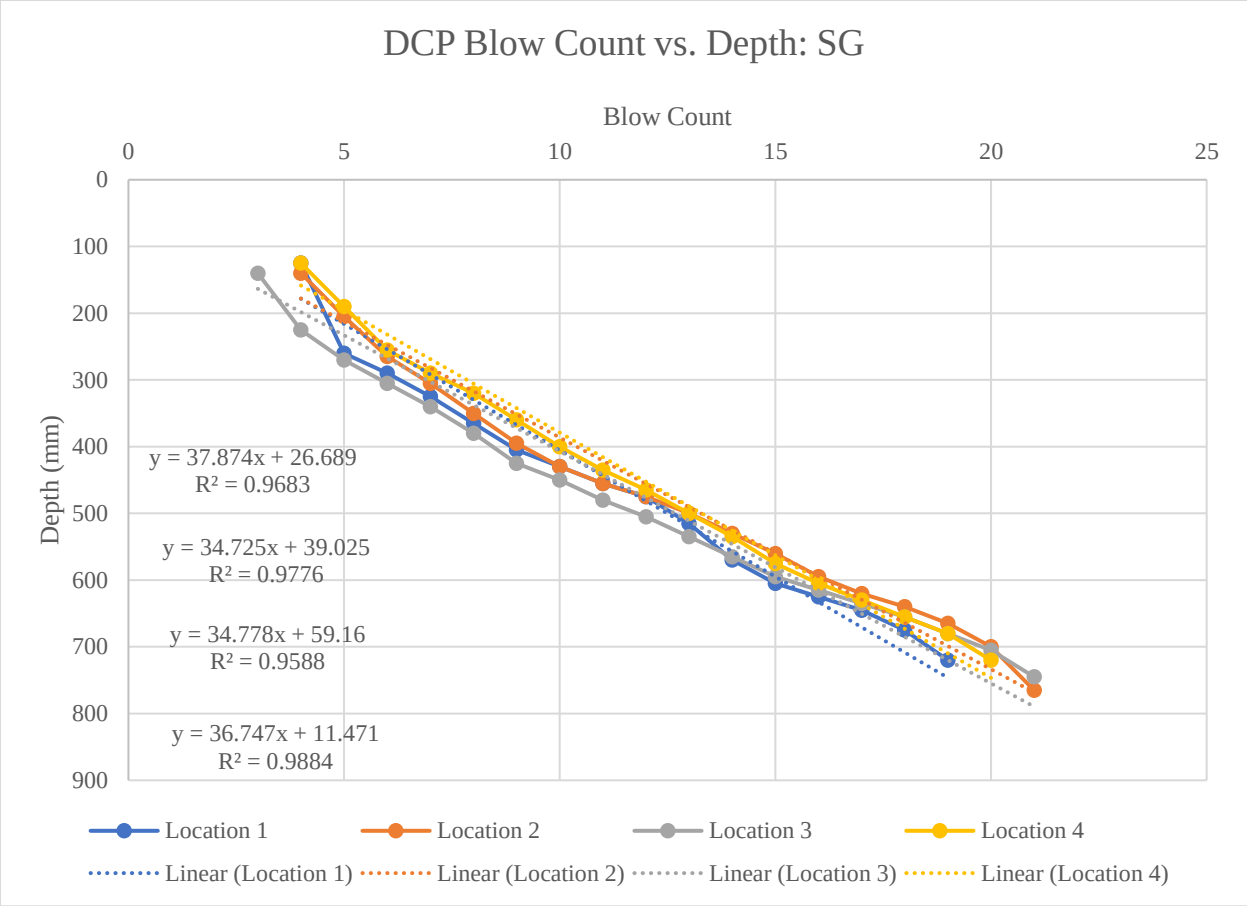

Figure 20. Test 07 DCPI: Subgrade.

Table A.16. Test 07 DCPI and CBR.

	DCPI (mm/Blow): BC	**DCPI (mm/Blow): SG**	**CBR (%): BC**	**CBR (%): SG**
Loc. 1	27.5	37.874	7.1	5.0
Loc. 2	34.667	34.725	5.5	5.5
Loc. 3	36.869	34.778	5.1	5.5
Loc. 4	30.883	36.747	6.3	5.2

Table A.17. Test 07 CBR Output, Standard Deviation, Coefficient of Variation.

	Base Course	**Subgrade**
Mean CBR (%)	6.0	5.3
Std. Dev. (σ)	0.884	0.252
CV	14.71%	4.77%

Test 08: RCA/ GG/ 5%-CBR SG (old load sequence)

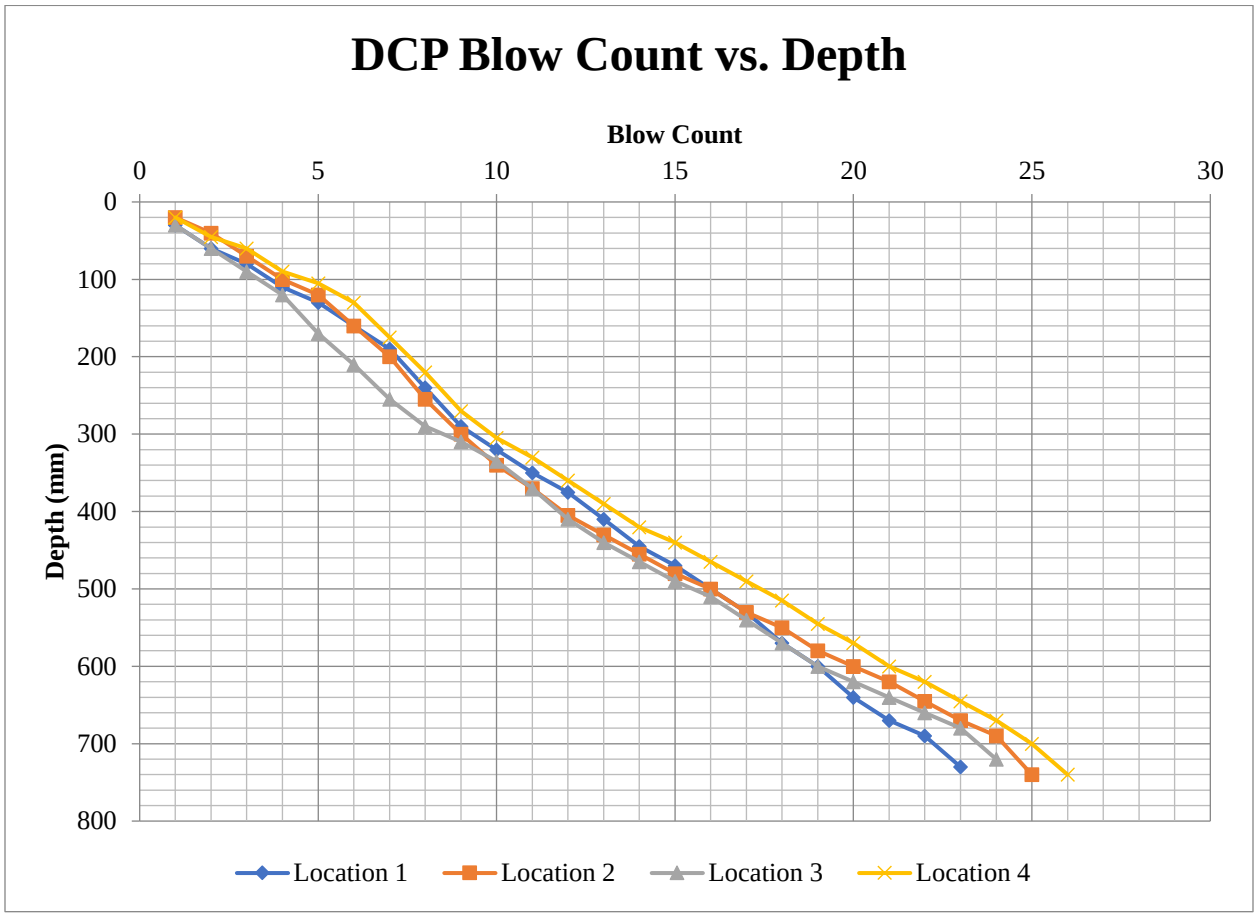

Figure 21. Test 08 DCP Blow Count vs. Penetration Depth.

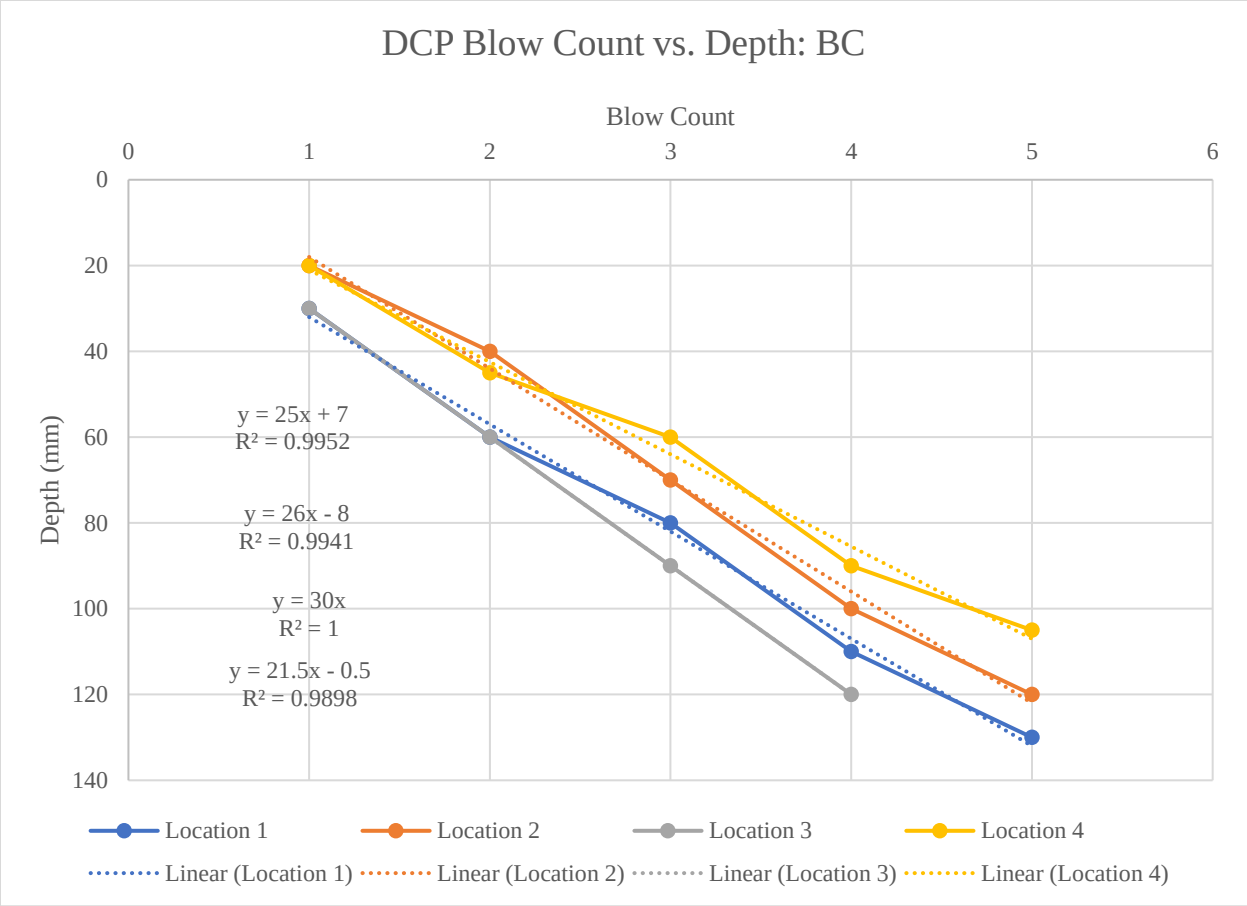

Figure 22. Test 08 DCPI: Base Course.

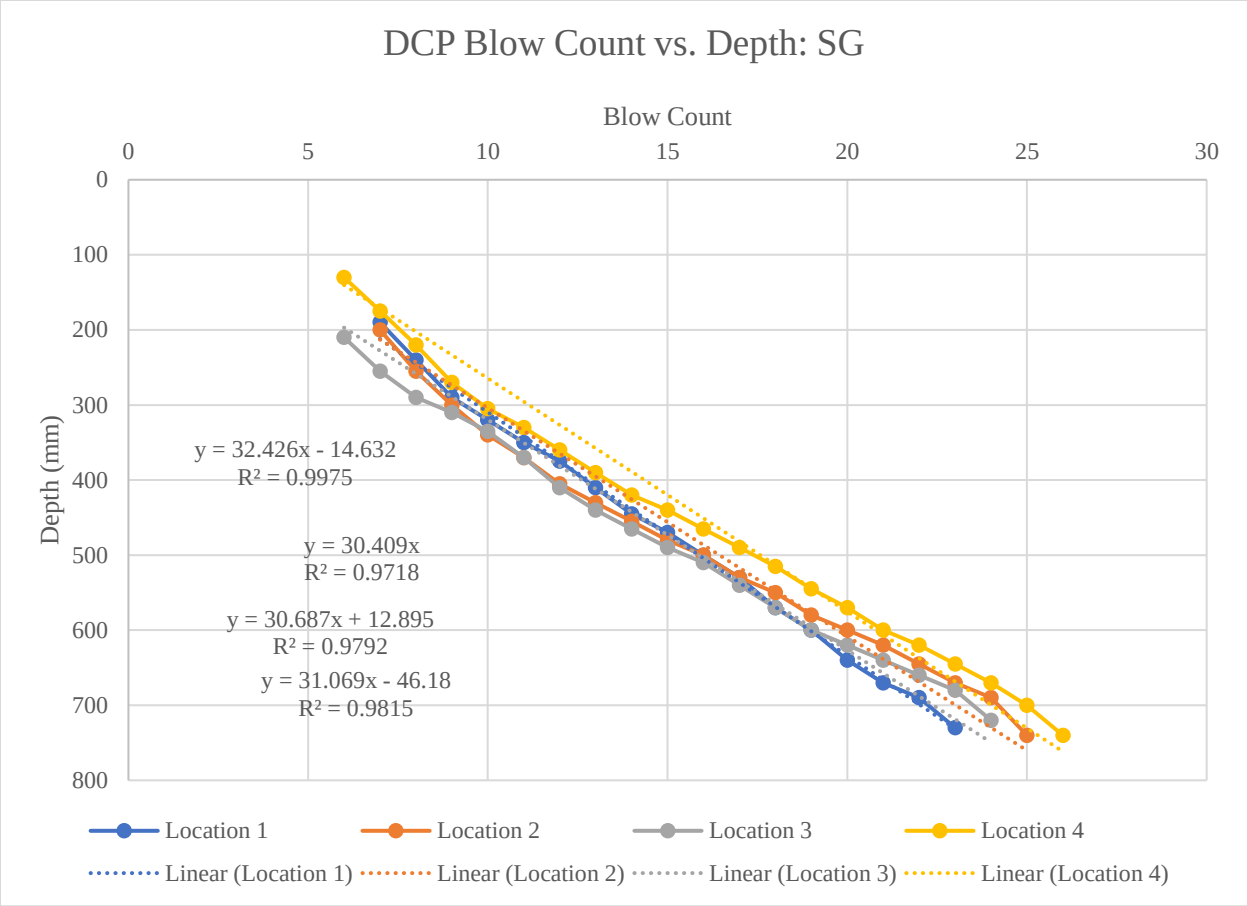

Figure 23. Test 08 DCPI: Subgrade.

Table A.18. Test 08 DCPI and CBR.

	DCPI (mm/Blow): BC	**DCPI (mm/Blow): SG**	**CBR (%): BC**	**CBR (%): SG**
Loc. 1	25	32.426	7.9	5.9
Loc. 2	26	30.409	7.6	6.4
Loc. 3	30	30.687	6.5	6.3
Loc. 4	21.5	31.069	9.4	6.2

Table A.19. Test 08 CBR Output, Standard Deviation, Coefficient of Variation.

	Base Course	**Subgrade**
Mean CBR (%)	7.9	6.2
Std. Dev. (σ)	1.207	0.195
CV	15.37%	3.15%

Test 09: VGB/ NW/ 2%-CBR SG (old load sequence)

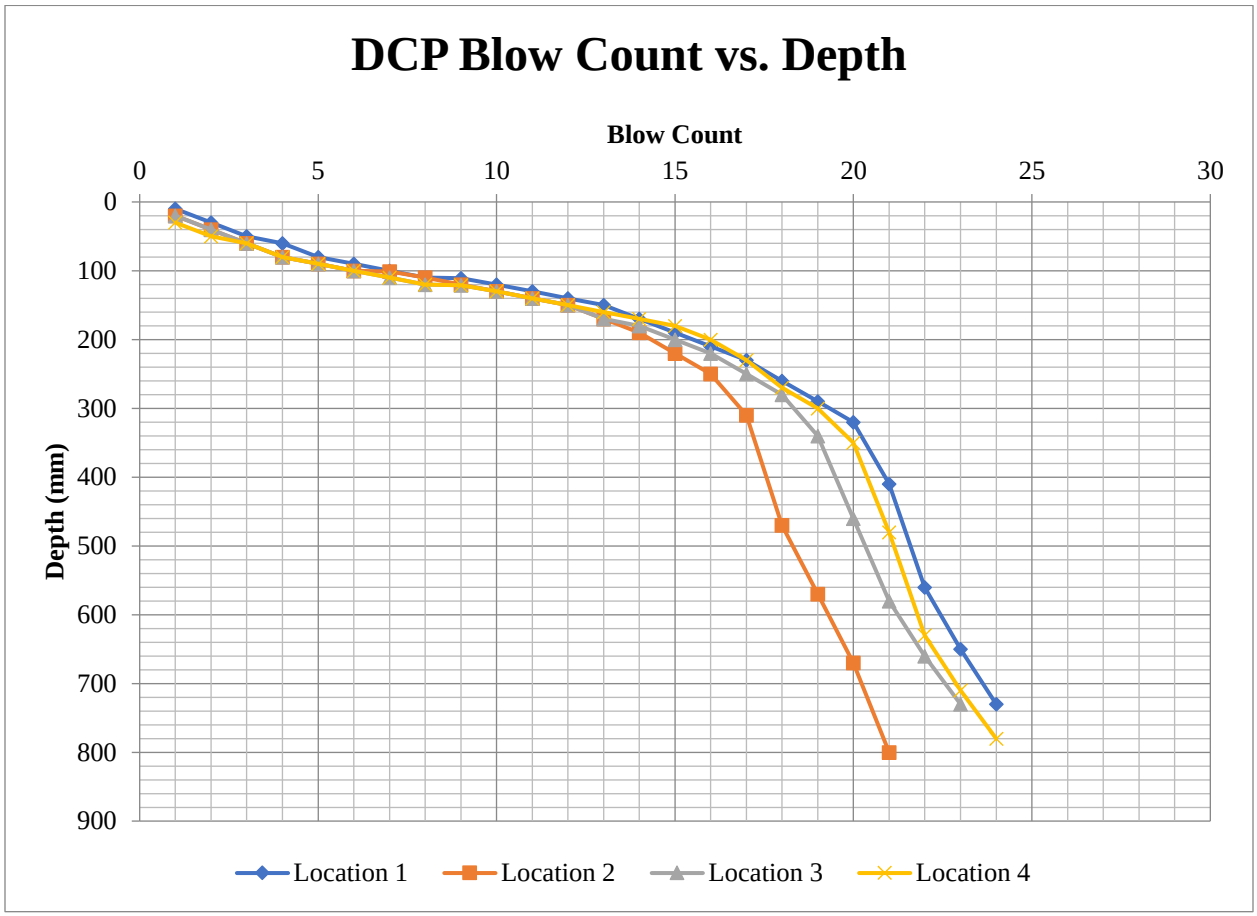

Figure 24. Test 09 DCP Blow Count vs. Penetration Depth.

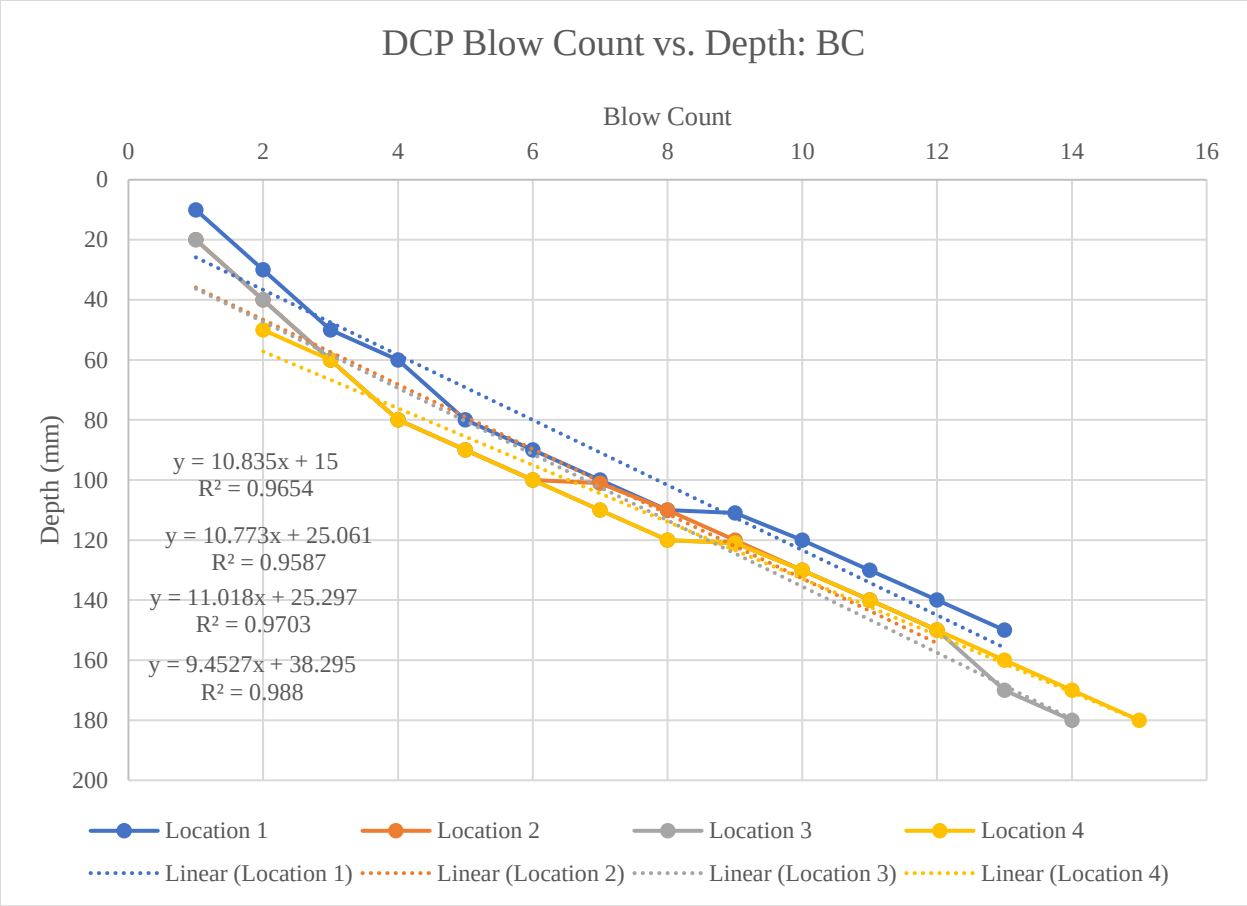

Figure 25. Test 09 DCPI: Base Course.

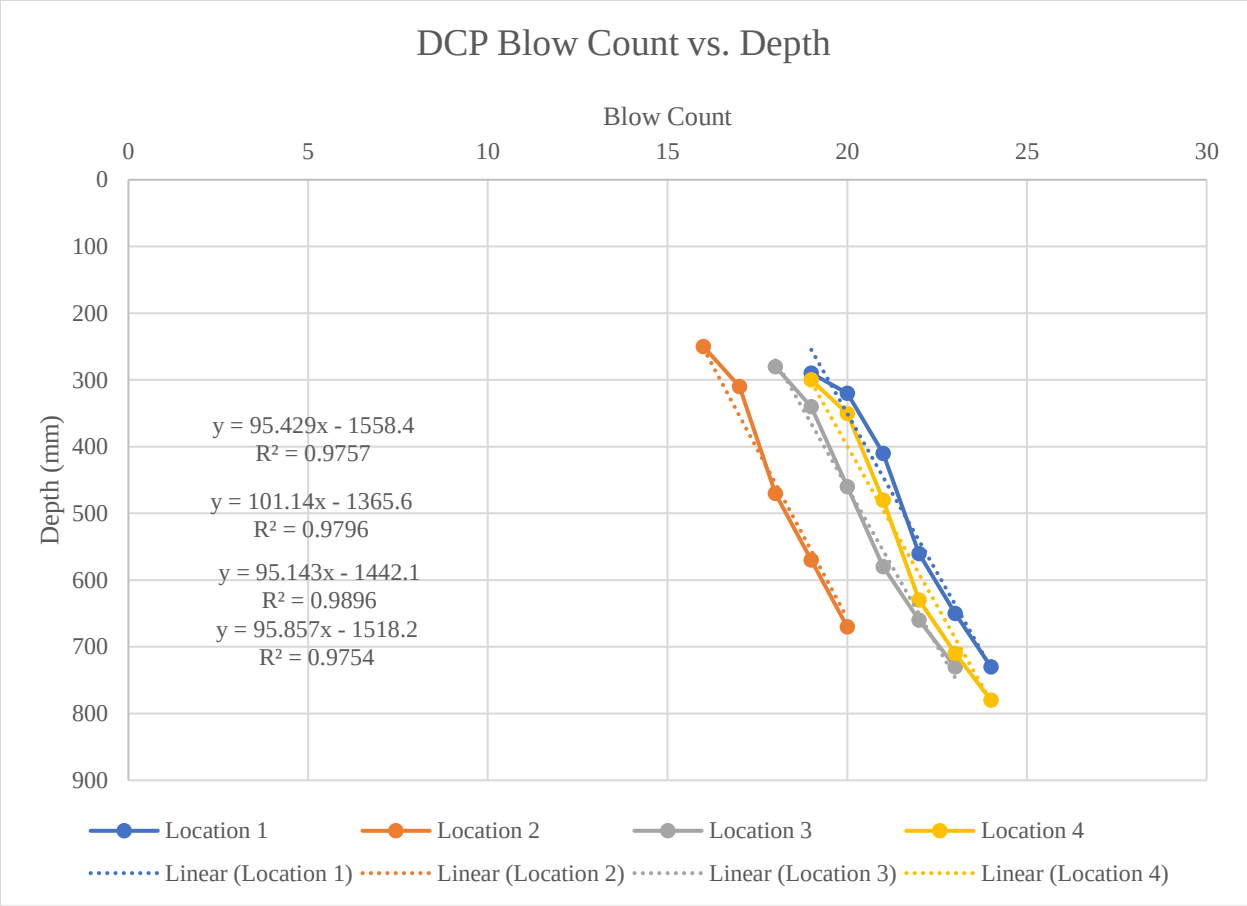

Figure 26. Test 09 DCPI: Subgrade.

Table A.20. Test 09 DCPI and CBR.

	DCPI (mm/Blow): BC	**DCPI (mm/Blow): SG**	CBR (%): BC	CBR (%): SG
Loc. 1	10.835	95.429	20.2	1.8
Loc. 2	10.773	101.14	20.4	1.7
Loc. 3	11.018	95.143	19.9	1.8
Loc. 4	9.4527	95.857	23.6	1.8

Table A.21. Test 09 CBR Output, Standard Deviation, Coefficient of Variation.

	Base Course	**Subgrade**
Mean CBR (%)	21.0	1.8
Std. Dev. (σ)	1.726	0.050
CV	8.21%	2.82%

Test 10: VGB/ W/ 2%-CBR SG (alt. load sequence)

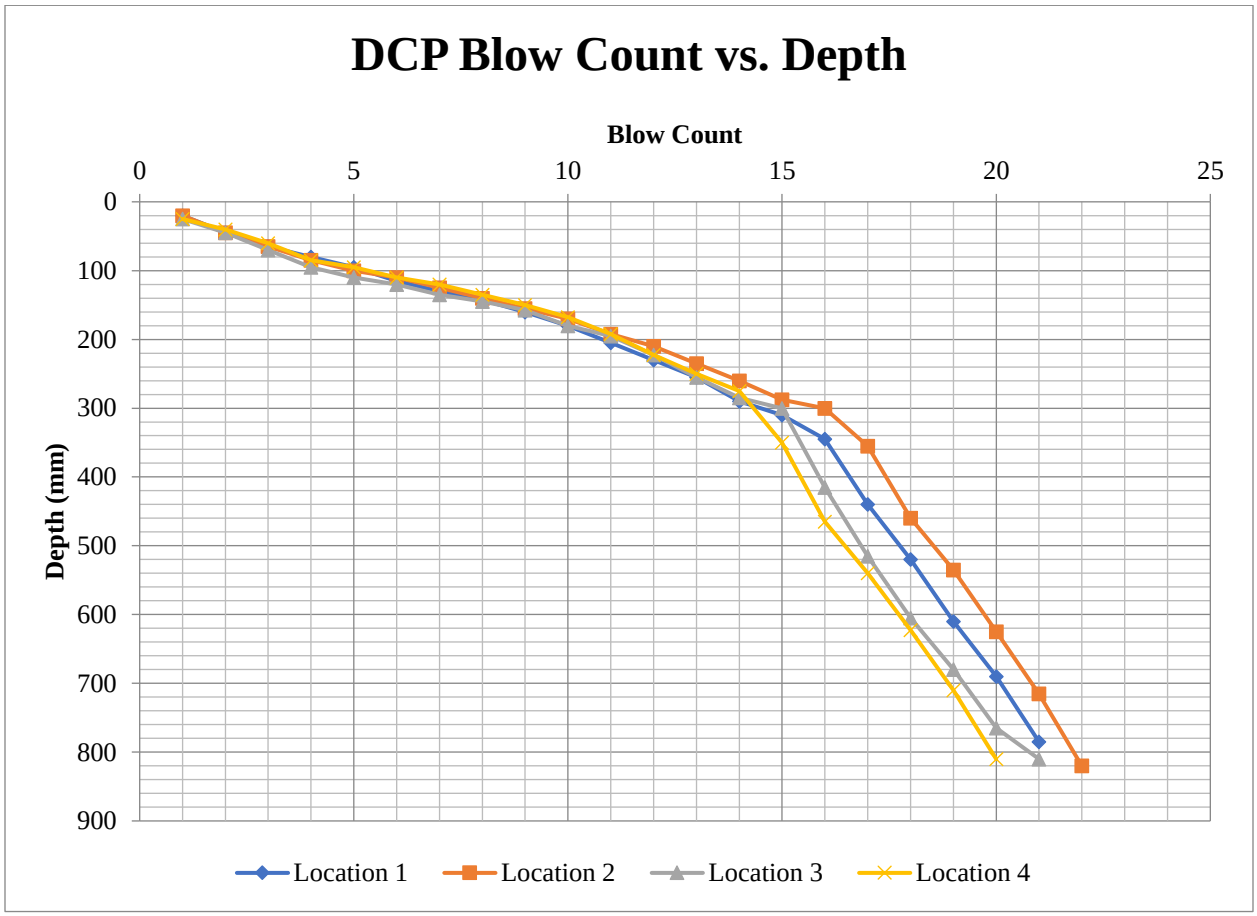

Figure 27. Test 10 DCP Blow Count vs. Penetration Depth.

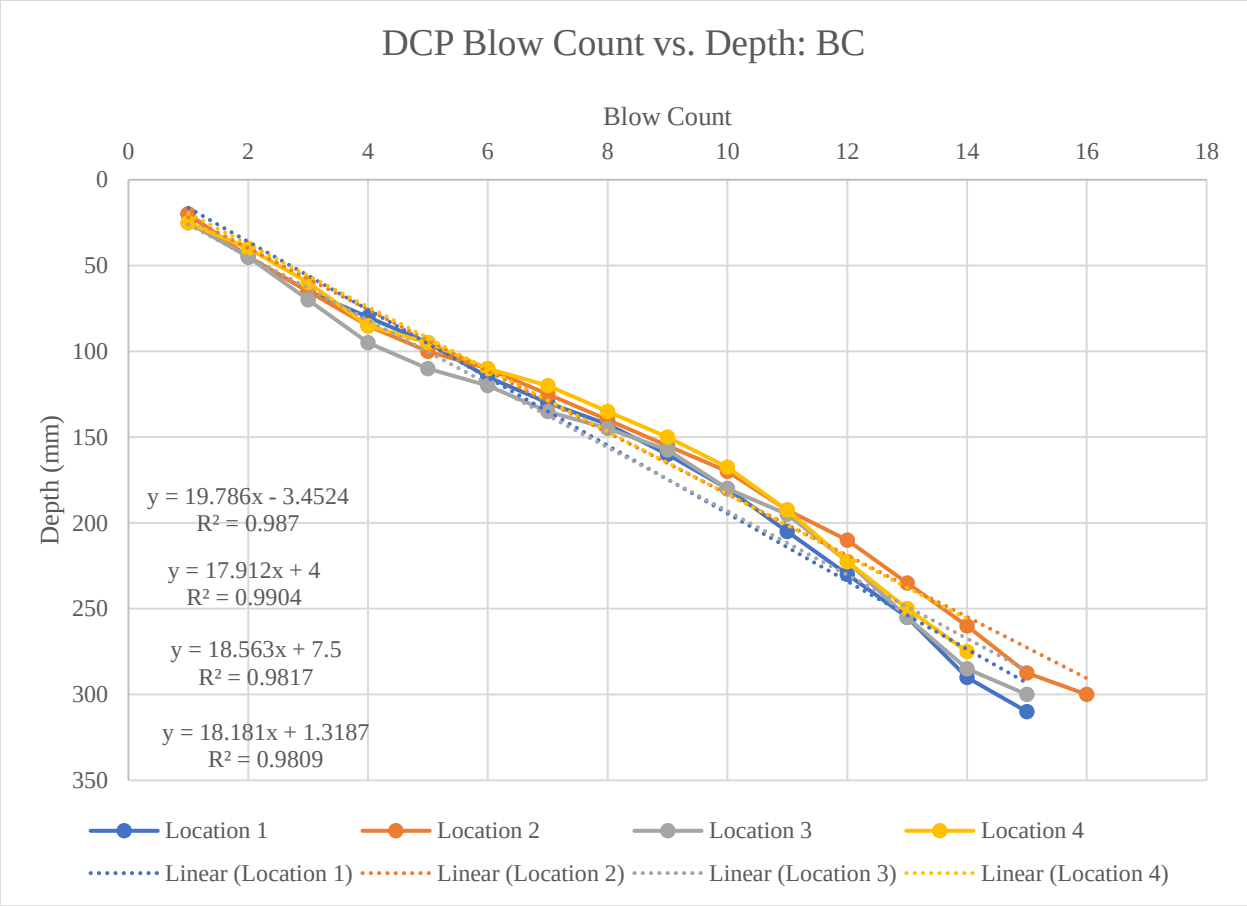

Figure 28. Test 10 DCPI: Base Course.

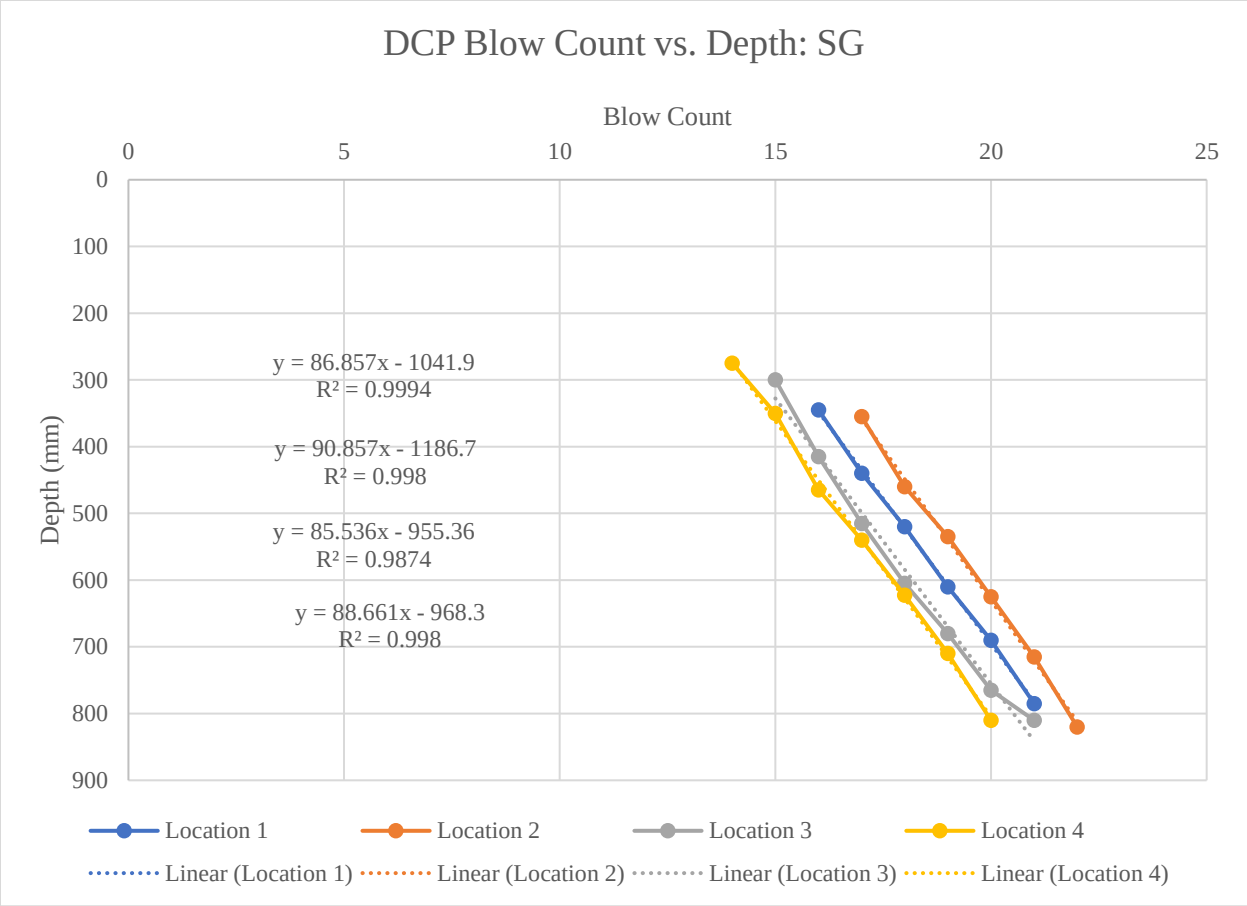

Figure 29. Test 10 DCPI: Subgrade.

Table A.22. Test 10 DCPI and CBR.

	DCPI (mm/Blow): BC	**DCPI (mm/Blow): SG**	**CBR (%): BC**	**CBR (%): SG**
Loc. 1	19.786	86.857	10.3	2.0
Loc. 2	17.912	90.857	11.5	1.9
Loc. 3	18.563	85.536	11.1	2.0
Loc. 4	18.181	88.661	11.3	1.9

Table A.23. Test 10 CBR Output, Standard Deviation, Coefficient of Variation.

	Base Course	**Subgrade**
Mean CBR (%)	11.1	1.9
Std. Dev. (σ)	0.534	0.057
CV	4.83%	2.92%

Test 11: VGB/ W/ 2%-CBR SG (retest)

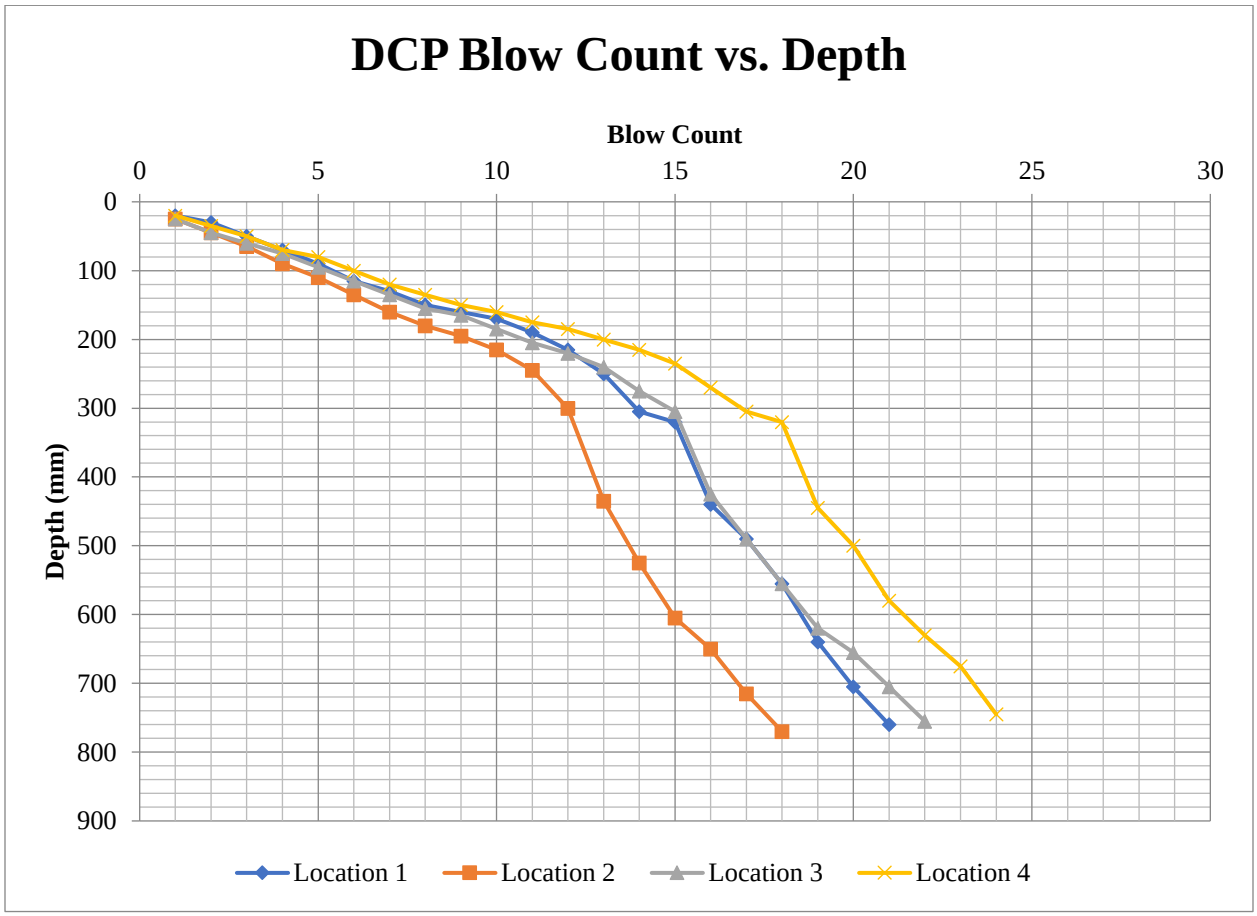

Figure 30. Test 11 DCP Blow Count vs. Penetration Depth.

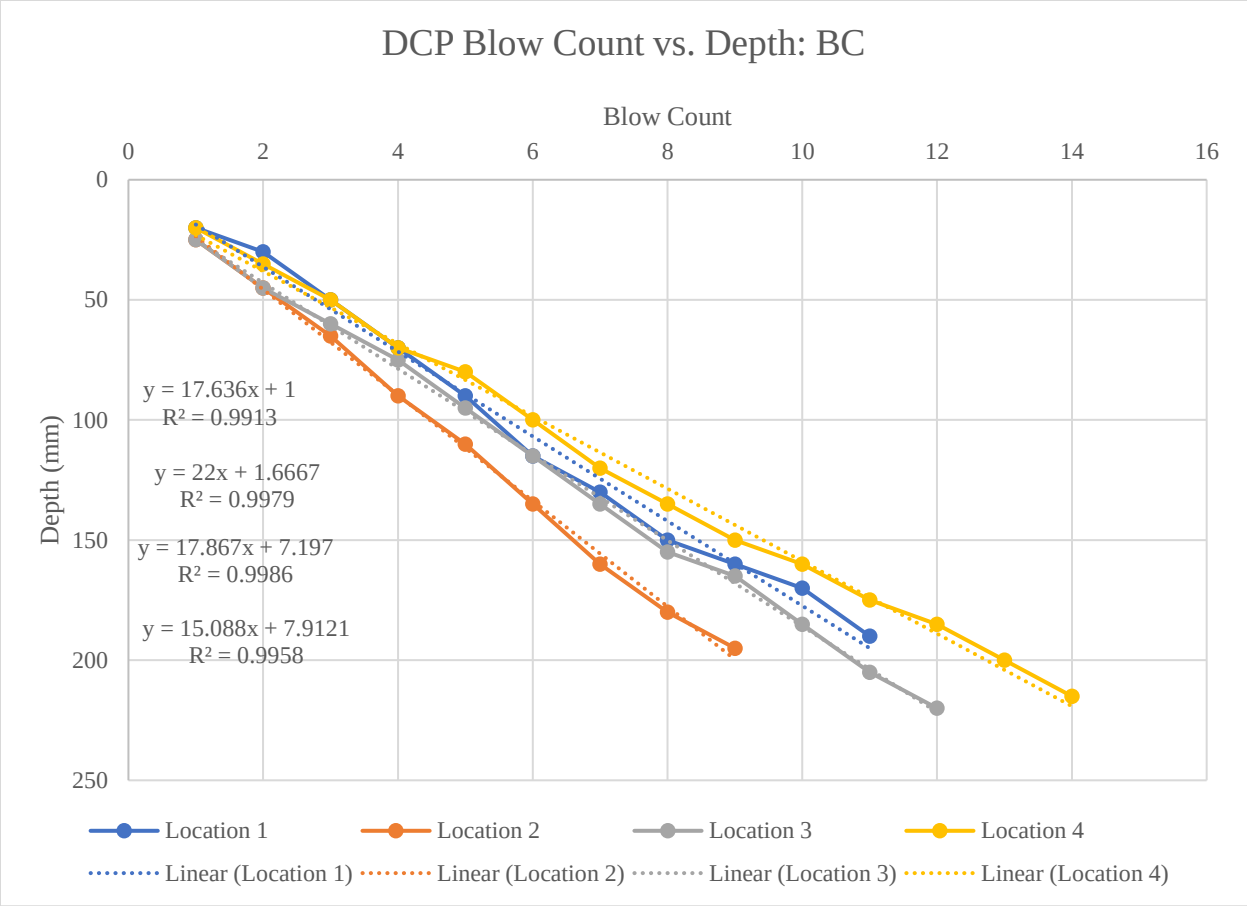

Figure 31. Test 11 DCPI: Base Course.

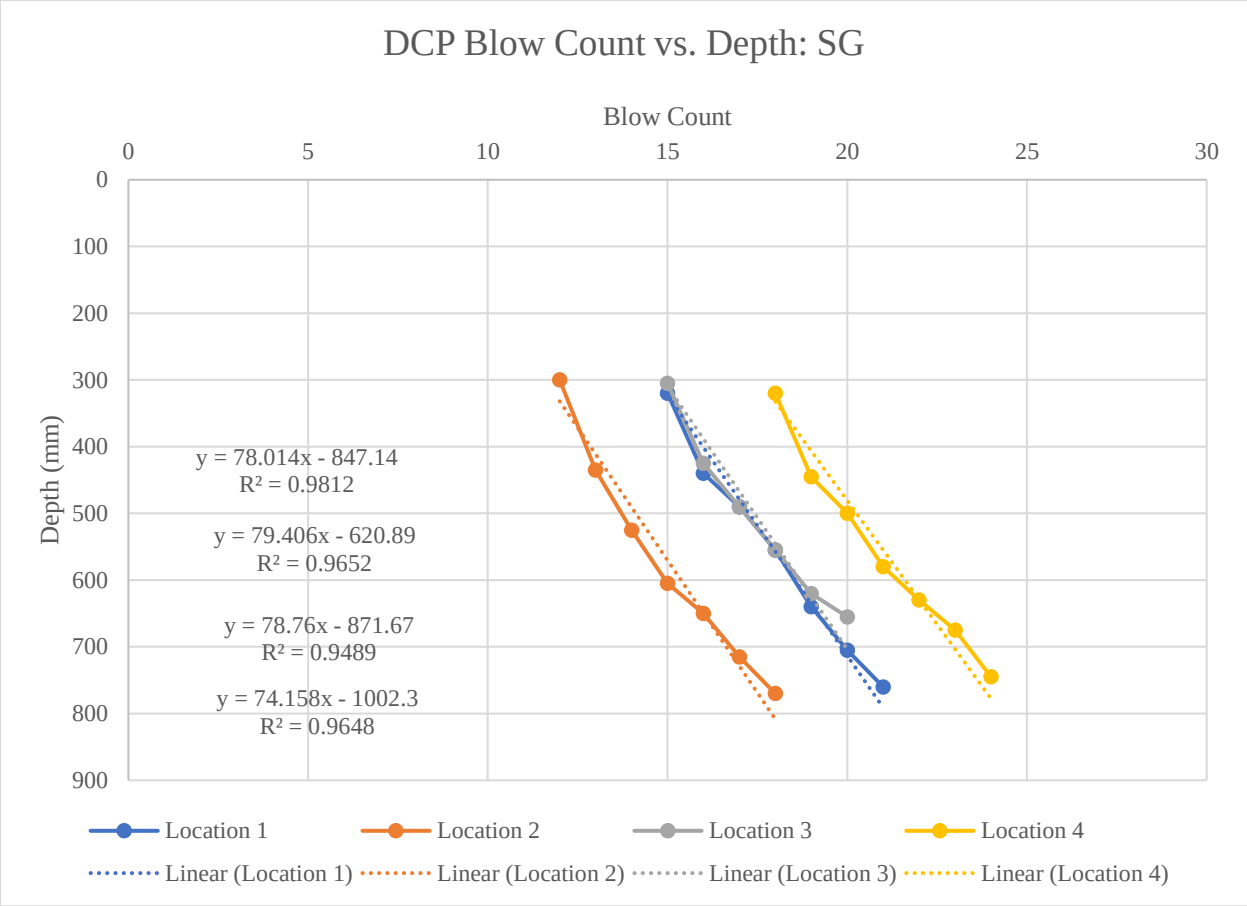

Figure 32. Test 11 DCPI: Subgrade.

Table A.24. Test 11 DCPI and CBR.

	DCPI (mm/Blow): BC	**DCPI (mm/Blow): SG**	**CBR (%): BC**	**CBR (%): SG**
Loc. 1	17.636	78.014	11.7	2.2
Loc. 2	22	79.406	9.2	2.2
Loc. 3	17.867	78.76	11.6	2.2
Loc. 4	15.088	74.158	14.0	2.3

Table A.25. Test 11 CBR Output, Standard Deviation, Coefficient of Variation.

	Base Course	**Subgrade**
Mean CBR (%)	11.6	2.2
Std. Dev. (σ)	1.967	0.078
CV	16.95%	3.49%

Test 12: RCA/ W/ 2%-CBR SG

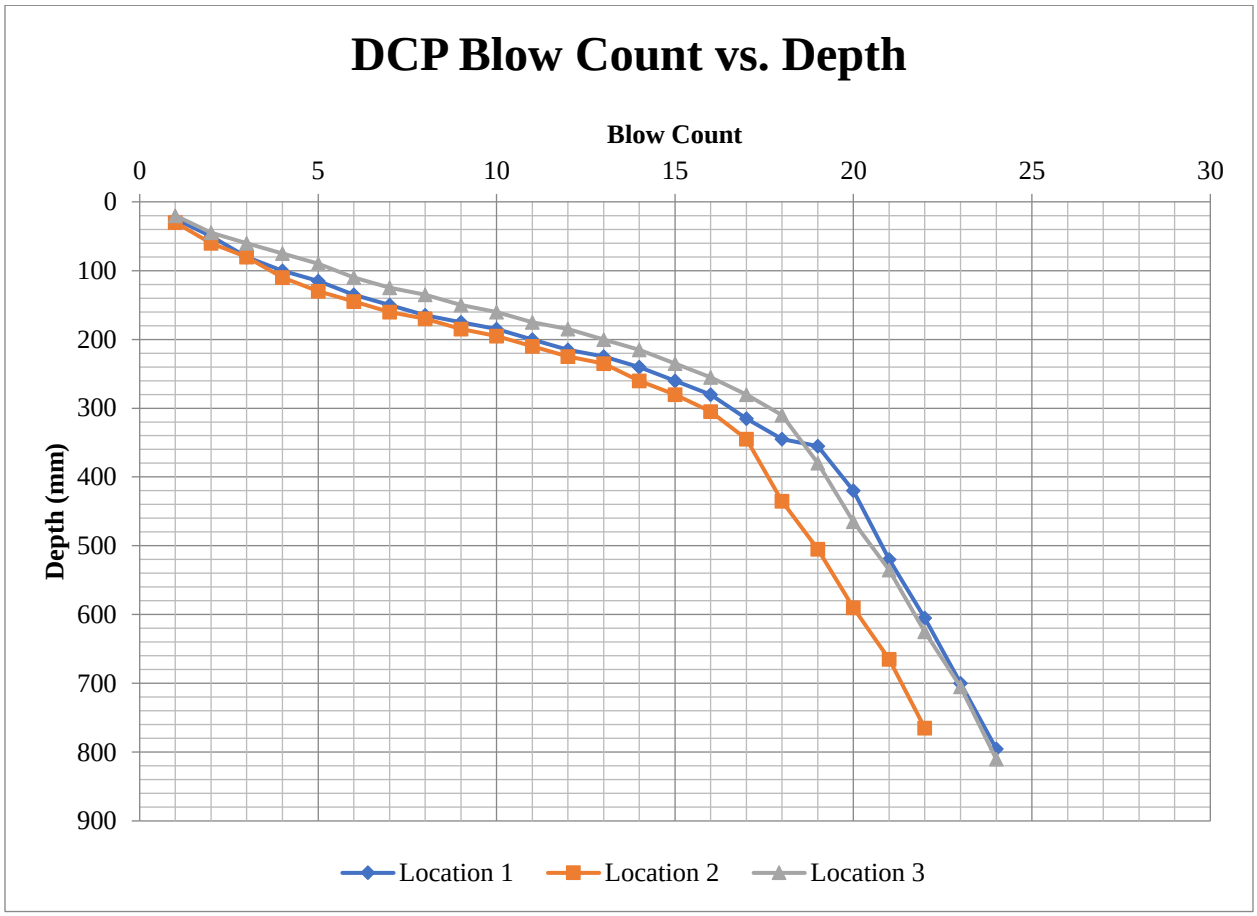

Figure 33. Test 12 DCP Blow Count vs. Penetration Depth.

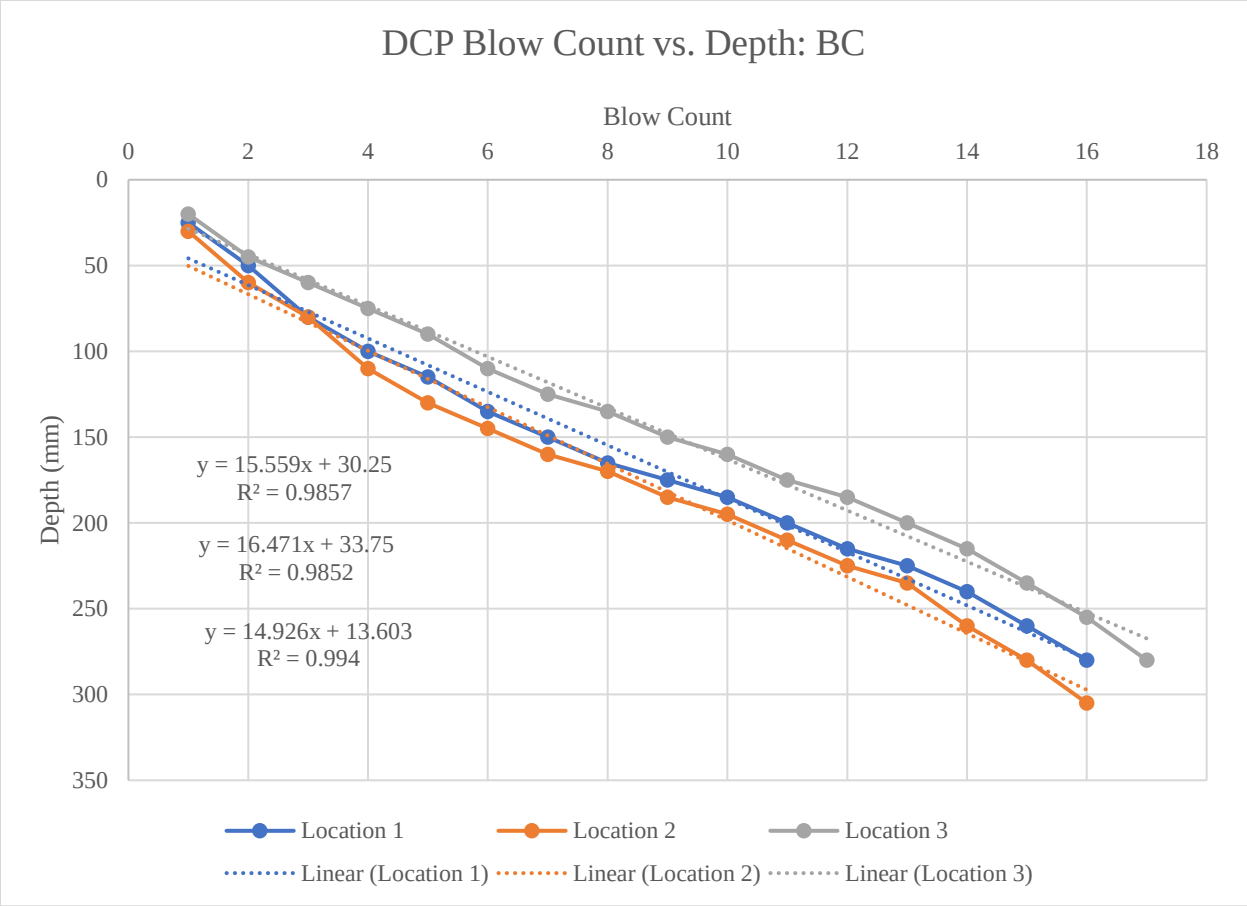

Figure 34. Test 12 DCPI: Base Course.

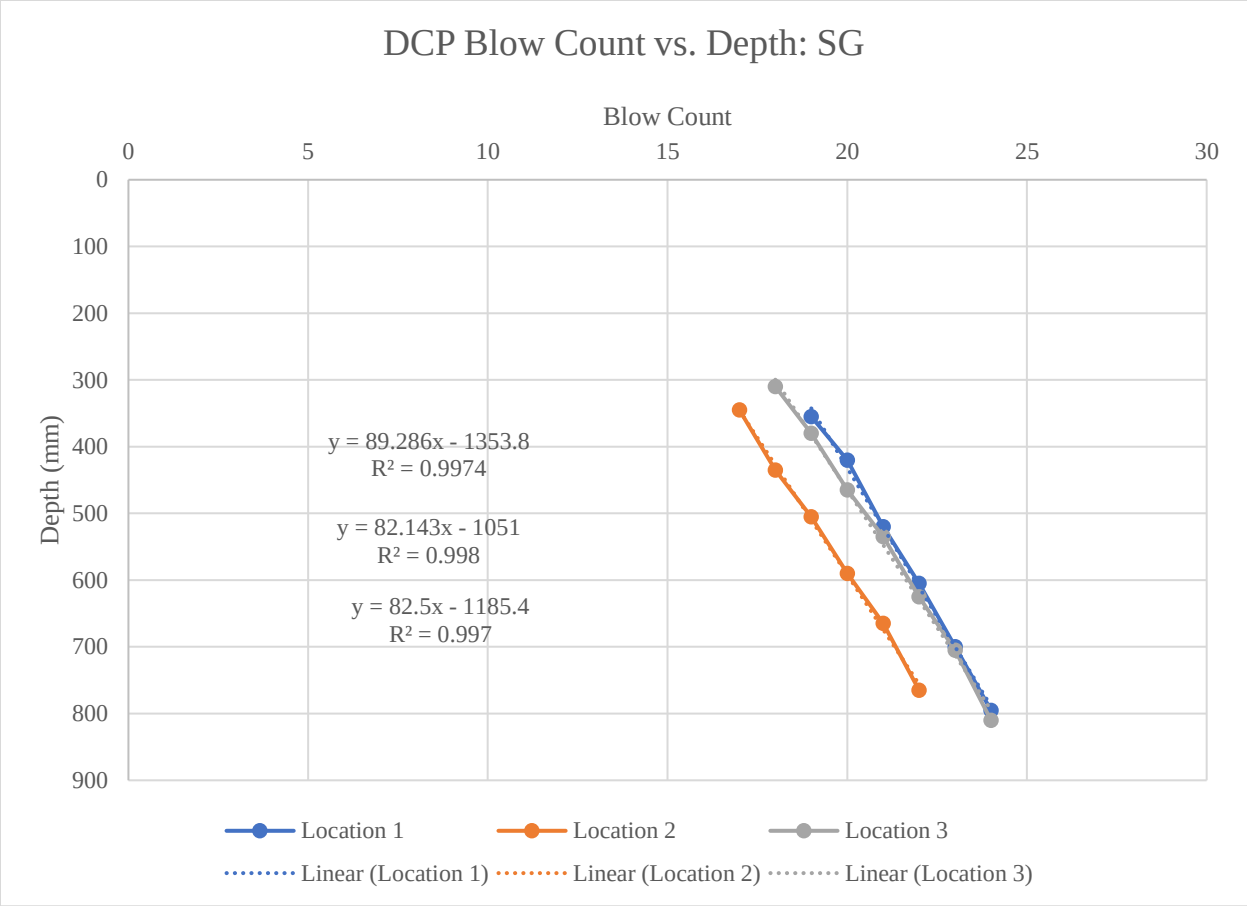

Figure 35. Test 12 DCPI: Subgrade.

Table A.26. Test 12 DCPI and CBR.

	DCPI (mm/Blow): BC	**DCPI (mm/Blow): SG**	**CBR (%): BC**	**CBR (%): SG**
Loc. 1	15.559	89.286	13.5	1.9
Loc. 2	16.471	82.143	12.7	2.1
Loc. 3	14.926	82.5	14.1	2.1

Table A.27. Test 12 CBR Output, Standard Deviation, Coefficient of Variation.

	Base Course	**Subgrade**
Mean CBR (%)	13.4	2.0
Std. Dev. (σ)	0.741	0.105
CV	5.51%	5.18%

Test 13: RCA/ 2%-CBR SG (Control)

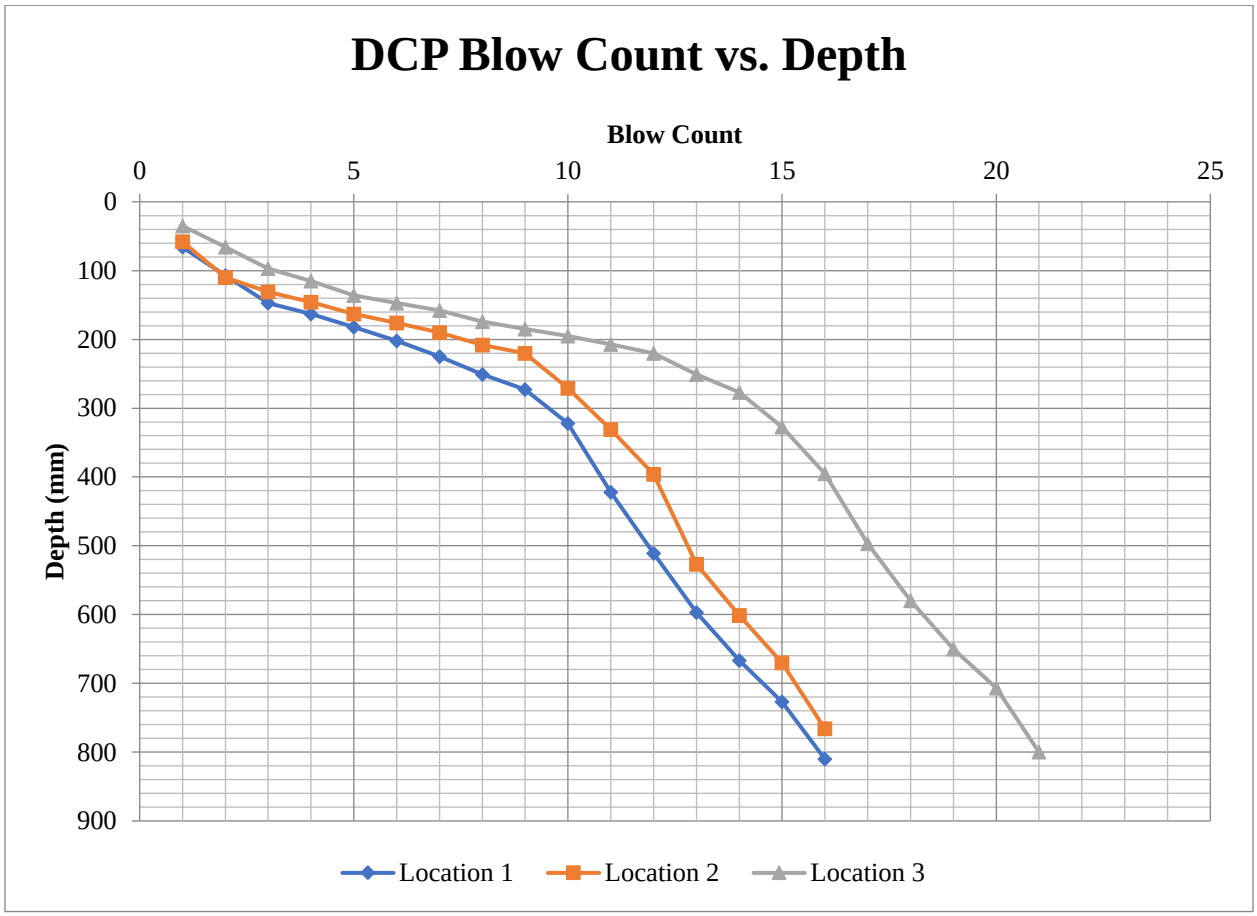

Figure 36. Test 13 DCP Blow Count vs. Depth.

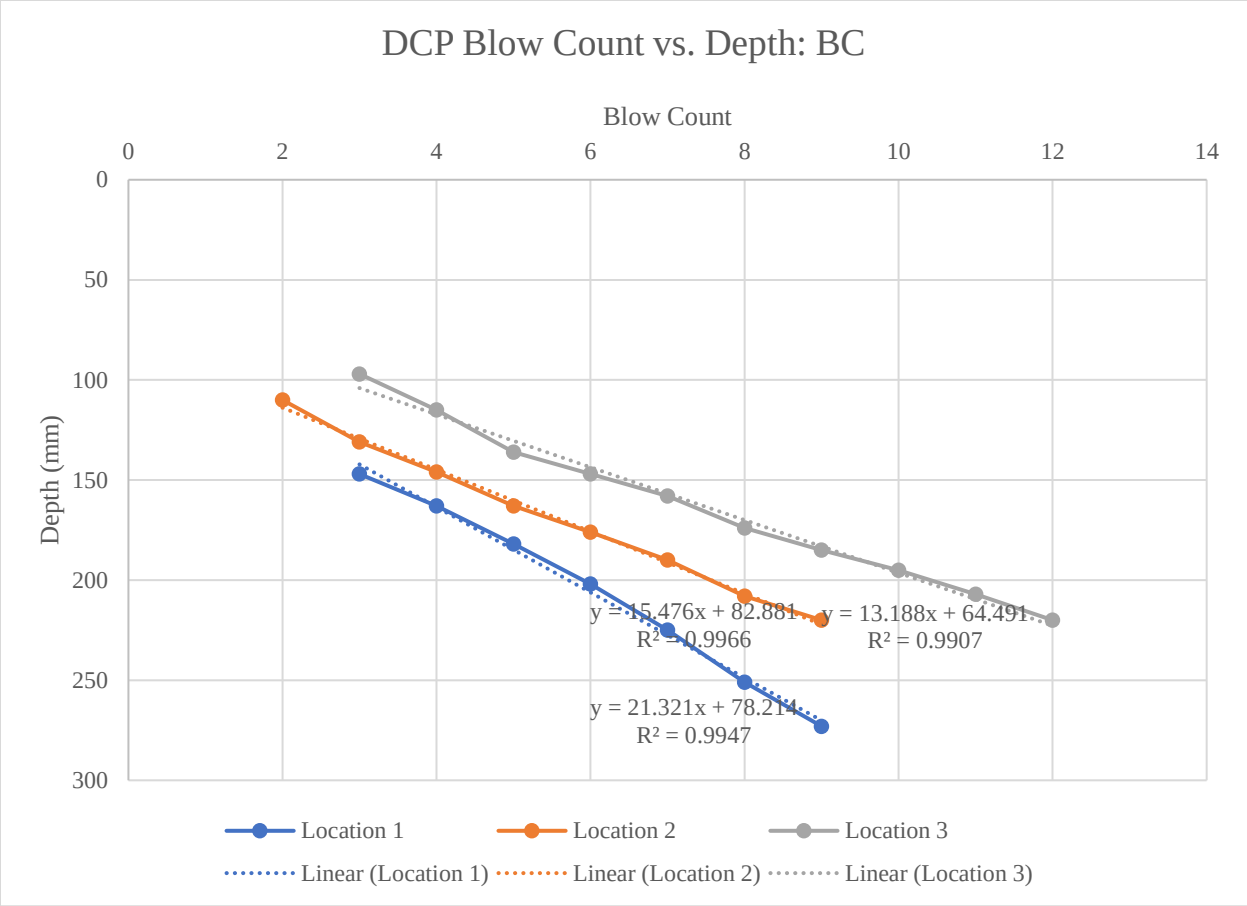

Figure 37. Test 13 DCPI: Base Course.

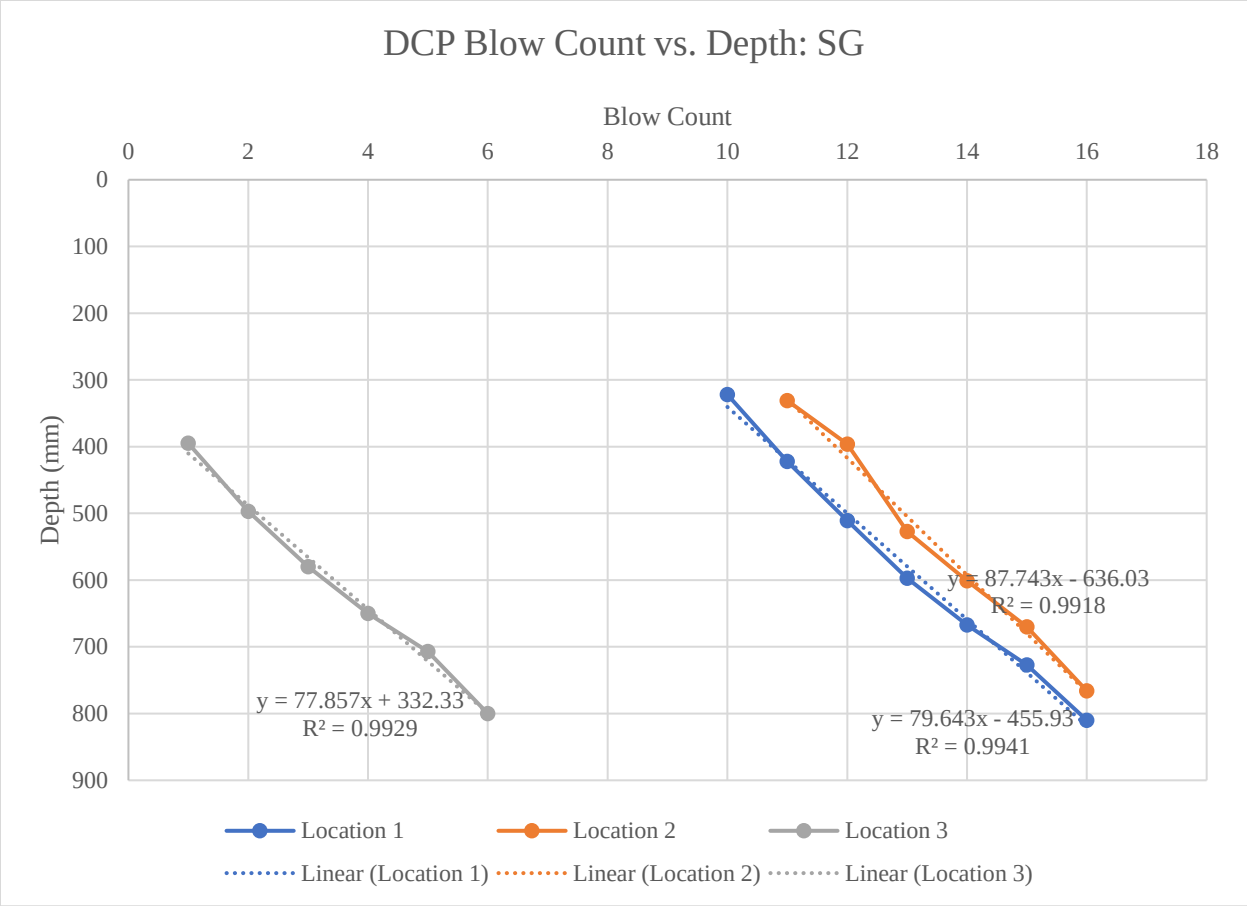

Figure 38. Test 13 DCPI: Subgrade.

Table A.28. Test 13 DCPI and CBR.

	DCPI (mm/Blow): BC	**DCPI (mm/Blow): SG**	**CBR (%): BC**	**CBR (%): SG**
Loc. 1	21.321	79.643	9.5	2.2
Loc. 2	15.476	87.743	13.6	1.9
Loc. 3	13.188	77.857	16.2	2.2

Table A.29. Test 13 DCP Output, Standard Deviation, Coefficient of Variation.

	Base Course	**Subgrade**
Mean CBR (%)	13.1	2.1
Std. Dev. (σ)	3.405	0.147
CV	25.98%	6.98%

Test 14: VGB/ 2%-CBR SG (Control)

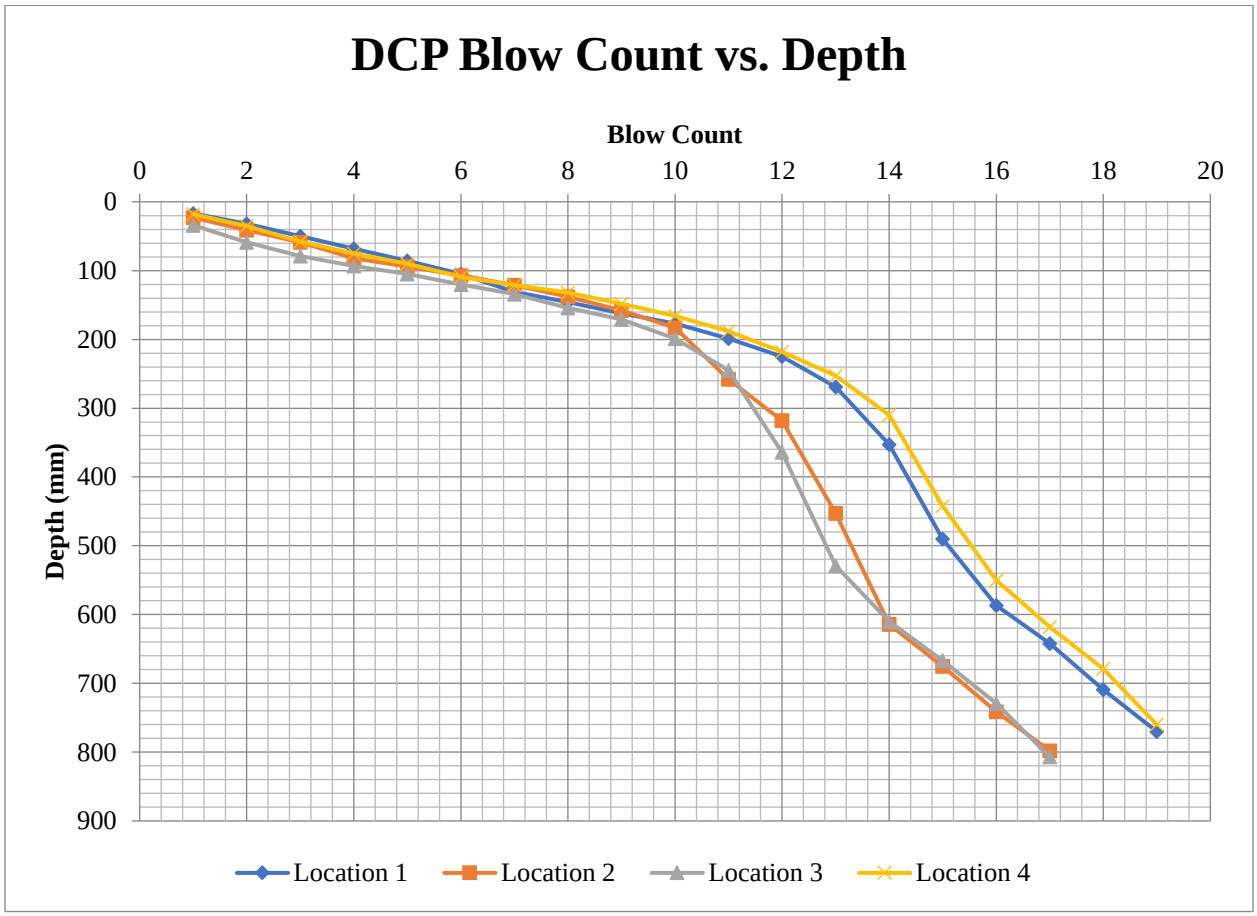

Figure 39. Test 14 DCP Blow Count vs. Penetration Depth.

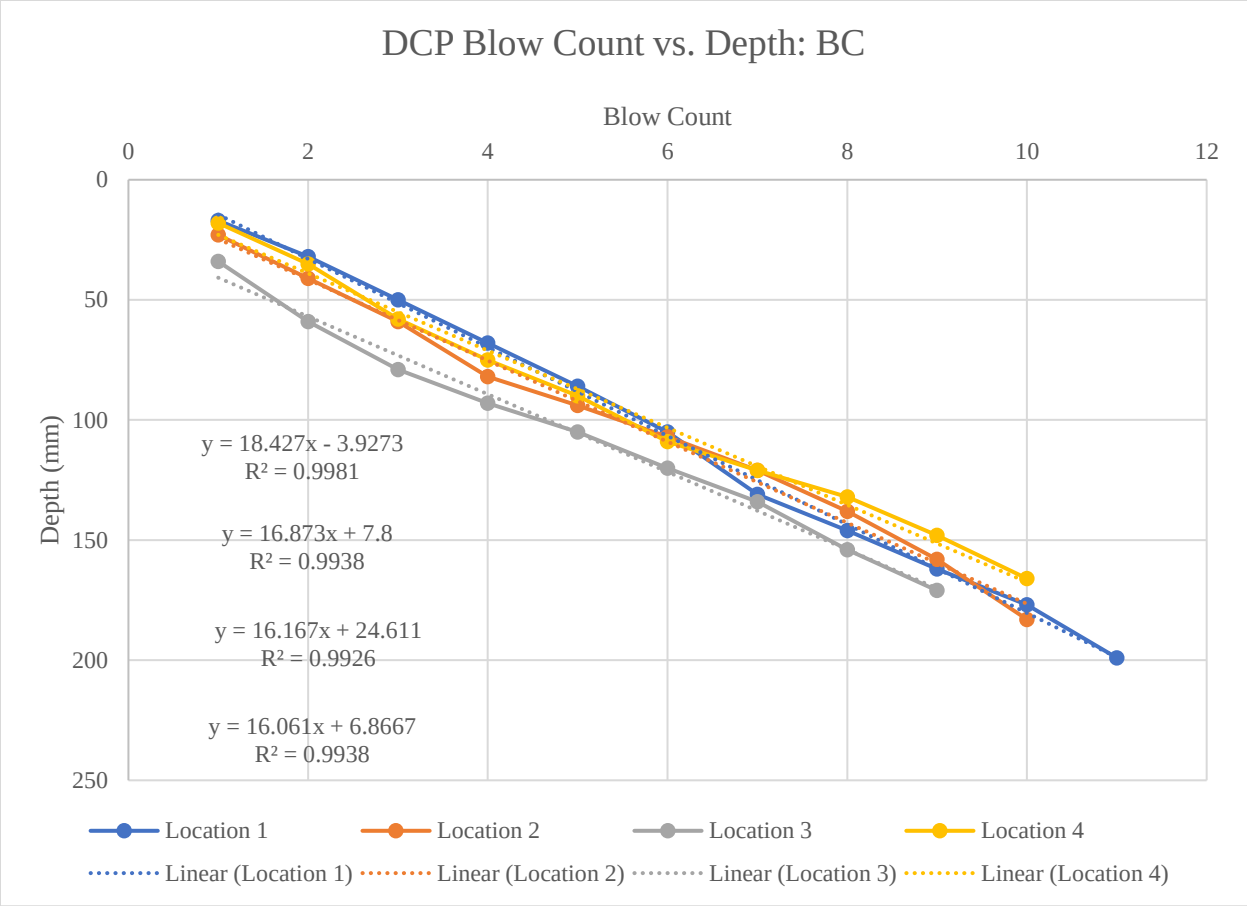

Figure 40. Test 14 DCPI: Base Course.

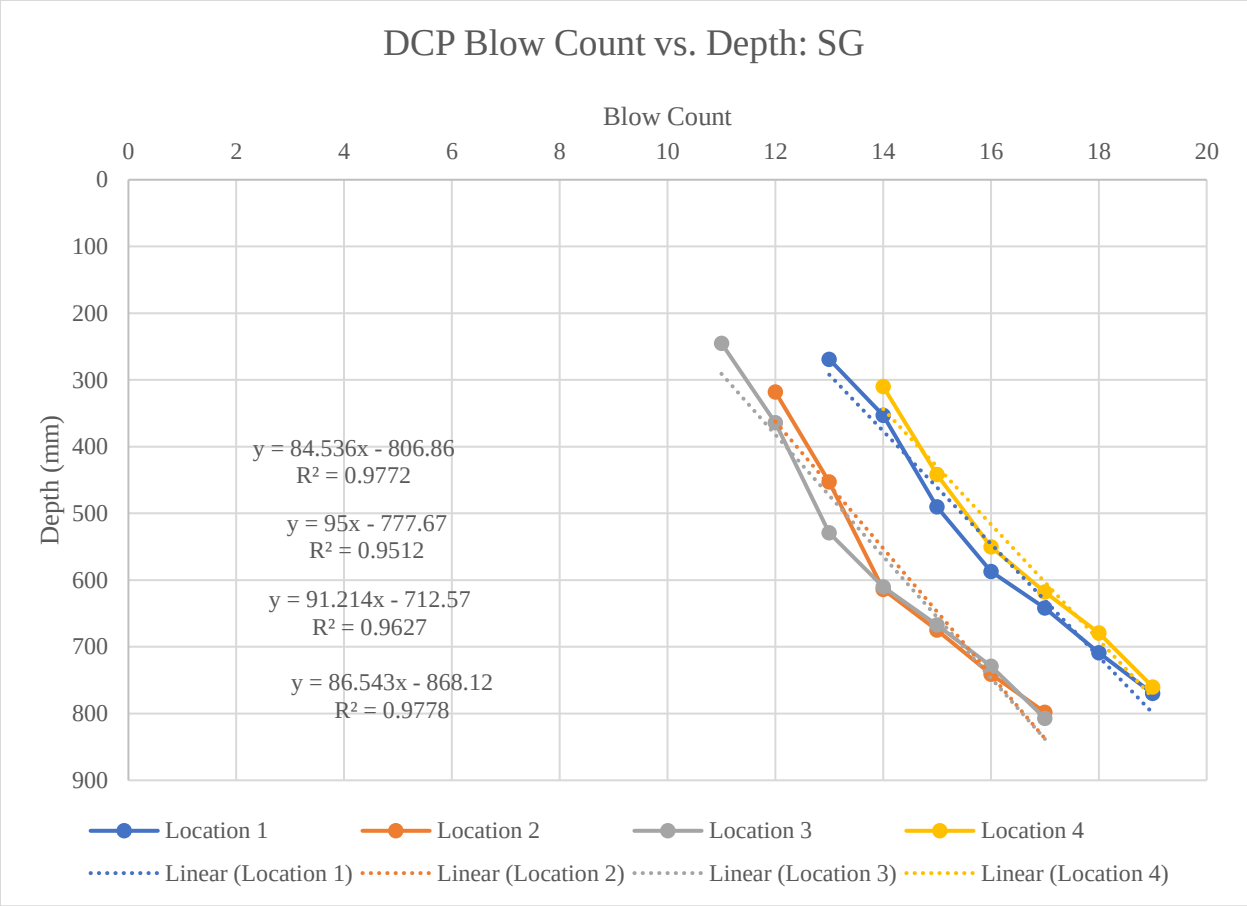

Figure 41. Test 14 DCPI: Subgrade.

Table A.30. Test 14 DCPI and CBR.

	DCPI (mm/Blow): BC	**DCPI (mm/Blow): SG**	**CBR (%): BC**	**CBR (%): SG**
Loc. 1	18.427	84.536	11.2	2.0
Loc. 2	16.873	95	12.3	1.8
Loc. 3	16.167	91.214	12.9	1.9
Loc. 4	16.061	86.543	13.0	2.0

Table A.31. Test 14 CBR Output, Standard Deviation, Coefficient of Variation.

	Base Course	**Subgrade**
Mean CBR (%)	12.4	1.9
Std. Dev. (σ)	0.855	0.112
CV	6.91%	5.85%

Test 15: VGB/ GG/ 2%-CBR SG (Breakdown during test)

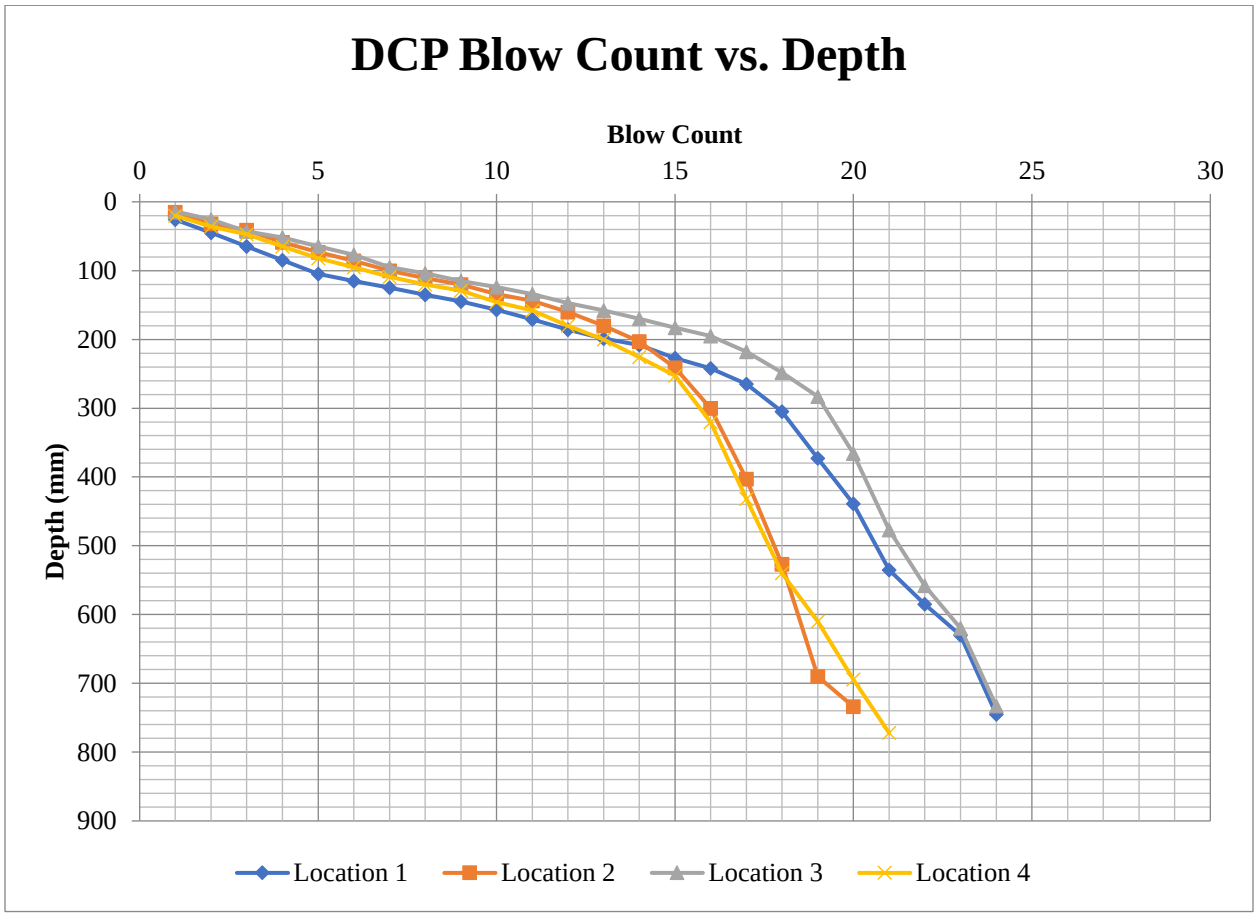

Figure 42. Test 15 DCP Blow Count vs. Penetration Depth.

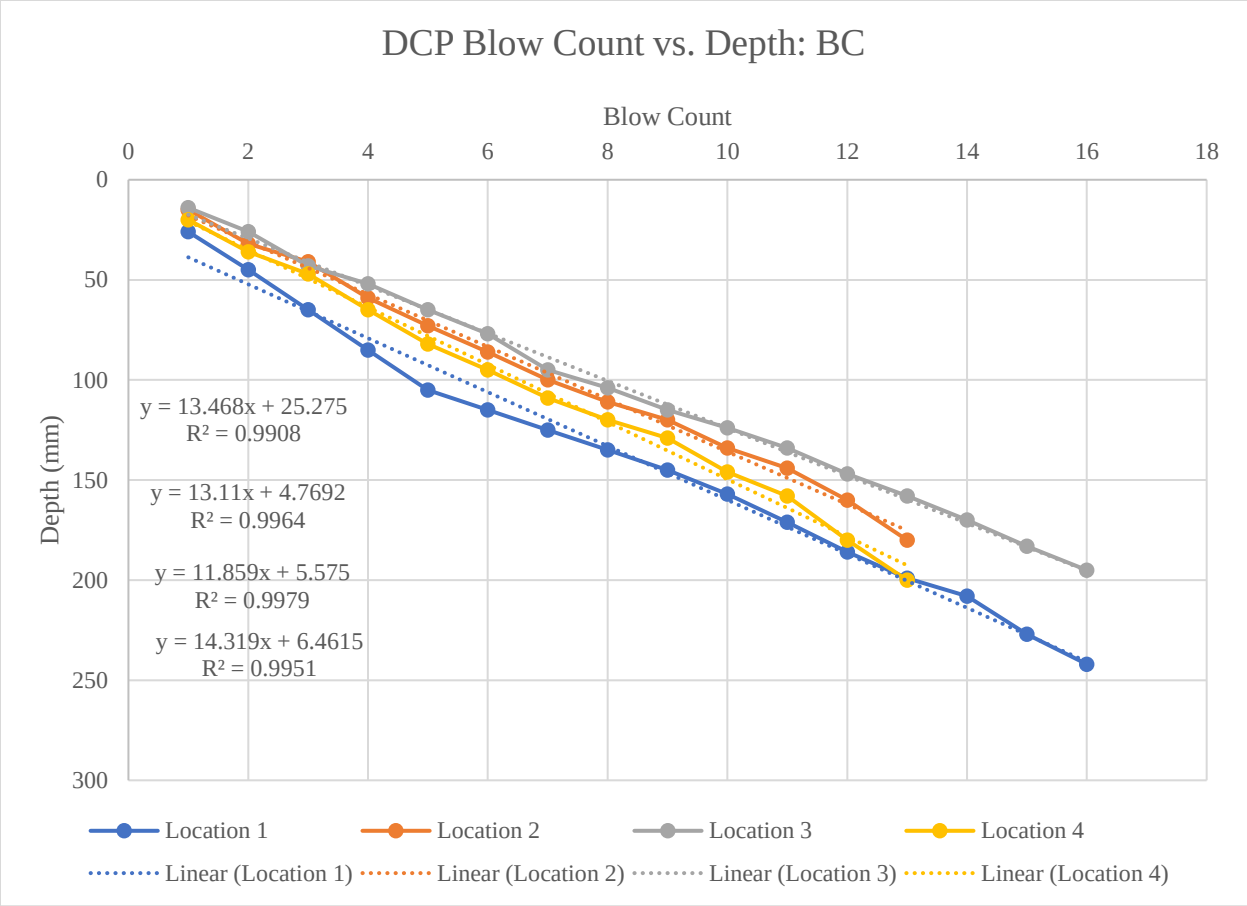

Figure 43. Test 15 DCPI: Base Course.

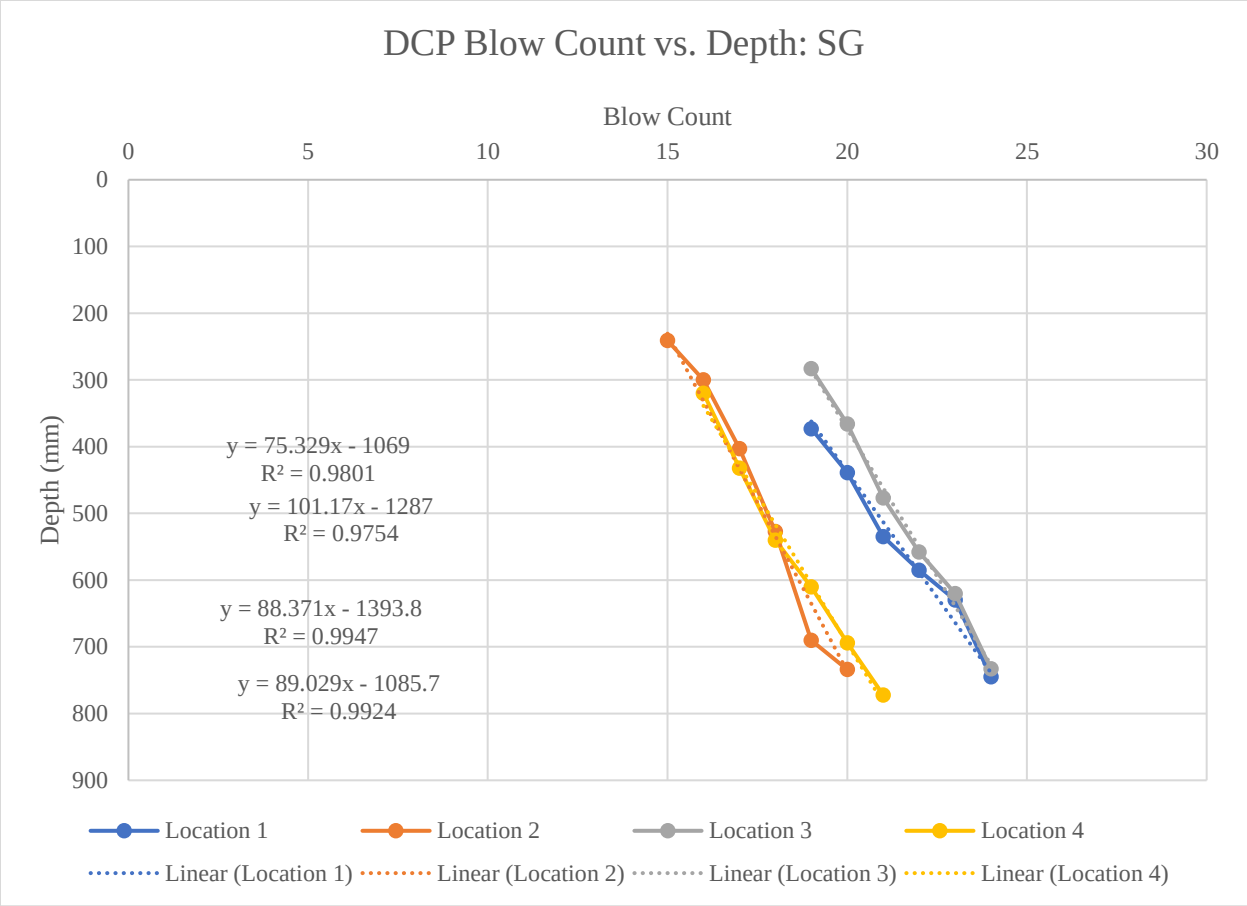

Figure 44: Test 15 DCPI: Subgrade.

Table A.32. Test 15 DCPI and CBR.

	DCPI (mm/Blow): BC	**DCPI (mm/Blow): SG**	**CBR (%): BC**	**CBR (%): SG**
Loc. 1	13.468	75.329	15.9	2.3
Loc. 2	13.11	101.17	16.4	1.7
Loc. 3	11.859	83.371	18.3	2.1
Loc. 4	14.319	89.029	14.8	1.9

Table A.33. Test 15 CBR Output, Standard Deviation, Coefficient of Variation.

	Base Course	**Subgrade**
Mean CBR (%)	16.3	2.0
Std. Dev. (σ)	1.459	0.272
CV	8.93%	13.69%

Test 16: RCA/ GG/ 2%-CBR SG

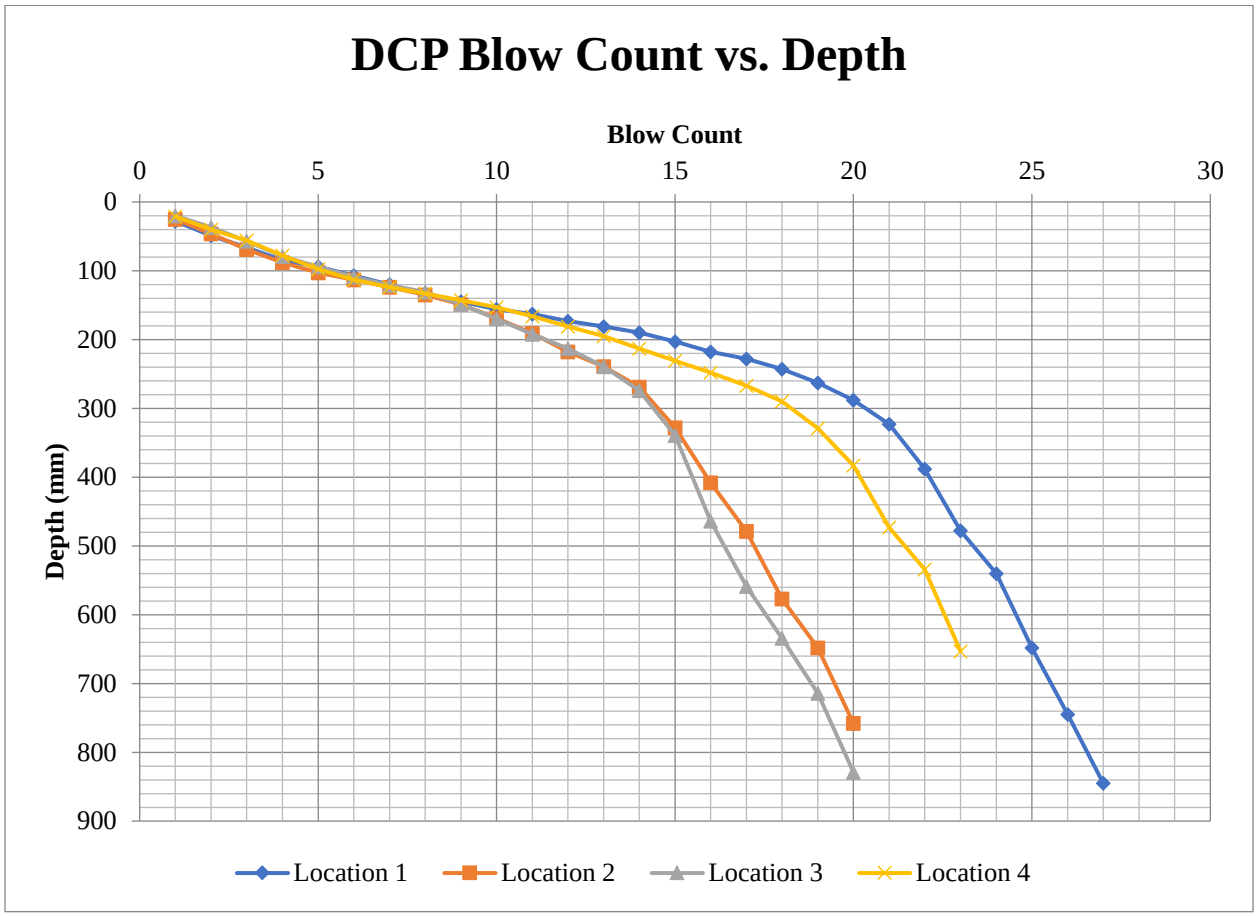

Figure 45. Test 16 DCP Blow Count vs. Penetration Depth.

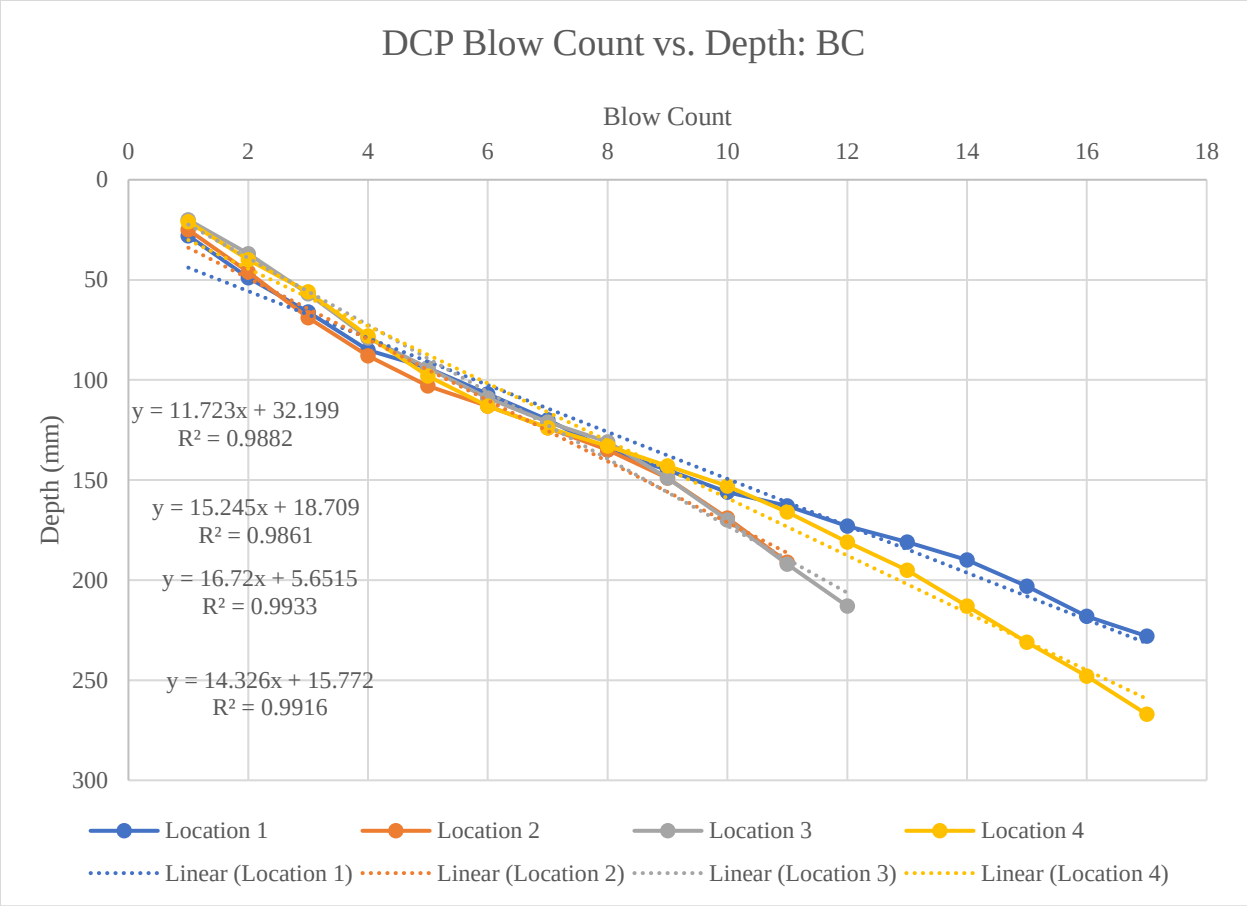

Figure 46. Test 16 DCPI: Base Course.

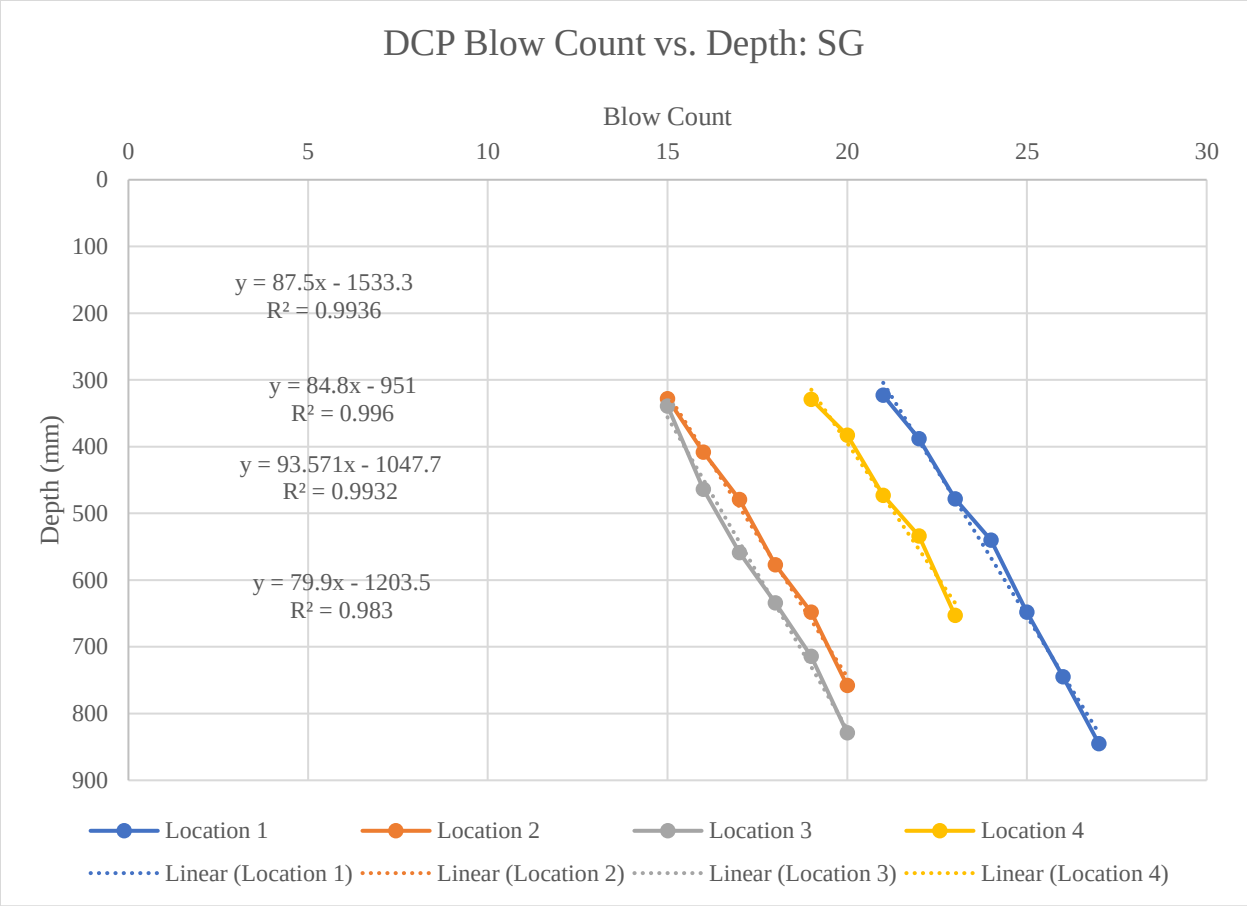

Figure 47. Test 16 DCPI: Subgrade.

Table A.34. Test 16 DCPI and CBR.

	DCPI (mm/Blow): BC	**DCPI (mm/Blow): SG**	**CBR (%): BC**	**CBR (%): SG**
Loc. 1	11.723	87.5	18.5	2.0
Loc. 2	15.245	84.8	13.8	2.0
Loc. 3	16.72	93.571	12.5	1.8
Loc. 4	14.326	79.9	14.8	2.2

Table A.35. Test 16 CBR Output, Standard Deviation, Coefficient of Variation.

	Base Course	**Subgrade**
Mean CBR (%)	14.9	2.0
Std. Dev. (σ)	2.608	0.146
CV	17.50%	7.34%

Test 17: VGB/ NW/ 2%-CBR SG

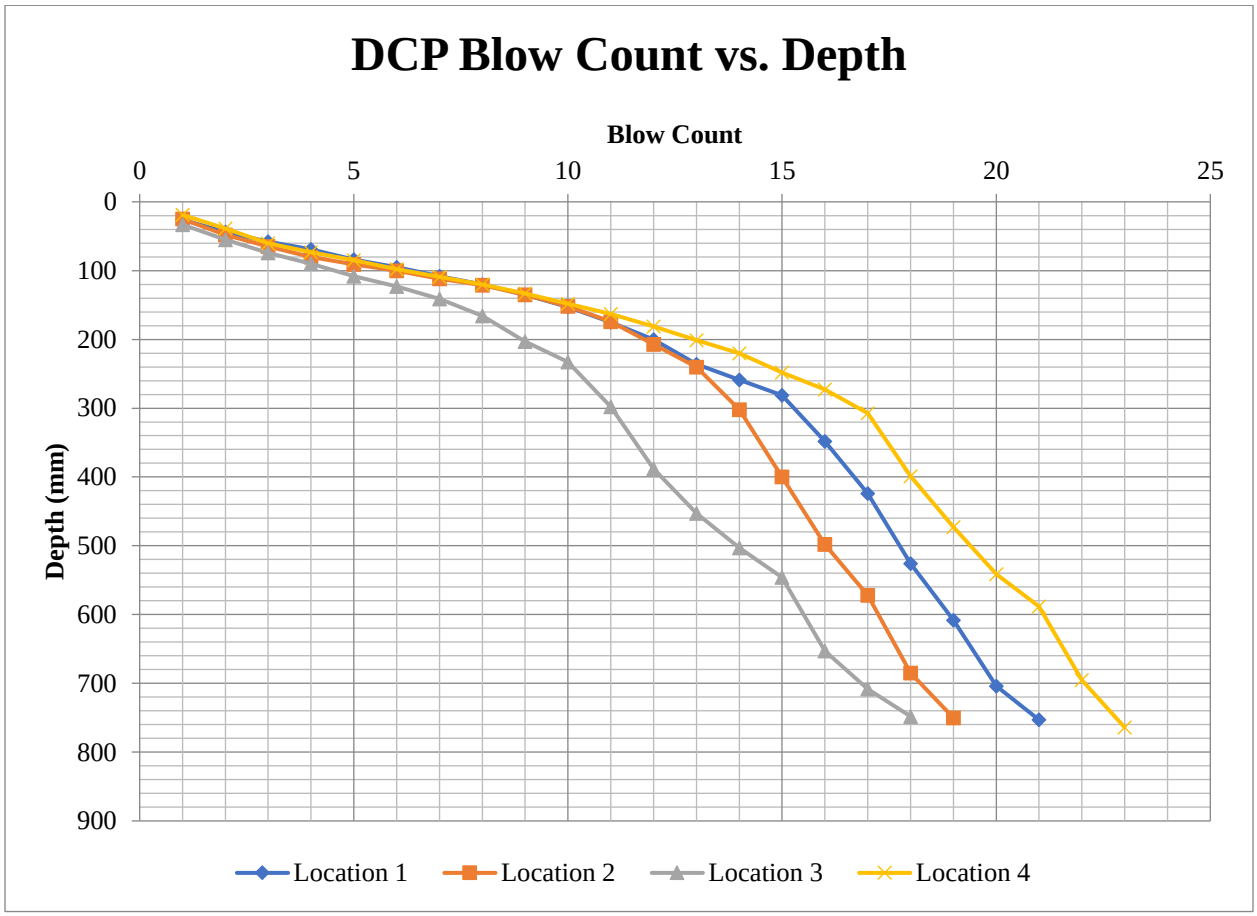

Figure 48. Test 17 DCP Blow Count vs. Penetration Depth.

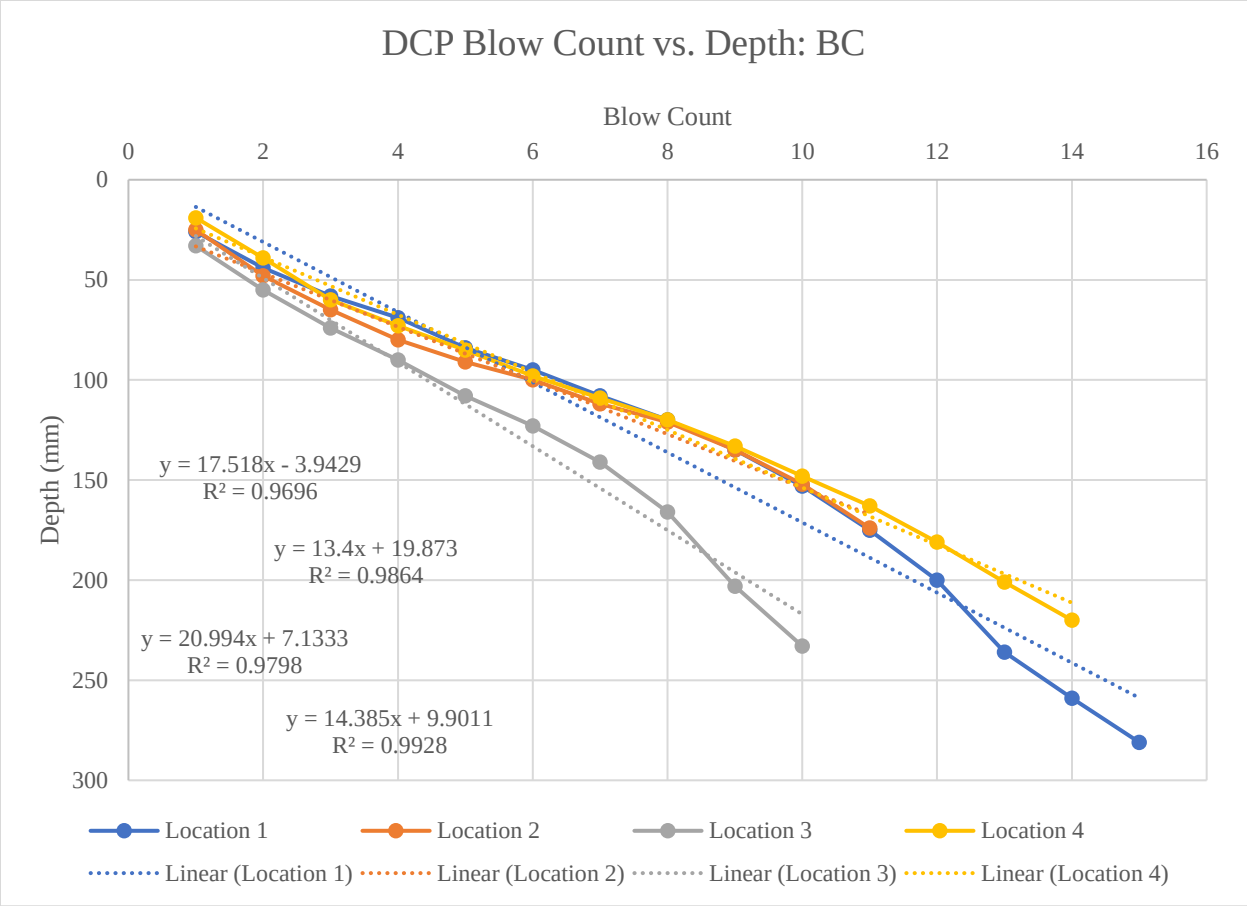

Figure 49. Test 17 DCPI: Base Course.

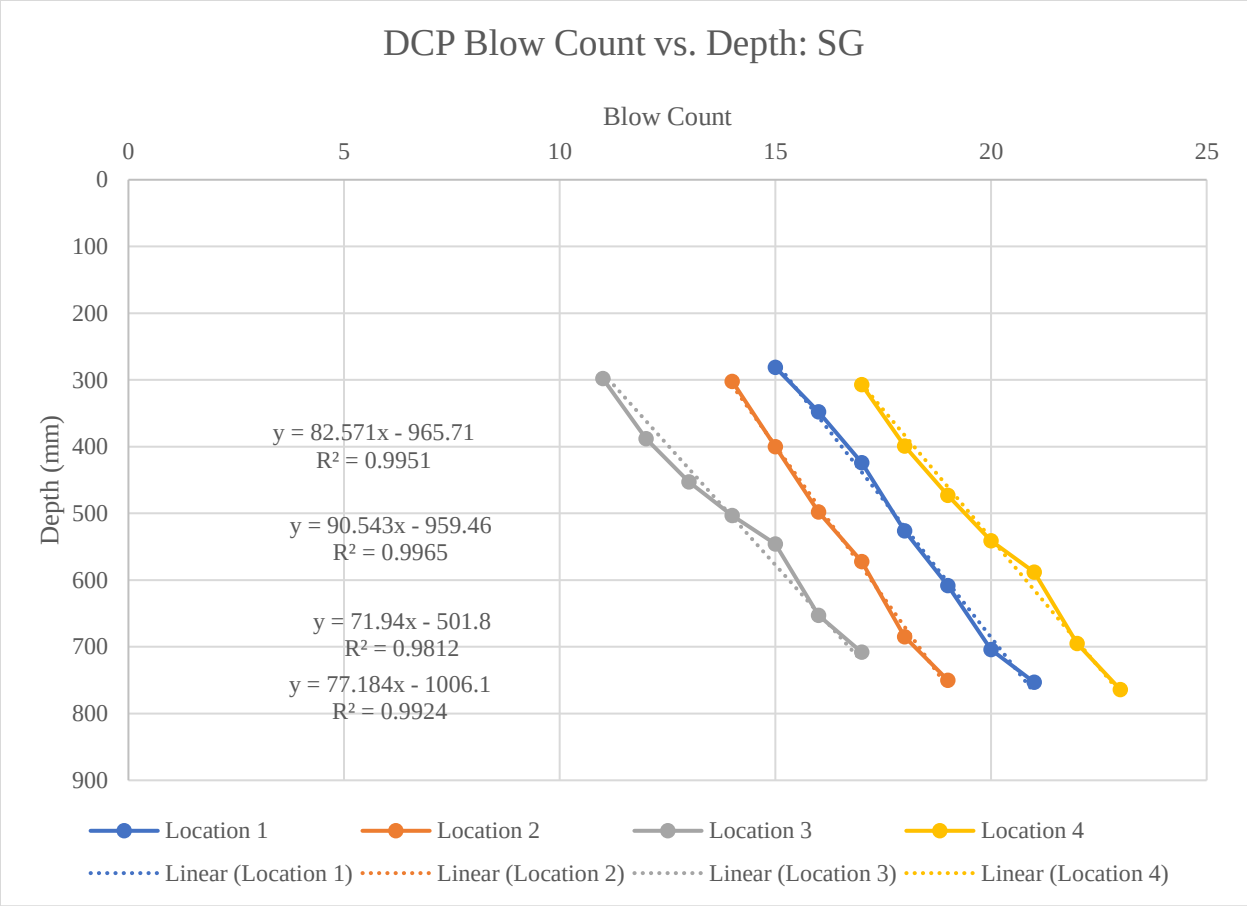

Figure 50. Test 17 DCPI: Subgrade.

Table A.36. Test 17 DCPI and CBR.

	DCPI (mm/Blow): BC	**DCPI (mm/Blow): SG**	**CBR (%): BC**	**CBR (%): SG**
Loc. 1	17.518	82.571	11.8	2.1
Loc. 2	13.4	90.543	16.0	1.9
Loc. 3	20.994	71.94	9.7	2.4
Loc. 4	14.385	77.184	14.7	2.2

Table A.37. Test 17 CBR Output, Standard Deviation, Coefficient of Variation.

	Base Course	**Subgrade**
Mean CBR (%)	13.0	2.2
Std. Dev. (σ)	2.851	0.235
CV	21.85%	10.89%

Test 18: RCA/ NW/ 2%-CBR SG

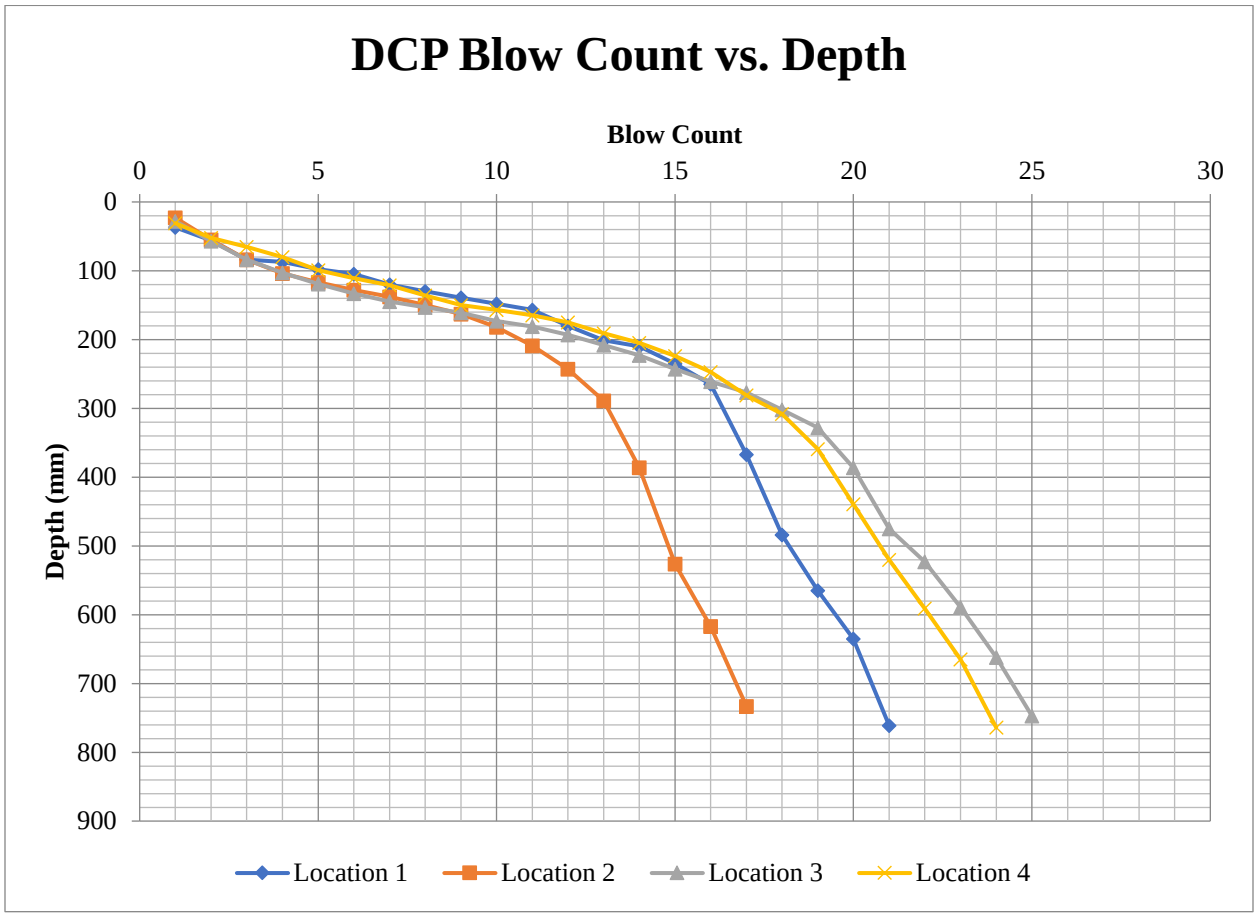

Figure 51. Test 18 DCP Blow Count vs. Penetration Depth.

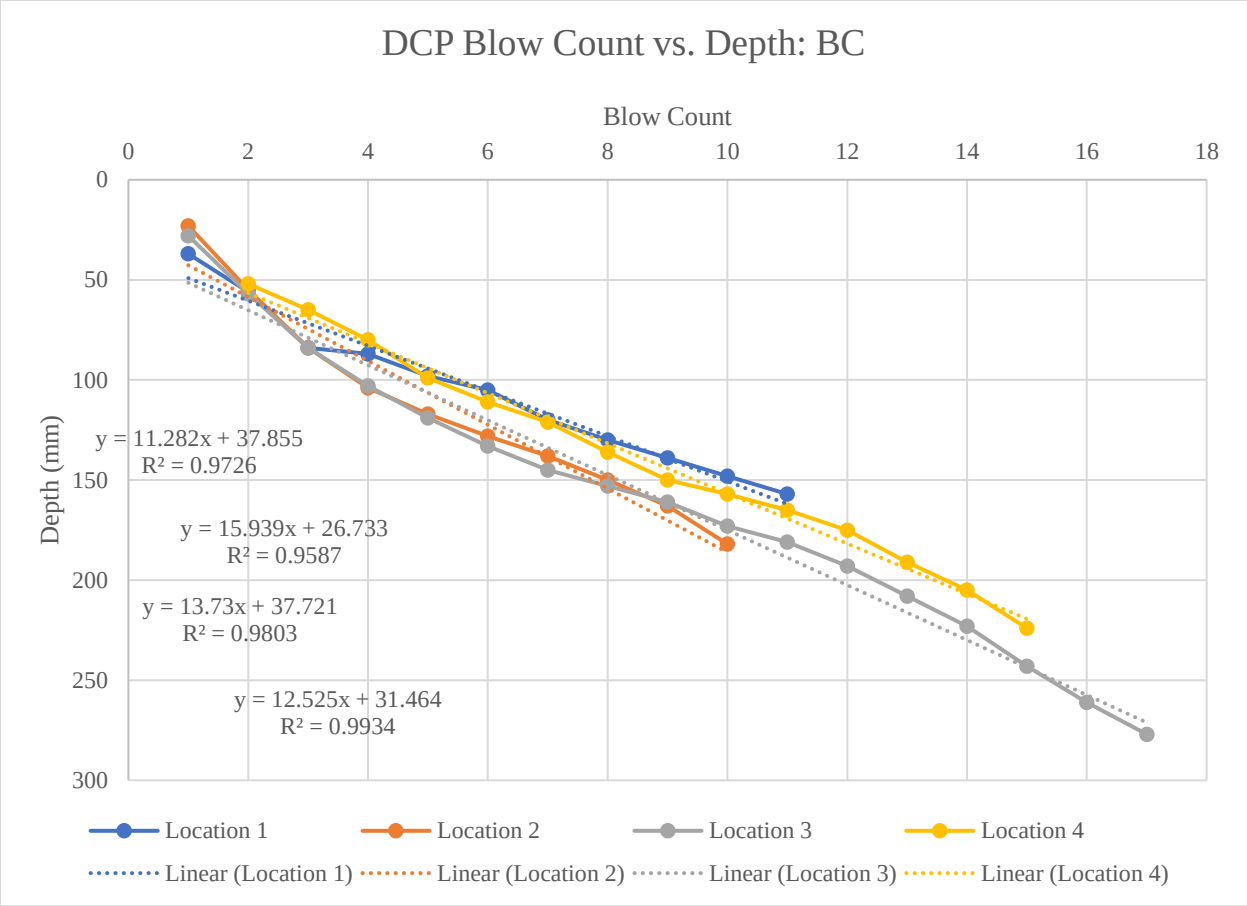

Figure 52. Test 18 DCPI: Base Course.

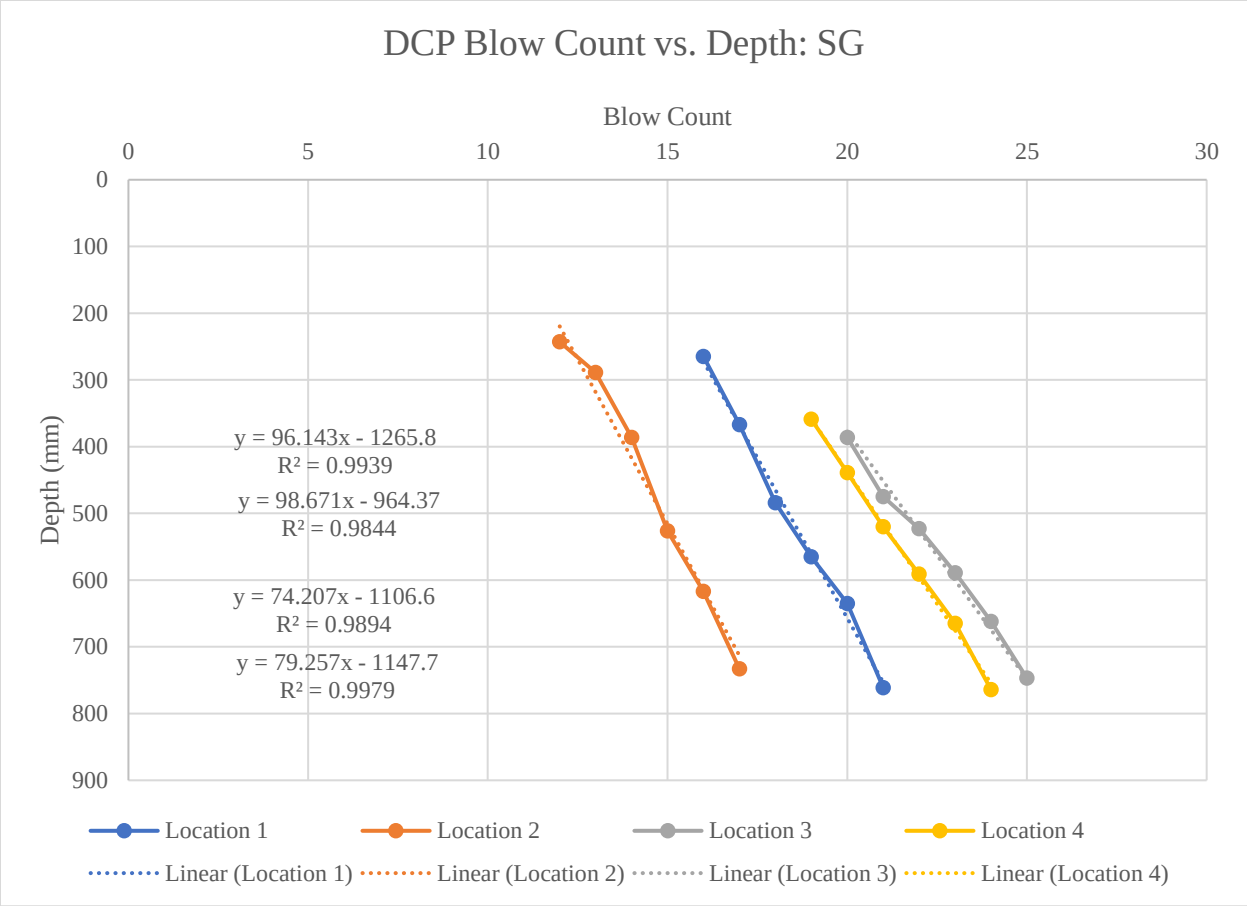

Figure 53. Test 18 DCPI: Subgrade.

Table A.38. Test 18 DCPI and CBR.

	DCPI (mm/Blow): BC	**DCPI (mm/Blow): SG**	**CBR (%): BC**	**CBR (%): SG**
Loc. 1	11.282	96.143	19.4	1.8
Loc. 2	15.939	98.761	13.1	1.7
Loc. 3	13.73	74.207	15.5	2.3
Loc. 4	12.525	79.257	17.2	2.2

Table A.39. Test 18 CBR Output, Standard Deviation, Coefficient of Variation.

	Base Course	**Subgrade**
Mean CBR (%)	16.3	2.0
Std. Dev. (σ)	2.628	0.316
CV	16.11%	15.83%

Test 19: VGB /GG/ 2%-CBR SG

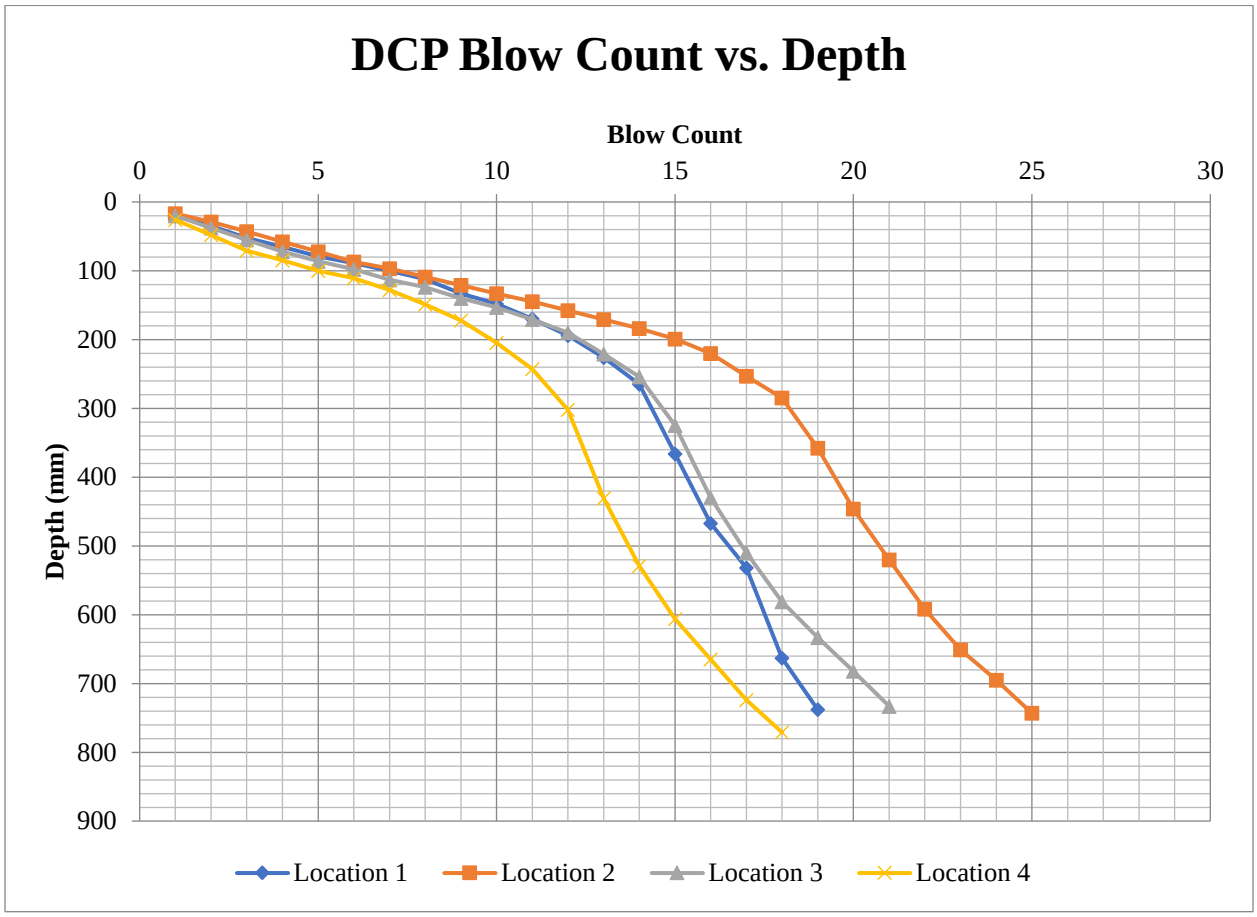

Figure 54. Test 19 DCP Blow Count vs. Penetration Depth.

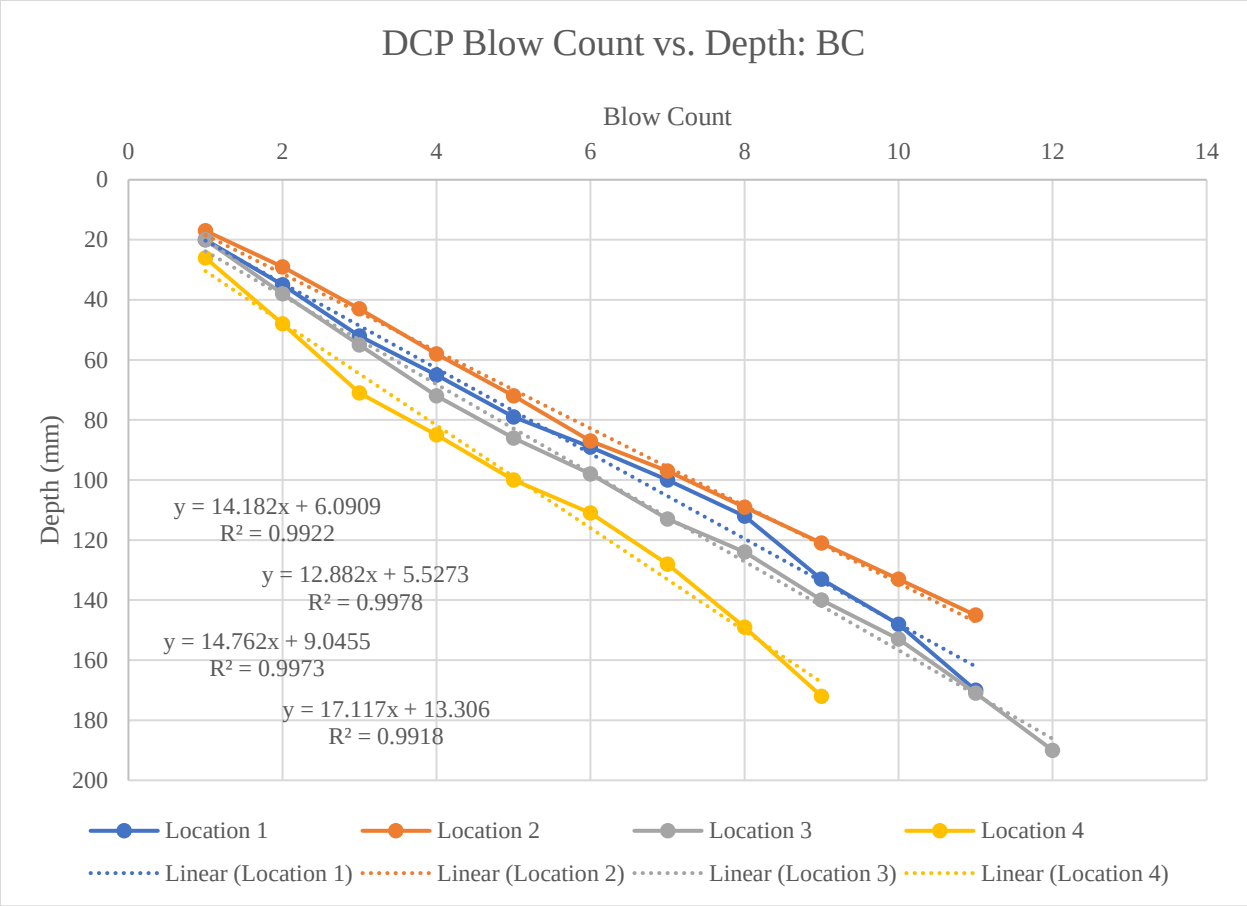

Figure 55. Test 19 DCPI: Base Course.

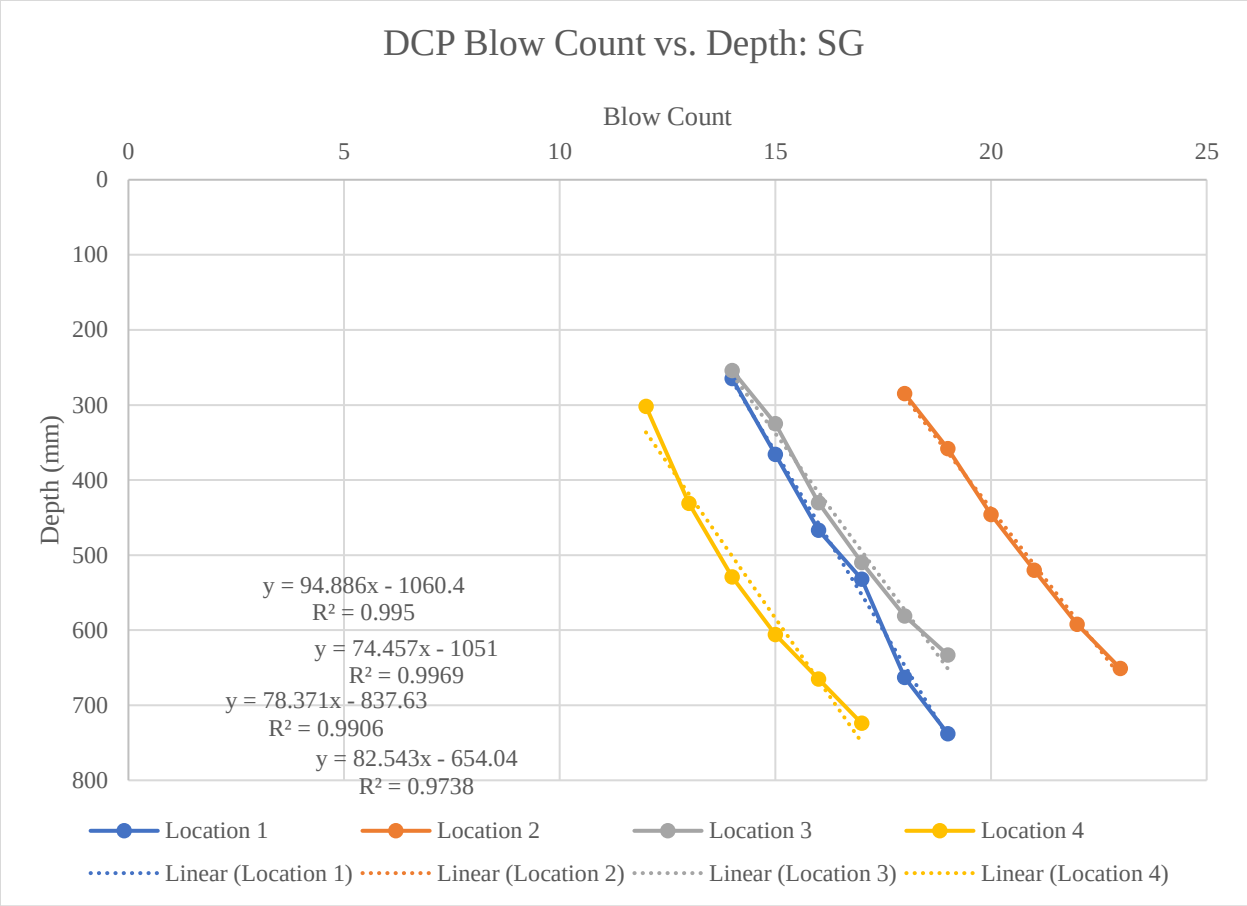

Figure 56. Test 19 DCPI: Subgrade.

Table A.40. Test 19 DCPI and CBR.

	DCPI (mm/Blow): BC	**DCPI (mm/Blow): SG**	**CBR (%): BC**	**CBR (%): SG**
Loc. 1	14.182	94.886	15.0	1.8
Loc. 2	12.882	74.457	16.7	2.3
Loc. 3	14.762	78.371	14.3	2.2
Loc. 4	17.117	82.543	12.1	2.1

Table A.41. Test 20 CBR Output, Standard Deviation, Coefficient of Variation.

	Base Course	**Subgrade**
Mean CBR (%)	14.5	2.1
Std. Dev. (σ)	1.881	0.238
CV	12.95%	11.31%

Test 20: VGB (100 mm) /NW/ 3%-CBR SG

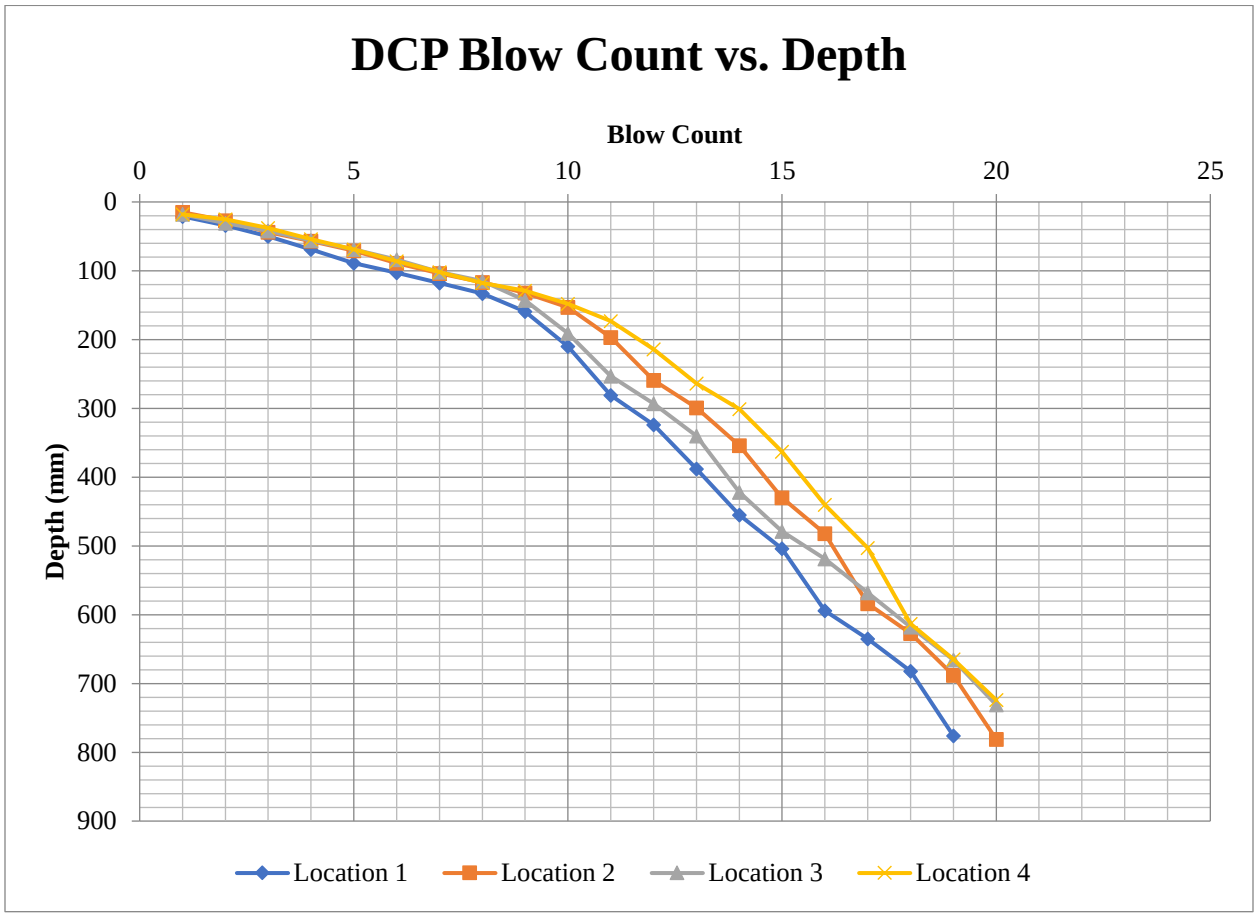

Figure 57. Test 20 DCP Blow Count vs. Penetration Depth.

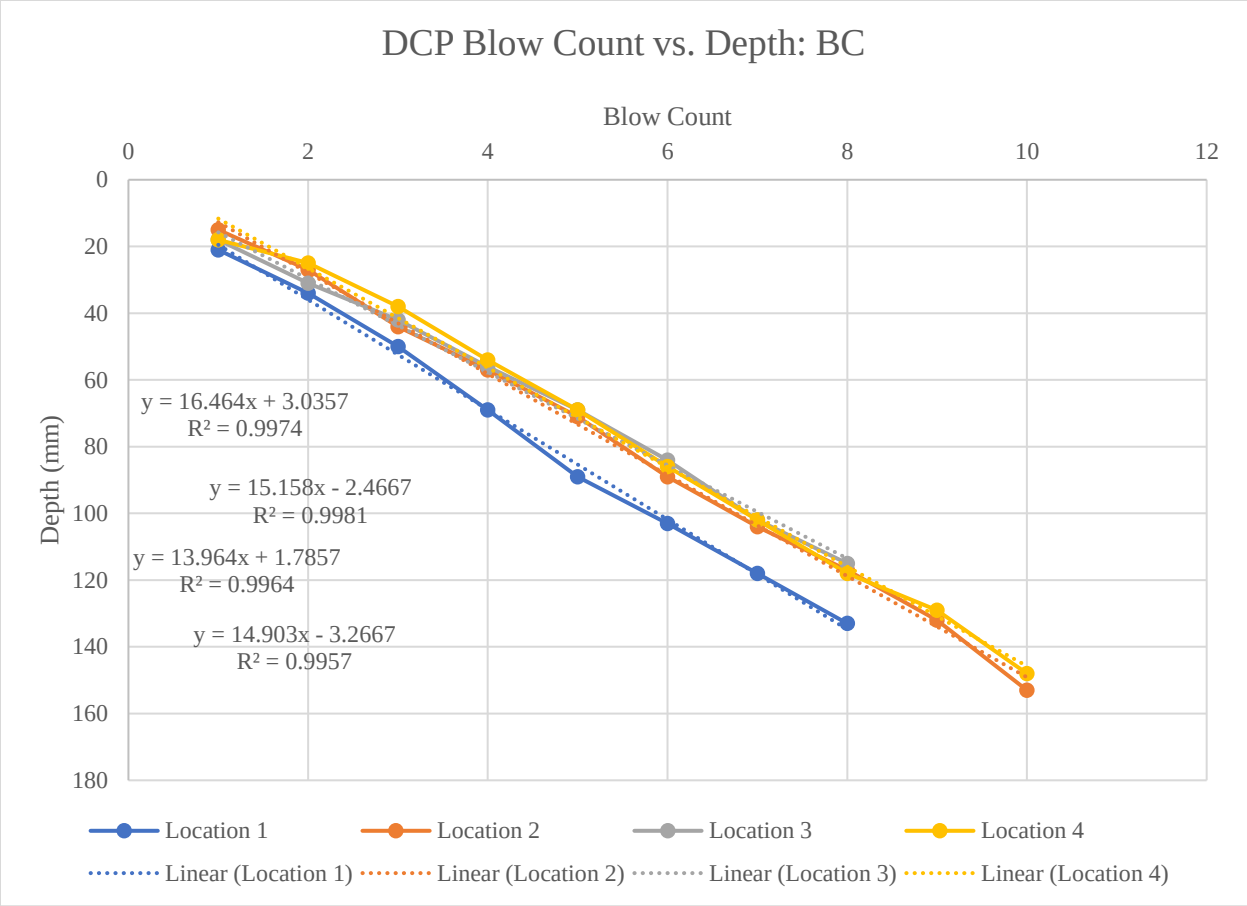

Figure 58. Test 20 DCPI: Base Course.

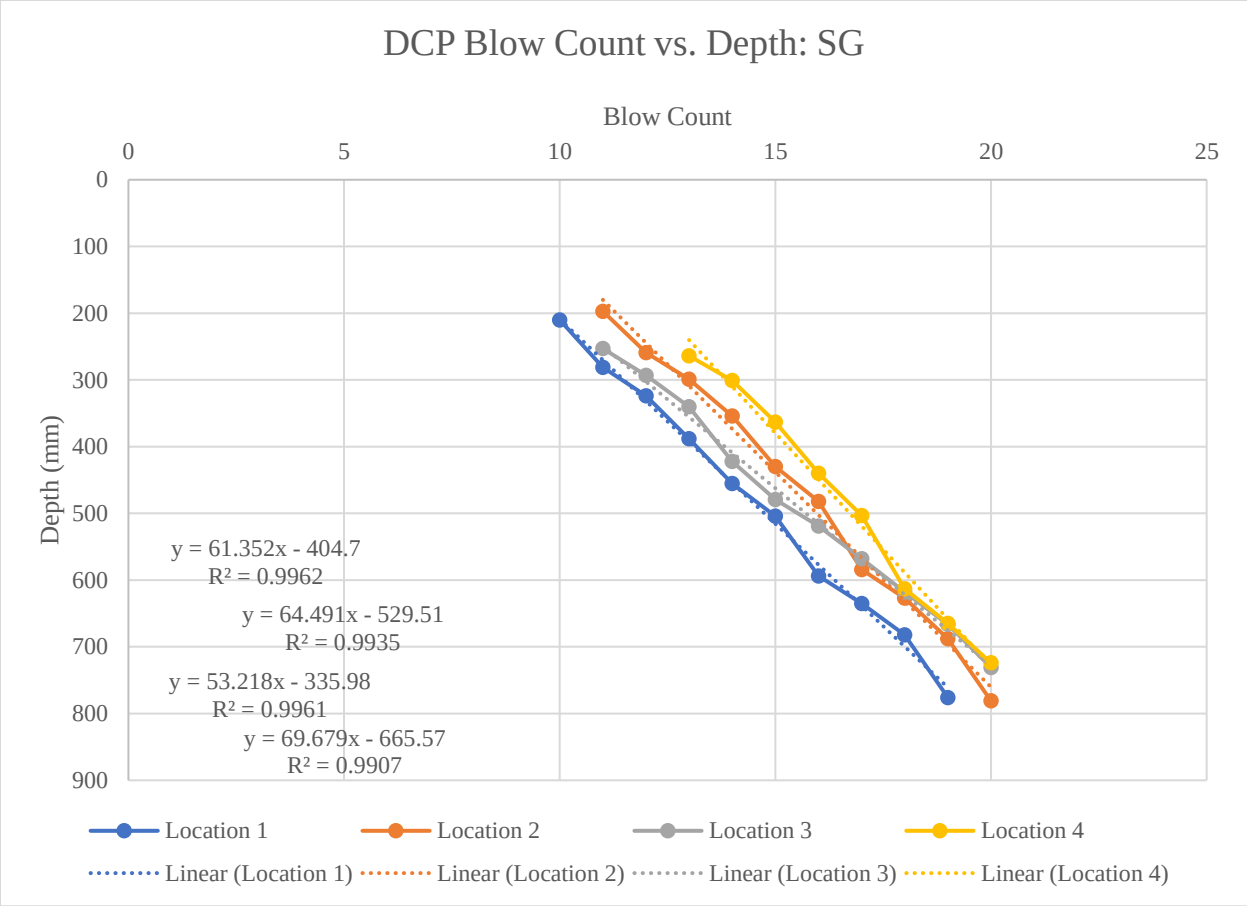

Figure 59. Test 20 DCPI: Subgrade.

Table A.42. Test 20 DCPI and CBR.

	DCPI (mm/Blow): BC	**DCPI (mm/Blow): SG**	**CBR (%): BC**	**CBR (%): SG**
Loc. 1	16.464	61.352	12.7	2.9
Loc. 2	15.158	64.491	13.9	2.7
Loc. 3	13.964	53.218	15.2	3.4
Loc. 4	14.903	68.679	14.2	2.6

Table A.43. Test 20 CBR Output, Standard Deviation, Coefficient of Variation.

	Base Course	**Subgrade**
Mean CBR (%)	14.0	2.9
Std. Dev. (σ)	1.055	0.363
CV	7.54%	12.50%

Test 21: RCA/GG/NW/ 2%-CBR SG

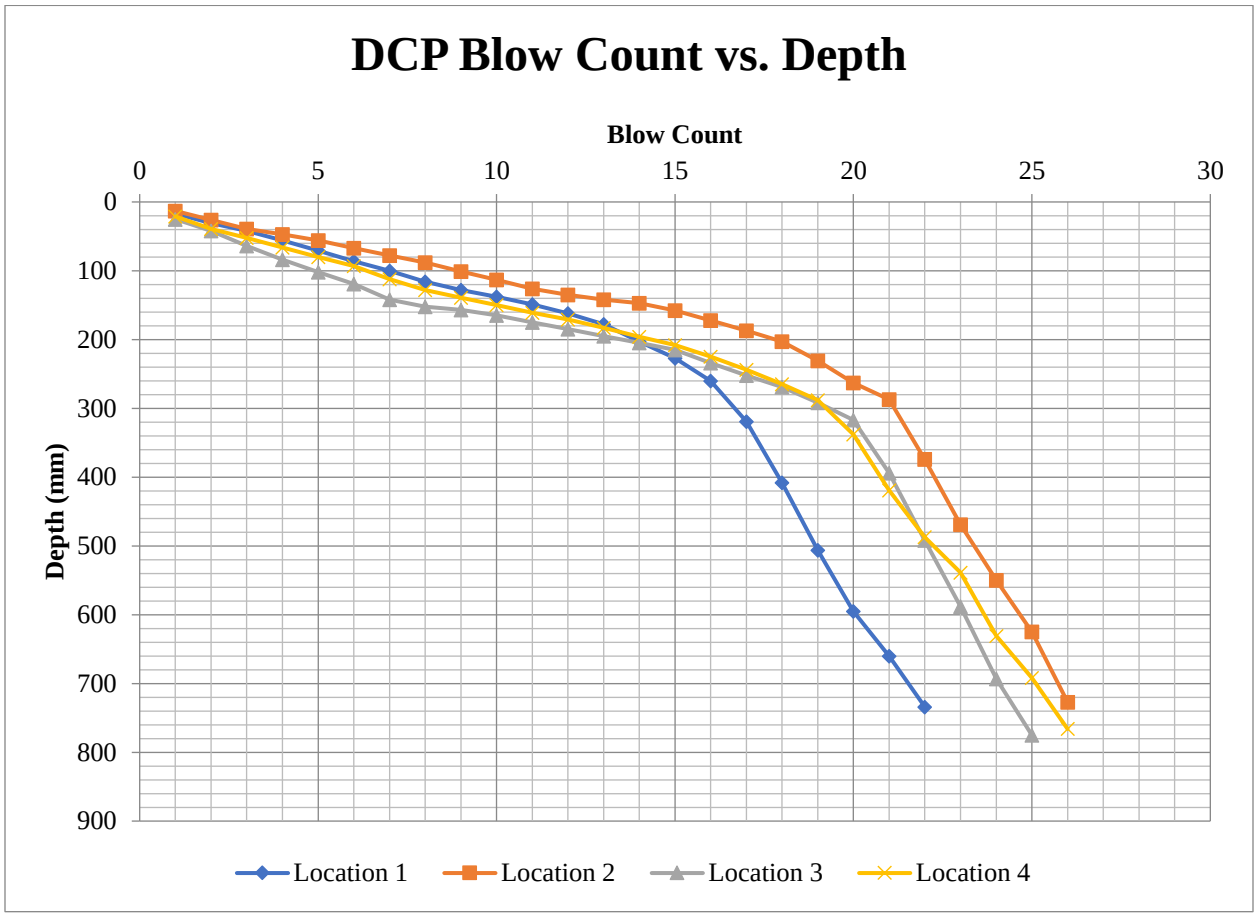

Figure 60. Test 21 DCP Blow Count vs. Penetration Depth.

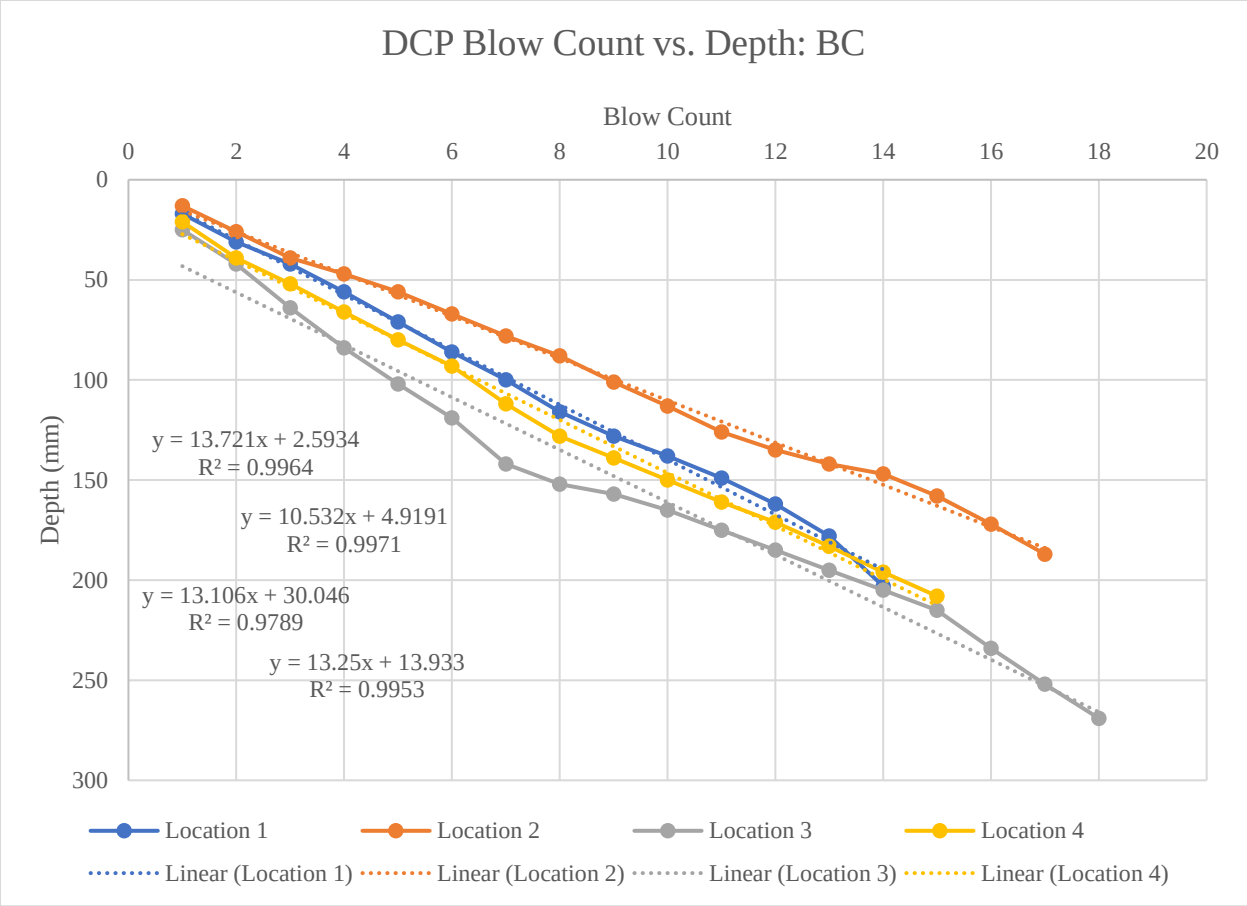

Figure 61. Test 21 DCPI: Base Course.

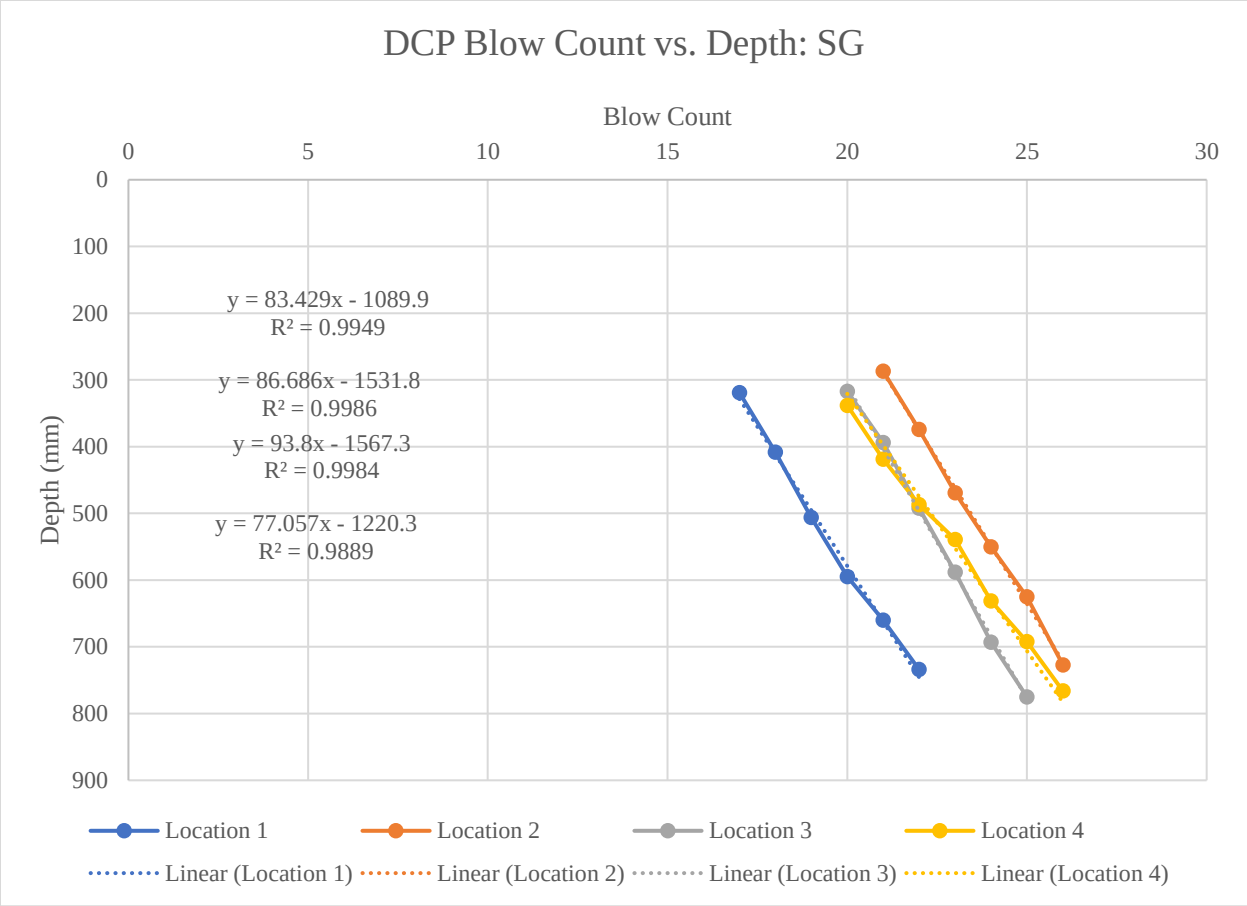

Figure 62. Test 21 DCPI: Subgrade.

Table A.44. Test 21 DCPI and CBR.

	DCPI (mm/Blow): BC	**DCPI (mm/Blow): SG**	**CBR (%): BC**	**CBR (%): SG**
Loc. 1	13.721	83.429	15.5	2.1
Loc. 2	10.532	86.686	20.9	2.0
Loc. 3	13.106	93.8	16.4	1.8
Loc. 4	13.25	77.057	16.2	2.2

Table A.45. Test 21 CBR Output, Standard Deviation, Coefficient of Variance.

	Base Course	**Subgrade**
Mean CBR (%)	17.2	2.0
Std. Dev. (σ)	2.464	0.185
CV	14.29%	9.16%

Test 22: VGB/GG/NW/ 2%-CBR SG

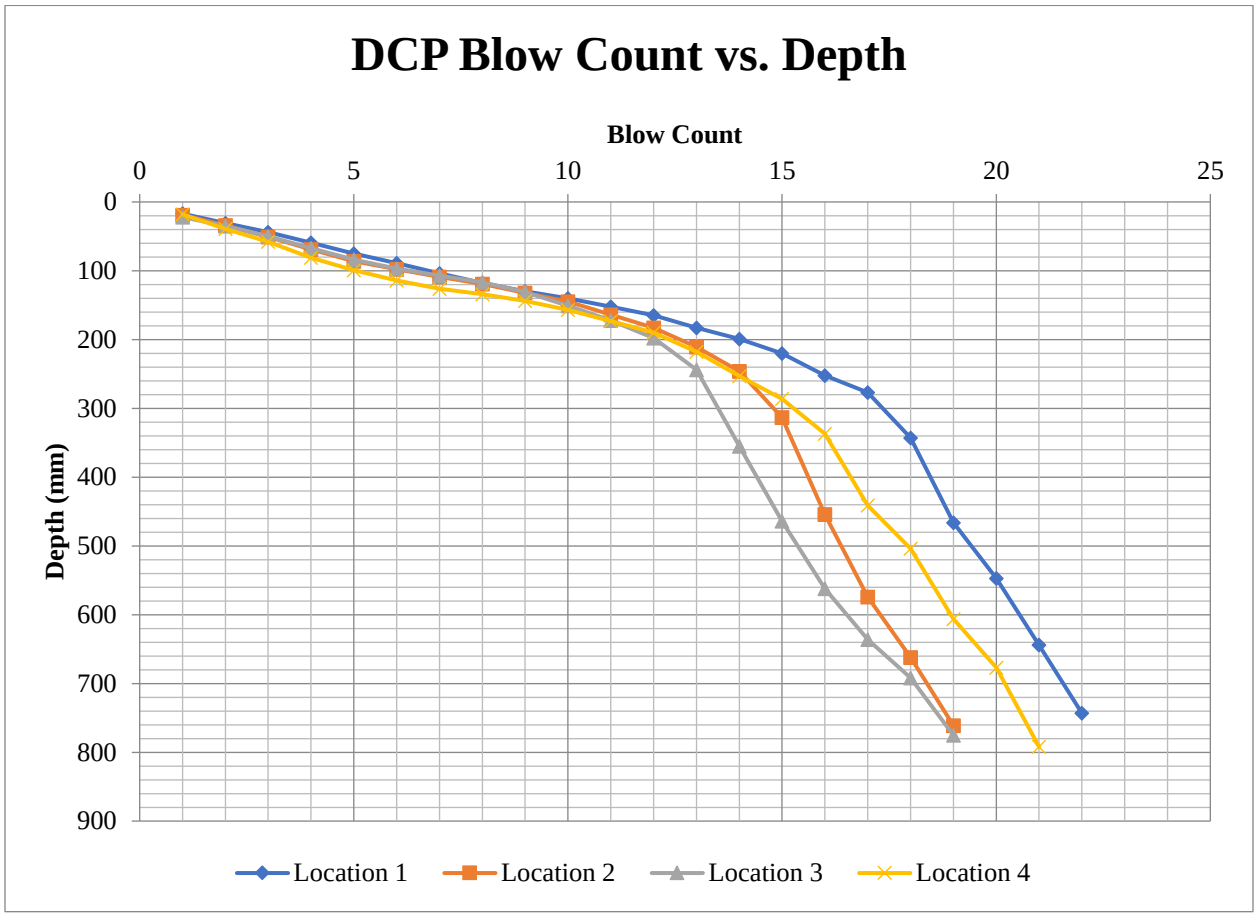

Figure 63. Test 22 DCP Blow Count vs. Penetration Depth.

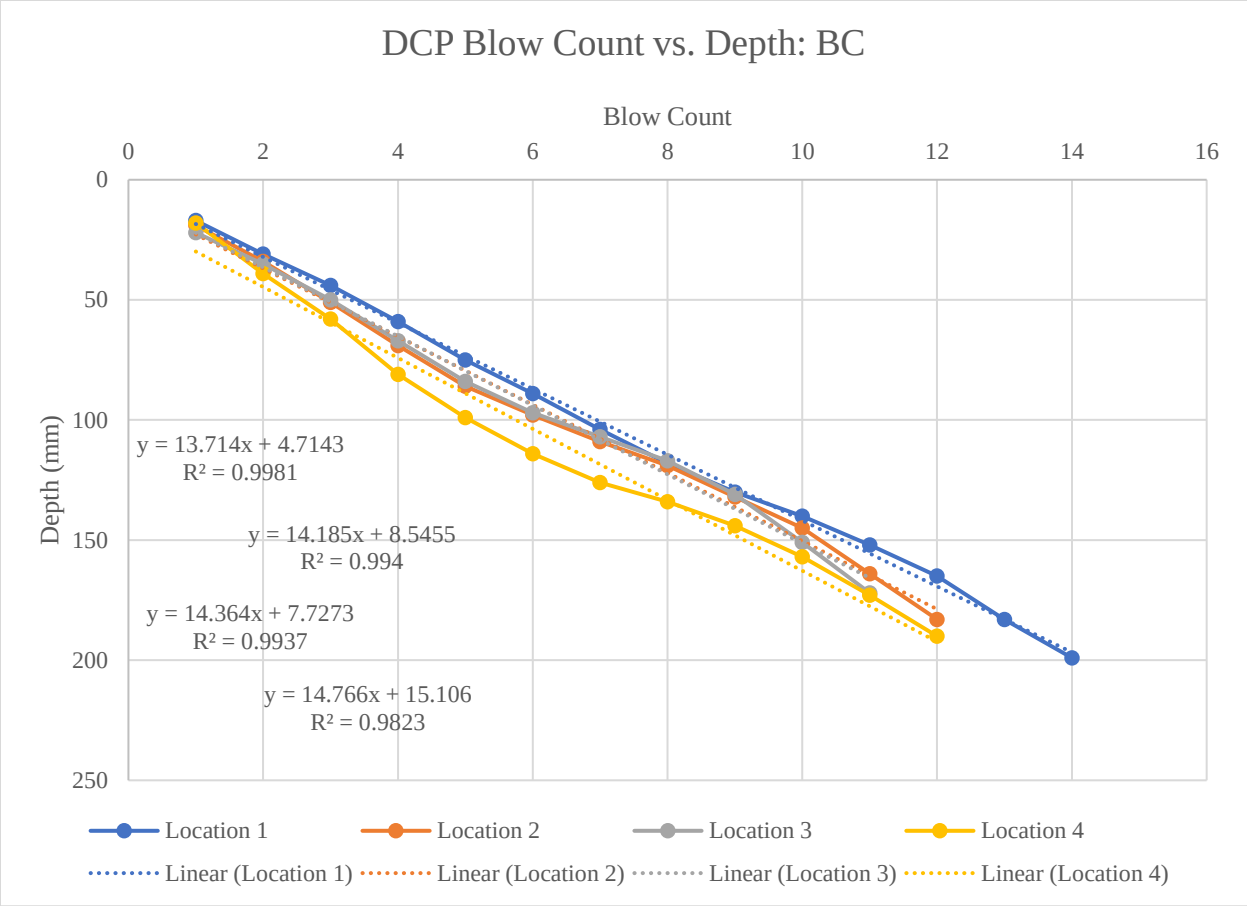

Figure 64. Test 22 DCPI: Base Course.

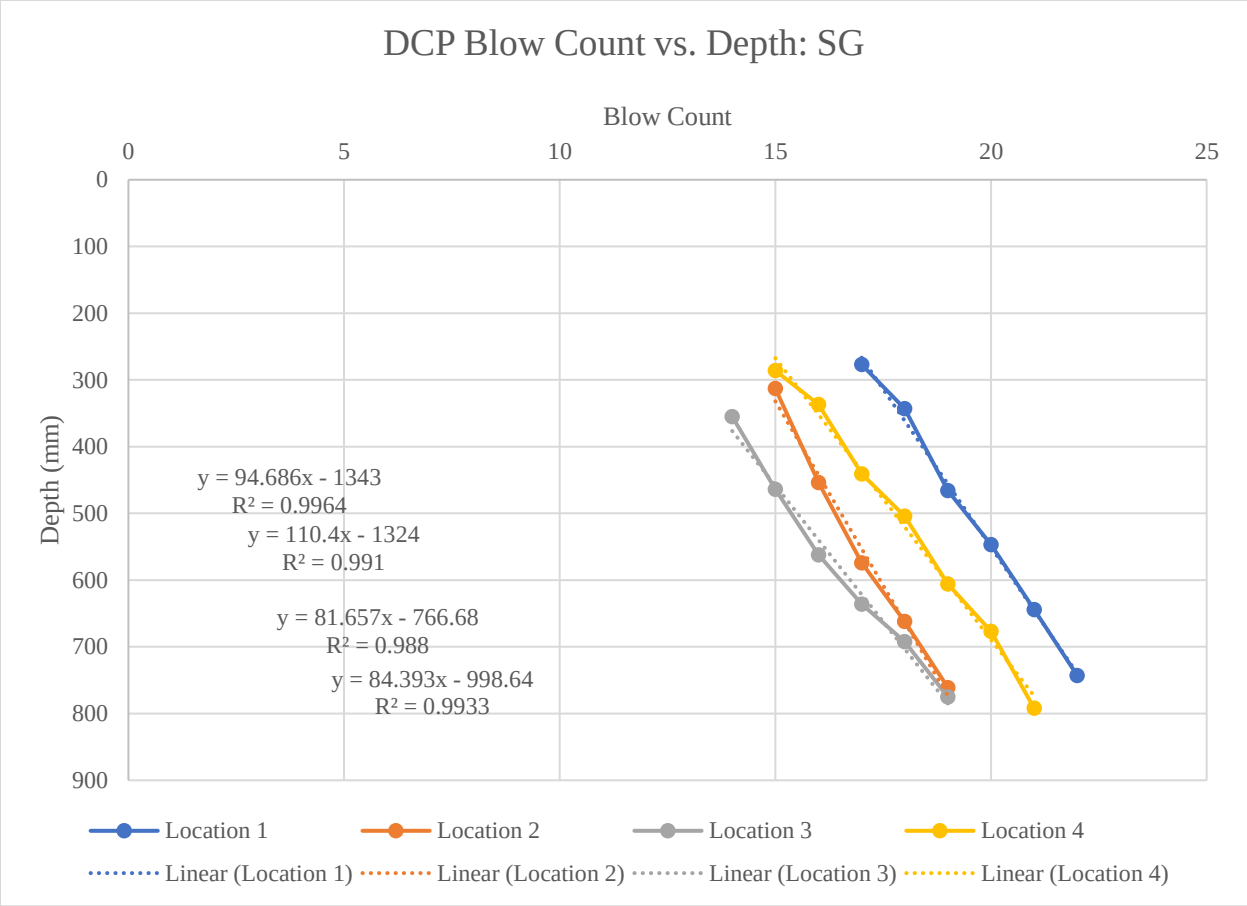

Figure 65. Test 22 DCPI: Subgrade.

Table A.46. Test 22 DCPI and CBR.

	DCPI (mm/Blow): BC	**DCPI (mm/Blow): SG**	**CBR (%): BC**	**CBR (%): SG**
Loc. 1	13.714	94.686	15.6	1.8
Loc. 2	14.185	110.4	15.0	1.5
Loc. 3	14.364	81.657	14.8	2.1
Loc. 4	14.766	84.393	14.3	2.0

Table A.47. Test 22 CBR Output, Standard Deviation, Coefficient of Variation.

	Base Course	**Subgrade**
Mean CBR (%)	14.9	1.9
Std. Dev. (σ)	0.513	0.273
CV	3.44%	14.69%

Test 23: VGB/ 5%-CBR SG

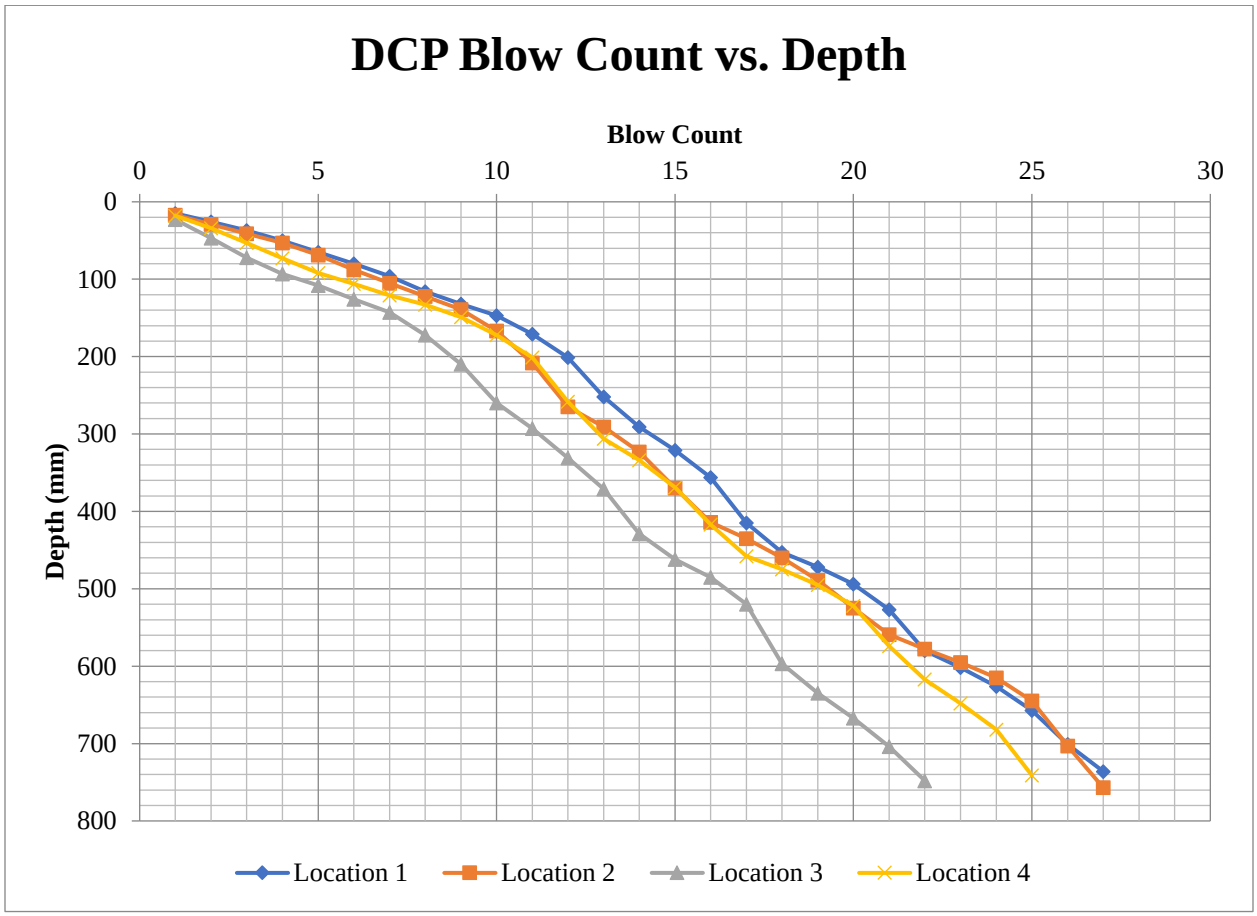

Figure 66. Test 23 DCP Blow Count vs. Penetration Depth.

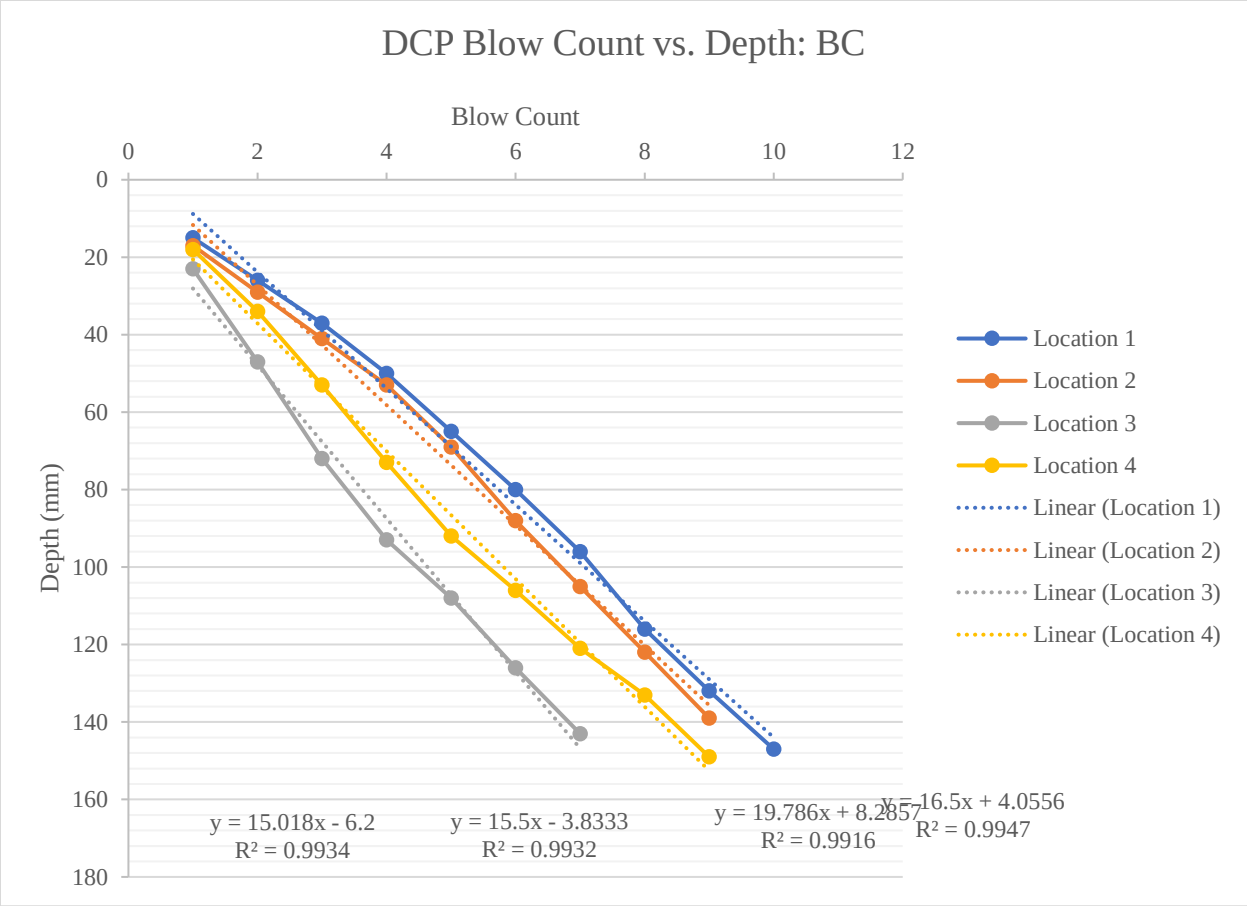

Figure 67. Test 26 DCPI: Base Course.

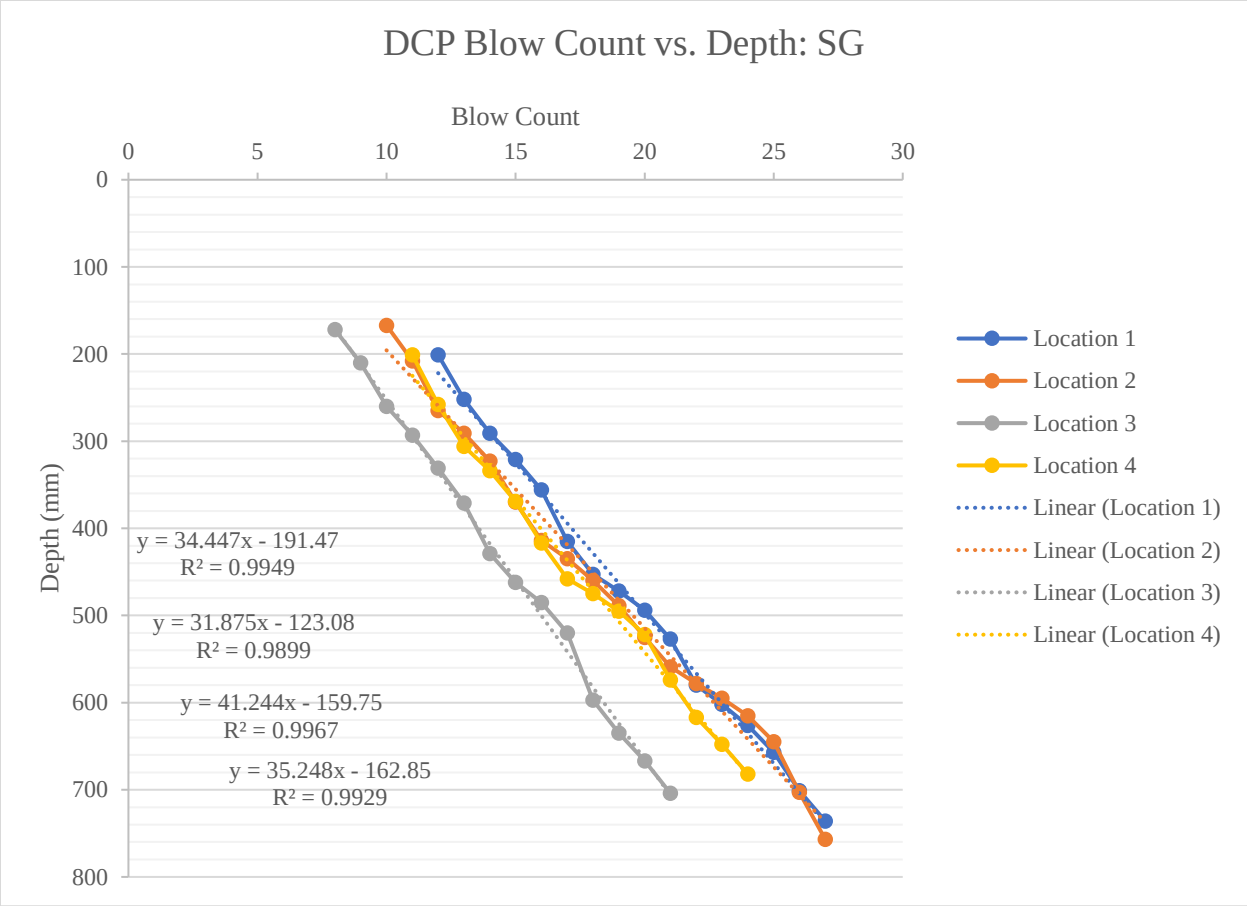

Figure 68. Test 26 DCPI: Subgrade.

Table A.48. Test 23 DCPI and CBR.

	DCPI (mm/Blow): BC	**DCPI (mm/Blow): SG**	**CBR (%): BC**	**CBR (%): SG**
Loc. 1	15.018	34.447	14.0	5.5
Loc. 2	15.5	31.875	13.6	6.0
Loc. 3	19.786	41.244	10.3	4.5
Loc. 4	16.5	35.248	12.6	5.4

Table A.49. Test 23 CBR Output, Standard Deviation, Coefficient of Variation.

	Base Course	**Subgrade**
Mean CBR (%)	12.6	5.4
Std. Dev. (σ)	1.656	0.631
CV	13.10%	11.72%

Test 24: VGB/ NW/ 5%-CBR SG

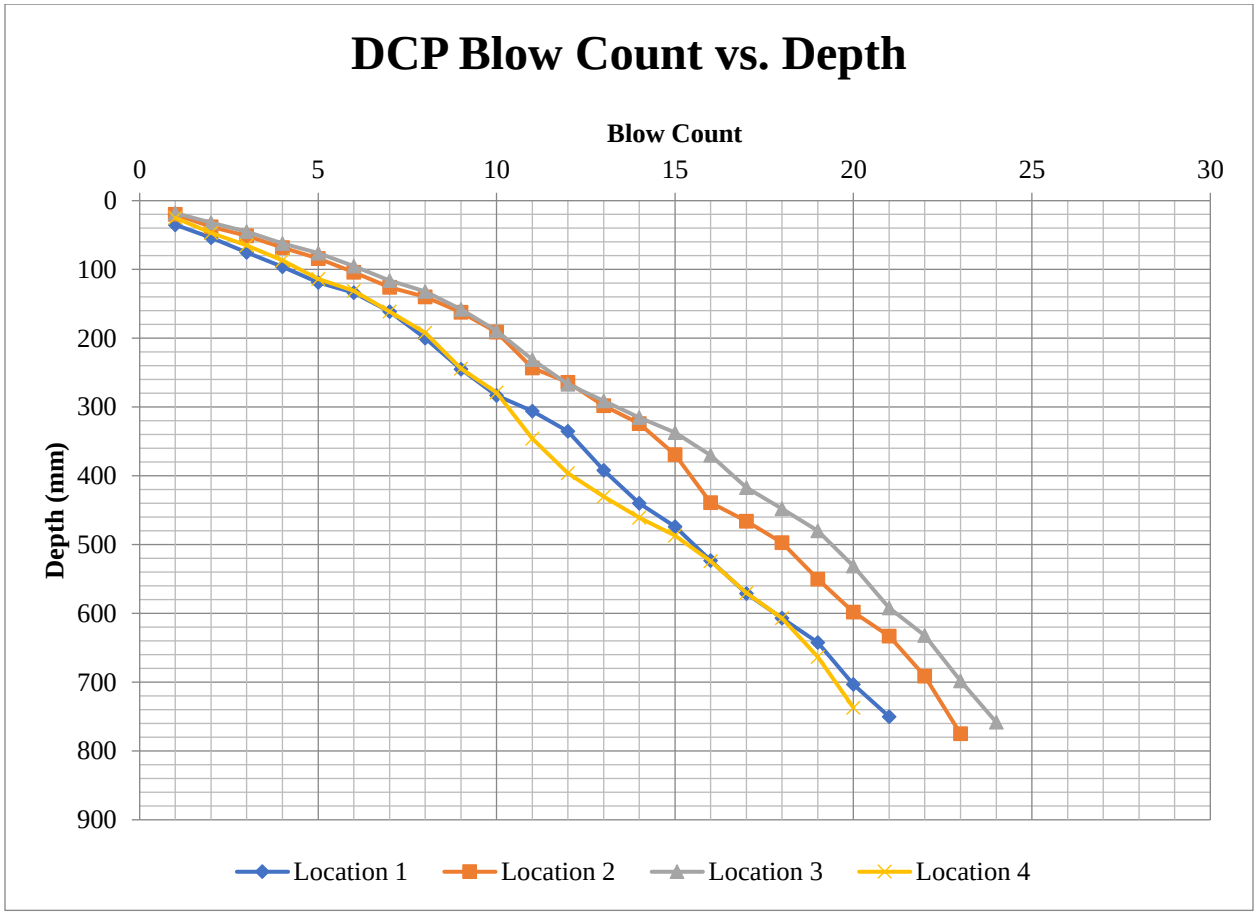

Figure 69. Test 24 DCP Blow Count vs. Depth.

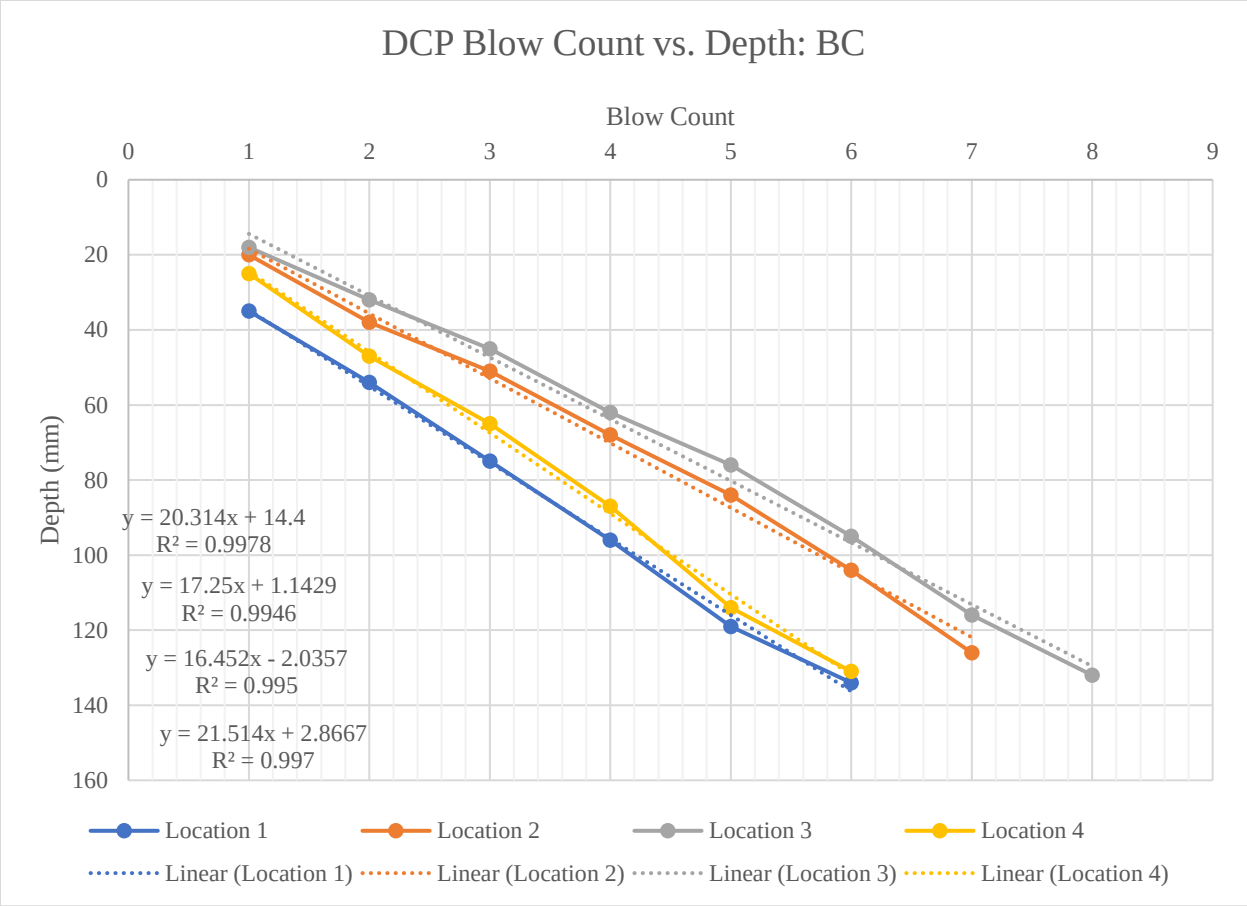

Figure 70. Test 24 DCPI: Base Course.

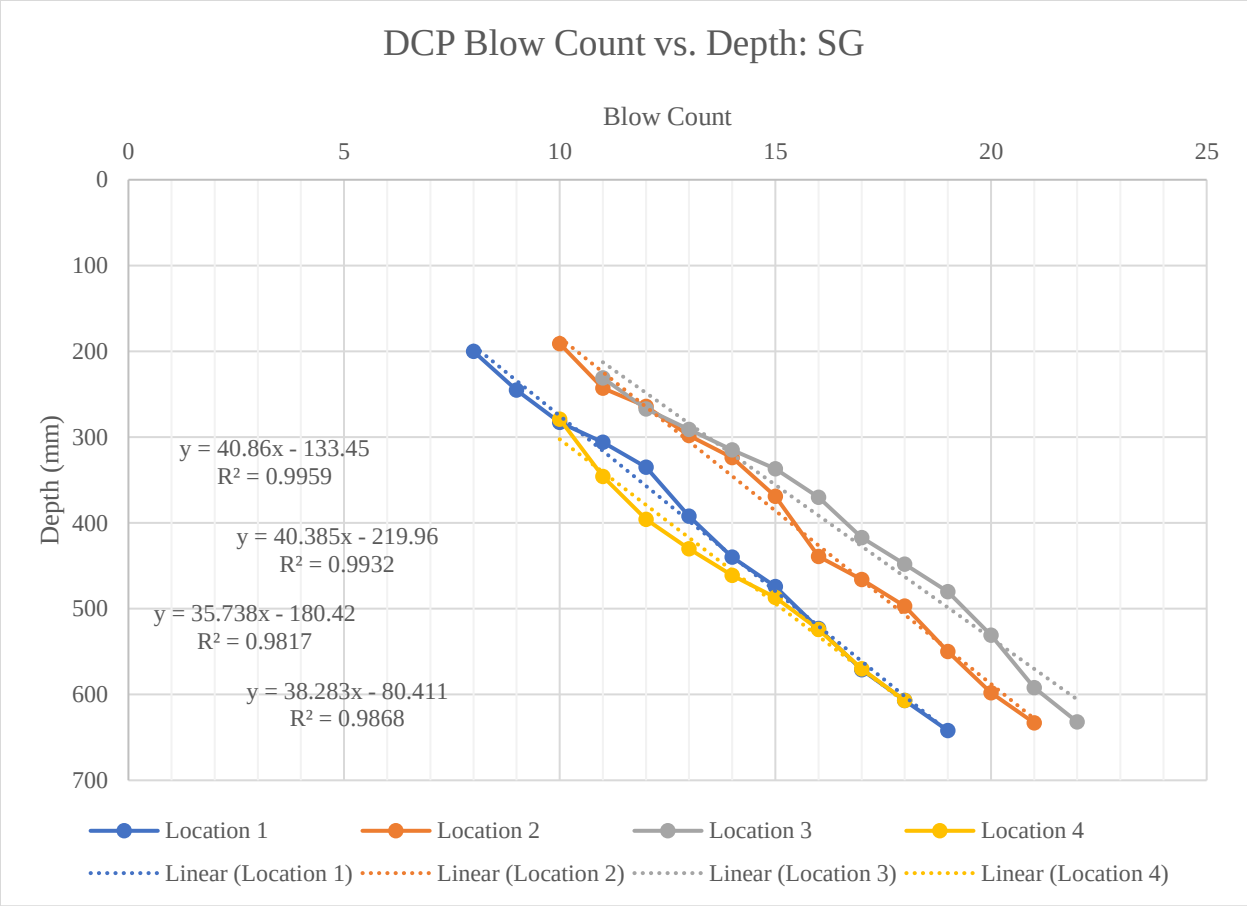

Figure 71. Test 24 DCPI: Subgrade.

Table A.50. Test 24 DCPI and Calculated CBR from DCP.

	DCPI (mm/Blow): BC	**DCPI (mm/Blow): SG**	**CBR (%): BC**	**CBR (%): SG**
Loc. 1	20.314	40.86	10.0	4.6
Loc. 2	17.25	40.385	12.0	4.6
Loc. 3	16.452	35.738	12.7	5.3
Loc. 4	21.514	38.283	9.4	4.9

Table A.51. Test 24 CBR Output, Standard Deviation, Coefficient of Variation.

	Base Course	**Subgrade**
Mean CBR (%)	11.0	4.9
Std. Dev. (σ)	1.575	0.338
CV	14.28%	6.95%

Test 25: RAP/ 5%-CBR SG

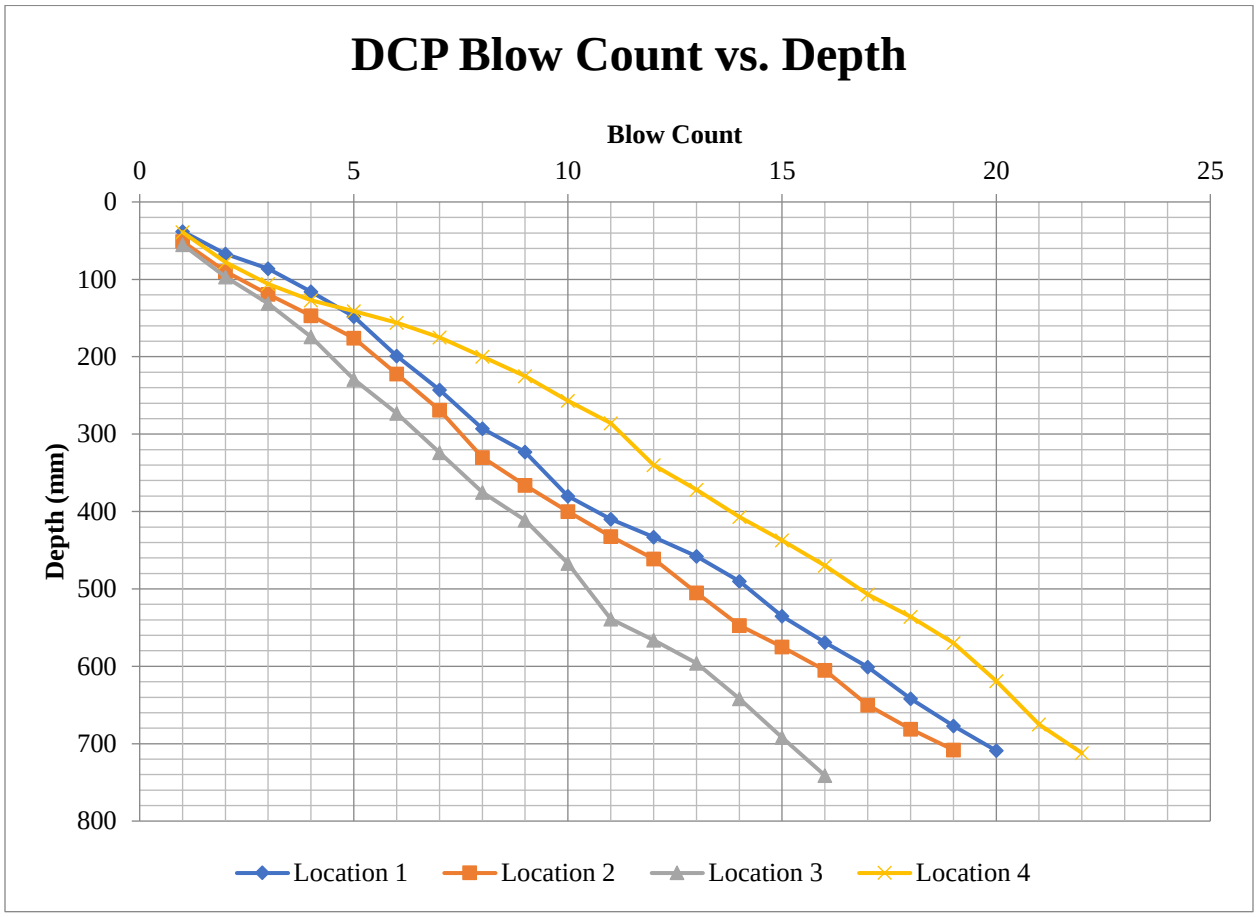

Figure 72. Test 25 DCP Blow Count vs. Penetration Depth.

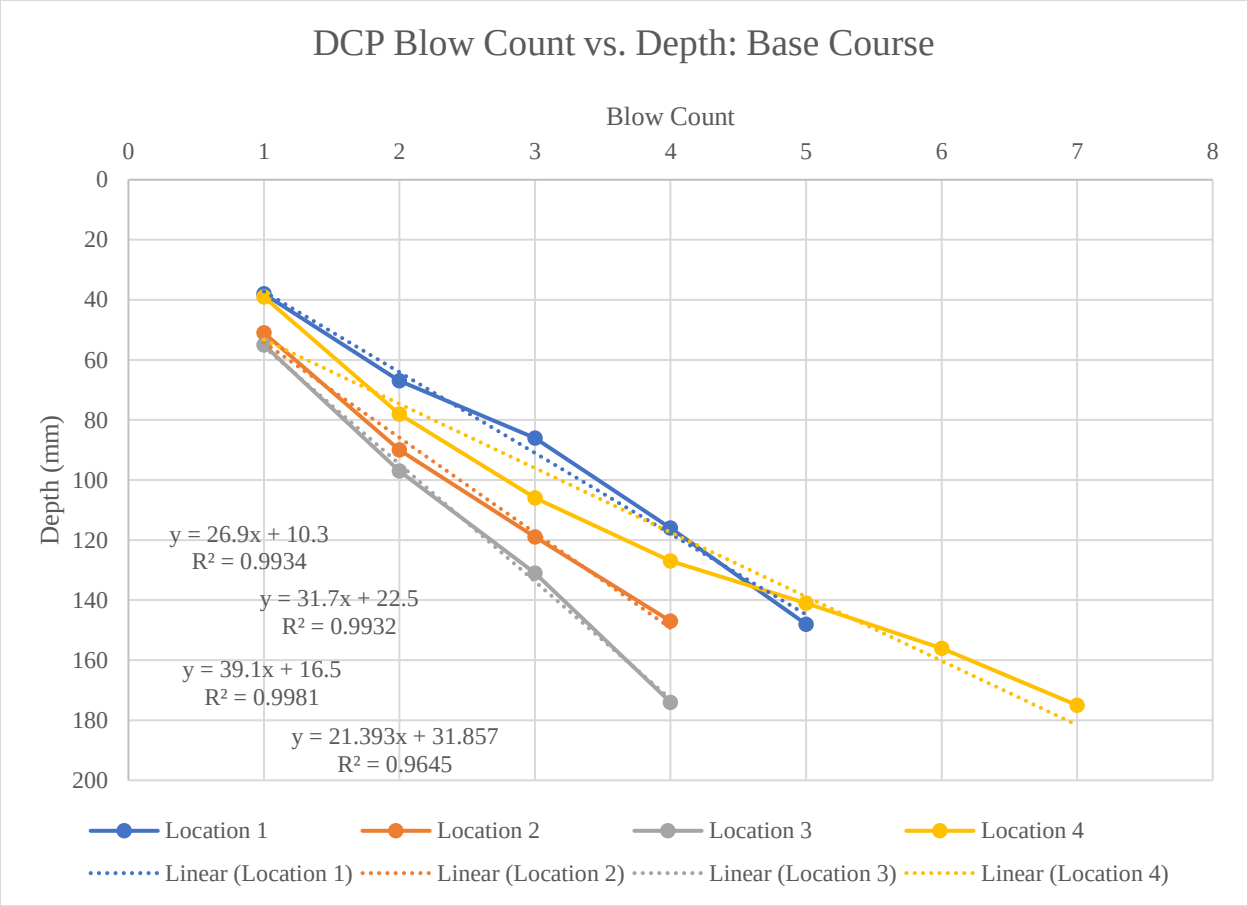

Figure 73. Test 25 DCPI: Base Course.

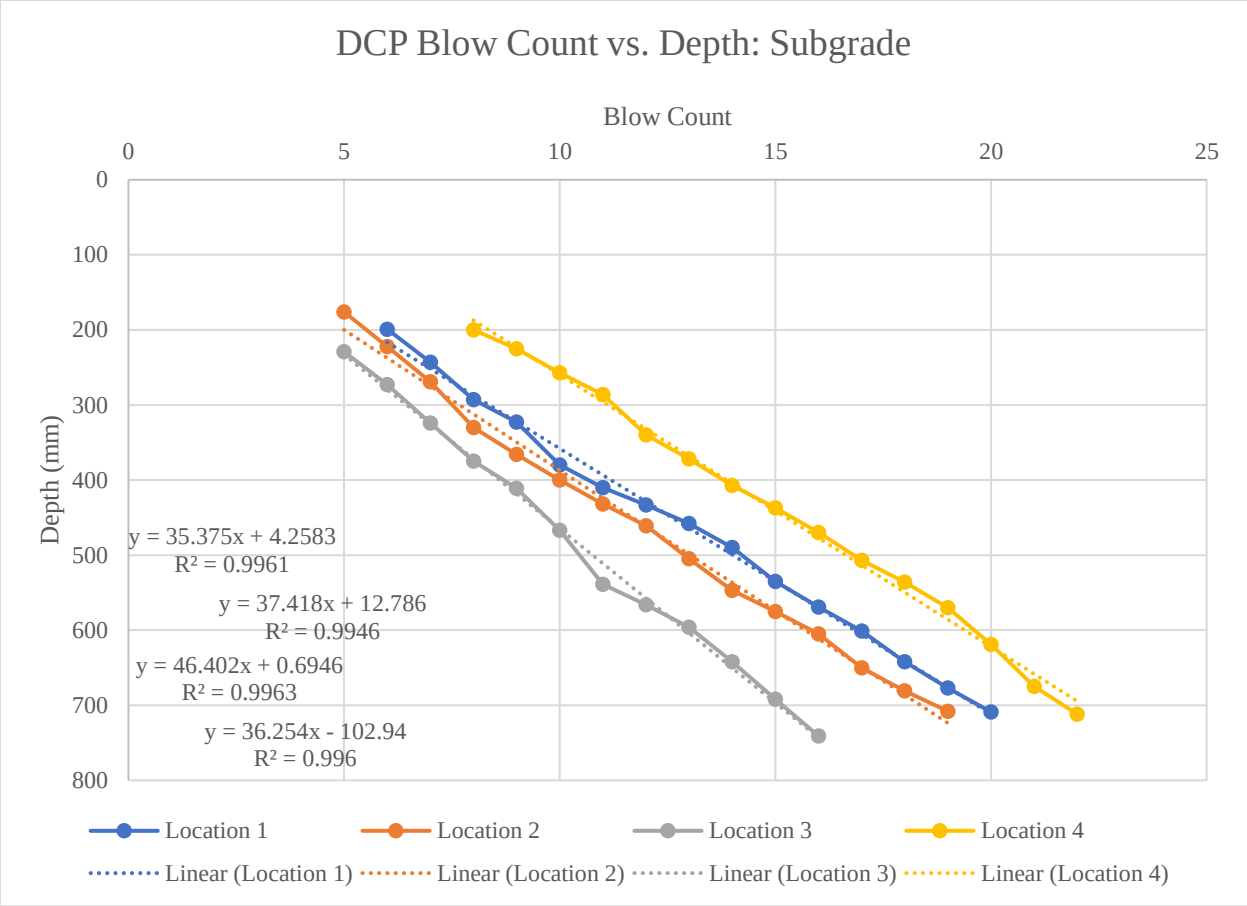

Figure 74. Test 25 DCPI: Subgrade.

Table A.52. Test 25 DCPI and CBR.

	DCPI (mm/Blow): BC	**DCPI (mm/Blow): SG**	**CBR (%): BC**	**CBR (%): SG**
Loc. 1	26.9	35.375	7.3	5.4
Loc. 2	31.7	37.418	6.1	5.1
Loc. 3	39.1	46.402	4.8	4.0
Loc. 4	21.393	36.254	9.5	5.2

Table A.53. Test 25 CBR Output, Standard Deviation, Coefficient of Variation.

	Base Course	**Subgrade**
Mean CBR (%)	6.9	4.9
Std. Dev. (σ)	1.976	0.640
CV	28.57%	13.04%

Test 26: RAP/ NW/ 2%-CBR SG

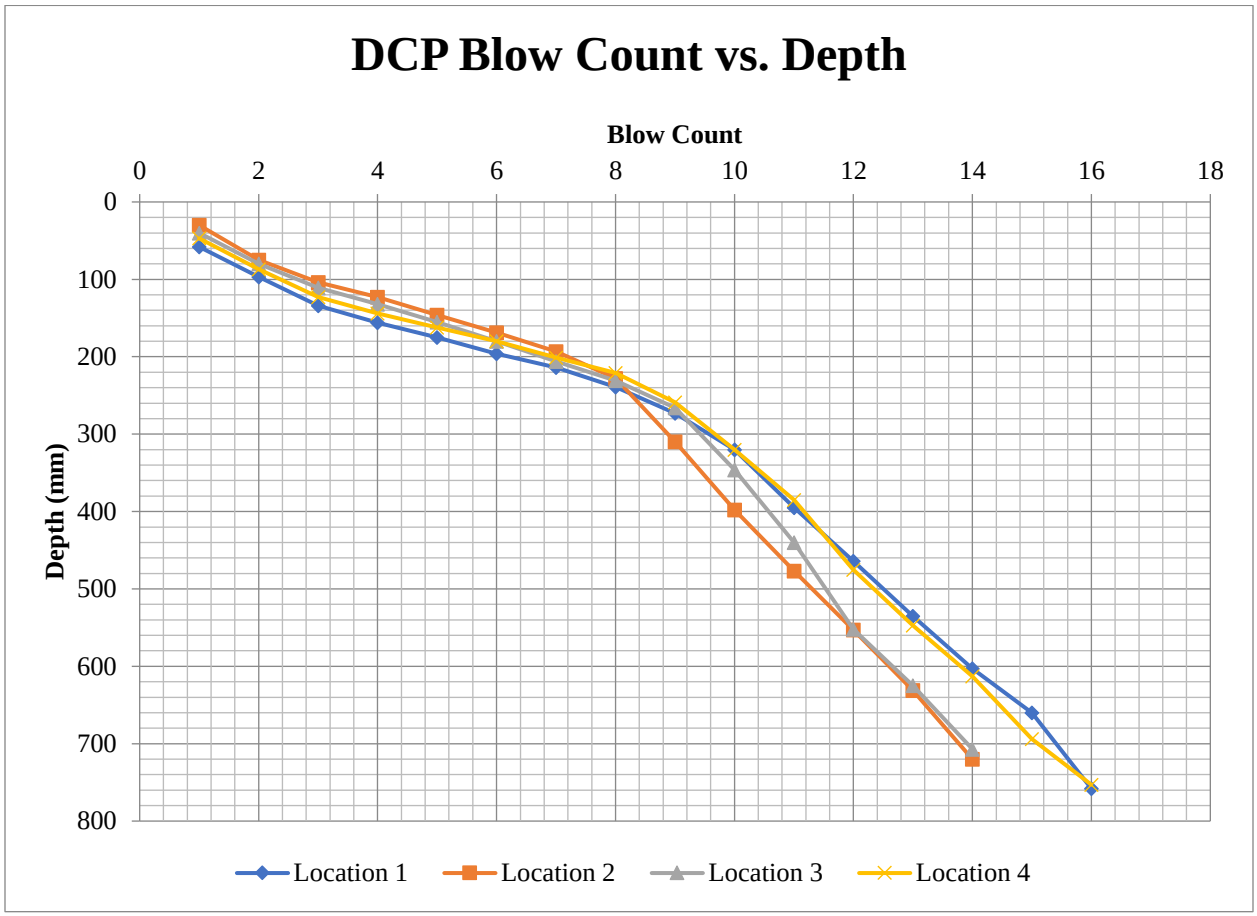

Figure 75. Test 26 Blow Count vs. Depth from DCP.

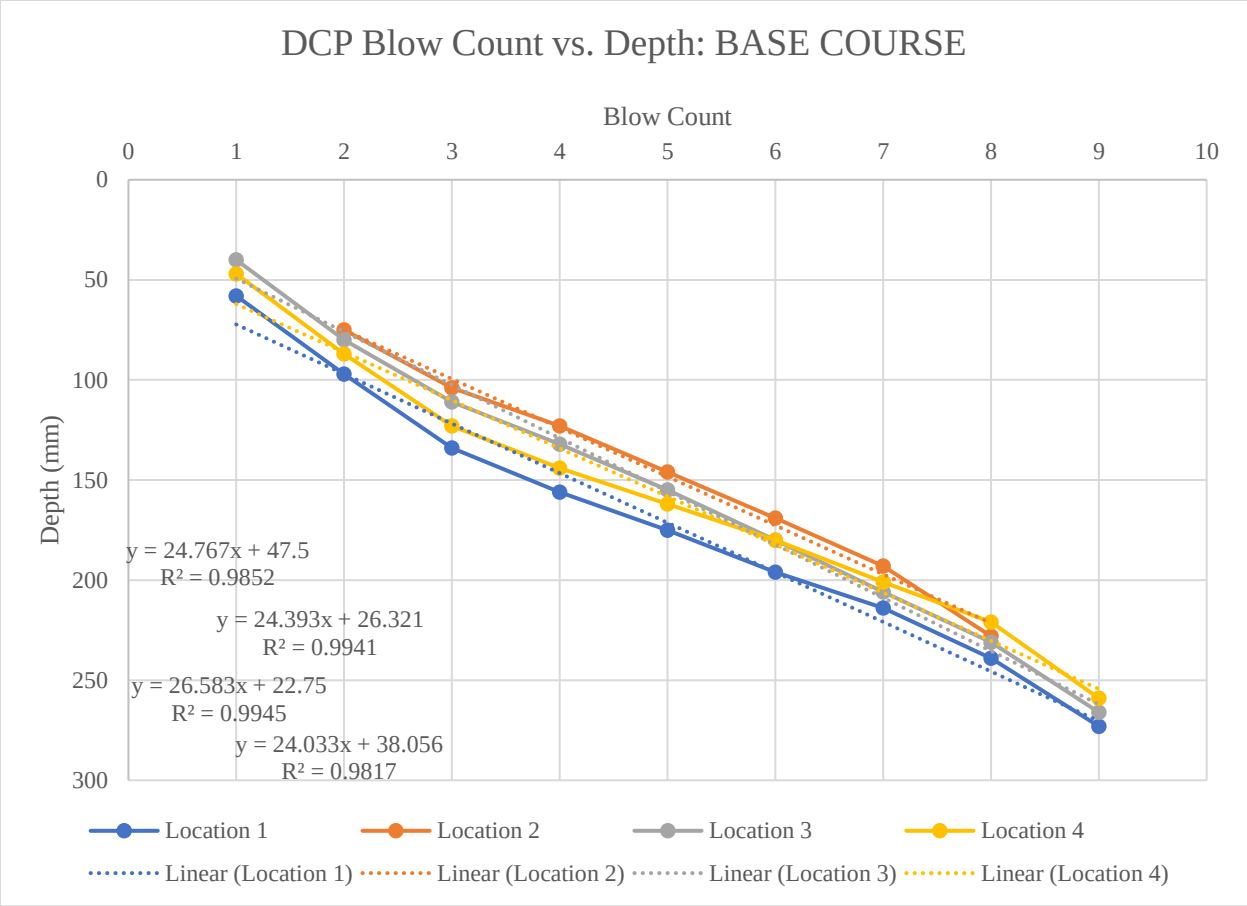

Figure 76. Test 26 DCPI: Base Course.

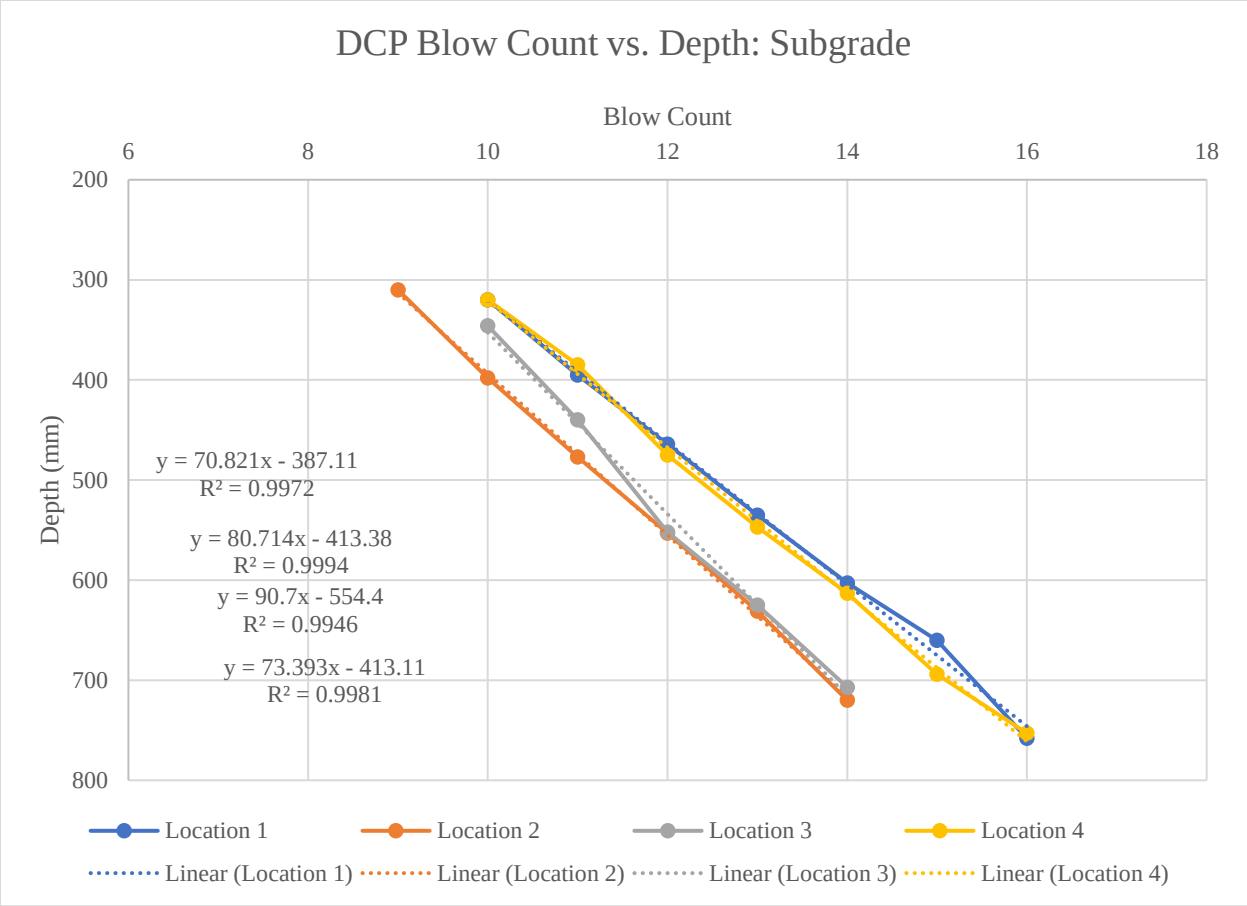

Figure 77. Test 26 DCPI: Subgrade.

Table A.54. Test 26 DCPI and CBR.

	DCPI (mm/Blow): BC	**DCPI (mm/Blow): SG**	**CBR (%): BC**	**CBR (%): SG**
Loc. 1	24.767	70.821	8.0	2.5
Loc. 2	24.393	80.714	8.2	2.1
Loc. 3	26.583	90.7	7.4	1.9
Loc. 4	24.033	73.393	8.3	2.4

Table A.55. Test 26 CBR Output, Standard Deviation, Coefficient of Variation.

	Base Course	**Subgrade**
Mean CBR (%)	8.0	2.2
Std. Dev. (σ)	0.391	0.268
CV	4.90%	12.08%

Test 27: RAP/ W/ 5%-CBR Subgrade

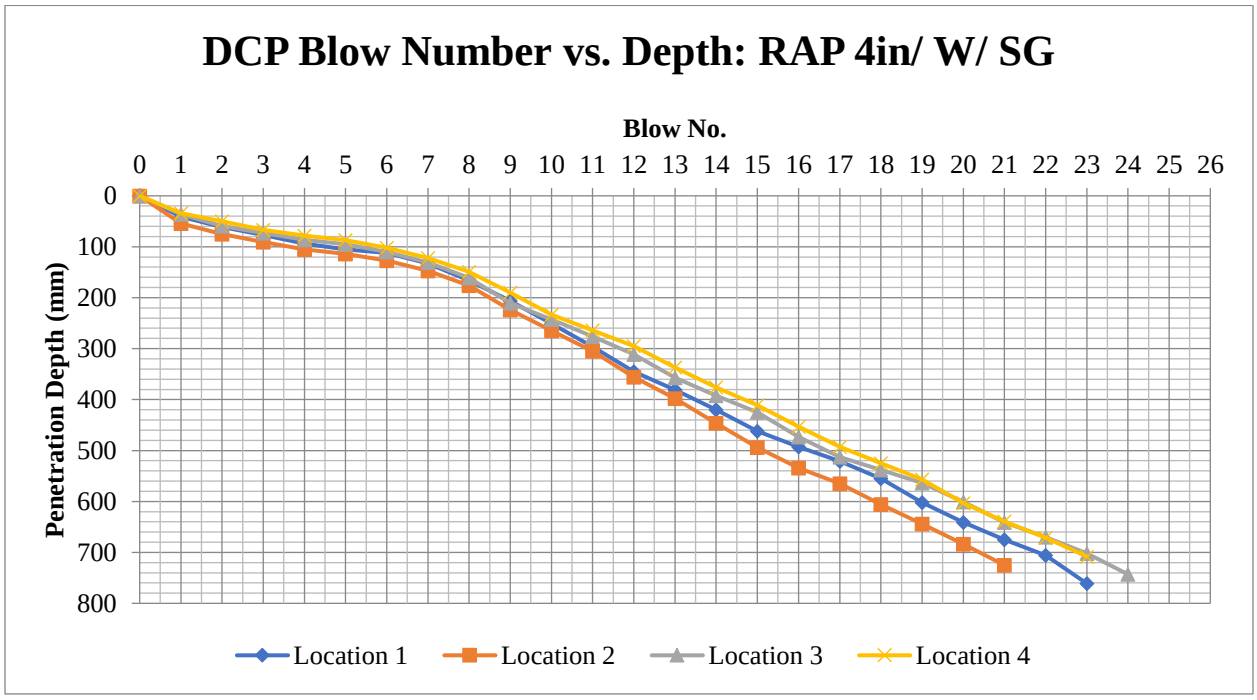

Figure 78. Test 27 DCP Blow Number vs. Penetration Depth.

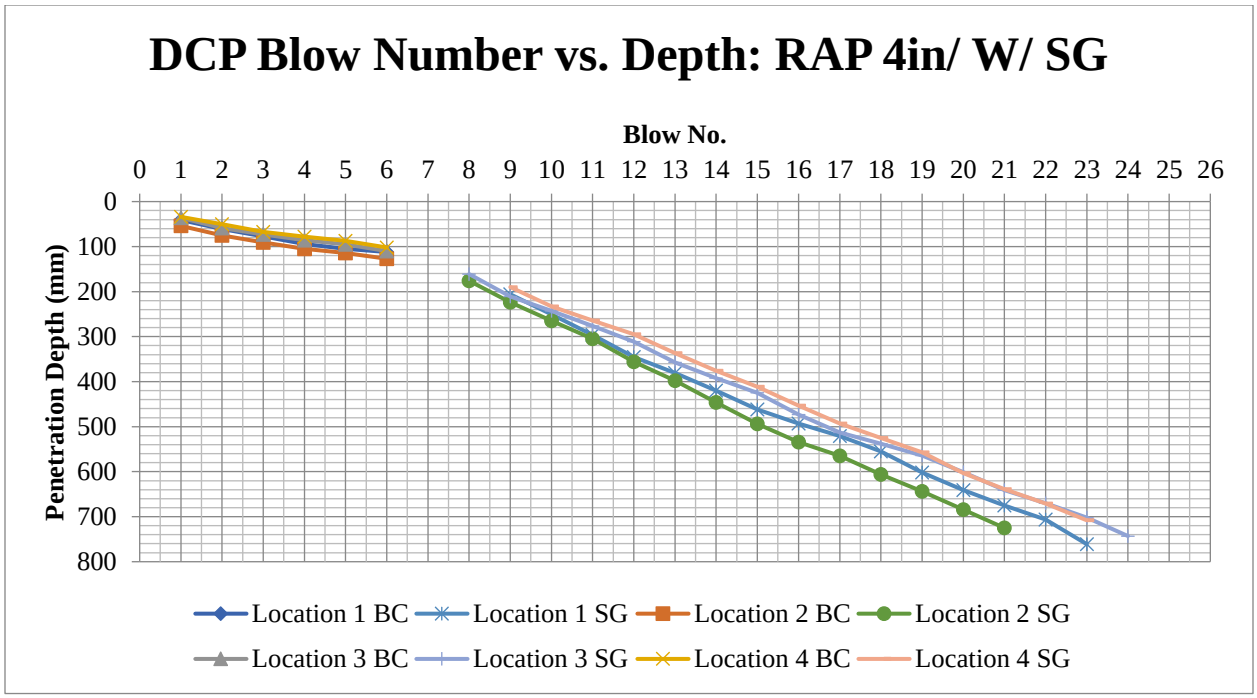

Figure 79. Test 27 Base Course and Subgrade Separated, DCP Blow No. vs. Penetration Depth.

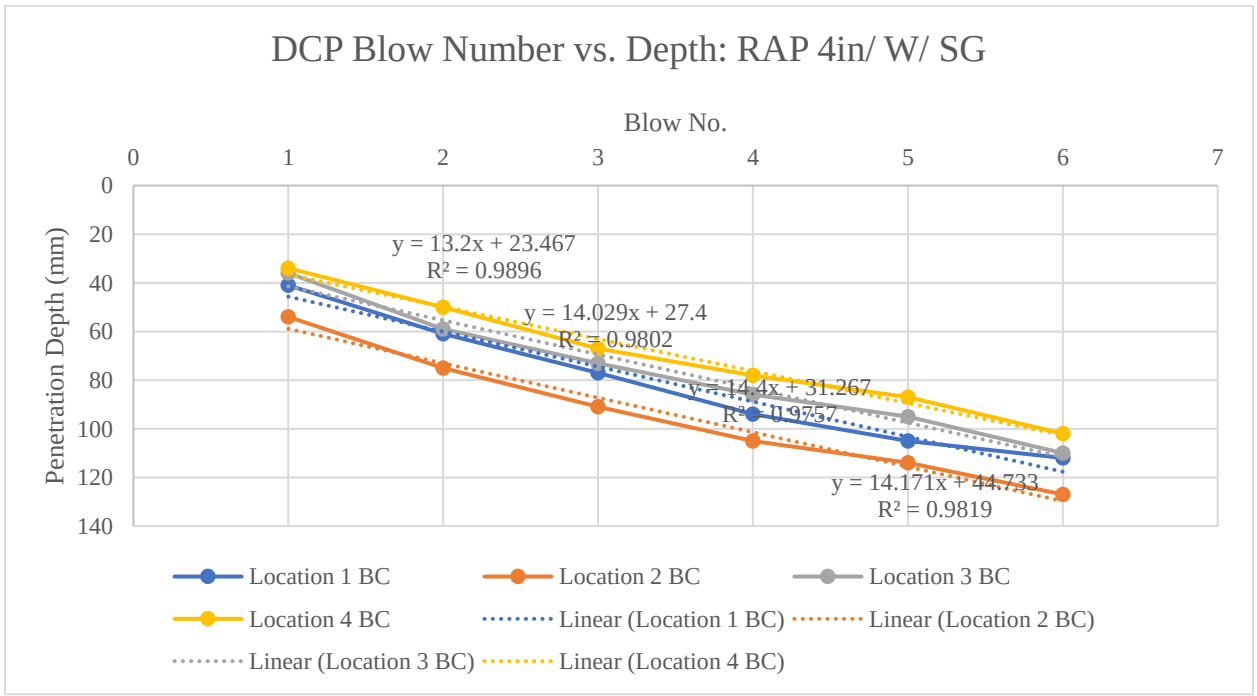

Figure 80. Test 27 Base Course Section Only DCP Blow Number vs. Penetration Depth.

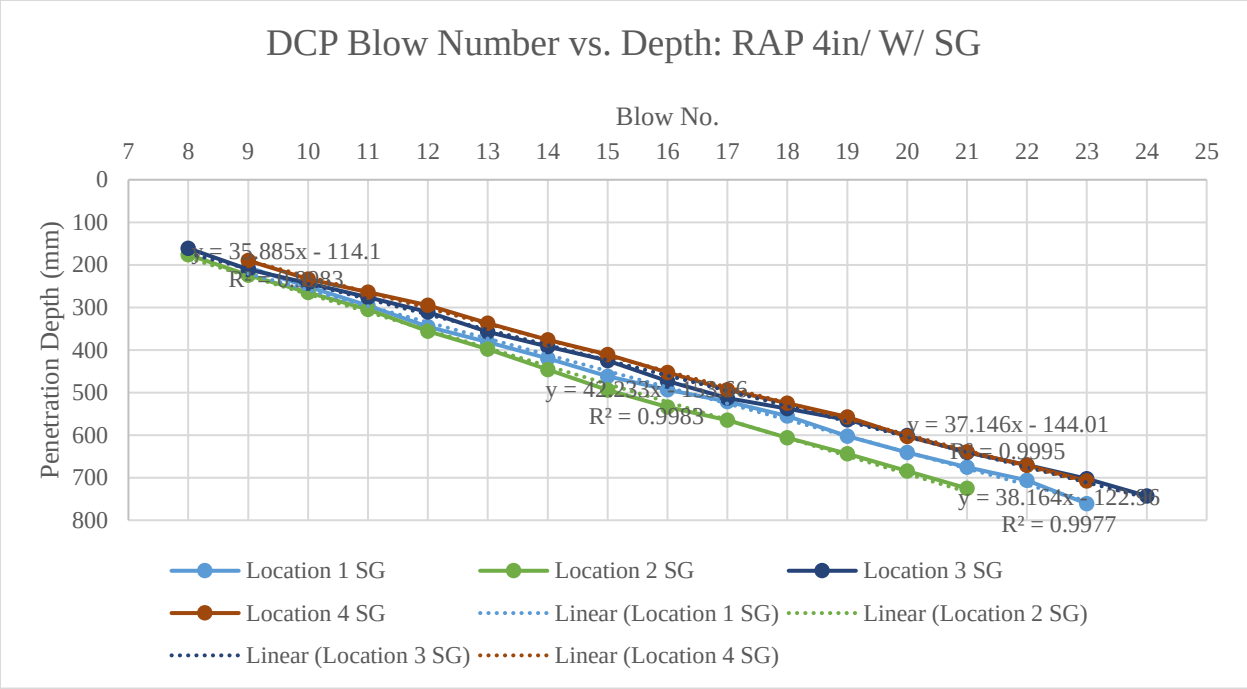

Figure 81. Test 27 Subgrade Only DCP Blow Number vs. Penetration Depth.

Table A.56. Test 27 DCP Penetration Index (DCPI) from Trendlines.

DCPI (mm/Blow)	**BC**	**SG**
Loc. 1	14.4	38.164
Loc. 2	14.171	42.233
Loc. 3	14.029	35.885
Loc. 4	13.2	37.146

Table A.57. Test 27 CBR from DPI.

CBR (%)	**BC**	**SG**
Loc. 1	14.7	4.9
Loc. 2	15.0	4.4
Loc. 3	15.2	5.3
Loc. 4	16.2	5.1
AVG	**15.3**	**4.9**

Table A.58. Test 27 CBR Output, Standard Deviation, Coefficient of Variation.

	BC	**SG**
Mean CBR (%)	15.3	4.9
Std. Dev. (σ)	0.661	0.378
CV	4.33%	7.66%

Test 28: Concrete Pavement/ VGB/ 2%-CBR Subgrade

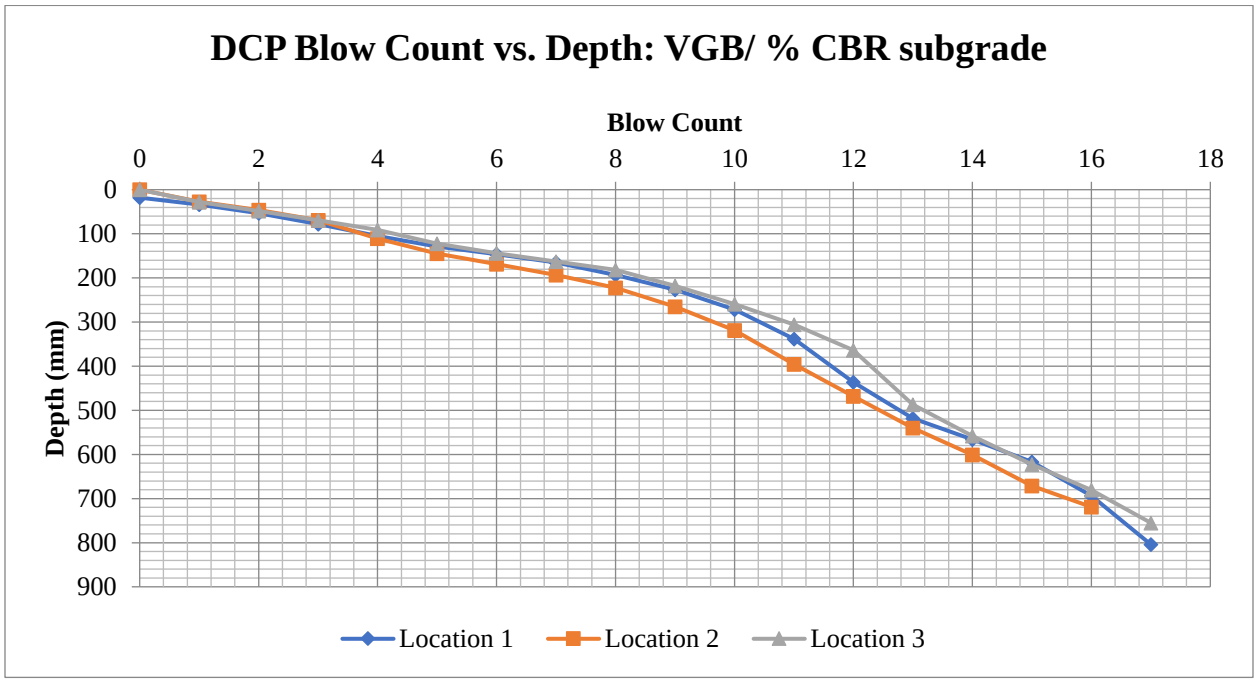

Figure 82. Test 28 DCP Blow Number vs. Penetration Depth.

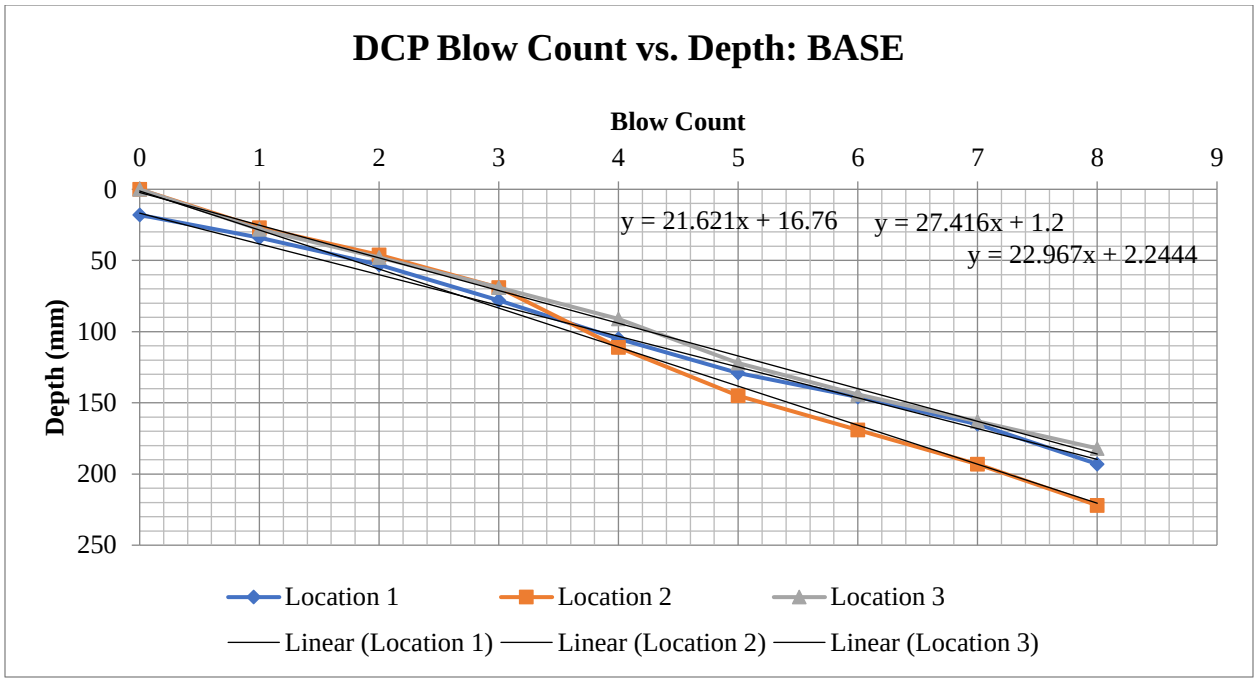

Figure 83. Test 28 Base Course Section Only DCP Blow Number vs. Penetration Depth.

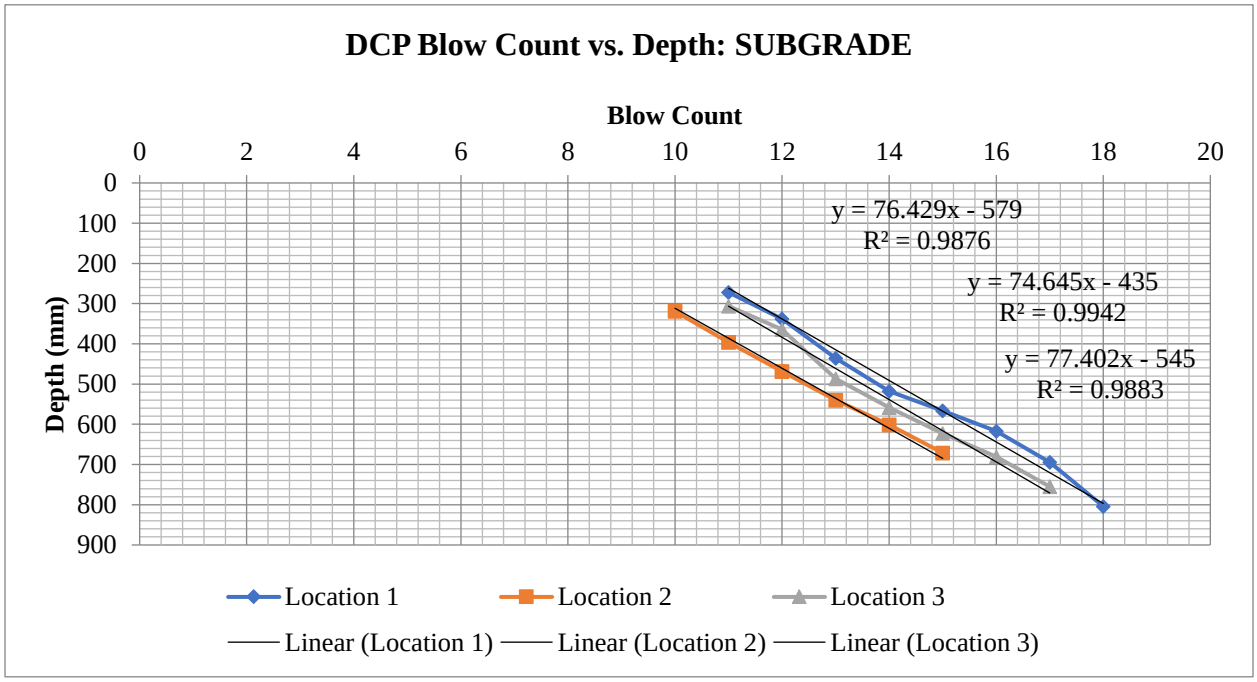

Figure 84. Test 28 Subgrade Only DCP Blow Number vs. Penetration Depth.

Table A.59. Test 28 DCP Penetration Index (DCPI) from Trendlines.

DCPI (mm/Blow)	**BC**	**SG**
Loc. 1	22.167	76.429
Loc. 2	27.416	74.645
Loc. 3	21.621	77.402

Table A.60. Test 28 CBR from DPI.

CBR (%)	**BC**	**SG**
Loc. 1	9.1	2.3
Loc. 2	7.2	2.2
Loc. 3	9.3	2.2
AVG	8.5	2.2

Table A.61. Test 28 CBR Output, Standard Deviation, Coefficient of Variation.

	BC	**SG**
Mean CBR (%)	8.5	2.2
Std. Dev. (σ)	1.192	0.047
CV	13.98%	2.07%

Test 29: Concrete Pavement/ VGB/ NW/ 2%-CBR Subgrade

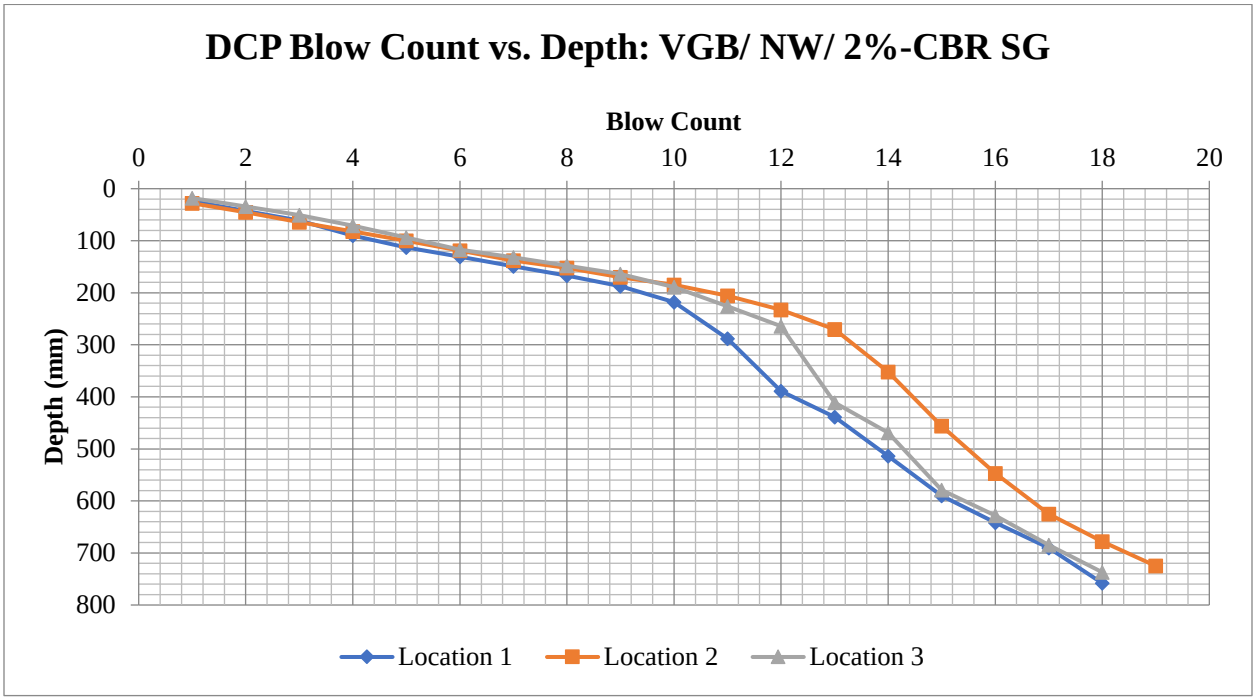

Figure 85. Test 29 DCP Blow Number vs. Penetration Depth.

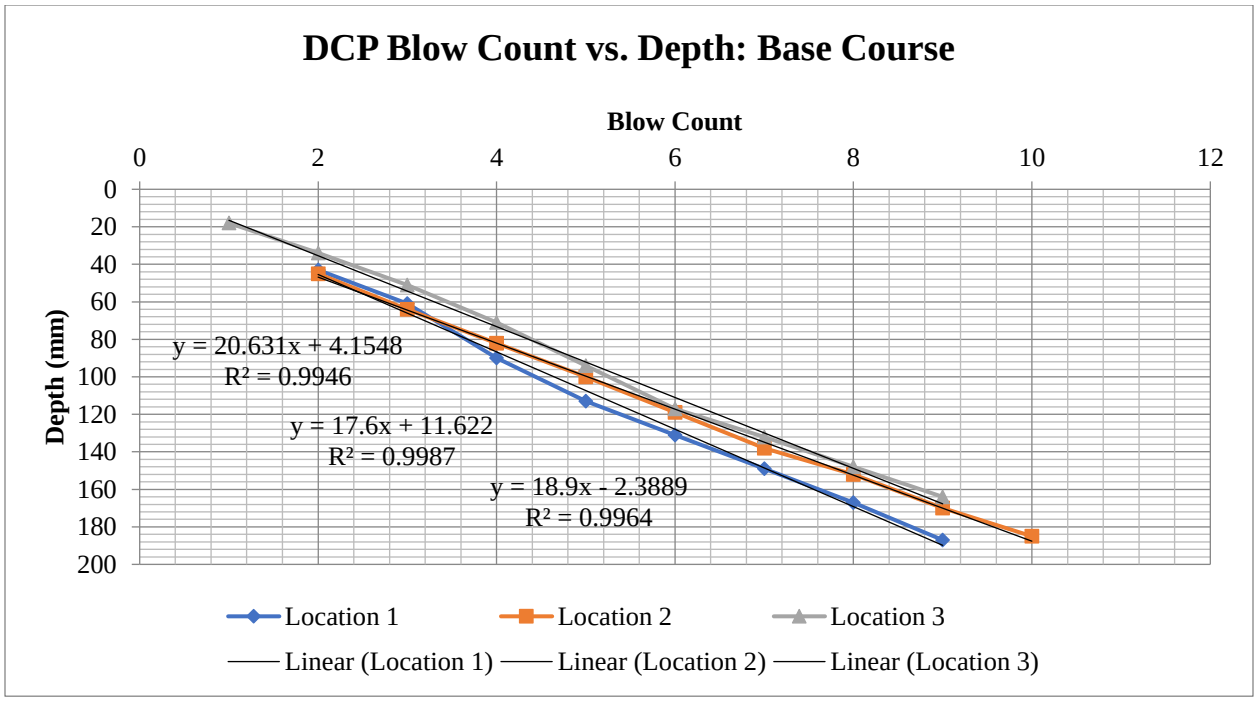

Figure 86. Test 29 Base Course Section Only DCP Blow Number vs. Penetration Depth.

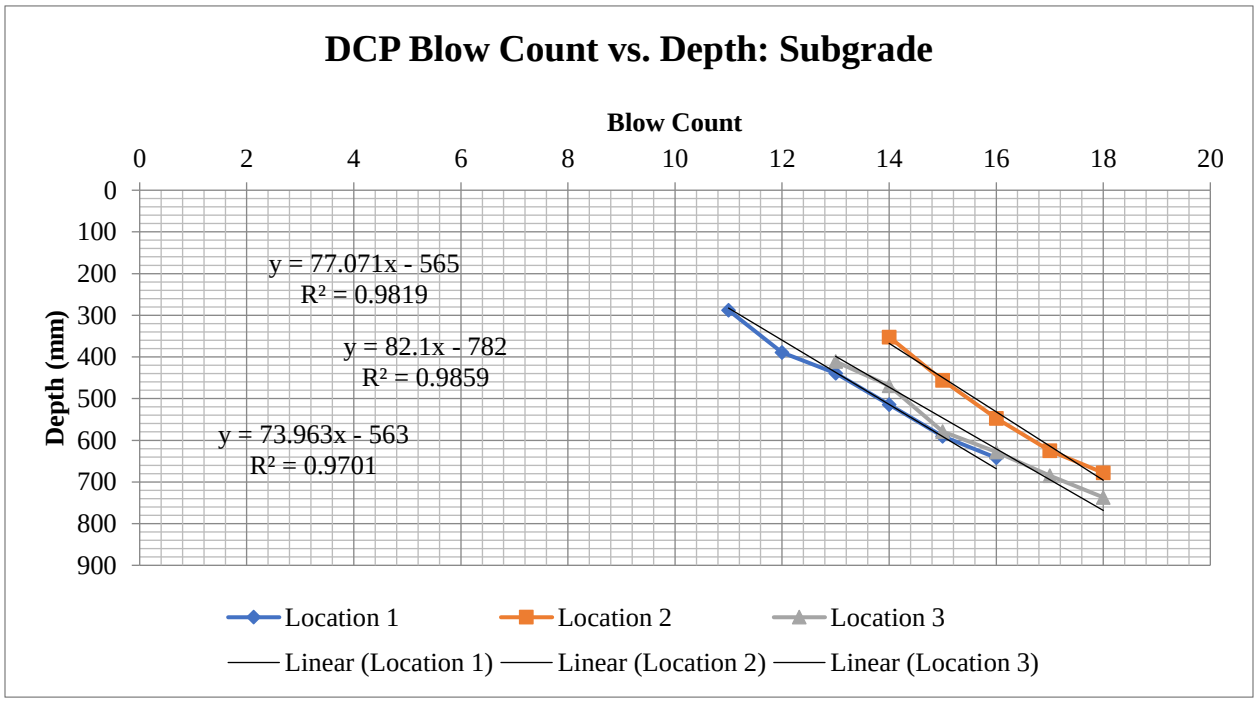

Figure 87. Test 29 Subgrade Section Only DCP Blow Number vs. Penetration Depth.

Table A.62. Test 29 DCP Penetration Index (DCPI) from Trendlines.

DCPI (mm/Blow)	**BC**	**SG**
Loc. 1	20.631	77.071
Loc. 2	17.6	82.1
Loc. 3	18.9	73.963

Table A.63. Test 29 CBR from DPI.

CBR (%)	**BC**	**SG**
Loc. 1	9.8	2.2
Loc. 2	11.8	2.1
Loc. 3	10.9	2.4
AVG	10.8	2.2

Table A.64. Test 29 CBR Output, Standard Deviation, Coefficient of Variation.

	BC	**SG**
Mean CBR (%)	10.8	2.2
Std. Dev. (σ)	0.959	0.131
CV	8.86%	5.85%

Test 30: Concrete Pavement/ RCA/ NW/ 2%-CBR Subgrade

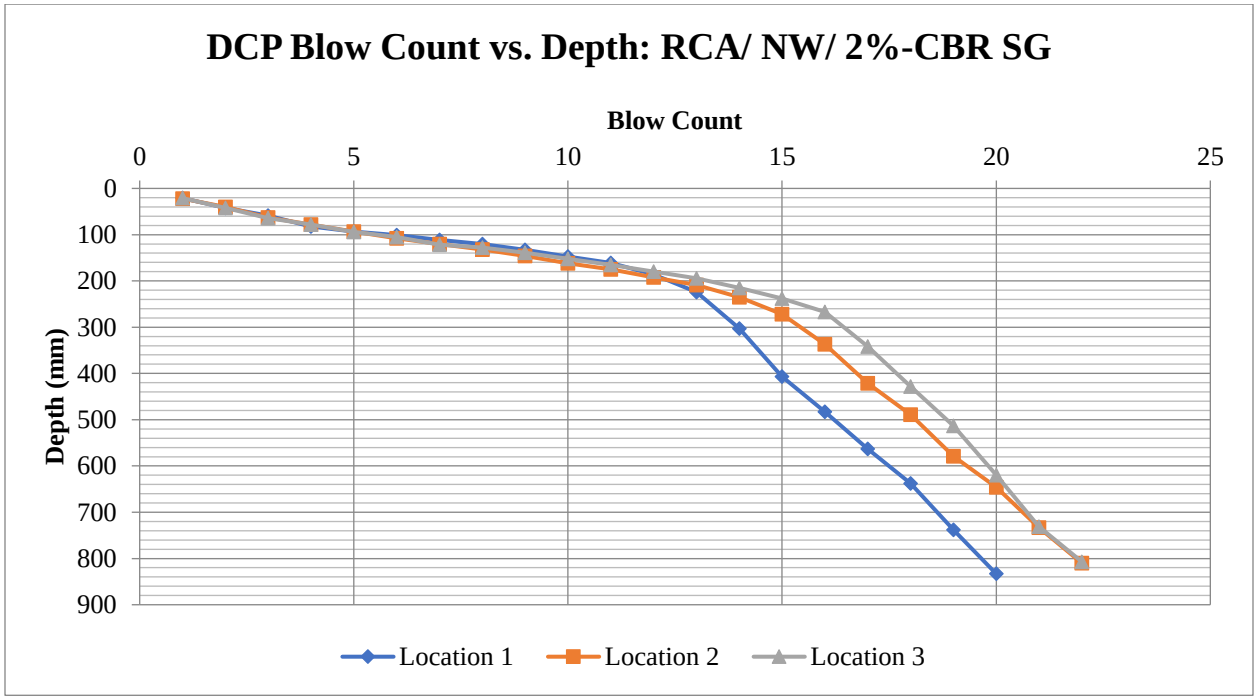

Figure 88. Test 30 DCP Blow Number vs. Penetration Depth.

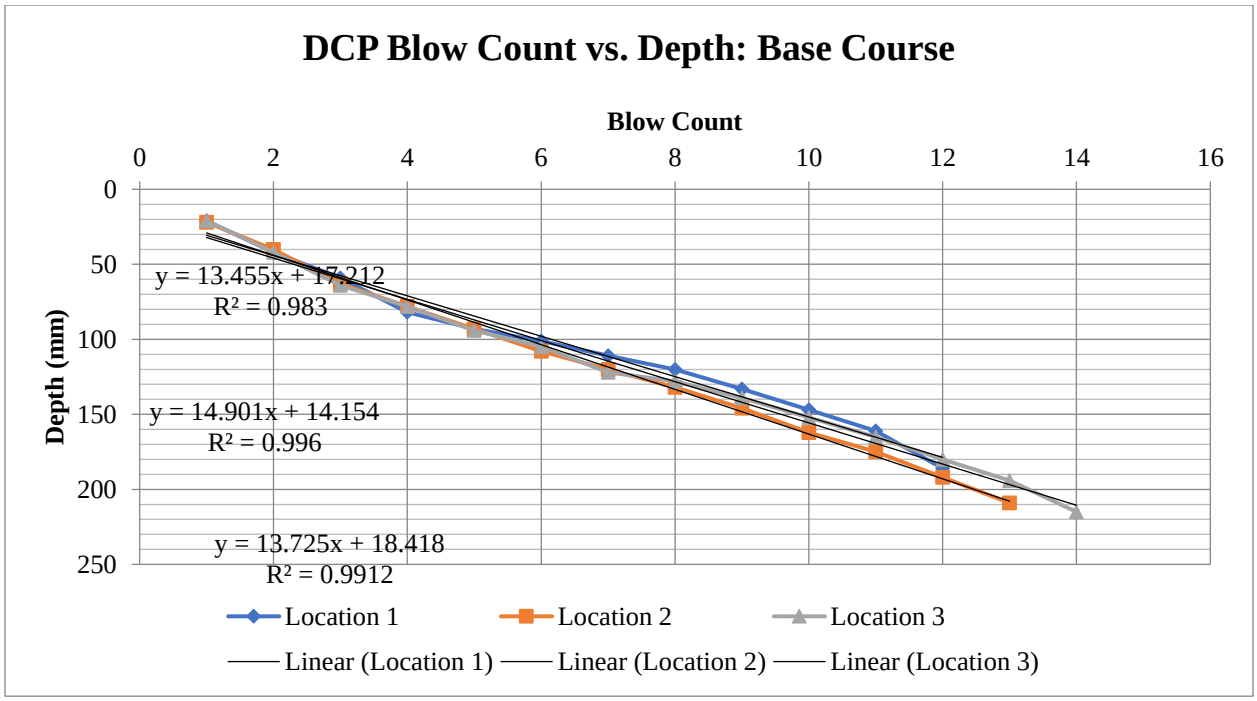

Figure 89. Test 30 Base Course Section Only DCP Blow Number vs. Penetration Depth.

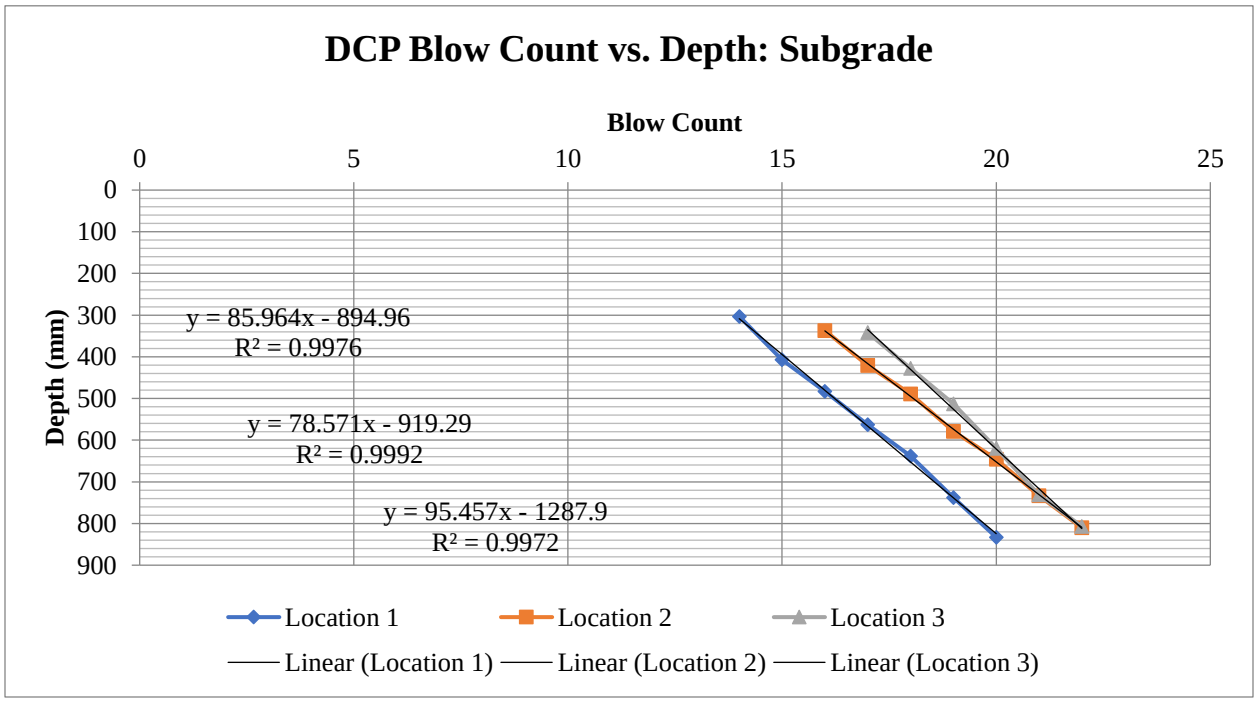

Figure 90. Test 30 Subgrade Section ONLYDCP Blow Number vs. Penetration Depth.

Table A.65. Test 30 DCP Penetration Index (DCPI) from Trendlines.

DCPI (mm/Blow)	**BC**	**SG**
Loc. 1	13.455	85.964
Loc. 2	14.901	78.571
Loc. 3	13.725	95.457

Table A.66. Test 30 CBR from DPI.

CBR (%)	**BC**	**SG**
Loc. 1	15.9	2.0
Loc. 2	14.2	2.2
Loc. 3	15.5	1.8
AVG	15.2	2.0

Table A.67. Test 30 CBR Output, Standard Deviation, Coefficient of Variation.

	BC	**SG**
Mean CBR (%)	15.2	2.0
Std. Dev. (σ)	0.907	0.216
CV	5.97%	10.85%

Appendix B. KENPAVE Inputs

The following notes describe the plethora of variable inputs in the KENSLABS module of the KENPAVE program (Huang 2004) used for simulation in this dissertation. There were two basic simulation models used in this analysis. The first setup matched the slab dimensions in the large-scale box tests and was intended to mimic the use of the Westergaard (1926) equations that KENPAVE simulations are based on (Huang 2004). The second setup was intended to mimic a typical single-axle-loaded slab consistent with AASHTO (1993) to verify the paved test analysis as well as provide a typical slab section for analysis using the unpaved road section results (M_r values). Some sections of the KENPAVE input are not detailed if input values were designated as "default" based on the inputs in the "General" section; they were not addressed in the simulation setup as they would not have an effect on the outputs (Huang 2004). Additional information on use of this software can be found in Huang's program or his corresponding textbook (Huang 2004).

B.1 Large Box Simulation

B.1.1 General Information for Set No. 1

- "TITLE" = adjusted to describe the appropriate road section.
- "with uniform load/ without uniform load" = ***with***.
- "with temperature curling/ without temperature curling" = ***without***.
- "with concentrated load/ without concentrated load" = ***with***.
- "Type of foundation (0=liquid, 1=solid, 2= layer) (NFOUND)" = **1**.
- "Damage analysis (0=no, 1=PCA criteria, 2- user specified) (NDAMA)" = **0**.
- "Number of periods per year (NPY)" = **1**.
- "Number of load groups (NLG)" = **1**.
- "Number of slab layers (NLAYER)" = **1**.
- "Bond between two slab layers (0=unbonded, 1=bonded)" = **0**.

- "Number of slabs (NSLAB)" = **2**.
- "Number of joints (NJOINT)" = **1**.
- "Nodal number for checking convergence (NNCK)" = **49**.
- "Number of nodes for stress printout (NPRINT)" = **0**.
- "Number of nodes on X axis of symmetry (NSX)" = **0**.
- "Number of nodes on Y axis of symmetry (NSY)"= **0**.
- "More detailed printout (0=no, 1=yes) (MDPO)" = **1**.
- "Number of nodes with different thicknesses of slab layer 1 (NAT1)" = **0**.
- "Number of nodes with different thicknesses of slab layer 2 (NAT2)" = **0**.
- "System of units (0=English, 1=SI) (NUNIT)" = **1**.

B.1.2 Curling

- On the *Main Menu* screen, the *Curling* menu was listed as "default." No values were changed.

B.1.3 Slab

B.1.3.1 Arrangement

Slab No.	NX	NY	JONO1	JONO2	JONO3	JONO4
1	7	8	0	1	0	0
2	6	8	1	0	0	0

- NX is the number of nodes in the X direction for each slab.
- NY is the number of nodes in the Y direction for each slab.
- JONO1 is the joint no. on the left of each slab.
- JONO2 is the joint no. on the right of each slab.
- JONO3 is the joint no. on the bottom of each slab.
- JONO4 is the joint no. on the top of each slab.

B.1.3.2 X-coordinate

Values listed for each slab are the distance from the lower right corner in the x (right-hand) direction of the given slab for each node.

Slab 1

Sequence	**X (cm)**
1	0
2	18.75
3	37.5
4	56.25
5	75
6	93.75
7	112.5

Slab 2

Sequence	**X (cm)**
1	0
2	15.76
3	31.52
4	47.28
5	63.04
6	78.8

B.1.3.3 Y-coordinate

Values listed in the table below are node distances in the y (vertical) direction from the bottom (in plan/ top view) of the given slab.

Slab 1, 2 (uniform)

Sequence	**Y (cm)**
1	0
2	17.7
3	35.4
4	53.1
5	70.8
6	88.5
7	106.2
8	123.8

B.1.3.4 Properties

- Layer No. 1 (only 1 layer in slab, should match)
- Thickness of the slab, T = 15.24 cm
- PR = Poisson's ratio of slab = 0.15
- YM = Young's Modulus of slab = 2.5E+07 kPa

B.1.4 Uniform

- NUDL = number of uniformly-distributed areas = **1**.

B.1.4.1 Loaded Areas for Load Group No 1 and Data Set No. 1

Load Sequence	LS	XL1 (cm)	XL2 (cm)	YL1 (cm)	YL2 (cm)	QQ (kPa)
1	1	84.3	111.3	95.8	122.7	550

- LS is the slab number on which the load is applied.
- XL1, XL2 are left and right limits of loaded area in local x coordinates.
- YL1, YL2 are lower and upper limits of loaded area in local y coordinates.
- QQ is the tire contact pressure in the loaded area.

B.1.5 Raft

- Number of concentrated vertical nodal forces (NCNF) = 1
    - NN = nodal number at which the concentrated load is applied.
    - FF = concentrated force at a given node. (This was measured during testing.)

Sequence N	NN	FF (kN)
1	1	25.1

- Number of nodal moments in x direction (NNMX) = 0
- Number of nodal moments in y direction (NNMY) = 0

B.1.6 Optional

- On the *Main Menu* screen, the *Curling* menu was listed as "default." No values were changed.

B.1.7 Foundation

- Young's Modulus of subgrade in kPa (YMS): **values estimated in Chapter 4 using Westergaard's (1926) solution vary based on test section. THIS WAS VARIED TO NOTE THE CHANGES IN SLAB TENSILE STRESSES.**
- Poisson's ratio of subgrade (PRS) = 0.45.

B.1.8 Adjust

- FSAF = seasonal adjustment, **1** left as default.

B.1.9 Joint

- SPCON1 (spring constant for shear transfer) = **0.0000000001 kN/cm^2**. (Entering zero yields an error in the program despite its recommended use in Huang 2004.)
- SPCON2 (spring constant for moment transfer) = **0 cm-kN/cm**.
- SCKV (modulus of dowel support or steel-concrete k value)= **0 MN/m^3** because no dowel support or interlock.
- BD (dowel bar diameter) = **0 cm**
- BS (dowel bar spacing) = **0 cm**
- WJ (width of joint) = **1.27 cm**
- GDC (gap between dowel and concrete) = **0 cm**
- NNAJ (Number of nodes at each joint) = **0**.

B.1.10 Damage

- On the *Main Menu* screen, the *Curling* menu was listed as "default." No values were changed.

B.2 Single Axle Load Simulation

B.2.1 General Information for Set No. 1

- "TITLE" = adjusted to describe the appropriate road section.
- "with uniform load/ without uniform load" = ***with***.
- "with temperature curling/ without temperature curling" = ***without***.
- "with concentrated load/ without concentrated load" = ***without***.
- "Type of foundation (0=liquid, 1=solid, 2= layer) (NFOUND)"
    - For Paved sections, chose **1**.
    - For Unpaved section simulations, chose **2**.
- "Damage analysis (0=no, 1=PCA criteria, 2- user specified) (NDAMA)" = **0**.
- "Number of periods per year (NPY)" = **1**.
- "Number of load groups (NLG)" = **1**.
- "Number of slab layers (NLAYER)" = **1**.
- "Bond between two slab layers (0=unbonded, 1=bonded)" = **0**.
- "Number of slabs (NSLAB)" = **2**.
- "Number of joints (NJOINT)" = **1**.
- "Nodal number for checking convergence (NNCK)" = **49**.
- "Number of nodes for stress printout (NPRINT)" = **0**.
- "Number of nodes on X axis of symmetry (NSX)" = **0**.
- "Number of nodes on Y axis of symmetry (NSY)"= **0**.
- "More detailed printout (0=no, 1=yes) (MDPO)" = **1**.
- "Number of nodes with different thicknesses of slab layer 1 (NAT1)" = **0**.
- "Number of nodes with different thicknesses of slab layer 2 (NAT2)" = **0**.
- "System of units (0=English, 1=SI) (NUNIT)" = **1**.

B.2.2 Curling

- On the *Main Menu* screen, the *Curling* menu was listed as "default." No values were changed.

B.2.3 Slab

B.2.3.1 Arrangement

Slab No.	NX	NY	JONO1	JONO2	JONO3	JONO4
1	7	8	0	1	0	0
2	7	8	1	0	0	0

- NX is the number of nodes in the X direction for each slab.
- NY is the number of nodes in the Y direction for each slab.
- JONO1 is the joint no. on the left of each slab.
- JONO2 is the joint no. on the right of each slab.
- JONO3 is the joint no. on the bottom of each slab.
- JONO4 is the joint no. on the top of each slab.

B.2.3.2 X-coordinate

Values listed for each slab are the distance from the lower right corner in the x (right-hand) direction of the given slab for each node.

Slab 1,2 (uniform)

Sequence	**X (cm)**
1	0
2	50
3	100
4	150
5	200
6	250
7	300

B.2.3.3 Y-coordinate

Values listed in the table below are node distances in the y (vertical) direction from the bottom (in plan/ top view) of the given slab.

Slab 1, 2 (uniform)

Sequence	**Y (cm)**
1	0
2	50
3	100
4	150
5	200
6	250
7	300
8	350

B.2.3.4 Properties

- Layer No. 1 (only 1 layer in slab, should match)
- Thickness of the slab, T = 15.24 cm
- PR = Poisson's ratio of slab = 0.15
- YM = Young's Modulus of slab = 2.5E+07 kPa

B.2.4 Uniform

- NUDL = number of uniformly-distributed areas = **2**.

B.2.4.1 Loaded Areas for Load Group No 1 and Data Set No. 1

Load Sequence	LS	XL1 (cm)	XL2 (cm)	YL1 (cm)	YL2 (cm)	QQ (kPa)
1	1	271.3	298.3	321.3	348.3	550
2	1	271.3	298.3	185.3	212.3	550

- LS is the slab number on which the load is applied.
- XL1, XL2 are left and right limits of loaded area in local x coordinates.
- YL1, YL2 are lower and upper limits of loaded area in local y coordinates.

- QQ is the tire contact pressure in the loaded area.

B.2.5 Raft

- On the *Main Menu* screen, the *Curling* menu was listed as "default." No values were changed.

B.2.6 Optional

- On the *Main Menu* screen, the *Curling* menu was listed as "default." No values were changed.

B.2.7 Foundation

- For Paved Section simulations:
    - Young's Modulus of subgrade in kPa (YMS): **values estimated in Chapter 4 using Westergaard's (1926) solution vary based on test section. THIS WAS VARIED TO NOTE THE CHANGES IN SLAB TENSILE STRESSES.**
    - Poisson's ratio of subgrade (PRS) = 0.45.
- For Unpaved Section simulations:
    - Maximum number of integration cycles for layered foundation (MAXIC) = **30**.
    - Number of layers for layered foundation (NL) = **2**.
    - For the table:
        - TH = thickness of each layer; lowest layer assumed to have infinite thickness.
        - E = Elastic Modulus (Resilient modulus M_r used) for each layer.
        - PRBF = Poisson's Ratio of each Burmister's layer.

Layer No.	TH (cm)	E (kPa)	PRBF
1	25	VARIES[1]	0.45
2	XXXXXXXX	VARIES[2]	0.25

[1] Base Course *E* determined in Chapter 6 using the modified Burmister solution.
[2] Subgrade *E* estimated using CBR from DCP and AASHTO (1993) correlation to M_r.

B.2.8 Adjust

- FSAF = seasonal adjustment, **1** left as default.

B.2.9 Joint

- SPCON1 (spring constant for shear transfer) = **0.0000000001 kN/cm^2**. (Entering zero yields an error in the program despite its recommended use in Huang 2004.)
- SPCON2 (spring constant for moment transfer) = **0 cm-kN/cm**.
- SCKV (modulus of dowel support or steel-concrete k value)= **0 MN/m^3** because no dowel support or interlock.
- BD (dowel bar diameter) = **0 cm**
- BS (dowel bar spacing) = **0 cm**
- WJ (width of joint) = **1.27 cm**
- GDC (gap between dowel and concrete) = **0 cm**
- NNAJ (Number of nodes at each joint) = **0**.

B.2.10 Damage

- On the *Main Menu* screen, the *Curling* menu was listed as "default." No values were changed.